Regulation of kinesin- and dynein-based intracellular transport:
A stochastic modeling approach

Dissertation

zur Erlangung des Grades
der Doktorin der Naturwissenschaften

der Naturwissenschaftlich-Technischen Fakultät
der Universität des Saarlandes

von
Gina Antonieta Monzon

Saarbrücken
2023

Tag des Kolloquiums: 13.09.2024

Dekan: Prof. Dr.-Ing. Michael Vielhaber

Berichterstatter: Prof. Dr. Ludger Santen
                   Prof. Dr. Stefan Diez
                   Prof. Dr. Stefan Klumpp

Vorsitz: Prof. Dr. Jochen Hub

Akad. Mitarbeiterin: Dr. Daniel Krug

Abstract

Intracellular transport is crucial for the functioning of living cells. Intracellular cargo is transported in a complex manner. For intracellular cargos to reach their destination in time, transport needs to be highly regulated. The regulation of microtubule-based transport by the opposing motors kinesin and dynein is poorly understood. In this thesis, stochastic simulations are used to study the regulation by number and type of motors, ATP concentration, roadblocks, the microtubule-associated protein tau and the cargo surface, which determines how the motors are coupled. Here it is found that the relative number of kinesin and dynein motors determine the net transport direction and the way motors are coupled the transport mode: unidirectional or bidirectional. Moreover, a mechanical dynein activation is found to influence the transport mode of dynein-driven transport. ATP concentration and single roadblocks had no effect on the transport direction of unidirectionally transported cargo, but might influence the transport of bidirectionally transported cargo. Furthermore, simulations hypothesize that tau island formation depends on the MT track identifying the MT track as an additional regulation factor. In conclusion, transport regulation is different for different transport modes.

Keywords: Intracellular transport, kinesin, dynein, microtubule, tau protein, stochastic simulations

Kurzzusammenfassung

Intrazellulärer Transport ist von entscheidender Bedeutung für die Funktionsfähigkeit von lebenden Zellen. Intrazellulärer Cargo Transport ist sehr komplex. Damit der Cargo seinen Bestimmungsort zur rechten Zeit erreicht, muss der Transport hochgradig reguliert werden. Die Regulierung des Transports entlang von Mikrotubuli durch die gegenläufigen Motoren, Kinesin und Dynein, wirft noch einige Fragen auf. In dieser Arbeit werden stochastische Simulationen verwendet, um die Regulierung durch Motorkonfiguration, ATP-Konzentration, Hindernisse entlang der Mikrotubuli, Mikrotubuli assoziierte Tau Proteine und Cargo-Oberfläche zu untersuchen. Es stellte sich heraus, dass die Motorkonfiguration die Netto-Transportrichtung bestimmt und die Cargo-Oberfläche, welche die Art der Motor-Kopplung vorgibt, den Transportmodus: unidirektional oder bidirektional. Eine mechanische Dynein-Aktivierung, des Weiteren, beeinflusst den Modus von Dynein-getriebenem Transport. Die ATP-Konzentration und Hindernisse beeinflussen die Transportrichtung von unidirektional transportiertem Cargo nicht, eventuell aber den Transport von bidirektional transportiertem Cargo. Weitere Simulationen lassen eine Abhängigkeit der Bildung von Tau-Inseln von der Mikrotubuli-Oberfläche vermuten. Kurz, die Regulierung des Transports ist für verschiedene Transportarten unterschiedlich.

Stichworte: Intrazellulärer Transport, Kinesin, Dynein, Mikrotubuli, Tau-Proteine, stochastische Simulationen

Contents

List of Figures

2

List of Tables

Chapter 1

Introduction

Intracellular transport is essential for the functioning of living cells. Intracellular transport can be divided into (passive) diffusion or active transport. Ions and small molecules typically diffuse in the cytoplasm of the cell or through biological membranes following a concentration gradient [1]. Facilitated diffusion uses channels and carrier proteins to transport molecules through membranes [1]. Long-range transport of huge vesicles on cellular scales cannot be realized by diffusion. Since the cellular environment is very crowded [2], diffusion would not be fast enough. Therefore, active transport processes are needed. Active transport, for instance, is used to transport mitochondria to locations of low ATP concentrations inside the cell or to divide chromosomes between the two daughter cells during cell division [3–5].

Long-range intracellular transport is typically carried out along the microtubule-network. The microtubule-network is a street-like network consisting of polar, intracellular filaments called microtubules (from now on MT). In basic cells, the MT-network typically grows radially from the cell center to the cell periphery [2, 6]. Molecular motors from the kinesin and dynein family move and transport cargo along the MTs. While kinesin motors move towards the MT plus-end, i.e. the cell periphery, dynein moves towards the MT minus-end, i.e. the cell center. Previous studies showed that kinesin and dynein motors are bound to the same cargo simultaneously leading to bidirectional cargo motion, which includes phases of diffusive or no motion, unidirectional motion and directional reversals . [3, 7–24]. The study by Soppina et al. [25] even show that endosomes are stretched during bidirectional transport indicating that a tug-of-war between opposing kinesin and dynein motor teams happens. How the cargo reaches its destination despite this complex motion patterns remains poorly understood.

Malfunctioning of intracellular transport is linked to neurodegenerative diseases and cancer [26–28]. In cancer cells, for instance, an altered number of motor proteins has been found. This is associated with an altered distribution of mitochondria throughout the cell, which in turn influences the spread of the cancer cells [28]. In tau-related neurodegenerative diseases it is known that tau detaches from MTs. One of the main functions of tau is to stabilize MTs. Tau detachment from the MT leads to failing intracellular transport and eventual the death of the cell [26, 29–31]. That is why it is important to study motor-driven, directed intracellular active transport and the question arises

How is intracellular cargo transport by opposing kinesin and dynein teams regulated such that the cargo reaches its destination?

Different approaches can be taken to study potential regulation factors of bidirectional transport by teams of opposing kinesin and dynein motors. *In vivo* experiments use artificially induced changes of the cellular environment to see how the system of interest reacts to such changes. Due to the complex intracellular environment, *in vivo* systems are often difficult to analyze. By contrast, well controlled *in vitro* assays allow to study simplified transport systems

outside of the cell. In *in vitro* experiments, components that lead to a certain observation are well defined. However, the mechanism of how the components work together to produce the observed effect often remains unclear. Therefore, *in silico* experiments, i.e. simulations are needed. Simulations can give concepts, explanations and models of the underlying processes. Furthermore, simulations can give predictions and forecast important factors to look at experimentally for further improvement of the understanding of a process. Here, simulations are used in close cooperation with *in vitro* experiments to further understand intracellular transport mechanism and their regulations.

But before transport under different conditions can be simulated, kinesin and dynein models have to be developed. Several theoretical studies introduced models for kinesin and dynein [32–36]. The models used here are based on the work by Klein et al. [35]. These models are adjusted to the given *in vitro* experiments such as bead and liposome transport or MT gliding assays. In MT gliding assays a glass coverslip is coated with motors and MTs are propelled above the coverslip. Simulating unidirectional kinesin and dynein gliding assays the question is addressed *why the velocity of unidirectional kinesin transport does not depend on the number of motors, while the velocity of unidirectional dynein transport increases with the number of motors.*

Previous experimental *in vivo* studies show that a few kinesin and dynein motors are simultaneously bound to the same cargo [3, 9–24]. Changing the configuration of kinesin and dynein motors can change the transport manner. Rezaul et al. [37], for instance, could show that adding kinesin to a dynein-driven cargo *in vivo* could reverse the transport direction. Moreover, previous MT gliding assays driven by kinesin and ciliary dynein could show that the transport direction can be tuned by changing the kinesin density [38]. However, for a better understanding how the number and type of motors regulate the direction of bidirectional transport, a more systematical approach is needed. Systematically changing dynein and kinesin numbers in *in vitro* MT gliding assays shows how the relative motor concentration determines the transport direction. To understand *how teams of kinesin and dynein motors counteract opposing forces and how the number of motors regulate bidirectional transport*, the here presented bidirectional gliding assay simulations are used.

Yet another factor influencing the transport manner might be the cargo itself. Besides the size of the cargo, also the diffusion of the motors on the cargo surface might play a role. While many *in vitro* studies use beads, where motors are rigidly bound to the cargo (rigid cargo surface), *in vivo* cargos often have a membrane in which motors can diffuse (fluid cargo surface). It is unclear *how a diffusion of motors on the cargo surface changes transport compared to rigidly coupled motors*. In this work, first unidirectional cargo transport models are used to study the influence of the cargo surface. Thereby the question is also addressed whether the dimension of the model (one or three dimensions) plays a role. After that the motor-cargo model with diffusive motor tails is used to simulate bidirectional vesicle transport and to understand *why a fluid cargo (motor diffusion on cargo surface) is transported bidirectionally including reversals, while a rigid cargo shows unidirectional motion or is stalled.*

Besides the motor-cargo complex itself, also environmental control parameters such as ATP concentration or the presence of roadblocks on the MT are potential regulation factors. The theoretical work by Klein et al. [35] shows that the transport direction can be tuned by changing the ATP concentration and the experimental work by Ferro et al. [39] shows that single kinesin motors are more affected by roadblocks than single dynein motors. Consequently, it can be hypothesized that ATP and roadblock concentrations regulate bidirectional transport. *In vitro* MT gliding assays show that unidirectional dynein and kinesin transport is indeed

influenced differently by ATP and roadblock concentrations. The directionality of bidirectional MT gliding assays, however, remains unchanged upon changes in ATP and roadblock concentrations. Here, the simulations of bidirectional MT gliding assays at different ATP and roadblock concentrations are used to understand *why ATP and roadblock concentrations influence the velocity of unidirectional transport but do not change the directionality of bidirectional transport.*

Although point-like roadblocks do not change the directionality of bidirectional MT gliding assays, it is still assumable that spatially extended obstacles such as clusters of MT associated proteins have an effect on the transport direction. For MT associated proteins it is known that they can change MT-motor affinities or even detach specific motors, while others remain unaffected. Tau islands, for instance, leave dynein unaffected but detaches kinesin [31, 40]. Thus, MT associated proteins are expected to change the number of motors and therefore the directionality of intracellular transport. Before a potential regulation of clusters such as stable tau islands can be discussed, the tau island formation needs to be understood. Here, a tau adsorption model is introduced to *shed light on the formation of stable tau islands* which let dynein pass, but detach kinesin [31, 40].

This thesis is structured as follows: After this introduction, first (chapter 2) the biological background of intracellular, MT-based transport by teams of kinesin and dynein motors and the State of Art of bidirectional transport regulation mechanism are introduced. Thereafter (chapter 3), the theoretical basics of Monte Carlo simulations and stochastic processes are presented as the main methods used in this thesis. Having introduced the biological and theoretical background, the studied projects are outlined and the above introduced research questions are discussed: This means, in chapter 4 unidirectional and bidirectional MT gliding assays are simulated to understand how kinesin and dynein motors work in a team. Moreover, this chapter deals with the influence of the environmental factors ATP and roadblock concentrations. As a different kind of roadblocks, chapter 5 investigates the formation of stable tau islands on the MT. Chapter 6 and 7 then deal with cargo transport. While in chapter 6 different cargo transport models including rigid (beads) and fluid cargo (liposomes) models are analyzed, chapter 7 covers bidirectional liposome transport by kinesin and dynein. Throughout all result chapters, simulation work is directly compared to experiments. In the end, chapter 8 draws overall conclusions of the presented regulation mechanisms.

Chapter 2

Biological aspects of intracellular transport

Contents

In the first part of this chapter microtubules will be introduced as intracellular streets for molecular motors. Then, the molecular motors will be presented with the focus on mammalian cytoplasmic dynein as a motor walking towards the microtubule minus-end and on kinesin-1 and kinesin-3 as examples for motors walking towards the microtubule plus-end.
In the second part three models for bidirectional transport will be discussed: the exclusionary presence model, the straight coordination model, and the tug-of-war model. Then, the state of the Art understanding of unidirectional transport by multiple motors will be presented. Finally bidirectional transport and possible mechanisms to regulate bidirectional cargo transport by teams of oppositely directed motors will be introduced. The presented regulation mechanisms are classified as i) regulation by the type and number of motors, ii) by environmental factors, iii) by the MT track and iv) by the cargo surface.

The basis of all living organisms are cells [6]. Dysfunctional cells, like tumor cells, which unstoppably multiply and spread, can lead to the death of an organism [41, 42]. Cells can be classified into two categories: eukaryotic and prokaryotic cells. Bacteria i.a. are made of prokaryotic cells, while plants and animals of eukaryotic cells [6]. Eukaryotic cells have a nucleus and membrane-bound organelles. The cell organelles are surrounded by the cytosol, a gel-like fluid, and enclosed by the cell membrane [6]. Various essential cellular functions are carried out by the different cell organelles and cell compartments. Examples of cell organelles and cell compartments are mitochondria, the energy-producing factories of the cell, the nucleus which contains the genetic information, and the ribosomes which translate the genetic information into proteins. The genetic information is then packed by the Golgi apparatus, another cell organelle, and sent to where it is needed [2, 6]. For a functioning cell, all the cell organelles and cell compartments need to work properly together. If all cell organelles just were to diffuse in the cytosol, the cell would not function. Instead, organelles need to be actively located where they are needed at a specific time of the cell life cycle. Mitochondria, for example, are transported to spots of low energy [3]. Thus, an intracellular organization is needed.

The cytoskeleton, "the backbone of the cell", is the basis for organizing cell components and maintaining the cell shape [43]. The cytoskeleton consists of three types of intracellular filaments: actin filaments, intermediate filaments, and microtubules [6, 43]. The actin filaments form a dense mesh on the inner side of the cell membrane, the so-called actin cortex. On the one hand, the actin cortex protects the cell from external deformations and mechanical stress and on the other hand, when actively rearranging, it generates forces and cell locomotion [44]. Intermediate filaments can be found throughout the cell, connecting the inner of the cell (microtubules, nucleus) with the actin cortex [45, 46]. The main function of intermediate filaments is to compensate tensile and compressive forces [45, 46]. Furthermore, they contribute to cell stiffness, and recent studies show that intermediate filaments play a role in intracellular regulations and signaling [46]. Microtubules (from now on MTs) are the stiffest and longest intracellular filaments [45, 47]. They mostly grow radially from the cell center to the cell periphery, giving the cell its shape and an intracellular orientation [6]. This intracellular orientation is essential for an intracellular organization of the cell compartments and because of their star-like arrangement throughout the cell, MTs are the basis of long-range intracellular transport towards the cell center (retrograde) or towards the cell periphery (anterograde). In the following paragraph a more detailed overview of MTs and their role in intracellular organization will be given.

2.1 The microtubule cytoskeleton: an intracellular street network

Microtubules (from now on MTs) are $1\,\mu m$ to $1\,mm$ long [47], stiff (persistence length of $6\,mm$ [47]), (hollow[1]) tubes [2, 6]. MTs are composed of $\alpha\beta$-tubulin heterodimers, which give the MT an intrinsic polarity throughout the filament. Therefore, a clear plus (β-tubulin) and minus-end (α-tubulin) can be defined [2, 6, 49]. In a cell cycle, during interphase for most of the time, the minus-end is in the cell center and the plus-end protrudes towards the cell periphery [6]. That is how the MT array, gives a robust intracellular orientation for

---

[1]It was previously thought that MTs are hollow [2, 6]. However, nowadays it is known that various MT internal proteins are inside the MT [48].

organelle transport. However, the MT array is further known to flexibly rearrange. During mitosis, for example, MTs first form the mitotic spindle, shrinking spindle MTs then separate the chromosomes and growing MTs finally reposition the nucleus in the center of the divided cell [49–51]. This means on a time scale of seconds to minutes [50], MTs shrink, grow, and dynamically rearrange to adopt different situations and intracellular functions.

To understand how the MT array can rearrange at such short time scales, the MT assembly
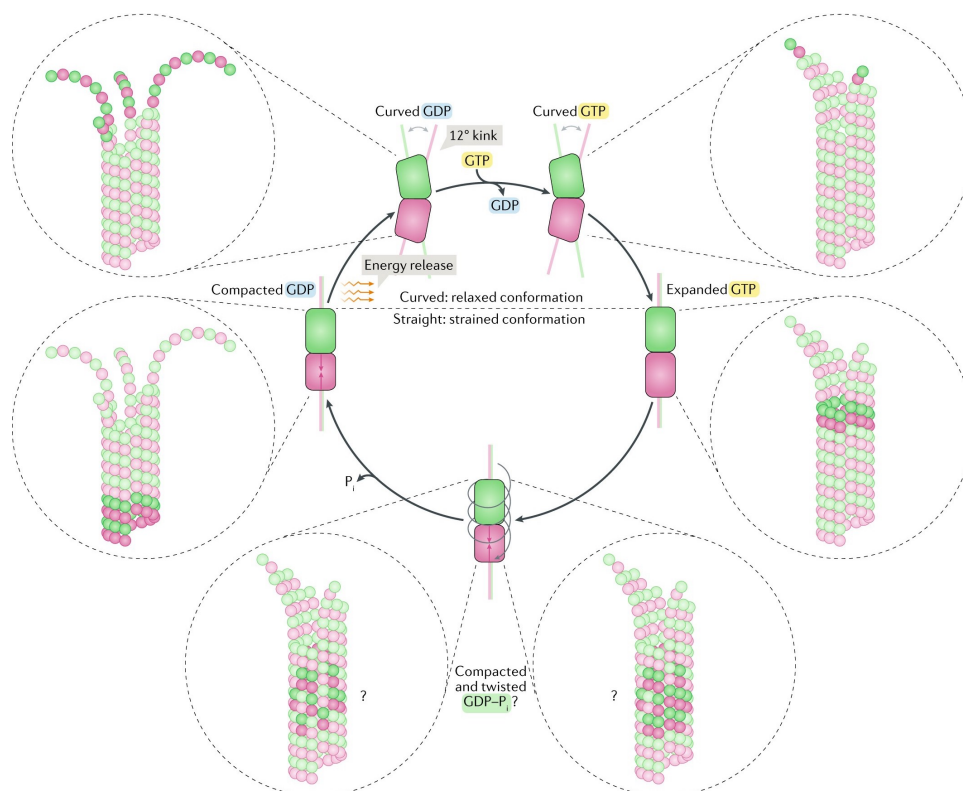
Figure 2.1: MT conformational cycle.
The illustration shows the mechanochemical cycle of tubulin binding and unbinding. Circles show where the particular tubulin conformation can be found in the MT lattice. The tubulin polymerization and depolymerization is a mechanochemical cycle with constant energy consumption in form of ATP. The curved GTP tubulin can bind to a free protofilament at the plus-end of a growing MT. After binding, the curved GTP tubulin straightens into an expanded GTP state. GTP hydrolysis then guides the tubulin into a compact conformation, which is $3\mathring{A}$ shorter. There is also a "compact and twisted" conformation (GDP-Pi state). It is not yet clear where this conformation is located in the MT lattice (indicated by the "?"). When depolymerizing, the compact GDP tubulin goes back to a curved conformation under the release of energy. To be able to bind again to the MT, GDP must be exchanged by GTP [49]. *Reproduced with permission from Springer Nature*. Originally published in *Nature Reviews Molecular Cell Biology*, volume 19, pages 451–463 (2018) [49].

and disassembly need to be understood. MTs are composed of heterodimers of α- and β-tubulin, which string to protofilaments [49]. Usually, 9 to 16 protofilaments are arranged in the form of a (hollow) cylinder forming a MT [52]. Tubulin heterodimers undergo a conformational cycle to assemble and disassemble into a MT. The current understanding of the conformational cycle is reviewed by Brouhard and Rice [49] and summarized in the

following (see also fig. 2.1 for an illustration)[2]. The conformational cycle of tubulin binding and unbinding is a non-equilibrium process because of a constant energy consumption in form of GTP (an energy deliverer) hydrolysis by tubulin heterodimers. For assembly, free GTP-tubulin heterodimers bind to a protofilament at the MT plus-end. The plus-end is the faster growing MT end, where β-tubulin is pointing outwards [50, 53]. Here, the α-tubulin of the free GTP-tubulin heterodimer binds to the β-tubulin of the existing protofilament. Since the free GTP-tubulins are curved, free protofilaments, which are not laterally bound, are curved as well. That is why the plus-end of MTs is often drawn as a funnel indicating the curved free protofilaments. However, when free protofilaments laterally bind to form "sheets", the GTP-tubulin starts to straighten. Most of the lateral bonds are homogeneous, meaning α-α or β-β bonds [2]. However, when the sheet closes to form the tube, the seam bond is mostly a heterologous bond (α-β). After straightening the tubulin goes into a compact GDP-state under releasing phosphate (In between, there might be a special, twisted GDP-Pi state, see fig. 2.1 for more information). Thus, the MT is usually composed of GDP-tubulin dimer. For disassembly, a GDP-tubulin heterodimer unbinds from the MT end under the release of energy and goes back to the relaxed, expanded curved state (curved GDP-tubulin). Now, GDP has to be exchanged with GTP so that the tubulin will be able to bind again to the MT. *In vivo*, we have a constant polymerization and depolymerization of tubulin. If the polymerization prevails, the MT is in the growing state, otherwise in the shrinking state. In the growing state, there is a cap consisting of GTP-tubulin preventing the MT from depolymerization. Thus, the cap stabilizes the growing plus-end of the MT [49, 54–56]. A transition to the rapid shrinking state starts if the MT loses this cap due to GTP hydrolysis, stochastic loss of GTP-tubulin, or if not enough new GTP tubulin was added [49, 54, 55]. This transition is called catastrophe and can lead to a complete MT disassembly [50]. However, if the MT can rescue its cap, it starts growing again. *In vivo*, the MT is known to frequently undergo catastrophe and rescue events at the plus-end, while the minus-end is anchored. These frequent transitions from the growing to the shrinking state are called dynamic instability. In addition to the dynamic instability, there is another mode called treadmilling. In this case, the MT plus-end continuously grows while the minus-end continuously shrinks and the MT migrates [50]. This dynamic instability enables MTs to rearrange at a relatively fast time scale during different phases of a cell cycle. However, to have a working cell, the (re)arrangement of the MT array needs to be regulated. MT-associated proteins (MAPs) are known to regulate the MT assembly and disassembly [49, 57, 58]. The MT dynamics are influenced by MAPs in different ways. First, MAPs can either induce or inhibit MT nucleation by stabilizing or destabilizing bonds between tubulin dimers [49, 59]. Second, they can suppress or trigger catastrophe or rescue events by influencing the mechanochemical tubulin cycle [49, 59, 60]. One way to influence the mechanochemical cycle is when MAPs preferentially bind to either the curved or the straight conformation of tubulin and therefore favor a particular conformation. A favored curved conformation causes that free curved protofilaments do not laterally bind to form sheets and finally the tube [49]. A third way to influence MT stability is when MAPs interfere with the MT lattice dynamic. It is known that besides polymerization and depolymerization at the MT tip, MTs also lose and incorporate tubulin along the MT bulk [61–63]. Thus, MTs are able to self-repair [63]. MAPs were shown to facilitate the MT repairment and thereby might prevent MTs from catastrophe [64, 65]. Besides non-motor MAPs, also enzymes or molecular motors from the kinesin and dynein superfamilies regulate the MT stability in the balk. Molecular motors damage the MT lattice when walking on the MT and modulate the MT assembly at the

---

[2]Additional information, taken from other sources, are marked in the text.

MT end [57, 61]. MT-severing enzymes like katanin or spastin cut the MT in pieces or destroy MTs from the middle. The MAP tau, in contrast, protects the MT from being severed [31, 40]. In section 2.4.3.1 tau proteins are discussed in detail. To conclude, several regulation factors enable the cell to control the dynamic instability of MTs and as a consequence precisely guide the rearrangement of the MT array.

We have seen the MT array is a flexibly rearrangeable, polar network throughout the cell. Therefore it seems to be a good basis for intracellular organization. However, the remaining question is how does the cell use the MT array for organizing cell compartments. It had been observed that rearrangement of the MT array helps in positioning specific cargo. For instance, the nucleus is repositioned in the cell center after cell division [49, 51]. However, rearranging the MT array by polymerization and depolymerization is not an efficient way to move organelles. Nevertheless, because of its intrinsic polarity and long range, the MT array can be seen as a street network that can be used to precisely locate organelles or other cargo along it. Molecular motors are known to walk along the MTs guided by the intrinsic polarity of the MTs [6, 66, 67]. These motors have a so-called tail, which can bind cargo and transport it along MTs. Moreover, to ensure a processive motion along the MT, most motors have two heads to ensure that at any instance one head is bound to the MT lattice [68, 69].

In summary, the MT array is a flexible street network throughout the cell. Because of its long range and intrinsic polarity, it provides the basis for intracellular organization through cargo transport by molecular motors. The next section gives more details about molecular motors.

2.2 Molecular motors

Molecular motors are mechanochemical enzymes that convert the chemical energy of the energy deliverer ATP into mechanical work. Upon hydrolysis of ATP, they undergo conformational changes to perform a step on a MT [70–75]. The intrinsic structure of the MT gives the motors an orientation, such that each motor develops a preferred stepping direction. This means, motors either preferably step towards the MT plus-end or the MT minus-end ensuring transport to any location within the cell [2, 6, 69, 76–78]. MT-based molecular motors can be divided into two superfamilies: the kinesin and the dynein superfamily. Members of the dynein superfamily preferentially step towards the MT minus-end, while most of the members of the kinesin superfamily preferentially step towards the MT plus-end [69, 76–78]. An exception is kinesin-14, which preferably steps towards the MT minus-end [79]. Molecular motors are further classified into processive and non-processive motors. Processive motors take multiple successive steps before detaching from the MT, while non-processive motors detach after each step ([80–82]. Most relevant for long-range cargo transport are processive motors. Processive motors usually have two heads and a tail domain. The tail domain binds to the cargo (or another filament) and the head domains alternatingly bind and unbind from the MT in order to step forward. While stepping on the MT, the motors exert a force on the cargo and move it forward.

Taken together, to transport cargo to any part of a cell, the opposite directed molecular motors kinesin and dynein bind to cargo and step processively along the MT array. In the next subsection details of the molecular motor properties and their functionality are given. Here, the focus is on the two most prominent motors: cytoplasmic dynein and conventional kinesin (kinesin-1) as well as the less studied motor KIF16B from the kinesin-3 family [78].
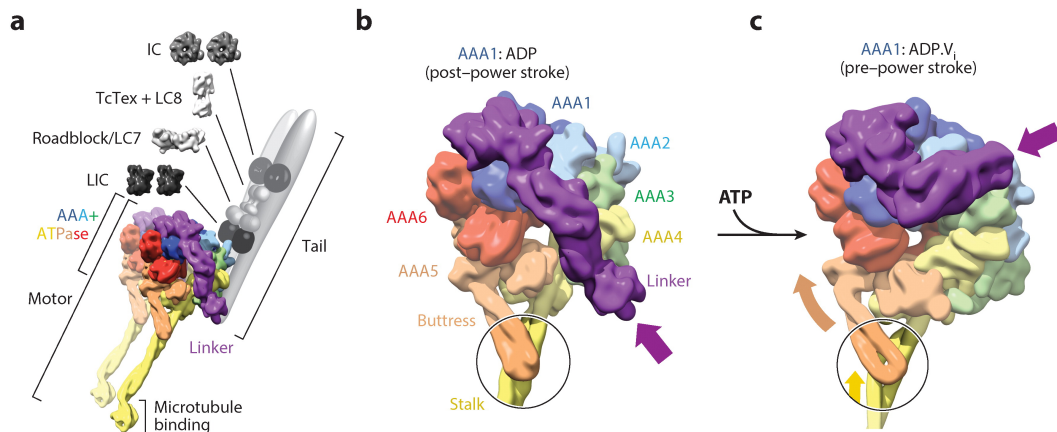
Figure 2.2: Dynein structure.
The illustration shows the complete dynein molecule (left, a), the AAA ring of the motor domain with a straight linker (middle, b), and with a bent linker (right, c). a) The complete molecule can be divided into a tail (grey) and a head region (colored). The latter, the part relevant for transport, consists of two identical motor domains ('Motor'). The linker (purple), which is part of the motor domain, binds the motor domain to the tail region. The motor domains consist of a MT binding domain, which interacts with the tubulin of the MT, and a stalk, which connects the MT binding domain to a AAA ring. The AAA ring is the ATPase active region of the molecule. b) The AAA ring consists of six AAA domains, from which AAA1- AAA4 can bind ATP. Conformational changes of the AAA ring are communicated via the buttress, an appendage of the AAA ring, to the stalk. Conformational changes of the stalk change the MT binding affinity of the MT binding domains. ATPase activity at AAA1 is essential for motor stepping. If ADP is bound to AAA1, the linker is in a straight conformation expanding over the complete AAA ring (post-power stroke state). c) Binding of ATP to AAA1 (b → c) bends the linker (pre-power stroke state). The bending of the linker shifts the buttress and thereby changes the conformational state of the stalk. *Used with permission of Annual Reviews, Inc., from Mechanism and Regulation of Cytoplasmic Dynein, Michael A. Cianfrocco, Morgan E. DeSantis, Andres E. Leschziner, and Samara L. Reck-Peterson, volume 31, pages 83-108 (2015); permission conveyed through Copyright Clearance Center, Inc.* Originally published in *Annual Review of Cell and Developmental Biology*, volume 31, pages 83-108 (2015) [83].

2.2.1 Cytoplasmic dynein

Members of the dynein superfamily are processive minus-end directed motors [69, 76]. Within the dynein superfamily two classes of dynein motors are distinguished: cytoplasmic dynein and axonemal dynein. While axonemal dynein is involved in the movement of cilia and flagella, which are filamentous structures carrying out cell locomotion or act as a sensory organelle [69, 76] the task of cytoplasmic dynein is intracellular transport and building the mitotic spindle during cell division [4, 69, 76]. Cytoplasmic dynein is again subdivided into the two members dynein-1 and dynein-2. While cytoplasmic dynein-2 only carries out transport within cilia and flagella, dynein-1 is involved in transport mechanisms throughout the cell. Among others, dynein-1 transports mRNA, certain proteins, and organelles and is involved in the nuclear migration during cell division [69, 76, 84]. Since the main aspect of this thesis lies in long-range intracellular transport throughout the cell, the focus must be on cytoplasmic dynein-1. Initial studies often used the easier-to-handle and less complex yeast dynein-1 for *in vitro* experiments [69, 81, 85, 86]. However, it is known that the more complex

cytoplasmic dynein-1 extracted from mammalian cells has substantially different properties [69, 87–89]. That is why it is relevant to study cytoplasmic dynein-1 from mammalians. Here, the focus is on mammalian cytoplasmic dynein-1 (from now on referred to as "dynein"). However, since yeast dynein-1 (referred to as "yeast dynein") is better studied, sometimes yeast dynein is referred to.

To understand dynein processive movement, we have to zoom into dynein's submolecular structure (see also fig. 2.2). The dynein molecule can be divided into a head and a tail region. The head region is the region interacting with the MT and is a homodimer, which consists of two identical heavy chain motor domains [69, 76, 84, 90, 91]. The tail region holds the two motor domains together and binds them to a cargo with the help of additional adaptor proteins [69, 76, 84, 90]). The motor domains bind to the MT and step on it under the consumption of ATP [70, 92]. Each motor domain consists of an AAA ring, the ATPase activity component of the motor domain [69, 76, 89]. The AAA ring contains six AAA domains, from which AAA1 to AAA4 can bind ATP and AAA1, AAA3, and AAA4 can also hydrolyze ATP. The ATP hydrolysis at AAA1 is thought to be essential for the motor stepping, while the others are assumed to have regulatory roles [69, 76, 91, 92]. The AAA ring has three appendages: the stalk, the buttress, and the linker (see fig. 2.2 for an illustration). The stalk, a helical, 15 nm long, coiled coil connects the hexametric AAA ring to a small, globular MT binding domain (MTBD). With the MTBD the dynein motor domain interacts with the MT [69, 76]. Depending on the conformational state of the stalk, the MTBD has a strong, an intermediate, or a weak MT binding affinity [92, 93]. A so-called α-registry of the stalk leads to a strong MT binding, a β-registry to a weak MT binding and a γ-registry to an intermediate MT binding [92] (see also fig. 2.4). The second appendage of the AAA ring, the buttress is a small coiled coil, which interacts with the stalk. The buttress communicates conformational changes of the AAA ring to the stalk, which then changes the registry. [69, 92]. The third appendage, the linker, connects the AAA ring to the tail domain of the motor and acts as a power stroke for stepping [69, 92]. If ADP is bound to AAA1, the linker extends over the complete AAA ring and docks at AAA4/AAA5. In this straight linker conformation the AAA ring adapts an open conformation, which leads to an α-registry of the stalk and a strong binding of the MTBD [69, 92]. However, if ATP binds to AAA1, the linker undocks from AAA4/5 and adapts a bent conformation. In the bent conformation the AAA ring is in a more closed conformation, which leads to a β-registry of the stalk and a weak MT binding affinity of the MTBD [69, 92]. While it is known that the ATPase activity at AAA1 is essential for motor stepping [69, 92], the regulatory roles of AAA2 and AAA4 remain less well understood [69, 92]. In summary, to perform a step on the MT, the motor heads need to unbind and rebind. Thus, the binding affinity needs to be changed. ATP binding and hydrolysis mediate conformational changes in the motor domain resulting in changes of the MT binding affinity.

We have seen the MT binding affinity changes in an ATP-dependent manner. But changing the binding affinity does not directly lead to a processive minus-end directed movement of dynein. Previous studies show that mammalian dynein exists largely in an auto-inhibited state [90]. In this auto-inhibited state mammalian dynein is only weakly processive and shows diffusion-like motion instead of minus-end directed stepping. Note that this auto-inhibited state does not exist for yeast dynein. Yeast dynein is always active showing processive, minus-end directed motion. Mammalian dynein, in contrast, needs to be activated to perform such a motion. Binding dynactin and a cargo adaptor (BicD or Hook3 for instance) at the motor tail, is known to activate dynein [90, 94–96]. Dynein with dynactin and cargo adaptor shows (ultra)processive, minus-end directed motion at high velocities [94, 95, 97]. Velocities
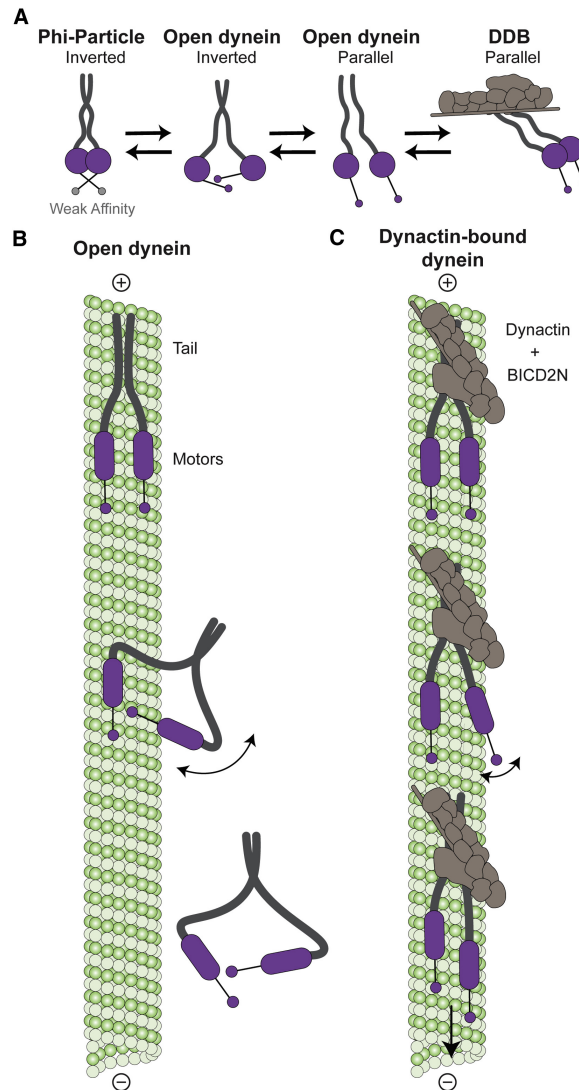
Figure 2.3: Dynein activation by adaptor proteins.

This figure explains the dynein activation by adaptor proteins. A) Different forms of dynein. Dynein without adaptor proteins can either be in the phi-particle state (motor domains are in the inverted conformation) or in the open form. In the phi-particle state, the linker of the two motor domains are connected and hold the AAA ring in a closed conformation, which leads to a weak MT binding affinity. For the open dynein again two forms exist, one where the motor domain stalks are inverted and one where the stalks are parallel. The DDB complex drives the dynein in a stable open form with parallel stalks. B) The sketch shows how open dynein walks on the MT. The drawing starts with an open dynein bound to the MT. When one head detaches to perform a step, the detached head likely goes to the inverted state because this is the favorite state. In the inverted form, it is harder for the detached motor head to reattach. That is why the complete dynein is likely to detach from the MT. This explains why dynein without adaptor proteins is poorly processive. C) The sketch shows how the DDB complex walks along a MT. As the open dynein without adaptor proteins, the DDB complex starts with both heads bound to the MT. The difference to the dynein without adaptor proteins is that when one head detaches, the stalks stay in the parallel conformation. In this conformation the detached (*Continuation on next page.*)

Figure 2.3 *(previous page)*: head can easily reattach and the DDB can continue stepping. The figure is reprinted from the article Cryo-EM Reveals How Human Cytoplasmic Dynein Is Auto-inhibited and Activated by *Kai Zhang, Helen E. Foster, Arnaud Rondelet, Samuel E. Lacey, Nadia Bahi-Buisson, Alexander W. Bird, and Andrew P. Carter* published in *Cell 169, 1303–1314, 2017* [90] under the Creative Commons CC-BY license.

and run-length of activated mammalian dynein are even longer than for yeast dynein [94]. Looking at the submolecular level (see fig. 2.3), it can be understood why additional adaptor proteins are needed for a processive and directed motion. Recent Cyro-EM studies by Zhang et al. [90] found that for single dynein two molecular states exist: a phi-stacked state (phi-dynein) and an open state [90]. From dynein produced in insect cells more than 85% were found to be in the phi-stacked state [90]. In the phi-stacked state the two linkers of the two motor domains are connected and the AAA ring is held in the closed conformation with the stalk causing a weak MT affinity. Besides a weak MT affinity, phi-dynein additionally has a weak binding affinity for dynactin and cargo adaptor proteins [90]. This means the phi-dynein is auto-inhibited. This auto-inhibition is thought to arise in connection with the (self-)dimerization of dynein motors [90]. Unlike phi-dynein, open dynein has its motor domains separated from each other. The motor domains are therefore more flexible [90]. Open-dynein shows a higher affinity of MT binding [90]. Because of the lacking linker connection and the higher flexibility of the single motor domains, the motor domains are not held in the low-affinity state anymore. However, also open-dynein shows only a weak processivity and only diffusion-like motion on the MT [89, 90]. This means there is a second level of inhibition. A closer look to the open dynein shows two sub-states: The inverted state where the two motor domains point towards each other and a parallel state where the two motor domains are aligned [90] (see illustration 2.3). For open-dynein the inverted motor domain state is predominant [89, 90]. EM images show that dynein with adaptor proteins have their motor domains in a parallel orientation [90]. Thus, it is thought that dynactin binding aligns the two motor domains for better binding to the MT lattice. This alignment of the two motor domains is thought to activate the open dynein for processive minus-end directed motion [90]. Besides an activation by adaptor proteins, several past studies also give hints to a mechanical or mutual dynein activation without adaptor proteins [13, 89]. Torisawa et al. [89] shows that dynein motors with truncated tails can be activated when physically separating the two motor domains. When the two motor domains are physically separated by a stiff stick, the dynein motor shows processive, unidirectional movement while otherwise only diffusion-like motion is observed. Belyy et al. [88] also sees a slight increase in velocities when a single dynein is bound to a bigger cargo compared to a smaller cargo. However, the velocity remained slower than for dynein activated with dynactin and BICD [88]. These two studies indicate that there might also be a mechanical dynein activation. Moreover, a more directed motion with higher velocities is observed when multiple dynein motors are attached to a cargo [88, 89] or in MT gliding assays [89, 98]. The directed motion in multiple motor systems gives hint to a mutual dynein activation. However, how mechanical activation could work inside the cell or how multiple dynein motors can mutually activate each other remain poorly understood. In summary, there might be several ways how dynein can be activated and differently activated dynein might have different properties. Past studies show that the way of activation, mechanically or with adaptor proteins using BICD2, hook1, or another cargo adaptor leads to slightly different active dynein properties [70, 89, 96]. A first difference is the

stall force. It is known that dynein motors activated by adaptor proteins have a high stall force (4.4pN) [88] which is comparable to the stall force of yeast dynein (3.6- 4.8pN) [88, 99, 100], but higher than the stall force of mechanically activated or single dynein (1-2 pN) [87–89, 99, 101–103]. Second, the run length and velocity of dynein activated by adaptor proteins (8.7 µm and 892 nm/s) [94] were reported to be higher than from yeast dynein (1.9 µm and 85 nm/s) [69, 104] which is automatically active. And third, the velocity of dynein along the MT, the sideways stepping, and the helical pitch along the MT were shown to vary depending upon which adaptor protein was involved [70]. Taken together, dynein shows a complex, two-level auto-inhibition, which needs to be released. While dynein activation by adaptor proteins was shown on a molecular level, the potential mechanical activation remains less well understood. However, it is intriguing to understand the different activation mechanisms because different activation mechanisms lead to slightly different dynein properties. The two-level auto-inhibition in combination with different activation mechanisms are thought to be used as regulation mechanisms inside the cell [90, 96, 105, 106].

How an active dynein complex steps processively along a MT complex is still poorly understood. It is known that under the consumption of one ATP the dynein motor domain undergoes a mechanochemical cycle to perform a step [70, 71]. However, the complete mechanochemical cycle including the functions of all AAA is not fully known. In the model of Rao et al. [92] (see fig. 2.4), the changes in the nucleotide state of AAA1 and AAA3 are taken into account, while AAA2 and AAA4 are not considered. AAA2 is known to be always in the ATP bound state when the motor is stepping while the regulatory role of AAA4 is not yet understood [92]. The mechanochemical cycle by Rao et al. [92] describes how the rear head steps while the front head is strongly bound to the MT (α-registry of the stalk). The rear head starts in an intermediate binding state (γ-registry of the stalk). In the first state of the cycle, there is ATP or ADP·Pi (transition state) bound at AAA3 and ADP at AAA1. The exchange of ADP with ATP at AAA1 leads to an undocking of the linker from AAA5 (open conformation of the AAA ring). The undocking of the linker causes the β-registry of the stalk, which lead to a weak MT binding of the MTBD (state 2). A weak binding of the MTBD can only be achieved when ADP·Pi is bound to AAA3 [71, 92]. It is known that ATPase mutations at AAA3 prevent the detachment of the MTBD from the MT [71]. However, when ADP·Pi or ADP is bound at AAA3 the MTBD detaches from the MT (state 3). Driven by the power stroke of the linker, the free head moves forward (state 4) [69]. Under phosphate release at AAA1 the free head reattaches to the MT in the weak binding state (state 5). Then the linker moves back to AAA5 and causes a strong MT binding (state 6) [92]. That is how the rear head becomes the new front head and the dynein motor moves forward (towards the minus-end).

The model of Rao et al. [92] describes a step where one head passes the other. One head alternatingly passing the other is called hand-over-hand stepping and is not the only way dynein motors step [69, 81, 85]. Another way is the inchworm stepping mechanism where the front head steps forwards and the rear head follows the front head without passing it [69, 81]. Besides the hand-over-hand and the inchworm stepping, it was also observed that one head takes various successive steps while the other did not move at all [69, 81, 85]. Furthermore, dynein was observed to frequently take backward steps and steps to the side changing the protofilament [69, 70, 85, 100]. Besides the stepping mechanism, also the step size varies between 8 to 32 nm, which are 1 to 4 tubulin dimers [69, 70, 81, 100, 107]. This variety of stepping mechanisms is thought to be caused by the flexible linker and the size of the motor domains. Because of the flexible linker and the size of the motor domain, the reattachment
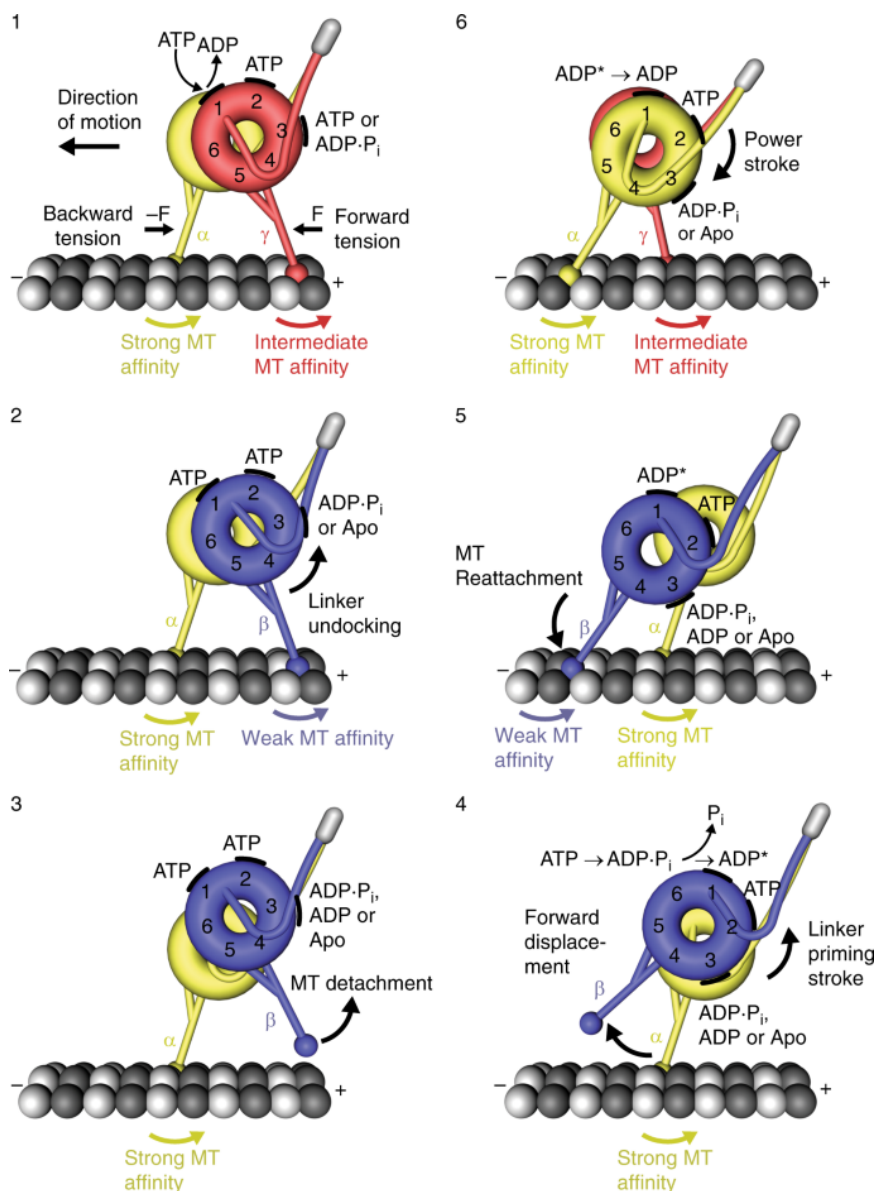
Figure 2.4: Dynein stepping cycle.
The drawing shows a state-of-the-art model for the dynein stepping taking the nucleotide states at AAA1 and AAA3 into account. In the model ATP is always bound to AAA2. In the first state (state 1) of the model, the front head (yellow, left) is in a strong binding α-registry, and the rear head (right, red) is in an intermediate binding γ-registry. The model describes how the rear head steps forward (towards the left). ATP binding to AAA1 leads to a bent linker (linker undocking) and a weak MT binding of the rear head (β-registry of the stalk, state 2). When ADP·Pi or ADP is bound at AAA3 the rear head detaches (state 3). In the next step, the power stroke of the linker (linker priming stroke) moves the rear head forward. The rear became now the front head (state 4). ATP hydrolysis at AAA1 leads to a reattachment of the detached head in a weak binding β-registry (state 5). When the linker moves back to the straight conformation, the new front head goes into the strong binding state (α-registry, state 6). The figure is reprinted from (*Continuation on next page.*)

Figure 2.4 (*previous page*): the article Molecular mechanism of cytoplasmic dynein tension sensing by *Lu Rao, Florian Berger, Matthew P. Nicholas, and Arne Gennerich* published in *Nature Communications 10, 3332, 2019* [92] under the Creative Commons CC-BY license.

area of the detached head is large [85]. Thus, the detached head might pass the attached head or not, or the detached head might change the protofilament or not. Additionally, because of the flexible linker, the detached head might even step backward. Taken together, dynein shows a variety of apparently uncoordinated steps giving the impression that there is no inter-head coordination [69, 85].

As mentioned before, especially dynein activated by adaptor proteins shows a very high processivity. For a processive motion, it has to be made sure that not both heads detach from the MT at the same time. Although the different ways of dynein stepping give the impression of an uncoordinated dynein stepping, the observed high processivity is an indication of an inter-head communication [91]. Past studies show that at low inter-head separations the two heads step stochastically with both heads most of the time being bound to the MT [69, 81, 85, 86, 100]. However, at high inter-head separations a communication between the heads is observed [81, 86]. At high inter-head separations it was observed that preferentially the rear head moves forward while the front head pauses [69, 81, 85, 86, 88, 100, 108]. This means under backward load (=pulled towards the MT plus-end) the head seems to bind more stably to the MT while under forward load (=pulled towards the MT minus-end) the motor favorably steps. Indeed, recent studies show that a backward load induces the strong binding α-registry of the stalk [92]. However, a forward load does not directly induce the weak binding β-registry, but an intermediate γ-registry [92]. The transition then to the weak binding β-registry only occurs in the presence of ATP [86, 92]. According to Rao et al. [92] these load and ATP-dependent changes of the MT binding affinity hold one motor head in the strong binding state when the other steps [92]. Note that the references [81, 86, 92] used yeast dynein for their measurements. However, Elshenawy et al. [70] also showed an asymmetric response to load for mammalian dynein activated by adaptor proteins indicating that this might be a universal behavior for all active dynein-1. Taken together the asymmetric response of the heads to load is thought to cause an inter-head communication, which leads to a processive motion of activated dynein [70, 86, 92].

The asymmetric responses to load on a sub-molecular level also cause asymmetric responses to load for the complete dynein molecule. Previous studies show that the detachment rate of dynein motors increases with forward load indicating that dynein forms a slip-bond with the MT under forward load [86, 92, 108]. Under backward load previously a catch-bond behavior was supposed, meaning that the detachment rate decreases under backward load [33]. However, recent studies refute the catch-bond and propose a "slip to ideal bond" instead, where the detachment rate increases only very slowly with backward load[3] [70, 86, 92, 108]. In total dynein's detachment rate increases faster under forward load than under backward load and the state of the art proposes a slip-bond under forward load and a "slip to ideal" bond under backward load [69, 86, 92].

Besides influencing the detachment rates of dynein, load also influences the stepping velocities of dynein. The stepping behavior of dynein is influenced differently by forward and backward

---

[3]"Slip bond" means that the detachment rate increases with load and "ideal bond" means that the detachment rate remains constant under load.

loads [70, 109]. The forward stepping rate reduces under backward load up to reaching the stall force [70, 109]. Under load forces beyond the stall force, dynein steps backward (towards the MT plus-end) with a small rate independent of the load force [70]. Under forward loads the forward stepping rate increases with force [70, 109]. The forward stepping behavior under load of dynein plus adaptor proteins and yeast dynein coincides [70, 109]. However, under backward loads beyond the stall force a constant backward stepping rate is found for dynein plus adaptor proteins [70] and an increasing backward stepping rate with load for yeast dynein [109]. Though both were similarly small [70, 109]. If the stepping rates of mechanically activated dynein change differently under load remains unclear. Taken together, dynein forward-stepping rates increase with forward loads and decrease with backward loads. Under backward loads higher than the stall force, dynein steps backward [70, 109].

In summary, the minus-end directed dynein motor is a complex macromolecule with several substructures. Up to date the functioning of the complete molecule is not yet fully understood. Furthermore, the auto-inhibition and especially the different activation mechanisms still raise various questions and it remains unclear how the cell uses the two-level auto-inhibition and the several activation mechanisms to precisely regulate dynein activity inside the cell.

2.2.2 Kinesin-1 (Conventional kinesin)

"Kinesin" comes from the Greek word "kinein" meaning "to move" and was given to the first discovered member of the kinesin superfamily [110–112]. Over the years more and more members of the kinesin superfamily were discovered, which needed to be sorted and classified. In 2004 Lawrence et al. [112] proposed a new standardized nomenclature for the members of the kinesin superfamily. In this nomenclature all the found kinesin motors (also called KIF = "kinesin superfamily" and KLP = "kinesin-like protein") were classified into 14 families [112, 113]. Each family has several members with a member-specific structure and name [68, 113]. What all kinesin motors have in common is a globular domain, which can attach to the MT, and hydrolyses ATP to step forward [68, 77, 113]. The globular domain, also called head, is mostly bound to a stalk followed by a tail connecting the two heads. The tail binds to the cargo (or another filament), which should be transported [113]. A neck, which is family-specific, connects tail and stalk. Tail and stalk, in contrast, vary within and between families [113]. The neck is responsible for motor activity and gives the direction of motion [77, 113]. The majority of kinesin motors move towards the MT plus-end [77], however, members of the kinesin-14 family move preferentially towards the MT minus-end [77] and others (kinesin-13 family) do not perform directed motion at all (non-motor kinesins) [77]. In this subsection the focus lies on the most intensively studied KHC (KHC = kinesin heavy chain), a member of the kinesin-1 family (from now on referred to as kinesin-1) and in the next subsection the less known member KIF16B (from now on referred to as kinesin-3) from the kinesin-3 family [78].
Kinesin-1, also called "conventional kinesin" [73], is a plus-end directed motor, which transports organelles, mRNA strings, or mitochondria, positions the nucleus, or slides MTs against each other [73, 113]. To understand how kinesin-1 moves along the MT and transports cargo, an understanding of its structure has to be gained. Kinesin-1 is a heterotetramer formed by two kinesin heavy chains (KHC) and two kinesin light chains (KLC) (see fig. 2.5 for an illustration of the kinesin structure) [68, 73, 114]. While the two heavy chains build the two MT-binding heads of the motor, the two light chains form the cargo-binding tail [68, 73, 91]. Each of the two heavy chains contains one of the two identical, globular motor

domains [73, 91, 115]. Unlike dynein, where the nucleotide site is spatially separated from the MTBD [69], for kinesin the globular motor domain is both, ATP and MT binding site [68, 77]. Depending on the nucleotide state of the motor domain, the motor domain undergoes

Verhey KJ, et al. 2011.
Annu. Rev. Biophys. 40:267–88
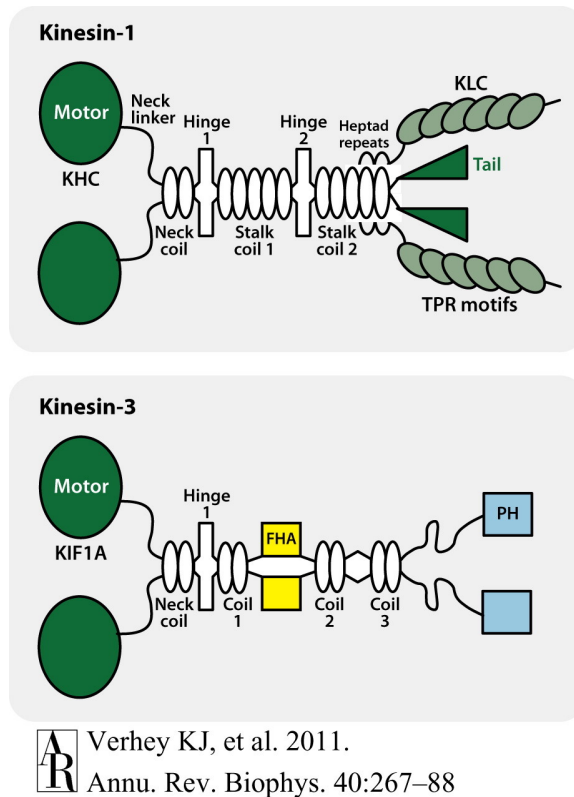
Figure 2.5: Structure of kinesin-1 and kinesin-3.
The drawing shows the main components of the kinesin-1 (top) and the kinesin-3 (bottom) structure. Both consist of two identical motor domains (dark green, KHC = kinesin heavy chain), held together by a neck (neck coil). The neck is followed by a stalk region, which connects the motor domain to the tail. Kinesin-1 and kinesin-3 have the same motor domains but differ in their stalk and their tail regions. Kinesin-1 has two coiled coils in the stalk region, while kinesin-3 has three and a kinesin-3 specific forkhead associate (FHA). The FHA is thought to drive kinesin-3 self-regulation. In this drawing kinesin-3 is shown as a dimer, however, kinesin-3 also exists as a monomer [77]. *Used with permission of Annual Reviews, Inc., from Kinesin Assembly and Movement in Cells, Kristen J. Verhey, Neha Kaul, and Virupakshi Soppina, volume 40, pages 267-288 (2011); permission conveyed through Copyright Clearance Center, Inc.* Originally published in *Annual Review of Biophysics*, volume 40, pages 267-288 (2011) [73].

conformational changes, which leads to different MT binding affinities of the motor domain [68, 114]. Having ATP bound at the motor domain, the motor domain strongly binds to the MT. In contrast, having ADP bound leads to a weaker bond with the MT [69, 116]. Besides changing the conformational state of the motor domain, the nucleotide state also changes the conformational state of the neck linker [68, 115]. The neck linker together with the neck coiled-coil forms the family-specific neck of the motor [73, 113]. The neck connects the motor domain with the stalk [91, 115]. If ATP is bound at the motor domain, the neck linker is in a docked conformation and if ADP is bound, the neck linker is in a flexible conformation [68]. These conformational changes ensure a processive motion of the motor towards the

MT plus-end [73]. The stalk of the motor, which connects the neck with the tail, consists of two coiled-coil domains connected by two hinges [73]. The construction of the stalk is responsible for the flexibility of the motor [73]. In summary, kinesin-1 changes its structure in dependence of the nucleotide state of its motor domains to processively move towards the MT plus-end.

We have seen that dynein is a priori in an auto-inhibited state. This rises the question whether kinesin needs to be activated as well before processively walking towards the MT plus-end. Indeed, also kinesin exists in an active and inactive state [117]. In the inactive state, the tail interacts with the motor domains (folded conformation). This prevents the motor domain from binding to the MT [73, 77, 117]. Cargo binding separates the tail from the motor domain and thereby activates kinesin-1 [73, 77, 90, 117, 118]. In the active state, kinesin-1 is in an extended conformation, where the two motor domains moved closer together [73, 77, 117]. Since the interest lies in kinesin-1, which transports cargo and cargo binding activates kinesin-1, the focus lies, from now on, only on the kinesin-1 structure in the active state (referred to as kinesin-1).

We have seen that the MT binding affinity of kinesin-1 changes with the conformational state of the neck depending on the nucleotide state of the motor domain. However, it remains to be understood how the changes of the MT affinity lead to a kinesin-1 step towards the MT plus-end. It is known that kinesin-1 uses a hand-over-hand stepping mechanism, where one head alternatingly passes the other [68, 69, 91, 115, 119]. For the stepping a mechanochemical cycle is performed, where the energy of one ATP is converted in a step of 8 nm [72, 73]. The mechanochemical cycles of both motor heads are coupled and shifted towards each other [91, 114]. Individual steps of the cycle are ATP and force-dependent [69, 120]. For describing the cycle (see fig. 2.6), kinesin-1 starts with having one head strongly bound to the MT containing neither ATP nor ADP (state 1) [121, 122]. The other head (rear head) is detached or in a weakly bound state [116, 123]. This state of the kinesin-1 molecule is the so-called "ATP waiting state", in which the kinesin-1 spends most of the time [116, 123, 124]. The ATP waiting state ends, when ATP binds to the strongly bound motor head. The ATP binding induces the partial docking of the neck, which extends the neck linker towards the MT plus-end. This propels the detached or weakly bound motor domain towards the MT plus-end and ensures the kinesin-1 stepping directionality [68, 91, 116, 121, 122, 125]. Thus, the motor domains change place (state 2). A hydrolysis of ATP to the transition state $ADP \cdot P_i$, induces the complete docking of the neck linker (state 3) and ensures a high MT affinity of the bound head. The detached head now performs a diffusional search in order to find the next binding site (tubulin dimer) [91, 122, 124]. In this state it could happen that the bound motor goes to the ADP state under release of the P_i. Having then both heads in the detached or weakly bound state, the complete kinesin motor detaches from the MT. However, when the detached head strongly rebinds to the MT under the release of ADP, a step is performed (state 4) [121, 122]. The detached head thereby advances 16 nm and the whole kinesin-1 molecule 8 nm [91, 115, 116]. To go back to the ATP waiting state, the new rear head needs to go to the weakly bound state releasing P_i. This hydrolysis is known to be induced by inter-head tension. For this, two models exist: The rear-gated and the front-gated model [69, 116, 122]. While the rear-gated model proposes that tension weakens the MT affinity of the rear head and induces ATP hydrolysis, the front-gated model says that the tension lowers the ATP binding rate to the front head while waiting for the rear head to hydrolyze ATP [116, 122]. Probably both, the rear- and the front-gated mechanism contribute to ATP hydrolysis at the rear head before the front head leaves the ATP waiting state again [116, 122]. For the backward stepping, there are
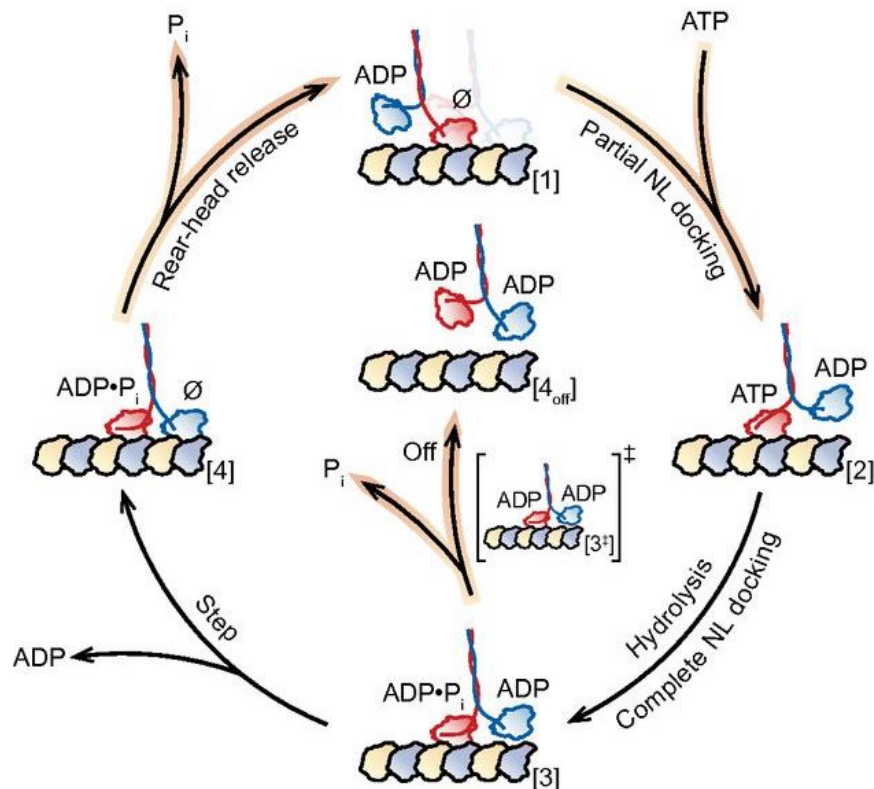
Figure 2.6: Stepping cycle of kinesin-1.
The drawing shows the state-of-the-art model for the kinesin hand-over-hand stepping mechanism. In state [1], the front head is strongly bound in the ATP waiting state and the rear head contains ADP (detached or weakly bound). ATP binding to the strongly bound front head induces a partial docking of the neck linker, which moves the rear head forward (state [2]). The rear head now becomes the new front head. Hydrolyzing ATP to the transition state $ADP \cdot P_i$ induces the complete docking of the neck linker. In this state (state [3]), the detached or weakly bound head performs a biased diffusional search to find its next MT binding site. During this process it could happen that the strongly bound head completely hydrolyzes its ATP and goes to the weakly bound ADP state (state [3^+]). In this case the complete kinesin molecule would detach from the MT (state [4_{off}]). Otherwise, if the diffusional search is successful, the new front head releases ADP and goes to the strongly bound state (state [4]). In the final step, the new rear head releases P_i and goes to the ADP bound state (state [1] with exchanged heads). *Reprinted with permission of the Proceedings of National Academy of Sciences*. Originally published in the *Proceedings of the National Academy of Sciences of the United States of America (PNAS)*, volume 111, no. 39, pages 14136-14140 (2014) [121].

two situations where this forward stepping cycle can be interrupted. First, especially under high backward loads, it can happen that the diffusional search ends at the side behind the front head resulting in an reattachment of the detached head behind the front head. Second, it might happen that in the ATP waiting state the weakly bound head strongly binds behind the front head under the release of ADP. In this case both heads are in the ATP waiting state and ATP binding and hydrolysis at the front head is proposed to result in a backward step [116]. Taking together, both motor domains of kinesin-1 undergo coupled mechanochemical cycles to perform a step. For both, backward and forward stepping, one ATP per step is consumed and

the kinesin-1 molecule is displaced 8 nm, the length of one tubulin dimer [72, 114, 116, 124]. We have seen that the individual steps of the mechanochemical stepping cycle depend on the state and position of the partner motor domain. ATP binding to the front head, first, ensures that the front head stays strongly bound to the MT, while the other head is detached and second, extends the neck linker of the bound head towards the MT plus-end such that the detached head moves forward. Thus, unlike dynein where the inter-head communication is less obvious, there is a clear inter-head coordination for kinesin-1. This coordination ensures unidirectional, processive motion, where kinesin-1 can take hundreds of consecutive steps following one protofilament [72, 91, 114, 116, 125, 126]. Doing so, it can reach speeds of $0.6 - 0.8\,\mu m/s^{-1}$ [73]. Even under (backward) loads kinesin-1 processively steps [72, 114]. Under forward load the velocity remains constant [124, 127, 128]. However, the velocity reduces with increasing backward load until reaching the kinesin-1 stall force. With even more increasing backward load the outcome of the diffusional search becomes more and more biased towards the MT minus-end and backward steps become more frequent [91, 124]. At the kinesin-1 stall force of $6 - 7\,pN$ forward and backward steps balance each other and kinesin-1 stalls [72, 122]. Under loads higher than the stall force, kinesin-1 steps processively backward. The backward stepping is ATP dependent, but independent of the load [91, 124]. In this case the kinesin-1 motor domains follow a cycle where the neck docking and extension towards the MT plus-end are inhibited and the diffusional search is biased towards the MT minus-end [124, 125]. Besides influencing the stepping, load also increases the detachment rate of kinesin-1. This means kinesin-1 forms a so-called slip-bond with the MT [33, 108, 127].

Taking together, kinesin-1 is a two-headed motor, which processively steps towards the MT plus-end following one protofilament and consuming one ATP per step of 8 nm [72, 73, 91, 114, 116, 125]. Under backward load its velocity decreases until reaching stall. For backward loads higher than the stall force, kinesin-1 inverts its stepping direction [91, 124]. Unlike dynein, which can still be auto-inhibited when bound to a cargo, kinesin-1 is always active when bound to a cargo [73, 77, 90, 117, 118].

2.2.3 Kinesin-3

Kinesin-3 is a fast, plus-end directed motor with high processivity [78]. It is involved in transport of organelles, vesicles, viruses, signaling proteins, endosomes, and mitochondria [78, 129, 130]. Because of its high processivity, kinesin-3 is especially responsible for long-range intracellular transport [78]. Furthermore, it was seen that kinesin-3 enhances retrograde mitochondria transport by dynein [129]. Thus, besides transporting itself, it might also have a regulatory role. So far, there are 5 subfamilies of the kinesin-3 family discovered: KIF1, KIF13, KIF16 (KIF16B), KIF14 and KIF28 and some kinesin-3-like proteins [73, 78, 113]. KIF1, also called Unc-104, is the first found member of the kinesin-3 family and the member, which was studied the most [78, 131]. Here, the main interest lies in KIF16 (KIF16B). However, since subfamily members of the kinesin-3 family are structurally related and not much is known about KIF16B, general knowledge about kinesin-3 is gathered.
To understand how its transport properties might differ from kinesin-1, we need to have a look at structural differences between kinesin-1 and kinesin-3. As all kinesin motors, kinesin-3 has the kinesin-specific globular motor domain [77] and as for kinesin-1 the motor domain is bound to the stalk by a neck linker [73]. However, the family-specific neck and stalk differ from kinesin-1 [73]. For kinesin-3 the neck consists of a β-sheet and an α-helix, and the neck is bound to the stalk by a hinge [73, 78]. The stalk consists of three coiled-coil and a kinesin-3

specific fork-head associated domain (FHA) [73]. It has been shown that the FHA interacts with the second coiled-coil and that an interruption of these interactions leads to a higher motor motility [132]. Thus, the FHA is thought to self-regulate the kinesin-3 activity [73, 113, 132]. Another kinesin-3-specific feature is the K-loop, an insert at the motor domain. The K-loop is shown to be responsible for a high MT affinity of the motor domain in the ADP-state, where kinesin-1 motor domains are only weakly bound or detached from the MT [116, 133]. The K-loop might play a role in the kinesin-3 stepping mechanism [73]. It has been shown that the K-loop increases the MT binding rate of kinesin-3 motors, but does not influence its processivity [133]. Another property, which is unique for the kinesin-3 family, is that it exists not only as a homodimer but also in a monomeric form [68, 77, 78, 113, 130, 134]. The monomer just consists of one motor domain [77] and only shows slow, diffusion-like motion, while the dimer shows fast and processive motion [78]. The dimer to monomer transition might be another regulation mechanism [78]. Taking together, special kinesin-3 elements like the FHA, the K-loop, or the monomer and dimer state, makes it worth looking in detail how kinesin-3 functions differently from kinesin-1. The structural differences might lead to differences in the motor dynamic and motor inhibition.

As also seen for kinesin-1 and dynein, auto-inhibition might be an essential mechanism for regulating motor activity. For kinesin-3 two distinct activation mechanisms have been described: The monomer-dimer switch model and the tail-blocked model [78]. While monomers showed only low velocities and mostly diffusion-like motion, a processive and fast motion is only observed for dimers [73, 75, 135]. Therefore, the first model suggests a motor dimerization to activate kinesin-3 motors [78, 135]. The dimerization was often supposed to be cargo-induced or concentration-dependent [68, 75, 77]. One argument against the monomer-dimer switch model is that dimers also have been shown to not move processively at high velocities [73, 75]. Thus, dimerization might not be sufficient for activation [73, 75]. This leads to the second, the tail-blocked model. The tail-blocked model suggests a compact kinesin-3 conformation, similar to the inhibited state of kinesin-1. In this state the tail interacts with the motor domain or neck region and therefore inhibits motor activity [78]. Cargo-binding is supposed to release the motor from this auto-inhibited state [73, 75, 77, 78, 136]. The current understanding is that the activation mechanism differs between subfamilies of kinesin-3 [78]. There are kinesin-3 motors which use the monomer-dimer switch and kinesin-3 motors which use the tail-blocked model. Others use a combination of both (two-level inhibition) [75, 77, 78]. It has been shown that kinesin-3 exists in a monomeric state as well as in the dimer state in the cytoplasm [75, 78, 130]. This underlies the current understanding that both activation mechanisms exist. For KIF16B it was found that a stalk inhibition prevents binding to the MT [137]. This is taken as an indication of the tail-blocked model [78]. Moreover, it has been found that KIF16B exists as a monomer in the cytoplasm and that cargo-induced dimerization activates KIF16B [78, 130]. Thus, for KIF16B a combination of both models might activate the motor. This means KIF16B as a monomer is a priori inhibited on two levels. Furthermore, besides these two structural activation models, there is also evidence for mutual, mechanical activation. It has been shown that multiple monomers move at higher velocities [78] and Ally et al. [13] suggests that kinesin-3 and dynein mechanically activated each other in *Drosophila* neurons [13]. Taking together, depending on the subfamily, kinesin-3 experiences different auto-inhibition mechanisms presumably to control kinesin-3 activity inside the cell.

The stepping mechanism of an active kinesin-3 dimer is supposed to be similar to the stepping of kinesin-1. Both undergo a mechanochemical cycle to perform a hand-over-hand stepping under the consumption of ATP [73–75]. Doing so, kinesin-3 steps at velocities around

950 nm/s [130] similar to kinesin-1, but with a ten-fold higher processivity than kinesin-1 [73, 74]. Unlike active kinesin-3 dimers, inactive kinesin-3 dimers show diffusion-like motion on the MT as observed for kinesin-3 monomers [73, 75]. For the monomer a biased diffusion was observed with low velocities (140-150nm/s) [78, 138]. Surprisingly, however, the monomer shows a processive motion [68, 73, 78, 138]. The processivity of the one-headed kinesin-3 motor can be reached by the positively charged K-loop of its motor domain [68, 138]. The positive charge of the K-loop is thought to interact with the negatively charged C-terminal of β-tubulin [68, 78]. This electrostatic potential avoids that the monomer moves away from the MT but allows the motor to diffuse on the MT in the otherwise weakly bound ADP state [68, 138]. The anisotropy or the power stroke of the motor induced by the conformational changes due to ATP binding biases the diffusion towards the MT plus-end, but is not enough to completely displace the motor to the next binding site [138]. To completely displace the motor, the thermal diffusion on the MT in the electrostatic potential is necessary [138]. This is how the monomeric kinesin-3 can processively step on the MT without a second head. In summary, the stepping mechanism of active kinesin-3 does not differ much from kinesin-1. However, active kinesin-3 steps with much higher processivity and even an inactive monomeric kinesin-3 moves processively along the MT.

2.3 Subconclusion

In the first part of this chapter, the long-range, polar MT array is presented as the structural basis for intracellular organization. The MT array serves as a dynamic street network for molecular motors to navigate throughout the cell. Molecular motors transport cell organelles, vesicles, or other intracellular cargo along these "streets". MT-associated molecular motors can be divided into two classes: the MT minus-end directed dynein motors and the mostly plus-end directed kinesin motors. Here, the focus is on mammalian cytoplasmic dynein-1 from the dynein superfamily and kinesin-1 as well as kinesin-3 from the kinesin superfamily. Although we have seen that all of the presented motors step along the MT under the consumption of one ATP per step using force-sensitive stepping mechanisms, the three motors differ essentially in their structures and properties. The main difference is their stepping direction, which is towards the MT plus-end for kinesin and MT minus-end for dynein. The opposite stepping directions ensure that transport in all directions inside the cell is possible. However, how the cell uses the different motor properties to organize the precise positioning of cargos at a specific location and time point still remains an open question. In the first part of this chapter we have seen that for all three presented motors a more or less complex motor inhibition and some kind of activation mechanisms exist. Furthermore, kinesin-3 and dynein present some additional assumed regulatory subparts in their molecular structure. But, how the cell uses these regulatory mechanisms to regulate transport inside the cell remains unclear. Moreover, controlling motor activity is not the only proposed regulatory mechanism. In the following part of this chapter the state of the art of regulation mechanisms presumably used to precisely control intracellular transport by molecular motors will be summarized.

2.4 State of the Art of regulating bidirectional intracellular transport

How intracellular transport by kinesin and dynein motors is regulated has been widely studied in the last decades but there are still many open questions [9, 10, 21, 23, 35, 139]. As already described in the last chapter, kinesin-1, kinesin-3, and dynein are all auto-inhibited when diffusing in the cytoplasm and not being bound to a cargo [78, 90, 117]. Not being active in the absence of a cargo gives the cell two obvious advantages. First, it avoids an unnecessary consumption of energy (ATP) and second, it avoids a crowding of unloaded motors on the MTs [73, 75, 78, 136]. For kinesin-1, we learned that cargo binding disconnects the tail from the motor domain and thereby activates kinesin-1 for stepping pointedly towards the MT plus-end [73, 77, 90, 117, 118]. For kinesin-3, we have seen that the auto-inhibition is a bit more complex. Depending on the subfamily, kinesin-3 exists as dimer or monomer in the cytoplasm, which were both shown to be auto-inhibited [68, 73, 75, 77, 78, 113, 130, 134]. Activation of kinesin-3 is mediated either by cargo binding (for dimers) or by cargo- or concentration-induced dimerization. Also a combination of both is suggested [73, 75, 78]. As described before, for dynein an even more complex, two-level auto-inhibition mechanism was found. At the first level, dynein is in the phi-stacked state. Though, just a release from the phi-stacked state is not enough for dynein activation. At the second level the motor domains of dynein need to be parallelized [90] and binding of dynactin along with cargo adaptor proteins have been shown to activate dynein. Cargo binding does not automatically activate dynein [88–90, 94]. Thus, while kinesin-1 and kinesin-3 can be assumed to be active when bound to a cargo, dynein can still be in an auto-inhibited state. Taken together, inhibition in the absence of a cargo is a first, useful mechanism to regulate the activity of the opposing, kinesin and dynein, motors *in vivo*. Further, it might be a way to control the directionality of cargo transport.

To achieve an efficient transport by the opposite directed motors kinesin and dynein, three different models have been proposed: i) the exclusionary presence model, ii) the straight coordination model and iii) the tug-of-war model [10, 21, 23]. While the exclusionary presence model assumes that just one kind of motor is bound to the cargo at the time, the straight coordination model and the tug-of-war model presume that both kinds of motors are bound to the same cargo simultaneously [10, 21, 23]. The straight coordination further says that the activity of the cargo-bound motors is regulated meaning that just one motor is active at the time. On the downside, the tug-of-war model expects that both motor teams actively exert forces against each other and the stronger team determines the transport direction. We have seen in the absence of cargo, motors are auto-inhibited and one could assume that the cell controls the direction of transport by just binding one kind of motor to the cargo. Thus, when a cargo needs to be transported towards the plus-end, only kinesin would bind to the cargo, while when the cargo needs to be transported towards the minus-end, only dynein would bind. Support for this exclusionary presence model comes from Kamal and Goldstein [140]. In Kamal and Goldstein [140] different kinesin-binding and dynein-binding proteins are listed and it is assumed that these proteins serve as receptors for cargo binding. In addition, it is assumed that the cell can use these "receptor proteins" to control the (kind of) motors bound to a cargo [140]. Indeed, Bielska et al. [141] shows that a *Hook* protein induces an unbinding of kinesin-3 and a binding of dynein to early endosomes. This indicates that *Hook* might be used to control the kind of motors bound to early endosomes in the fungus *Ustilago maydis* [141]. If regulatory proteins would always control that only one kind of motor is

attached to a cargo, one would expect only long, unidirectional cargo runs *in vivo*. The cargo would always move till the end of the MT without stopping nor changing the direction. Or if it changes the direction, it would take some time, because the cell needs to unbind one type of motor and needs to bind the other one while holding the cargo close to the MT [21]. However, inside the cell many cargos, including mitochondria, chromosomes, endosomes, vesicles, and more are observed to be transported bidirectionally including pauses of the cargo and rapid directional switches [11, 19, 21, 142]. Ma and Chisholm [19], for example, show that cargos inside living *Dictyostelium* cells move bidirectionally with frequent and fast directional changes [19] and Hendricks et al. [142] show that latex beads containing kinesin-1, kinesin-2, and dynein motors move bidirectionally with frequent reversals inside living mammalian macrophages [142]. Moreover, frequent directional changes were also observed by Hendricks et al. [11] for vesicles inside cells [11]. The fast directional changes are in the order of 0.5 s [21] indicating that changes induced by exchanging the motors bound to the cargo are unlikely. Besides directional changes, also stationary or pausing cargos were observed [11, 19, 142]. Encalada et al. [18] show that vesicles of live neurons move bidirectionally with long (up to three seconds) and frequent pauses. Pauses were similar for anterograde and retrograde transport [18]. The list of bidirectional moved cargo can be extended and is reviewed by Gross [21] and Welte [23]. Furthermore, if just one motor kind would be bound to the cargo, inhibiting one motor should not affect the movement of the other. However, past studies show a mutual dependence of anterograde and retrograde transport [13–15, 18, 78, 129, 143–146]. Martin et al. [144], for instance, show that both, retrograde and anterograde transport in extruded axoplasm is impaired if either kinesin or dynein is inhibited [144]. Haghnia et al. [146] investigated organelle transport in *Drosophila* axons and found that defect dynactin, which leads to a dysfunctional dynein, causes a complete inhibition of anterograde and retrograde organelle transport [146]. The same is found by Ally et al. [13] showing that in *Drosophila melanogaster S2* cells inhibiting kinesin-1 leads to a disruption of dynein-driven transport and vice versa. Hancock [143] call this mutual dependence "paradox of co-dependence" and review mutually dependent cargo transport in [143]. With the exclusionary presence model neither pauses, nor fast directional changes, nor a mutual dependence of anterograde and retrograde transport can be explained. This means, while there are hints for the exclusionary presence model, it cannot explain the full range of observations. The exclusionary presence model reaches its limits when it comes to explaining how a cargo can be transported bidirectionally including fast reversal, pauses of the cargo and mutual dependencies between transport directions [21, 23].

While the exclusionary presence model is not completely refuted, many past studies in fact show that oppositely directed motors are simultaneously bound to the same cargo [3, 9–24]. Hendricks et al. [11] found a small number of kinesin and dynein motors attached to purified neuronal vesicles [11]. Encalada et al. [18] investigated the motors attached to mammalian prion protein vesicles of live neurons. They found that mainly kinesin-1 and cytoplasmic dynein is bound and that their activity is co-dependent [18]. Using an optical trap and measuring *in vivo* stall forces, Blehm et al. [147] shows that both motors are attached to lipid vesicles in human epithelial cells and that dynein reduces kinesin's stall force [147]. A review of the topic is included in Jolly and Gelfand [9] and Blehm and Selvin [10]. Together, past studies show that oppositely directed motors are bound to the same cargo simultaneously. This supports the coordination or the tug-of-war model but is contradictory to the exclusionary presence model.

Previous studies give hints for both, the coordination [10, 16, 17, 19, 21, 148, 149] and the

tug-of-war model [10, 12, 25, 37, 142, 150]. Rai et al. [17], for instance, observe latex bead phagosomes containing both, kinesin-1 and cytoplasmic dynein, at single molecule resolution in macrophage cells. Looking at the trajectories they see that phagosomes move with long, persistent unidirectional runs (about 4 μm for plus-end directed motion and 7 μm for minus-end directed runs) inside the macrophage cells. The long runs do not show reversals nor interruptions. They conclude that during the long runs only one kind of motor is transporting the phagosome [17]. Laib et al. [148] see a similar behavior for transport within flagella of *Chlamydomonas*. Additionally, they show that eliminating retrograde transport, the transport behavior of anterograde transport did not change and vice versa [148]. Thus, retrograde and anterograde transport are independent [148]. Another study by Leidel et al. [16] use optical force trap experiments to investigate lipid droplet transport by kinesin-1 and cytoplasmic dynein in *Drosophila* embryos. They found that when detaching and reattaching in an optical trap, the probability is higher to move in the same direction than reverse the direction after reattachment [16]. This memory effect suggests that only one kind of motor is active [16]. How the cell coordinates the activity of oppositely directed motors remains unclear. One possibility would be that scaffolding proteins control the activity of the motors. The possible regulation by scaffolding proteins is reviewed by Fu and Holzbaur [149]. While there are studies supporting the coordination model, there are also evidences for a tug-of-war between oppositely directed motors [10, 25, 37, 142, 150]. The most famous example is an observed stretching of bidirectional transported endosomes [25]. Soppina et al. [25] investigate bidirectional endosomes transport in live *Dictyostelium* cells and see an elongation and sometimes a fission of endosomes during periods of slow motion, after which the endosome changes its direction [25]. In addition to this, Gennerich and Schild [150] observe size changes of bidirectionally moved mitochondria inside dendritic cells [150]. The elongation in connection with reversals and also the size changes of mitochondria in bidirectional movements are strong evidences that a tug-of-war between opposing motors occurs and stretches the cargo. Besides measuring size changes, also optical trapping experiments were performed to measure forces inside cells [142]. Hendricks et al. [142] measure forces exerted on latex beads transported by kinesin-1, kinesin-2 and dynein inside mouse macrophage cells. They found that equally large forces were exerted in both directions and that at high forces 8-nm steps were performed in both directions. They conclude that "opposing teams of stably bound motors (...) operate near force balance" [142]. Moreover, Rezaul et al. [37] found that a dynein-driven cargo can be reversed by adding kinesin-1 motors indicating that a tug-of-war competition between the opposing teams determines the transport direction [37]. Taken together, both models can explain certain experiments but will fail for others. The coordination model, for instance, could not explain the size changes observed for mitochondria or endosomes *in vivo* [25, 150] and the tug-of-war model could not explain the memory effect found by Leidel et al. [16]. This means, neither a pure tug-of-war model nor a pure coordination model can explain all experimental findings.

As neither the tug-of-war model nor the coordination model fits as a universal model for bidirectional transport, we need to look for another, more refined understanding. Previously, the understanding of the tug-of-war was a complete stalling of the motion or a motion with frequent interruptions [10]. Because this seemed to be unlikely to explain efficient bidirectional transport, the tug-of-war model was often refuted in the past [21, 23]. However, using a theoretical mean-field tug-of-war model, where motors of both directions stochastically bind to and unbind from the MT, Müller et al. [151] show that seven motility states exist in dependence of the motor properties. These motility states also include unidirectional long

runs[4]. This means the tug-of-war model in principle could also explain unidirectional runs as observed by Rai et al. [17] or Laib et al. [148]. A closer look to the studies of Rai et al. [17] and Laib et al. [148] reveal that the cargo pauses before changing the direction [17, 148]. These pauses could be situations where both motor teams stochastically engage in a tug-of-war. Support for a mixture of the tug-of-war model and the coordination model also comes from the dynein dragging model [10, 11, 147]. Several studies show that kinesin is detached during dynein-driven motion, but dynein remains attached when the cargo is transported in kinesin direction [10–12, 147]. This leads to a reduction of the total kinesin force during plus-end directed motion [147]. This means there seems to be a mechanism regulating that during minus-end motion only dynein motors are attached (coordination model) while during plus-end motion dynein is exerting forces against the leading kinesin (tug-of-war model). Consequently, the tug-of-war and the coordination model are not mutually exclusive and rather a combination of both might be the way to explain efficient bidirectional transport. A current understanding is that basically a tug-of-war occurs between oppositely directed motors but the outcome of the tug-of-war can be highly regulated [143].

In fact, in the past, several regulation mechanisms have been proposed. Here, the regulation mechanisms are categorized into 4 groups: (i) self-regulation by the number and kinds of bound motors, (ii) regulation by environmental parameters like ATP concentration, (iii) regulation by the MT track, and (iv) regulation by the cargo. In the next subsections these four categories of regulation mechanisms will be described in more detail.

2.4.1 The number of motors

As pointed out before, inside the cell cargos are often transported by teams of oppositely directed dynein and kinesin motors, which engage occasionally in a tug-of-war [9, 10, 25, 143, 150]. In the past it has been shown that multiple motors working in a team behave differently than single molecular motors [16, 142, 145, 154]. To understand the tug-of-war between these teams of oppositely directed motors, first the collective behavior of many motors of the same kind needs to be understood.

Collective kinesin-1 motion   *In vivo* force measurements of lipid droplets in *Drosophila* embryos show a peak at 2.6 pN and 5.2 pN for plus-end directed droplets[15]. Assuming that forces by multiple motors are additive, Shubeita et al. [15] conclude that peaks correspond to one and two involved kinesin motors indicating that lipid droplets are transported by multiple kinesin motors. Knowing that the *in vitro* stall force of kinesin is in the order of $6 - 7$ pN [72, 122, 124] (note *in vivo* stall force are thought to be smaller [15, 16]), one could still assume that the higher force peak comes just from one kinesin motor. However, other previous studies of lipid droplets in *Drosophila* embryos [16] and kinesin-driven latex beads in mouse macrophage cells [142] found broad force distribution with forces up to 20 pN. They assume

---

[4]While the mean-field model reproduces run lengths observed for lipid droplet transport in *Drosophila*, it could not reproduce the detachment behavior of two kinesin or dynein motors bound to a bead in an optical trap [33, 151]. The mean field model assumes an equal force sharing between motors. However, it is known that forces are not equally shared between motors [152]. Distinct motility states are expected when taking the explicit motor positions into account [153]. However, also when taking the explicit motor positions into account, high velocities of more than ±500 nm/s could be observed [153] underlying the fact that also when having both motors engaged in a tug-of-war, unidirectional runs with high velocities are possible.

that the broad force distribution comes from multiple kinesin motors transporting the latex bead adding to the assumption of Shubeita et al. [15] [15, 16, 142]. Confirming the results of Hendricks et al. [142], Rai et al. [17] use western blotting and optical trap measurements to show that multiple kinesin motors are attached to latex bead phagosomes in macrophage cells. As Hendricks et al. [142], also Rai et al. [17] and Reddy et al. [155] found high forces, higher than the usual kinesin stall force [17, 142, 155]. In addition, Reddy et al. [155] see that forces decrease with decreasing kinesin number indicating that indeed multiple motors are involved. Taking together these studies show that *in vivo* transport is often carried out by multiple kinesin-1 motors.

This rises the question how do multiple kinesin motors work in a team. Using a bead assay with multiple kinesin motors, Vershinin et al. [139] show that travel distances were longer than those of single kinesin motors. Run length measurements using DNA scaffolds with 1-2 [156], 1-4 [157] and 1-7 [158] kinesin motors show that the run length increases with an increasing number of motors. Thereby run lengths up to 15 μm could be reached [157, 158]. 5-10 motors on giant unilamellar vesicles show even longer travel distances of up to one millimeter [159]. A longer run length for two kinesin motors is also predicted by the theoretical work of Khataee and Howard [160] using a transition rate model and numerically solving the master equations for this model. While *in vitro* studies all agree that run length increases with an increasing number of kinesin motors, an *in vivo* study of lipid droplets in *Drosophila* embryos sees no increase of run length if more kinesin-1 motors are engaged [15]. This is confirmed by Norris et al. [161] using scaffold proteins with 2 motors inside mammalian cells. Consequently, there needs to be another mechanism cutting the run length *in vivo* [15]. Taking together, *in vitro* studies show that multiple kinesin motors help each other to increase the run length.

Besides helping each other to increase the run length, also higher forces could be observed for multi-motor transport [15, 17, 142, 155]. As discussed before, force measurements *in vivo* found forces up to 20 pN for cargos transported by multiple motors [16, 17, 142, 155]. This is in agreement with *in vitro* studies [162]. All previous studies agree that forces increase linearly with an increasing number of motors [16, 17, 139, 142, 157]. *In vivo* studies further show that forces by multiple motors are additive. Force histograms clearly show peaks at the single kinesin force, at two times the single kinesin force, at three times the single kinesin force, etc. [15–17, 142]. A good agreement between *in vitro* and *in vivo* studies can be achieved by Rai et al. [17] showing a clear additive force dependence on the number of motors. Additive forces are also seen by Vershinin et al. [139] investigating bead assays *in vitro* [139]. However, other *in vitro* studies cannot reproduce the additive behavior of forces exerted by multiple kinesin motors. The force histograms of Jamison et al. [162] show a force peak at 7.6 pN and no forces beyond 8 pN for a single kinesin motor and a force peak at 5.6 pN with a tail up to 14 pN for two kinesin motors [162]. Furthermore, Furuta et al. [157] show just a weak number of motor dependence of the maximal force produced by kinesin motors in DNA scaffold assays. This subadditive force behavior can be reproduced by the theory of Uçar and Lipowsky [163] using a coarse-grained stochastic model. Uçar and Lipowsky [163] assume that the discrepancies between *in vivo* and *in vitro* experiments rise from a lower kinesin-1 stall force *in vivo* of approximately 2.5 pN [15, 16] than *in vitro* of $6 - 7$ pN [72, 122, 124]. However, taking together, we can say that forces exerted by multiple kinesin motors are higher than the force exerted by a single kinesin [16, 17, 139, 142, 157].

Pulling on the cargo with a higher force is expected to lead to a higher cargo velocity according to Newton's equation of motion. This means having a higher force production by multiple kinesin motors is expected to produce higher velocities of cargos transported by teams of

kinesin motors. However, *in vivo* studies of giant unilamellar vesicles [159] or lipid droplets [15] found that velocities are independent of the number of kinesin motors. Also experiments with DNA scaffolds *in vivo* [161] and *in vitro* [157, 158] observe constant velocities for an increasing number of kinesin motors. In addition to this, MT gliding experiments, where motors are fixed at a glass cover and propel MTs above them, show that MT gliding velocities are independent of the motor density on the glass cover [164–167]. Just for very high kinesin densities Bieling et al. [165] see reduced MT gliding velocities. This is presumably due to a mutual steric hindrance of the motors [165]. However, an increase of the velocity with an increasing number of motors could only be observed when motors were bound to fluid membranes (vesicles) [145, 168, 169] or non-processive kinesin-14 motors as well as monomeric kinesin-1 motors [157, 170]. The fluid membrane might be the reason for the divergent behavior and for both, the non-processive and the monomeric kinesin motors, the velocity increased with increasing motor number but could by far not reach the kinesin-1 level [157, 170]. Furthermore, using a transition rate model Jamison et al. [162] predict higher velocities when the spacing between two motors is less than 12 nm [162]. In summary, teams of processive kinesin-1 motors poorly cooperate in transporting cargo.

We have seen that multiple kinesins can exert higher forces on cargos, but cannot transport the cargo at higher velocities. This rises the question why kinesin motors poorly cooperate in transporting cargo. Previous studies of two kinesin motors in MT gliding assays [171] and DNA scaffold [156] were zooming into the trajectories and found fractional steps of about 4 nm. These fractional steps of transport trajectories of two kinesin motors indicate that the two kinesin motors step asynchronously and uncoordinatedly [156, 171]. This might lead to an unequal force distribution between the motors engaged in the transport. An unequal force distribution was previously hypothesized by Uçar and Lipowsky [163]. Indeed, labeling single motors in MT gliding assays, Tjioe et al. [152] found that two-thirds of the motors are pulling the MT, while the rest of the motors are resisting the MT motion. The resisting motors are slowing down the MT [152] and the tensions between the engaged motors lead to shorter run lengths of the single motors involved in the transport. Moreover, the fractions of pulling and resisting motors were independent of the total motor number [152]. This supports the idea that the tensions between motors are the reason why multi-motor velocities are independent of the number of motors. Before the study of Tjioe et al. [152], a gliding assay modeling, using a coarse-grained kinesin model, predicted that one-fourth of the motors are exerting forces against each other, while the rest is near zero load [164]. While in multi-motor transport motors exert forces against each other, in optical trap measurements motors are supposed to be aligned and motor forces might therefore be additive. Taking together multiple kinesin motors poorly cooperate to transport cargo because they presumably exert forces against each other due to their unsynchronized stepping. That is why multiple motors cannot transport cargos at higher velocities than single kinesin motors.

Collective dynein motion   Many previous *in vivo* studies have reported several dyneins bound to one cargo [13, 17, 20, 142, 147]. In detail, using force measurements of latex bead phagosomes in macrophage cells, Rai et al. [17] found a broad force histogram with peaks in 2 pN intervals. Knowing that the used effector (RILP) binds two dynein complexes and assuming a stall force of 1 pN for a single dynein motor, they conclude that 6-10 dynein motors are present on the latex bead in their study [17]. A similar experiment was performed by Hendricks et al. [142]. They reported a broad force histogram with several peaks and forces

up to 20 pN [142]. The dynein stall force has been widely debated in the past [89, 142, 147]. As discussed before, for dynein without adaptor proteins a stall force of about $1 - 2$ pN was found [33, 87, 88, 99, 101, 102], while activated by dynactin and BICD2 a stall force of 4 pN was found [88][5]. For *in vivo* experiments, it is unclear if dynein plus dynactin is attached to the cargo or if dynein is somehow activated by adaptor proteins (adaptor proteins other than BICD might lead to even other stall forces [96]). However, since several clear peaks and forces up to 20 pN were observed, it is clear that several dynein motors are attached to the latex bead phagosomes [17, 142]. Combining *in vivo* and *in vitro* experiments, Blehm et al. [147] measure forces exerted on "lipid vesicles in human epithelial cells and on polystyrene beads in *Dictyostelium discoideum*" [147]. For both experiments they found a similar broad force histogram with forces up to 7 pN (occasionally 10 pN) . Assuming a dynein stall force of $1 - 2$ pN they suggest that two to four dynein motors are on lipid vesicles in human epithelial cells [147]. Taking together these *in vivo* studies show that intracellular cargos are often transported by teams of multiple dynein motors.

This rises the question how well multiple dynein motors cooperate when working in a team. Using DNA origami scaffolds of 1-7 yeast dynein motors, Derr et al. [158] could show that the run length increases with an increasing number of dynein motors. In addition to this, Mallik et al. [172] used polystyrene beads coated with mammalian dyneins at different concentrations and could show that at higher dynein concentrations the run length increased up to 8 µm, while for single mammalian dynein a run length of approximately 0.7 µm was measured [172]. Thus, as seen for kinesin, also dynein motors working in a team help each other to achieve longer run lengths of cargos.

As already described before, *in vivo* experiments show a higher force production for multiple dynein motors than for a single dynein motor [17, 142, 147]. This is confirmed by *in vitro* experiments by Mallik et al. [172] and Torisawa et al. [89] showing clear peaks in force histograms of polystyrene beads coated with mammalian dyneins. The peaks were at multiples of $0.8 - 1$ pN, the dynein stall force *in vitro* [33, 87, 88, 99, 101, 102]. This indicates that forces exerted by multiple dynein motors are equal to the sum of the single dynein stall forces. Thus, forces are additive [89, 172]. In addition to this, the several peaks of the *in vivo* studies are also assumed to be at multiples of dynein stall forces [17, 142]. A theoretical study of Uçar and Lipowsky [163] compared the force production of strong and weak dynein motors [163]. A motor is commonly referred to as "strong" when the stall force to detachment force ratio is high and as "weak" when this ratio is low [151, 163]. In the study by Uçar and Lipowsky [163] the strong dynein has a stall force of 7 pN and the weak dynein a stall force of 1.1 pN, while both have a detachment force of 2.9 pN [163]. They found that for weak dynein motors, the collective force is close to the sum of the single dynein stall force, while for strong dynein the force is close to the sum of the forces exerted by single strong dynein. The force exerted by a single strong dynein is significantly lower than the single dynein stall force [163]. Uçar and Lipowsky [163] connect this to the fact that strong dynein frequently detaches before reaching stall. However, for both, the strong and the weak motor, forces are expected to be additive [163]. Mammalian dynein motors without adaptor proteins, which have a stall force of approximately 1 pN, fall in the class of weak motors and are therefore expected to produce forces which are multiples of their single dynein stall force.

We have seen that multiple dyneins produce additive force. Thus again, we would expect that multiple dyneins also transport cargo at higher velocities compared to single dyneins. Indeed, Torisawa et al. [89] see velocities up to 1.1 µm/s for dynein-driven gliding assays

[5]It could be that BICD2 bound two dynein motors in this study.

using mammalian dynein without adaptor proteins. This velocity is much higher than single dynein velocities [89]. Moreover, using polystyrene beads coated with mammalian dynein [88] or mammalian dynein motor domains [87] it could be shown that the motile fraction of these beads increased with increasing dynein concentration [87, 88]. In a more detailed study, Torisawa et al. [89] used DNA origami scaffolds with 1-8 dyneins and showed that the drift part of the motion increased up to 400 nm/s with an increasing number of motors. Thus, multiple mammalian dynein motors without adaptor proteins can produce velocities higher than the single dynein velocity. Furthermore, previous gliding assay experiments using axonemal dynein [173], one-headed inner arm dynein [174], monomeric or dimeric dynein 2 [98] showed an increasing gliding velocity with increasing dynein concentration. However, while gliding assays were performed for axonemal dynein and dynein2 [98, 173, 174] a detailed analysis of the relationship between the velocity of multiple mammalian cytoplasmic dynein motors and the number of motors is still missing. Further, it remains unknown how many motors are needed to transport cargo at such high velocities as seen by Torisawa et al. [89] and it remains questionable if a better cooperation of mammalian dynein - not activated by adaptor proteins - alone can lead to such velocities higher than the single molecule velocity of dynein activated by adaptor proteins [89, 94, 95]. Mammalian dynein without adaptor proteins is thought to be a weak, non-processive motor [89, 90]. As said before, in theoretical studies non-processive, weak motors are predicted to cooperate better [163, 175]. Thus, an increase in velocity is expected with increasing motor numbers. However, multiple non-processive, monomeric kinesin-1 motors could increase the velocity, but not reproduce the high, single dimeric kinesin-1 velocity [157, 170]. Thus, it is not yet fully understood how dynein can produce such high velocities. Moreover, as previously stated (see chapter 2.2.1), various studies give hints towards a mechanical or mutual dynein activation [13, 88, 89]. How such a mutual mechanical activation influences the cooperation between dynein motors remains unknown. In summary, it remains unclear how mammalian dynein motors without adaptor proteins cooperate to transport MT at velocities higher than the single molecule velocity of activated dynein.

Taken together, we have seen that even though both, kinesin and dynein forces are additive, the kinesin velocity remains constant with an increasing number of motors, while the dynein velocity increases. The influence of this behavior and if it could regulate the tug-of-war between kinesin-1 and mammalian cytoplasmic dynein remains unclear. Moreover, it remains unknown whether a mechanical activation plays a role in the tug-of-war competition of dynein and kinesin motors when simultaneously bound to a cargo.

Tug-of-war between teams of kinesin and dynein motors As said before, teams of kinesin and dynein motors were found to be simultaneously present on *in vivo* cargo and a tug-of-war between the opposing teams of motors is likely to happen [25, 142, 150]. Measuring phagosomes inside cells [17], endosomes inside live *Dictyostelium* cells [25] or latex beads in macrophages [142], previous studies find that mostly a few (1-3) kinesin motors compete against several dynein motors (4-12) [17, 25, 142]. Trajectories of these cargos include pauses and eventually directional reversals after pauses [17, 25]. Using *in vivo* cargos such as neuronal vesicles or purified phagosomes similar trajectories are obtained *in vitro* [11, 22]. Combining *in vivo* and *in vitro* studies, Blehm et al. [147] observe a presence of dynein even when the cargo is transported in kinesin direction. They concluded that dynein cannot win the competition against kinesin alone due to its small stall force [147]. This is

verified by Belyy et al. [88], which let one dynein compete against one kinesin. They found that motion is always carried out in kinesin direction [88]. While most studies agree that more dynein is needed than kinesin, studying lipid droplets in *Drosophila* Leidel et al. [16] found a similar amount of kinesin and dynein motors on the cargo [16]. Note that in all the mentioned studies it is not exactly known how many motors actually exert force against each other. Thus, it is not known how many of the available motors are attached to the MT. The attachment rates might vary between experiments. However, the theoretical force study by Uçar and Lipowsky [163] supports the fact that more dynein than kinesin motors are needed. In this study, they predict that three kinesin motors are necessary to balance 7 dynein motors [163]. But further theoretical studies using a tug-of-war model predict a balance between the opposing teams also when having the same number of motors attached to the cargo. However, here again, it is unclear how many motors are attached to the MT and actively engaged in a tug-of-war [35, 151]. Moreover, other studies using other kinds of dynein or kinesin motors show different results [11, 70, 98, 158]. Derr et al. [158], for example, shows that yeast dynein normally wins against mammalian kinesin [158]. However, here the focus lies on the competition between conventional kinesin (kinesin-1) and pure cytoplasmic dynein without adaptor proteins. In summary, previous studies lead to the conclusion that more dynein motors are needed to work against kinesin. However, it remains unclear how many motors really are attached and actively produce forces against each other.

Several studies give hints that changing the motor number could change the transport direction [11, 37, 38, 176]. An *in vivo* study by Rezaul et al. [37] could add kinesin motors on dynein-driven organelles inside pigment cells. By adding kinesin, they could reverse the direction of the organelle [37]. In addition to this, partially inhibiting dynein in *in vitro* experiments, Hendricks et al. [11] could increase processive runs of purified vesicles and change the directional bias towards the plus-end [11]. Additionally, they performed theoretical modeling and predict that the ratio of dynein to kinesin motors determines the transport direction [11]. Using antiparallel MT doublets, Leduc et al. [176] show different velocity regimes in dependence of the number of antagonistically acting kinesin-1 motors [176]. Moreover, using ciliary dynein against kinesin in MT gliding assay, Vale et al. [38] show that the transport directions can be tuned by changing the kinesin density [38]. Taking together, the number of motors might regulate the tug-of-war competition. But it remains unclear how many kinesin or dynein motors are needed to constantly win against the opposing team. Moreover, it remains unclear how motors of the two different teams cooperate (to work against the opposing team) or influence each other. Additionally, the influence of an eventual mutual mechanical dynein activation on the outcome of the tug-of-war remains unknown.

To better understand how the number of motors changes the outcome of the tug-of-war and how many motors are needed for dynein or kinesin-driven motion, a more detailed analysis is needed.

2.4.2 Environmental control parameters

Different motor properties are predicted to lead to different outcomes of the tug-of-war [151]. Modifying motor properties by external parameters was previously predicted by theoretical studies to change the outcome of the tug-of-war between oppositely directed motors [35, 151]. Using a corse-grained, mean-field model, where attached motors equally share forces, Müller et al. [151] could show that in dependence of the motor properties,

different motility states could be observed [151]. In dependence of the motor properties, they found up to 7 motility states including, i.a., fast minus-end and plus-end runs as well as stalled cargos [151]. In addition to this, the theoretical study by Klein et al. [35] predicts that changes in the motor properties induced by environmental factors lead to different transport directions [35]. Experimentally, several studies show that motor properties depend on environmental factors [89, 101, 120, 158, 165, 170, 173, 177]. But, to my knowledge, it could never be directly shown experimentally that the transport direction can be changed by modifying the motor properties by environmental control parameters. However, some studies indicate that a regulation mechanism by environmental factors or signaling pathways exist [3, 178, 179]. Investigating the axonal outgrowth Morris and Hollenbeck [3], for instance, found that mitochondria were always transported to locations of intensive ATP consumption [3]. Moreover, Rodionov et al. [178] show that whether a cargo is transported over the MT cytoskeleton or the actin cytoskeleton is determined by the second messenger cAMP (cyclic adenosine monophosphate) [178].

This means that it is interesting to understand whether bidirectional transport is regulated by environmental factors. Here, the focus will be on the ATP concentration as an environmental factor. Moreover, at the end of this section, other environmental factors, which could potentially regulate bidirectional transport, are briefly mentioned.

ATP concentration If the ATP concentration could be a regulation factor depends on the spatial and temporal distribution of the ATP concentration inside the cell. Having always a homogenous ATP distribution inside the cell, even though the motor properties might depend on the ATP concentration, the ATP concentration could not change the transport. Measuring the ATP level inside HeLa cells, Imamura et al. [180] could show that the ATP concentration varies between different cell compartments [180]. Moreover, Albert and Brown [181], found that the ATP concentration varies temporally in response to extracellular changes. In addition to this, significantly different ATP concentrations were found in cells of Huntington patients [182]. This means the ATP concentration is not constantly homogeneously distributed throughout the cell but varies spatially and temporally. It is therefore intriguing to understand the impact of the different ATP levels on bidirectional transport.

To better understand the potential impact of the ATP concentration on bidirectional transport, we need to know how motor properties change with ATP concentration. Potential regulation of bidirectional transport by the ATP concentration requires an asymmetric response to changes of the ATP concentration by oppositely directed molecular motors. If, for instance, an increase in ATP concentration would slow down kinesin, which is engaged in a tug-of-war with dynein, dynein is expected to take over and drive the motion. For single motors, we know that both, kinesin and dynein, consume one ATP per step [70–73, 183]. Thus, a dependence of the stepping velocity on the ATP concentration is expected. Measuring the velocity of single kinesin motors attached to a quantum dot [184] or in a force clamp [128], it is found that the velocity increases with the ATP concentration showing a Michaelis-Menten dependence on the ATP concentration [128, 184]. This dependence is confirmed by several other single kinesin experiments also using monomeric kinesin-3 [120, 185–187]. Using multi-motor gliding assays the Michaelis-Menten dependence on the ATP concentration is also shown for teams of multiple kinesin motors [188, 189]. While the velocity-ATP dependence is well known for kinesin, less is known about how dynein velocities change with the ATP

concentration. We know that the dynein molecule has several ATP binding sites, which are partly supposed to have regulatory functions (compare chapter 2.2.1) [69, 87, 92]. Thus, the ATP dependence could be more complex than for kinesin-1. Supporting this idea, Ross et al. [190] show that processive minus-end and plus-end runs have a similar ATP dependence. However, the found ATP dependence could not be fitted by a simple Michaelis-Menten function. Instead, two ATP-dependent parameters had to be used indicating that the multiple ATP binding sites of dynein play a role [190]. Ross et al. [190] were using single dynein dynactin-GFP complexes. Using individual cytoplasmic dynein motors without adaptor proteins, Torisawa et al. [89] show a Michaelis-Menten dependence of the single molecule velocity [89]. Mechanically separating the two dynein heads by a stiff stick, Torisawa et al. [89] observe an enhanced ATPase activity of the single molecules [89]. This suggests that a mechanical activation might influence the ATP dependence. Using a MT gliding assay, the same study shows a Michealis-Menten dependence of the velocity of many dynein motors [89]. Moreover, also the ATP dependence of inner-arm dynein c and e and single- and double-headed cytoplasmic dynein was previously studied. Both studies find a Michealis-Menten dependence of the ATPase activity [191, 192]. Taking together, it is known that the kinesin velocity depends on the ATP concentration in a Michaelis-Menten-like manner. For dynein also a Michealis-Menten dependence is suggested, but it remains unclear how a mechanical activation could influence this dependence. Moreover, further studies are needed to say whether the velocity of kinesin and dynein change with ATP dependence differently such that the ATP could potentially regulate bidirectional transport by teams of kinesin and dynein motors.

Besides the velocity, also the stall forces could change with the ATP concentration. For kinesin it was previously seen that the stall force slightly varies between 5 and 7.5 pN for low ATP concentrations less than 100 μM [186]. This is supported by Schnitzer et al. [120], showing a slightly higher stall force for 2 mM compared to 5 μM. For dynein without adaptor proteins, the stall force was found to be ATP dependent for low and intermediate ATP concentrations lower than 1000 μM. For these ATP concentrations a linear increase from 0.3 to 1.1 pN was observed [101]. Thus, for different ATP regimes, the stall force of dynein and kinesin vary differently with the ATP concentration. This means varying the ATP concentration could lead to other outcomes of the tug-of-war between competing teams of dynein and kinesin motors. This rises the question whether ATP concentration can control bidirectional transport. Previous experimental studies give hints that the bidirectional transport can be controlled by the ATP concentration [3]. As said before, bidirectional mitochondria were seen to be transported to locations where ATP was needed [3]. However, to my knowledge, it could never be experimentally verified that the ATP concentration can change the transport direction. A theoretical model by Klein et al. [35] predicts a directional change in dependence of the ATP concentration. In the model a constant kinesin stall force was used and a changing dynein stall force as found by Mallik et al. [101]. For both, kinesin and dynein, a Michaelis-Menten dependence of the single molecule velocity was applied [35]. Taking together, how the velocity of dynein depends on the ATP concentration is not yet fully understood. Moreover, it is unknown whether the changes in the stall forces could lead to a different outcome when a kinesin team is competing against a dynein team. Thus, further experimental studies are needed to test whether the ATP concentration can change the transport direction.

Further environmental factors influencing motor properties Besides the ATP concentration, many other environmental factors influence the motor properties [23, 35, 70, 78, 88, 132, 178, 193]. Among others there is the viscosity, which is known to change motor properties [193] and is predicted to change the outcome of the tug-of-war between kinesin and dynein motors [35]. Yet another environmental factor is the temperature, which differs spatially and temporally between cell compartments and within the cell cycle [194, 195]. The velocity of single motors as well as motors working in a team is known to depend on the temperature in a Arrhenius-like manner [177, 187, 189, 196–199]. Whereby the exact temperature dependence is different for kinesin-1, kinesin-3 and dynein motors [177, 187, 197, 199]. Thus, also the temperature is a potential regulation factor of intracellular transport. Other environmental factors can be the dynein adaptor proteins, which are known to change dynein properties [23, 88, 94, 95]. Also, second messengers are supposed to change bidirectional transport [178]. Please see reviews [9–11, 21, 23, 78, 143, 145, 200] for further information.

In summary, motor properties can be regulated by environmental factors and different motor properties could change the directionality of bidirectionally moving cargo. However, little is known about how the environmental factors influence bidirectional transport.

2.4.3 The microtubule track

The inside of the cell is a crowded environment. Inside the cell are molecular motors, vesicles, cell organelles, proteins, and intracellular filaments among other cell compartments [2, 6]. On the MT track, there are molecular motors, but also other, non-motor MT-associated proteins (from now on called MAPs) [31, 40, 59, 201, 202]. *In vitro* studies normally use MTs without associated proteins, however, inside the cell molecular motors need to make their way over a very crowded MT surface [31, 203–205]. Previous *in vivo* studies show a clear influence of non-motor MAPs on MT-based transport [29, 201, 204, 206–208]. Ebneth et al. [29], for instance, show that changing the concentration of the MAP tau leads to an altered distribution of cell organelles. Mitochondria, for instance, were found to be clustered at the MT organization center (MTOC) indicating that the kinesin-driven anterograde transport failed [29]. An inhibition of kinesin-driven transport by tau was also found by LaPointe et al. [207] for fast axonal transport. In contrast to kinesin-1 and kinesin-3, dynein-driven transport is not affected by tau *in vivo* [204]. While most *in vitro* studies confirm an inhibition of kinesin-driven transport by tau proteins [24, 139, 154, 209], Lopez and Sheetz [205] found a kinesin and dynein inhibition by MAP2 but not by tau using MT gliding assays [205]. *In vitro* studies further show that dynein is not at all or way less affected by tau than kinesin [24, 31, 154, 209]. Further previous studies also show that other MAPs differentially alter the functioning of motor proteins too [201, 204, 208]. Semenova et al. [201] show a negative influence on dynein and a positive regulation of kinesin-2 while transporting pigment granules in live cells [201]. In *Drosophila* cells, an enhanced kinesin binding and activity induced by the MAP ensconsin were found [208]. In addition to this, it was found that MAP7 recruits kinesin, has no effect on dynein but inhibits kinesin-3 [204]. One possible reason why MAPs influence intracellular transport by kinesin and dynein motors is that they compete for the same MT binding site [203, 210]. Hagiwara et al. [203], for instance, showed that kinesin, dynein, tau, and MAP2 compete for the same MT binding site [203]. Taken together, these asymmetric effects of non-motor MAPs on molecular motors are thought to be used as intracellular regulation mechanisms of bidirectional transport [77, 204, 207].

To better understand the effects of non-motor MAPs on molecular motor transport, it is crucial to know how molecular motors interact with roadblocks. For kinesin, it was previously found that the motor stops when encountering a roadblock and pauses for 0.2 up to a few seconds [39, 211, 212]. After that, most studies found kinesin motors which detach from the MT [39, 40, 209, 211–213]. As a result the overall run length and the overall velocity were strongly reduced in the presence of roadblocks [39, 209, 211, 213]. Note, however, the speed between pauses was found to remain unchanged [214, 215]. Besides detaching after pausing, it was frequently observed that kinesin motors continue moving [211, 212, 214, 215]. While Telley et al. [212] observe just occasional bypass events, Korten and Diez [215] found that half of the stopped motors continued after pausing [212, 215]. Previous studies agree that kinesin motors do not perform side steps but stay on the same protofilament [39, 126, 216]. Thus, it remains unclear how kinesin motors can circumvent roadblocks. Schneider et al. [211], found shifts of up to $\pm 25\,\mathrm{nm}$ along the MT axis in connection with bypass events. Because these long shifts cannot come from stepping events, they propose that in order to circumvent a roadblock, kinesin needs to detach and reattach after the roadblock again [211]. Unlike Telley et al. [212], who could not find a distinct behavior in dependence of the kind of roadblock, Ferro et al. [39] found that the pause time depends on whether antibodies or rigor binding kinesin mutants were used as roadblocks [39, 212]. This indicates that kinesin might react differently upon different roadblocks. While the velocity of single kinesin motors strongly decreased with increasing motor concentration [39, 211], the velocity reduction could be weakened when using multiple kinesin motors [39, 152]. Tjioe et al. [152] explain that the better performance of multiple kinesin motors is reached by the moving motors, pulling the stuck motors off the MT [152]. In summary, the movement of single kinesin motors is strongly impaired by roadblocks but can be improved when using multiple kinesin motors. A potential bypassing mechanism of kinesin remains not fully understood.

A distinct behavior is observed when dynein encounters a roadblock. Dynein was found to either reverse direction when encountering a roadblock or not be influenced by the roadblock at all [31, 209]. Dixit et al. [209] find that dynein plus dynactin reverse direction when encountering tau patches [209]. Controversially, Tan et al. [31] find that dynein activated by dynactin and BIC D (DDB) passes tau patches [31]. In addition, using single molecules of DDB and yeast dynein, Ferro et al. [39] find that dynein remains largely unaffected by roadblocks [39]. They find that both the run length and the velocity did not change in the presence of roadblocks [39]. The different behavior of different dynein is likely due to its activation state: Inhibited dynein might reverse the direction when encountering a roadblock as observed by Dixit et al. [209], while the movement of active dynein might remain unchanged [31, 39]. As previously stated, dynein is able to change the protofilament [39, 217]. This side-stepping ability of dynein is thought to enable dynein to maneuver around obstacles resulting in similar velocities and run lengths as in the absence of roadblocks [39]. While this is a valid model for dynein to circumvent single roadblocks, it remains unclear how dynein can pass through tau patches (see below for more details on tau and tau patches). While Ferro et al. [39] find that cargos transported by multiple dynein motors rotate around the MT to overcome the roadblocks [39], it remains unknown how multiple dynein motors without adaptor proteins react in the presence of roadblocks. Thus, more studies are needed on multiple dynein motors without adaptor proteins in the presence of roadblocks. Moreover, the role of a potential mechanical activation in the presence of roadblocks remains unknown.

In summary, kinesin and dynein react differently to roadblocks and are supposed to

use distinct mechanisms to overcome roadblocks. This means roadblocks are a potential regulation mechanism for bidirectional transport [209].

As said before, many *in vivo* studies give hints that MAPs regulate bidirectional transport [29, 201, 204, 206–208]. Three-dimensional measurements of *in vivo* cargo transport show that cargos rotate around MTs and it is supposed that molecular motors help each other to overcome obstacles. A cooperation between kinesin and dynein motors to overcome obstacles was previously suggested [10, 13, 23, 143, 218]. Past *in vivo* studies especially show a regulation of bidirectional transport by tau [29, 207]. Having a closer look at tau, we see that tau is not stationary on the MT but diffuses on the MT track. Moreover, tau is found to form patches of several molecules on the MT surface [31, 40] (see the following subsection for more details on tau). Thus, the regulation by tau and also other MAPs, which recruit a special motor to the MT, might be very different from the possible regulation of single, neutral roadblocks. To my knowledge, the influence of single neutral roadblocks on bidirectional transport has not been studied before. This means it remains unknown how the distinct behavior of dynein and kinesin upon encountering a roadblock and the distinct bypass mechanisms influence bidirectionally transported cargos in the presence of roadblocks.
Besides roadblocks or MAPs, also the MT track itself might regulate bidirectional transport. In fact, previous studies find kinesin-1 motors only on a subset of MTs *in vivo* [161, 219]. It is further found that kinesin-1 prefers stable MTs [219–221] while kinesin-2 and kinesin-3 are thought to be non-selective [161, 219, 221]. Besides kinesin-1 being selective with regard to the MT state, it is also observed, that when stepping on the MT, kinesin-1 leaves a trace behind itself. This trace shows a higher binding affinity for other kinesin-1 motors [222, 223]. A theoretical work by Jose and Santen [224] shows that the trace of higher binding affinity can lead to a lane formation of bidirectionally moved cargos in axons [224]. Unlike kinesin-1, it is not known how dynein is influenced by the MT itself. For mammalian dynein with dynactin and BICD2 it was found that post-translational modifications of the MT influence the motor motility [225]. Furthermore, post-translational modifications were found to also influence kinesin-1 [226]. This means it is also crucial to understand how the MT itself influences bidirectional transport. However, this is beyond the focus of this thesis.

In summary, the MT cytoskeleton *in vivo* can be considered as a very crowded street network. How single motors react when encountering a roadblock is partly understood. However, further studies are needed to understand whether roadblocks can change the direction of cargo transport by teams of oppositely directed motors.

As said before, first single neutral roadblocks need to be studied to understand the influence of the different motor properties on bidirectional transport in the presence of obstacles. However, the MAP tau is known to form patches, also called islands, on the MT lattice [31, 40]. These clusters of tau might regulate transport differently [31, 40]. That is why at the same time, it is crucial to look at tau islands formed by several molecules in detail. The following subsection will therefore introduce and discuss the MT-associated protein tau in more detail.

2.4.3.1 Tau proteins

The MT-associated protein (MAP) tau, also called MAPT, was discovered in 1975 as a protein that promotes MT polymerization [227, 228]. Besides triggering MT polymerization, tau bundles and stabilizes MTs for transport especially in axons [30, 210, 227, 229, 230]. Furthermore, tau influences motor transport and protects the MT from severing enzymes [24, 29, 31, 40, 204]. Malfunctioning of tau is known to cause neurodegenerative diseases, called tauopathies. Tauopathies include Alzheimer's disease and frontotemporal dementia accompanied by parkinsonism [26, 229, 231–233]. In cells of patients with tauopathies, it is seen that tau does not bind to MTs anymore, but forms filamentous aggregates, also called neurofibrillary tangles. The formation of these insoluble tau aggregates is known to cause neuron death [30, 31]. Previous *in vivo* studies showed that malfunctioning of tau leads to failing anterograde transport and consequently a distinct distribution of cell organelles [29]. It is conceivable that this causes cell death. That is why it is crucial to understand the fundamental functionality of tau and its role in bidirectional transport.

To understand how tau interacts with MTs to regulate transport, the tau structure needs to be known. In solution, tau is an intrinsically disordered protein not showing any stable secondary structure [30, 210, 230]. A detailed look reveals that tau has a filamentous structure. It can be divided into a N-terminus and a C-terminus [30, 234]. The N-terminus is also called "projection domain" because it projects away from the MT and the C-terminus "assembly domain" because it supports the MT assembly [234]. To support the MT assembly and stabilization, the C-terminal contains a positively charged MT binding region, which binds to several tubulin dimers [30, 235]. The binding region consists of three to four MT binding repeats, which differ in their MT affinity (R1-R3 or R1-R4) [30, 210, 229, 236]. The more binding repeats a tau has, the higher is its MT binding affinity [210, 236]. In dependence of the number of binding repeats tau is called 3R tau or 4R tau [30, 236]. In total, there exist six tau isoforms, which differ in the number of MT binding repeats (3R and 4R) and the number of N-terminal inserts (0N, 1N, or 2N) [30, 229, 237]. How the different numbers of N-terminal inserts influence the tau-MT interaction remains unclear. A recent study shows that the tau-isoform influences the cell size and the number of MTs and predicts that different tau isoforms might influence the MT dynamic differently [237]. In summary, a positively charged MT binding region including three to four MT binding repeats enables tau to interact with the MT.

To attach the MT, the positively charged MT binding region is supposed to interact with the negatively charged C-terminal of tubulin [210, 236]. The electrostatic interaction explains the MT binding affinity of tau [236]. High-resolution cryo–electron microscopy finds that tau binds longitudinally along MT protofilaments having the MT binding repeats bound in tandem [210, 238]. In combination with computational modeling, Kellogg et al. [210] suppose that tau bridges an intra- and an inter-tubulin connection. Ranging from the middle of one β-tubulin to the middle of the next β-tubulin, one MT binding repeat stretches over the length of approximately 8 nm, the length of an heterodimer [210, 238]. This is how tau is supposed to stabilize MTs [210, 236]. While Kellogg et al. [210] only find longitudinal bonds, Li et al. [239] also suggests lateral bonds [239]. Other previous studies suppose multiple conformations of tau binding to MTs [240]. Taken together, the electrostatic interaction between tau and tubulin binds tau to the MT and thereby stabilizes the MT lattice [210, 238]. Due to the electrostatic potential a stable tau MT bond is expected. Previous studies indeed show static tau on MTs [241, 242]. However, many other studies see rapid diffusing tau on the MT as well as transitions from static to diffusive tau and vice versa. This indicates a

flexible MT-tau bond [40, 230, 241–243]. Previous studies report diffusion constants mostly in the range $0.15 - 0.27\,\mu m^2/s$ [40, 241, 242]. Furthermore, Hinrichs et al. [241] find that the diffusion is independent of the tau concentration indicating that tau can bypass each other and might even change the protofilament [241]. This means for intracellular transport, it is unlikely that tau acts as a static roadblock for kinesin or dynein motors [241]. Presumably, there needs to be another mechanism by which tau differentially influences kinesin and dynein [29, 209]. Taking together, tau can be static or diffusive on MTs, and can most likely not be considered just as a static roadblock for molecular motors. Moreover, it is unclear why some tau proteins are static while others diffuse.

In some studies, a tau-tau interaction has been observed, which may also give an indication of how tau interacts with molecular motors [31, 235]. As already mentioned before in tauopathy cells, tau is observed to form aggregates of several molecules [30, 235]. These tau aggregates were found to be solid-like [235]. Besides forming these solid-like structures inside cells, *in vitro* also liquid-liquid phase separation (LLPS) forming liquid-like drops were observed [31, 228, 235]. These drops were found to undergo fusion and fission and it could be shown that the positively charged MT binding region is responsible for forming tau drops [228, 235]. The latter result indicates a close connection between tau-tau and MT-tau interaction. Supporting this, Tan et al. [31] found that the C-terminus is responsible for forming tau condensates on MTs and Hernández-Vega et al. [228] show that inducing tubulin into tau drops leads to the formation of MT bundles *in vitro* [31, 228]. Thus, tau-tau interactions might also be relevant for the tau-MT interaction and therefore for motor-driven transport.

Because of the observed tau-tau interaction in solution a tau-tau interaction on the MT is expected too. Indeed, a previous study by Rosenberg et al. [243] suggests that tau forms dimer to stabilize MTs [243]. Furthermore, other studies observe larger tau accumulations, so-called tau condensates, tau islands, or tau patches [10, 31, 40, 234, 242]. These tau accumulations are observed to be mainly stationary. Only a slow diffusion of tau molecules inside the islands could be seen and occasionally a bidirectional movement of small clusters [40, 234]. Thus, the previously observed static tau [241, 242] could actually be small accumulations of tau proteins. While diffusive tau binds to the MT independently of the MT track itself [31, 242], the formation of tau islands or condensates depends on the nucleotide state of the MT lattice or how the MT is stabilized [31, 242]. On GMPCPP-stabilized MTs, which have a more expanded tubulin lattice, no island formation could be observed [242, 244]. Because of this dependence on the MT lattice, Tan et al. [31] suggest that the island formation could be guided by the MT lattice and local lattice distortion could act as nucleation points for islands to form [31]. Moreover, Tan et al. [31] found that the C-terminus of the tau molecule is required for island formations [31]. However, the underlying physical mechanism of stable cluster formation including the four MT binding domains is unknown. It is crucial to understand the formation of stable clusters in order to understand how tau potentially regulates bidirectional transport. Additionally, the interaction of molecular motors with stable tau islands might be different from the interaction with diffusive tau.

A first hint that tau islands interact differently with molecular motors is given by McVicker et al. [242] showing that kinesin is not inhibited by tau on GMPCPP-stabilized MTs, where no tau islands form [242]. Previous *in vivo* studies, however, showed a severe impairment of anterograde, kinesin-driven transport by tau [29]. Siahaan et al. [40] then explicitly showed that kinesin-1 cannot pass tau islands but is not hindered by diffusive tau [40]. In contrast, they find that kinesin-8 passes tau islands and destroys them at the same time [40]. The ultra

processive kinesin-3 motor, in contrast, is again inhibited by tau [204]. Investigating the interaction of dynein with tau islands, Tan et al. [31] find that dynein passes tau islands [31]. Interestingly, for both passing motors, kinesin-8 and dynein, traffic jams at island boundaries were observed [31, 40]. This indicates that there might be an interaction or even a competition between tau and molecular motors. This might be the previously reported competition for MT binding sites [203, 210]. Besides interacting with molecular motors, tau also interacts with other MAPs. While tau islands were found to protect the MT from MT-severing enzymes such as katanin or spastin, MAP7 was seen to inhibit tau binding to the MT [31, 40, 204]. Taken together, tau islands selectively inhibit molecular motors. This might be because binding sites of kinesin, dynein, and tau overlap and they therefore are competing for the MT binding sites [203, 210]. However, it remains unclear why dynein can pass tau islands, while kinesin cannot.

2.4.4 The cargo surface

In the previous subsections the influence of the motor number, the environment, and the MT track were discussed without drawing the attention especially to the cargo and its properties. However, cargo properties are also thought to have an impact on motor transport [88, 169, 206, 245–248]. Cargo properties which could influence the transport are the cargo size or the cargo surface. The cargo size was shown to lead to different motility properties [88, 206, 247, 248]. Belyy et al. [88] find slightly increased velocities for bigger beads transported by mammalian dynein motors without adaptor proteins. Using myosin motors Nelson et al. [248] find that velocities increase with cargo size for membrane cargos, but remain constant for membrane-free cargos. A modeling approach finds slightly reduced velocities for bigger cargos, which contradicts the experimentally observed tendencies [247]. Regarding the force production, Pyrpassopoulos et al. [249] find a faster single motor detachment for bigger cargos due to a higher vertical force. This is underlined by the modeling of Bovyn et al. [250], which find shorter run lengths for bigger cargos sizes. Taken together, previous studies show that the cargo size has an effect on transport. However, the exact contribution of the cargo size on transport by multiple motors is poorly understood.

Besides the cargo size, also the cargo surface might have an effect [248, 250, 251]. The surface of *in vivo* organelles often consists of an organelle-specific membrane containing different lipids [252–254]. Those lipids are known to differently interact with motor proteins [253]. It is assumed that pathogens can alter the interaction between motor proteins and lipids. They might use this feature to establish themselves in the host cell [253]. That is why it is relevant to study the relative contribution of the interaction of molecular motors with the cargo surface toward intracellular cargo transport.

Different motor cargo interactions could i) influence the motor distribution on the cargo surface, ii) the mobility of motors on the cargo surface and iii) the flexibility of the motor cargo bond. An altered motor distribution on the cargo can change the transport [245, 247, 250]. Rai et al. [245] find that a clustering of dynein motors on late phagosomes leads to longer minus-end run lengths and higher minus-end directed forces. A higher run length of clustered motors is also found when modeling transport [250]. Thus, clusters seem to perform better than having all motors individually distributed over the surface of the cargo.

Furthermore, the mobility of motors on the cargo surface may play a role. The mobility of motors on the cargo differs between most *in vitro* cargos and *in vivo* vesicles. On artificial, *in vitro* cargos such as quantum dots, latex, or polystyrene beads, molecular motors have an anchored position on the cargo. The membrane of membrane-enclosed organelles, however,

is highly dynamic. It is known that lipids and proteins diffuse in the membrane [255, 256]. Thus, motor proteins are not anchored on the cargo surface but rather diffuse on it [22, 169]. Previous studies suggest that diffusion coefficients of molecular motors on the cargo surface are in the range of a few μm^2/s [22, 169, 256]. The mobility of molecular motors on the cargo surface can be altered, for instance by cholesterol [169, 253], but also by the lipid composition of the cargo surface [246]. This rises the question, how does the mobility of motors on the cargo surface influence cargo transport by teams of motors. Jiang et al. [246] find that the kinesin (re)attachment, consisting of a diffusing rate into the attachment zone and an ordinary kinesin attachment rate, is independent of the motor mobility on the cargo surface. The theoretical paper by Bovyn et al. [250], in contrast, predicts a faster cargo binding in the presence of surface diffusion of molecular motors indicating a higher global attachment rate [250]. Moreover, they and the theoretical paper by Sarpangala and Gopinathan [251] find a higher number of engaged motors resulting in a longer run length in the presence of motor diffusion. This indicates that motor transport might be more robust when motors diffuse on the cargo surface.

But, when the motor can diffuse on the cargo surface, also the motor cargo bond is flexible and it remains the question, what is the influence of the flexible motor cargo bond on the motor force production by teams of (opposing) motors and on the cargo transport velocity. While the work by Sanghavi et al. [22] finds that the force production of kinesin-1 is unaffected by the flexible motor cargo bond, Campàs et al. [257] says that force production differs because the tangential component of the force vanishes and only the component normal on the cargo surface play a role. Both, the theoretical paper by Bovyn et al. [250] and Sarpangala and Gopinathan [251] predict that a flexible motor cargo bond promotes force sharing between attached motors. A load sharing is also assumed by the *in vivo* work of Reis et al. [258] investigating vesicle transport by multiple kinesin motors in *Drosophila*. Thus, while experimental studies find ambiguous results for the influence of the flexible motor cargo bond on the force production of motors, simulation studies coincide in predicting a better load sharing when having a flexible motor cargo bond.

The altered force production of motors with a flexible motor-cargo bond could also affect the velocity of cargo transport. For single motors it was previously found that the membrane does not influence the motor movement [168]. However, results are ambiguous for transport by teams of motors. For teams of motors transporting a cargo with a flexible motor cargo bond, Li et al. [168] and Herold et al. [159] found that the transport velocity is unaffected by the motor number. An *in vivo* study of *Drosophila*, however, finds up to three times single kinesin-1 velocities and suggests that the velocity increases with an increasing number of motors [258]. An *in vitro* study using myosin, which is a molecular motor walking on actin filaments, also finds velocities higher than single-molecule velocities for membrane cargos. But, the velocity decreases with an increasing number of motors in this study [248]. To explicitly study the influence of the flexible motor cargo bond, Grover et al. [169] study MT gliding on lipid bilayers coated with kinesin-1 motors. They find that velocities increase with increasing density but are independent of the MT length [169]. This indicates that spacing between the motors may play a role. It remains to compare the performance of multiple motors for a flexible motor cargo bond versus a rigid motor cargo bond. Studying the MT gliding, Grover et al. [169] find higher velocities for reduced flexibility. Different behaviors are observed when studying cargo transport [168, 248]. Nelson et al. [248] find reduced transport velocities when having a rigid bond between the cargo and myosin motors. Li et al. [168], however, find equal velocities for low number of motors and reduced velocities when
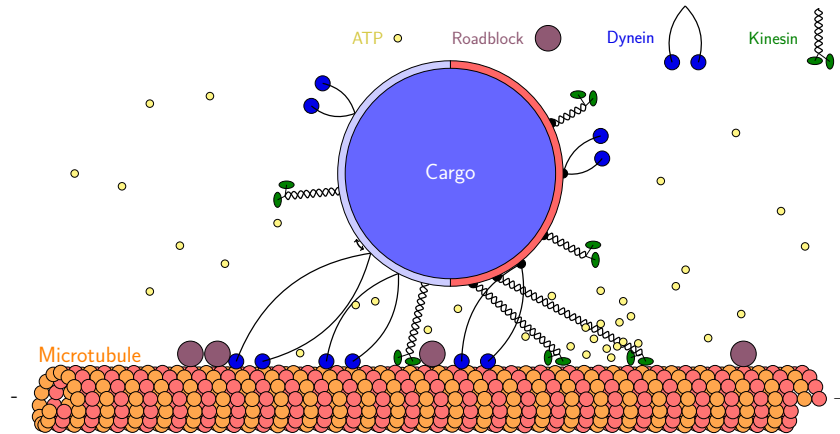
Figure 2.7: Summary of regulation mechanism covered in this thesis.
The illustration shows a MT-based, bidirectional cargo transport by teams of minus-end directed dynein (blue) and plus-end directed kinesin (green) motors. To be efficient, intracellular cargo transport needs to be highly regulated. Different factors might regulate the transport direction. The number and type of engaged motors influence the transport direction. But how is the number of engaged motors regulated? The here addressed regulation mechanisms are classified into environmental factors, the MT track, and the cargo surface. As an example for environmental factors, it is investigated how the ATP concentration (yellow dots) influences the transport direction. For the MT track, it is tested how single roadblocks (circles in dark magenta on the MT) influence unidirectional and bidirectional transport and furthermore, a look into the cluster formation of the MT-associated tau proteins is taken. Clusters of roadblocks, like indicated on the left side of the very left dynein motor, might regulate transport differently than single roadblocks. At the end, the cargo surface is addressed. Motors might be rigidly (right side of the cargo with the red surface) or flexibly (left side of the cargo with the light blue surface) bound to the cargo surface. In the latter case motor tails are able to diffuse on the cargo surface. The motor-cargo bond might influence cargo transport as well.

having more kinesin-1 motors on a rigid cargo. Nelson et al. [248] on the other hand finds that reduction of the velocity starts earlier in the case of a flexible motor cargo bond. Thus, past studies report different influences of the motor-cargo bond on transport velocity. Differences might be due to different experimental set-ups (MT gliding assay versus cargo transport) or different motor types (myosin versus kinesin-1).

In summary, past studies indicate that a flexible motor-cargo bond might have an effect on cargo transport. However, the underlying mechanism remains poorly understood. Moreover, it remains unknown how the flexible motor cargo bond influences the force production when having an opposing force like in bidirectional transport.

2.5 Chapter conclusion

This chapter introduces the current understanding of MT-based intracellular transport performed by the opposite-directed motors dynein and kinesin. We have seen that on intracellular cargos often teams of both, kinesin and dynein motors, are attached and occasionally engage

in a tug-of-war. The current model of how the cell manages efficient bidirectional transport of a cargo to a specific location and at a specific time in the cell cycle is a regulated tug-of-war. Here, four categories of regulation mechanisms are introduced: i) a regulation by the number of motors, ii) a regulation by environmental control factors such as ATP concentration, iii) a regulation by the MT track (including MAPs) and iv) a regulation by the cargo surface. See fig. 2.7 for a summary of the regulation mechanism discussed in this thesis.

To contribute to the understanding of regulating bidirectional transport, the known kinesin and dynein models will be adjusted to the state-of-art understanding of molecular motors (chapter 4). Then these models will be used to better understand transport by multiple kinesin or multiple dynein motors (chapter 4). In the next step bidirectional transport by multiple kinesin and dynein motors is modeled and the question how they depend on the number of motors and environmental control parameters is addressed (chapter 4). To better understand the regulation by the MT track, a tau adsorption model is developed and the cluster formation of tau proteins on the MT is discussed (chapter 5). Moreover, liposome versus bead transport by kinesin-3 is simulated to see how the motor-cargo bond influences the transport (chapter 6). At the end, bidirectional liposome transport by kinesin-3 and cytoplasmic dynein is modeled (chapter 7).

Chapter 3

Methods

Contents

In this thesis, stochastic processes are used as a tool to describe intracellular transport by teams of opposing kinesin and dynein motors. This chapter first gives details on stochastic processes as such and how they are modeled. Afterward, transport-related stochastic processes are presented. These processes include equilibrium processes such as diffusion processes and Langmuir adsorption kinetics as well as non-equilibrium processes such as driven lattice gas models. At the end, the state of the Art of modeling intracellular transport by kinesin and dynein motors is reviewed.

The previous chapter introduced motor-driven, intracellular transport processes relevant for this thesis. Intracellular transport processes are systems of many interacting particles of different types in a "highly noisy environment" [259]. While *in vivo*, it is not clear which components (agents) are involved in the complex system, the types of interacting agents are well defined and controlled in *in vitro* experiments. Therefore, *in vitro* experiments are used as a reference to study the underlying processes of intracellular transport. Because of the stochastic nature of the process, intracellular transport is best described by stochastic processes (see definition below). Moreover, the cargo, the MT, and multiple, interacting molecular motors build an example of a complex system. Complex systems consist of the following characteristics defined by Boccara [260]:

- "They consist of a large number of interacting agents."

- "They exhibit emergence."

- "Their emergent behavior does not result from the existence of a central controller." [260]

Emergence means that there is a collective behavior of the interacting particles, which is "difficult to anticipate from the knowledge of the agents' behavior" solely [260]. Therefore, a model is needed. "A model is a simplified mathematical representation of a system" [260]. A model only includes the characteristics of a process, which are likely to be necessary to produce the observed behavior [260].
Here, models are the basis of the stochastic processes, which describe intracellular transport. These stochastic processes are simulated by means of Monte Carlo simulations to see whether the, in the models, included characteristics of molecular motors, cargos, and MTs are sufficient to explain the observed behavior of *in vitro* experiments.
In the following, first stochastic processes and basics of simulating stochastic processes will be introduced before examples of typical, transport-related stochastic processes will be discussed. At the end, previously published models for molecular motors will be presented.

3.1 Stochastic processes

Stochastic process   Before defining the stochastic process, *random variables* need to be introduced. A random variable, also called *stochastic variable* or *random number* is a variable X, which takes a value x out of a set of possible values with a certain probability. The probabilities of all possible values need to sum up to one [259, 261]. One famous random variable is the outcome of throwing a coin. In this case, both possible values, head and tail, are taken with equal probabilities if the coin is fair. A stochastic process is then defined by a random variable or a function of a random variable(s), which evolve in time:

$$X \to X(t) \quad \text{or} \quad X \to f(X, t). \tag{3.1}$$

One of the first studied stochastic process is the motion of pollen grains in water discovered and named after the botanist *Robert Brown* [259]. The motion of these passive particles is determined by thermal fluctuations of the surrounding water molecules. In this example, the random variable, i.e. the position of the particle, takes different values over time [259, 261, 262].

Langevin equation   After Einstein presented a theoretical description of the Brownian motion [263], Langevin presented, according to him, an "infinitely more simple" description of the Brownian motion [262, 264]. Langevin argued that the pollen grain moves according to its Newton's equation of motion, where the thermal motion of the water molecules is added as a stochastic force $\mathfrak{f}(t)$:

$$m\frac{d^2x}{dt^2} = -\xi\frac{dx}{dt} + \mathfrak{f}(t).$$

$$(3.2)$$

Thereby is ξ is the drag coefficient [259, 265]. The so-called Langevin equation is a stochastic differential equation and remains one common way to describe stochastic motion.

Markov process   Another way to define a stochastic process is to describe how the probability density function of a random variable evolves over time. The joint probability density function of all realizations of the random variable X at any time t

$$p(x_0, t_0; x_1, t_1; \dots; x_n, t_n)$$

$$(3.3)$$

describes the stochastic process completely [262]. A special class of stochastic processes are Markov processes. Using conditional probabilities, the probability of being in states $x_{k+1}, x_{k+2}, \dots, x_n$ at times $t_{k+1}, t_{k+2}, \dots, t_n$, when having been in states $x_1, x_2, \dots, x_k$ before at times $t_1, t_2, \dots, t_k$[1], respectively, is given by

$$p(x_{k+1}, t_{k+1}; x_{k+2}, t_{k+2}; \dots; x_n, t_n | x_0, t_0; x_1, t_1; \dots; x_k, t_k)$$
$$= \frac{p(x_0, t_0; x_1, t_1; \dots; x_k, t_k; x_{k+1}, t_{k+1}; x_{k+2}, t_{k+2}; \dots; x_n, t_n)}{p(x_0, t_0; x_1, t_1; \dots; x_k, t_k)}.$$

$$(3.4)$$

When having a Markov process, the subsequent states $x_{k+1}, x_{k+2}, \dots, x_n$ at times $t_{k+1}, t_{k+2}, \dots, t_n$ are determined only by the present state x_k. Consequently, the conditional probability becomes:

$$p(x_{k+1}, t_{k+1}; x_{k+2}, t_{k+2}; \dots; x_n, t_n | x_0, t_0; x_1, t_1; \dots; x_k, t_k)$$
$$= p(x_{k+1}, t_{k+1}; x_{k+2}, t_{k+2}; \dots; x_n, t_n | x_k, t_k).$$

$$(3.5)$$

This means Markov processes have no memory effects. The joint probability density function of a Markov process is consequently given by

$$p(x_0, t_0; x_1, t_1; \dots; x_n, t_n)$$
$$= p(x_n, t_n | x_{n-1}, t_{n-1}) \times p(x_{n-1}, t_{n-1} | x_{n-2}, t_{n-2}) \times \dots \times p(x_1, t_1 | x_0, t_0) \times p(x_0, t_0).$$

$$(3.6)$$

This means the stochastic process is completely defined by the initial state probability $p(x_0, t_0)$ and the transition probability $p(x_{k+1}, t_{k+1} | x_k, t_k)$. Taking together, in a Markov process the subsequent state is determined only by the present state and past states can be neglected [261, 262].

---

[1]Note it holds $t_1 \leq t_2 \leq t_3 \dots$.

Chapman-Kolmogorov equation   As said before, a Markov process is fully determined by the initial state probability and the transition probability. Equation 3.6 is therefore considered for $n = 2$:

$$p(x_0, t_0; x_1, t_1; x_2, t_2) = p(x_2, t_2 | x_1, t_1) \times p(x_1, t_1 | x_0, t_0) \times p(x_0, t_0). \tag{3.7}$$

Integrating over x_1 gives

$$\int dx_1 p(x_0, t_0; x_1, t_1; x_2, t_2) = \int dx_1 p(x_2, t_2 | x_1, t_1) \times p(x_1, t_1 | x_0, t_0) \times p(x_0, t_0) \tag{3.8}$$

$$\Longleftrightarrow \quad p(x_0, t_0; x_2, t_2) = \int dx_1 p(x_2, t_2 | x_1, t_1) \times p(x_1, t_1 | x_0, t_0) \times p(x_0, t_0). \tag{3.9}$$

When dividing by $p(x_0, t_0)$ and using the conditional probability density rule, the Chapman-Kolmogorov equation is obtained:

$$p(x_2, t_2 | x_0, t_0) = \int dx_1 p(x_2, t_2 | x_1, t_1) \times p(x_1, t_1 | x_0, t_0). \tag{3.10}$$

The Chapman-Kolmogorov equation says that the transition probability of going from state 0 to state 2 is given by the transition probabilities for going from state 0 to an intermediate state 1 and from 1 to 2. It thereby has to be summed over all possible intermediate states 1. The Chapman-Kolmogorov equation fully describes a Markov stochastic process [261, 262].
In praxis, it is often easier to deal with the differential form of the Chapman-Kolmogorov equation instead of using the given integral form (eq. (3.10)). The differential form of the Chapman-Kolmogorov equation is (see book by *C.W. Gardiner* [262] for the derivation of the differential form):

$$\frac{\partial p(x, t | x_0, t_0)}{\partial t} = - \frac{\partial}{\partial x} \left[A(x, t) p(x, t | x_0, t_0) \right] \tag{3.11}$$

$$+ \frac{1}{2} \frac{\partial^2}{\partial x^2} \left[B(x, t) p(x, t | x_0, t_0) \right] \tag{3.12}$$

$$+ \int dy \left[W(x | y, t) p(y, t | x_0, t_0) - W(y | x, t) p(x, t | x_0, t_0) \right] \tag{3.13}$$

with the initial condition (x_0, t_0) (see also reference [262]). The first term on the right side of the differential Chapman-Kolmogorov equation describes drift motion, the second term diffusion and the third term jump processes. From the differential Chapman-Kolmogorov equation, the time evolution of the probability density function $p(x, t)$ can be calculated.

Fokker-Planck equation   Having a Markov process without jump processes ($W(x | y, t) = 0$), the differential Chapman-Kolmogorov equation converts to the Fokker-Planck equation:

$$\frac{\partial}{\partial t} p(x, t) = -\frac{\partial}{\partial x} \left[A(x, t) p(x, t) \right] + \frac{1}{2} \frac{\partial^2}{\partial x^2} \left[B(x, t) p(x, t) \right]. \tag{3.14}$$

The Fokker-Planck equation describes Brownian particles with a drift. The first term describes the drift caused by an external force $A(x, t) \propto F(x, t)$ and the second term the diffusion of the Brownian particle: $B(x, t) \propto D(x, t)$ [259, 262].

Diffusion equation   Without a drift ($A(x,t) = 0$), the Fokker-Planck equation becomes the diffusion equation:

$$\frac{\partial}{\partial t} p(x,t) = \frac{1}{2} \frac{\partial^2}{\partial x^2} [B(x,t)p(x,t)] \tag{3.15}$$

or

$$\frac{\partial}{\partial t} p(x,t) = D \frac{\partial^2}{\partial x^2} p(x,t) \tag{3.16}$$

if $B(x,t) = 2D(x,t) = 2D$ (homogeneous diffusion). The diffusion equation describes, for instance, a Brownian particle [259, 262].

Master equation   When setting the drift part and the diffusion part of the differential Chapman-Kolmogorov equation to zero ($A(x,t) = 0$ and $B(x,t) = 0$), the Chapman-Kolmogorov equation converts to the continuous Master equation:

$$\frac{\partial}{\partial t} p(x,t) = \int dy \left[W(x|y,t)p(y,t) - W(y|x,t)p(x,t) \right]. \tag{3.17}$$

If the state space of x is discrete, the Master equation is given by

$$\frac{\partial}{\partial t} p(n,t) = \sum_m \left[W(n|m,t)P(m,t) - W(m|n,t)P(n,t) \right]. \tag{3.18}$$

The Master equation describes jump processes with transition rates given by the matrix W. In detail, the probability of being in state x is equal to the probability of all transitions into this state $W(x|y,t)p(y,t)$ ("gain term") minus all transitions out of this state $W(y|x,t)p(x,t)$ ("loss term"). Master equations can describe a wide range of Markov processes [262].

Stationary process   A process is called stationary if the statistical properties of the process do not change with time anymore. This means the joint probability density is invariant regarding time translation:

$$p(x_0,t_0; x_1,t_1; \dots; x_n,t_n) = p(x_0,t_0 + \tau; x_1,t_1 + \tau; \dots; x_n,t_n + \tau). \tag{3.19}$$

The master equation then becomes:

$$\int dy W(x|y,t)p(y,t) = \int dy W(y|x,t)p(x,t). \tag{3.20}$$

It can clearly be seen that for stationary Markov processes the flux into the state x is identical to the flux out of the state x [261, 262, 265].

Detailed balance   If for a stationary process, the transition from state x to state y is balanced by the transition from state y to state x, the process fulfills detailed balance. In detail this means that the integrands of equation 3.20 are equal:

$$W(x|y,t)p(y,t) = W(y|x,t)p(x,t). \tag{3.21}$$

If the process is in thermal equilibrium, the probability density functions are given by the Boltzmann distribution and the detailed balance is given by the following equation:

$$\frac{W(x|y,t)}{W(y|x,t)} = \frac{p(x,t)}{p(y,t)} = e^{-\beta(E_y - E_x)} = e^{-\beta \Delta E} \tag{3.22}$$

where ΔE is the energy difference between state x and y.

First passage times   The partial differential equations for the probability density function of a stochastic process (equations eq. (3.14), (3.15), (3.17)) can be solved analytically or numerically. Knowing the probability density function $p(x,t)$ mean values and higher moments of the probability density function can be calculated. Besides mean values, another observable is the first passage time distribution, which is often of interest. The first passage time distribution describes the time the system first reaches a specific state. An example is a one-dimensional diffusion in a box with adsorbing boundaries. This means, once the particle reaches one of the boundaries, it is absorbed by the boundary and stops diffusing in the box. The so-called survival probability $S(t)$ gives the probability a particle is still alive, i.e. is still diffusing at a time t. For a one-dimensional diffusion in a box with boundaries at a and b, the survival probability is calculated as [259, 262]:

$$S(t) = \int_a^b dx p(x,t). \tag{3.23}$$

In contrast, the probability of being dead, i.e. absorbed by the boundary, is on one hand given by $1 - S(t)$ and on the other hand by integrating over the first passage time distribution. Thus, the following equation [261, 266]:

$$1 - S(t) = \int_0^t dt' f(t') \tag{3.24}$$

holds with $f(t)$ being the first passage time distribution. Consequently, the first passage time distribution can be calculated by [262, 266]

$$f(t) = -\frac{\partial}{\partial t} S(t) \tag{3.25}$$

and the mean first passage time by [259, 265]

$$\langle t \rangle = \int_0^\infty dt f(t)t. \tag{3.26}$$

3.2 Simulating stochastic processes

The previous section introduced master equations to describe probability density functions of stochastic processes. Master equations can be solved analytically, numerically or can be simulated. Having a system of many interacting particles and many degrees of freedom, simulating master equations and calculating ensemble averages are the methods of choice.

To simulate a stochastic process, Monte Carlo simulations, named after the famous Casino of Monte Carlo can be used [267]. Monte Carlo simulations use random numbers to generate different samples of the process. Having generated a high number of samples, probability distributions and mean values can be approximated. Monte Carlo simulations are therefore considered to be a statistical approach [267].

When solving master equations, the Monte Carlo simulations generate random trajectories/realizations of the stochastic process. A trajectory of a stochastic process described by master equations consists of multiple consecutive transitions (jumps) between states [265]. The transition rates are given by the transition matrix W of the master equation. The time update can either be performed in continuous time or approximated in discrete time. In the case of the discrete-time update mechanism, a small, but fixed Δt is chosen. After each Δt, the probability of a transition is calculated. Transitions are performed with the calculated probabilities. It thereby has to be made sure that the time update Δt is small enough [265]. For the continuous time update mechanism, a stochastic simulation algorithm, originally developed by Gillespie [268], is used. The Gillespie algorithm generates continuous waiting times between transitions and chooses transitions according to these waiting times. The Gillespie algorithm is presented in detail below.

Gillespie's algorithm for time-independent rates   The Gillespie algorithm was originally developed to describe chemical reactions. To introduce the waiting time distribution, first, a one-reaction process is considered. Let a_1 be the reaction rate, then $a_1 d\tau$ is the probability that a reaction occurs during the time step $d\tau$. The probability that no reaction occurs during the time interval $(t, t + \tau)$ is

$$P_0(\tau) = \left[1 - a_1 \frac{\tau}{N}\right]^N \tag{3.27}$$

with the number of time steps $N = \frac{\tau}{d\tau}$. For an infinitesimally small time step $d\tau \to 0$, the number of time steps goes towards infinity $N \to \infty$ and the probability that no transition occurred during the waiting time τ becomes

$$P_0(\tau) = \lim_{N \to \infty} \left[1 - a_1 \frac{\tau}{N}\right]^N = e^{-a_1 \tau}. \tag{3.28}$$

The probability that no reaction occurs during the waiting time τ and then a reaction occurs directly after, at $t + \tau + d\tau$, is

$$P(\tau) = P_0(\tau) a_1 d\tau = e^{-a_1 \tau} a_1 d\tau = p(\tau) d\tau \tag{3.29}$$

with the waiting time distribution

$$p(\tau) = e^{-a_1 \tau} a_1. \tag{3.30}$$

To simulate a one-reaction process, waiting times are generated according to the waiting time distribution. After each waiting time, the reaction is performed [265].

However, when having several possible reactions, not only the waiting times but also the reaction needs to be chosen. Gillespie [268] describes $P(\tau, \mu)d\tau$ as the probability that μ is the next reaction, which occurs within the time interval $(t + \tau, t + \tau + d\tau)$. If a_μ is the reaction rate of the reaction μ, then is $a_\mu d\tau$ the probability that the reaction μ occurs in $d\tau$. The probability that no reaction occurs during the waiting time τ is given by

$$P_0(\tau) = \lim_{N \to \infty} \left[1 - \sum_{\nu}^{M} a_\nu \frac{\tau}{N} \right]^N = e^{-\sum_{\nu}^{M} a_\nu \tau} \tag{3.31}$$

with the number of time steps $N = \frac{\tau}{d\tau}$ and the number of possible reactions M. For the probability of the next reaction being μ and occurring after a waiting time τ holds:

$$P(\tau, \mu) = a_\mu P_0(\tau) = a_\mu e^{-\sum_{\nu}^{M} a_\nu \tau}. \tag{3.32}$$

To generate a trajectory of a multiple reaction stochastic process, a waiting time and a reaction need to be sampled according to $P(\tau, \mu)$ [268].

Gillespie [268] published two standard methods to generate the reaction and the waiting time according to $P(\tau, \mu)$ (eq. (3.32)): The *direct method* and the *first reaction method*. For the *direct method*, the conditional probability given by

$$P(\tau, \mu) = P(\tau)P(\tau|\mu) \tag{3.33}$$

is considered. The probability that the next reaction, no matter which, occurs after the waiting time τ is given by

$$P(\tau) = \sum_{\nu=1}^{M} P(\tau, \nu) = \sum_{\nu=1}^{M} a_\nu e^{-\sum_{\nu}^{M} a_\nu \tau} = a e^{-a\tau} \tag{3.34}$$

with the reaction rate of all rates

$$a = \sum_{\nu=1}^{M} a_\nu. \tag{3.35}$$

The conditional probability is then

$$P(\mu|\tau) = \frac{P(\tau, \mu)}{P(\tau)} = \frac{a_\mu e^{-a\tau}}{\sum_{\nu=1}^{M} a_\nu e^{-a\tau}} = \frac{a_\mu}{a}. \tag{3.36}$$

To generate the next reaction and the next waiting time, the waiting time can be generated from $P(\tau)$ (eq. (3.34)) and the next reaction can be chosen according to $P(\mu|\tau)$ (eq. (3.36)) [268]. For the *first reaction method*, each reaction is considered independently. For each reaction μ holds that the probability that a reaction μ occurs within $d\tau$ is $a_\mu d\tau$ and the probability that no reaction μ occurs during the waiting time τ is

$$P_0(\tau) = \lim_{N \to \infty} \left[1 - a_\mu \frac{\tau}{N} \right]^N = e^{-a_\mu \tau}. \tag{3.37}$$

Thus, as for the one-reaction process, the waiting time for each reaction follows the distribution:

$$p(\tau) = a_\mu e^{-a_\mu \tau}. \tag{3.38}$$

When considering all reactions independently from one another, it can occur that during the waiting time τ of one reaction another reaction occurs. In order to maintain the correct reaction order, the reaction with the shortest waiting time is carried out. This means, at each update, the respective waiting times for all reactions are calculated according to eq. (3.38) and the reaction with the smallest waiting time is performed. If the rates do not change, the other waiting times can be kept for the next update, otherwise, they are rejected and need to be recalculated. Depending on the stochastic process, either the *direct method* or the *first reaction method* can be more efficient [268].

Using Gillespie's algorithm, random trajectories of a stochastic process can be generated by throwing a waiting time and a transition/reaction. Both, the waiting time and the transitions, are following a certain probability distribution. The question remains how to generate numbers/samples that follow a given probability density function.

Tower sampling   Tower sampling is a simple sampling method that can be used when having a finite number of possible states of a distribution, such as the number of reactions/transitions for instance. For the tower sampling, probabilities are added up to a tower (=cumulative probabilities). The tower consists of several "boxes". Each box represents one possible transition and the height of the box reflects the probability for this transition. To choose a transition a uniformly distributed random variable between 0 and the height of the tower $a = \sum_{\nu=1}^{M}$ is thrown:

$$u = rand(0, 1) \times a \tag{3.39}$$

where rand(0,1) is a uniformly distributed random variable between zero and one as provided by several random generators. The box into which the random number u falls is the chosen transition [267].

When having many possible transitions, a **Bisection search algorithm** is often used to find the chosen box. In the bisection search algorithm, the tower (or the search interval) is divided into two parts and it is checked whether the random number u lies in the upper or lower part. If the random number is in the upper/lower part, only the upper/lower part is further considered and again divided into two parts. Then it is again checked whether the random number u is in the upper or lower part of the chosen part. Continuing this process, the chosen box can be found more efficiently than going through all the boxes of the tower individually [267].

Inverse sampling   The inverse sampling is the analogous to the tower for a continuous probability density function, such as an exponential waiting time distribution (see eq. (3.38)) for instance. Instead of adding single probabilities up to a tower consisting of unequally high boxes, for the inverse sampling the cumulative distribution function is calculated:

$$F(x) = \int_{-\infty}^{x} p(x)dx. \tag{3.40}$$

In the continuous case, all "boxes" of the "tower" have the same height of dx and would sum up to 1. Throwing a uniformly distributed random number u in the interval $[0, 1]$, the box with a corresponding realization x can be found by solving $F(x) = u$:

$$F(x) = \int_{-\infty}^{x} p(x)dx = u. \tag{3.41}$$

Thus, solving this equation for x gives a random realization x distributed according to $p(x)$ [265, 267].

One frequently used example are random numbers following an exponential probability density function:

$$p(x) = \lambda e^{-\lambda x}. \tag{3.42}$$

Calculating the cumulative distribution function up to x gives:

$$F(x) = \lambda \int_{-\infty}^{x} e^{-\lambda x}dx = \left(1 - e^{-\lambda x}\right). \tag{3.43}$$

Setting $F(x)$ equal a uniformly distributed random number u and solving this equation for x gives a random number x following the exponential probability density function:

$$\left(1 - e^{-\lambda x}\right) = u \quad \Longleftrightarrow \quad x = -\frac{1}{\lambda}\ln(1 - u) = -\frac{1}{\lambda}\ln(\tilde{u}) \tag{3.44}$$

where $\tilde{u} = 1 - u$ is also a uniformly distributed random number between zero and one. Thus, eq. (3.44) gives an exponentially distributed random number x calculated from a uniformly distributed random number u [265, 267].

Metropolis algorithm   A process in thermal equilibrium can benefit from the fact that the process follows the detailed balance and state probabilities are given by the Boltzmann distribution (see above). Thus, the following equation applies for the transition rates:

$$\frac{W(x \to y)}{W(y \to x)} = e^{-\beta(E_y - E_x)} = e^{-\beta \Delta E}. \tag{3.45}$$

One way to sample a process in thermal equilibrium is to use the Metropolis algorithm, where a proposed transition is accepted with the following probability

$$W(x \to y)dt = \begin{cases} e^{-\beta(E_y - E_x)} = e^{-\beta \Delta E}, & \text{if} \Delta E \geq 0 \\ 1, & \text{else.} \end{cases} \tag{3.46}$$

Thus, the Metropolis algorithm suggests that when a proposed transition reduces the energy, it will be performed in any case, otherwise with probability $p = e^{-\beta \Delta E}$ [265, 267].

Gaussian distributed random numbers   Another distribution, which is often used, is a Gaussian or normal distribution. In the following, the generation of Gaussian distributed random numbers is described using the so-called *Box-Muller transform* [265, 267]. When sampling a Gaussian distributed random variable, the variable first needs to be transformed to a standard, normal distributed random variable x using

$$x = \frac{(y - \mu_y)}{\sigma_y}. \tag{3.47}$$

where μ_y is the mean and σ_y the standard deviation of the Gaussian distributed random variable y. x follows then a normal distribution with zero mean and a variance of one. To transform the uniformly distributed random variable back to the given Gaussian distribution, the inverse transform of

$$y = \sigma_y x + \mu_y \tag{3.48}$$

has to be applied. To derive a formula for how to generate a normally distributed random number from a uniformly distributed random number, we first rewrite the integration of the normal distribution:

$$1 = \int_{-\infty}^{\infty} dx \frac{1}{\sqrt{2\pi}} e^{-\frac{x^2}{2}} \tag{3.49}$$

$$\iff 1 = \left[\int_{-\infty}^{\infty} dx \frac{1}{\sqrt{2\pi}} e^{-\frac{x^2}{2}} \right]^2 = \int_{-\infty}^{\infty} dx \frac{1}{\sqrt{2\pi}} e^{-\frac{x^2}{2}} \int_{-\infty}^{\infty} dy \frac{1}{\sqrt{2\pi}} e^{-\frac{y^2}{2}} \tag{3.50}$$

$$= \int_{-\infty}^{\infty} \int_{-\infty}^{\infty} dx dy \frac{1}{2\pi} e^{-\frac{x^2+y^2}{2}}. \tag{3.51}$$

Using the polar coordinates two independent integrals can be obtained:

$$1 = \int_{0}^{2\pi} \int_{-\infty}^{\infty} dr d\varphi \frac{1}{2\pi} r e^{-\frac{r^2}{2}} = \underbrace{\int_{0}^{2\pi} d\varphi \frac{1}{2\pi}}_{=1} \underbrace{\int_{-\infty}^{\infty} dz \, e^{-z^2}}_{=1} \tag{3.52}$$

with $z = \frac{r^2}{2}$. The distributions of both integrals can be sampled independently using the inverse sampling method. Thus, r and φ are generated from uniformly distributed random variables u, v as follows:

$$\varphi = 2\pi v \qquad \text{and} \qquad r = \sqrt{2z} = \sqrt{-2 \ln u}. \tag{3.53}$$

Transforming back to cartesian coordinates, two normally distributed random variables are obtained:

$$x = r \cos(\varphi) = \sqrt{-2 \ln u} \cos(2\pi v) \tag{3.54}$$

$$y = r \sin(\varphi) = \sqrt{-2 \ln u} \sin(2\pi v). \tag{3.55}$$

This means, with two uniformly distributed random variables u and v, we can generate two independent normally distributed random variables x and y [265, 267].

Uniformly distributed positions on a sphere   Besides random numbers in one dimension, often also random positions on a sphere are needed. Here, it is described how uniformly distributed positions on a sphere can be generated. Therefore, a sphere with radius $r = 1$ is considered. The surface area of such a sphere is:

$$\int\int_S dA = 4\pi \tag{3.56}$$

$$\Longleftrightarrow \quad 1 = \int\int_S \frac{1}{4\pi} dA. \tag{3.57}$$

Using spherical coordinates, it is obtained

$$1 = \int_0^\pi \int_0^{2\pi} \frac{\sin(\theta)}{4\pi} d\varphi d\theta = \int_0^\pi \int_0^{2\pi} p(\varphi, \theta) d\varphi d\theta. \tag{3.58}$$

Where the joint probability density for the angles is defined as

$$p(\varphi, \theta) = \frac{\sin(\theta)}{4\pi}. \tag{3.59}$$

Integrating over the joint probability density gives the separated probability density functions for φ and θ:

$$p(\varphi) = \int_0^\pi \frac{\sin(\theta)}{4\pi} d\theta = \frac{1}{2\pi} \tag{3.60}$$

$$p(\theta) = \int_0^{2\pi} \frac{\sin(\theta)}{4\pi} d\varphi = \frac{\sin\theta}{2}. \tag{3.61}$$

Plugging in the two separated probability density functions splits the two-dimensional integral into two independent integrals:

$$1 = \underbrace{\int_0^\pi \frac{\sin\theta}{2} d\theta}_{=1} \underbrace{\int_0^{2\pi} \frac{1}{2\pi} d\varphi}_{=1}. \tag{3.62}$$

Using the inverse sampling method, both angles, φ and θ can be generated separately from uniformly distributed random numbers v and u, respectively:

$$\theta = \arccos\left(1 - 2u\right) \quad \varphi = 2\pi v. \tag{3.63}$$

That is how random points on a unit sphere can be generated [267].

   Taking together, this subsection described how to simulate master equations by means of Monte Carlo simulations. The Gillespie algorithm has been introduced to generate random trajectories in continuous time and several methods have been presented to generate random numbers according to given distributions.

3.3 Transport-related stochastic processes

In this section transport-related, stochastic processes are presented. The here discussed processes are the basis of the later presented modeling of intracellular transport (chapter 4, 6 and 7) and tau adsorption (chapter 5).

Diffusion process The first process which is relevant for transport is the one-dimensional diffusion process. Inactive or passive dynein motors as well as microtubule-associated proteins such as tau are known to perform diffusion-like motion on microtubules [31, 40, 89, 94, 269]. Moreover, the cargo itself or the MT itself might diffuse in the solution. The diffusion process is described by the diffusion equation eq. (3.16). Using the Fourier transform

$$\hat{p}(k,t) = \int_{-\infty}^{\infty} e^{ikx} p(x,t) dx \tag{3.64}$$

the diffusion equation can be solved in the Fourier space [259]:

$$\frac{\partial \hat{p}(k,t)}{\partial t} = -k^2 D \hat{p}(k,t) \quad \Longleftrightarrow \quad \hat{p}(k,t) = \hat{p}_0(k) e^{-k^2 Dt} \tag{3.65}$$

with the initial condition $\hat{p}_0(k)$. Using the fact that the product of two functions in the Fourier space is a convolution of the two functions in the position space, the inverse transform is:

$$p(x,t) = \int_{-\infty}^{\infty} dx' p_0(x') \left[\frac{1}{2\pi} \int_{-\infty}^{\infty} e^{-ik(x-x')} e^{-k^2 Dt} dk \right] = \int_{-\infty}^{\infty} dx' p_0(x') \frac{1}{\sqrt{4\pi Dt}} e^{-\frac{(x-x')^2}{4Dt}}. \tag{3.66}$$

Applying the initial condition $p_0(x) = \delta(x)$, the solution of the diffusion equation is found to be a Gaussian distribution:

$$p(x,t) = \frac{1}{4\pi Dt} e^{-\frac{x^2}{4Dt}} \tag{3.67}$$

with zero mean and mean square displacement

$$\langle x^2 \rangle = 2Dt. \tag{3.68}$$

Diffusion in a harmonic potential The diffusive motion along the MT of a passive motor attached to the cargo cannot be considered as free diffusion. It is rather a diffusion in a harmonic potential assuming that the motor acts like a linear harmonic spring. For diffusion in a harmonic potential $V(x) = \frac{1}{2}\kappa x^2$, the Fokker-Planck equation (see eq. (3.14)) becomes:

$$\frac{\partial}{\partial t} p(x,t) = D \left[\frac{\partial^2}{\partial x^2} + \beta\kappa \frac{\partial}{\partial x} x \right] p(x,t) \tag{3.69}$$

where $B(x, t) = 2D$, $A(x, t) = -\frac{1}{\gamma}\frac{\partial V(x)}{\partial x}$ and $\frac{1}{\gamma} = D\beta$ is applied.

The stationary solution of the Fokker-Planck equation for diffusion in a harmonic potential is Boltzmann distributed:

$$p_{\text{st}}(x) = \sqrt{\frac{\kappa\beta}{2\pi}}e^{-\frac{\beta\kappa x^2}{2}}. \tag{3.70}$$

Due to the special form of the harmonic potential, the stationary solution is Gaussian distributed as the solution of the diffusion equation. However, while the Gaussian distribution of the free diffusion widens over time, the stationary solution of the diffusion in a harmonic potential is clearly localized by the confinement given by the harmonic potential.

Physics at low Reynold numbers   The Reynold number describes the ratio of inertial to viscous force. The inertial force scales as $\rho l^2 v^2$ and the viscous force as $\eta l v$. Thus, the Reynold number is defined as:

$$\mathcal{R} = \frac{\rho l^2 v^2}{\eta l v} = \frac{\rho l v}{\eta} \tag{3.71}$$

where ρ is the density of the fluid, v the velocity and l the characteristic length of the object, and η the viscosity of the fluid [259, 270]. If the Reynold number is high, i.e. $\mathcal{R} \gg 1$ the inertial force dominates the motion and if the Reynold number is low $\mathcal{R} \ll 1$ the viscous force. Hence, at low Reynold numbers, the inertia term can be neglected and the Langevin equation becomes:

$$\xi_{\text{MT}}\frac{dx}{dt} = F(x, t) + \mathfrak{f}(t) \tag{3.72}$$

where ξ_{MT} is the drag coefficient of the MT and $F(x, t)$ an eventual external force, which acts on the particle additionally to the noise $\mathfrak{f}(t)$ [259, 270].

Stoke's drag force   For a spherical particle with radius R, which moves at low Reynold numbers through a viscous medium, Stoke's found the following expression for the drag force [270, 271]:

$$F_{\text{s}} = \xi v \tag{3.73}$$

with the drag coefficient:

$$\xi = 6\pi\eta R. \tag{3.74}$$

Hydrodynamics of a MT   The typical motion of a MT *in vitro* can usually be considered to be a motion at low Reynold numbers (see chapter 4). The MT itself is a rigid rod. Thus, to describe the viscous force of a MT, the drag coefficient of a cylinder has to be used. Various approximations of the drag coefficient of a cylinder can be found in literature [272]. The drag coefficient differs for one-dimensional motions parallel to the MT length axis, perpendicular

to the MT length axis or for random directions [272, 273]:

$$\xi_{||} = \frac{2\pi\eta L}{\log(L/(2b)) + \gamma_{||}} \quad \text{(parallel)} \tag{3.75}$$

$$\xi_{\perp} = \frac{4\pi\eta L}{\log(L/(2b)) + \gamma_{\perp}} \quad \text{(perpendicular)} \tag{3.76}$$

$$\xi_{r} = \frac{3\pi\eta L}{\log(L/(2b)) + \gamma_{r}} \quad \text{(random)}. \tag{3.77}$$

L is thereby the length of the cylinder, b the radius and $\gamma_{||}, \gamma_{\perp}$ and γ_{r} the end-effect corrections. Among the different expressions for the end-effect corrections given in literature [272], in this thesis, the expressions by Broersma [274] are used:

$$\gamma_{||} = -0.207 + 0 - 980 * \frac{2b}{L} - 0.133 \left(\frac{2b}{L}\right)^2 \tag{3.78}$$

$$\gamma_{\perp} = 0.839 + 0.185\frac{2b}{L}0.233 \left(\frac{2b}{L}\right)^2 \tag{3.79}$$

$$\gamma_{r} = 0.312 + 0.565\frac{2b}{L}0.100 \left(\frac{2b}{L}\right)^2. \tag{3.80}$$

$$\tag{3.81}$$

Having the drag coefficient, also the one-dimensional diffusion coefficient can be calculated using the Einstein relation [259]:

$$\xi D = k_{\mathrm{B}}T. \tag{3.82}$$

One-dimensional random walk   Since the MT consists of α-β-tubulin subunits, and the molecular motors orientate their steps along this discrete lattice, the motion of molecular motors along the MT or along one protofilament of a MT can be described in discrete space. The one-dimensional random walk model describes diffusion in one-dimensional, discrete space. In discrete space, the particle hops to neighboring sites on the one-dimensional lattice with equal transition rates $r_p = \frac{1}{2\Delta t}$. The corresponding master equation describing the random walk on a lattice with lattice spacing Δx is:

$$\frac{\partial p(x,t)}{\partial t} = \frac{1}{2\Delta t}p(x - \Delta x, t) + \frac{1}{2\Delta t}p(x + \Delta x, t) - \frac{1}{\Delta t}p(x,t). \tag{3.83}$$

In the continuum limit $\Delta x, \Delta t \to 0$ with the definition of the diffusion constant $D = \lim_{\Delta x, \Delta t \to 0} \frac{(\Delta)^2}{2\Delta t}$, the master equation becomes the diffusion equation (see eq. (3.16)). See eq. (3.67) for the solution of the one-dimensional diffusion equation.

Exclusion process   The random walk model describes the random motion of an ensemble of particles, where particle-particle interactions can be neglected (diffusion). In the context of the thesis, however, spatially extended particles eventually step along the same protofilament of a MT. Particles interact with the protofilament at specific binding sites, which makes the lattice-type structure important and hardcore particle-particle interactions cannot be neglected. Interacting particles in discrete space can be described by lattice gas models. Processes describing many particles with hardcore repulsion/interaction are called exclusion processes [275, 276].

a) Random walk

b) Symmetric exclusion process

c) TASEP

d) TASEP + Langmuir kinetics
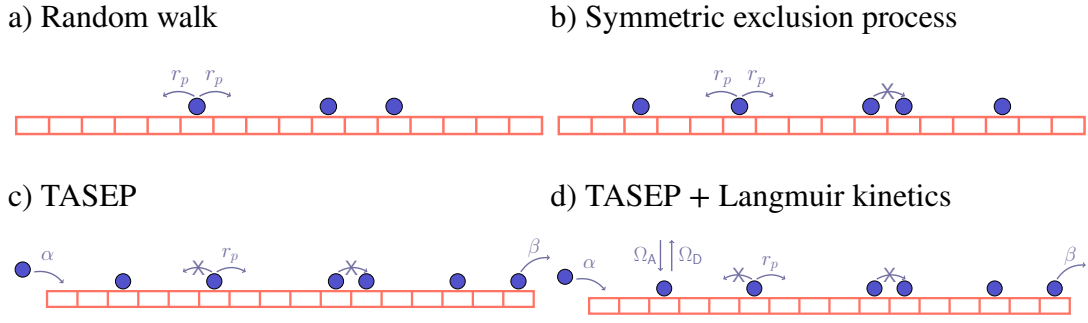
Figure 3.1: Lattice gas models. a) The random walk model describes the one-dimensional diffusion of random particles on a one-dimensional lattice, where particle-particle interactions can be neglected. The particles hop with equal rates r_p to neighboring sites (left/right). b) The symmetric exclusion process describes several random walkers on a one-dimensional lattice. Hardcore interactions are taken into account such that no more than one particle can occupy one lattice site (exclusion). c) The total asymmetric exclusion process (TASEP) is the extreme case of the asymmetric exclusion process and describes driven particles, which stochastically step only in one direction on a one-dimensional lattice. Particles hop to the right neighboring site with rate r_p, enter the lattice on the left site with rate α and leave the lattice on the right site with rate β. Hardcore interactions are taken into account (exclusion effect). d) In the TASEP with Langmuir kinetics, the particles can additionally attach and detach to and from the bulk of the lattice to the solution with rates Ω_A and Ω_D, respectively.

For exclusion processes, each particle occupies one lattice site and hops to neighboring lattice sites with specific rates. A particle can thereby only hop to a neighboring lattice site if this site is empty (see fig. 3.1b or 3.1c for a schematic). Consequently, a lattice site can either be empty or occupied by one particle. The simplest exclusion process, i.e. the simple symmetric exclusion process (SEP), describes multiple particles with hardcore interactions, which perform a random walk (see fig. 3.1b). Let $p(x,t)$ describe the probability density that site x is occupied at time t. Then the following master equation describes how the site occupation evolves in time:

$$\frac{\partial p(x,t)}{\partial t} = \frac{1}{2} p(x+1,t)\,(1 - p(x,t)) + \frac{1}{2} p(x-1,t)\,(1 - p(x,t)) \tag{3.84}$$

$$- \frac{1}{2} p(x,t)\,(1 - p(x+1,t)) - \frac{1}{2} p(x,t)\,(1 - p(x-1,t)). \tag{3.85}$$

Thereby, the first two terms describe the probability density that the neighboring sites are occupied times the probability density that the site x is empty such that the particle could hop to site x with rate one. The two last terms describe the probability density that site x is occupied, while the neighboring site is empty such that the particle could hop to the neighboring site. Simplifying this master equation, one obtains:

$$\frac{\partial p(x,t)}{\partial t} = \frac{1}{2}\,(p(x+1,t) - p(x-1,t)) - p(x,t) \tag{3.86}$$

which is the master equation for a single random walker with hopping rate one (see eq. 3.83). Thus, the density of the system behaves as a normal diffusion without interactions [276]. However, a single particle moves differently in the simple symmetric exclusion process compared to the free random walk. In the case of the exclusion process, the particle moves less far since it cannot pass other particles. See [276] for more details.

Totally asymmetric exclusion process   While diffusive/passive dynein motors and tau molecules diffuse along the MT, active intracellular motors step directedly along the MT under the consumption of energy. The directed, far from equilibrium motion of active motors can be described by driven lattice gas models. The totally asymmetric exclusion process (TASEP) describes active, hardcore interacting particles, which stochastically step in one direction on a discrete lattice. The TASEP is often studied with open boundaries such that particles enter the one-dimensional, finite lattice on one side with rate α and leave the system on the other side with rate β (see fig. 3.1c). The master equation describing the occupation probability density function $p(x, t)$ for the one-dimensional TASEP with open boundaries and hopping rate one is given by

$$\frac{\partial p(x, t)}{\partial t} = p(x - 1, t)(1 - p(x, t)) - p(x, t)(1 - p(x + 1, t)) \tag{3.87}$$

for the bulk lattice and by

$$\frac{\partial p(1, t)}{\partial t} = \alpha(1 - p(1, t)) - p(1, t)(1 - p(2, t)) \quad \text{left boundary} \tag{3.88}$$

$$\frac{\partial p(N, t)}{\partial t} = p(N - 1, t)(1 - p(N, t)) - \beta p(N, t) \quad \text{right boundary} \tag{3.89}$$

$$\tag{3.90}$$

for the boundaries. For the non-equilibrium steady state, three different phases can be distinguished in dependence of α and β: first the high-density phase for $\beta < 0.5$ and $\alpha < \beta$, second the low-density phase for $\alpha < 0.5$ and $\beta < \alpha$ and third the maximal current phase for $\alpha, \beta > 0.5$. For more details see [259, 276].

Langmuir adsorption model   While the TASEP only considers particle entry and leaving at the beginning and end of the lattice, molecular motors as well as tau proteins usually attach and detach from the bulk of the MT. The Langmuir adsorption model describes particle adsorption and desorption on a one-dimensional lattice taking hardcore particle-particle interactions into account. Particle motion along the lattice is not considered. In the Langmuir adsorption model, particles attach to an empty lattice site with the adsorption rate Ω_A and detach to the solution with the desorption rate Ω_D (see fig. 3.1d). The master equation describes the particle density $\rho(x, t)$ on the one-dimensional lattice:

$$\frac{\partial \rho(x, t)}{\partial t} = \Omega_A(1 - \rho(x, t)) - \Omega_D \rho(x, t). \tag{3.91}$$

From the master equation, the stationary state density

$$\rho^{\text{st}} = \frac{\Omega_A}{\Omega_A + \Omega_D} \tag{3.92}$$

and the time evolution of the particle density

$$\rho(t) = \frac{\Omega_A}{\Omega_A + \Omega_D} \cdot \left(1 - e^{-(\Omega_A + \Omega_D) \cdot t}\right) \tag{3.93}$$

can be obtained [259, 277]. The time evolution of the particle density is used in the tau adsorption model in chapter 5. See Swenson and Stadie [277] for a centennial review of the Langmuir adsorption model.

TASEP with Langmuir adsorption model Intracellular transport can be described as a combination of the Langmuir adsorption model and the TASEP. Combining the two models, the master equation for the occupation probability density function $p(x, t)$ becomes

$$\frac{\partial p(x, t)}{\partial t} = p(x - 1, t)(1 - p(x, t)) + \Omega_A(1 - p(x, t)) - p(x, t)(1 - p(x + 1, t)) - \Omega_D p(x, t)$$

(3.94)

for the bulk lattice and

$$\frac{\partial p(1, t)}{\partial t} = \alpha(1 - p(1, t)) + \Omega_A(1 - p(1, t)) - p(1, t)(1 - p(2, t)) - \Omega_D p(1, t)$$

(3.95)

$$\frac{\partial p(N, t)}{\partial t} = p(N - 1, t)(1 - p(N, t)) + \Omega_A(1 - p(N, t)) - \beta p(N, t) - \Omega_D p(N, t)$$

(3.96)

(3.97)

for the boundaries [259]. Here, the Langmuir reservoir given by Ω_A and Ω_D competes with the side reservoirs given by α and β. If the Langmuir reservoir is dominant, the influences of α and β are not visible and vice versa.

This section introduced stochastic processes, which are the basis of modeling intracellular transport and MT tau interactions. For molecular motors and MT-associated proteins, however, rates and interactions are more complex. In many particle transport systems, for instance, particles are mechanically coupled such that their stepping and detachment rates are force dependent (see chapters 4, 6 and 7). In the case of the tau adsorption, additional particle-particle and particle-lattice interactions lead to quite a distinct behavior than expected from the basic stochastic models (see chapter 5). In the following, the State of Art of more advanced multi-motor transport models is presented.

3.4 State of the Art of modeling multi-motor transport

When being interested in the collective motion and the mutual interplay of multiple, mechanically coupled molecular motors, explicit motor positions and forces as well as the mechanical coupling via the cargo need to be taken into account. In the following, typical molecular motor models, their coupling in multi-motor transport systems and the simulation of multi-motor trajectories are presented.

Molecular motor heads are usually coarse-grained modeled as point-like particles not resolving the two motor heads separately [35, 36, 151, 163, 247, 278]. The motor body should be able to exert a force on the cargo, which scales with the stretching of the motor. The simplest way is to model the motor body as a linear, Hookean spring. The used Hookean spring models mostly show no resistance under compression and have a non-zero rest length reflecting the motor contour length [34–36, 157, 163, 163, 166, 247, 278–281]. Deviating from this standard, Li et al. [278] tested several kinds of springs with and without a rest length. They found that the linear spring with a non-zero rest length reproduces the experimental behavior best supporting the standard model of molecular motors [278].

When not being interested in the mutual interplay between attached motors, but only in the number and kind of attached motors, a mean-field approach is used to calculate the force. The mean field approach assumes that forces are equally shared between members of the same

team [25, 33, 160, 163, 163, 282–284]. However, since motors are stochastic steppers, the load is not supposed to be equally shared between motors. Thus, when being interested in the mutual interplay between attached motors the explicit motor positions need to be taken into account. When taking the explicit motor positions into account, the exerted force is calculated by the difference between motor head and motor tail positions [33, 35, 153, 163, 281]:

$$F = \kappa \left(x_{\mathrm{h}} - x_{\mathrm{t}} - L_0 \right) \tag{3.98}$$

with x_{h} and x_{t} being the motor head and motor tail positions, respectively, κ the motor stiffness, and L_0 the non-zero motor rest length. While the mean-field approach is often considered when solving the master equation numerically or analytically [32, 151, 160, 283, 285], the explicit position model is often used in combination with MC simulations [34–36, 153, 163, 247, 286]. Since this work focuses on the mutual interplay between multiple motors, the explicit position model will be considered in the following.

Having characterized the motors themselves, the motor actions still need to be described. Motors are typically supposed to be permanently bound to the cargo, but stochastically attach and detach from the MT or step on the MT when being attached. Motors are modeled to attach with a constant attachment rate [32–34, 163, 247, 282, 285, 287, 288]. Deviating from this standard, Khataee and Howard [160] and Li et al. [278] take an attachment potential into account and use an Arrhenius-like attachment rate. Since there is no reason for motors to stretch without experiencing a force, the motors are modeled to attach in a relaxed conformation [32–34, 163, 247, 282, 285, 287, 288]. While the attachment procedure is identical for kinesin and dynein, the value of the attachment rate can differ between kinesin and dynein motors [33, 288, 289].

For the detachment of the motor, often the Kramer's escape rate or the Bell theory is used [290, 291]. In this case, the detachment rate increases exponentially with the applied load force

$$k(F) = k_{\mathrm{d}}^0 \cdot e^{\frac{F \delta_0}{k_{\mathrm{B}} T}} = k_{\mathrm{d}}^0 \cdot e^{\frac{F}{F_{\mathrm{d}}}} \tag{3.99}$$

with $F_{\mathrm{d}} = \frac{k_{\mathrm{B}} T}{\delta_0}$ being the detachment force and δ_0 the length scale of the detachment potential. The unloaded detachment rate k_{d}^0 can be calculated from single motor run length L_{run} and velocity v:

$$k_{\mathrm{d}}^0 = \frac{v}{L_{\mathrm{run}}}. \tag{3.100}$$

While most studies use the exponentially increasing detachment rate with different k_{d}^0 and F_{d} for dynein and kinesin respectively [32, 34, 151, 157, 163, 165, 176, 257, 278–283, 285, 286, 288, 292], Kunwar et al. [33], Klein et al. [35], and Klein et al. [36] adjust the detachment in the super stall regime ($F > F_{\mathrm{s}}$) to the experimental findings of Kunwar et al. [33] for kinesin-1 and cytoplasmic dynein to have a more realistic model [33, 35, 36].

As the detachment, also the stepping depends on the load force a motor experiences. While some studies use force-dependent backward and forward stepping probabilities [34, 163, 281], most studies use a piecewise force-velocity relation [25, 32–36, 151, 153, 157, 164, 257, 278, 279, 283, 285, 288]. It is thereby distinguished between three force regimes: i) the regime under assisting load force, ii) the regime under resisting load force up to the stall force and iii) the super stall regime beyond the stall force. In the assisting force regime either a velocity,

which increases with increasing assisting force [25, 32, 33, 151, 257], is used or a constant, force-independent velocity [34, 153, 157, 164, 278, 279, 283, 285, 288]. Kunwar et al. [280], for instance, use a force-independent velocity, which depends on the ATP concentration in a Michaelis-Menten-like manner [280]:

$$v = \frac{v_{\mathrm{max}} \, [\mathrm{ATP}]}{K_m + [\mathrm{ATP}]}. \tag{3.101}$$

In the resisting force regime, the velocity decays in an algebraic manner [25, 32–34, 99, 151, 153, 157, 164, 165, 257, 278–280, 283, 285, 288, 292]:

$$v(F) = v \left(1 - \left(\frac{F}{F_{\mathrm{s}}} \right)^w \right). \tag{3.102}$$

In most cases the exponent is set to one $w = 1$, generating a linear force-velocity relation [25, 32, 33, 99, 151, 153, 157, 164, 165, 257, 278, 279, 283, 285, 288]. Some studies also include an ATP dependence in this regime. Klein et al. [35] and Klein et al. [36], for instance, use the combined ATP and force dependence of the velocity found by Schnitzer et al. [120] for kinesin-1. Moreover, a complex dependence on load and ATP concentration is also used by Ohashi et al. [34]. In the super stall regime, the backward velocity is either set to zero [157, 164, 165, 257, 279, 283, 285], constant [35, 36, 153] or increasing with increasing load [25, 32, 33, 151, 288]. For dynein and kinesin mostly the same force dependencies of the velocity are used with motor-specific stall forces, force-independent and backward stepping velocities. An exception is the study by Khetan and Athale [288], which uses a linear force-velocity relation for kinesin, while for dynein the step sizes reduce with load at a constant velocity. Moreover, when focusing on motor stepping, some studies even take sub-steps of the stepping mechanism into account [175, 286, 293].

Taking together, in the standard molecular motor model, motors are modeled as linear springs with non-zero rest length. Motors attach to the MT at a constant rate in a relaxed confirmation. Attached to the MT, they can step along the MT or detach again. The detachment rate depends exponentially on the force, while the stepping rate decreases with force in the resisting force regime, which is the most relevant force regime for bidirectional transport.

Having characterized the motors, next the MT and the cargo need to be defined. Since lateral movements are not of interest in most studies, the MT is mostly modeled as a one-dimensional (discrete) line, reflecting just one protofilament [33, 35, 36, 164, 257, 280, 292]. However, since the MT normally has several protofilaments, no steric exclusion effects (steric hindrance) of the motors are taken into account [35, 164, 280]. Since most studies focus on the MT attached motors, detached motors on the cargo are not simulated explicitly. The cargo is therefore mostly modeled as an infinitesimally small point. This means all motor tails are bound to the same spot [32, 33, 35, 36, 151, 153]. Deviating from the standard, Chen et al. [286], Korn et al. [279] and Erickson et al. [247] simulate the cargo-MT system in three dimensions. All of them distribute the motors randomly on the surface of the cargo and calculate the three-dimensional force [247, 279, 286]. MT gliding assays in contrast are modeled both, in one [164, 166, 292] and two dimensions [278, 285, 294–296]. Two dimensions mean that the coverslip is a two-dimensional surface and the motors are distributed randomly on this surface [278, 285, 294–296]. In this case, motor forces are calculated in two dimensions and the MTs are characterized by a position, an orientation and a length [294–296]. Motors are allowed to attach the MT when the MT is within a sphere with a

certain radius (contour length) around the motor coverslip position [295]. In one-dimensional gliding assay simulations, the coverslip is one-dimensional as the MT. For calculating motor forces, mostly only parallel components are taken into account [164, 166, 292]. Taking together, while cargo transport is mostly considered just in one dimension with the cargo being an infinitesimally small point, MT gliding assay simulations can be found in one and two dimensions.

Monte Carlo (MC) simulations are used to generate a sample of the time development of the considered system. Thereby, most algorithms implement a discrete time update [33, 157, 164, 247, 280, 286, 292, 293, 295, 297]. They therefore use either a time interval, which is smaller than the fastest expected update time [33], or a random sequential update where several motors are updated at the time [297]. Moreover, MC simulations are also used with continuous time updates [32, 34, 163, 287]. In this case, the Gillespie Algorithm for time-independent or time-dependent rate is applied [34–36, 298].
Besides the time, also the cargo position needs to be updated. The cargo can be propagated by solving its equation of motion or Langevin equation. Because inertia effects are small compared to friction and motor forces [278, 285, 294], mostly the over-damped limit is considered and the acceleration term is neglected [34, 164, 278, 279, 285, 294–296]. The inertia term is found to be small for cargo transport [279] as well as for MT gliding assays [278, 294]. Besides solving the equation of motion, another approach propagates the cargo to its equilibrium position [33, 34, 278], which is a valid approach in the over-damped limit where relaxation times are shorter than next event times (see also chapter 4).

In summary, intracellular transport has been intensively modeled in the past and basic molecular motor models have been developed. However, molecular motors differ in their properties and not all motor properties are fully studied. That is why molecular motor models always need to be adjusted to the motor of interest and the recent experimental findings. Moreover, to study a specific transport experiment, the simulations need to be adjusted to the given experimental conditions such as transport geometry, temperature, ATP concentration, buffer solution, etc.

Chapter 4

Microtubule gliding assays

Contents

In this chapter, MT gliding assays are simulated and compared to MT gliding experiments. The MT gliding assay set-up is implemented and existing kinesin and dynein models are incorporated in the gliding assay implementation. Comparing simulation results to experimental results, the kinesin and dynein models are calibrated. To align the simulation to the experimental findings, a mechanical activation is added to the dynein model. Having well-calibrated dynein and kinesin models, bidirectional gliding assays are studied at varying numbers of kinesin and dynein motors. Moreover, the ATP concentration and the presence of roadblocks at different concentrations are studied as possible regulation factors of the directionality of bidirectional transport.

In vivo, teams of kinesin-1 and cytoplasmic dynein motors are known to be simultaneously bound to the same cargo [9, 13, 14, 16, 25]. Teams of motors were previously observed to behave differently than single motors [16, 17, 142, 145, 147, 154, 155]. Hence, it is important to first understand how multiple kinesin-1 or multiple cytoplasmic dynein motors work together in a team before considering how oppositely directed teams of kinesin-1 and cytoplasmic dynein motors work against each other.

To investigate how multiple kinesin-1 (from now on called "kinesin") or multiple mammalian, cytoplasmic dynein motors without adaptor proteins (from now on called "dynein") work in a team, MT gliding assays are a suitable tool. In MT gliding assays, the cooperation between multiple motors can be studied without a potential or additional influence of the cargo. Furthermore, the motor density can be changed systematically to understand how the transport depends on the number of involved motors. However, simulations are needed for a more detailed picture of the transport process on a molecular level. Unlike in the experiment, where transport velocities can be measured, simulations can additionally give detailed insights into how many and what kind of motors are involved in the transport and how these motors work in a team to transport the MT. To model MT gliding assays, previously published kinesin and dynein models [33, 35] are adapted to the particular kinesin and dynein studied, and implemented in the gliding assay set-up. All shown experimental results are from experiments performed by the Stefan Diez lab[1].

In the following, it will be presented first the modeling of the MT gliding assay set-up, second the separate study of unidirectional kinesin and dynein gliding assays, and third the study of bidirectional gliding assays and the influence of regulation mechanisms such as the number of motors, the ATP concentration, and roadblocks.

4.1 Modeling gliding assays

In experimental gliding assays, a coverslip is coated with molecular motors and a MT is placed above. Motors bind to the MT and step on it until detaching stochastically under load or at the end of the MT. When stepping on the MT, motors exert forces on the MT and propel it forward. Gliding assays were modeled before in one [164, 166, 292] and in two dimensions [246, 278, 285, 294–296]. Gliding trajectories from the here presented experiments (fig. 4.1a), however, reveal that MTs move along straight lines. That is why, here, a one-dimensional model is used. The used one-dimensional model is presented in the following.

In the one-dimensional model, the coverslip (from now on called surface) coated with molecular motors is modeled as a line, on which motors with a finite radius R are stringed. The surface presents the global, fixed coordinate systems. In this coordinate system, the position of the rigidly bound tail of the ith motor is denoted as x_{t}^i. Because it is a priori not known how far the MT will move in which direction, new motors need constantly be added to the surface during the simulation to make sure that there are always the amount of motors under the MT, which represents the given surface density. In detail this means, if the MT is moving in positive direction, motors are added at the positive end of the line and vice versa. The motor line density on the one-dimensional modeling surface should always reflect the experimentally given motor surface density σ_{s}. Therefore, the two-dimensional surface density σ_{s} needs to be appropriately transformed into a line density. To calculate the line density, first, the number

---

[1]Experiments were performed by Lara Scharrel from the Stefan Diez lab at B CUBE, TU-Dresden. See also the thesis [299]. I did not perform any experiments myself.
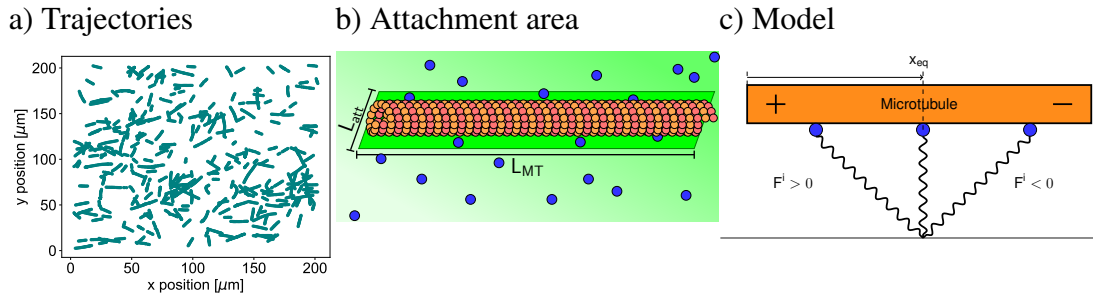
Figure 4.1: Illustration of gliding assays. a) Figure shows example MT trajectories (x-y-plane). The shown MTs are bidirectionally transported by kinesin and dynein motors. It can be seen that MTs move in straight lines. That is why the transport of a MT in a MT gliding assay can be modeled in one dimension. b) Figure shows an illustration of an experimental gliding assay. The cover slip (green background) is coated with motors (blue circles) and a MT (orange-red tube) is placed above. All the motors within the attachment area (dark green rectangle under the MT) are assumed to be able to reach the MT. The attachment area is given by the rectangle $L_{att} \times L_{MT}$. c) Figure shows a sketch of a gliding assay model. The MT (orange rectangle), with its plus-end on the left and its minus-end on the right side, is placed above the surface (=coverslip, gray axis line). Here, only one motor, coarse-grained modeled as a dot, with three different MT positions is drawn (blue dots with a curvy line representing the motor spring). If the motor has the left MT position, it experiences a positive force ($F^i > 0$) and if the motor has the right MT position, it experiences a negative force ($F^i < 0$). If the motor has the middle MT position, it experiences no force because the motor is attached at its equilibrium position x_{eq}. The equilibrium position x_{eq}, given in the coordinate system of the MT, is the position of the motor head on the MT directly above the motor tail position on the surface. Thus, at the equilibrium position the motor extension $\Delta x^i(t)$ is zero.

Experiments were performed by Lara Scharrel from Stefan Diez lab at B CUBE, TU-Dresden. *Fig. c) is reproduced/adapted with permission from The Company of Biologists LTd., Journal of cell science.* Originally published in *Journal of cell science*, volume 132(4), page jcs220079 (2019) [300]. *Print permissions for fig. a was given in a private communication by the Stefan Diez lab at B CUBE, TU-Dresden.*

of motors, which can reach the MT in the experiment, needs to be calculated. Assuming that motors within the lateral width L_{attach} around the MT can reach the MT, the area on the surface from where motors are able to attach the MT (from now on called attachment area, see fig. 4.1b) is:

$$A_{attach} = L_{attach} \times L_{MT} \tag{4.1}$$

with L_{MT} being the MT length. The number of motors within this attachment area A_{attach} is obtained by:

$$N_{attach} = A_{attach} \times \sigma_s = L_{attach} \times L_{MT} \times \sigma_s \tag{4.2}$$

with the experimentally given surface density σ_s. Having the number of motors, which can potentially attach the MT, the motor line density can be calculated

$$\lambda_{attach} = \frac{N_{attach}}{L_{MT}} = L_{attach} \times \sigma_s \tag{4.3}$$

and the mean distance between motors on the line:

$$\delta_{\text{attach}} = \frac{1}{\lambda_{\text{attach}}} = \frac{1}{L_{\text{attach}} \times \sigma_{\text{s}}}. \tag{4.4}$$

Thus, λ_{attach} is the one-dimensional motor line density corresponding to the two-dimensional experimental motor surface density σ_{s}. To distribute motors randomly over the one-dimensional modeling surface, motor tail positions are subsequently calculated as

$$x_{\text{t}}^{i+1} = x_{\text{t}}^{i} + u \tag{4.5}$$

whereby u is a random number uniformly distributed in the interval $\left[2R, \delta_{\text{attach}} - 2R\right]$ with R being the radius of the motor (see table A.1 of the appendix for parameter values and references). Once set, the motor tails are permanently bound at x_{t}^{i} during the complete simulation. As the surface, also the MT is modeled in one dimension as a one-dimensional rigid rod. Modeling the MT in one dimension can be considered the standard approach [33, 35, 36, 164, 257, 280, 292]. To characterize the MT, it is therefore sufficient to store the MT plus-end position $X_{\text{MT},+}(t)$ (or the minus-end position $X_{\text{MT},-}(t)$) in the global coordinate system and the MT length L_{MT}. A second coordinate system (body-fixed coordinate system of the MT, from now on called MT coordinate system) is chosen such that the plus-end is fixed (origin of the coordinate system) and the motors move in this coordinate system between zero and the MT length L_{MT}. Positions of MT-attached motor heads, denoted by $x_{\text{h}}^{i}(t)$, are stored in the MT coordinate system.

As a consequence of the one-dimensional representation of the MT gliding assay, molecular motors are modeled as one-dimensional, linear springs. Molecular motors have been modeled as linear springs before [33–36, 157, 160, 163, 164, 166, 176, 247, 278–280, 288, 292, 294]. The one-dimensional motor extension is calculated as the difference between head and tail positions in the global coordinate system:

$$\Delta x^{i}(t) = x_{\text{t}}^{i} - \left(X_{\text{MT},+}(t) + x_{\text{h}}^{i}(t)\right) \tag{4.6}$$

with $X_{\text{MT},+}(t) + x_{\text{h}}^{i}(t)$ being the position of the motor head in the global coordinate system. In accordance with previous studies [35, 36, 157, 163, 166, 247, 278–281], a non-zero motor rest length L_0 is assumed. This means, if the motor extension is less than the motor rest length L_0, the motor is not exerting any force on the MT. Thus, compression forces are neglected. Consequently, the motor force is given by

$$F^{i}(t) = \begin{cases} \kappa \left(\Delta x^{i}(t) - L_0\right), & \Delta x^{i}(t) > L_0 \\ 0, & \left|\Delta x^{i}(t)\right| < L_0 \\ \kappa \left(\Delta x^{i}(t) + L_0\right), & \Delta x^{i}(t) < -L_0 \end{cases} \tag{4.7}$$

with κ being the stiffness of the motor. Thereby, negative forces are defined as forces pulling the MT in negative direction of the global coordinate system and positive forces as forces pulling the MT in positive direction of the global coordinate system. See fig. 4.1c for force directions and the MT orientation. Taking together, motors, modeled as linear springs with non-zero rest lengths, exert one-dimensional forces parallel to the MT length axis.

Having characterized the geometry of the gliding assay and the motors, the update mechanism needs to be described. Motors attach with a constant rate and step and detach with force-dependent rates. MT-attached motors can exert a force on the MT. Having N_{att} motors attached

to the MT and therefore a total motor force of

$$F_{\text{tot}}(t) = \sum_{I=0}^{N_{\text{att}}} F^i(t) \tag{4.8}$$

acting on the MT, the MT needs to be moved according to the equation of motion

$$m\frac{\partial^2}{\partial t^2}X_{\text{MT},+}(t) = F_{\text{tot}}(t) - \zeta \cdot v_{\text{MT}}. \tag{4.9}$$

Thereby, Stoke's law is used with the drag coefficient ζ and the velocity of the MT v_{MT}. The efficient drag coefficient for a cylinder moved along the cylinder axis is given by [273, 301, 302]:

$$\zeta = \frac{2\pi\eta L_{\text{MT}}}{\ln(p) + \gamma_{||}} \tag{4.10}$$

with the viscosity η, the MT length L_{MT}, the MT length to MT radius ratio $p = L_{\text{MT}}/2r$ and the end-effect correction $\gamma_{||}$ for movements parallel to the cylinder axis. Approximations for the end-effect correction were used as found by de la Torre and Bloomfield [302] (based on the standard expressions of Broersma [274]). The inertia term

$$m\frac{\partial^2}{\partial t^2}X_{\text{MT},+}(t) \tag{4.11}$$

could be neglected, if the inertial force is much smaller than the viscous force, that is, if the Reynold number is low. The Reynold number is defined as

$$\mathcal{R} = \frac{F_{\text{inertial}}}{F_{\text{viscous}}} = \frac{lv\rho}{\eta} \tag{4.12}$$

with l being the characteristic length, v the speed of the object relative to the fluid, ρ the density of the fluid and η its viscosity [294, 303]. Using the viscosity and density of water, a typical MT length of $L_{\text{MT}} = 10\,\mu\text{m}$ and a speed of $v = 1\,\mu\text{m/s}$ (approx. the maximal speed of kinesin-driven gliding assays [164–167]), a small Reynold number of $\mathcal{R} \sim 10^{-5} \ll 1$ is obtained [301]. Thus, it is indeed appropriate to neglect the inertia term and model the MT in the over-damped limit. The equation of motion of the MT movement under the total force $F_{\text{tot}}(t)$ becomes:

$$m\frac{\partial^2}{\partial t^2}X_{\text{MT},+}(t) = F_{\text{tot}}(t) - \zeta \cdot v_{\text{MT}} = 0. \tag{4.13}$$

When the MT moves in the over-damped limit, the MT may reach its equilibrium position (i.e. force-free position) before the next motor event (attachment, stepping, or detachment) occurs. To check whether the MT reaches its equilibrium position before the next motor event, the time needed until reaching the equilibrium position $\Delta t_{\text{to-eq}}$ needs to be compared with the update time Δt_{update}, the time passing until the next event occurs. According to eq. (4.13), a force of $F_{\text{tot}}(t)$ generates a MT velocity of:

$$v_{\text{MT}} = \frac{F_{\text{tot}}(t)}{\zeta}. \tag{4.14}$$

This means, if the difference between the current MT position and its equilibrium position is $\Delta x_{\text{to-eq}}$, the MT approximately needs the following time

$$\Delta t_{\text{to-eq}} = \frac{\Delta x_{\text{to-eq}}}{v_{\text{MT}}} \tag{4.15}$$

to reach this equilibrium position. The MT could reach its equilibrium position before the next event occurs, if

$$\Delta t_{\text{to-eq}} < \Delta t_{\text{update}} \tag{4.16}$$

holds. Δt_{update} is thereby the time passing until the next motor event (next update of the motors) occurs. Comparing $\Delta t_{\text{to-eq}}$ and Δt_{update} from simulations[2], it can be found that Δt_{update} is typically in the order of $10^{-4} - 10^{-2}$ s, while $\Delta t_{\text{to-eq}}$ is typically in the order of $10^{-7} - 10^{-6}$ s [300]. Thus, $\Delta t_{\text{to-eq}}$ is at least 2 orders of magnitude smaller than Δt_{update}. This means the MT can indeed be moved immediately to its force-free, equilibrium position. Consequently, instead of solving the equation of motion, the MT can be updated by finding its equilibrium position after each motor event.

To find the closest force-free position of the MT, two runs of bisection search (see section 3.2) are used. The first run of the bisection search tries to find a force-free (equilibrium) MT position. Therefore, the first search interval is set as follows:

$$\Delta_{\text{first}} = \left[x_{\text{t}}^{\text{most left}} - L_0, x_{\text{t}}^{\text{most right}} + L_0 \right] \tag{4.17}$$

with the tail position of the most left, MT-attached motor $x_{\text{t}}^{\text{most left}}$ and the tail position of the most right, MT-attached motor $x_{\text{t}}^{\text{most right}}$. The first run of bisection search ends, when a force-free MT position is found. However, since motors have a non-zero rest length L_0, within which there are force-free, the found force-free MT position is not unique. Because the MT moves in the over-damped limit, it has to be found the force-free position closest to the previous MT position. To find the force-free position closest to the previous MT position, a second run of bisection search is applied. For the second run of bisection search, the first search interval ranges from the previous MT position to the force-free position found by the first run of bisection search. The second run of bisection search ends when having found the force-free position, which is closest to the previous MT position. That is how the MT is moved in the over-damped limit.

Moving the MT in the over-damped limit by finding the closest force-free position, means that rates can be considered to be time-independent. Thus, Gillespie's algorithm for time-independent rates (see section 3.2) can be used to propagate the system in continuous time [268, 298]. Since rates cannot be restored, Gillespie's first reaction method is used to select the next event [268, 298].

In summary, a complete simulation run is as follows: at the beginning, no motor is attached to the MT. In the course of the simulation the motors attach, detach and step on the MT, the time is updated by means of Gillespie's Algorithm and the MT is moved by finding the

---

[2]In this simulation, the equilibrium position is found by a bisections search algorithm (see below) and the MT is immediately moved to this position. Δt_{update} comes out of the Gillespie algorithm, which is used to find the next motor event and to propagate the time. $\Delta t_{\text{to-eq}}$ could be calculated using 4.15 when knowing the equilibrium position from the bisection search algorithm.

closest force-free position. The simulation is ended either when the simulation time is over or if no motor is attached to the MT anymore. From the experiment, it is known that if no motor is attached, the MT diffuses away from the surface. One simulation run represents the transport of one MT. In total, the simulation is run N_{samples} times to mimic several MTs in the experiment.

4.2 Unidirectional gliding assays

In this section, unidirectional kinesin- and dynein-driven gliding assays are studied. The here presented work has been published in Monzon and Scharrel et al. 2019 [300] (see chapter appendix D).

4.2.1 Kinesin-driven gliding assay

It has been previously shown that multiple kinesin motors are bound to intracellular cargo simultaneously [16, 17, 142, 155]. It is therefore intriguing to understand how multiple kinesin motors work together. This has been intensively studied before [15–17, 139, 142, 155–159, 164–167]. It has been shown that the run length of the cargo and the total force increase with increasing number of kinesin motors [15–17, 139, 142, 155–158], but the cargo velocity is independent of the number of kinesin motors [158, 159, 164–167]. Kinesin is therefore considered to weakly cooperate. The reason for the weak cooperation is thought to be the random motor extensions due to the stochastic stepping of the single kinesin motors. This results in motors, which pull the cargo back while others try to advance the cargo [152, 156, 164, 171].

As a control for the here presented gliding assay model, unidirectional, kinesin-driven gliding assay simulations are performed and compared to experiments by the Stefan Diez lab[3] to calibrate model parameters. The aim is to test whether the simulation can confirm the predictions of former studies about a weak kinesin cooperation. Having already described the geometry and the update mechanism of the gliding assay implementation, only the description of the kinesin model is missing. As said before, the model is based on previously published models by Klein et al. [35] and Kunwar et al. [33]. Here, the model is adjusted to the state-of-the-art understanding of kinesin motors. For completeness, the whole kinesin model will be presented in the following.

Kinesin model   Kinesin is modeled as a one-dimensional, linear spring with spring constant (i.e. kinesin stiffness) κ_{kin} and the kinesin-specific non-zero rest length $L_{0,\text{kin}}$. Within this rest length, the kinesin motors do not exert any force. Thus, the force a kinesin motor exerts is calculated as:

$$F^i(t) = \begin{cases} \kappa_{\text{kin}} \left(\Delta x^i(t) - L_{0,\text{kin}} \right), & \Delta x^i(t) > L_{0,\text{kin}} \\ 0, & \left| \Delta x^i(t) \right| < L_{0,\text{kin}} \\ \kappa_{\text{kin}} \left(\Delta x^i(t) + L_{0,\text{kin}} \right), & \Delta x^i(t) < -L_{0,\text{kin}} \end{cases} \tag{4.18}$$

---

[3]Experiments were performed by Lara Scharrel from Stefan Diez lab at B CUBE, TU-Dresden. See also the thesis [299]. I did not perform any experiments myself.

with $\Delta x^i(t)$ given by eq. (4.6).

Kinesin motors can perform the following events: i) attachment to the MT, ii) stepping on the MT, and iii) detachment from the MT. A kinesin motor in the attachment area under the MT (see eq. (4.1) and fig. 4.1b) binds to the MT with the kinesin-specific attachment rate $k_{a,kin}$. As in previously published molecular motor models [32–34, 163, 247, 282, 285, 287, 288], motors attach in a relaxed conformation. Here, the motor attaches at its equilibrium position x_{eq}, where the head is exactly positioned above the tail such that $\Delta x^i = x_t^i - \left(X_{MT,+}(t) + x_h^i(t) \right) = 0$ (see fig. 4.1c for an illustration). For the force-dependent stepping the previously published model by Klein et al. [35] uses the force and ATP-dependent stepping rate found by the experimental study of Schnitzer et al. [120]. In the here presented model, the same ATP and force-dependent stepping rate is applied. The force dependence of the stepping rate can be divided into three force regimes: i) assisting forces ($F^i < 0$), ii) resisting forces below stall ($F_{s,kin} > F^i > 0$) and iii) super stall forces ($F^i \geq F_{s,kin}$). In the assisting force regime ($F^i < 0$) the stepping rate does not depend on the force, but on the ATP concentration in the following Michaelis-Menten-like way:

$$s_{kin}([ATP]) = \frac{k_{cat}^0 \cdot [ATP]}{[ATP] + k_{cat}^0/k_b^0} \tag{4.19}$$

with k_{cat}^0 being the unloaded catalytic turnover rate constant and k_b^0 the unloaded second-order rate constant for ATP binding. The unloaded catalytic turnover rate is defined by the maximal kinesin forward velocity $v_{f,kin}$ divided by the step size d: $k_{cat}^0 = v_{f,kin}/d$ [35, 120]. For the unloaded second order rate constant k_b^0, the value found by Schnitzer et al. [120] is applied. A constant stepping rate under assisting forces is supported by previous single molecule experiments [124, 127, 128].

Under resisting forces ($F_{s,kin} > F^i > 0$), experimental, single molecule studies previously observed a decrease of the velocity with increasing force up to the stall force [17, 120, 124, 127, 128, 304–306]. Schnitzer et al. [120] suggested a Boltzmann-type force dependence of the rate constants:

$$k_m(F^i) = \frac{k_m^0}{p_m + q_m e^{F^i \delta / k_B T}} \quad \text{with} \quad m \in \{cat, b\} \tag{4.20}$$

with $q_m + p_m = 1$. The fraction of the unloaded catalytic cycle q_{cat} and the fraction of the unloaded ATP binding p_b are taken from Schnitzer et al. [120] and the characteristic length δ is determined such that the stepping rate is small at the stall force:

$$s_{kin}(F_{s,kin}, [ATP]) = \frac{k_{cat}(F_{s,kin})[ATP]}{[ATP] + k_{cat}(F_{s,kin})/k_b(F_{s,kin})} \overset{!}{=} 0.1 \, \text{s}^{-1}. \tag{4.21}$$

This equation is numerically solved using MATLAB. Using the Boltzmann-type force dependence of the rate constants, the stepping rate in the resisting force regime below stall ($F_{s,kin} > F^i > 0$) becomes:

$$s_{kin}(F^i, [ATP]) = \frac{v_{f,kin}/d \cdot [ATP]}{[ATP] + K_M} = \frac{k_{cat}(F^i)[ATP]}{[ATP] + k_{cat}(F^i)/k_b(F^i)}. \tag{4.22}$$

The force dependence under resisting forces is in accordance with experimental findings [17, 120, 124, 127, 128, 304].

In the super stall regime ($F^i \geq F_{s,kin}$), the kinesin motor was observed to step backward with constant velocity [116, 124, 305]. Thus, the stepping rate in the super stall regime is:

$$s_{kin} = \frac{v_{b,kin}}{d} \tag{4.23}$$

whereby $v_{b,kin}$ is the kinesin backward velocity (see table A.1 of the appendix for parameter values). If a motor is chosen to perform a step, the motor head is moved $d = 8\,nm$ back or forth in the MT coordinate system. Reaching one of the MT ends, the motor cannot step further. As only one protofilament is modeled, but the motors are supposed to reach multiple protofilaments on the MT, exclusion effects (mutual sterical hindrances) are not taken into account as in previous work [35, 164, 280].

While Klein et al. [35] and Kunwar et al. [33] used a linearly increasing detachment rate in the super stall regime, here a purely exponentially increasing detachment rate is used. The exponential detachment behavior was used in previously published kinesin models [32, 34, 151, 157, 163, 165, 176, 257, 278–283, 285, 286, 288, 292] and is predicted by the Kramer's or Bell theory [290, 291]:

$$k_{d,kin}(F^i) = k^0_{d,kin} \cdot e^{\frac{|F^i|}{F_{d,kin}}}. \tag{4.24}$$

The force dependence of all kinesin rates are shown in figure 4.14b and the parameter values used for the kinesin model are listed and discussed in table A.1 of the appendix A. Parameter values are taken from literature whenever possible. Kinesin gliding assay simulations were robust upon parameter changes.

Taking together, kinesin is modeled as a linear spring with a non-zero rest length. In the model, kinesin attaches at a constant rate, detaches at a rate that increases exponentially with the load force, and steps with a force and ATP-dependent stepping rate. Unlike the stepping where the behavior found by Schnitzer et al. [120] for kinesin-1 is used, this model reflects the standard kinesin model (see section 3.4 for a review of previous models). Having characterized the motors and the modeling of the gliding assay, results from MT gliding assay experiments and simulations will be presented in the following.

Results and discussion   As kinesin gliding assay simulations should be used to understand gliding assay experiments, first the experiments will be described. In the experiment, coverslips were coated with kinesin-1 motors at low ($\sigma_{s,\,kin} = 10\,\mu m/s$), intermediate ($\sigma_{s,\,kin} = 51\,\mu m/s$) and high densities ($\sigma_{s,\,kin} = 102\,\mu m/s$). Fluorescent labeled MTs with varying lengths were put on the motor-coated coverslip (from now on called surface). The position of the MT was measured at each second ($\Delta t_{mes} = 1\,s$). From the position, median instantaneous velocities plus interquantil ranges are calculated. Kinesin-driven velocities are denoted positive in our set-up[4]. For a better comparison with the simulation, the given MT lengths and surface densities were transformed to a median number of kinesin motors under the MT using eq. (4.2). Median instantaneous velocities are depicted as a function of the calculated median number of motors under the MT once for fixed MT length intervals and varying kinesin densities (fig. 4.2b), and once for fixed kinesin densities and varying MT lengths (fig. 4.2d). It can be seen that the MT gliding velocity neither changes with

---

[4]The geometry is chosen such that when kinesin steps towards the MT plus-end, it exerts a positive force on the MT, which generates a positive gliding velocity of the MT. See also fig. 4.1c.

a) Simulation: density dependence

b) Experiment: density dependence

c) Simulation: length dependence

d) Experiment: length dependence
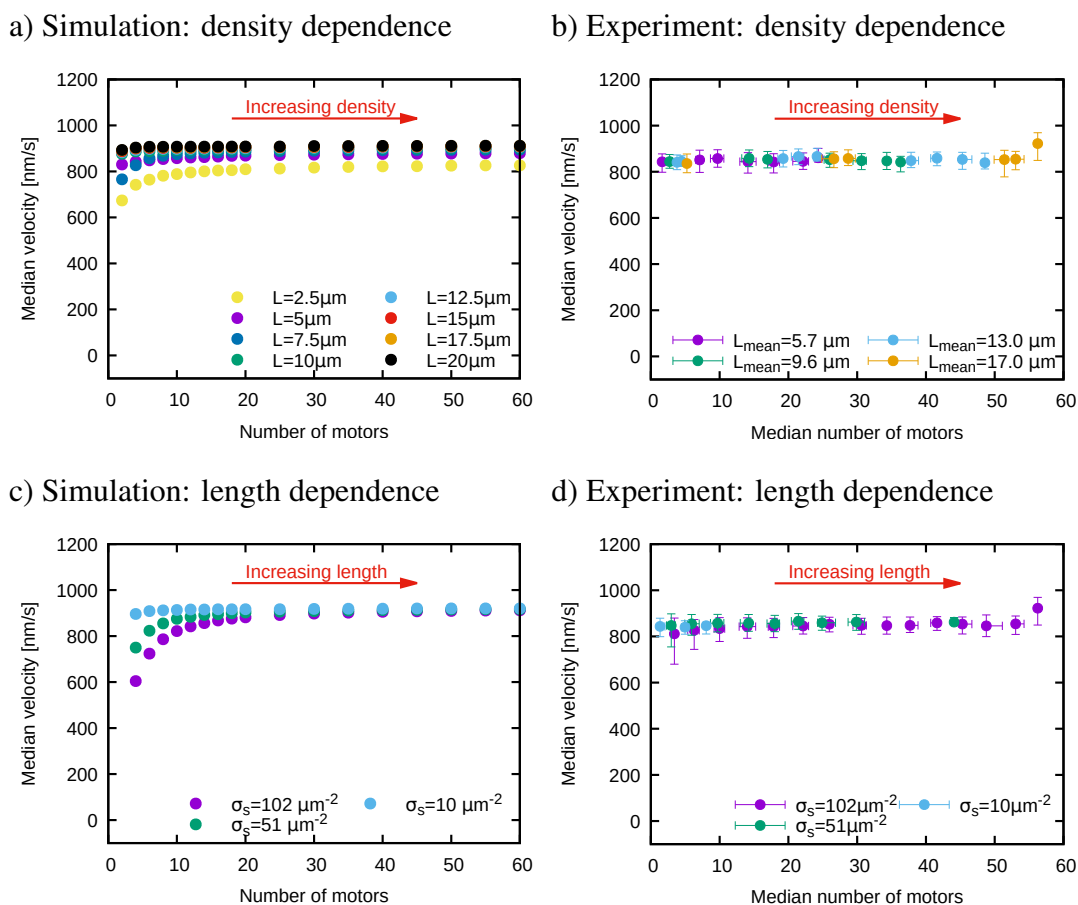
Figure 4.2: Multiple kinesin motors transport the MT at constant high velocity. For simulation (left) and experiment (right) median velocities (and interquantil range for the experiment) are depicted as a function of the number of motors. The number of motors is either varied by varying the kinesin surface density at a constant MT length (upper panels) or by varying the MT length at constant kinesin densities (lower panels). In the experiments, MT lengths were binned into intervals and mean values are given for the density dependence (fig. 4.2b). Median number of motors was calculated for MT lengths and surface densities. In the simulation, constant MT lengths were applied. For simulation and experiment, constant high median gliding velocities are observed for varying kinesin densities (fig. 4.2a and 4.2b) as well as varying MT lengths (fig. 4.2c and 4.2d). All shown experiments were performed by Lara Scharrel from Stefan Diez lab at B CUBE, TU-Dresden. *Reproduced/adapted with permission from The Company of Biologists LTd., Journal of cell science.* Originally published in *Journal of cell science*, volume 132(4), page jcs220079 (2019) [300].

increasing density at a fixed MT length (fig. 4.2b), nor with increasing MT length at a fixed surface density (fig. 4.2d). For all measured densities and MT lengths, the MT gliding velocity was around 850 nm/s. In addition, velocity histograms (fig. 4.3d and 4.3b) show sharp peaks around 850 nm/s. The findings are in accordance with previous studies saying that the velocity of multiple kinesin motors is independent of the number of kinesin motors [15, 157–159, 161, 164, 166, 167]. Thus, the experiment confirms the weak cooperation of multiple kinesin motors.

However, while most studies observed a constant high velocity for multiple kinesin motor

transport [15, 157–159, 161, 164, 166, 167], Bieling et al. [165] finds a reduction of the velocity at very high motor densities. This reduction of the velocity is presumably due to mutual steric hindrance of the motors (exclusion effects). Here, such a reduction of the velocity at high motor densities is not observed and it can be concluded that exclusion effects (mutual steric hindrance) are still negligible at the highest experimentally used kinesin density ($\sigma_s = 102\,\mu m^{-2}$). This means the model assumption that MT-attached kinesin motors do not sterically hinder each other to step or attach, is in accordance with the experiment (see model description above). Note, however, at even higher kinesin densities, exclusion effects are expected to become relevant and velocities are expected to decrease. In total, not taking exclusion effects on the MT into account is in accordance with the experiment for the applied motor densities.

To simulate the MT gliding assay, the above described gliding assay model with the above described kinesin model and the parameter values listed in table A.1 of the appendix A are used. For "measurements" during the simulation, the same measurement interval $\Delta t_{mes} = 1\,s$ as in the experiment is applied. However, when measuring the MT position in the simulation, a Gaussian noise with zero mean and variance $\sigma_p = 30\,nm$ is added to the MT position mimicking the experimental measurement uncertainty. From the MT position and the time interval of Δt_{mes}, median instantaneous velocities are calculated as for the experiment. Taking the same kinesin densities and mean MT lengths as used in the experiment, the simulation tries to reproduce the experimental data to calibrate the model.

Simulation results (fig. 4.2a and 4.2c) show high median velocities around $850 - 900\,nm/s$ as in the experiment. The velocities are widely independent of the motor number. Only at small number of motors ($N_{kin} < 8$) velocities are slightly reduced for very small MTs ($L_{MT} = 2.5\,\mu m$) and high ($\sigma_{kin} = 102\,\mu m^{-2}$) and intermediate ($\sigma_{kin} = 51\,\mu m^{-2}$) densities. If MTs are short, motors often reach the end of the MT and cannot step any further. Motors at the end of the MT need to be pulled off by other advancing motors and new motors need to attach. If not enough motors attached to the bulk of the MT exists, this causes a slight reduction of the velocity. Taking together, as the experiment, the simulation does not show a strong dependence of the velocity on the number of motors. Thus, the simulation confirms the weak cooperation between kinesin motors, which is in accordance with previous experimental and theoretical studies [159, 162, 164–167]. Hence, the simulation can be used to further investigate kinesin-driven gliding assays.

It was previously suggested that apart from sterical hindrance, MT-attached motors impair each other because of stochastically oriented motor forces [152, 156, 164, 171]. Here, the simulation is used to measure forces, which the attached motors exert on the MT (fig. 4.4b and 4.4c). It can be seen that while many motors exert positive forces (trying to move the MT in kinesin-direction) up to the kinesin stall force ($F_{s,kin} = 6\,pN$), there are also motors exerting high negative forces (holding the MT back) up to $20\,pN$ on the MT. Consequently, the latter exerts forces against the advancing motors and slows them down. In detail, about 90% of the motors exert forces close to zero, $7 - 9\%$ exert positive forces, pulling the MT in kinesin direction and $1 - 3\%$ of the attached motors hold the MT back. Because of the symmetric force dependence of the detachment rate, advancing motors need to combine forces to be able to pull the kinesin motors off, which hold the MT back. Moreover, the force histograms show that forces are not equally shared by MT-attached motors. The same was found before by the theoretical study of Uçar and Lipowsky [163]. Moreover, previous experimental studies of gliding assays observed that most motors are near zero force [164] and that there is always a small fraction of motors holding the MT back [152].
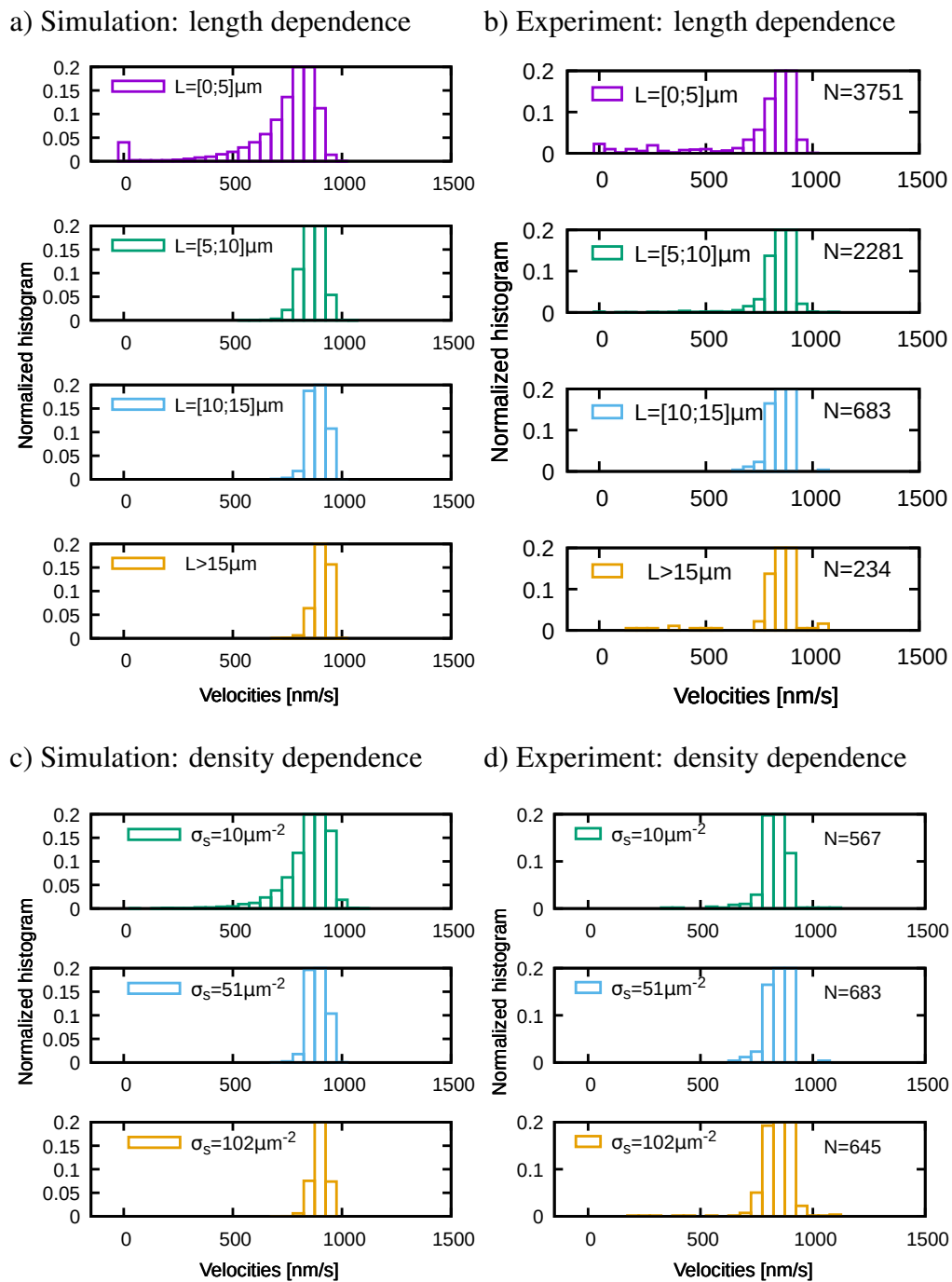
Figure 4.3: Instantaneous MT gliding velocities of kinesin gliding assay simulations and experiments. Histograms of instantaneous MT gliding velocities from simulation (left) and experiment (right). Upper panels show histograms for different MT lengths at intermediate kinesin density ($\sigma_{s,kin} = 51\,\mu m^{-2}$) and lower panels show histograms for different kinesin densities at a fixed MT length interval of $L_{MT} = [10, 15]\,\mu m$. For all simulations, the corresponding length distribution of the experiment is applied. All histograms show a peak at high MT gliding velocities ($850 - 900\,nm/s$) and the simulation reproduces the velocity histograms of the experiment. All shown experiments were performed by Lara Scharrel from Stefan Diez lab at B CUBE, TU-Dresden. *Reproduced/adapted with permission from The Company of Biologists LTd., Journal of cell science.* Originally published in *Journal of cell science*, volume 132(4), page jcs220079 (2019) [300].

Furthermore, when comparing force histograms for different number of motors, it can be seen that the force histograms do not change with the number of motors (for high number of motors; compare fig. 4.4b with fig. 4.4c). This means the percentage of motors pulling the

a) $N_{kin} = 4$ b) $N_{kin} = 30$ c) $N_{kin} = 50$
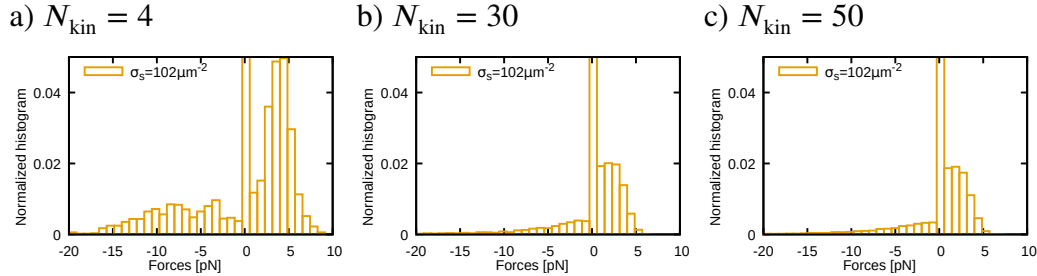
Figure 4.4: **Force distribution of MT-attached kinesin motors.** Normalized histograms of forces that MT-attached kinesin motors exert on the MT in the simulations. Positive forces pull the MT in positive direction (kinesin-driven direction) and negative forces pull the MT in negative direction (see 4.1c for the force definition). In all simulations, a kinesin density of $\sigma_{s,kin} = 102\,\mu m$ is applied and the MT length is chosen such that on average $N_{kin} = 4$ (fig. 4.4a), $N_{kin} = 30$ (fig. 4.4b) or $N_{kin} = 50$ (fig. 4.4c) motors can potentially attach the MT. For long enough MTs ($N_{kin} = 30$ and $N_{kin} = 50$) the force distribution is independent of the number of motors. For short MTs ($N_{kin} = 4$) negative and positive forces are more pronounced. In all simulations there exist motors, which pull the MT in negative direction and thereby impair the other motors from further stepping and advancing the MT.

MT back is independent of the total number of available motors under the MT. This has been shown before by the experimental study by Tjioe et al. [152]. Thus the reason for the weak kinesin cooperation is that kinesin motors are identical stochastic steppers such that a constant percentage of motors pull the MT back and slow the advancing motors down. This results in a MT gliding velocity, which is independent of the number of motors.

As previously mentioned, velocities are slightly reduced for small number of motors ($N_{kin} < 8$) in the simulation (fig. 4.2a and 4.2c). In detail, the velocities slightly reduce for small number of motors on short MTs ($L_{MT} = 2.5\,\mu m$) or at high ($\sigma_{s,kin} = 102\,\mu m^{-1}$) or intermediate densities ($\sigma_{s,kin} = 51\,\mu m^{-1}$) (see fig. 4.2a and fig. 4.2c). To obtain a small number of available motors at high (or intermediate) densities, the MT needs to be very short. Thus, slightly reduced velocities are only observed for very short MTs. Looking in detail at experimental results, it can be seen that for the smallest number of motors at the high density ($\sigma_{s,kin} = 102\,\mu m^{-1}$), the median velocity is also reduced to a very slight extent (fig. 4.2d). This indicates that also in the experiment the velocity is slightly reduced for short MTs. Thus, the reduced velocity is not an artifact of the simulation, but rather a weak, but real effect. Since the effect is less pronounced in the experiment, it can be concluded that the experimentally given surface density might be overestimated. In the experiment, it is difficult to measure the surface densities. The experimentally given surface densities are therefore just rough extrapolations from the kinesin concentration in solution. See our publication Monzon and Scharrel et al. 2019 [300] (see appendix D) for more information about the estimation procedure.

Even though the experiment supports the observation that the velocity reduces for very short MTs, it remains unclear why the velocity is reduced. Measuring the forces motors exert on (very) short MTs (fig. 4.4a), it is observed that positive forces, as well as negative forces, are more pronounced and the peak at zero is reduced. This indicates that motors impair each

other more when the MT is very short. For short MTs, the MT length becomes comparable with the motor run length ($\approx 1.5\,\mu m$ for this simulation, which is in accordance with previous experimental studies [157, 158]). If this is the case, most motors reach the MT plus-end. In the simulation (and the same is expected for the experiment), motors do not detach automatically at the end of the MT but need to be pulled off by other motors advancing the MT. For short MTs, they are not many other motors, which advance the MT and can pull off the motors at the MT end. Consequently, for short MTs, the motors at the end of the MT carry a high weight and reduce the MT gliding velocity.

Finally, the simulation is used to gain some further insides into the number of engaged motors. As previously mentioned, neither the exact number of available motors under the MT nor the number of motors attached to the MT is given by the experiment. Having calibrated the kinesin model by aligning the simulation and experiment, the simulation can be used to give an estimate for the number of available and MT-attached motors. Figure 4.5a and 4.5b show the median number of MT-attached kinesin motors as a function of the number of available kinesin motors, which are under the MT. It can be observed that almost all motors, which are
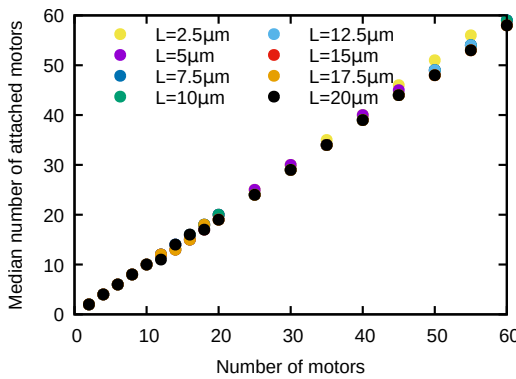
a) Simulation: density dependence b) Simulation: length dependence
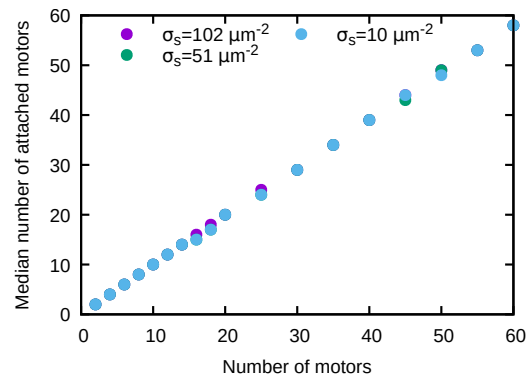
Figure 4.5: All available kinesin motors are attached to the MT. Median number of MT-attached kinesin motors as a function of the available number of motors in the simulation. The number of available motors is varied either by varying the kinesin density at a fixed MT length (left) or by varying the MT length at a fixed kinesin density (right). Both cases show that all available motors are attached to the MT.

able to attach the MT, are attached to the MT. From that, it can be predicted that up to 60 motors are expected to transport the MT at constant high velocities.

In summary, experiment and simulation show widely constant high gliding velocities independent of the number of MT-attached kinesin motors. These findings are conform with previous gliding assay studies [164, 166, 167]. Using the simulation, it can be shown that MT-attached motors exert forces against each other and thereby impede a cooperation between multiple kinesin motors. Weak kinesin cooperation was found before theoretically and experimentally [152, 157, 162, 164]. Having well-calibrated the kinesin model, the here presented kinesin model will be used in section 4.3 to investigate bidirectional, kinesin, and dynein gliding assays.

4.2.2 Dynein-driven gliding assay

It is known that intracellular cargo is transported by multiple dynein motors [13, 17, 20, 142, 147]. To get a better understanding of the pure system without any additional influence factors, mammalian, cytoplasmic dynein without adaptor proteins is studied. Single mammalian dynein motors without adaptor proteins (from now on referred to as dynein) are known to be weakly processive and to only perform diffusion-like motion [89, 90, 307]. How multiple such dynein motors work in a team has been studied before [89, 158, 163, 172]. It has been observed that run length increases with increasing number of motors [158, 172] and forces generated by multiple dynein motors are additive [17, 89, 142, 172]. Unlike single dynein, multiple dynein motors were observed to perform directional motion [172]. The velocity of multiple dynein motors without adaptor proteins has been shown to be very high (1000 nm/s) [89]. Moreover, it could be shown that the drift part of the multiple dynein motility increases with increasing number of motors [89]. However, a complete analysis of how the transport velocity depends on the number of dynein motors is missing. Moreover, it remains unclear how dynein motors, which show non-processive and diffusive motion on the single molecule level, can produce such high velocities when working in a team.

To understand how multiple dynein motors work in a team, the dynein-driven gliding assay is modeled. The gliding assay is modeled as introduced in section 4.1 and for dynein, a model is used, which is based on the previously reported models by Kunwar et al. [33] and Klein et al. [35]. Here, the model is adjusted to the current knowledge of single dynein properties. In the following, the complete model is presented.

Dynein model Dynein is modeled as a one-dimensional linear spring with a non-zero rest length $L_{0,\mathrm{dyn}}$, as in previous studies [33–36, 163, 288]. Because dynein is a big, roundish molecule, the here presented model assumes that dynein even exerts a small force when being stretched less than its rest length ($|\Delta x^i| < L_{0,\mathrm{dyn}}$). Therefore a non-zero, but small spring constant is applied when the dynein extension is less than its rest length and a higher spring constant (stiffness) when it is stretched more than its rest length ($|\Delta x^i| > L_{0,\mathrm{dyn}}$). Different spring constants in dependence of the motor extension have not been used in the previously published models by Kunwar et al. [33] and Klein et al. [35]. The dynein force production can be summarized as follows:

$$F^i(t) = \begin{cases} \kappa_{1,\mathrm{dyn}} \cdot L_{0,\mathrm{dyn}} + \kappa_{2,\mathrm{dyn}} \cdot \left(\Delta x^i(t) - L_{0,\mathrm{dyn}}\right), & \Delta x^i > L_{0,\mathrm{dyn}} \\ \kappa_{1,\mathrm{dyn}} \cdot \Delta x^i(t), & |\Delta x^i| < L_{0,\mathrm{dyn}} \\ -\kappa_{1,\mathrm{dyn}} \cdot L_{0,\mathrm{dyn}} + \kappa_{2,\mathrm{dyn}} \cdot \left(\Delta x^i(t) + L_{0,\mathrm{dyn}}\right), & \Delta x^i < -L_{0,\mathrm{dyn}} \end{cases} \quad (4.25)$$

with the motor extension $\Delta x^i(t)$ given by eq. (4.6), the motor stiffness $\kappa_{1,\mathrm{dyn}}$ when the motor is stretched less than its rest length and $\kappa_{2,\mathrm{dyn}}$ when the motor is stretched more than its rest length. Thus, it holds $\kappa_{1,\mathrm{dyn}} < \kappa_{2,\mathrm{dyn}}$.

During the simulation, dynein can perform the following events: i) attach to the MT, ii) step on the MT, or iii) detach from the MT. All dyneins within the attachment area (see eq. (4.1)) can potentially attach to the MT with their head region. Dynein motors attach with the constant rate $k_{a,\mathrm{dyn}}$. Like kinesin, they attach in a relaxed conformation. Exerting a force even when being stretched less than its rest length, the only force-free position is when tail and head positions are identical and $\Delta x^i(t) = 0$. Thus, dynein attaches to its equilibrium position (compare fig.

4.1c). Unlike kinesin, where exclusion effects are neglected, dynein can only attach when its equilibrium position on the MT is empty. Because dynein covers a higher area on the MT (radius $R_{dyn} = 24$ nm [89, 95, 308]) than kinesin (radius $R_{kin} = 4$ nm [193]), it is assumed that exclusion effects (mutual steric hindrance) need to be taken into account. This is in accordance with the experimental results (see below). As in the model by Klein et al. [35], the same piecewise defined force-velocity curve is applied for dynein as previously found for kinesin [120]. Please see equations (4.19), (4.22) and (4.23) for motor stepping in the different force regimes: i) assisting forces ($F^i > 0$), ii) resisting forces below stall ($-F_{s,dyn} < F^i < 0$) and iii) super stall forces ($F^i < -F_{s,dyn}$). Note that assisting/resisting forces have the opposite sign for dynein than for kinesin. However, while the curve is the same as for kinesin, the parameters are adjusted to known dynein values: for the stall force, a previously reported mammalian dynein stall force is applied (see table A.1 of the appendix A). For the maximal, force-free velocity, the dynein single molecule velocities from the experiment are used as mean force-free forward velocities. While for kinesin, a constant maximal velocity is applied, for dynein a wide maximal forward velocity distribution is used to generate individual force-free forward velocities for dynein motors. A wide maximal single molecule velocity has previously been experimentally observed for single dynein motors [94, 95, 104]. Here, a Gaussian distribution with mean $v_{f,dyn,mean}$ and standard deviation $\sigma_{v,dyn}$ truncated at $v_{f,dyn,lowest}$ and $v_{f,dyn,\,highest}$ is used. The Gaussian is truncated to avoid too small or even negative velocities. $v_{f,dyn,lowest}$ and $v_{f,dyn,\,highest}$ are chosen in such a way that the distribution remains symmetric around the mean. During the simulation, each motor obtains its own maximal velocity drawn from the truncated Gaussian distribution. Having a different stall force, also a different characteristic length for the Boltzmann-type force dependence of the first and second order rate constants is found (see eq. 4.21). Finally, for the constant backward velocity a previously reported yeast dynein value is applied, which is almost double the kinesin value. As for the attachment also for the stepping exclusion effects need to be considered. This means, dynein can only perform a step when the next site on the MT is empty and dynein can only attach to the MT when its equilibrium position is empty. To perform a step, the same step size as for kinesin is used: $d = 8$ nm.

While Klein et al. [35] and Kunwar et al. [33] implemented a catch-bond detachment in the super stall regime for dynein, the state of art knowledge is that dynein performs a "slip-bond" under assisting forces and a "slip-ideal bond"[5] under resisting forces [86, 92]. In particular, Cleary et al. [86] find that the detachment rate increases faster under assisting loads than under resisting loads. The detachment behavior of Cleary et al. [86] is modeled here:

$$k_{d,dyn}(F^i) = \begin{cases} -0.1\,F^i + 0.4 & \text{for} \quad F^i \leq 0 \\ 3.2\,F^i + 0.4 & \text{for} \quad F^i > 0. \end{cases} \tag{4.26}$$

The force dependence of all dynein rates is shown in figure 4.14c and the parameter values used for the dynein model are listed and discussed in table A.1 of the appendix A.

Taking together, the dynein model is based on the previously published models by Klein et al. [35] and Kunwar et al. [33]. Compared to previous models, here, it is added that dynein exerts a small force when being stretched less than its rest length. Moreover, a linear detachment is modeled adjusting the model to the state-of-art knowledge of dynein. Furthermore, a more realistic maximal velocity is used by applying a truncated Gaussian distribution.

---

[5]Meaning a detachment rate which increases only very slowly with force, i.e. a detachment behavior somewhere in between a slip bond and an ideal bond.

a) Simulation: density dependence

b) Experiment: density dependence

c) Simulation: length dependence

d) Experiment: length dependence
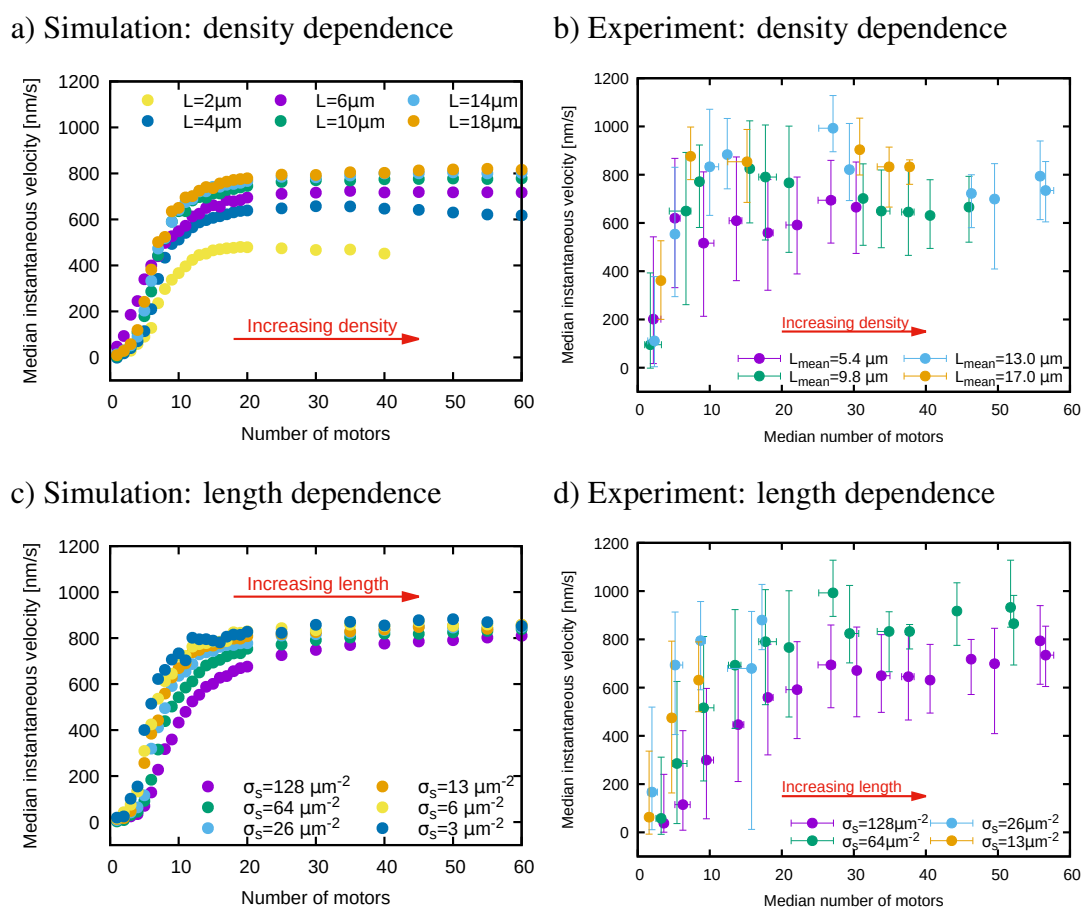
Figure 4.6: Mechanical dynein activation model reproduces the increased dynein cooperation with increasing number of motors. Median instantaneous velocities (plus interquantil range for experiment) are depicted as a function of the number of motors for simulation (left) and experiment (right). Motor numbers are varied by the dynein density at fixed MT length (upper panels) or by the MT length at fixed dynein densities (lower panels). For experimental fig. 4.6b MT lengths are binned into intervals and mean values are given. Constant MT lengths are applied in all depicted simulations. All simulations are performed using the mechanical dynein activation model. For simulation and experiment a transition from small velocities (< 100 nm/s) to high velocities (> 800 nm/s) can be seen as a function of the number of motors. Moreover, a slightly reduced velocity is seen for high motor numbers on short MTs (high densities, see fig. 4.6a and fig. 4.6b) for simulation and experiment. Thus, when using the mechanical dynein activation model a good alignment between simulation and experiment has been achieved. All experiments were performed by Lara Scharrel from Stefan Diez lab at B CUBE, TU-Dresden. *Reproduced/adapted with permission from The Company of Biologists LTd., Journal of cell science.* Originally published in *Journal of cell science*, volume 132(4), page jcs220079 (2019) [300].

Results and discussion In the experiment[6], the coverslip (referred to as surface) was coated with dynein at varying densities. Fluorescent-labeled MTs with varying lengths were placed on the surface. MT positions were measured after each $\Delta t_{\mathrm{mes}} = 1$s to calculate

---

[6]Experiments were performed by Lara Scharrel from Stefan Diez lab at B CUBE, TU-Dresden. See also the thesis [299]. I did not perform any experiments myself.

instantaneous gliding velocities. To investigate the influence of the number of motors, the dynein surface density was varied as well as the MT length. For a better comparison with the simulation, the MT length at a given dynein density was transformed to a number of motors using eq. (4.2). Median instantaneous velocities are depicted as a function of the number of motors. The number of motors is once varied by the dynein density at a fixed MT length interval (fig. 4.6b) and once by the MT length at a fixed dynein density (fig. 4.6d). Note that even though, dynein-driven velocities are negative in this set-up (compare fig. 4.6), velocities are shown as positive values in this section for simplicity.

Experimental results (fig. 4.6b and 4.6d) show low instantaneous median gliding velocities ($\sim 50 - 100\,\text{nm/s}$) at low number of motors ($\lesssim 5$ motors) and an increase in median velocities up to approximately $900\,\text{nm/s}$ for higher number of motors. Thus, knowing that single dynein motors diffuse on the MT, the experiment suggests that with increasing number of motors the diffusive dynein motion becomes a directed transport at high velocities. This indicates

a) Simulation: density dependence

b) Simulation: length dependence
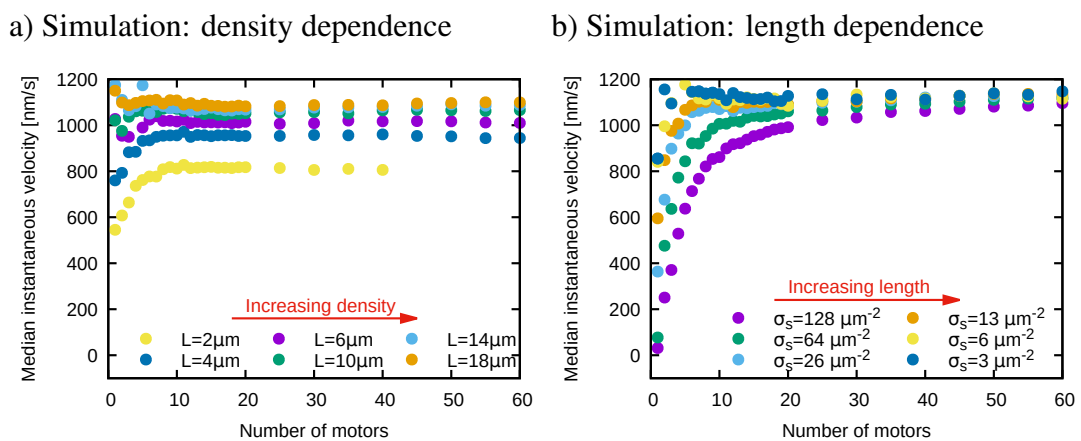
Figure 4.7: High gliding velocities in the absence of passive dynein motors. Median instantaneous velocities are depicted as a function of the number of motors varied by the dynein density at a fixed MT length (left) or by the MT length at a fixed dynein density (right). All simulations were performed using the dynein model, where only active dynein motors exist, but no passive dynein motors and no mechanical dynein activation. The simulation almost exclusively shows high MT gliding velocities and no transition from small to high velocities. Reduced velocity can only be seen for short MTs (low number of motors at high densities, see fig. 4.7b). *Reproduced/adapted with permission from The Company of Biologists LTd., Journal of cell science.* Originally published in *Journal of cell science*, volume 132(4), page jcs220079 (2019) [300].

strong cooperation between dynein motors. When varying the number of motors by the dynein density (fig. 4.6b), the velocity first increases with motor number, but then decreases again at very high motor numbers. This indicates that at high dynein density, the dynein motors sterically hinder each other. That is why, exclusion effects cannot be neglected when modeling the dynein assay at these dynein densities. When comparing median velocities for the same number of motors, but different MT lengths (see fig. 4.6b), it can be seen that longer MTs are transported at higher velocities. Thus, the same number of dynein motors performs better on longer MTs. To summarize, the experiment shows an increasing dynein cooperation with increasing number of motors, exclusion effects at high densities and higher velocities for longer MTs.

High velocities for a high number of dynein motors have been observed before [89]. Several previous studies suggest that the transport performed by multiple dynein motors depends on the number of motors. For instance, it has been shown that the motile fraction [87, 88] or the drift part of cargo transport by multiple dynein motors [89] increases with increasing number of motors. Moreover, gliding assays were performed for axonemal [173], inner-arm dynein c [174], and dynein 2 [98]. They all show an increase in the velocity for increasing number of motors. The here shown experimental results confirm the number of motor dependence for mammalian cytoplasmic dynein without adaptor proteins and explicitly show how the velocity depends on the number of motors. The MT gliding velocity was found to continuously increases with the number of motors as long as exclusion effects do not play a role. At high dynein densities, however, motors sterically hinder each other (exclusion effect) and the velocity reduces. A reduced velocity at high motor numbers has been observed before for kinesin [165], but not for dynein. Moreover, the experiment shows higher velocities for longer MTs at the same number of motors. This has not been observed before and might be a hint for the underlying mechanism of cooperation. Forces applied by multiple dynein motors were shown to be additive [89, 163, 172]. That is why a better performance of multiple dynein motors would be expected. However, multiple kinesin motors also produce higher forces but do not cooperate to produce higher velocities (see above). This means, even though for both motors higher forces are observed when working in a team [15–17, 142, 142], the kinesin velocity does not depend on the number of motors, while the dynein velocity increases with increasing number of motors. Moreover, kinesin teams never reach velocities higher than the single kinesin molecule velocity. Dynein teams, however, reach velocities more than 30-fold higher than the drift velocity of single dynein motors (ca. 21 nm/s) [89]. Yet another difference is that at high motor numbers, for kinesin, velocity histograms show sharp peaks at high velocities, while for dynein, histograms show a wide distribution of intermediate and high velocities. It remains unclear why for dynein, velocity histograms show such wide distributions of high velocities and how dynein motors increase the velocity with increasing number of motors up to values higher than the single molecule velocity.

To shed light on dynein-driven multi-motor transport, the dynein-driven gliding assay is simulated using the above introduced dynein model. As in the experiment, the number of motors is once varied by the dynein density at a fixed MT length and once by the MT length at a fixed dynein density. Fig. 4.7a and fig. 4.7b show median instantaneous velocities as a function of the motor number at fixed MT lengths or at fixed dynein densities, respectively. Almost exclusively high MT gliding velocities are observed, when the number of motors is increased by the dynein density at fixed MT lengths. When increasing the motor number by the MT length at fixed dynein densities, also mainly high MT gliding velocities are observed. In this case, however, some smaller velocities could be observed for high dynein densities and small number of motors. The same effect has been observed for kinesin at high densities and small number of motors. As previously mentioned, realizing a small number of motors at a high density means that the MT is very short. For kinesin, it was found that at very short MTs, the motors which reached the end of the MT slow down the MT (see above). The slowing down due to motors reaching the end of very short MTs, could also be the reason for the smaller velocities at high dynein densities and small motor numbers in the dynein-driven gliding assay simulation.

The comparison between experiment and simulation reveals that the simulation shows mainly constantly high velocities for all numbers of motors, while the experiment shows a slow transition from small to high velocities as a function of motor numbers (see fig. 4.7 for the

a) Simulation: length dependence

b) Experiment: length dependence

c) Simulation: density dependence

d) Experiment: density dependence
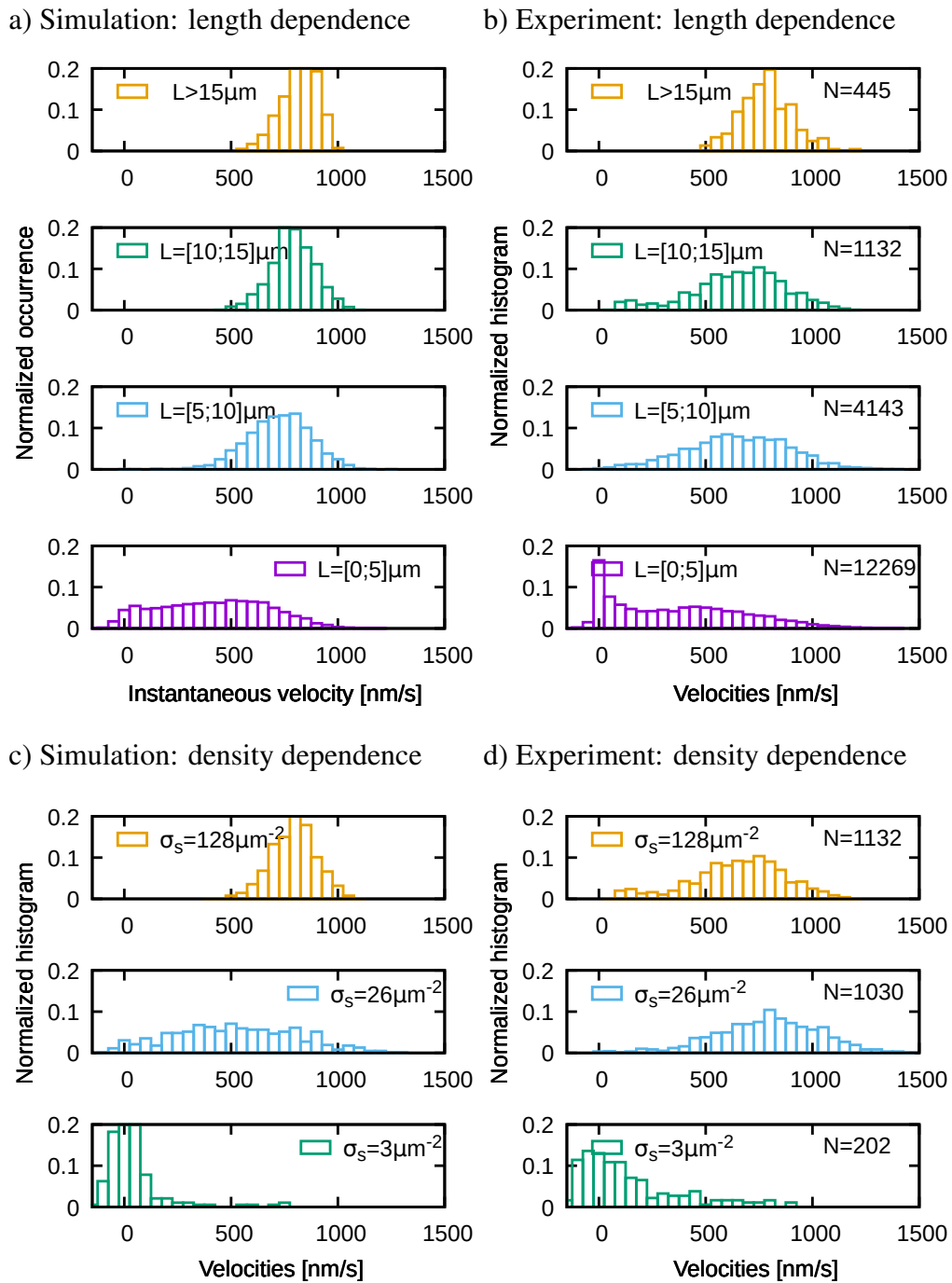
Figure 4.8: Simulation reproduces histograms of instantaneous dynein velocities. Normalized histograms of instantaneous MT gliding velocities from simulation (left) and experiment (right). Upper panels show histograms for different MT lengths at a dynein density of $\sigma_{s,dyn} = 128\,\mu m^{-2}$ and lower panels show histograms for different dynein densities at a fixed MT length interval of $L_{MT} = [10, 15]\,\mu m$. For all simulations, the corresponding length distribution of the experiment is applied. For the length dependence (upper panels) as well as for the dynein density dependence (lower panels) an increase of the velocity with increasing length or increasing dynein density is observed, respectively. The simulation reproduces the velocity histograms of the experiment. (*Continuation on next page.*)

Figure 4.8 *(previous page)***:** All experiments were performed by Lara Scharrel from Stefan Diez lab at B CUBE, TU-Dresden. *Reproduced/adapted with permission from The Company of Biologists LTd., Journal of cell science*. Originally published in *Journal of cell science*, volume 132(4), page jcs220079 (2019) [300].

simulation and fig. 4.6 for the experiment). Thus, the experimentally observed, increasing cooperation between dynein motors is missing in the simulation.

Previous experimental studies show that single dynein without adaptor proteins show (biased) diffusion-like motion [89, 94]. In the current dynein model, however, all dynein motors step directedly toward the MT minus-end when experiencing a load force smaller than the dynein stall force. The missing diffusion-like motion of single dynein motors might be the reason why only high velocities are observed for all numbers of motors. Furthermore, Torisawa et al. [89] show first that the drift part of MT gliding velocities increases with increasing number of dynein motors and second that dynein can be mechanically activated (directed motion in the active state) when physically separating the dynein heads with a rigid rod. That is why, here, a mutual, mechanical dynein activation is hypothesized for dynein attached to the MT. Since high velocities (assumed to come from active dynein motors) can also be seen for long MTs with low dynein density, a mutual activation via direct motor-motor interactions can be ruled out. Consequently, here it is assumed that MT-attached dynein motors activate each other when indirectly being coupled via the rigid MT.

In the following, the dynein activation model is presented. For the dynein activation model, diffusive dynein motors (called passive dynein motors), which activate when being stretched by the other MT-attached motors, are added to the above presented dynein model.

Mechanical dynein activation model To add passive motors, which diffuse on the MT to the above presented dynein model, first, the diffusion coefficient of these motors needs to be estimated from the experiment. Therefore, it is assumed that negative velocities (MT gliding in positive direction), which are frequently observed for low number of motors, come from the diffusive motion of passive dynein motors[7]. To calculate the diffusion coefficient, the distribution of negative velocities is mirrored at the y-axis and fitted by a Gaussian function. Having a one-dimensional Gaussian with zero mean, the diffusion coefficient can be calculated from the variance of the Gaussian (see section A.1 of appendix A for a detailed calculation). The calculated diffusion coefficients ($D \sim 10^{-3}$) are three orders of magnitude smaller than the diffusion coefficient of a freely diffusive rigid cylinder with a length similar to the used MTs ($D_{MT} \sim 10^{-6}$ using the formulas given by [302], compare chapter 3). This rules out that the negative velocities come from freely diffusing MTs. Fig. 4.9 shows the calculated, experimental diffusion coefficients as a function of the number of motors. With increasing number of motors the diffusion coefficient decreases. This is expected for a diffusion in a harmonic potential which increases with the number of motors.

From the experimental data, the diffusion coefficients could be calculated for 2, 6, 10, 14, and 18 dynein motors. To determine the single motor diffusion coefficient, the diffusive motion of multiple passive MT-attached dynein motors is implemented and adjusted to the experimentally given diffusion coefficients for 2,6,10,14 and 18 dynein motors. For the

---

[7]It can be ruled out that the negative velocities come from a freely diffusive MT because a freely diffusing MT would immediately move out of the focus of the camera and would therefore not be tracked any longer.

"dynein-diffusion" simulation, the MT is modeled with periodic boundaries for simplicity. Moreover, a fixed number of passive dynein motors is applied, which are permanently attached to the MT. The one-dimensional diffusion of the passive motors in the harmonic potential of the motors springs is simulated using the Metropolis algorithm (see section 3.2). Thereby, for the stepping of the motors on the MT, exclusion effects are taken into account. By varying the free diffusion rate s_0 of the passive motors (diffusion rate in the absence of a harmonic potential), the simulation diffusion coefficients can be fitted to the experimental results (see fig. 4.9). That is how the best choice for the free diffusion rate s_0 of single passive dynein motors is found (see table A.1 of the appendix A for parameter values). Having the diffusion rate of passive dynein motors, passive dynein motors can be added to the above presented dynein model.

In the refined dynein model, called mechanical dynein activation model, dynein motors have two states: active and passive. All dynein motors attach in the passive state with the same attachment behavior as described before and all dynein motors detach with the same detachment rate as introduced previously (see eq. 4.26). While the at- and detachment rates do not change, the stepping of the passive motors differs from the above introduced stepping of active motors. Passive MT-attached motors perform a random walk in the harmonic potential of their motor springs. Thus they step with the following rate:

$$s_{\pm}\left(F^i\right) = s_0 e^{\mp\beta\frac{F^i \cdot d}{2}} \tag{4.27}$$

Figure 4.9: **To estimate the single dynein diffusion constant, the simulation diffusion constant is aligned to the experimental diffusion constant.** The distribution of negative experimental velocities was mirrored at the y-axis and fitted by a Gaussian distribution. From the obtained variance of the Gaussian fit, the diffusion constant as a function of the number of motors can be calculated (see section A.1 of appendix A). In the simulation, the energy landscape of the diffusion in the harmonic potential of the motor springs is implemented using the Metropolis algorithm (see section 3.2). Diffusion coefficients as a function of the number of motors decrease with increasing number of motors. By optimizing the force-free diffusion constant (s_0), simulation results could be fitted to the experimental diffusion coefficients. All shown experiments were performed by Lara Scharrel from Stefan Diez lab at B CUBE, TU-Dresden. *Reproduced/adapted with permission from The Company of Biologists LTd., Journal of cell science.* Originally published in *Journal of cell science*, volume 132(4), page jcs220079 (2019) [300].

with the step size d, the thermal energy β, the individual motor load force F^i and the free diffusion rate s_0, which was found with the dynein-diffusion simulation. $\pm$ stands for stepping towards the plus- and minus-end, respectively. Besides stepping and detaching, passive MT-attached motors can activate and active MT-attached motors can deactivate. Because a direct coupling of the motors (direct motor-motor interaction) could be ruled out, a mechani-
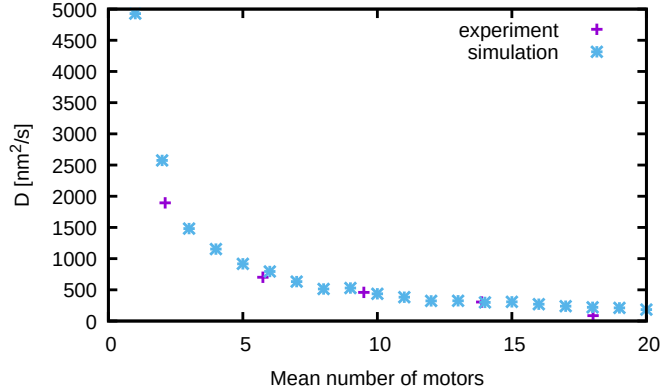
cal dynein activation by stretching the motors is assumed. In detail, if a passive MT-attached motor is stretched outside the deactivation region around its equilibrium position $x_{\text{eq}}^i \pm L_{0,\text{dyn}}$ (i.e. the motor extension $|\Delta x^i|$ is bigger than the untensioned length $L_{0,\text{dyn}}$, see fig. 4.10), it stochastically activates. For the stochastic activation process, an Arrhenius activation rate is used:

$$r_{\text{a}}\left(\Delta x^i\right) = r_{\text{a}}^0 \left(1 - e^{-\frac{E_{\text{a}}}{k_{\text{B}}T}}\right) \tag{4.28}$$

whereby the activation energy E_{a} is given by

$$E_{\text{a}} = \frac{1}{2}\left(\kappa_{1,\text{dyn}} L_{0,\text{dyn}}^2 + \kappa_{2,\text{dyn}}\left(|\Delta x^i| - L_{0,\text{dyn}}\right)^2\right). \tag{4.29}$$

The maximal activation rate r_{a}^0 and the stiffness $\kappa_{1,\text{dyn}}$ are a priori unknown parameters, which were determined by aligning the simulated median velocity to the experimental median velocity as a function of the number of available dynein motors. If an active MT-attached motor is stretched inside the deactivation region (see fig. 4.10), it deactivates with the constant rate r_{d}. Multiple passive MT-attached dynein motors are mechanically coupled via the rigid MT. When diffusively stepping and thereby diffusively transporting the MT, passive MT-attached dynein motors stochastically exert forces on each other and thereby stretch each other. A passive MT-attached motor can thereby occasionally be stretched outside the deactivation region and activate (see illustration fig. 4.10). An active MT-attached motor then starts to pointedly step towards the MT minus-end and directedly transports the MT. It thereby stretches other passive MT-attached motors even more such that they also start to activate. That is how a mutual mechanical dynein activation can be achieved.

To see whether the dynein activation model can capture the increase in velocity with increasing number of motors, dynein densities and MT lengths are varied and median instantaneous velocities were measured as above. Median instantaneous velocities are depicted as a function of the number of motors once for fixed MT lengths varying the number of motors by the dynein density (fig. 4.6a) and once for fixed dynein densities varying the number of motors by the MT length (fig. 4.6c). Simulation results using the dynein activation model show small velocities (< 100 nm/s) for small number of motors ($\lesssim 5$ motors) for all MT lengths and all dynein densities as it was observed in the experiment. Furthermore, the velocity increases up to high velocities (> 800 nm/s) with increasing number of motors in accordance with the experiment. For high motor densities (high motor numbers on short MTs: $L_{\text{MT}} = 2\,\mu\text{m}$ or $L_{\text{MT}} = 4\,\mu\text{m}$ in fig. 4.6a), the simulation shows slightly reduced velocities due to exclusion effects (steric hindrance). The same is seen in the experiment. Besides the median instantaneous velocities, also velocity histograms of the simulation show a similar behavior as the experiment (see fig. 4.8). This means, using the mechanical dynein activation model, the simulation can be aligned with the experiment. Consequently, the mechanical activation based on the indirect, mechanical coupling of the motors via the MT explains the increasing cooperation between dynein motors with increasing number of motors.
A mechanical dynein activation has not been introduced to any theoretical dynein model before. Earlier experimental studies, however, suggest some kind of mechanical activation or gave hints to it [13, 88, 89].

The *in vivo* experiment by Ally et al. [13], for instance, finds that opposite-directed kinesin and dynein motors need each other for transport and demonstrates that impairing one kind of motor will stop the complete movement. They hypothesize that a mutual mechanical activation is the underlying mechanism for their findings. Another hint gives the study by Belyy et al. [88], which shows that single dynein motors transport larger beats at higher velocities than smaller beats. Since a higher force is needed to transport a larger beat, it can be suggested that the larger beat stretches the dynein motors. According to our model, a stretching of the dynein motor would occasionally activate the motor and could explain the slightly higher velocities. Moreover, as previously mentioned, Torisawa et al. [89] show that dynein motors, where the two motor heads were physically separated by a rigid rod, move processively and directedly

Figure 4.10: Deactivation region. Illustration shows the dynein deactivation region ($x_{eq} \pm L_{0,dyn}$; green), given by the dynein untensioned length $L_{0,dyn}$. The right passive motor (light blue) is stretched outside the deactivation region and therefore activates with rate $r_a(\Delta x^i)$ and the left active motor (dark blue) is stretched inside the deactivation region and therefore deactivates with rate r_d.

towards the MT minus-end. This suggests that besides adaptor proteins there might be another, mechanical mechanism to pull dynein out of its inhibited state. Zhang et al. [90] found that adaptor proteins align the dynein motor heads to pull dynein out of the inverted (inhibited) state (see section 2.2.1 for details). Here, it is hypothesized that when stretching the complete molecule, the two heads align automatically and are thus mechanically pulled out of the inhibited state. Moreover, it is hypothesized that dynein without adaptor proteins, but with mechanically aligned heads, show high velocities as observed for dynein activated by adaptor proteins. In summary, the mechanical dynein activation model is supported by previous studies.

The experiment showed higher velocities for longer MTs at the same number of motors (see fig. 4.6b). The simulation shows the same effect and can explain it. Therefore, the dynein activation ratio, defined as the ratio of active MT-attached to passive MT-attached motors, is calculated:

$$f_a = \frac{\text{Number of active MT-attached dynein motors}}{\text{Number of passive MT-attached dynein motors}} = \frac{N_a}{N_p}. \tag{4.30}$$

The activation ratio gives the relative contribution of active to passive MT-attached motors. The activation ratio is displayed as a function of the number of motors for fixed MT lengths (fig. 4.11a) or fixed dynein densities (fig. 4.11b). It can be seen that the activation ratio strongly increases with the number of motors for $N_{dyn} < 20$ and levels off for higher number of motors or even slightly decreases, where exclusion effects become relevant (fig. 4.11a, for $L_{MT} = 2\,\mu m$ and $L_{MT} = 4\,\mu m$). Comparing the activation ratio with the median velocity, it can be seen that both show a similar dependence on the number of motors. This suggests that the activation ratio determines the MT gliding velocity. Moreover, the median velocity as the activation ratio are higher for longer MTs at the same number of motors. This implies on longer MTs more of the attached motors are activated. A motor presumably stays activated
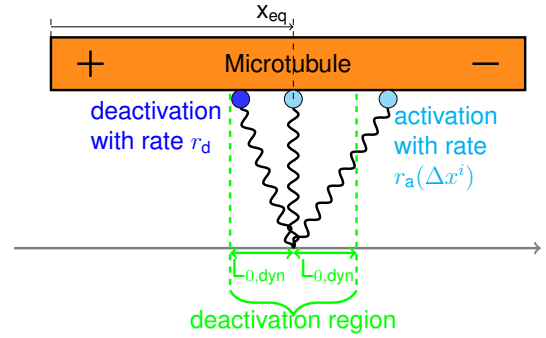
a) Simulation: density dependence   b) Simulation: length dependence

Figure 4.11: Dynein activation ratio determines median velocities. Dynein activation ratio is depicted as a function of the number of motors for fixed MT lengths (right) and fixed dynein densities (left). The activation ratio is calculated by dividing the mean number of actively MT-attached motors by the mean number of passive MT-attached motors. All simulations were performed using the mechanical dynein activation model. For both cases, the activation ratio increases with increasing number of motors. For motor numbers over 20, the activation ratio starts to level off. Comparing the activation ratio with the median velocity as a function of the number of motors (see fig. 4.6), it can be seen that the dependence is similar. Thus, the simulation suggests that the activation ratio determines the median gliding velocity. *Reproduced/adapted with permission from The Company of Biologists LTd., Journal of cell science.* Originally published in *Journal of cell science*, volume 132(4), page jcs220079 (2019) [300].

until reaching the end of the MT, if it is not hindered by other motors or stochastically detaches. Hence, the longer the MT, the longer a motor can stay activated. On shorter MTs, the attached motors have to detach more frequently and new motors have to attach. Each time a new motor attaches, it first needs to be stretched outside the deactivation region to activate. Only when being activated, a motor contributes to the directed movement of the MT. That is why more of the attached motors are activated on longer MTs leading to a higher activation ratio and consequently a higher median velocity. Additionally, the number of active MT-attached motors is reduced and the number of passive MT-attached motors increased when exclusion effects play a role (see fig. 4.11a). This means, if an active motor is hindered by other MT-attached motors, it is likely to deactivate again because it cannot continue stepping. That is why, the activation ratio and therefore, the median velocity is slightly reduced, where exclusion effects are relevant (fig. 4.11a for $L_{MT} = 2\,\mu m$ and $L_{MT} = 4\,\mu m$). Taking together, higher median velocities come along with a higher activation ratio and reduced median velocities with a reduced activation ratio. Consequently, the simulation suggests that the median velocity is directly determined by the activation ratio.

Besides measuring the activation ratio, active MT-attached and passive MT-attached motors are depicted as a function of the number of available motors, separately. Both passive MT-attached and active MT-attached motors increase with increasing number of motors at a fixed MT length (fig. 4.12c and fig. 4.12a) and for a fixed dynein density (fig. 4.12d and 4.12b). Neither for actively MT-attached motors nor for passive MT-attached motors a saturation of the number of MT-attached motors is visible. However, for high number of motors ($N_{dyn} > 20$), active and passive MT-attached motors increase with a similar slope

a) Simulation: density dependence

b) Simulation: length dependence

c) Simulation: density dependence

d) Simulation: length dependence
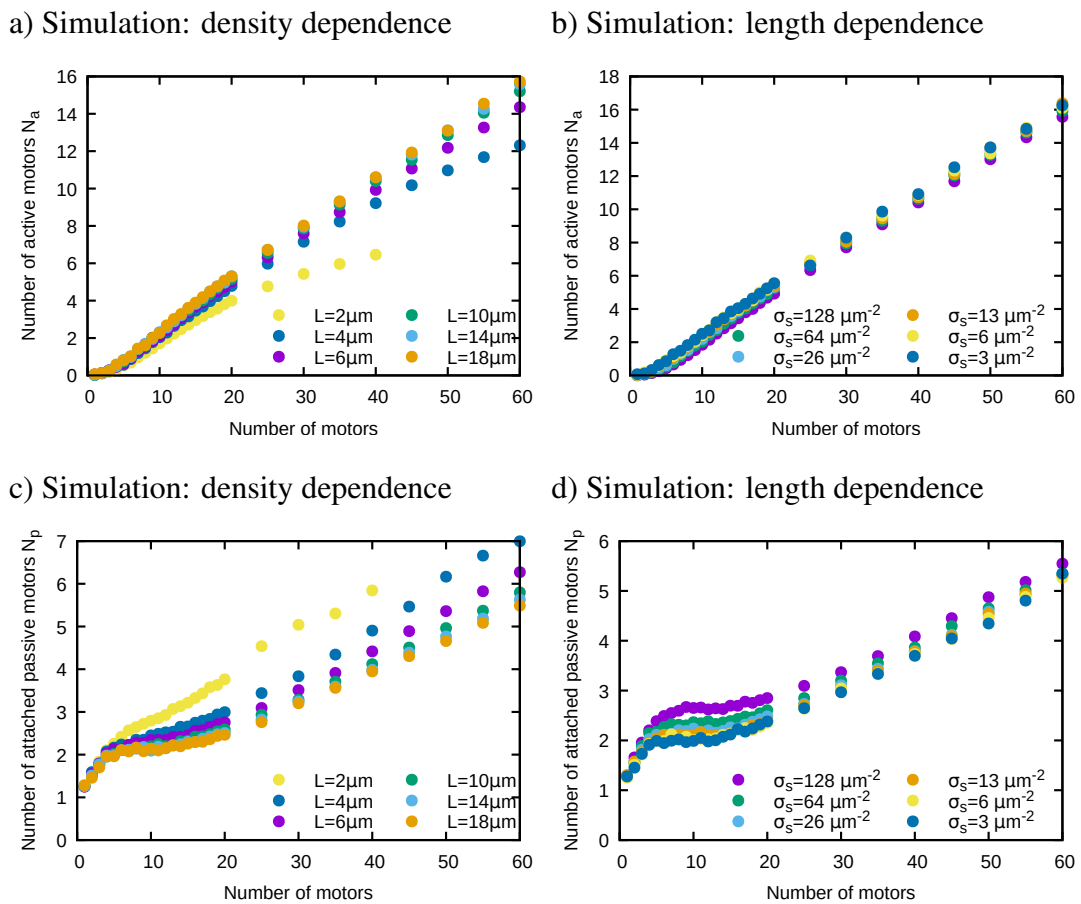
Figure 4.12: Number of active and passive MT-attached motors increases with the number of motors. Mean number of active MT-attached (upper panels) and passive MT-attached motors (lower panels) as a function of the number of available motors. The number of motors is once increased by the dynein density at a fixed MT length (left) and once by the MT length at a fixed dynein density (right). Active and passive MT-attached motors monotonically increase with the number of motors. When increasing the number of motors by the dynein density, the number of passive MT-attached motors increases faster than the number of actively MT-attached motors at high densities (compare fig. 4.12a with fig. 4.12c for $L_{MT} = 2\,\mu m$ or $L_{MT} = 4\,\mu m$). All simulations were performed using the mechanical dynein activation model. *Reproduced/adapted with permission from The Company of Biologists LTd., Journal of cell science.* Originally published in *Journal of cell science*, volume 132(4), page jcs220079 (2019) [300].

such that the activation ratio does not change significantly anymore (compare with fig. 4.11a). Consequently, the activation ratio and therefore the median velocity are saturated. This implies that in this regime, dynein motors do not further increase their cooperation to produce even higher velocities and the influence of the hindering passive MT-attached motors, causing reduced velocities, is negligible. Thus, in this regime, the dynein cooperation resembles the kinesin cooperation.

As it has been done for kinesin, also dynein load forces are measured in the simulation. Histograms of dynein forces are shown for the mechanical dynein activation model (fig. 4.13a) and for the dynein model (fig. 4.13b). For both models, dynein forces are more peaked around

a) Mech. dynein activation model   b) Dynein model
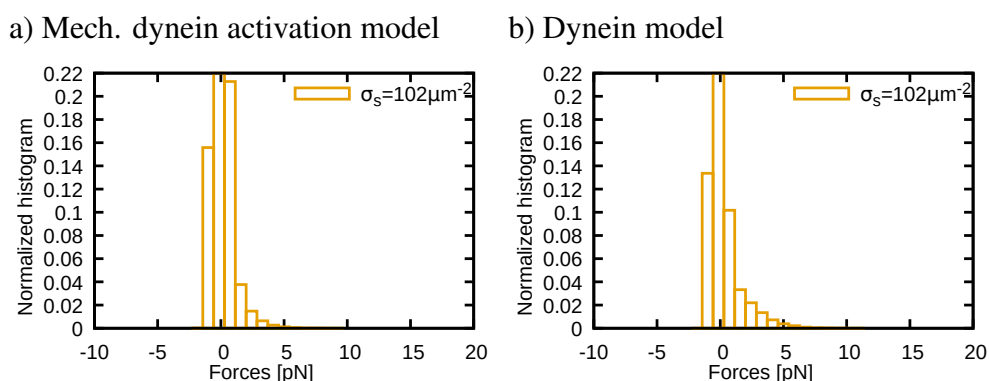
Figure 4.13: Dynein force distribution is peaked around zero. Normalized histograms of forces that MT-attached dynein motors exert on the MT in the simulations. Negative forces pull the MT in negative direction (dynein-driven direction) and positive forces pull the MT in positive direction (see 4.1c for the force definition). In all simulations, a dynein density of $\sigma_{s,kin} = 128\,\mu m$ is applied and the MT length is chosen such that $N_{kin} = 40$ motors can potentially attach the MT. Force histograms are depicted for the mechanical dynein activation model (left) and the dynein model (right). Forces are more peaked around zero for the mechanical dynein activation model because of the passive motors, which are biased towards their equilibrium position at zero force.

zero than kinesin forces. The reason is the smaller dynein stall force of $F_{s,dyn} = 1.25\,pN$ compared to the kinesin stall force of $F_{s,kin} = 6\,pN$. The small dynein stall force leads to smaller forces of leading motors (negative forces). Additionally, if leading motors cannot step very far until reaching stall they do not stretch non-advancing motors. That is why non-advancing/slowly advancing motors (positive forces) do not exert high forces on the MT either. Moreover, motor forces are even more peaked around zero in the presence of passive motors (fig. 4.13a). Passive motors perform a diffusion in the harmonic potential. Because of the harmonic potential of the motor spring, the diffusive motion is biased towards the motor equilibrium position, where motors exert no force on the MT. That is why the force histogram for the mechanical dynein activation model (fig. 4.13a) is even more peaked around zero than for the dynein model (fig. 4.13b). Taking together, a small stall force and passive MT-attached motors lead to a force distribution of MT-attached dynein motors which is peaked around zero.

In summary, using the mechanical dynein activation model, the simulation results are in alignment with the experimental results. The simulation suggests that a mutual mechanical stretching of multiple MT-attached motors leads to a mutual mechanical motor activation. The simulation shows that the activation ratio directly determines the median instantaneous velocities. That is how the simulation explains the increased dynein cooperation with increasing number of motors. The dynein activation model should be used for future simulations when modeling cytoplasmic mammalian dynein without adaptor proteins.

4.2.3 Subconclusion

For kinesin, this work shows that the velocity of multiple motors is independent of the number of motors. The reason, given by the simulation, is that a constant fraction of MT-attached kinesin motors always impairs and slows down the advancing motors. Multiple kinesin motors

can therefore not produce higher velocities than their single molecule velocity. For dynein, it is observed that the velocity increases with increasing number of motors until reaching a saturated median velocity. Using a "simple" kinesin-like motor model with dynein parameters, this unconventional dynein behavior could not be reproduced by the simulation. Therefore, a mutual mechanical dynein activation is postulated here. Adding this mechanical dynein activation to the dynein model, the increase of the velocity with increasing number of motors is reproduced by the simulation. In the mechanical dynein activation model, MT-attached dynein motors stochastically stretch each other by (diffusively) transporting the MT. The mutual stretching of the motors leads to a mutual, mechanical motor activation. Thus, dynein motors cooperate in order to pull each other out of the inhibited state. The simulation showed that the median velocity is determined by the activation ratio, the ratio of active to passive MT-attached motors. Since the mutual activation of dynein is required to reproduce the experimental data, this effect should be always considered when investigating cytoplasmic dynein without adaptor proteins. In the following, the here presented kinesin and mechanical dynein activation models are used to investigate bidirectional transport by kinesin and cytoplasmic mammalian dynein.

4.3 Bidirectional gliding assays

In vivo, vesicles are known to be transported bidirectionally [7, 14, 25]. Moreover, it is known that kinesin and dynein motors are bound simultaneously to the same cargo [9, 13, 14, 16, 25]. However, how teams of oppositely directed motors influence each other, remains unclear. Here, bidirectional gliding assay simulations in close cooperation with corresponding experiments are used to investigate the transport by teams of kinesin-1 and cytoplasmic, mammalian dynein motors without adaptor proteins. The here presented work is published in Monzon et al. 2020 (see appendix D).

To model the bidirectional gliding assay, the above introduced kinesin and dynein models (mechanical dynein activation model) need to be combined in the gliding assay set-up (see section 4.1 for the one-motor gliding assay model). While the dynein and kinesin models remain unchanged, the gliding assay model needs to be slightly modified in order to incorporate two different types of motors. In the following, the modifications for the bidirectional gliding assay are presented.

In bidirectional gliding assays, the surface is coated with dynein and kinesin at certain surface densities σ_{dyn} and σ_{kin}, respectively. In the simulation, these densities are transformed into number of dynein (N_{dyn}) and kinesin motors (N_{kin}) using eq. (4.2) for a given MT length L_{MT}. Thus, on the one-dimensional surface, N_{dyn} dynein and N_{kin} kinesin motors need to be subsequently aligned such that they represent the given experimental surface densities. Therefore, random distances between the motors are drawn while taking motor-motor exclusion effects into account. To build up the surface coated with dynein and kinesin motors at the given ratio, dynein motors are chosen with the constant probability p_{dyn} and kinesin motors with the constant probability p_{kin}, where p_{dyn} and p_{kin} are given by

$$p_{\text{dyn}} = \frac{N_{\text{dyn}}}{N_{\text{kin}} + N_{\text{dyn}}} \quad \text{and} \quad p_{\text{kin}} = \frac{N_{\text{kin}}}{N_{\text{kin}} + N_{\text{dyn}}}. \tag{4.31}$$

To choose the next motor position on the surface, a uniformly distributed random number in the interval

$$\left[x_{\text{t}}^{\text{last}} + R_{\text{last}} + R_{\text{current}}; \quad 2 \cdot \delta_{\text{attach}} - R_{\text{current}} - R_{\text{next}} \right] \tag{4.32}$$

is drawn. Where R_{last} is the radius of the last motor, R_{current} the radius of the current motor, R_{next} the radius of the subsequent motor and δ_{attach} the mean distance between motors, given by

$$\delta_{\text{attach}} = \frac{L_{\text{MT}}}{N_{\text{dyn}} + N_{\text{kin}}}. \tag{4.33}$$

To know the radius of the subsequent motor, the type of the subsequent motor should be chosen and stored at the time when setting the current motor.

Besides the surface, also the mutual motor-motor hindrance for MT-attached motors need to be modified. While for kinesin, exclusion effects on the MT could have been neglected, for dynein, exclusion effects had to be taken into account. That is why, for the bidirectional assay, exclusion effects on the MT need to be considered for both motors. A motor can therefore only attach when its equilibrium position on the MT is empty and an attached motor can only perform a step if the next motor position on the MT is empty.
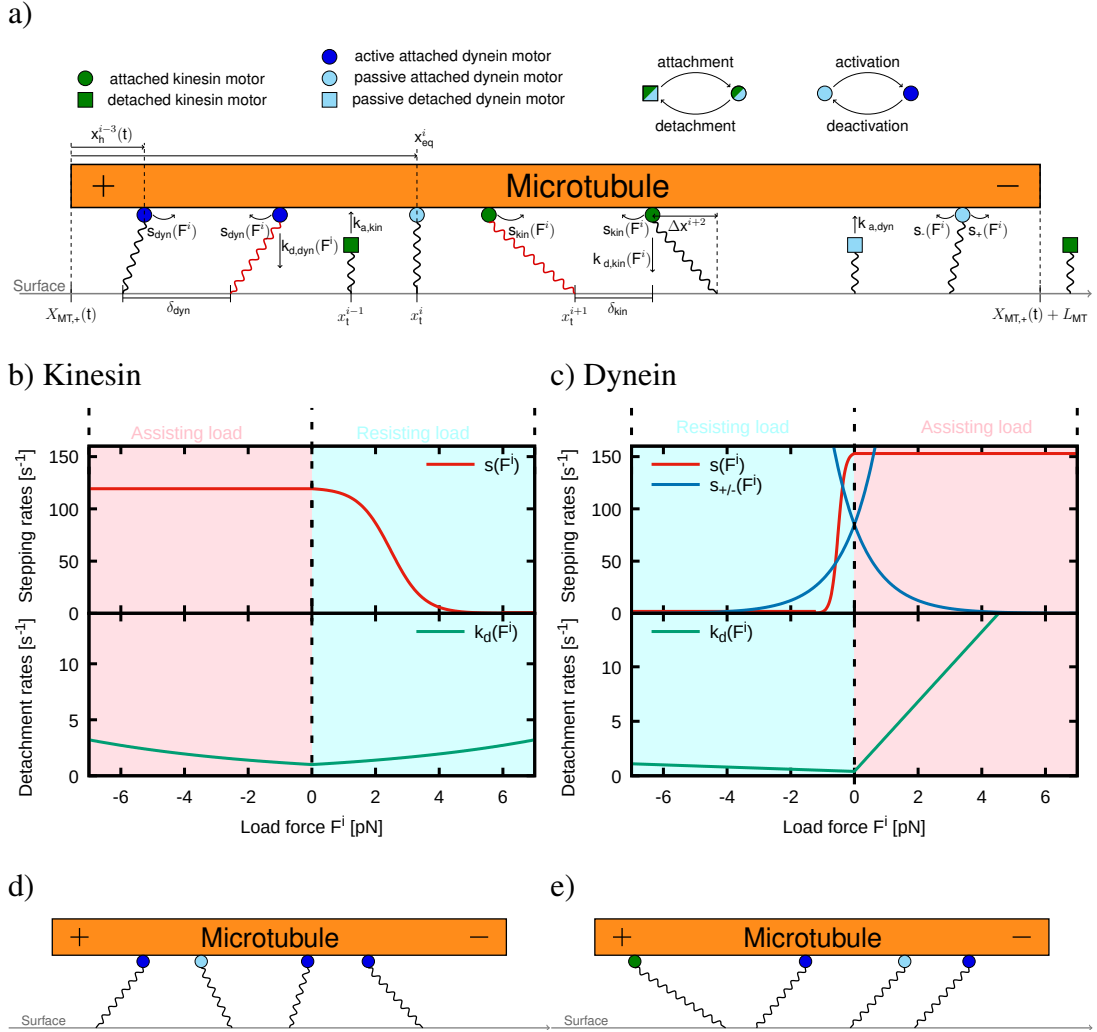
Figure 4.14: Bidirectional MT gliding assay model. a) Figure shows an illustration of the bidirectional gliding assay. The gliding assay is modeled in one dimension neglecting any motion in y- and z-direction, as well as any rotational degree of freedom. The surface (= coverslip, gray line) gives the orientation of the global, one-dimensional coordinate system. The MT (orange rectangle) is placed above the surface with its minus-end on the right and its plus-end on the left side. If kinesin motors (green) transport the MT, the MT moves towards the right (positive values) side, while when dynein motors (blue) transport the MT, the MT moves towards the left side (negative values). The MT is characterized by the MT plus-end position in the global coordinate system $X_{\mathrm{MT},+}(t)$ together with the MT length L_{MT}. Motor tail positions x_{t}^i are uniformly distributed on the surface with mean distances δ_{kin} and δ_{dyn} between kinesin and dynein motors, respectively. Motors are drawn by a curvy line, representing the motor spring, and a square for detached motors or a circle for MT-attached motors. Kinesin motors are drawn in green, passive dynein motors in light blue and active dynein motors in dark blue. The motor head positions in the MT coordinate system (body-fixed coordinate system of the MT ranging from 0 to L_{MT}) are denoted by x_{h}^i and the equilibrium position in the MT coordinate system by x_{eq}^i. The equilibrium position is the position of the motor head on the MT, where the motor extension Δx^i is zero. The motor extension Δx^i is defined by the (*Continuation on next page.*)

Figure 4.14 *(previous page)*: one-dimensional difference between the motor head and the motor tail positions (see eq. 4.6). Kinesin and dynein motors attach to the MT with the constant rates $k_{a,kin}$ and $k_{a,dyn}$, respectively, and step and detach with the force dependent rates $s_{kin}(F^i)$, $s_{dyn}(F^i)$, $k_{d,kin}(F^i)$ and $k_{d,dyn}(F^i)$. While kinesin steps towards the MT plus-end for forces smaller than the kinesin stall force $F_{s,kin}$, active dynein steps towards the MT minus-end for forces smaller than the dynein stall force $F_{s,dyn}$. However, both motors step backward under forces higher than the stall forces (denoted by the red curved lines of the motors). While the attachment and the detachment of passive and active dynein motors are similar, the stepping differs. An active dynein steps directely towards the MT minus-end with the stepping rates $s_{dyn}(F^i)$, while a passive dynein diffuses in the harmonic potential of the motor spring with rates $s_\pm(F^i)$. b) Kinesin stepping (red curve, upper panel) and detachment rates (green curve, lower panel) as a function of the motor load force. Negative forces are assisting forces, which pull the kinesin towards the MT plus-end and positive forces are resisting forces, which hold the kinesin back. Under resisting forces, the stepping rate is constantly high while under resisting forces, the stepping rate decreases. For forces higher than the kinesin stall force $F_{s,kin} = 6\,\text{pN}$, kinesin steps backwards with a constant low rate. The kinesin detachment increases exponentially for assisting and resisting forces with the detachment force $F_{d,kin} = 6\,\text{pN}$. c) Dynein stepping (upper panel) and detachment rates (lower panel) as a function of the motor load force. Negative forces are resisting forces for dynein, which hold the motor back and positive forces are assisting forces, which pull the motor towards the MT minus-end. The active dynein stepping rate (red curve) is constantly high under assisting forces and decreases with increasing resisting forces. For resisting forces higher than the stall force ($F^i < -F_{s,dyn} = -1.25\,\text{pN}$), the dynein motor steps backwards with a constant small rate. Passive dynein diffusive stepping rates $s_\pm(F^i)$ (blue curves), for stepping towards the MT plus- and MT minus-end, are mirrored at the y-axis. Both increase exponentially for stepping away from the equilibrium position x^i_{eq} ($F^i = 0$). Dynein detaches with linearly increasing detachment rates (green curve). Detachment rates increase faster with increasing assisting forces than resisting forces. d) Example configuration of MT-attached dynein motors. If only active and passive dynein motors are attached, the motor extensions are random. Some motors are holding the MT back (negative forces), while others try to advance the MT (positive forces). e) Example configuration of MT-attached kinesin and dynein motors. If dynein is attached in the presence of kinesin, kinesin aligns the attached dynein motors under resisting forces (backward load). *Reproduced/adapted with permission from The Company of Biologists LTd., Journal of cell science.* Originally published in *Journal of cell science*, volume 133(22), page jcs249938 (2020) [309].

In the following, the bidirectional gliding assay simulations are used together with bidirectional gliding assay experiments from Stefan Diez lab[8] to investigate how the number and kind of motors, the ATP concentration and roadblocks on the MT track influence the transport directionality.

4.3.1 Regulation by the number of motors

Previous *in vivo* studies found that multiple dynein and kinesin motors are simultaneously bound to the same cargo and that a tug-of-war is likely to happen between teams of kinesin and dynein motors [9, 10, 25, 143, 150]. The number of motors might influence the tug-of-war between opposing teams. The number of kinesin and dynein motors might vary inside the cell and between different kinds of cargos [17, 25, 142, 310, 311]. It is therefore intriguing to understand how the number of kinesin and dynein motors influences bidirectional transport. Previous studies showed that varying the kinesin number or density can change the transport direction [37, 38]. However, it is unknown how the dynein number or the mechanical dynein activation influences bidirectional transport. Moreover, a detailed analysis of how many dynein and kinesin motors are able to compete against each other is missing in the literature. A previous MT gliding assay study showed that varying the kinesin densities in gliding assays could change the transport direction [38]. Therefore, as a first step, the kinesin density is varied to see whether we see a similar effect. Before describing simulation results, the experimental results are presented. At a constant dynein density, the kinesin density is varied from $0.1\,\mu\text{m}^{-2}$ to $100\,\mu\text{m}^{-2}$ including an "only dynein" and an "only kinesin" case. For the constant dynein density, a high density of $64\,\mu\text{m}^{-2}$ is chosen, where influences of passive dynein motors are expected to be negligible (see section 4.2.2). MT positions of fluorescence-labeled MTs with lengths in the interval $L_{\text{MT}} = 10 - 15\,\mu\text{m}$ are measured for each measurement time interval $\Delta t_{\text{mes}} = 1\,\text{s}$. MT gliding trajectories go from unidirectional, dynein-driven trajectories for the "only dynein" case and low kinesin densities, over stalled trajectories for partly low and intermediate kinesin densities to unidirectional kinesin-driven trajectories for high kinesin densities and the "only kinesin" case (see fig. 4.15b). From MT positions and time intervals, instantaneous gliding velocities are calculated. Histograms of instantaneous gliding velocities are depicted at different kinesin densities (see fig. 4.16b). Velocities are thereby shown as positive when the MT is transported by kinesin motors, which step towards the MT plus-end and as negative velocities when the MT is transported by dynein motors, which step towards the MT minus-end. Fig. 4.16a shows that only kinesin transports the MT at high positive velocities producing a narrow peak at around $800\,\text{nm/s}$. The same is seen for high kinesin densities ($\sigma_{\text{kin}} = 20 - 100\,\mu\text{m}^{-2}$). Thus, for these densities, the influence of dynein is still negligible. At intermediate kinesin densities ($\sigma_{\text{kin}} = 1 - 2\,\mu\text{m}^{-2}$), however, a balance between kinesin and dynein can be seen producing a peak around zero velocity. At a very low kinesin density ($\sigma_{\text{kin}} = 0.1\,\mu\text{m}^{-2}$), kinesin is still able to strongly slow down dynein producing a velocity distribution with a peak at low negative velocities and a small tail towards higher negative velocities. The "only dynein" velocity distribution spreads over a wide range of values (zero to high negative velocities) with a peak at around $-800\,\text{nm/s}$. To conclude, this means the experiment shows that the gliding direction can be changed by changing the kinesin density. This is in accordance with previous studies [37, 38].

---

[8]Experiments were performed by Lara Scharrel from Stefan Diez lab at the B CUBE, TU-Dresden. See also the thesis [299]. I did not perform any experiments myself.
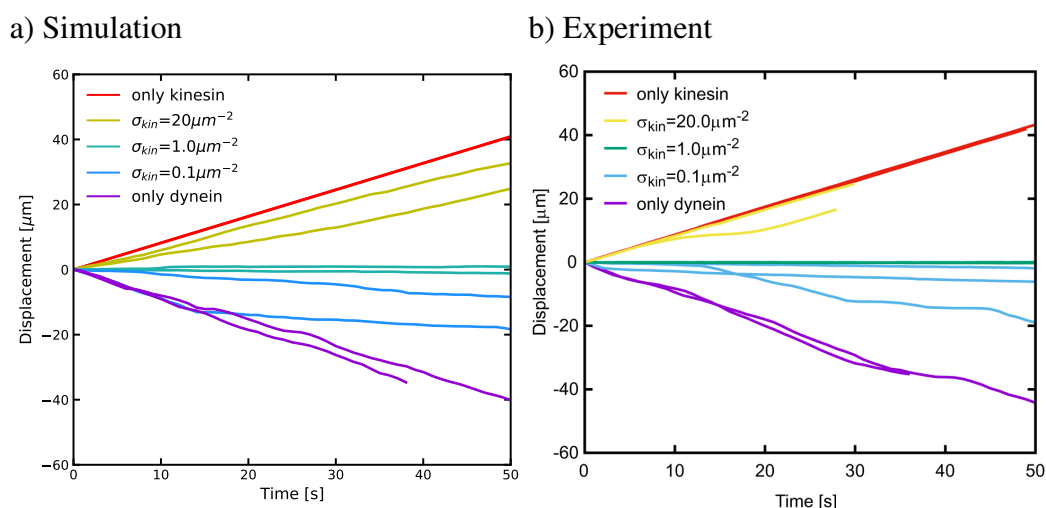
a) Simulation

b) Experiment

Figure 4.15: MT gliding trajectories from simulations and experiments. MT gliding trajectories from simulation a) and experiment b). For both a dynein density of $\sigma_{\text{dyn}} = 64\,\mu\text{m}^{-2}$ is applied and MT lengths are in the range of $L_{\text{MT}} = 5 - 10\,\mu\text{m}$ for experiments and $L_{\text{MT}} = 25\,\mu\text{m}$ for simulations. Kinesin densities are as written in the plots. In the "only kinesin" case a kinesin density of $\sigma_{\text{kin}} = 100\,\mu\text{m}^{-2}$ is applied. Positive directions are kinesin-driven and negative directions dynein-driven. Simulations and experiments show unidirectional kinesin-driven trajectories for the "only kinesin" case and for high kinesin densities ($\sigma_{\text{kin}} = 20\,\mu\text{m}^{-2}$), stalled trajectories for intermediate kinesin densities ($\sigma_{\text{kin}} = 1.0\,\mu\text{m}^{-2}$) and unidirectional dynein-driven or partly stalled trajectories for low kinesin densities ($\sigma_{\text{kin}} = 0.1\,\mu\text{m}^{-2}$) and the "only dynein" case. The shown experiments were performed by Lara Scharrel from Stefan Diez lab at B CUBE, TU-Dresden. *Reproduced/adapted with permission from The Company of Biologists LTd., Journal of cell science*. Originally published in *Journal of cell science*, volume 133(22), page jcs249938 (2020) [309].

In summary, three different motility states can be distinguished: a kinesin-driven state (high positive velocities), a dynein-driven state (up to high negative velocities) and a balanced state, where the dynein and kinesin teams balance each other and almost no net-movement is observed.

While we have seen that the experimental results are in accordance with previous studies, it remains to be shown that the simulation shows the same results when using the above introduced kinesin and dynein models. For the simulation, the same dynein and kinesin densities and the same MT length distribution are used as in the experiment. Moreover, the MT position is determined after each experimentally given time measurement interval $\Delta t_{\text{mes}} = 1\,\text{s}$ and a Gaussian noise with zero mean and variance $\sigma_{\text{P}} = 30\,\text{nm}$ is added to mimic the experimental measurement uncertainty. Simulation trajectories show, similar to the experiment, a transition from unidirectional dynein-driven, over stalled, up to unidirectional kinesin-driven trajectories with increasing kinesin concentrations (see fig. 4.15a). From the MT position and the time interval, instantaneous gliding velocities are calculated. Histograms of instantaneous velocities from the simulation are shown in fig. 4.16a. As in the experiment, sharp velocity peaks at high, positive velocities can be seen for kinesin densities higher or equal $20\,\mu\text{m}^{-2}$. For small kinesin densities ($\sigma_{\text{kin}} = 1 - 2\,\mu\text{m}^{-2}$), a peak around zero is observed and for the very small kinesin density and the "only dynein" case, a wide distribution

of negative velocities can be seen. A comparison of experimental and simulation results reveals that similar effects are observed in simulation and experiment. Thus, the simulation is a reliable tool to give further insights and explanations of bidirectional transport at a molecular level.

We have seen that varying the kinesin density can change the transport direction of bidirectional transport. To show this, the kinesin density was varied at a high, constant dynein density, where the influence of passive motors is expected to be negligible. The previously presented unidirectional dynein gliding assays (see section 4.2.2), however, showed that the gliding velocity is strongly influenced by passive MT-attached motors. To understand the influence of passive motors and the mechanical dynein activation on bidirectional transport, the dynein density needs to be varied. The influence of the dynein density on bidirectional transport has not been studied before. To study the influence of the dynein density, three different constant dynein densities are applied at varying kinesin densities and median instantaneous velocities are depicted as a function of the kinesin density for simulation (fig. 4.17a) and experiment (fig. 4.17b). For all three dynein densities, a transition from the dynein- to the kinesin-driven state can be seen and the balanced state was shifted to lower kinesin densities, the lower the dynein density was. Hence varying the dynein density also changes the transport direction of bidirectional transport in MT gliding assays.

To learn more about the influence of the passive motors and the mechanical dynein activation, the results of the lowest dynein density, where passive dynein motors play a role (compare section 4.2.2 for the dependence on the dynein density) need to be considered in detail. At the lowest dynein density, the simulation (fig. 4.17a), finds that the median instantaneous velocity is zero for the "only dynein" case (only dynein-driven) and for small kinesin densities (balanced state)[9]. This means, the balanced state and dynein driven-state merge. There are two possible explanations for why the velocity is zero: i) First no dynein motor is attached at all for the "only dynein" case or ii) second only passive dynein is attached in the "only dynein" case. As previously mentioned, in the experiment, the number and types of MT-attached motors cannot be measured. However, this can easily be done in the simulations. Fig. 4.17d depicts the number of MT-attached dynein motors in the simulation. The upper panel shows the median number of total (passive and active) MT-attached dynein motors and the lower panel the median number of actively MT-attached dynein motors. It can be seen that for small kinesin densities ($\sigma_{\text{kin}} < 0.5\,\mu\text{m}$, balanced and dynein-driven state) one dynein is attached on average ruling out the first explanation that no dynein is attached at all. However, looking at the lower panel, it can be seen that the number of actively MT-attached dynein motors is zero for all kinesin densities at the lowest constant dynein density. This means the MT-attached dynein motor is passive and hence the second explanation holds. In the "only dynein" case, the single passive MT-attached dynein motor has no chance to activate because there are no other motors that transport the MT and thereby could stretch the single MT-attached dynein motor. However, in the presence of kinesin ($\sigma_{\text{kin}} > 0\,\mu\text{m}^{-2}$), there could be a MT-attached kinesin transporting the MT and thereby occasionally stretching and activating the passive MT-attached dynein motor. For $\sigma_{\text{kin}} = 0.5\,\mu\text{m}^{-2}$, for instance, one passive dynein and one kinesin motor are attached (the median kinesin and dynein number is one, while the median active dynein number is zero). In this case, median transport velocities reveal that the MT is

---

[9]The median instantaneous velocity is not zero in the experiment for the "only dynein" case. Discrepancies between experiment and simulation most likely come from an uncertain motor density estimation. Experimentally, it is not easy to determine the motor density on the coverslip and therefore, the given motor densities are rough estimates.
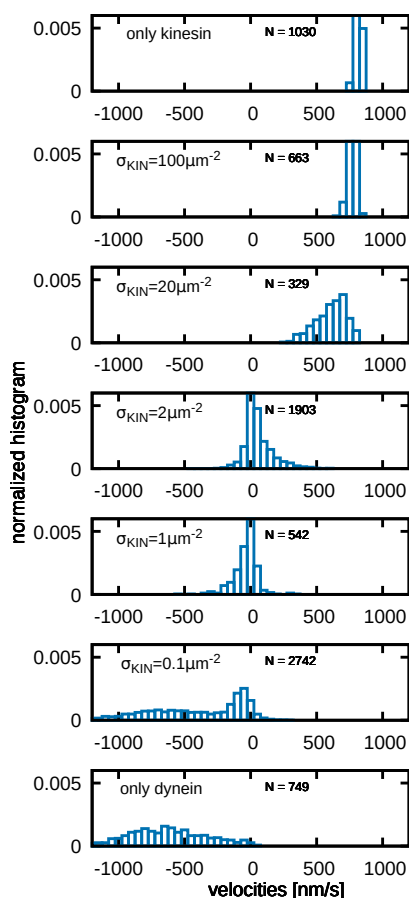
a) Simulation   b) Experiment
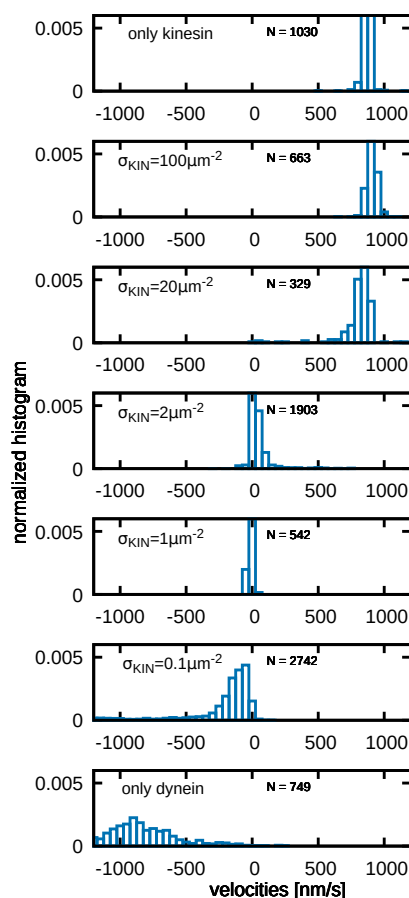
Figure 4.16: The simulation reproduces the experimental histograms. Normalized histograms of instantaneous bidirectional gliding velocities from simulation a) and experiment b). For simulation and experiment a dynein density of $\sigma_{\mathrm{dyn}} = 64\,\mu m^{-2}$ is applied and MT lengths were in the range of $L_{\mathrm{MT}} = 10 - 15\,\mu m$. In the simulation, the same length distribution as in the experiment is used. Kinesin densities were as written in the plots. In the "only kinesin" case a kinesin density of $\sigma_{\mathrm{kin}} = 100\,\mu m^{-2}$ was applied. At high kinesin densities ($\sigma_{\mathrm{kin}} = 20 - 100\,\mu m^{-2}$), a peak around 800 nm/s can be seen characterizing the kinesin-driven state. At low kinesin densities ($\sigma_{\mathrm{kin}} = 1 - 2\,\mu m^{-2}$) velocities were peaked around zero indicating the balanced state. At very low kinesin density ($\sigma_{\mathrm{kin}} = 0.1\,\mu m^{-2}$) and the "only dynein" case, a wide distribution of negative velocities can be seen indicating the dynein-driven state. The simulation shows similar velocity histograms as the experiment for the kinesin-driven state, the balanced state and the dynein-driven state. The shown experiments were performed by Lara Scharrel from Stefan Diez lab at B CUBE, TU-Dresden. *Reproduced/adapted with permission from The Company of Biologists LTd., Journal of cell science*. Originally published in *Journal of cell science*, volume 133(22), page jcs249938 (2020) [309].

transported by kinesin (see fig. 4.17a). Thus, the passive MT-attached dynein is not activated, but dragged by the kinesin motor as previously predicted by the dynein dragging model [10, 11, 147]. This means, one MT-attached dynein motor cannot stop a kinesin motor and no

balanced state exists at the lowest dynein density. Hence, one dynein cannot hold against one kinesin.

It has been shown that at the lowest dynein density, dynein is not able to resist kinesin at all. This raises the question of how many dynein motors are needed to resist kinesin. To answer this question a detailed look at the intermediate dynein density ($\sigma_{\text{dyn}} = 13\,\mu\text{m}^{-2}$) is taken. For the intermediate dynein density, a clear separation between dynein-driven (negative velocities) and balanced (median velocities around zero) states is observed (see fig. 4.17a). This indicates that the MT-attached dynein motors are able to resist the MT-attached kinesin motors. Looking at the number of MT-attached dynein motors (fig. 4.17d) reveals that in the "only dynein" case, two dynein motors are attached, which are passive on average. However, since the median velocity is non-zero, the two passive MT-attached dynein motors need to activate each other temporarily. In the balanced state, however, a passive and an active dynein is attached (see fig. 4.17d). This means, once kinesin plays a role, the MT-attached kinesin activates one of the passive MT-attached dynein motors. This raises the question if an active dynein is strong enough to hold back one kinesin motor. Previously it was established that the strength of a motor is determined by the stall force to detachment force ratio [151]. A strong motor is said to have a large ratio and a weak motor, a small ratio. Having a stall force of $F_{\text{s,kin}} = 6\,\text{pN}$ and a detachment force of $F_{\text{d,kin}} = 6\,\text{pN}$, kinesin has a stall force to detachment force ratio of one. Dynein has a stall force of $F_{\text{s,dyn}} = 1.25\,\text{pN}$ and an asymmetric detachment behavior. Dynein detaches faster under forward load (positive forces) than under backward load (negative forces). This means it has a smaller detachment force under forward load than under backward load. In the competition with kinesin, detachment under backward load is relevant. In this case, dynein has a stall force to detachment force ratio of approximately 0.3125, which is significantly smaller than the stall force to detachment force ratio of kinesin. This means dynein is the weaker motor in the competition with kinesin. It is therefore likely that kinesin will pull off the one active MT-attached dynein, as observed at the lowest dynein density, and take over. However, at the intermediate dynein density, typically a second, passive dynein is attached. When the kinesin pulls off the active dynein, there is still the passive dynein which could substitute the active dynein. Once the passive dynein is activated by kinesin, it tries to maintain the balanced state. However, as seen before, one dynein is not able to resist kinesin. That is why to maintain the balanced state, in the meantime another passive dynein should attach. Together, that is how on average an active dynein with a passive dynein as a substitute could temporarily hold back kinesin and it can be concluded that one active dynein together with a passive MT-attached dynein can temporarily resist a kinesin. The passive dynein helps out in the case the active dynein is pulled off by the kinesin but does not exert a directed force.

It could be seen, that two dynein motors can balance one kinesin. However, because dynein is continuously pulled off by kinesin, more dynein might be necessary to have a more stable balanced state. Indeed, at a dynein density of $\sigma_{\text{s,dyn}} = 64\,\mu\text{m}^{-2}$, fewer fluctuations of the instantaneous velocity can be observed (see fig. 4.17a). For this dynein density, six dynein motors are competing against two kinesin motors in the balanced state. Moreover, the number of actively MT-attached dynein motors reaches its maximum in the balanced state (see fig. 4.17d). This means, increasing the kinesin density increases the number of activated dynein motors until reaching the balanced state. This clearly shows that the activity of kinesin activates dynein. By activating more MT-attached dynein motors, kinesin stabilizes the balanced state. Besides the number of actively MT-attached dynein motors, also the total number of active and passive MT-attached dynein motors is maximal in the balanced state
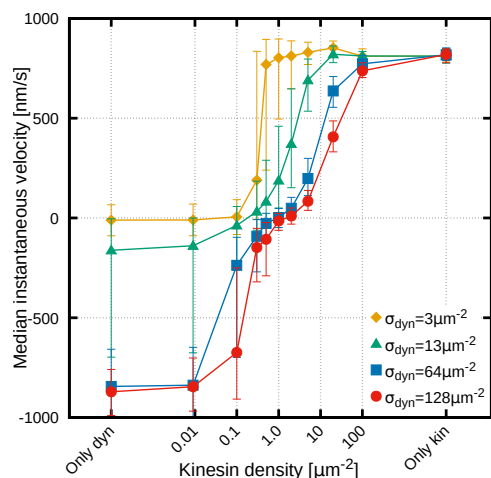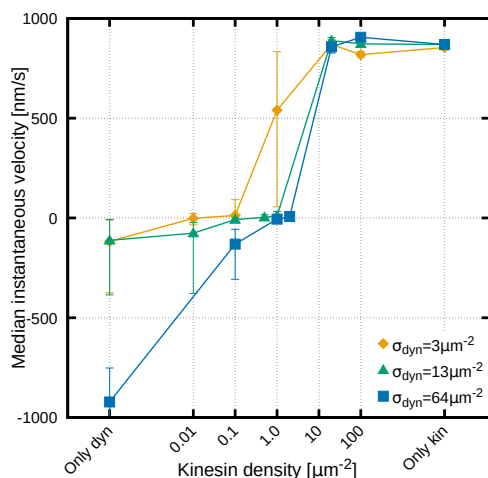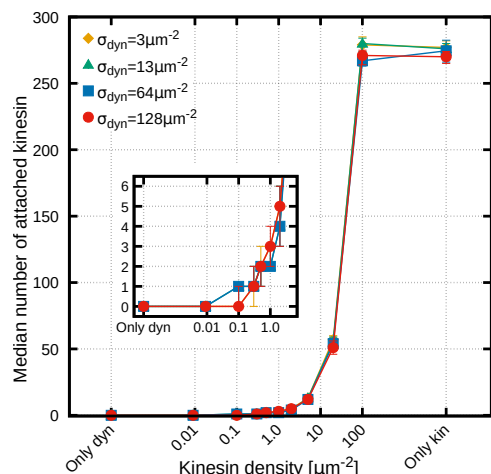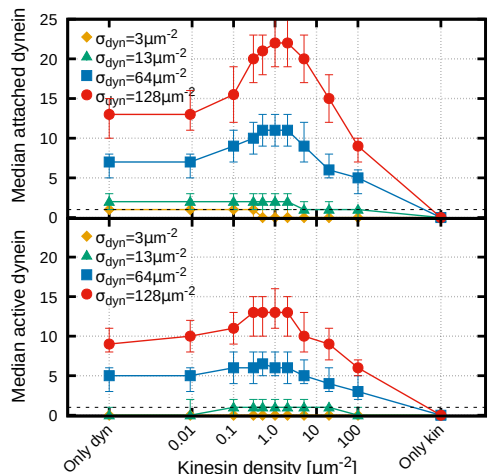
Figure 4.17: The number of kinesin and dynein motors regulates the direction of bidirectional transport. Median instantaneous gliding velocities of bidirectional gliding assays: simulations a) and experiments b). Median velocities are depicted as a function of varying kinesin densities at a constant dynein density. In the simulation a MT length of $L_{MT} = 25\,\mu m$ is chosen and experimental lengths were $L_{MT} > 12\,\mu m$. At all dynein densities, a kinesin-driven state was found for kinesin densities $\sigma_{kin} \geq 20\,\mu m^{-2}$ and a dynein-driven state for $\sigma_{kin} \leq 0.1\,\mu m^{-2}$ ($\sigma_{kin} \leq 0.01\,\mu m^{-2}$ for the intermediate dynein density in the experiment). The balanced state is shifted towards lower kinesin densities, the lower the dynein density is. Thus, the dynein and the kinesin density regulate the directionality of bidirectional transport. Median numbers of MT-attached kinesin c) and MT-attached dynein motors d) are depicted for different constant dynein densities as a function of the varying kinesin densities corresponding to a). The monotonically increasing number of MT-attached kinesin motors does not show a significant dependence on the dynein density. The number of MT-attached dynein motors is split into the total (passive and active) number of MT-attached dynein motors (*Continuation on next page.*)

Figure 4.17 *(previous page)***:** (upper panel) and the number of actively MT-attached dynein motors (lower panel). The dashed black line shows the one motor value. The number of MT-attached motors shows that an active and a passive dynein can resist one kinesin, while one dynein alone cannot. For high dynein densities ($\sigma_{\text{dyn}} = 64\,\mu\text{m}^{-2}$ and $\sigma_{\text{dyn}} = 128\,\mu\text{m}^{-2}$) the total number of MT-attached dynein as well as the number of actively MT-attached dynein motors show a clear maximum at the kinesin density of the balanced state. Thus, kinesin stabilizes the balance state by first maximizing the number of MT-attached dynein and second by activating the maximum number of passive MT-attached dynein motors. All shown experiments were performed by Lara Scharrel from Stefan Diez lab at B CUBE, TU-Dresden. *Reproduced/adapted with permission from The Company of Biologists LTd., Journal of cell science*. Originally published in *Journal of cell science*, volume 133(22), page jcs249938 (2020) [309].

(see fig. 4.17d). Hence the overall dynein detachment is reduced when kinesin is competing against dynein. Past studies found a dynein catch-bond behavior at large backward loads [33]. However, the current understanding of dynein detachment is a slowly increasing detachment rate under backward load [86, 92]. The latter detachment behavior is implemented in the here presented dynein model. This rules out the catch-bond as an explanation for the reduced overall detachment in the balanced state. What happens here is that when competing against kinesin, the MT-attached dynein motors are aligned under backward load (see fig. 4.14e for an illustration). Under backward load, the detachment rates are smaller than under forward load. In contrast, when only dynein motors are attached, the motor extensions (and therefore the motor forces) are randomly distributed (see fig. 4.14d for an illustration and fig. 4.13 for the force distribution of MT-attached dynein motors in the unidirectional gliding assay). Dynein extensions are random because single dynein motors step stochastically with different single molecule velocities. This means some motors are under backward load, while others are under forward load. This increases the overall detachment rate in the dynein-driven state compared to the case where MT-attached dynein motors are aligned under backward load by kinesin. Aligning dynein under backward load and therefore reducing the overall dynein detachment, increases the number of dynein motors and therefore stabilizes the balanced state. Thus, the balanced state is stabilized by kinesin, which on one hand activates MT-attached dynein and on the other hand reduces the dynein detachment by aligning MT-attached dynein under backward load.

This study showed that kinesin stabilizes the balanced state between the kinesin and dynein team by increasing the number of MT-attached dynein motors. This is in agreement with previous *in vivo* studies showing that in the tug-of-war multiple dynein motors compete against a few kinesin motors [11, 25]. Moreover, by activating passive MT-attached dynein motors, kinesin produces a stable force balance between the kinesin and dynein team. This means besides antagonistic effects, also cooperative effects exist between the oppositely directed kinesin and dynein teams. Inside the cell, the stable force balance might be used to hold a cargo at a specific position.

Here, it was shown that increasing the available number of dynein or kinesin motors can shift the force balance to the dynein- or the kinesin-driven state. *In vivo*, there might be different mechanisms, which can change the number of engaged motors and thereby shift the force balance. The number of engaged motors might be changed by locally different motor concentrations [310, 311] or by different binding affinities. Shima et al. [223] and Peet

et al. [222] showed that when kinesin steps on the MT, it slightly changes the MT lattice in such a way that the binding affinity of following up kinesin motors is increased. Jose and Santen [224] modeled bidirectional axonal transport with a floor field model and showed that the increased affinity of following-up motors of the same kind and a reduced affinity of the opposing motors may produce a lane formation in the axon. The increased affinity of following-up motors produces one lane for kinesin-driven transport and one for dynein-driven transport. That is one way how regulation of the number of motors leads to different transport directions.

Besides shifting the force balance by the number of motors, also adaptor proteins might influence the force balance between kinesin and dynein motors. Activating dynein by adaptor proteins is known to increase the dynein stall force from $\approx 1\,\text{pN}$ [33, 87, 88, 99, 101–103] to $4.4\,\text{pN}$ [88]. An increased stall force could strengthen the dynein team and therefore shift the force balance toward the dynein-driven state. In future work, it would therefore be intriguing to investigate adaptor proteins in terms of regulatory mechanisms.

Taking together, cooperative effects between kinesin and dynein motors lead to a stable force balance between the oppositely directed kinesin and dynein team. Changing the number of motors is one way to regulate this stable force balance. Another way might be strengthening one team. One way to strengthen the dynein team might be adding adaptor proteins and therefore increasing the stall force. Future work should focus on factors influencing the force balance between kinesin and dynein motors.

4.3.2 Regulation by ATP concentration

The ATP concentration varies temporally and spatially inside the cell [180, 181] and single molecule velocities of kinesin and dynein strongly depend on ATP concentrations [71, 88, 120, 190]. To be a potential regulation factor of bidirectionally transported cargo, teams of dynein and kinesin motors need to react differently to changes in the ATP concentration. That is why, it is first studied how unidirectional kinesin and dynein gliding assays change with ATP concentration.

Unidirectional gliding assay experiment and simulation were performed at kinesin and dynein motor densities of $\sigma_{\text{kin}} = 18\,\text{µm}^{-2}$ and $\sigma_{\text{dyn}} = 18\,\text{µm}^{-2}$, respectively and the ATP concentration is varied between $2 - 5000\,\text{µM}$. In the simulation, the stepping rates of kinesin and active dynein motors are ATP dependent (see eq. (4.19) and eq. (4.22) for kinesin, for dynein the same equations but dynein-specific parameter values are used). For passive MT-attached dynein, a Michaelis-Menten-like ATP dependence is added to the force-free diffusion rate:

$$s_0 = s_0\,([\text{ATP}]) = \frac{s_{0,\text{max}} \cdot [\text{ATP}]}{[\text{ATP}] + s_{0,\text{max}}/k_{\text{b}}^0} \tag{4.34}$$

with k_b^0 being the unloaded rate constant for ATP binding as used for the active motors (see eq. (4.19)). $s_{0,\text{max}}$ is determined by setting $s_0\,([\text{ATP}] = 2000\,\text{µM})$ equal the value of s_0 found above for $2000\,\text{µM}$ (see section 4.2.2). Using this force-free diffusion rate, the force-dependent stepping rate is given by

$$s_{\pm} = s_0\,([\text{ATP}])\,e^{\mp \frac{F^i \cdot d}{2k_{\text{B}}T}}, \tag{4.35}$$

using eq. (4.27). For simulation and experiment, median instantaneous velocities are

a) Kinesin

b) Dynein

c) Simulation

d) Experiment
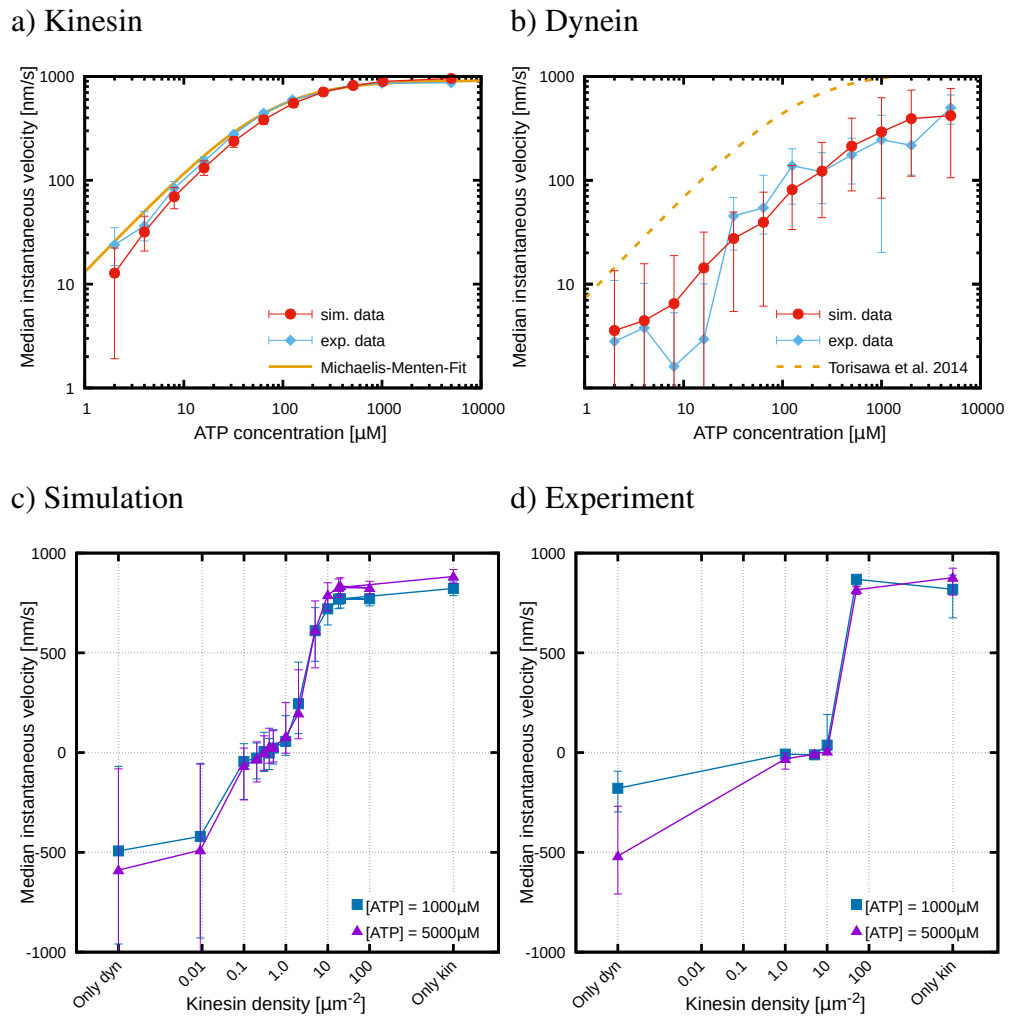
Figure 4.18: Different reactions of unidirectional gliding assays to varying ATP concentrations do not lead to a shift of the balanced state in bidirectional gliding assays. a)+b): Median instantaneous gliding velocities plus IQR are depicted as a function of ATP concentration for the unidirectional kinesin a) and dynein gliding assay b), for simulation (red curve) and experiment (light blue curve). For simulation and experiment, kinesin and dynein densities of $\sigma_{\mathrm{kin}} = 18\,\mu\mathrm{m}^{-2}$ and $\sigma_{\mathrm{dyn}} = 18\,\mu\mathrm{m}^{-2}$ were applied, respectively. Experimental and simulation results match for the kinesin and the dynein assay. The experimental data of the kinesin assay could be fitted by a Michaelis Menten equation ($v = v_{\mathrm{max}} \times [\mathrm{ATP}]/(K_m + [\mathrm{ATP}])$ with $v_{\mathrm{max}} = 914\,\mathrm{nm\,s}^{-1}$ and $K_m = 69\,\mu\mathrm{M}$, solid fit, yellow curve). The ATP dependence of the dynein assay could not be fitted by a Michaelis-Menten equation because the experimental data shows a more linear increase with ATP concentration instead of a Michaelis-Menten-like dependence. The dashes yellow line shows the Michaelis-Menten equation found by Torisawa et al. [89] for dynein gliding assays. For unidirectional dynein assay simulations, the experimental MT length distribution of MT lengths $L_{\mathrm{MT}} > 15\,\mu\mathrm{m}$ was used and for the unidirectional kinesin assay, a MT length of $L_{\mathrm{MT}} = 25\,\mu\mathrm{m}$. c)+d): Median instantaneous velocities plus IQR of bidirectional gliding assay simulations (c) and experiments (d) at different ATP concentrations. Median velocities are depicted as a function of varying (*Continuation on next page.*)

Figure 4.18 (*previous page*): kinesin densities at the constant dynein density of $\sigma_{\mathrm{dyn}} = 18\,\mu\mathrm{m}^{-2}$. In the simulation a MT length of $L_{\mathrm{MT}} = 25\,\mu\mathrm{m}$ was used and in the experiment MTs with lengths $L_{\mathrm{MT}} > 15\,\mu\mathrm{m}$. Simulation and experiment show a stronger reduction of the velocity in the dynein-driven state than in the kinesin-driven state. The balanced state ($\sigma_{\mathrm{kin}} = 0.1 - 1.0\,\mu\mathrm{m}^{-2}$ for simulation and $\sigma_{\mathrm{kin}} = 1 - 10\,\mu\mathrm{m}^{-2}$ for experiment), however, remained stable upon different ATP concentrations. This means ATP concentration cannot regulate the directionality of MT transport in bidirectional gliding assays. All shown experiments were performed by Lara Scharrel from Stefan Diez lab at B CUBE, TU-Dresden. *Reproduced/adapted with permission from The Company of Biologists LTd., Journal of cell science.* Originally published in *Journal of cell science*, volume 133(22), page jcs249938 (2020) [309].

measured as a function of the ATP concentration (see fig. 4.18a and 4.18b). Simulation and experimental results of the kinesin assay coincide well and could be fitted by a Michaelis-Menten equation. For dynein, the simulation is also in alignment with the experiment. However, median velocities of experiment and simulation do not show a Michaelis-Menten-like dependence on the ATP concentration. For the dynein assay, the median velocity increases more in a linear manner with the ATP concentration and might not be saturated at the highest applied ATP concentration of $5000\,\mu\mathrm{M}$. Consequently, the unidirectional gliding assays indeed react differently to changes in ATP concentration and ATP concentration could be a potential regulation factor for bidirectional transport.

The absence of a Michaelis-Menten-like ATP dependence is in conflict with previous experimental studies [87, 89]. To investigate this discrepancy, the unidirectional gliding assay is simulated at a higher dynein density for the same ATP concentrations. At the higher dynein density, indeed a Michaelis-Menten dependence of the gliding velocity can be seen (see fig. 4.19a). In section 4.2.2, it has been shown that the influence of passive motors can be neglected at the higher dynein density. However, at the lower dynein density, the gliding velocity is strongly influenced by passive MT-attached motors. Passive MT-attached motors slow down the transport velocity at low number of dynein motors. The stepping of passive motors is modeled to be dependent on the ATP concentration using a Michaelis-Menten dependence (see eq. (4.34)). This means at lower ATP concentrations the passive MT-attached motors slow down the MT gliding even more. This explains why, a slower, almost linearly increasing gliding velocity with increasing ATP concentration is found instead of a Michaelis-Menten-like ATP dependence. Consequently, the ATP dependence of dynein depends on the number of motors. At saturated number of motors, a Michaelis-Menten dependence is expected as seen by previous experimental studies [87, 89]. However, at low number of dynein motors, passive MT-attached dynein motors slow down the transport and a more linearly increasing velocity as a function of the ATP concentration is found. Future studies should take into account this number dependence.

While at higher dynein densities a Michealis-Menten dependence on the ATP concentration is expected as seen for kinesin, at lower dynein densities the dependence on the ATP concentration differs for kinesin and dynein motors. That is why, bidirectional gliding assays are performed at a low dynein density and two ATP concentrations, $1000\,\mu\mathrm{M}$ and $5000\,\mu\mathrm{M}$, where the differences between dynein and kinesin motors were found to be substantive. Going from $1000\,\mu\mathrm{M}$ to $5000\,\mu\mathrm{M}$, the median velocity of the kinesin assay remained almost constant, while the median velocity of the dynein assay nearly doubled. As for the number dependence,

the kinesin density is varied at a constant dynein density. A low constant dynein density of $\sigma_{\text{dyn}} = 18\,\mu\text{m}^{-2}$ is applied as used in the unidirectional assay (see fig. 4.18a and 4.18b for the unidirectional assay). Median instantaneous velocities of simulation (fig. 4.18c) and experiment (fig. 4.18d) are depicted as a function of the kinesin density at the two different ATP concentrations 1000 μM and 5000 μM. It can be seen that the simulation is aligned with
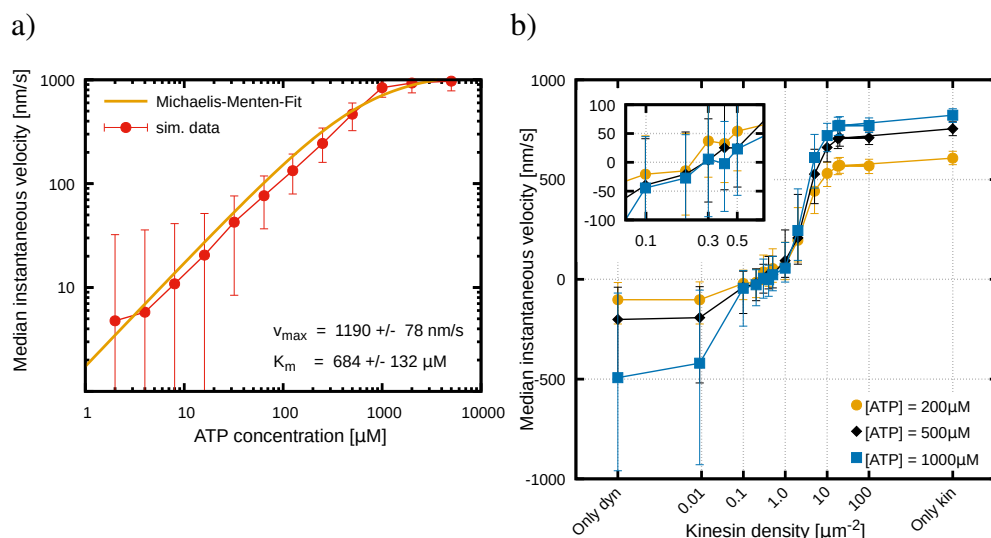
Figure 4.19: Unidirectional gliding assay at high dynein density and bidirectional gliding assay at low ATP concentrations. a) Unidirectional gliding assay simulations performed at a high dynein density of $\sigma_{\text{dyn}} = 64\,\mu\text{m}^{-2}$. Median instantaneous velocities plus IQR are depicted as a function of ATP concentration. In this simulation a MT length of $L_{\text{MT}} = 25\,\mu\text{m}$ was applied. The data of the unidirectional gliding assay simulation at higher dynein density could be fitted by a Michaelis-Menten equation $V_{\text{max}} \times [\text{ATP}]/(K_m + [\text{ATP}])$ with $V_{\text{max}} = 1190\pm78$ nm/s and $K_m = 684\pm132\,\mu\text{M}$. b) Bidirectional gliding assay simulations at varying low ATP concentrations. A MT length of $L_{\text{MT}} = 25\,\mu\text{m}$ was applied. Median instantaneous gliding velocities plus IQR are depicted as a function of varying kinesin densities at a fixed dynein density of $\sigma_{\text{dyn}} = 18\,\mu\text{m}^{-2}$. A slight tendency of a shift of the balanced state towards smaller kinesin densities for lower ATP concentrations can be seen (see inset). *Reproduced/adapted with permission from The Company of Biologists LTd., Journal of cell science.* Originally published in *Journal of cell science*, volume 133(22), page jcs249938 (2020) [309].

the experimental observations. Both experiment and simulation show the dynein-driven state, the balanced state and the kinesin-driven state for both ATP concentrations. In accordance with the unidirectional assay, median velocities are reduced for the lower ATP concentration in the dynein- and kinesin-driven states. As expected, the velocity is stronger reduced in the dynein-driven state than in the kinesin-driven state (see results of the unidirectional assays fig. 4.18a and fig. 4.18b). If ATP concentration would regulate the directionality of bidirectional transport, the balanced state should be shifted to different kinesin densities in dependence of the ATP concentration. However, the balanced state does not change with the ATP concentration but remains at the same kinesin density (between $0.1 - 1.0\,\mu\text{m}^{-2}$). Thus, the balanced state remains stable upon varying ATP concentrations indicating that the ATP concentration might not regulate the directionality of bidirectional transport.

To understand why the balanced state remains stable upon varying ATP concentrations, the

simulation is used for a detailed look at events happening at the balanced state on a molecular level. Fig. 4.20a shows that predominantly passive dynein stepping occurs at the balanced state. Passive dynein stepping is modeled as ATP-dependent stepping. However, passive
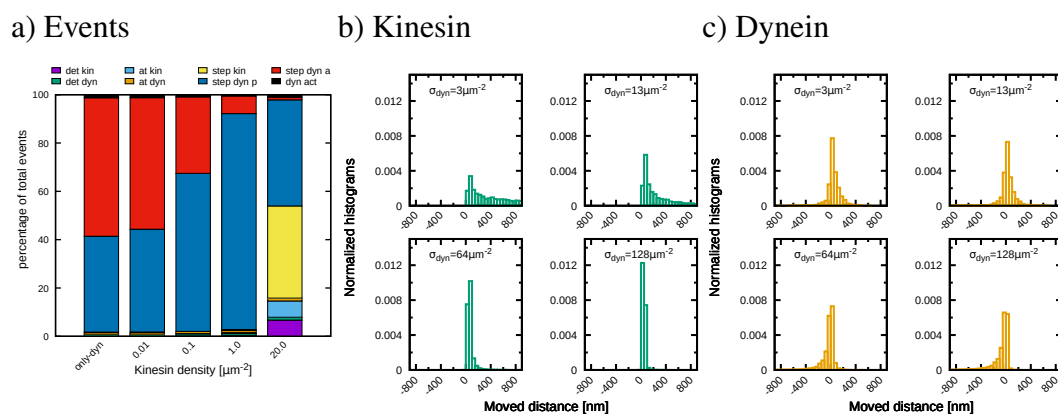

Figure 4.20: Insights into the balanced state at the sub-molecular level. a) Percentage of events that occur on a molecular level are depicted as a function of varying kinesin densities. For all simulations the fixed dynein density was $\sigma_{\mathrm{dyn}} = 64\,\mu\mathrm{m}^{-2}$. The following events can occur on the molecular level: kinesin detachment (purple), dynein detachment (green), kinesin attachment (light blue), dynein attachment (orange), kinesin stepping (yellow), passive dynein stepping (blue), active dynein stepping (red) and dynein (de)activation (black). At the balanced state ($\sigma_{\mathrm{kin}} = 1.0\,\mu\mathrm{m}^{-2}$) mainly passive dynein stepping occurs. Kinesin almost did not step at all and active dynein only stepped occasionally ($< 10\%$). b)+c) Histograms of moved kinesin b) and dynein distances c) in bidirectional gliding assay simulations. The kinesin density was $\sigma_{\mathrm{kin}} = 1.0\,\mu\mathrm{m}^{-2}$ and the dynein density as given in the sub-figures. The balanced state occurred at $\sigma_{\mathrm{dyn}} = 64\,\mu\mathrm{m}^{-2}$. At the balanced state, the moved kinesin and the moved dynein densities are peaked around zero. Thus, at the balanced state, the motors are strongly localized. *Reproduced/adapted with permission from The Company of Biologists LTd., Journal of cell science.* Originally published in *Journal of cell science*, volume 133(22), page jcs249938 (2020) [309].

dynein stepping is a diffusive motion in a harmonic potential, rather than a directed motion. Passive dynein, therefore, does not contribute to the force balance between kinesin and dynein. Consequently, passive dynein and therefore the ATP concentration does not change the force balance between kinesin and dynein motors.

Using MT gliding assays, either unidirectional or stalled trajectories can be observed in dependence of the relative motor concentrations (see fig. 4.15). Stalled trajectories mean that there is a stable force balance between kinesin and dynein. In order to regulate the directionality of bidirectional MT gliding assays, this force balance needs to be shifted. Since the active motors hardly step during the force balance (balanced state), factors that influence the stepping velocity of the motors cannot shift the stable force balance. Thus, the ATP dependence of the motor stepping velocity changes the velocity of the unidirectionally moving cargos, but not the directionality of MT gliding assays.

However, previous studies showed that the ATP concentration also influences the stall force of kinesin and dynein motors. Since the force balance is determined by the number and kind of motors as well as the strengths of individual motors, changing the stall force could influence the force balance. A detailed look at the previous studies reveals that the kinesin stall varies only slightly at very low ATP concentrations ($< 100\,\mu\mathrm{M}$), but remains

constant for higher ATP concentrations [186]. Consequently, the kinesin stall force is mostly considered independent of the ATP concentration [35]. The dynein stall force, in contrast, increases linearly with the ATP concentration until saturating at a value of $\approx 1\,\mathrm{pN}$ and an ATP concentration of $1000\,\mu\mathrm{M}$ [101]. The experiments, which were taken as a reference for the here shown simulations, only applied ATP concentrations in a regime where neither the dynein nor the kinesin stall force changes. Simulating, however, the bidirectional MT gliding assay at lower ATP concentrations (see fig. 4.19), where dynein has a smaller stall force, shows a small tendency of a shift of the balance state towards lower kinesin densities as expected. A clearer dependence on the ATP concentration could be observed for a simulated cargo transport with fixed number of motors [35]. It might be, that when having a fixed number of available motors, the shift of the balanced state can be clarified due to reduced fluctuations[10]. However, the number of motors is not expected to be fixed in real systems. Thus, whether the ATP concentration can shift the force balance in real systems need to be tested in future.

A difference between the trajectories of *in vivo* cargo transport and MT gliding assays is that while MT gliding assays only show stalled or unidirectionally moving cargos (fig. 4.15), single *in vivo* cargos often move in both directions including pauses and directional reversals [7, 8]. This means the balance state might not be as stable *in vivo* as observed here for MT gliding assays. Consequently, reducing the stepping velocity of one motor more than the other in dependence of the ATP concentration would lead to a shorter distance traveled during the moving (run) state in one direction than in the other. As a result, the overall directionality would be changed. Thus, influencing the stepping velocity rather than the force balance could still be a mechanism for how the ATP concentration could regulate *in vivo* cargo motion. Future work should focus on testing the influence of the ATP concentration on transport systems which resembles the mode of motion of *in vivo* cargos.

4.3.3 Regulation by roadblocks

Previous work showed that kinesin and dynein are asymmetrically influenced by roadblocks [31, 40, 204, 312]. The reason is a different reaction of the kinesin and dynein motors when encountering a roadblock [209, 211, 212]. While kinesin shows pausing or detachment events when encountering a roadblock [209, 211], dynein is thought to change to the neighboring protofilaments in order to circumvent roadblocks [39]. Consequently, (eventually) detaching kinesin, roadblocks could shift the force balance between kinesin and dynein. Thus, it is therefore thought that roadblocks could regulate bidirectional transport [31, 40, 204, 312].

Before studying bidirectional transport in the presence of roadblocks, it needs to be known how teams of multiple kinesin or teams of multiple dynein motors react separately to roadblocks. Therefore, unidirectional gliding assays were performed at kinesin and dynein densities of $\sigma_{\mathrm{kin}} = 50\,\mu\mathrm{m}^{-2}$ and $\sigma_{\mathrm{dyn}} = 50\,\mu\mathrm{m}^{-2}$, respectively. In the experiments, the MTs were coated with rigor-binding kinesin-1 mutants (from now on referred to as roadblocks) at different concentrations. In the simulation, permanently occupied spots on the MT at a given line density λ_{RB} are implemented. The occupied spots have the radius of a kinesin motor $R_{\mathrm{kin}} = 4\,\mathrm{nm}$. Both, dynein and kinesin motors are not allowed to attach or step on these occupied spots. Unidirectional gliding assays were performed at different roadblock concentrations (experiments) and line densities (simulation). Relative median instantaneous velocities are depicted

---

[10]Note that in this work fluctuations are in the same range as the observed shift of the balance state.

as a function of the roadblock concentration for the experiment (fig. 4.21b) and as a function of the roadblock line density for the simulation (fig. 4.21a). For simulation and experiment, the median velocities decrease with increasing roadblock concentrations/line densities for kinesin and dynein. In the experiment and the simulation, a faster decrease is observed for dynein. Consequently, dynein is more affected by roadblocks than kinesin. This is in contrast to expectations from single molecules, where dynein was observed to overcome roadblocks more successfully or not be influenced by roadblocks at all [31, 39]. Furthermore, the result is in contrast to a previous study showing that cargo transport by multiple kinesin motors is as affected by roadblocks as multiple dynein motors [39].

Dynein being more affected by roadblocks than kinesin in MT gliding assays might be due to the gliding assay set-up. As said before, the bypassing mechanism of dynein is to take side steps to neighboring protofilaments. In the simulation, however, only one protofilament is modeled and dynein motors are not able to sidestep in order to overcome a roadblock. Differences between kinesin and dynein assays raise only from different detachment and (re)attachment properties. While for the simulation it is known that dynein motors are not able to side step, it is unknown whether dynein motors are able to perform side steps in the gliding assay set-up. To test whether the same results would be obtained if dynein were able to side step, the gliding assay is simulated with seven protofilaments instead of just one protofilament. In the multiple protofilament simulation, kinesin motors are able to attach to different protofilaments, but not change the protofilament while being attached. Attached dynein motors, in contrast, change the protofilament with the side-stepping rate s_{side} (see table A.1 for parameter values and references). Using the multiple protofilament simulation, multiple dynein motors were as affected by roadblocks as multiple kinesin motors (see 4.22a). Using the multiple protofilament simulation, but not allowing dynein to take side steps, multiple dynein motors were again more affected by roadblocks than multiple kinesin motors as it has been seen for the one protofilament simulation (see fig. A.1 of the appendix A). Consequently, it is expected that dynein motors are not able to take side steps in the gliding assay experiments.

Not being able to sidestep, dynein motors need to detach and attach again after the roadblock to overcome it. Comparing the dynein attachment rate ($k_{\mathrm{a,dyn}} = 0.2\,\mathrm{s}^{-1}$) with the kinesin attachment rate ($k_{\mathrm{a,kin}} = 20\,\mathrm{s}^{-1}$), reveals that kinesin is able to reattach much faster than dynein (see table A.1 for the parameter values). That is why, in gliding assays, multiple dynein motors are more affected by roadblocks than multiple kinesin motors.

Since roadblocks impair multiple kinesin and dynein motors to different degrees, the question arises, whether roadblocks can change the transport direction in bidirectional gliding assays. Bidirectional gliding assays are therefore performed in the presence of roadblocks at different roadblock concentrations, in the experiment, and different roadblock line densities, in the simulation. As before, the kinesin densities are varied at the constant dynein density of $\sigma_{\mathrm{dyn}} = 50\,\mu\mathrm{m}^{-2}$ used in the unidirectional assay. Median velocities are depicted as a function of the kinesin density for different roadblock line densities for the simulation (fig. 4.21c) and roadblock concentrations for the experiment (fig. 4.21d). Simulations and experiments show dynein-driven states, balanced states, and kinesin-driven states. Median velocities reduce in the dynein- and kinesin-driven state the higher the roadblock concentration or the roadblock line density. The reduction of the velocity is stronger in the dynein-driven state, which is expected from the results of unidirectional gliding assays. The balanced state, however, remains at the same kinesin density for all roadblock concentrations in the experiment and all line densities in the simulation. Consequently, roadblocks cannot change the transport direction in bidirectional gliding assays. With the multiple protofilament simulation, the same results are

a) Simulation

b) Experiment

c) Simulation

d) Experiment
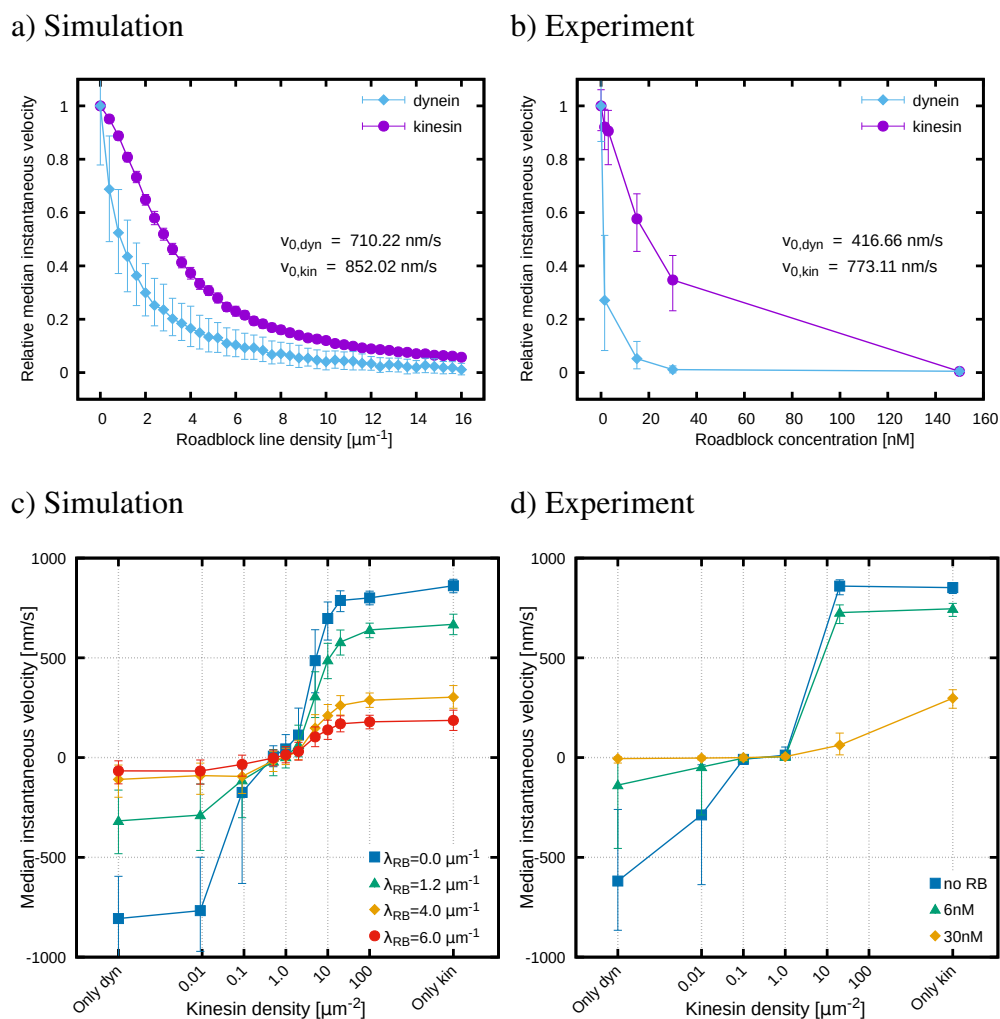
Figure 4.21: Different reactions of unidirectional kinesin and dynein assays to roadblocks do not lead to a shift of the balanced state in bidirectional gliding assays. Rigor-binding kinesin mutants were put on the MTs as roadblocks. While in the simulation a roadblock line density λ_{RB} is applied, in the experiment the roadblock concentration is given. a)+b) Relative median instantaneous velocities with IQR for unidirectional kinesin (purple curve) and dynein (light blue curve) gliding assays in the presence of roadblocks. Relative velocities are calculated by the instantaneous velocities in the presence of roadblocks divided by the velocity in the absence of roadblocks. Relative median velocities are depicted as a function of the roadblock line density for simulation a) and as a function of the roadblock concentration for the experiment b). For simulation and experiment, kinesin and dynein densities were $\sigma_{kin} = \sigma_{dyn} = 50\,\mu m^{-2}$, respectively and the MT length was $L_{MT} = 25\,\mu m$ in the simulation and in the interval of $L_{MT} = 25 - 30\,\mu m$ in the experiment. Median velocities decreased with increasing number of roadblocks in unidirectional kinesin and dynein gliding assay simulations and experiments. The velocities decreased faster in the dynein assays than in the kinesin assays. c)+d) Bidirectional gliding assay simulations (c) and experiments (d) in the presence of roadblocks. At a fixed dynein density of $\sigma_{dyn} = 50\,\mu m^{-2}$, median instantaneous gliding velocities with IQR are shown as a function of varying kinesin densities. In the (*Continuation on next page.*)

Figure 4.21 (*previous page*)**:** simulation, a length of $L_{MT} = 25\,\mu m$ was applied. Relative median velocities were stronger reduced by roadblocks in the dynein-driven state than in the kinesin-driven state. The balanced state remained at a kinesin density of $\sigma_{kin} = 1.0\,\mu m^{-2}$ in the simulation and of $\sigma_{kin} = 0.1-1.0\,\mu m^{-2}$ in the experiment for all roadblock line densities and concentrations. All shown experiments were performed by Lara Scharrel from Stefan Diez lab at B CUBE, TU-Dresden. *Reproduced/adapted with permission from The Company of Biologists LTd., Journal of cell science.* Originally published in *Journal of cell science*, volume 133(22), page jcs249938 (2020) [309].

found (see fig. 4.22b). This means, independently of the side-stepping ability of dynein, roadblocks cannot regulate the directionality in bidirectional MT gliding assays.

To understand why the balanced state remains stable upon different roadblock concentrations, the distance a motor moves in the balanced state is measured using the simulation. Moved distances are depicted for kinesin and dynein motors at different dynein densities and a kinesin density of $\sigma_{kin} = 1.0\,\mu m^{-2}$ (fig. 4.20b and fig. 4.20c). At the balanced state ($\sigma_{dyn} = 64\,\mu m^{-2}$), it can be seen that kinesin and dynein motors move very little. In more detail, the median moved dynein and kinesin distance in the balanced state are 16 nm and 64 nm, respectively, while the mean distance between roadblocks is $\approx 166\,nm$ at a roadblock line density of $\lambda_{RB} = 6\,\mu m^{-2}$. Thus, the mean distance between roadblocks is more than double the moved distance of the motors. That is why the motors do not "see" the roadblocks in the balanced state. Taking together, because of the strong motor localization, the balanced state remains stable upon different roadblock concentrations. Consequently, roadblocks cannot regulate bidirectional transport.

Here, it is shown that roadblocks, which hinder both motors, cannot change the force balance. Having, however, motors that asymmetrically detach one kind of motor, while the other remains unaffected, could shift the absolute force direction during a moving phase and therefore change the direction. Tau islands, for instance, are such roadblocks (see chapter 5 for tau island modeling and 2.4.3.1 for background information about tau). Tau islands let dynein motors pass, but detach kinesin-1 motors [31, 40]. Thus, tau islands change the motor distribution and are therefore expected to regulate the direction of bidirectional transport.

Furthermore as mentioned before, *in vivo* cargos move bidirectionally including unidirectional runs, pauses, and directional reversals [7, 8]. Slowing down the cargos more during one transport direction than the other could change the overall transport direction of bidirectionally moving cargos. Thus, as for the ATP concentration, the influence of symmetric roadblocks should be tested using a transport system showing bidirectional, *in vivo*-like transport motion including reversals.

4.4 Conclusion

In this chapter, MT gliding assay simulations are used to study intracellular transport by multiple motors. Using unidirectional gliding assays, first, the collective motion of several kinesin or dynein motors was studied. While the kinesin assay simulations are in alignment with the experimental observations using a known kinesin model [33–35], the standard dynein model [33–35] could not reproduce the experimentally observed behavior. To reproduce the increase of MT gliding velocity with increasing number of dynein motors seen in experiments, a mechanical dynein activation is hypothesized and added to the dynein model. Under the assumption of
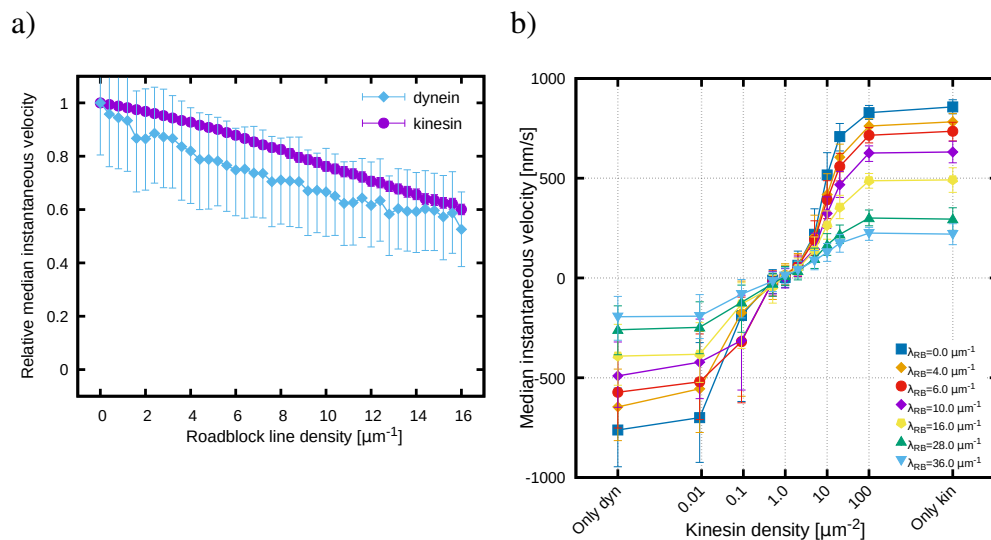
a)

b)

Figure 4.22: Dynein is as affected as kinesin in multiple protofilament simulations in the presence of roadblocks, but the balanced state remains stable. a) Multiple protofilament simulations of unidirectional kinesin (purple) and dynein (light blue) gliding assays in the presence of roadblocks. Using the multiple protofilament simulations seven protofilaments are modeled instead of just one protofilament. Dynein is thereby allowed to change the protofilament with rate $s_{\text{side}} = 4\,\text{s}^{-1}$, while kinesin stays at one protofilament. Kinesin and dynein densities were $\sigma_{\text{kin}} = \sigma_{\text{dyn}} = 50\,\mu\text{m}^{-2}$, respectively and a MT of $L_{\text{MT}} = 25\,\mu\text{m}$ was used. Relative median instantaneous velocities (instantaneous velocity divided by the velocity in the absence of roadblocks) are depicted as a function of the roadblock line density. In the multiple protofilament simulation, both motors are less affected by roadblocks and dynein is as strongly affected as kinesin. b) Multiple protofilament simulations of bidirectional gliding assays in the presence of roadblocks. Relative median instantaneous velocities are depicted as a function of varying kinesin densities at a fixed dynein density of $\sigma_{\text{dyn}} = 50\,\mu\text{m}^{-2}$. The MT length was $L_{\text{MT}} = 25\,\mu\text{m}$. Even if multiple protofilaments are involved in the transport, the balanced state stays at the same kinesin density for all roadblock concentrations. *Reproduced/adapted with permission from The Company of Biologists LTd., Journal of cell science.* Originally published in *Journal of cell science*, volume 133(22), page jcs249938 (2020) [309].

a mechanical activation, the simulation shows the experimentally found increased cooperation between multiple dynein motors with increasing number of motors. The here shown and in Monzon et al. [300] published, mechanical activation mechanism can explain how multiple dynein motors can transport a MT at high velocities while for single dynein without adaptor proteins, only diffusion-like motion is observed.

In a second step, the established kinesin and dynein models were incorporated into bidirectional gliding assay simulations. Results of the bidirectional gliding assays show that while the number and kind of motors determine the transport direction, the balanced state remains stable under varying ATP and roadblock concentrations. Thus, ATP concentration and roadblocks are no regulation factors for the directionality of bidirectional transport in MT gliding assays. Thus, in MT gliding assays, only factors influencing the force balance between kinesin and dynein motors rather than the single motor stepping, are potential regulation factors.

However, while in MT gliding assays only stalled or unidirectional trajectories (fig. 4.15)

could be observed, *in vivo* cargos often show bidirectional motion including directional reversals [7, 8]. Future studies should test whether influencing the motor stepping can regulate cargo transport directions, when the cargo is transported bidirectionally, including reversals.

Moreover, the simulation shows that MT-attached kinesin motors activate passive MT-attached dynein and increase the total number of MT-attached motors. Thus, the simulation reveals that besides antagonistic effects, there are also cooperative effects between kinesin and dynein motors.

The presented bidirectional gliding assay results including the dependence on the number of motors, ATP, and roadblock concentrations are published in Monzon et al. [309].

Chapter 5

Modeling tau adsorption

Contents

In this chapter, the adsorption of the MT-associated protein tau to the MT lattice is modeled. MT-associated proteins influence each other differently such that molecular motors (belonging to the MT-associated proteins) are also influenced by non-motor MT-associated proteins. On the one hand, non-motor MT-associated proteins can reduce molecular motor stepping or even lead to motor detachment. On the other hand, non-motor MT-associated proteins can have no effect on the molecular motor MT interaction or even enhance the molecular motor binding affinity to MTs [31, 40, 313–316]. Here, first, the tau adsorption to the MT and the formation of tau islands (= dense, stable accumulations of tau) on the MT are studied. The tau adsorption model is built up using the Langmuir adsorption model as a reference. Then, the simulated tau adsorption and island formation are compared to the experiments of Siahaan et al. [40]. Finally, model parameters are varied to discuss their influence on tau island formation.

The previous chapter showed that although point-like roadblocks have different effects on unidirectional kinesin and dynein transport, point-like roadblocks cannot regulate the transport direction in bidirectional gliding assays. However, inside the cell, not only point-like road-blocks exists but also spatially extended obstacles. Spatially extended obstacles could have a different effect on the directionality of bidirectional transport than point-like roadblocks. It could be that a cargo reverses its direction when encountering a spatially extended obstacle because the leading motor cannot step any further. Spatially extended obstacles could be other big cargos occupying the MT track or accumulations of other MT-associated proteins. Recent work showed that the MT-associated protein tau forms islands on MTs[1]. Tau islands are stable clusters of tau proteins, which protect the MT from MT-severing enzymes like katanin for instance [40]. Malfunctioning of tau is known to lead to neurodegenerative diseases like Alzheimer or fronto-temporal dementia [26, 229, 231–233, 318]. On the intracellular level, it has been shown that a higher tau concentration leads to different organelle distributions suggesting that tau has an impact on intracellular transport [29, 316]. That is why it is intriguing to understand the functioning of tau.

In vitro experiments showed that dynein and kinesin are differently affected by tau islands. While single DDB (dynein–dynactin–BicD2N) was observed to pass tau islands, kinesin-1 detached when encountering a tau island [31, 40]. However, the effect of tau islands on bidirectional intracellular transport remains obscure. To understand the impact of tau islands on intracellular transport, first, the tau adsorption and island formation need to be understood. Here, tau island formation is studied using stochastic simulations. Simulations are compared to the experimental work by Siahaan et al. [40]. Therefore, a tau adsorption model is developed based on the Langmuir adsorption model and known lattice gas models (see section 3.3 for details on the Langmuir adsorption model and lattice gas models).

5.1 Tau adsorption model

Previous work showed that tau binds longitudinally along MTs [210]. That is why the MT is modeled as a one-dimensional lattice taking only one protofilament (from now on abbreviated as PF) into account (see illustration fig. 5.6). The one-dimensional lattice consists of N_L sites. Each site is 8 nm long, the length of one tubulin dimer.

First, only the adsorption and desorption are modeled. Therefore, the adsorption and desorption rates are estimated from the experimental *in vitro* study by Siahaan et al. [40]. In this study, they measured the tau density within (denoted by ρ_I) and outside the islands (=surrounding, density denoted by $\rho_S(t)$) as a function of time, as well as the fraction of the MT covered with islands ($f_{\text{coverage}}(t)$). From that the total experimental tau density can be calculated:

$$\rho_{\text{exp}}(t) = f_{\text{coverage}}(t) \cdot \rho_I + \left(1 - f_{\text{coverage}}(t)\right) \cdot \rho_S(t).$$
(5.1)

The time dependence of the experimental density can be fitted with the time dependence given by the Langmuir adsorption model (see section 3.3 for details):

$$\rho_{\text{Langmuir}}(t) = \frac{\Omega_a}{\Omega_a + \Omega_d} \cdot \left(1 - e^{-(\Omega_a + \Omega_d) \cdot t}\right).$$
(5.2)

---

[1]These "tau clusters" were first called "tau islands" and "tau condensates" [31, 40]. A recent study calls them "tau envelops" [317].

Fitting $\rho_{\text{exp}}(t)$ with the Langmuir adsorption model (see fig. 5.1) gives an estimate for the tau adsorption rate Ω_a and desorption rate Ω_d:

$$\Omega_a = 0.003\,\text{s}^{-1} \quad \text{and} \quad \Omega_d = 0.046\,\text{s}^{-1}. \tag{5.3}$$

When simulating just tau adsorption and desorption, the simulation density (fig. 5.2a) follows the theoretical Langmuir density as expected and the kymograph (lower row of fig. 5.2a) shows tau molecules that attach to the MT lattice, stay attached for a while, and then detach again. The kymographs show various grey shades because a Gaussian filter is applied to better mimic the experimental kymographs. Note that using the Langmuir model neglects correlation effects between tau molecules.

In this first model, one tau molecule is just occupying one lattice site, i.e. one tubulin dimer. However, it is known that the tau isoform used in the experiment by Siahaan et al. [40] has four MT binding repeats (from now on called MT-BRs). Tau is a string-like molecule, where the four MTBRs are aligned next to each other (see fig. 5.4). Moreover, it is known that tau binds along one protofilament with one MTBR being attached from the middle of the beta-tubulin of one tubulin dimer to the middle of the beta-tubulin of the next tubulin dimer [210]. Thus, one MTBR covers a length of one tubulin dimer of approximately 8 nm. This means, when adding the four MTBRs to the tau adsorption model, one tau molecule occupies $1-4$ neighboring sites on the one-dimensional lattice. When adsorbing from the solution tau binds with one randomly chosen MTBR. While for the initial adsorption from the

Figure 5.1: Experimental tau density can be fitted with Langmuir adsorption model. The red curve shows an estimate of the tau density in the experiment of Siahaan et al. [40]. Using eq. (5.1), the density was calculated from the constant tau density within islands ρ_I, the tau density outside islands $\rho_S(t)$, and the fraction of the MT covered with islands $f_{\text{coverage}}(t)$. The tau densities inside and outside islands were estimated from fig. 1f and the MT coverage from fig. 1e (20nM tau) of Siahaan et al. [40]. The blue curve shows the fit using the Langmuir adsorption model (eq. (5.2)).

solution, the global adsorption rate Ω_a is used, for the further binding and unbinding of MT-BRs, the intrinsic attachment and detachment rates ω_a and ω_d are used, respectively. Since MTBRs are next to each other in the tau molecule (see fig. 5.4), it is assumed that only the next neighbor(s) of the MT-bound MTBR(s) can bind to neighboring sites on the lattice and only the outer bound MTBR(s) can unbind. This means combinations such as *bound-unbound-bound-bound* are not allowed. See also the schematic in fig. 5.3a. Since the binding and unbinding of the MTBRs are stochastic processes at equilibrium, the intrinsic attachment and detachment rates are connected via the detailed balance:

$$\frac{\omega_a}{\omega_d} = e^{-\beta \Delta E} = e^{-B} \tag{5.4}$$

with the thermal energy $\beta = \frac{1}{k_B T}$ and the binding energy B.

A tau molecule completely desorbs to the solution again if all four MTBRs are unbound. Including four MTBR(s) and intrinsic binding and unbinding processes, the tau molecule should
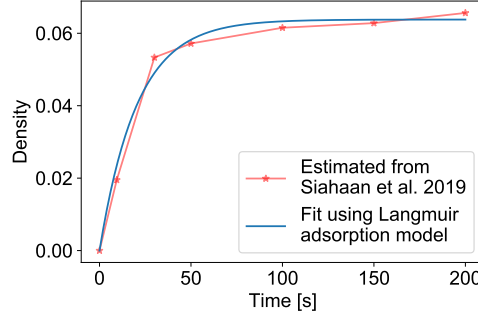
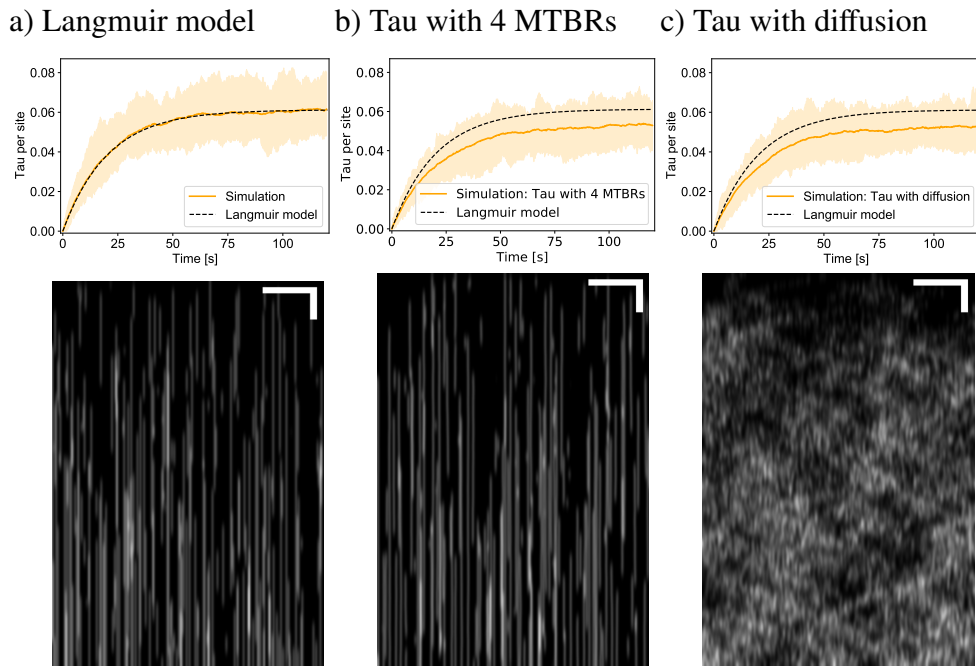a) Langmuir model   b) Tau with 4 MTBRs   c) Tau with diffusion

Figure 5.2: Building up the tau adsorption model: Langmuir adsorption model, tau with four MT binding repeats and tau diffusion. Figures show tau per site densities (upper row) and kymographs (lower row) for different states of the tau adsorption model. Tau per site density is calculated as the number of tau molecules bound to the one-dimensional lattice divided by the total number of lattice sites. Kymographs are generated by plotting the occupancy of the one-dimensional lattice for each measurement time ($\Delta t_{mes} = 0.12\,\text{s}$). A site, which is occupied, is plotted in white, and an empty site in black. Having tau with four MT binding repeats (MTBRs), the signal of one tau is equally distributed over the occupied sites resulting in grey points. Additionally, to better mimic experimental kymographs, the image is blurred using the Gaussian filter from the python package *scipy* with sigma = 5 (*scipy.ndimage.gaussian_filter*). Scale bars are $2\,\mu\text{m}$ (horizontal) and $5\,\text{s}$ (vertical). a) Only tau adsorption and desorption are modeled reproducing the Langmuir adsorption model. In this case, one tau molecule is only occupying one lattice site. Since tau molecules do not move, the kymograph just shows straight lines representing attached tau molecules. b) The model of a) is used but with tau with four MTBRs. In this case, one tau molecule can occupy one to four sites on the lattice resulting in a tau per site density lower than the density from the Langmuir adsorption model. The kymograph is similar to the kymograph in a). c) The tau diffusion is added to the model of b). When the tau molecule diffuses to the next site, all bound MTBRs are moved by one site. The tau per site density remains unchanged compared to b), but the kymograph now shows moving tau resulting in randomly distributed dots instead of straight lines.

still desorb to the solution with the rate Ω_d. This means the tau molecule should, on average, pass the desorbed state after a time of $1/\Omega_d$ after binding. This specifies the time scale for intrinsic binding and unbinding events. In detail, this means the mean time between binding and unbinding has to be equal $1/\Omega_d$. Note that initially one randomly chosen MTBR is bound. To calculate the mean first passage time to pass to the desorbed state, the set of master equations of all states is needed. For setting the master equations, it has to be distinguished between MTBRs in the middle (denoted by M, MTBR numbers two and three) and MTBRs at the edges

(denoted by E, MTBR numbers one and four). The state where all MT binding repeats are bound is then called P_{EMME}. Having three MTBRs bound can either be state P_{EMM} or P_{MME}. For two bound MTBRs, there are the states P_{EM}, P_{ME} and P_{MM} and when only one is bound, it can either be P_E or P_M. The state where no MTBR is bound is denoted by $P_{Desorption}$. Fig. 5.3b shows all possible transitions between the states, which result in the following set of master equations:

$$
\begin{cases}
\frac{d}{dt}P_{EMME} &= -2\omega_d P_{EMME} + \omega_a \left(P_{EMM} + P_{MME} \right) \\[4pt]
\frac{d}{dt}P_{EMM} &= \omega_d \left(P_{EMME} - 2P_{EMM} \right) + \omega_a \left(P_{EM} + P_{MM} - P_{EMM} \right) \\[4pt]
\frac{d}{dt}P_{MME} &= \omega_d \left(P_{EMME} - 2P_{MME} \right) + \omega_a \left(P_{MM} + P_{ME} - P_{MME} \right) \\[4pt]
\frac{d}{dt}P_{EM} &= \omega_d \left(P_{EMM} - 2P_{EM} \right) + \omega_a \left(P_E + P_M - P_{EM} \right) \\[4pt]
\frac{d}{dt}P_{MM} &= \omega_d \left(P_{EMM} + P_{MME} - 2P_{MM} \right) + 2\omega_a \left(P_M - P_{MM} \right) \\[4pt]
\frac{d}{dt}P_{ME} &= \omega_d \left(P_{MME} - 2P_{ME} \right) + \omega_a \left(P_E + P_M - P_{ME} \right) \\[4pt]
\frac{d}{dt}P_E &= \omega_d \left(P_{ME} + P_{EM} - P_E \right) - 2\omega_a P_E \\[4pt]
\frac{d}{dt}P_M &= \omega_d \left(P_{ME} + P_{EM} + 2P_{MM} - P_M \right) - 4\omega_a P_M \\[4pt]
\frac{d}{dt}P_{Desorption} &= \omega_d \left(P_M + P_E \right).
\end{cases}
\tag{5.5}
$$

Dividing by ω_d and using the detailed balance 5.4, the master equations become:

$$
\begin{cases}
\frac{d}{d\tau}P_{EMME} &= -2P_{EMME} + e^{-B} \left(P_{EMM} + P_{MME} \right) \\[4pt]
\frac{d}{d\tau}P_{EMM} &= P_{EMME} - 2P_{EMM} + e^{-B} \left(P_{EM} + P_{MM} - P_{EMM} \right) \\[4pt]
\frac{d}{d\tau}P_{MME} &= P_{EMME} - 2P_{MME} + e^{-B} \left(P_{MM} + P_{ME} - P_{MME} \right) \\[4pt]
\frac{d}{d\tau}P_{EM} &= P_{EMM} - 2P_{EM} + e^{-B} \left(P_E + P_M - P_{EM} \right) \\[4pt]
\frac{d}{d\tau}P_{MM} &= P_{EMM} + P_{MME} - 2P_{MM} + 2e^{-B} \left(P_M - P_{MM} \right) \\[4pt]
\frac{d}{d\tau}P_{ME} &= P_{MME} - 2P_{ME} + e^{-B} \left(P_E + P_M - P_{ME} \right) \\[4pt]
\frac{d}{d\tau}P_E &= P_{ME} + P_{EM} - P_E - 2e^{-B} P_E \\[4pt]
\frac{d}{d\tau}P_M &= P_{ME} + P_{EM} + 2P_{MM} - P_M - 4e^{-B} P_M \\[4pt]
\frac{d}{d\tau}P_{Desorption} &= P_M + P_E
\end{cases}
\tag{5.6}
$$

with the reduced time $\tau = \omega_d \cdot t$. The master equations were solved numerically using the initial condition $P_E = P_M = 0.5$. Knowing the time dependence of the probability densities of all states, the probability of still being attached (survival probability) can be calculated:

$$
P_A(\tau) = \sum_{i \in \{E,M,EM,MM,ME,EMM,MME,EMME\}} P_i(\tau). \tag{5.7}
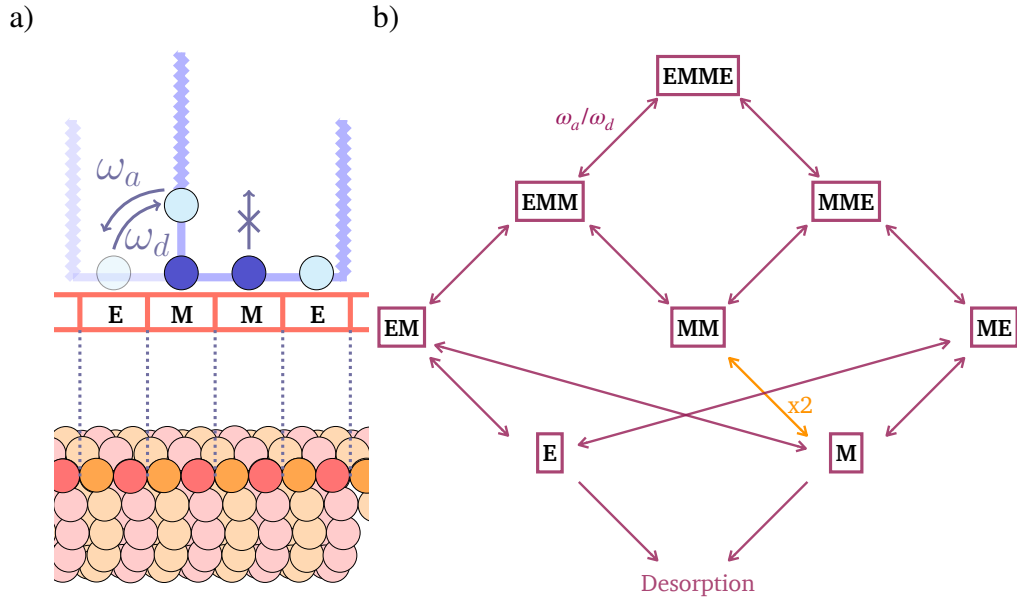$$

Figure 5.3: Tau has four MT binding repeats. a) The schematic shows the model of the four MT binding repeats (MTBRs) of the tau molecule. The four MTBRs are lined up in the tau molecule (see also fig. 5.4) such that it can be distinguished between edge (E) and middle (M) MTBRs. Each MT-bound MTBR occupies one site on the one-dimensional lattice (red), which represents one protofilament of the MT. Single MTBRs attach and detach from the MT with the intrinsic rates ω_a and ω_d, respectively. For intrinsic attachment, only the detached neighboring MTBR(s) of the bound MTBR(s) are allowed. For intrinsic detachment, only the outer-bound MTBRs are allowed. In the schematic the right middle (M) MTBR is therefore not allowed to detach (see crossed arrow). b) The diagram shows all possible states of a tau molecule: zhe tau molecule can be bound with all four MTBRs (EMME), with three of the four MTBRs (EMM or MME), with two MTBRs (EM, MM, or ME), with only one MTBR (E or M) or be desorbed ("Desorption"). Arrows show transitions between the states. Red arrows identify transitions, where only one process leads to this transition, while the orange arrow shows a transition, where two different processes can lead to (the left M or the right M can detach to get to the state M and another M can attach to the right or left of the one attached M). In the model, tau molecules initially land on the lattice either in state M or in state E.

From that the first detachment time density (first passage time density) can be obtained:

$$f_D = \frac{d}{d\tau}(1 - P_A(\tau)) = -\sum_{i \in \{E,M,EM,MM,ME,EMM,MME,EMME\}} \frac{d}{d\tau} P_i(\tau). \tag{5.8}$$

Plugging in the master equations (eq. (5.6)), it is found:

$$f_D = P_E + P_M. \tag{5.9}$$

To calculate the mean first detachment time in the reduced time, the first detachment time probability density has to be averaged over all times:

$$\langle \tau \rangle = \int_0^\infty \tau \cdot (P_E + P_M) d\tau. \tag{5.10}$$

The mean first detachment time in real-time t is calculated as $\langle t \rangle = \langle \tau \rangle / \omega_d$ and has to be equal to the inverse of the global desorption rate:

$$\langle t \rangle = \frac{\langle \tau \rangle}{\omega_d} \overset{!}{=} \frac{1}{\Omega_d}. \tag{5.11}$$

Using a binding energy of $B = -0.1$ (see section 5.2 for variation in the binding energy), the intrinsic detachment rate is found to be:

$$\omega_d = 0.207 s^{-1} \tag{5.12}$$

Using the detailed balance (see eq. (5.4)), the intrinsic attachment rate is:

$$\omega_a = \omega_d e^{-B} = 0.229 s^{-1}. \tag{5.13}$$

Modeling tau with four MTBRs, one tau molecule can occupy $1 - 4$ lattice sites instead of just one lattice site. That is why the tau per site density (fig. 5.2b) remains lower than the density given by the Langmuir adsorption model. Besides the tau per site density, which is defined as the number of bound tau molecules divided by the total number of lattice sites, also the number of occupied sites divided by the total number of lattice sites can be calculated (occupancy density). The occupancy density (fig. B.1a of the appendix B) is higher than the Langmuir density since one tau molecule can occupy up to four sites. In the kymographs, the signal of a bound tau is distributed equally over the sites, which are occupied by this tau molecule. However, because of the Gaussian filter and the low resolution, the spread of a tau molecule over several sites is not visible and the kymograph (lower row of fig. 5.2b) resembles the kymograph of the Langmuir model (lower row of fig. 5.2a).

Besides tau adsorption and desorption processes, previous experiments show tau diffusion along the MT [31, 40, 241]. In the next step, tau diffusion is added to the tau adsorption model. The one-dimensional diffusion constant is given by Siahaan et al. [40]. Tau diffusion along the lattice is modeled as a one-dimensional random walk (see chapter 3). A tau molecule is moved to the next site by shifting all bound MTBRs by one site (see fig. 5.6). Thus, if a tau molecule is initially occupying sites $[i, i + 2]$ (three bound MTBRs, which are occupying sites $i, i + 1$ and $i + 2$) and is chosen to move to the right, it afterward occupies sites $[i + 1, i + 3]$. Adding tau diffusion to the simulation leaves the tau per site density (fig. 5.2c) and the occupancy density (fig. B.1b of appendix B) unchanged. The tau kymograph (lower row of fig. 5.2c) now shows random dots instead of stationary lines. However, no bigger tau accumulations, which could have been identified as tau islands, can be observed.

It is known that in the presence of molecular crowding agents, tau molecules form tau droplets/condensates through liquid-liquid phase separation [235, 319, 320]. Moreover, it was shown that tubulin could be penetrated into the tau droplets and enhance tau droplet nucleation [228]. This indicates that tubulin reinforces a tau-tau interaction. Furthermore, previous studies show that the N-terminal and the C-terminal of the tau molecule (see fig. 5.4) are needed for island formation on the MT supporting also the existence of a tau-tau interaction [31, 40]. Therefore, a tau-tau interaction is added to the presented tau adsorption model. Although the C-terminal and the N-terminal are needed to see tau island formations [31, 40], it is not clear whether edge MTBRs (denoted by E, see fig. 5.3a) need to be next neighbors on the protofilament (i.e. need to be bound to the MT) or a spatial proximity is enough to interact with each other. Since tau-tau interactions are reinforced even in a liquid-like phase in the presence of tubulin, a spatial proximity of the C-terminal and the N-terminal is likely sufficient to experience a tau-tau interaction. That is why, in the tau adsorption model, a tau-tau interaction
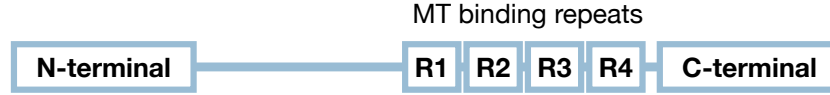
MT binding repeats

| N-terminal | ——————— | R1 | R2 | R3 | R4 | C-terminal |

Figure 5.4: Schematic of the tau molecule. Simplified schematic of the tau molecule. The tau molecule has the N-terminal at one end of the molecule and the C-terminal at the other end. Next to the C-terminal the four MTBRs (R1, R2, R3, and R4) are aligned [31, 40].

is added between tau molecules (see fig. 5.6), which are next neighbors on the MT, which is independent of the types of MTBRs bound. In the model, it is assumed that a tau-tau interaction between two tau molecules reduces the diffusion rate and the intrinsic detachment rate exponentially:

$$s \rightarrow s \cdot e^{-I} \quad \omega_d \rightarrow \omega_d \cdot e^{-I} \tag{5.14}$$

where I is the interaction energy. Due to the tau-tau interaction energy, which overall reduces tau desorption, both the tau per site and the occupancy density are drastically increased (fig. 5.5a and fig. B.1c of the appendix B) compared to the simulations without a tau-tau interaction energy (fig. 5.2c and fig. B.1b of the appendix B). Both densities increase in an almost linear manner as a function of time for the observed period of 120 s. Adding a tau-tau interaction energy, the tau kymograph (lower row of fig. 5.5a) clearly shows small, but stable accumulations of tau, which were not observed in the absence of tau-tau interactions (lower row of fig. 5.2c). A recent study shows that tau islands compact the MT lattice [317]. It can be assumed that the MT lattice is therefore also slightly deformed at the island boundaries leading to higher tau adsorption at island boundaries. That is why a preferential tau adsorption at the boundaries of existing tau islands is added. Having two interacting tau molecules, the tau molecules are identified as a tau island. The global adsorption rate is increased in the following way at empty neighboring sites of existing islands:

$$\Omega_{a,e} = \Omega_a \cdot \frac{(1 + p) \cdot (N_F + N_B)}{N_B \cdot (1 + p) + N_F} \tag{5.15}$$

with the preference $p = 500$ and the total number of free sites at the boundary of islands N_B and the total number of free sites not being next neighbors of existing tau islands N_F. To keep the total global adsorption rate the same as before ($\Omega_{a,tot} = \Omega_a (N_F + N_B)$), the adsorption to free sites not being next neighbors of tau islands is reduced:

$$\Omega_{a,r} = \Omega_a \cdot \frac{N_F + N_B}{N_B \cdot (1 + p) + N_F}. \tag{5.16}$$

While the tau per site (fig. 5.5b) and the occupancy density (fig. B.1d of the appendix B) do not change much, the kymograph (lower row of fig. 5.5b) now shows less but bigger tau islands.

While in the current model infinitely many tau molecules are available in solution to bind to the MT, it is expected that the number of available tau molecules is limited in the experiment. Simulating a reservoir of $N_{res} = 80$ molecules instead of infinitely many tau molecules limits the increase of the tau per site (fig. 5.5c) and the occupancy density (fig. B.1e of the appendix B). The tau per site density now resembles again more the density given by the fit of the experimental density using the Langmuir adsorption model. The kymograph still shows tau
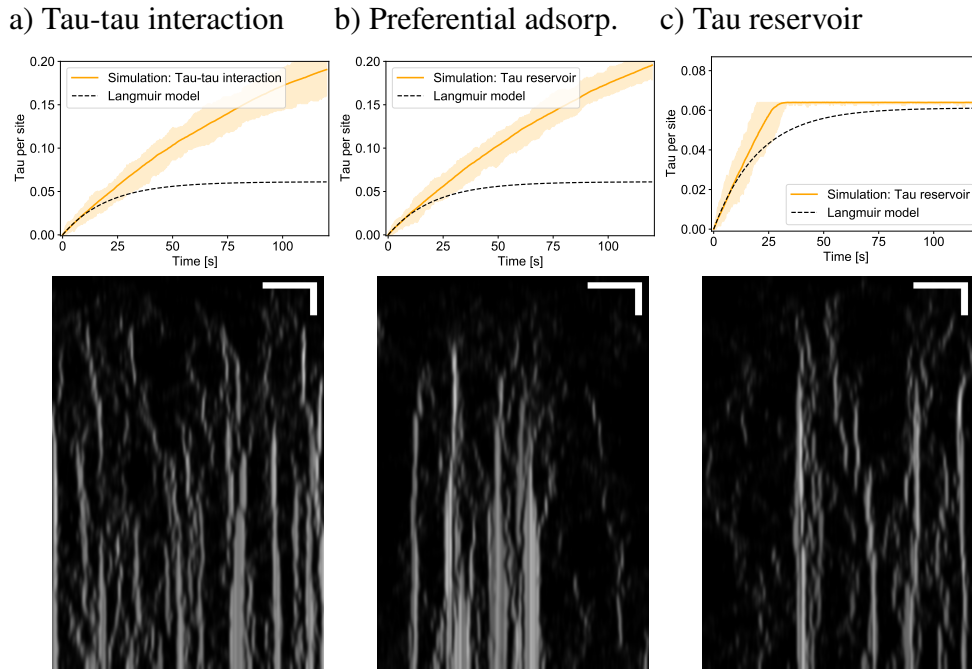
Figure 5.5: Building up tau adsorption model: tau-tau interaction energy, preferential adsorption at island boundaries, and limited tau reservoir. Figures show tau per site densities (upper row) and corresponding kymographs (lower row) for tau adsorption models where the tau-tau interaction was added (a), where the preferential adsorption was added (b) and where a limited tau reservoir was added (c). See the caption of fig. 5.2 for details on the calculation of the tau per site densities and the generation of the kymographs. Scale bars are 2 μm (horizontal) and 5 s (vertical). a) A tau-tau interaction energy is added when two tau molecules are next neighbors on the lattice. The tau-tau interaction energy decreases the intrinsic tau detachment rate and the diffusion rate of interacting tau molecules (see eq. (5.14)). This leads to higher tau per site densities and the kymograph shows accumulations of tau molecules. b) When increasing the global adsorption rate at empty boundary sites of existing islands and decreasing the global adsorption rate at the other empty sites, the tau per site density remains unchanged compared to a), but the kymograph shows fewer, but bigger islands. c) When limiting the number of tau molecules in the solution (tau reservoir), the tau per site density saturates and resembles the density given by the fit of the experimental density using the Langmuir adsorption model. The kymograph shows accumulations of tau molecules and regions with almost no tau.

accumulations and also regions with almost no tau (lower row of fig. 5.5c).

Fig. 5.6 summarizes the here introduced tau adsorption model. At all stages of the tau adsorption model, Gillespie's algorithm for time-independent rates (see section 3.2) is used to choose the next event and propagate the system in continuous time [268, 298]. The tau configuration on the lattice is measured after each Δt_{mes} and the simulation is terminated after T_{end}. See table B.1 for a list of the standard values for all model parameters.
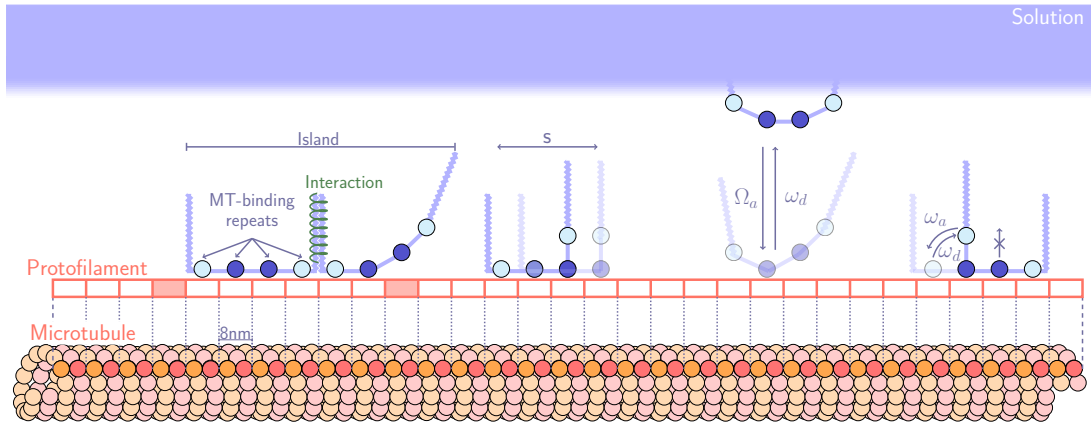
Figure 5.6: Tau adsorption model. The schematic shows a MT and the dynamics of the tau molecule in the tau adsorption model. For transitions between two states, one of the states is drawn with a lower opacity to be able to distinguish it from the other state.

Representing just one protofilament (higher opacity of the red-orange tube), the MT (red-orange tube) is modeled as a one-dimensional lattice of discrete sites (orange lattice). Each site is 8 nm long, the size of one tubulin dimer. Tau molecules are modeled as string-like molecules with four, lined up MT-binding repeats (MTBRs, see most left, blue tau molecule). It is distinguished between edge (denoted by E, light blue circles) and middle (denoted by M, dark blue circles) MTBRs. Tau molecules adsorb to the MT from the solution (blue cloud at the top of the schematic) with the global adsorption rate Ω_{a}. When adsorbing from the solution one of the four MTBRs is randomly chosen to bind to the MT (see second tau molecule from the right). When being attached, the individual MTBRs detach and attach with the intrinsic rates ω_{d} and ω_{a}, respectively (see most right tau molecule). Thereby, only the outer bound MTBRs are allowed to detach (the dark blue middle MTBR of the most right tau molecule is not allowed to detach, for instance, denoted by the crossed arrow). In the same way, only the detached neighbors of the MT-bound MTBRs are allowed to attach to the MT. In the second tau molecule from the right, which is just attached from the solution, only the left light blue and the dark blue MTBRs are allowed to attach, while the right light blue is not. To go back to the solution, the last MTBR needs to detach (rate ω_{d}, see second tau molecule from the right). Tau molecules diffuse along the lattice with rate s. To diffuse to the next binding site, all bound MTBRs are shifted by one site. See the third tau molecule from the right: all three bound MTBRs are shifted by one site on the lattice. If two tau molecules are next neighbors on the lattice (see first and second tau molecule from the left), a tau-tau interaction (see green spring connecting first and second tau molecule from the left) is added. The tau-tau interaction reduces the intrinsic detachment rate ω_{d} and the diffusion rate s (see eq. (5.14)) of the interacting tau molecules. If two tau molecules are next neighbors on the lattice (see the first and second tau molecules from the left), they are building an island (internal definition). Tau from solution preferentially adsorbs to empty boundary sites of existing tau islands (filled, orange lattice sites). See eq. (5.15) and (5.16) for adsorption rates in the case of preferential adsorption.

5.2 Comparison to experiment and parameter discussion

To further investigate and understand the tau adsorption model, in this subsection, first, the tau adsorption model will be compared to the tau island formation experiments by Siahaan et al. [40] and second, the impact of each model parameter will be discussed separately.

In the experiments of Siahaan et al. [40], a solution with tau molecules at different concentrations (20 nM − 90 nM) is mixed with stabilized MTs. The tau is labeled with fluorescent proteins to measure tau intensities along MTs (see [40] for more details about the experimental set-up). Kymographs (see fig. 5.7d and 5.7e for example kymographs at 20 nM tau concentration) of the experiment clearly show regions with high tau intensities surrounded by regions with low tau intensities. The kymographs were manually divided into regions of high tau intensity (called islands) and regions with low tau intensity (called surrounding). To calculate tau densities, for both types of regions, the tau intensities were summed up and divided by the intensity of a single tau and the total length of all regions of this type (island or surrounding). To calculate the number of tau molecules per tubulin dimer, the tau density was multiplied by the length of a dimer (8 nm) and divided by 13 accounting for 13 PFs [40]. The tau molecules per tubulin dimer density at 20 nM tau concentration (fig. 5.7a) clearly shows a difference between islands and surroundings. Islands have a density of slightly less than 0.3 tau per tubulin dimer and the surroundings a density of approximately 0.1 tau per tubulin dimer [40]. The fraction of the MT(s) covered with islands at a tau concentration of 20 nM (fig. 5.7b) slowly increases over time and does not seem to be saturated after the measurement time interval of 200 s [40]. Counting island nucleation events within time intervals of 20 s (fig. 5.7c) reveals that most islands nucleate within the first twenty seconds. After 40 s almost no islands nucleate anymore (especially at the lowest tau concentration of 20 nM) [40]. Kymographs show the high-intensity island regions clearly separated from the surroundings. Fig. 5.7d shows an example kymograph with three island nucleation events (white arrows) and two island fusion events (orange arrows). Interestingly, the borders of islands are stable over long periods. This means, in this state, island borders neither shrink nor continue growing [40]. It is not clear what holds islands stably together and what stops islands from further growing at their stable borders.[2]

To better understand the physical process, underlying island formation, the tau adsorption model presented in the previous section is used. The simulation results of the tau adsorption model are evaluated similarly to the experiment and then compared with the experimental results.

To measure island and surrounding properties separately from one another, in the experiment, island and surrounding regions are segmented manually. During the simulation an interaction between two tau molecules occurs when they are next neighbors. One way to identify islands in the simulation is to use this internal definition saying that tau molecules (at least two) form an island when they are next neighbors on the MT lattice. Since there might also be empty lattice sites within islands, the internal island definition allows up to three empty sites between two islands to still account as one island. Using this definition, already two neighboring tau molecules would form an island. However, due to limited resolution, it is unlikely that in experimental kymographs islands consisting of only two tau molecules

---

[2]Note that all experimental results including data analysis are taken from Siahaan et al. [40]. I did not perform any experiments myself and did not do any data analysis of the experimental data.

a) Density   b) Coverage   c) Nucleation

d) Kymograph 1   e) Kymograph 2
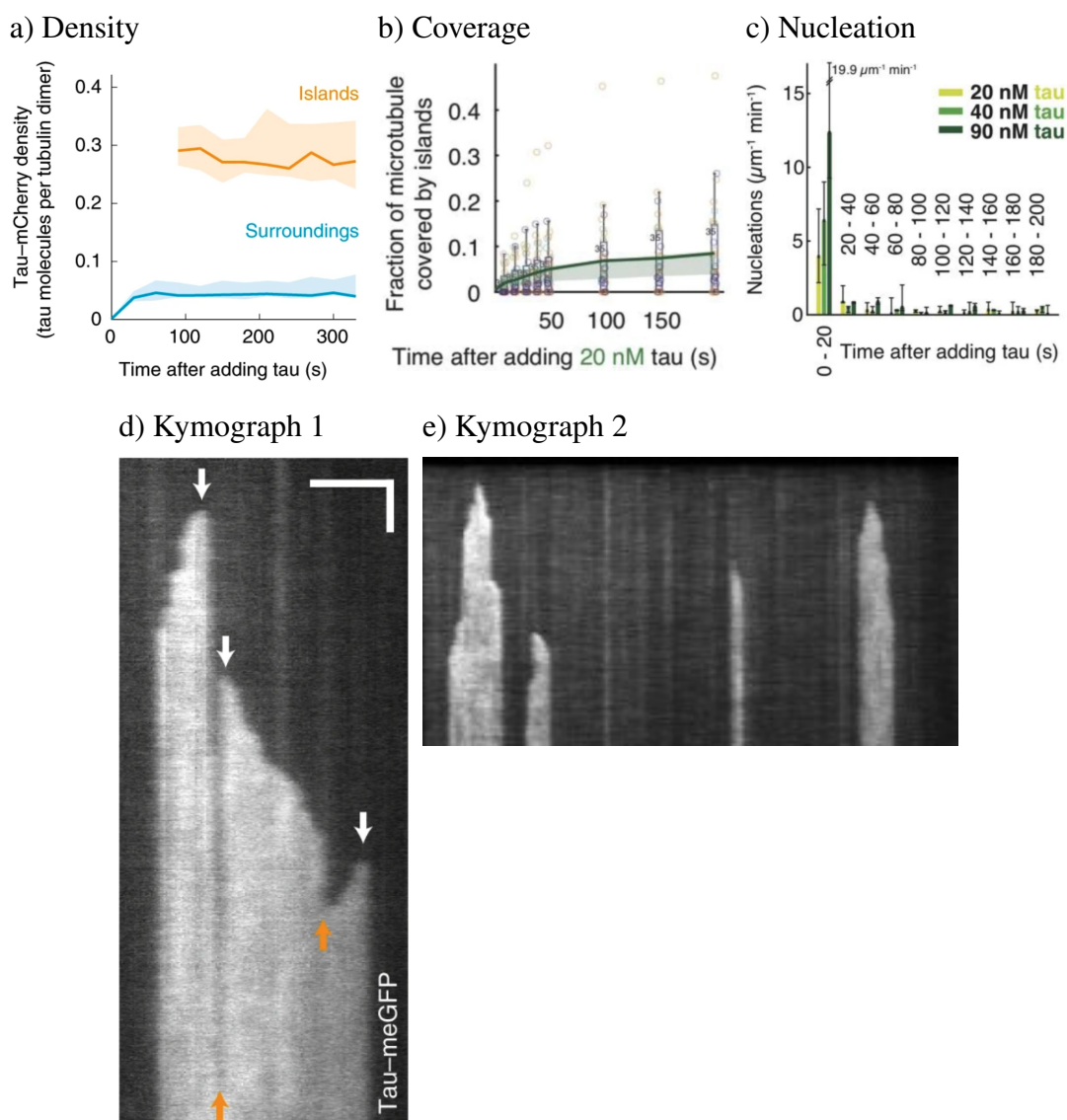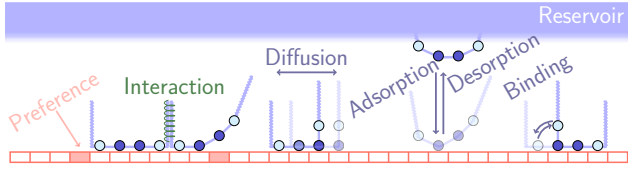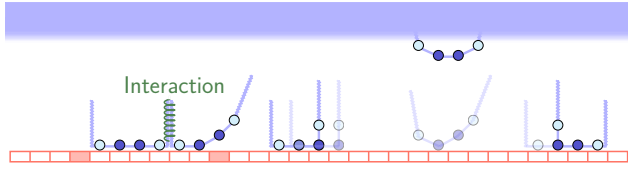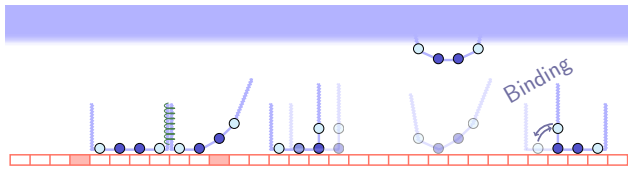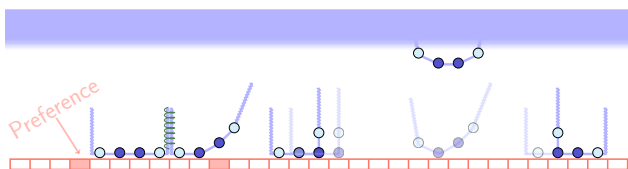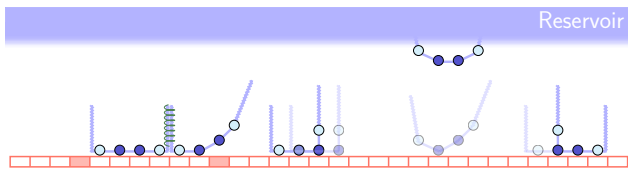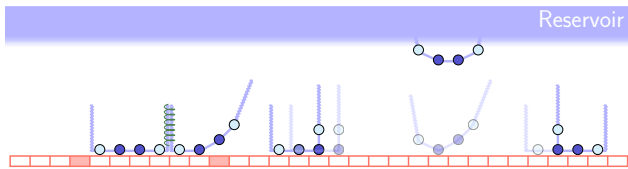
Figure 5.7: Tau adsorption experiments show tau island formations on MTs. The figure shows experimental tau adsorption results from Siahaan et al. [40]. In [40], the MT is manually segmented into regions of high tau density, i.e. tau islands, and regions of low tau density, i.e. surroundings. a) Example time development of tau density in islands and surroundings at 20 nM tau in solution (5 MTs). Tau density (tau molecules per tubulin dimer) is calculated by taking the sum of the intensity of a given category (island or surrounding), divided by the intensity of a single tau times the sum of lengths of the category regions and then multiplied by the length of a tubulin dimer and divided by 13 accounting for the 13 PFs. Tau density within the islands is higher than the tau density in the surroundings. Solid line shows the median and the shaded area the interquantil range. b) Figure shows the time development of the fraction of the MT covered by islands when having 20 nM tau in solution. Solid line and shaded area are the median and minimum/maximum when summing up the length of all islands in a field of view and dividing it by the sum of the lengths of all MTs in the field of view (3 experiments). The boxplot of the data points (open circles) is generated using the fraction of single MTs covered with islands. This (*Continuation on next page.*)

Figure 5.7 *(previous page)*: means one data point is calculated by summing up the lengths of the islands on one MT and dividing them by the length of this MT. c) Island nucleation rate (median plus/minus maximum and minimum) as a function of time for different tau densities in the solution. For all tau concentrations, most islands form in the first 20 seconds. In this thesis, we compare the simulation results to 20 nM tau in solution. d)+e) Example kymographs of tau island formations at 20 nM tau in solution. In d), the three white arrows indicate three island nucleation events and the orange arrows two island fusion events. Remarkably, it takes quite long until the first and second island fuse. Scale bars are 2 μm (horizontal) and 5 s (vertical). *Figures a-d are reproduced with permission from Springer Nature*. Originally published in *Nature Cell Biology*, volume 21, pages 1086–1092 (2019) [40]. The kymograph in e) was produced in the same experiments as published in [40]. *Print permissions were given in a private communication by Markus Braun from Lansky and Brain Lab at Institute of Biotechnology, Czech Academy of Sciences, BIOCEV, Prague West, Czech Republic.*

could already be identified as islands. That is why a second, external island definition is used. The external island definition identifies an island when at least N_{min} consecutive sites are occupied. Thereby, again up to three empty sites between two islands are allowed to still account for one island. Ideally, the results from the internal and external definitions should not differ much from one another, especially at later time points when islands are established. Comparing the fraction of the MT covered with islands (from now on referred to as "island coverage") calculated from the internal and external definition for three different values of N_{min} ($N_{min} \in \{5, 7, 9\}$; see fig. B.2d of the appendix B) reveals that the island coverages are similar for the internal definition and the external definition with $N_{min} = 5$ and $N_{min} = 7$. Using the external definition with $N_{min} = 9$, the island coverage is significantly smaller especially at later time points. This means the value $N_{min} = 9$ is too high so that small islands are neglected. That is why from now on the external definition with $N_{min} = 7$ is used to identify the island and surrounding regions.

The tau density of the simulation with the standard parameter set (see table B.1 of the appendix B) shows a clear separation between islands (slightly less than 0.3 tau per dimer) and surrounding regions (approximately 0.025 tau per dimer density; see fig. 5.9a). The simulated tau density in the islands shows less fluctuations than in the experiment, but the mean value matches well the experimental value (see fig. 5.7a). The tau density in the surrounding is lower in the simulation than in the experiment. The simulated island coverage (fig. 5.10a) increases faster at the beginning and reaches higher values than in the experiment (see fig. 5.7b). Moreover, the coverage saturates within the observation period, which is not the case for the experiment. The number of island nucleation events within 20 seconds time intervals (called nucleation rate) fit well with the experimental values (compare fig. 5.11a with fig. 5.7c). However, in the experiment the MT has 13 PFs [40], while in the simulation only one protofilament is modeled. To compensate for this, one could multiply the simulated nucleation rate by 13. However, because of the tau-tau interaction, it is likely that island nucleations on different PFs are not independent from one another. That is why comparing absolute values of the nucleation rate is difficult. But the trend is the same for experiment and simulation. The simulation kymographs (fig. 5.14a) show many small tau accumulations. Some of them disappear after a while. Occasionally, the kymographs also show bigger tau islands. The tau islands of the simulation are not as homogeneous as in the experiment and borders are not stable. In the simulation, islands even shrink occasionally. Fig. 5.13a shows the island length distribution after 300 seconds. It can be seen that most of the islands are less than 0.25 μm, and the biggest islands are up to 1.5 μm. Siahaan et al. [40] shows

only the island length distribution at higher tau concentration of 40 nM[3]. In this experiment, most islands are up to 1 μm long, but there are also many between 1 and 4 μm. The biggest experimental islands are up to 10 μm long. Even though islands are expected to be bigger at higher tau concentrations, it still seems that island lengths are underestimated in the simulation.

Model	Graphic	Description
a) Standard		Standard parameter set, see table B.1 of the appendix B
b) $I = 1.2\,I_0$		Increased interaction energy between neighboring tau molecules on the MT lattice; interaction energy is $I = 6$ instead of $I_0 = 5$
c) $B = 10\,B_0$		Increased binding energy between MTBRs and the MT lattice changes intrinsic attachment and detachment rates of MTBRs; binding energy is $B = 1$ instead of $B_0 = 0.1$
d) $p = 2\,p_0$		Increased preference for the preferential adsorption at free boundary sites of existing tau islands; preference is $p = 1000$ instead of $p_0 = 500$
e) $N_{res} = 0.75\,N_{res,0}$		Decreased number of tau molecules in reservoir/solution; reservoir is $N_{res} = 60$ molecules instead of $N_{res,0} = 80$ molecules
f) $N_{res} = 1.5\,N_{res,0}$		Increased number of tau molecules in reservoir/solution; reservoir is $N_{res} = 120$ molecules instead of $N_{res,0} = 80$ molecules

---

[3]The here presented simulation focus on the experiment at 20 nM since experimentally given tau densities and kymographs are from experiments with 20 nM tau in solution.
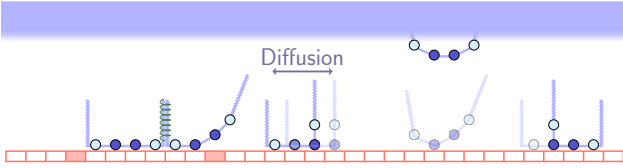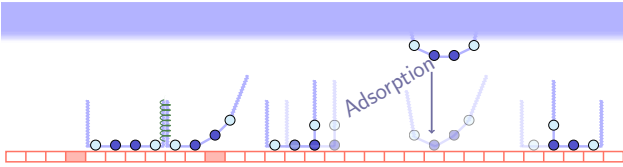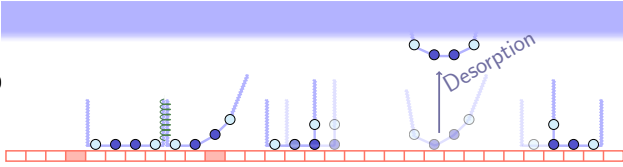
g) $s \approx 0.01\, s_0$		Decreased diffusion rate of MT bound tau molecules; diffusion rate is $s = 40\, \mathrm{s}^{-1}$ instead of $s_0 = 4220\, \mathrm{s}^{-1}$
h) $\Omega_\mathrm{a} = \frac{1}{3}\, \Omega_\mathrm{a,0}$		Decreased global adsorption rate for adsorption from the solution (reservoir); adsorption rate is $\Omega_\mathrm{a} = 0.001\, \mathrm{s}^{-1}$ instead of $\Omega_\mathrm{a,0} = 0.003\, \mathrm{s}^{-1}$
i) $\Omega_\mathrm{d} \approx 11\, \Omega_\mathrm{d,0}$		Increased global desorption rate for desorption from the MT to the solution (reservoir); desorption rate is $\Omega_\mathrm{d} = 0.5\, \mathrm{s}^{-1}$ instead of $\Omega_\mathrm{d,0} = 0.046\, \mathrm{s}^{-1}$

Table 5.1: Table shows the different models tested here. The first one ("a) Standard") uses the standard parameter set (see table B.1 of the appendix B). The corresponding illustration (middle column) shows all parameters that are changed individually for the other models (b) - i)). The illustrations of the other models just mark the parameter, which is changed for this particular model. The first column says how much the parameter is changed compared to the standard model and the third column gives a short description of the changed parameter.

Taking together, the simulation reproduces only partly the experiment (table 5.2 lists all measured variables and evaluates whether experiment and simulation match or not). The simulation shows similar results to the experiment for the tau island density and the nucleation rate. But the tau density in the surrounding is lower and the island coverage higher than in the experiment. Moreover, the number and length of islands together with kymographs reveal that the simulation produces a lot of small islands without stable boundaries instead of a few big islands with stable boundaries as seen in the experiment. This means bigger tau accumulations need to be stabilized and attractive for free tau molecules and small tau accumulations need to be destabilized such that they contribute more to the surrounding density.

In the following, single simulation parameters are changed to see their influence and whether changing individual parameters leads to simulation results closer to the experimental observations. All models with changed parameters as well as the standard model (standard parameter set, see table B.1 in appendix B) are defined in table 5.1. The first row of this table shows the standard model with an overview of all parameters which are changed individually in the other models. The following rows show all models with one changed parameter, respectively.

We have seen that islands are not as stable in the simulation as in the experiment. Building up the tau adsorption model showed that the symmetry of the homogeneous Langmuir density could be broken when introducing an interaction energy between neighboring tau

molecules such that islands form. That is why one way to stabilize islands could be to increase the interaction energy between neighboring tau molecules on the MT lattice. Increasing the interaction energy by a factor 1.2 (from $I = 5$ to $I = 6$, see table 5.1 for the model definition) keeps the island coverage and the nucleation rate similar (compare fig. 5.10b, 5.11b with fig. 5.10a, 5.11a). The tau density within islands (fig. 5.9b) saturates slower but to the same value as the simulation with the lower interaction energy (fig. 5.9a).

Having a higher interaction energy, the tau density in the surrounding is even lower. Kymographs (fig. 5.14b), however, show that island boundaries are more stable when having a higher interaction energy. Moreover, distributions of the number of MTBRs bound to the MT show that more tau molecules are bound with four MTBRs (see fig. 5.8). Comparing the number of islands (fig. 5.12b) and the island length distribution after 5 minutes (fig. 5.13b) reveals that there are less but bigger islands. To conclude, increasing the interaction energy favors the island state over the surrounding state, which results in more stable islands, but the tau density in the surrounding is even lower than for the standard simulation. Moreover, the island coverage remains too high. See table 5.2 for a summary of the influence of the interaction energy on all measured variables.

Figure 5.8: Most tau molecules bind with four MTBRs to the MT. The figure shows the percentage of tau, which is bound with four (grey blue), three (light blue), two (middle blue), or one (dark blue) MTBR after 300 seconds using the different models defined in table 5.1.

Another way to stabilize the islands could be to increase the binding energy B of the MTBRs. Changing the binding energy B also changes the intrinsic detachment and attachment rates ω_d and ω_a, respectively, according to equations (5.12) and (5.13). Note that thereby the experimentally given mean first passage time for tau to pass the desorbing state after landing remains the same. Thus, the global desorption rate Ω_d is not changed. Increasing the binding energy by a factor 10 (from $B = 0.1$ to $B = 1$, see table 5.1 for the model definition) results in slightly higher nucleation rates (fig. 5.11c) and a faster increasing island coverage (fig. 5.10c). This indicates again that islands are favored. Also, the fraction of taus bound with four MTBRs is enhanced even more (fig. 5.8). This leads to slightly decreased tau densities within the islands, while the surrounding density remained the same (fig. 5.9c). Island lengths distribution (fig. 5.13c) and the number of islands (fig. 5.12c), however, reveal that there are more, but smaller islands pointing towards less stable islands. This is underlined by the kymographs (fig. 5.14c) showing islands as for the standard simulation with lower binding energy B (fig. 5.14a), i.e. no stable borders. The latter is the case because the global desorption rate remained the same. The higher binding energy only favored the state, where tau is bound with four MTBRs, which leads to a faster increasing island coverage. See table 5.2 for a summary of the influence of the binding energy on all measured variables.

A third factor, which could influence the stability of the islands, is the preference p of the preferential adsorption (eq. (5.15)). Increasing the preference by twofold (from $p = 500$ to $p = 1000$, see table 5.1 for the model definition) does not change the tau density of the surroundings and islands (fig. 5.9d) nor the island coverage (fig. 5.10d). But the nucleation
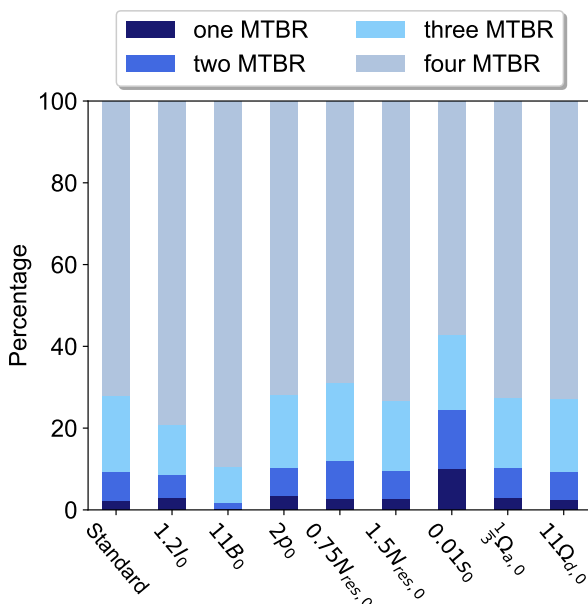
rate is slightly reduced (fig. 5.11d). This results in a lower number of islands (fig. 5.12d). Island length distribution (fig. 5.13d) after 5 minutes reveals that islands are bigger and kymographs (fig. 5.15a) show more stable island boundaries. However, islands are not yet as homogeneous as in the experiment. The reason might be that in the simulation only one protofilament is giving a signal, while in the experiment intensity signals come from 13 PFs [40]. Thus, increasing the preference of the preferential adsorption has a positive effect on island stability and the island coverage without changing the tau density in the surrounding. However, changes are not big enough to overcome discrepancies between experiment and simulation.

The amount of available tau, i.e. the tau reservoir might have an effect on tau density in islands and surroundings as well as on the island coverage and the nucleation rate. A higher tau concentration in the experiment leads to higher tau densities in both, islands and surroundings. Moreover, the island coverage is the higher, the higher the tau concentration in the solution of the experiment [40]. Reducing the reservoir in the simulation (see table 5.1 for the model definition) reduces the island coverage (fig. 5.10e) and increasing the reservoir (see table 5.1 for the model definition) increases the island coverage (fig. 5.10f). In both cases, however, the island coverage reached saturation, which is not observed in the experiment. The level of saturation coverage is determined by the reservoir. Reaching saturation means that the flow into the island state is in equilibrium with the flow out of the island state. In the experiment, however, the island coverage increases slightly but steadily, which means that the flow into the island state is greater than the flow out of the island state. Since the coverage is still lower in the experiment, there has to be another process/factor besides the reservoir, which limits and slows down the island coverage growth in the experiment. Besides influencing the coverage, a smaller/bigger reservoir also leads to slightly less/more nucleations within the first 20 seconds (fig. 5.11e and 5.11f), smaller/bigger islands (fig. 5.13e and 5.13f), and less/more islands (fig. 5.12e and 5.12f). Moreover, also the tau density in the surrounding could slightly be tuned with the reservoir (fig. 5.9e and 5.9f). The tau density in the islands (fig. 5.9e and 5.9f), however, as well as the percentages of tau bound with four, three, two, or one MTBR(s) did not significantly change (fig. 5.8). This suggests that the amount of available tau is too small. Having a lot of tau in the solution together with the preferential adsorption should lead to a higher tau density in the islands as observed in the experiment [40]. Having a higher tau density in the islands, it would be expected that less MTBRs of one tau are bound to the MT within island regions. Together with the finding that another process limits island coverage growth draws the picture that in the experiment a lot of tau molecules are available for potentially adsorbing to the islands, but the island growth (at the boundaries) is limited by another factor, not included in the simulation. In summary, a lower reservoir can down-regulate the island saturation coverage, but also leads to an even lower tau density in the surrounding. A bigger reservoir has the opposite effect. See table 5.2 for an overview of the influence of the reservoir on all measured variables.

Furthermore, island dynamics are determined by the interplay of the three parameters: diffusion, global adsorption, and desorption. The most efficient and fastest island growth is reached when a tau attaches, then diffuses to the next island and stays there until the next tau arrives. If the tau detaches or diffuses away before the next tau reaches the island, the tau island growth is less stable and many small islands nucleate. Here, the diffusion rate is given by the experiment and the global adsorption and desorption rates were estimated assuming the standard Langmuir adsorption model (see fig. 5.1). The standard Langmuir adsorption model ignores tau-tau interactions and assumes that one particle only can occupy one site on the lattice, which is not the case for real tau. This means the real rates can slightly differ from the estimates. In the standard parameter set, the diffusion rate is six orders of magnitude higher than the global adsorption rate and five orders of magnitude higher than the desorption rate (see table B.1 of the appendix B). This means a newly adsorbed tau should have enough time to find the next island before the next tau attaches to the MT or an existing tau detaches. When being part of an island, the diffusion rate is exponentially decreased (eq. 5.14) by

approximately two orders of magnitude but still significantly higher than the adsorption and desorption rates. This means the new island tau is likely to diffuse away again before the next tau reaches the island. Consequently, borders are not stable. When drastically decreasing the diffusion rate by two orders of magnitude (see table 5.1 for the model definition; not in agreement with the experimentally measured values), kymographs show strongly stabilized island boundaries. Stabilizing the island boundaries favors the island state resulting in a slightly higher tau density within islands, but a strongly reduced tau density in the surrounding (fig. 5.9g). Moreover, there are less (almost half the amount seen with the standard parameter set, fig. 5.12a) but bigger islands (fig. 5.12g and 5.13g). A lower number of islands leads to a slower increasing island coverage. To conclude, a lower diffusion rate favors the island state, which results in stabilized islands but even more reduced tau in the surrounding.

As already mentioned, one of the discrepancies between simulation and experimental results is that the island coverage increases faster and saturates in the simulation but not in the experiment. The speed of the growth of the island coverage is determined by the global adsorption rate. When reducing the global adsorption rate by a factor of three (from $\Omega_a = 0.003\,\mathrm{s}^{-1}$ to $\Omega_a = 0.001\,\mathrm{s}^{-1}$, see table 5.1 for the model definition), the island coverage indeed grows slower. However, it still saturates within the observed time period. Having a lower adsorption rate, the tau density within islands and surroundings does not significantly change (fig. 5.9h), and one obtains the same amount of islands with similar sizes (fig. 5.12h and 5.13h) compared to the simulation with the standard parameter set (fig. 5.9a, 5.12a and 5.13a). However, the nucleation rate (fig. 5.11h) and the kymographs (fig. 5.16b) show that islands nucleate later when having a lower adsorption rate. The nucleation rate in this case does not follow the trend of the experiment anymore. Consequently, the adsorption rate does not seem to be the right parameter to limit the speed of the island coverage growth.

Model	Island density		Surrounding density		Island coverage		Nucleations		Number of islands		Island lengths		Kymograph
a) Standard	✓		✗		✗		✓		✗		✗		✗
b) $I = 1.2\,I_0$	✓	0	✗	−	✗	0	✓	0	✗	+	✗	+	✗
c) $B = 10\,B_0$	✓	+	✗	0	✗	−	✓	+	✗	−	✗	−	✗
d) $p = 2\,p_0$	✓	0	✗	0	✗	0	✓	−	✗	+	✗	+	✗
e) $N_{\mathrm{res}} = 0.75\,N_{\mathrm{res},0}$	✓	0	✗	−	✗	+	✓	−	✗	+	✗	−	✗
f) $N_{\mathrm{res}} = 1.5\,N_{\mathrm{res},0}$	✓	0	✗	+	✗	−	✓	+	✗	−	✗	+	✗
g) $s \approx 0.01\,s_0$	✗	−	✗	−	✗	+	✓	−	✗	+	✗	+	✗
h) $\Omega_a = \frac{1}{3}\,\Omega_{a,0}$	✓	0	✗	0	✗	+	✗	−	✗	0	✗	0	✗
i) $\Omega_d \approx 11\,\Omega_{d,0}$	✓	+	✗	−	✗	−	✓	−	✗	−	✗	+	✗

Table 5.2: Table shows how the models, defined in table 5.1, perform with regard to the tau density of islands, tau density of surroundings, island coverage, island nucleation rate, number of islands, length of islands, and the kymograph. The marks ✓ and ✗ specify whether the model reproduces the experimental observation (see 5.7) or not. The marks +, 0, and − evaluate whether the model performs better, as good as or worse than the standard model. For the kymograph, it is difficult to evaluate whether the obtained results are better, as good as, or worse compared to the standard model because there are always aspects that are better and others that are worse. The experiment does not give the number of islands and the island lengths for the here considered tau concentrations in solution (20 nM). Only the length distribution of tau islands at a higher tau concentration in solution (40 nM) is given [40]. From this, it can be deduced that the standard model produces too many and too small islands. Thus, less and bigger islands are considered positive and more and smaller islands negative.

As described above, the desorption rate was estimated assuming the standard Langmuir

adsorption model combining the island and surrounding regions. In doing so, the tau-tau interaction is neglected as well as the fact that one tau molecule can occupy several sites. Another way of estimating the desorption rate is by just considering the surrounding regions and using the dwell time of tau in the surrounding given by the experiment [40]. Using the tau dwell time in the surrounding on the other hand ignores that the surrounding constantly loses tau particles to the islands since the islands constantly grow [40]. Thus, the desorption rate given by the dwell time can be considered as an upper limit, while the previously estimated desorption rate using the Langmuir adsorption model for surrounding and island regions is a lower limit. Using the higher tau desorption rate (approximately eleven-fold higher, see table 5.1 for the model definition) given by the dwell time of tau in the surrounding, drastically reduces the tau density in the surrounding (fig. 5.9h). Since the desorption is reduced within islands compared to the surrounding, the island borders seem to be stabilized (see kymographs in fig. 5.16c), which leads to bigger (fig. 5.13i) but less islands (fig. 5.12i) and a coverage which increases a bit slower but saturates at higher values (fig. 5.10i). However, the number of islands (fig. 5.12i) also shows a small reduction towards the end of the observation time showing that due to the high desorption rate some islands disassemble. Thus, a higher desorption rate on the one hand stabilizes island borders by almost completely emptying the surrounding. On the other hand, it leads to island disassembling, which is not observed in the experiment in the presence of tau in the solution (island disassembling only occurred when tau was removed from the solution) [40]. This indicates that using the dwell time of tau in the surroundings overestimates the tau desorption rate.

Taking together, in this subsection, the model parameters of the established tau adsorption model are changed individually to see if they can lead to simulation results closer to the experimental observations. All parameter changes had a positive effect on one part of the measured variables but a negative effect on the other part of the measured variables. Mostly, they stabilized/destabilized islands on the one hand and reduced/increased the surrounding on the other hand. Table 5.2 lists all parameter changes and their influence on all measured variables. In conclusion, the standard model performs best and all parameter deviations lead to further deficits.
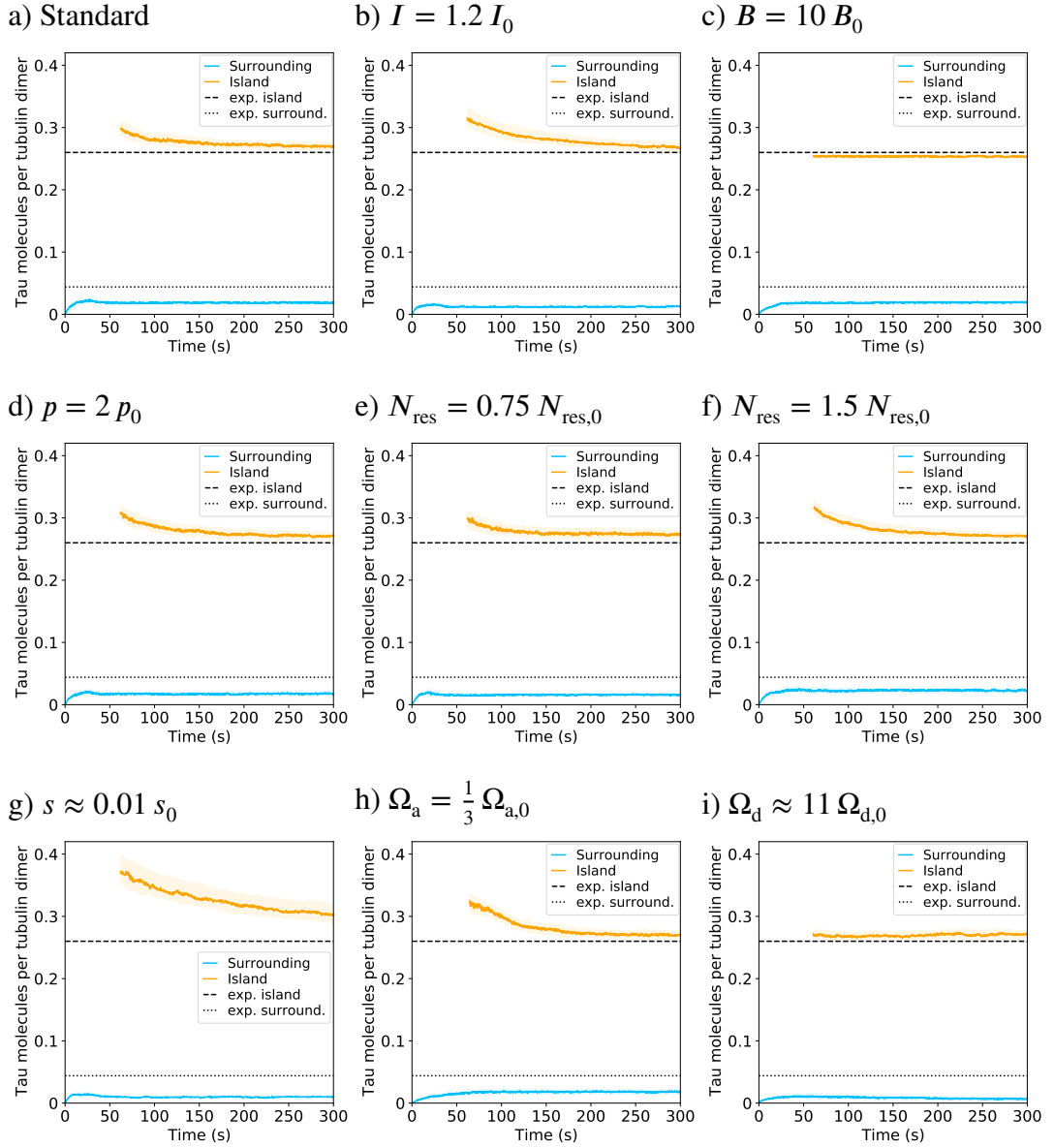
Figure 5.9: Simulations show high tau densities of islands and low tau densities of surroundings.
Tau densities of islands and surroundings for the different models defined in table 5.1. The
MT is divided into island and surrounding regions using the external definition ($N_{min} = 7$,
see main text for details). The tau density (tau per tubulin dimer) is calculated as the
number of tau molecules in the island/surrounding regions divided by the number of is-
land/surrounding sites. Solid line represents the median and shaded area the interquantil
range of 50 MTs ($L_{MT} = 10\,\mu m$). Black dashed line represents the experimental mean
density of islands [40] and black dotted line the approximated experimental density of the
surrounding (estimated from [40]; see fig. 5.7a).
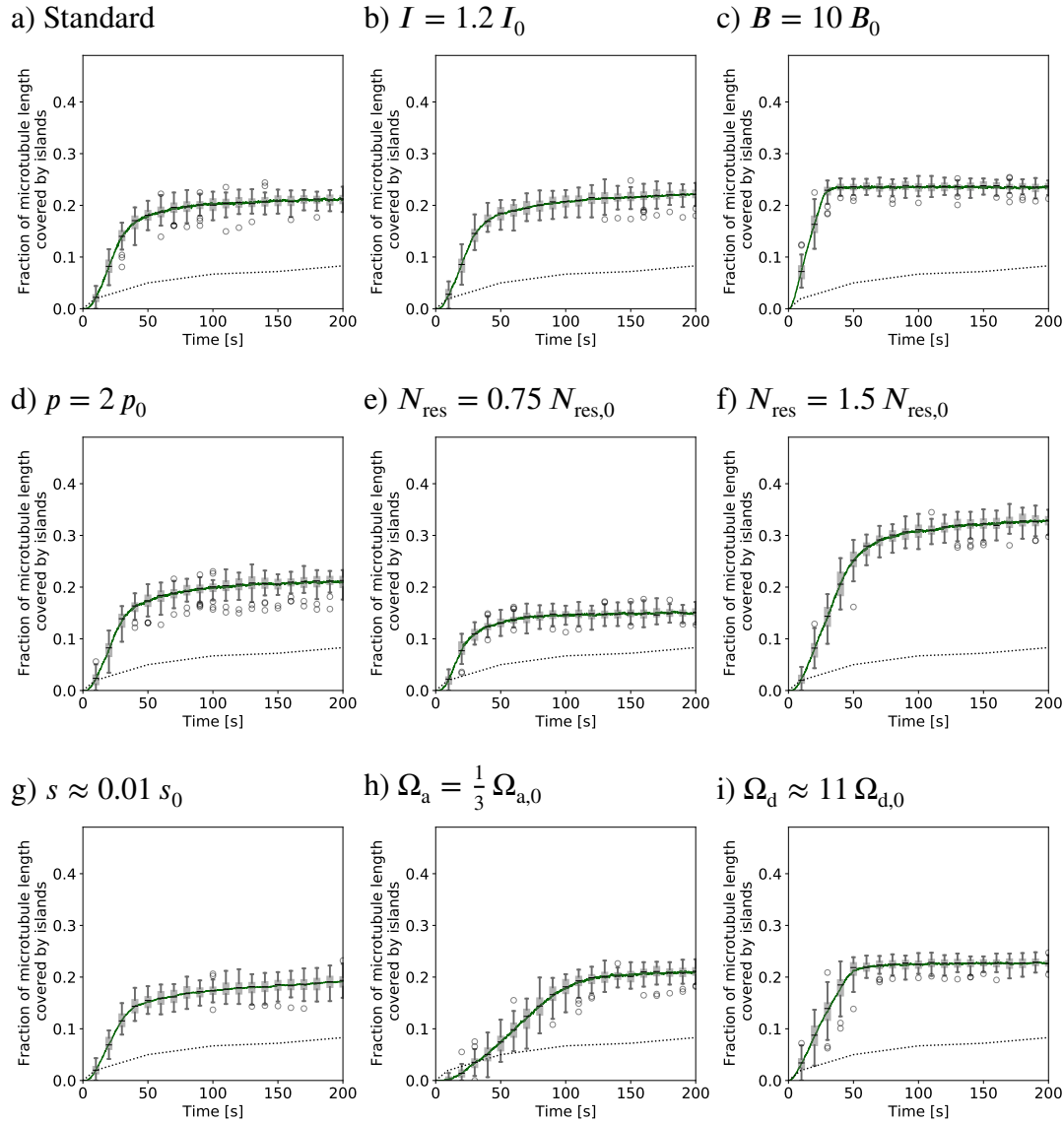
Figure 5.10: The island coverage from simulations increases fast and saturates within the measurement period. Fraction of the MT covered with islands (called island coverage) for the different models defined in table 5.1. Solid green line is calculated by summing up the length of all islands of all simulated MTs (50 MTs) and divided by the sum of the lengths of all MTs ($50 \times 10\,\mu$m). Dotted black line is the estimated experimental equivalent (estimated from [40]; see fig. 5.7b). The boxplot is generated using the fraction of single MTs covered with islands. This means one data point is calculated by summing up the lengths of the islands on one MT and dividing by the length of this MT.

a) Standard

b) $I = 1.2 \, I_0$

c) $B = 10 \, B_0$

d) $p = 2 \, p_0$

e) $N_{\text{res}} = 0.75 \, N_{\text{res},0}$

f) $N_{\text{res}} = 1.5 \, N_{\text{res},0}$

g) $s \approx 0.01 \, s_0$

h) $\Omega_{\text{a}} = \frac{1}{3} \, \Omega_{\text{a},0}$

i) $\Omega_{\text{d}} \approx 11 \, \Omega_{\text{d},0}$
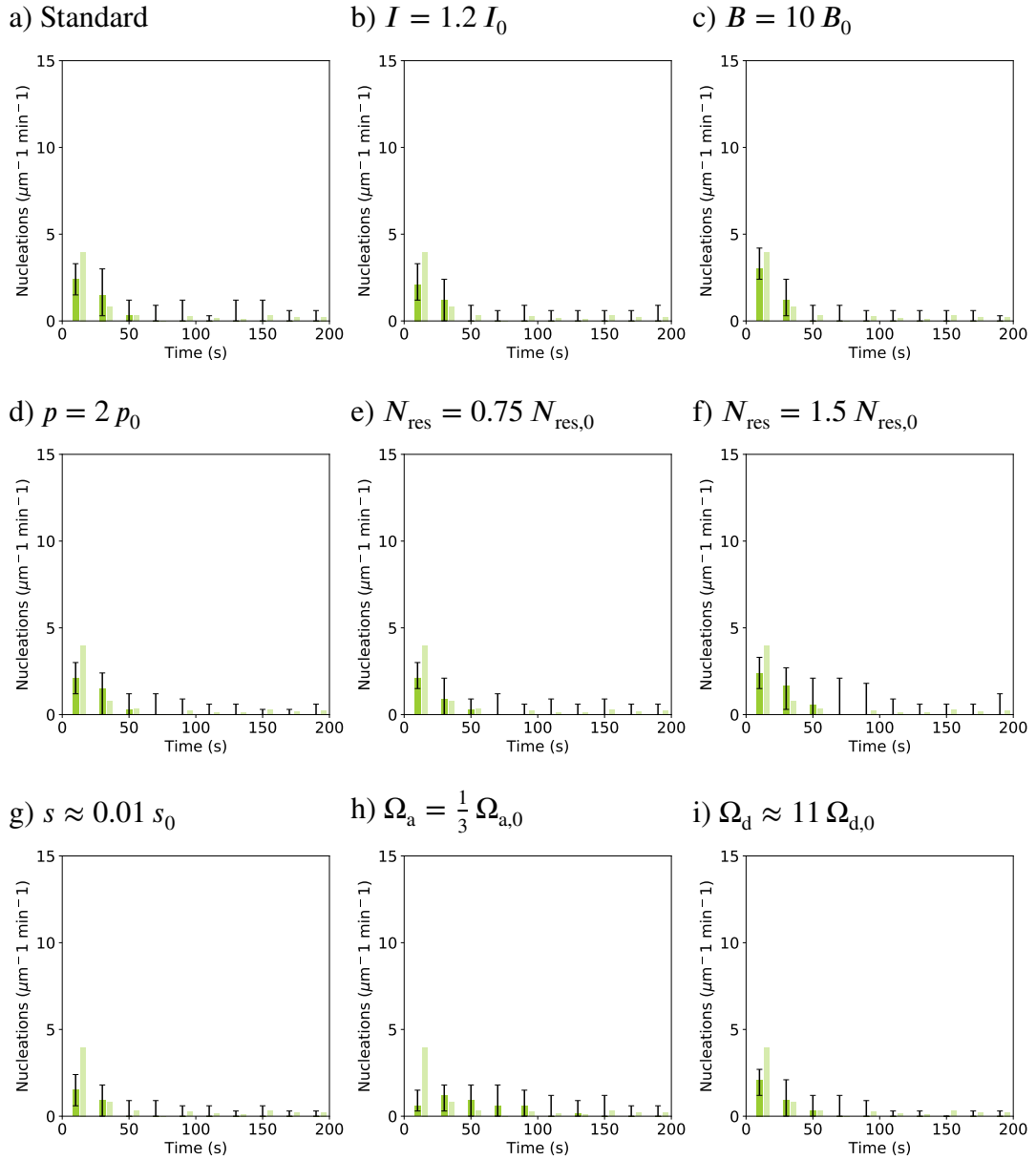
Figure 5.11: The simulated nucleation rate decrease with time. Nucleation rates as a function of time for the different models defined in table 5.1. The nucleation rate is calculated as the number of nucleations within 20 seconds multiplied by 3 (to convert in nucleations per minute) and divided by the MT length $L_{\text{MT}} = 10 \, \mu\text{m}$. Bars with high opacity are from simulations and bars with low opacity are estimated from the experiment at 20 nM tau in solution [40] (fig. 5.7c). Estimates are for the same time interval but slightly shifted to the right for better visibility.
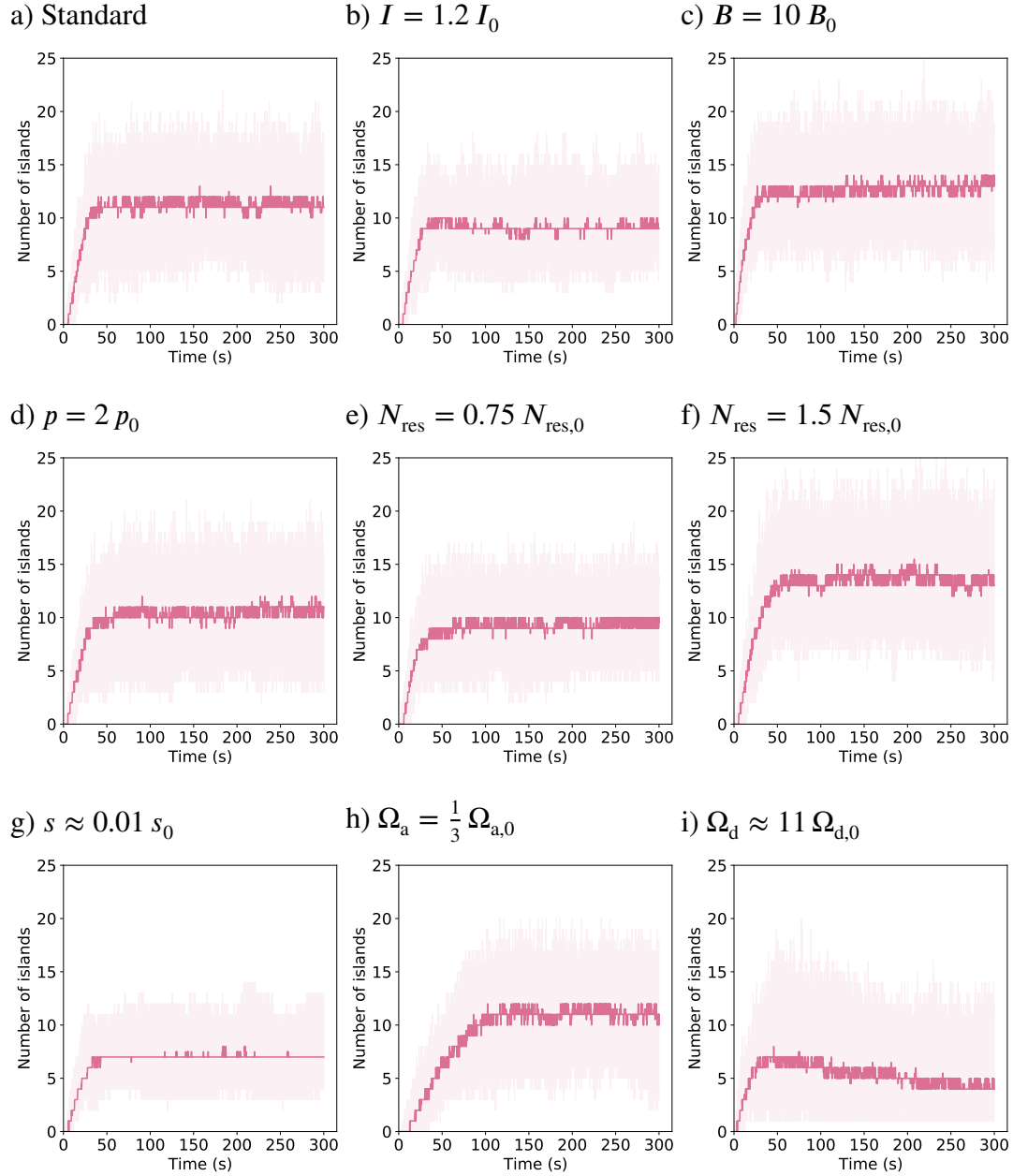
Figure 5.12: The number of islands saturates for almost all models. Number of islands as a function of time from simulation for the different models defined in table 5.1. Solid line shows the median and the shaded area the minimum and maximum.
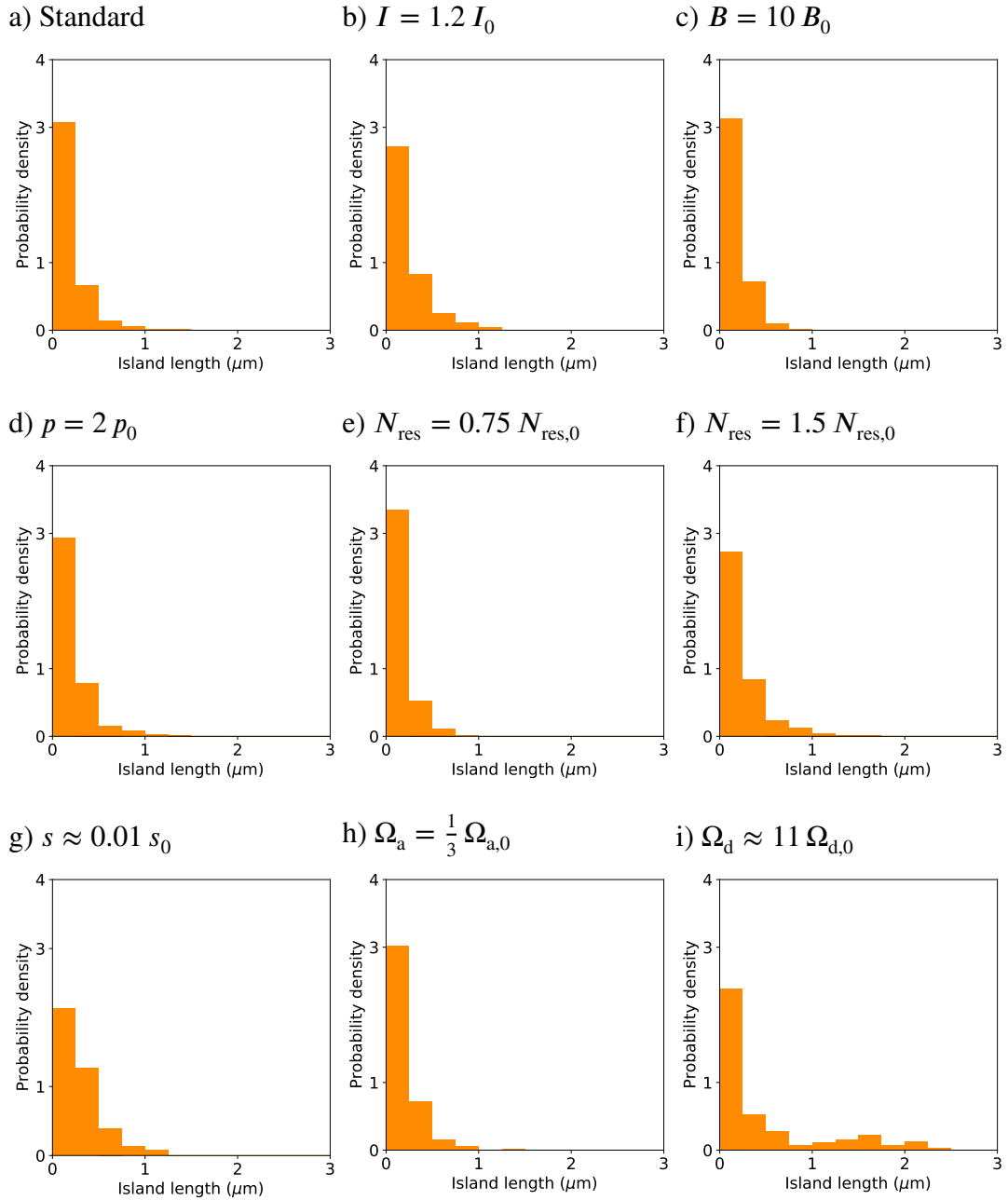
Figure 5.13: Most of simulated islands are shorter than 0.25 μm. Histograms of island lengths from simulations for the different models defined in table 5.1. Island length were measured after 300 seconds after the start of the adsorption process.

a) Standard
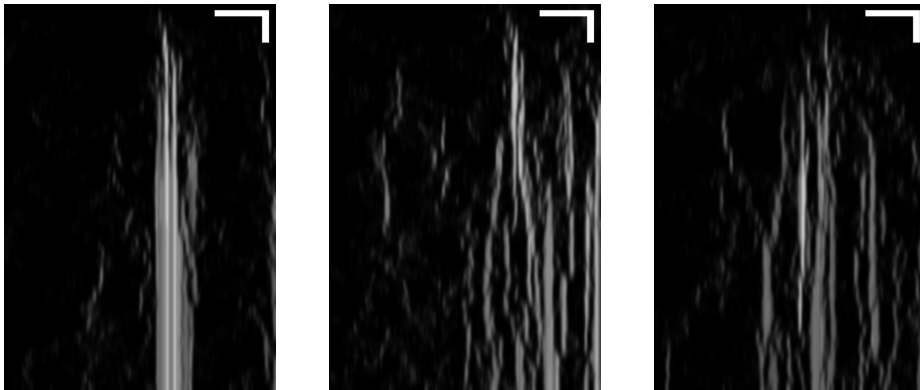
b) $I = 1.2\, I_0$
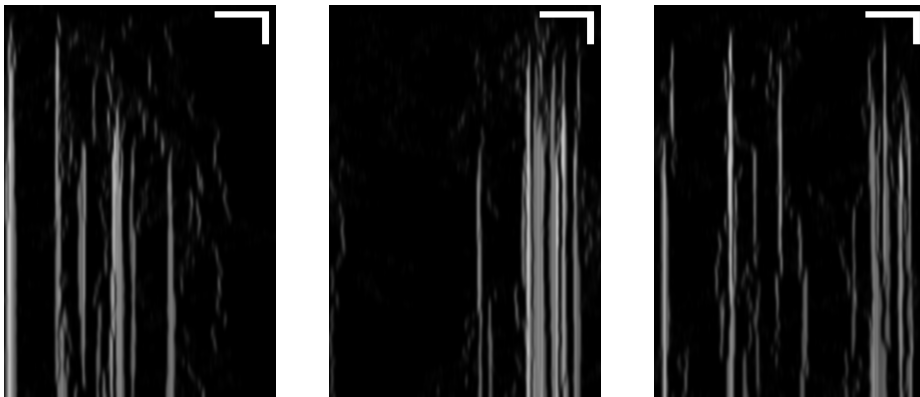
c) $B = 10\, B_0$
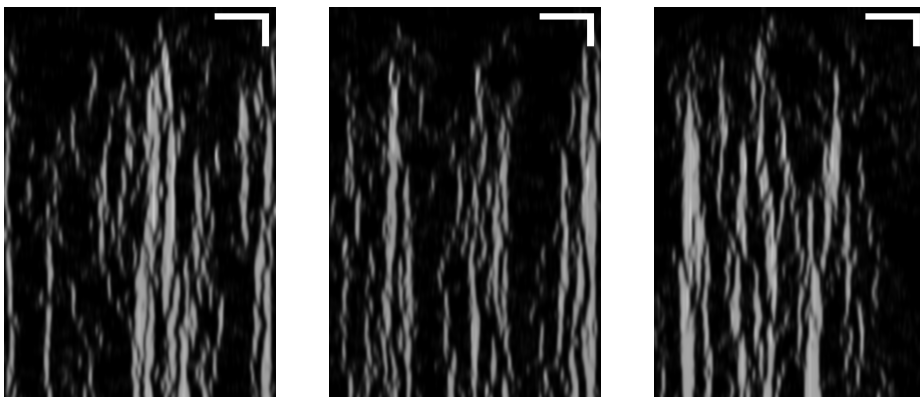
Figure 5.14: Example kymographs for standard parameters, higher interaction energy, and higher binding energy. Example simulation kymographs for the models a) to c) defined in table 5.1. See caption of fig. 5.2 for details on the generation of the kymographs. Scale bars are 2 μm (horizontal) and 5 s (vertical). A higher interaction energy (see fig. b)) leads to more stable island (boundaries), while a higher binding energy (see fig. c)) has little effect on island stability.

a) $p = 2\,p_0$
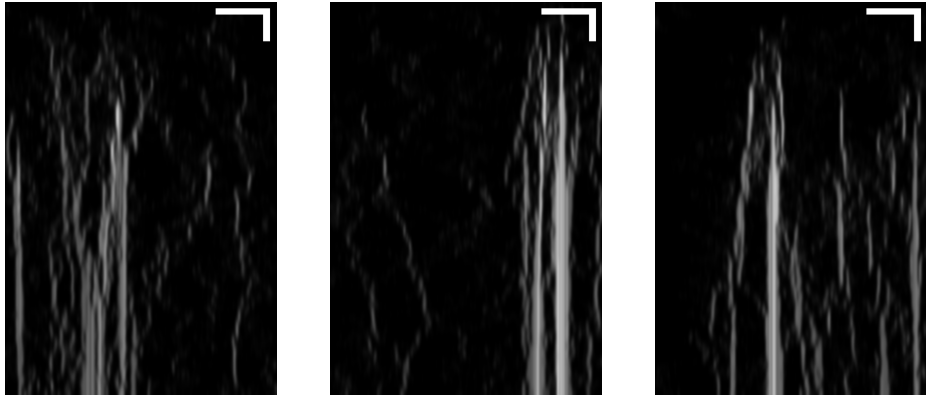
b) $N_{\mathrm{res}} = 0.75\,N_{\mathrm{res},0}$
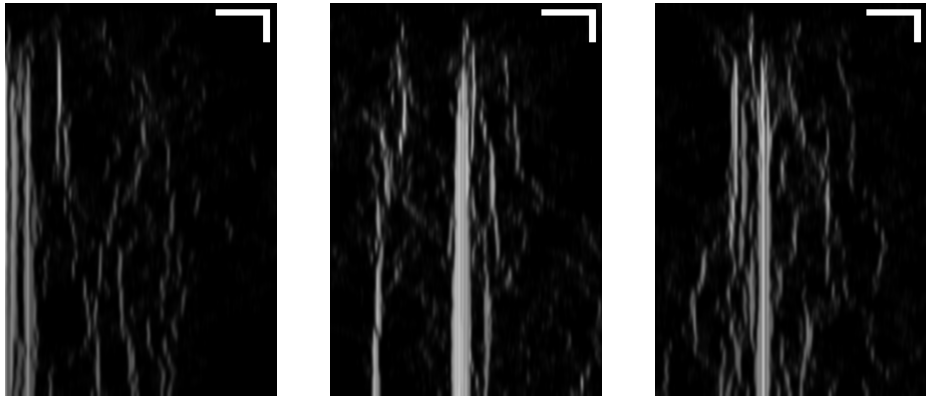
c) $N_{\mathrm{res}} = 1.5\,N_{\mathrm{res},0}$
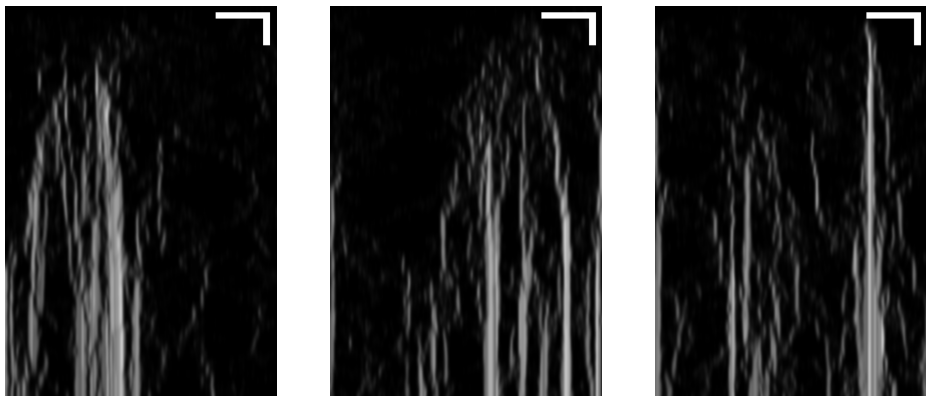
Figure 5.15: Example kymographs for higher preference, smaller and bigger reservoir. Example simulation kymographs for the models d) to f) defined in table 5.1. See caption of fig. 5.2 for details on the generation of the kymographs. Scale bars are 2 μm (horizontal) and 5 s (vertical). A higher preference (see fig. a)) slightly stabilizes bigger islands and the size of the reservoir influences island sizes (see fig. b) and c)).

a) $s \approx 0.01\, s_0$
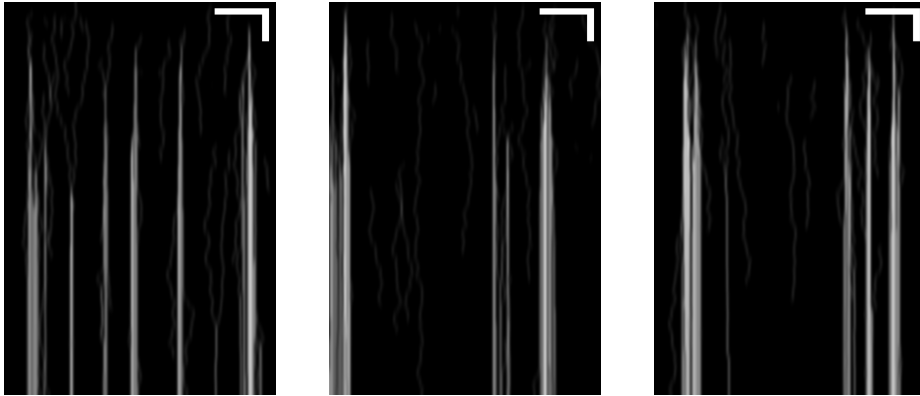
b) $\Omega_a = \frac{1}{3}\, \Omega_{a,0}$
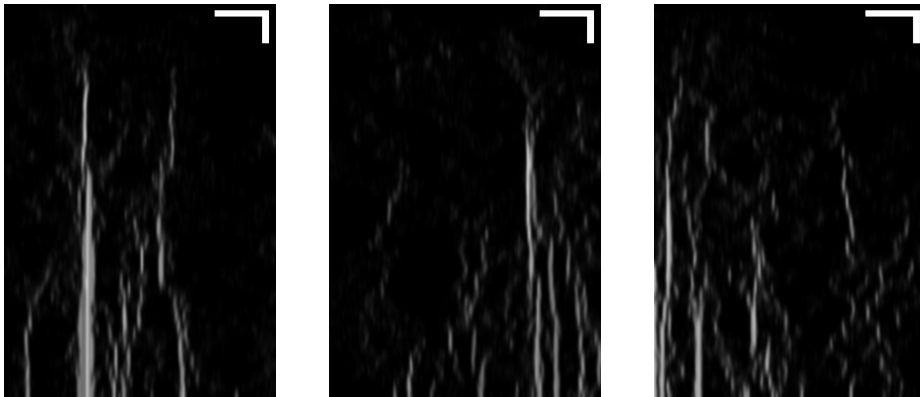
c) $\Omega_d \approx 11\, \Omega_{d,0}$
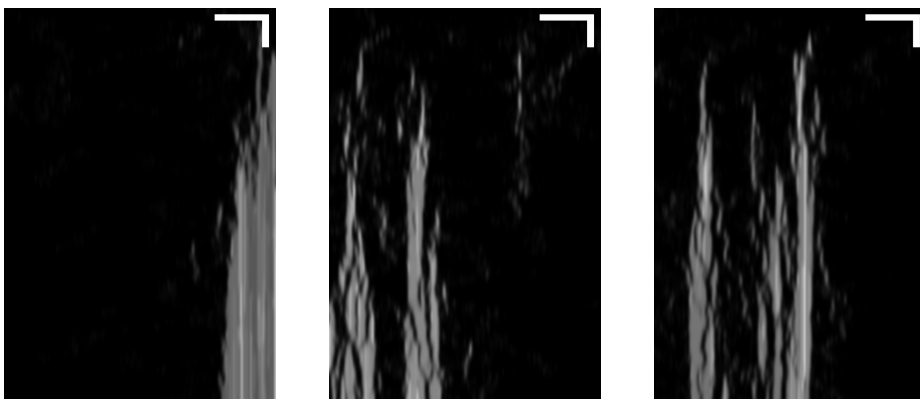
Figure 5.16: Example kymographs for slower diffusion, lower global adsorption, and higher global desorption. Example simulation kymographs for the models g) to i) defined in table 5.1. See caption of fig. 5.2 for details on the generation of the kymographs. Scale bars are 2 μm (horizontal) and 5 s (vertical). A lower diffusion rate (see a)) slightly stabilizes islands, a lower adsorption rate (see b)) reduces island sizes and nucleation events and a higher global desorption rate (see c)) reduces the tau density in the surrounding.

5.3 Discussion and outlook

The goal of this chapter was to understand the physical process underlying the formation of tau islands on the MT lattice. Tau island formation was experimentally studied among others by Siahaan et al. [40]. Here, a stochastic model with parameters, whenever possible, estimated from the experiment by Siahaan et al. [40] is used to simulate tau adsorption to the MT lattice. The model is based on the Langmuir and the one-dimensional diffusion model. Adding a tau-tau interaction when they are next neighbors on the lattice, breaks the symmetry of the homogeneous Langmuir density, and islands form. Moreover, a preferential adsorption at the boundaries of existing islands leads to slightly less but slightly bigger islands, and a limited reservoir of tau molecules in the solution limits the island growth. Simulating this model, islands nucleate with a similar rate as in the experiment (compare fig. 5.11a) with fig. 5.7c) and have a similar density (compare fig. 5.9a with fig. 5.7a). However, there are also discrepancies between simulation and experimental results: first, the simulated tau density in regions surrounding the islands (called surrounding) is half than that in the experiment. Second, the simulated islands are not as stable as seen in the experiment (compare fig. 5.14a with fig. 5.7d and 5.7e). While in the experiment island boundaries either grow or form clear, stable borders, in the simulation islands mostly either grow or even shrink. And third, there seem to be more, but smaller islands in the simulation than in the experiment (see fig. 5.12a and 5.13a for simulation). Thus, to better approximate the experiment, big clusters should be stabilized and favored such that less small islands nucleate and small islands should be dispersed such that they contribute to the surrounding. Changing model parameters (fig. 5.9, 5.10, 5.11, 5.12, 5.13, 5.14, 5.15, 5.16 and tables 5.1 and 5.2) reveals that parameter changes, which stabilize islands, lead often to more small islands and an even more reduced tau density in the surrounding, and parameter changes increasing the tau density in the surrounding destabilize the islands. This suggests that there must be other factors influencing the formation of tau islands that were not considered in this model.

The interaction between MT-bound tau molecules and the MT lattice itself is only partly considered. It is known that tau islands reduce the lattice spacing of taxol stabilized MTs[317]. This is incorporated in the model in the form of a preferential adsorption at the island boundaries. It is thereby assumed that the changed lattice spacing due to tau islands also changes the lattice in the direct proximity of islands such that tau from solution preferentially adsorbs at tau island boundaries. However, it might also be that the diffusion of free tau in direct proximity around islands on the MT is enhanced for diffusion towards the island and reduced for diffusion away from the island. Furthermore, the lattice spacing needs a few seconds to relax after island removal [317]. Thus, there might be a memory effect of the lattice spacing. The theoretical work by Jose and Santen [224] shows that a floor field with a memory effect leads to the formation of a plus and minus lane in bidirectional transport in neurons. In this work, the motor stepping on the MT changes the lattice and increases thereby the MT affinity for following-up motors of the same kind. A similar approach could lead to a higher tau affinity around islands, which could stabilize tau islands without increasing the island nucleation rate. Another factor, which is not considered in the tau adsorption model is the underlying MT lattice. In the model, it is assumed that the MT has a homogeneous lattice, where all sites are equal. However, previous studies show that the MT lattice often has defects [63, 321–323]. Here, changing the model parameters indicated that there needs to be another factor limiting the island coverage growth. Moreover, the simulation only shows clear, constant island boundaries at the MT end (fig. 5.16c). In the experiment, such clear borders, which neither grow

nor shrink over several seconds, are also observed within the bulk of the MT (see fig. 5.7d and 5.7e). MT lattice homogeneities could be the missing factor that stops island growth and leads to clear, not growing nor shrinking island boundaries. Lattice inhomogeneities could be lattice defects such as holes, a GTP-tubulin within the GDP-tubulin lattice, or changes in the protofilament number [323]. Tau molecules might not be able to diffuse over lattice defects such as holes. This leads to the fact that no island tau can diffuse away and also no new tau can be added to the island so that a clear, neither growing nor shrinking border forms. When having a GTP-tubulin within the GDP-tubulin lattice or irregularities in the tubulin lattice, tau might not be able to compress the lattice at these spots. If tau is not able to compress the lattice, which is the case for GMPCPP MTs, islands do not form [317]. Thus, it might be that at such defects tau still arrives at the island, but newly arriving tau cannot be added to the island (no tau-tau interaction) because the lattice cannot be compressed. The newly arrived tau would then either fast diffuse away again leading to a clear, neither growing nor shrinking border, or form a "new" island. In the kymograph, the latter case would look as if the island were growing again (see the experimental kymograph, fig. 5.7d for instance). Other lattice inhomogeneities could be the presence or absence of taxol. To stabilize the MT, taxol binds to tubulin and thereby expands the lattice [317]. Siahaan et al. [317] show that the amount of taxol is reduced for tau island regions. Consequently, random taxol-free lattice sites could serve as nucleation points and eventual sites with rigidly bound taxol could stop island growth and lead to stable island boundaries. To conclude, an inhomogeneous lattice could be the missing factor that stops island growth leading to clear, neither growing nor shrinking island borders.

Another difference between experiment and simulation is the dimension of the MT lattice. While, in the simulation, only one protofilament (PF) is modeled, there are about 13 PFs in the experiment [40]. This might be the reason why in the experiment islands seem to be more homogeneous, while in the simulation they often contain holes (compare fig. 5.7d and 5.7e with fig. 5.14a). Adding the second dimension and lateral interactions between tau molecules on the MT might not just lead to more homogeneous island signals of the kymographs but also stabilize the islands. Moreover, when having several PFs, tau molecules diffusing in the surrounding would be able to pass each other without interacting and directly nucleating an island as it is the case for the one protofilament simulation. In this way, one could have more tau in the surrounding without having too many nucleation events.

When performing the experiment at higher tau concentrations in the solution, the tau density within islands increased and saturated at approximately 0.75 tau per tubulin dimer [40]. Observing higher densities could either mean that there are several layers of tau or that tau binds with less MTBRs such that there is space for more tau. If the first were be the case, it would be expected that the density increases unlimitedly. However, the tau density within the islands seems to saturate at around 0.75 tau per tubulin dimer for high tau concentrations in the solution of the experiment [40]. This means it seems more likely that at high tau concentrations in solution, tau binds with only $1-2$ MTBRs within the islands and therefore the island density can be higher. A future version of the here presented tau adsorption model could then be used to test whether there are several layers of tau or if tau is "upstanding" aligned within the islands, i.e. bound with only $1-2$ MTBRs at high tau concentrations.

In the future, this model could also be used to study the influence of tau islands on bidirectional transport. Therefore, the tau adsorption model needs to be merged with either the unidirectional/bidirectional gliding assay models (see chapter 4) or with the unidirectional/bidirectional cargo transport models (see chapter 6 and 7). Doing so, the influence of tau islands first on single motors, then on teams of one motor specie, and finally on teams of opposite-directed

motors should be studied.

Chapter 6

Cargo transport by kinesin-3

Contents

This chapter explores the influence of the cargo itself on the motion of the motor-cargo systems. The focus will be on how the cargo surface composition regulates transport. Therefore, the two extreme cases of a fluid cargo surface, on which the motors perform rapid diffusion, and a rigid cargo surface, on which the motors have a fixed position, are studied. First the experimental results of liposome (fluid cargo surface) transport by kinesin-3 motors are presented. To understand the experimental results, liposome transport by kinesin-3 is simulated first with a point-like cargo model, second with a one-dimensional liposome model, and finally with a three-dimensional liposome model. To understand the impact of the diffusive motor tails on the cargo transport, also a bead (rigid cargo surface) is modeled in one dimension and three dimensions and the simulation results are compared with liposome transport.

Cargos are actively transported by molecular motors inside the cell [73, 179, 324]. Inside the cell, there exist various different kinds of cargos such as mitochondria, ribosomes, phagosomes, etc. [73, 76, 179, 324]. Different kinds of cargos can differ in size or surface composition [88, 168, 248, 324]. Previous studies report different transport behaviors for cargos of different sizes [88, 324] or different surface compositions [168, 248, 250].

Different surface compositions influences the mobility of the motors on the cargo surface. If cargos have dynamic lipids on their surface (fluid cargo surface), motors diffuse along the cargo surface. For membrane-free cargos, in contrast, motors have fixed positions on the cargo surface [169, 253, 256]. The two extreme cases are membrane-enclosed cargos, which have a fluid cargo surface, where motors perform rapid diffusion and membrane-free cargos, which have a rigid cargo surface, where motors have fixed positions. The effect of the fluid versus the rigid cargo surface (diffusive versus fixed motor positions on the cargo surface) remains poorly understood.

In *in vitro* experiments, i.a. liposomes are used as fluid cargos to investigate the role of the diffusive motor tails on

Figure 6.1: Experimental set-up. Shown is an illustration of the experimental set-up in real-size ratios. Due to the lipid bilayer on the liposome surface, kinesin-3 motors (KIF16B) can diffuse on the liposome surface. Kinesin-3 motors bind to the MTs and walk towards the MT plus-end. They thereby transport the liposome towards the MT plus-end.

cargo transport in a controlled environment. Liposomes are spherical cargos with a surface consisting of a lipid bilayer [2] such that motor tails perform rapid diffusion along the cargo surface [22, 169, 256, 325]. To gain further knowledge about how multiple kinesin-3 motors work in a team, kinesin-3 (KIF16B) motors are used to study the influence of fluid versus rigid cargo surfaces on cargo transport. In the following, results of liposome transport by teams of kinesin-3 motors are presented. All shown experimental results are from experiments performed by the Stefan Diez lab[1]. After presenting the experimental results, the liposome transport by kinesin-3 is modeled to gain further insights into the underlying physical transport processes. Thereafter, bead transport by kinesin-3 is modeled to study the transport of cargos with a rigid cargo surface. Beads do not have a lipid bilayer on their surfaces such that the motor tails have a fixed position on the cargo surface. A comparison of bead versus liposome transport then reveals how the cargo surface composition (fluid versus rigid) influences transport properties.

6.1 Experiments of liposome transport by kinesin-3

To investigate liposome transport by kinesin-3, an *in vitro* assay is used (see fig. 6.1 for an illustration). In the *in vitro* assay, stabilized MTs are fixed at the bottom of a glass coverslip. Fluorescent labeled liposomes with kinesin-3 motors at varying concentrations

---

[1]Experiments were performed by Akhil Sai Naidu, Rahul Grover, and Ashwin D'Souza from Stefan Diez lab at B CUBE, TU-Dresden. I did not perform any experiments myself.

($c_{kin3} = 1.5 - 90$ nM) are put on top of the MTs. From tracked positions of fluorescently labeled liposomes, trajectories can be drawn (see fig. 6.2b for example trajectories) and instantaneous velocities can be calculated. Velocity histograms (fig. 6.2a) are shown in dependence of the kinesin-3 concentration. For the lowest kinesin-3 concentration (1.5 nM) the histograms show two peaks: one low velocity peak close to zero and one high velocity peak at approximately 700 nm/s. The low velocity peak is higher for the lowest kinesin-3 concentration compared to the three higher kinesin-3 concentrations, where the low velocity peak remains constantly high. With increasing kinesin-3 concentration, the high velocity peak moves to lower velocities until it merges with the low velocity peak. At the highest kinesin-3 concentration, the velocity distribution shows only one peak at approximately 300 nm/s. Even though the low velocity peak is lower for the three higher motor concentrations, the overall mean velocity reduces (fig. 6.2c) suggesting a negative cooperation of multiple kinesin-3 motors at higher motor concentrations. In conclusion, the observations indicate that there are two motility states, a slow and a fast state, which changes differently with increasing motor concentrations.

Besides the velocity histograms, also the trajectories (fig. 6.2b) clearly show a stop- and go-like motion emphasizing the existence of a slow and fast state. To further analyze the slow and fast states, the trajectories are segmented using a segmentation algorithm. The segmentation algorithm is based on the local slope of the trajectory. To be able to calculate the derivative (slope), the trajectory is first fitted by a B-spline using a weighted least square interpolation (from python package *scipy.interpolate*) on a window of five data points (measurement interval: $\Delta t_{mes} = 100$ ms). To distinguish between the slow and the fast state, a threshold for the derivative is needed. To set a meaningful threshold v_{th}, the mean velocity of the slow and the fast state need to be known. Therefore, the velocity histogram is fitted by a double Gaussian:

$$p(x) = c_1 \exp\left[-\alpha \left(x - \mu_s\right)^2\right] + c_2 \exp\left[-\beta \left(x - \mu_f\right)^2\right]. \tag{6.1}$$

From the parameter fit (fig. 6.2a), the parameter values of c_1, c_2, α, β, μ_s and μ_f are obtained for each kinesin-3 concentration (see table C.2 of the appendix C). A threshold of $v_{th} = 200$ nm/s lies between the mean velocity of the slow μ_s and the fast velocity peak μ_f for all kinesin-3 concentrations and is, therefore, a meaningful threshold [2]. Using this segmentation algorithm, trajectories can be segmented into slow and fast states (see 6.3 for an example).

Having segmented the trajectories in slow and fast states, the velocity histograms can be split into histograms of the slow states and histograms of the fast states (see color code of fig. 6.2a). In doing so, the low velocity peak as well as the negative velocities can be related to the slow state. Comparing the shape and position of the slow state histograms, it can be seen that velocities of the slow state slightly increase with increasing kinesin-3 concentration. This means that while at low concentrations the liposome really pauses (slow state histogram is around zero), there is small drift towards the MT plus-end for higher kinesin-3 concentrations during the slow state.

Using the segmentation algorithm, also the duration (fig. 6.4a) and the frequency of the slow states (6.4b) can be calculated. Neither the slow state durations nor the slow state frequencies show a dependence on the kinesin-3 concentration. The slow state duration is about 2 seconds and the slow state frequency $0.2\,s^{-1}$ for all kinesin-3 concentrations. This means, getting in

---

[2] In more detail, using a threshold of $v_{limit} = 200$ nm/s, more than 92% of each Gaussian peak is higher/lower than the threshold for three out of four used kinesin-3 concentrations. The exceptions are the high velocity peak at 90 nM, where only a percentage of 73.14 % is higher than the threshold and the low velocity peak at 9 nM, where only a percentage of 82.55 % is lower than the threshold. Note that slightly different threshold values did not change the outcome.
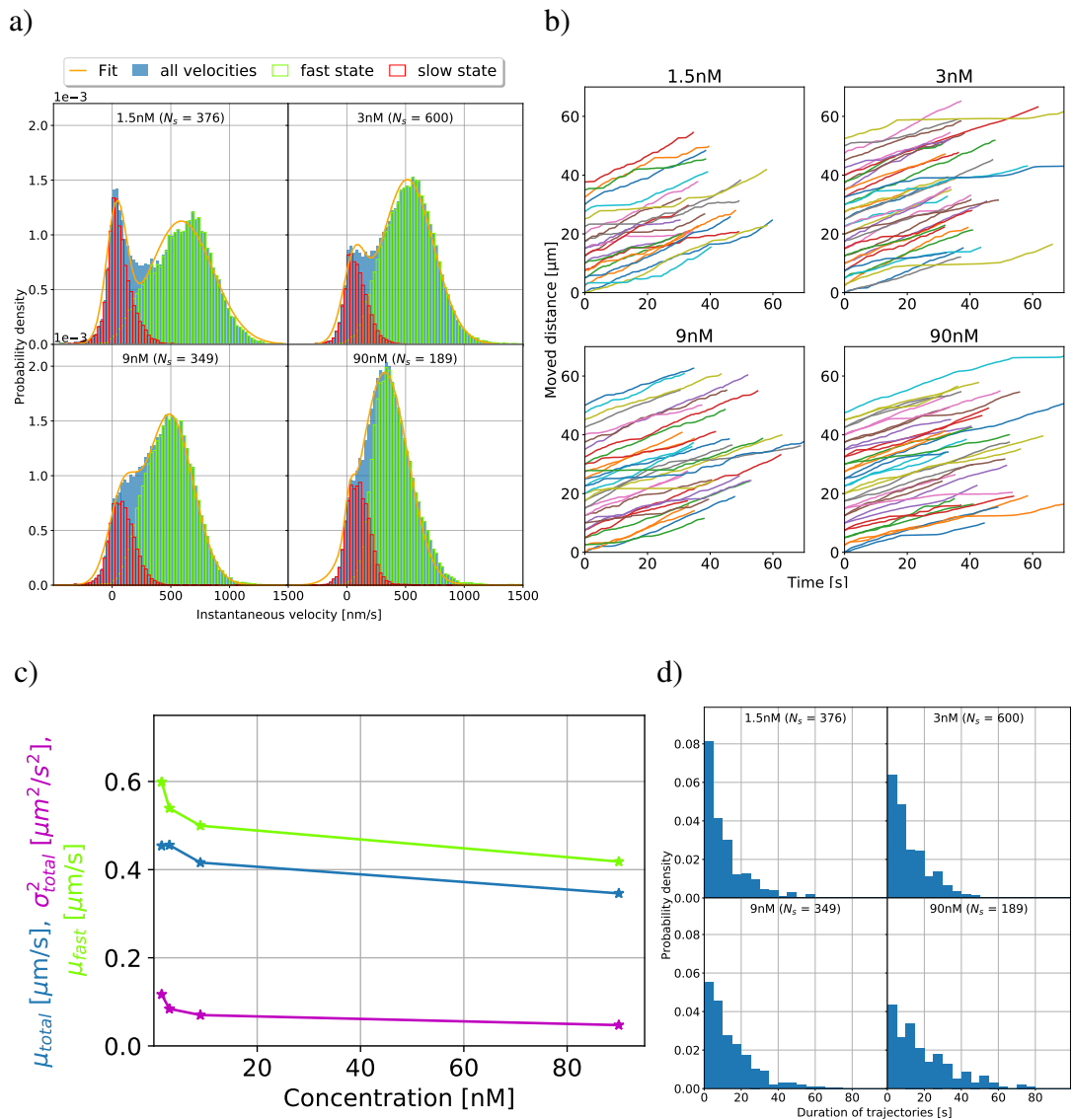
Figure 6.2: Experiment: liposome transport results. a) Histograms of liposome point-to-point velocities at varying kinesin-3 concentrations. Slow state velocities are drawn in red and fast state velocities in green. See main text and caption of fig. 6.3 for the segmentation into slow and fast states. A double Gaussian fit is shown in yellow. Derivations between the fit and the real values are small. Histograms show a low and a high velocity peak, which merge at higher kinesin-3 concentrations. b) Example cargo trajectories show a stop-and-go-like motion for all kinesin-3 concentrations. The shown trajectories are a random selection of trajectories longer than 30 seconds. c) This figure shows mean (blue) and variance (magenta) of all liposome velocities and mean velocities of only the fast state (green). Both means as well as the variances reduce with increasing kinesin-3 concentration. d) Histograms of trajectory durations. Trajectories are longer in time for high motor concentrations. Number of samples N_s are given in brackets (a+d). All experiments were performed by Akhil Sai Naidu, Rahul Grover, and Ashwin D'Souza from Stefan Diez lab at B CUBE, TU-Dresden. *Print permissions were given in a private communication by the Stefan Diez lab at B CUBE, TU-Dresden.*

a) Experiment
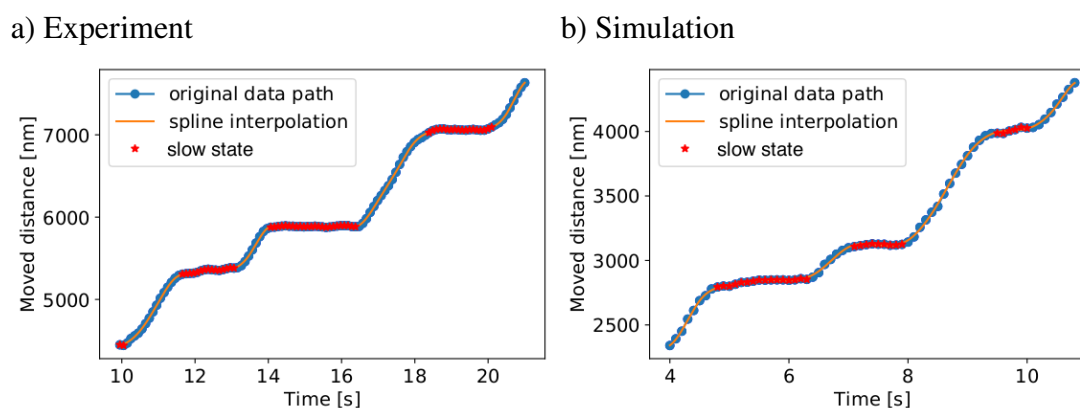
b) Simulation

Figure 6.3: The segmentation algorithm. Example, segmented trajectories from experiment (a) and simulation (b). Trajectories show the original data (blue and red dots) and the spline interpolation (yellow, solid line). Slow state segments are depicted in red and fast state segments in blue. In the segmentation algorithm, the original data is first approximated by a cubic spline (weighted least square interpolation from python package *scipy.interpolate*) over a fixed window of five data points (measurement interval $= 100\,$ms) to be able to calculate the derivative. If the derivative at a data point is less than the threshold $v_{th} = 200\,$nm/s, the data point is attributed to the slow state, otherwise to the fast state. See main text for the derivation of the threshold of $v_{th} = 200\,$nm/s. The experiments were performed by Akhil Sai Naidu, Rahul Grover, and Ashwin D'Souza from Stefan Diez lab at B CUBE, TU-Dresden. *Print permission was given in a private communication by the Stefan Diez lab at B CUBE, TU-Dresden.*

and getting out of the slow state does not depend on the kinesin-3 concentration.

Plotting the mean velocity of the fast state as a function of the kinesin-3 concentration reveals that the velocity of the fast state decreases in a similar manner with increasing kinesin-3 concentration as the mean velocity of the complete histogram. Consequently, the negative co-operation of multiple kinesin-3 motors at higher concentrations can be assigned to the fast state.

In summary, the experiment shows a slow and a fast velocity state. While the velocity of the slow velocity state slightly increases with increasing kinesin-3 concentration, the mean duration and frequency of the slow state remain unchanged. This means getting into and out of a slow state is equally likely for all motor concentrations. The reason which causes this slow state remains unclear. Unlike the slow state, the velocity of the fast state was seen to significantly reduce with the kinesin-3 concentration. Thus, kinesin-3 motors negatively cooperate at high motor concentrations. It remains to be found out whether the motor tail diffusion on the cargo surface is responsible for the slow velocity state or the negative motor cooperation at higher kinesin-3 concentrations. Previous theoretical studies predict a higher number of MT-attached motors due to the diffusion of motors on the cargo surface [250, 251]. However, whether the motor tail diffusion on the cargo surface influences the transport velocity or causes a slow velocity state remains unclear. Therefore, further theoretical work is needed that directly compares experiment and simulation and takes the geometry of the motor-cargo complex and the MT into account.

a)   b)
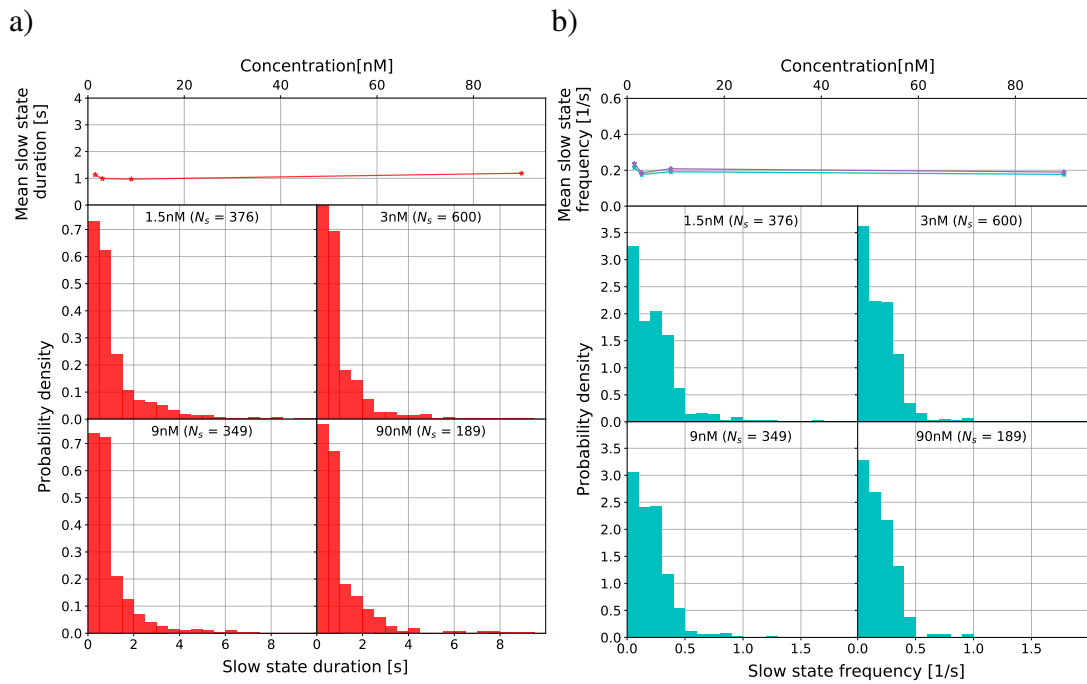
Figure 6.4: Experiment: duration and frequency of the slow state. a) Mean and histograms of slow state durations for varying kinesin-3 concentrations. Neither histograms nor means change significantly with changing kinesin-3 concentrations. b) Mean and histograms of slow state frequencies for varying kinesin-3 concentrations. The individual frequency of slow states (blue) is the number of slow states divided by the trajectory duration. The total frequency of slow states (magenta, independent of the duration of the trajectories) is total number of slow states per experiment divided by the sum of all trajectory durations. Slow state frequencies are independent of the kinesin-3 concentration. Number of samples N_s are given in brackets. All experiments were performed by Akhil Sai Naidu, Rahul Grover, and Ashwin D'Souza from Stefan Diez lab at B CUBE, TU-Dresden. *Print permission was given in a private communication by the Stefan Diez lab at B CUBE, TU-Dresden.*

6.2 One-dimensional models of cargo transport by kinesin-3

In this section, liposome transport by kinesin-3 is modeled. Therefore, in a first step, a known, point-like cargo transport model [35, 36, 153] is used. A point-like cargo model is a good first approximation because MT-attached motors are extended radially away from the cargo as it is expected when motor tails are able to move on the cargo surface. Afterward, the cargo is modeled with a radius R_C to study how sliding of diffusive motor tails (one-dimensional liposome model) versus fixed motor tails on the cargo surface (one-dimensional bead model) influence cargo transport. Illustrations of fig. 6.5 show all studied one-dimensional cargo transport models. Finally, the cargo is modeled in three dimensions to take all degrees of freedom, i.e. y- and z-extensions, cargo rotation, and orientation in relation to the MT, into account. The cargo is modeled with diffusive motor tails (three-dimensional liposome model) and with fixed motor tails (three-dimensional bead model) in three dimensions.
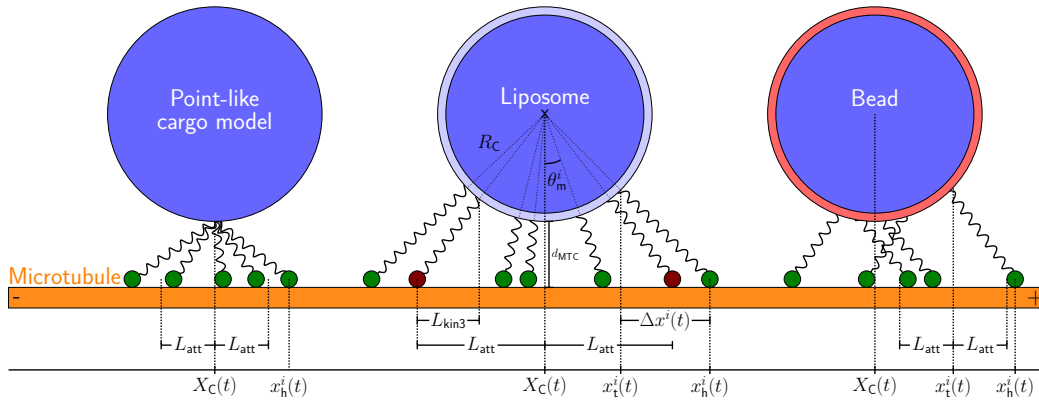
Figure 6.5: One-dimensional models: the point-like cargo model, the liposome model, and the bead model. All models neglect degrees of freedom in y- and z-direction as well as any rotation. **Point-like cargo model:** All motor tails are at the same point $X_C(t)$ (point-like cargo). Motor heads (green dots) attach to the MT within the attachment area $X_C(t) \pm L_{att}$, where they are force-free ($L_{att} = L_{kin3}$). The three middle motors therefore experience no force, motors on the left side of the attachment area (most left motor) experience a forward force, and motors on the right side (most right motor) a backward force. The head position of the ith motor on the MT is denoted by $x_h^i(t)$. **Liposome model:** Cargo has a radius of $R_C \geq 0$ and motors are able to slide on the cargo surface (x-direction only) to the position with the shortest motor extension. Motors attach to the MT within the attachment area $X_C(t) \pm L_{att}$ on the MT, where motors are force-free. Because of the motor sliding, L_{att} is bigger (or equal compared to the $R_C = 0$ case) than the rest length of the motor L_{kin3}. The one-dimensional motor extensions of the two red-marked motors are exactly equal to the motor rest length L_{kin3}. Any motor on the right/left of the left/right red motor experiences a force. The one-dimensional motor extension of the ith motor is denoted by $\Delta x^i(t)$, the corresponding head position by $x_h^i(t)$ and the tail position by $x_t^i(t)$. The angular θ_m^i denotes the angle under which the ith motor is attached. **Bead model:** Motor tails have a fixed position, denoted by $x_t^i(t)$, on the surface of the cargo with radius $R_C \geq 0$. In the bead model, motor heads attach the MT in the attachment area around the motor tail position $x_t^i(t) \pm L_{att}$. To assure that motors attach in a force-free position, the half length of the attachment area on the MT L_{att} is equal to the rest length L_{kin3} of the motor. The motor head position of the ith motor on the MT is denoted by $x_h^i(t)$ and the bead position by $X_C(t)$.

6.2.1 Point-like cargo model

Cargo transport by molecular motors has been modeled in the past [33, 35, 36, 151, 153]. Here, a point-like cargo model, which has been introduced and analyzed before [35, 35, 153] is used to study liposome transport by kinesin-3 motors. In this first approach, the focus lies on the cargo transport and interplay of multiple kinesin-3 motors in one direction (x-axis, one-dimensional model). MT, cargo, and motor extensions and motions in y- and z-direction as well as any rotational degree of freedom are neglected but will be considered in the following up sections.

In the point-like cargo model, all motor tails come together in one point, the cargo position, which is denoted by $X_C(t)$ in the one-dimensional coordinate system. The MT, modeled as one-dimensional line (one protofilament), is placed in the one-dimensional coordinate system such that movement towards the MT plus-end is considered positive. For simplicity, it is assumed that the MT is infinitely long.

  In the experiment, a total number of N_{tot} motors are bound with their tails to the cargo surface[3]. However, from the total number of motors N_{tot} only a subset of motors $N_{aa} < N_{tot}$ are in the area on the cargo (from now on called "attachment area on the cargo", see fig. 6.6), from where motors can reach the MT to attach. Since only these motors are contributing to the cargo transport, only these motors are modeled. To account for motors diffusing on the cargo surface and exchanging with the motors which cannot reach the MT (motors in the "reservoir"), individual motor properties are chosen randomly each time they attach to the MT. Unlike previously published versions of the point-like cargo model [35, 35, 153], where the number of motors is the same for each cargo, here fluctuations in the number of motors between cargoes are taken into account. To estimate the number of motors per cargo distribution, the distribution of motors among the cargos is simulated. In this simulation, there are supposed to be N_C cargos in the solution and N motors. To distribute the N motors randomly among the N_C cargos, a uniformly distributed random number between 1 and N_C is thrown N times. The histogram of the number of motors per cargo (see fig. 6.7a) can be fitted by a Gaussian distribution with mean μ and standard deviation σ. Performing the simulation for varying number of motors in the solution N, but a fixed number of cargos N_C, it can be seen that number of motors per cargo distributions widen and move to higher means for higher number of motors in the solution N. Fitting the number of motors per cargo distribution for each number of motors in solution N reveals that the standard deviation σ depends on the mean μ in a square-root-like manner (fig. 6.7b). Fitting a square root to the standard deviation σ as a function of the mean μ, the following dependence of mean and standard deviation is derived:

$$\sigma(\mu) = 1.0683\sqrt{\mu}. \tag{6.2}$$

To take fluctuations in the number of motors per cargo into account, for each cargo the number of motors N_{aa} is randomly thrown from a Gaussian distribution with mean given by the desired mean number of motors per cargo (given by the experimental concentration) and the standard deviation given by eq. (6.2). Since the mean number of motors per cargo is not given by the experiment, here the simulation is used to give a range of number of motors per cargo where simulation and experimental results fit bests.

  Motors are coarse-grained modeled as roundish objects, which occupy an area of $2 \times R_{kin3}$ on the MT when the motor is attached to the MT (MT-attached motors). Attached motors can exert a force on the cargo, which is proportional to the motor extension (Hookean spring). The

---

[3]It can be assumed that the number of motors per cargo does not change over time.
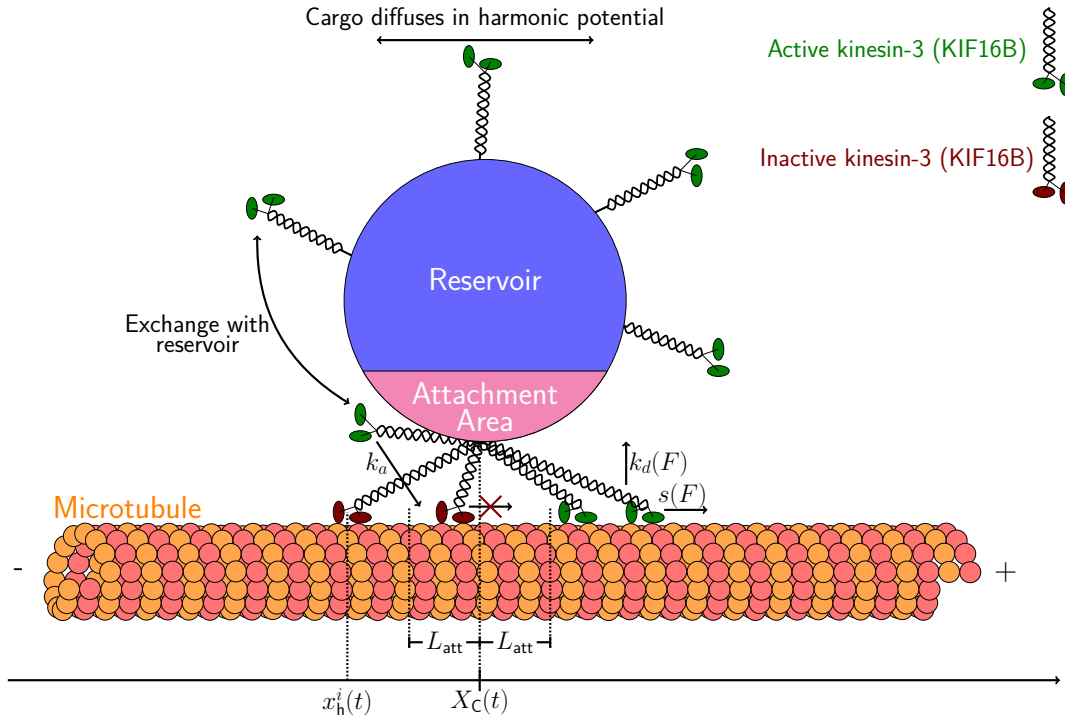
Figure 6.6: The point-like cargo model including all variations. For a better illustration an extended cargo and a finite MT is drawn (MT is infinitely long in the simulation). However, all tails of MT-attached motors come together in one point showing the point-like cargo model. The MT is drawn as an orange-red tube with the plus-end in positive direction of the one-dimensional coordinate system. Motors attach to 7 out of 14 protofilaments with the constant rate k_a. For simplicity, all protofilaments are modeled to be parallel to the x-axis and no super-twist of the protofilaments is taken into account (for one-dimensional models). Motors are drawn as springs with two circles presenting the two motor domains. Although both motor domains are drawn, in the simulation, the motor domains are coarse-grained modeled as a single sphere with radius R_{kin3}. Single molecule experiments of kinesin-3 (KIF16B) show that about 20 % of kinesin-3 motors are not moving (called "inactive" motors). Inactive motors (red) attach to and detach from the MT at the same rates as the active motors (green). In the model, only the motors in the attachment area (magenta), which can reach the MT, are modeled. Motors, which cannot reach the MT are in the reservoir (blue). Due to the motor diffusion on the cargo surface, motors in the attachment area are able to exchange with motors in the reservoir. That is why, with probability $p_{inactive} = 0.2$ a motor is chosen to be inactive each time it (re)attaches. A motor attaches with the constant rate k_a within the attachment area $X_C(t) \pm L_{att}$ on the MT. Because motors are supposed to attach in a force-free state, L_{att} is equal to the motor rest length L_{kin3}. The attachment probability to the protofilaments p_{PF} is Gaussian distributed over the 7 protofilaments. The mean is the central protofilament of the upper half space of the MT and the variance is $\sigma = 1$. The borders of the Gaussian are chosen such that the 7 protofilaments occupy $\mu \pm 3\sigma$ of the Gaussian distribution. Motors are modeled as linear, Hookean springs. Thus, motor forces (eq. (6.4)) are proportional to the motor extension $x_h^i(t) - X_C(t)$. The detachment rates (detachment from the MT) $k_d(F)$ increase exponentially with forward and backward forces F. The stepping rate $s(F)$ is constant under forward load force (forces pulling the motor towards the MT plus-end) and decreases with backward forces (forces pulling the motor towards the MT minus-end) smaller than the stall force $F_{s,kin3}$. For backward forces higher than the stall force, the motor steps backward with a small and constant rate [35, 120]. The cargo diffuses in the harmonic potential of MT-attached motors. Therefore, the Metropolis algorithm (see section 3.2) is used.
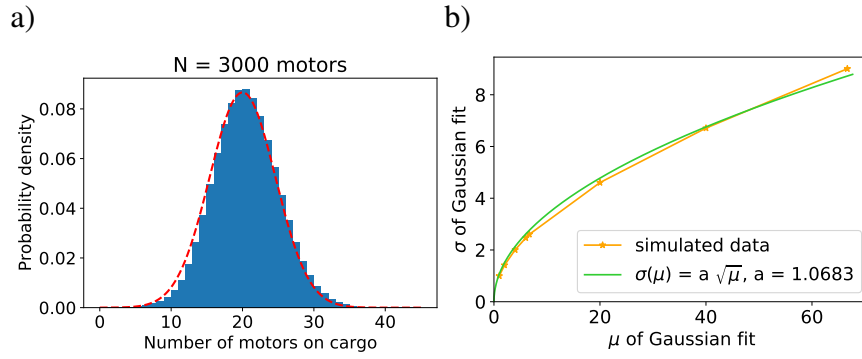
Figure 6.7: Number of motors per cargo distribution. In an extra simulation, a varying number of motors N is randomly distributed over a fixed number of cargos $N_c = 150$. The number of motors represents the number of motors in the solution. a) Shows an example number of motors per cargo distribution for $N = 3000$. The distribution could be fitted with a Gaussian with mean $\mu = 20$ and standard deviation $\sigma = 4.6052$. b) The figure shows the standard deviations σ of the Gaussian fits as a function of the respective means μ of the Gaussian fits of the number of motor per cargo distributions. The standard deviation as a function of the mean could be fitted by a square-root function $\sigma(\mu) = 1.0683\sqrt{\mu}$.

motor extension is given by the one-dimensional difference between the motor tail and the motor head attached to the MT:

$$\Delta x^i(t) = x_h^i(t) - x_t^i(t) = x_h^i(t) - X_C(t) \tag{6.3}$$

where in the last step it is applied that the motor tail position is identical to the cargo position for the point-like cargo model (see fig. 6.6 and fig. 6.5). Since kinesin-3 motors are modeled as linear Hookean springs with a rest length L_{kin3}, the force a MT-attached motor exerts on the cargo is:

$$F^i(t) = \begin{cases} \kappa_{kin3}\left(\Delta x^i(t) - L_{kin3}\right), & \Delta x^i(t) > L_{kin3} \\ 0, & \left|\Delta x^i(t)\right| \leq L_{kin3} \\ \kappa_{kin3}\left(\Delta x^i(t) + L_{kin3}\right), & \Delta x^i(t) < -L_{kin3} \end{cases} \tag{6.4}$$

with κ_{kin3} being the stiffness of a kinesin-3 motor.

All kinesin-3 motors can perform three different kinds of events: i) detached motors can attach to the MT, ii) MT-attached motors can detach from the MT, or iii) MT-attached motors can step along the MT. To model these events, the standard kinesin-1 model, which has been introduced in section 4.2.1, is used. Thus, motors attach with the constant rate k_a in the area $X_C(t) \pm L_{att}$ around the cargo position (see fig. 6.6). Since motors attach in a force-free position, the half length of the attachment area on the MT L_{att} is equal to the rest length of the motor L_{kin3}. For detachment, a rate is used, which increases exponentially with force:

$$k_d(F^i) = k_d^0 e^{\frac{|F^i|}{F_d}} \tag{6.5}$$

where k_d^0 is the force-free detachment rate and F_d the detachment force (see also eq. (4.24)). The stepping rate is divided into forward stepping under assisting forces, forward stepping under resisting forces smaller than the stall force F_s and backward stepping under resisting

forces bigger than the stall force. For the forward stepping rate, the force and ATP dependent stepping behavior of Schnitzer et al. [120] is used:

$$s_{\text{kin}}(F^i, [\text{ATP}]) = \frac{v_{\text{f}}/d \cdot [\text{ATP}]}{[\text{ATP}] + K_M} = \frac{k_{\text{cat}}(F^i)[\text{ATP}]}{[\text{ATP}] + k_{\text{cat}}(F^i)/k_{\text{b}}(F^i)} \tag{6.6}$$

with the stepsize d and $k_{\text{cat}}(F^i)$ and $k_{\text{b}}(F^i)$ given by eq. (4.20) (see section 4.2.1 for more details). For the forward stepping under assisting load, $s_{\text{kin}}(F^i = 0, [\text{ATP}])$ is used. The backward stepping rate is chosen to be constant and given by

$$s_{\text{kin}}(F^i) = \frac{v_{\text{b}}}{d} \tag{6.7}$$

with v_{b} being the backward stepping velocity of kinesin-3 and d the stepsize. Since in real systems, the MT has several protofilaments and motors are assumed to reach several PFs of the MT, no exclusion effects are taken into account on the MT for the standard point-like cargo model. This means motors do not sterically hinder each other when attaching or stepping on the MT. Modeling kinesin-3, different parameter values than for kinesin-1 in section 4.2.1 are used. The force-free detachment rate k_{d}^0 and the force-free forward stepping velocity v_{f} of kinesin-3 can directly be taken from single molecule experiments. However, other parameters such as F_{d}, F_{s}, v_{b}, k_{a} or L_{kin3} are not given by the experiment. Whenever available, literature values are used. See table C.1 for parameter values and references to the literature. Moreover, see fig. 6.8 for attachment, detachment, and stepping rates as a function of the motor force for different parameter values.

Figure 6.8: Kinesin-3 rates as a function of the motor load force. The attachment rate $k_{\text{a}} = 5\,\text{s}^{-1}$ (blue) is independent of the motor load force. The rate of motor detachment from the MT and the stepping rate depend on the motor force and are drawn for different values of the detachment force $F_{\text{d}} = F_{\text{d,kin3}}$ and the stall force $F_{\text{s}} = F_{\text{s,kin3}}$. The detachment rate (green) increases exponentially with forward and backward forces. The stepping rate (red) is constant under negative forces (forces pulling the motor towards the MT plus-end), decreases under positive forces (forces pulling the motor towards the MT minus-end) smaller than the stall force, and is constant and small for forces bigger than the stall force. Under forces bigger than the stall force, the motor steps backward. The stepping was previously published by Klein et al. [35] and is based on the findings of Schnitzer et al. [120] for kinesin-1.

Having motors exerting forces on the cargo, the cargo should move according to the following over-damped equation of motion:

$$m\frac{\partial^2}{\partial t^2}X_{\text{C}}(t) = \sum_{i=0}^{N_{\text{att}}} F^i - \zeta\frac{\partial}{\partial t}X_{\text{C}}(t) = 0 \tag{6.8}$$

where $N_{att} < N_{aa}$ is the number of MT-attached motors and $\zeta = 6\pi\eta R_C$ the drag coefficient with viscosity η and cargo radius R_C. The over-damped equation of motion is used because the Reynold number ($\mathcal{R} \sim 10^{-7} \ll 1$, see eq. (4.12)) of a cargo with a typical radius of $R_C = 60\,\mathrm{nm}$ is small and the inertia term can therefore be neglected. Instead of numerically solving this equation of motion, the cargo is immediately moved to the closest force-free position after each motor event in the simulation. The force-free position (equilibrium position, where motor forces balance each other) is found by using a bisection search algorithm (see section 3.2). It is thereby carefully checked that the next force-free position is reached according to the equation of motion before the next event occurs. See also section 4.1 for more details on this update mechanism.

Taking together, the point-like cargo model describes liposome transport in one dimension. Motor tails, therefore, come together in one point (cargo position), motors attach to one protofilament of the MT, and motor extensions are given by the one-dimensional difference between the motor tail position (=cargo position) and the motor head position on the MT. Motors are modeled as linear, Hookean springs, which attach the MT with a constant rate and detach and step on the MT with force-dependent rates. As a summary of the model, the pseudo-code is given:

Algorithm 1 Point-like cargo model

Initialize cargo:
    $X_C(t) = 0$
    $N_{aa} = $ **generate_number_of_motors_per_cargo**($\langle \mathbf{N_{aa}} \rangle$)
Initialize motors:
    being_attached $=$ **false**
Update:
    do:
        next_event $=$ **get_next_event**{*motor attachment, stepping or detachment*}
        update_simulation_time()
        output{**if**(simulation_time > next_output_time) : *output measurements*}
        update_motors{*motor attachment, stepping or detachment*}
        move_cargo{*closest force-free position or diffusion in harmonic potential*}

    while (number_of_measurements < max **and** number_of_attached_motors > 0)

In the following simulation results are presented.

Results: The above-presented point-like cargo model is used to simulate cargo transport by kinesin-3 for four different numbers of motors $N_{aa} = \{4, 10, 15, 30\}$. During the simulations, cargo positions are measured after Δt_{mes} seconds as in the experiment (see table C.1 of the appendix C for explicit values). From the cargo positions, instantaneous cargo velocities are calculated.
Instantaneous velocity histograms (fig. 6.9a) show narrowed peaks at high velocities of about $800 - 850\,\mathrm{nm/s}$ for all number of motors N_{aa}. Peaks become narrower the higher the motor number N_{aa}, which can also be seen when plotting velocity variances as a function of the number of motors (fig. 6.10). Mean velocities increase with increasing number of motors (fig.

a) Standard point-like cargo model

b) Variation I: velocities

c) Variation II: exclusion

d) Variation III: inactive motors
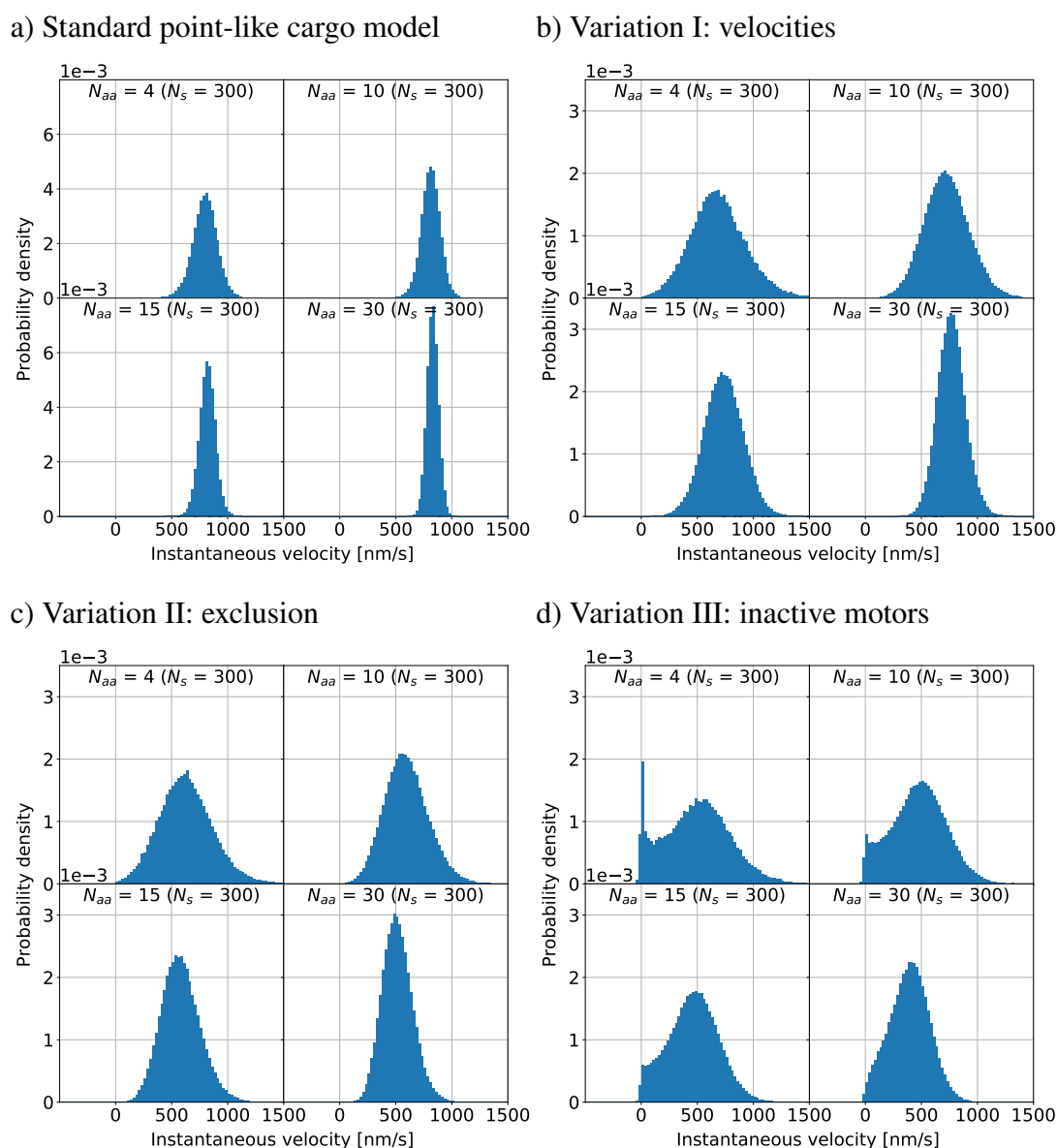
Figure 6.9: Varying the point-like cargo model: histograms. Point-to-point velocity histograms from the standard model (a) and three model variations I-III (b-d). Number of motors N_{aa} is varied for each model. a) Standard point-like cargo model: histograms show narrow peaks with decreasing width for higher number of motors N_{aa}. b) Variation I: point-like cargo model with Weibull distributed force-free forward velocities (see eq. (6.9) and fig. 6.11). Weibull-distributed forward velocities widen the velocity distribution. Peaks still become narrower for larger number of motors. c) Variation II: point-like cargo model with Variation I and exclusion on the MT. In total, 7 protofilaments are modeled, to which the motors attach with Gaussian distributed probabilities. Histograms show peaks similar to b), but moved to lower velocities for higher number of motors. d) Variation III: point-like cargo model with Variation I, II, and inactive motors. 20 % of the kinesin-3 motors are inactive, which means they do not move at all along the MT but attach to and detach from the MT as normal active kinesin-3 motors. Histograms (*Continuation on next page.*)

Figure 6.9 (*previous page*): show two peaks for low number of motors. One peak is at high velocities and one at low velocities close to zero. The low velocity peak disappears for high number of motors.

The number of simulated samples (cargos) N_s is given in brackets.

a) Standard point-like cargo model

b) Variation I: velocities

c) Variation II: exclusion

d) Variation III: inactive motors
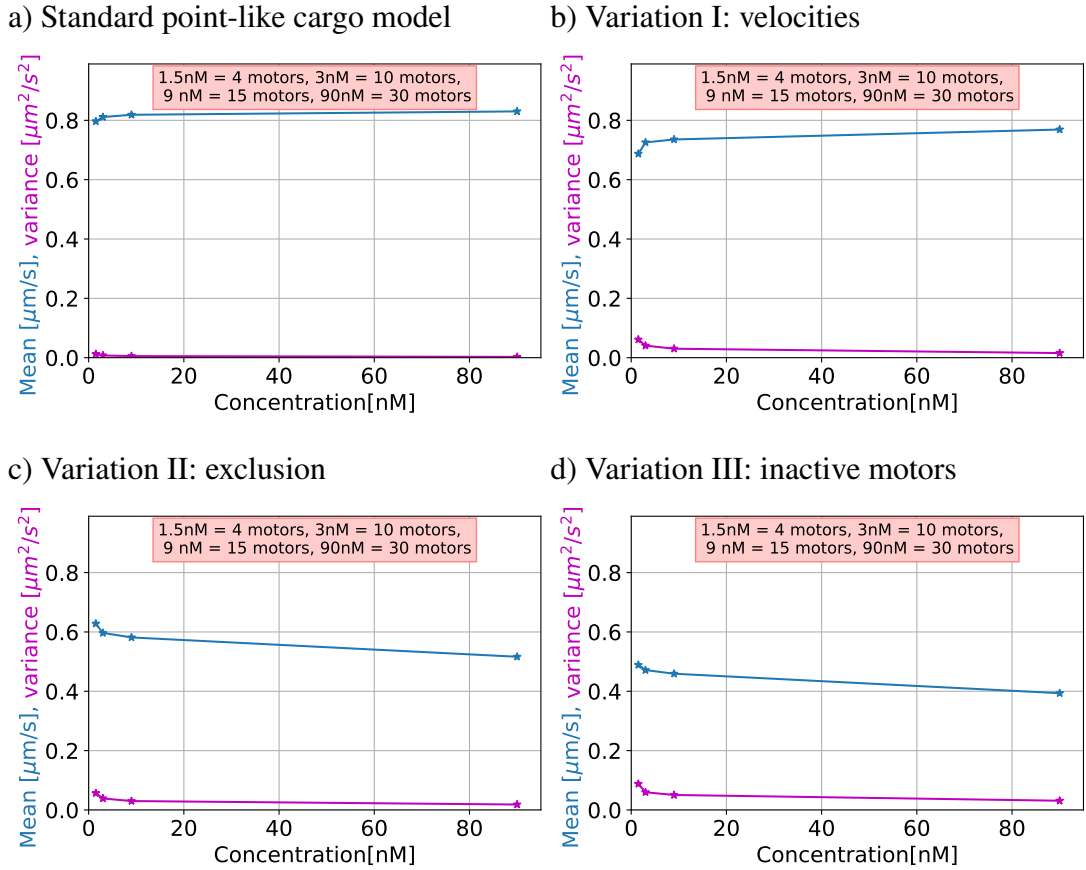
Figure 6.10: Varying the point-like cargo model: mean velocities. Mean and variance of cargo velocities as a function of motor concentration from the standard model (a) and three model variations I-III (b-d). The assumed, corresponding number of motors in the attachment area on the cargo N_{aa} is given in the heading. a) Standard point-like cargo model: variances are $\sigma^2 = \{0.012, 0.0075, 0.0053, 0.0027\}$ nm^2/s^2 for $N_{aa} = \{4, 10, 15, 30\}$ motors, respectively. Mean velocities increase with increasing number of motors N_{aa}, while the variance decreases. b) Variation I: point-like cargo model with Weibull distributed force-free forward velocities (see eq. (6.9) and fig. 6.11). Variances are higher and mean values lower compared to a). c) Variation II: point-like cargo model with Variation I and exclusion on the MT. In total, 7 protofilaments are modeled, to which the motors attach with Gaussian distributed probabilities. Mean velocities decrease with increasing number of motors. Variances, however, remain unchanged compared to b). d) Variation III: point-like cargo model with Variation I, II, and inactive motors. 20 % of motors are inactive motors, which means they attach to and detach from the MT as normal, active motors, but do not step at all on the MT. Mean velocities are reduced and variances increased compared to c).

6.10). A comparison of simulation and experimental results reveals the following differences between simulation and experiment:

- Velocity histograms from simulation (fig. 6.9a) show one peak at high velocities, while the experimental histograms (fig. 6.2a) show a high and a low (close to zero) velocity peak.

- The high velocity peaks are narrower in the simulation than in the experiment. In detail, the variance of the simulation is at least one order of magnitude smaller (see caption of fig. 6.10 for exact values) than in the experiment (fig. 6.2c).

- Mean velocities from simulation (fig. 6.10) increase with increasing number of motors, while mean velocities from experiments (fig. 6.2c) decrease with increasing motor concentration.

This means the model did not capture all details, which are needed to observe the experimentally seen dependence on the motor concentration.

In the next steps, the following features are added step-by-step to the point-like cargo model to better align simulations and experiments:

- Variation I: add Weibull distributed motor velocities

- Variation II: add motor-motor exclusion on the MT

- Variation III: add inactive motors

- Variation IV: add cargo diffusion in the harmonic potential of MT-attached motor springs

The features are added one after the other to see their influence and to assign them to specific results.

Variation I: add Weibull distributed motor velocities: Single motor stepping velocities influence the cargo velocity. Single motor stepping velocities depend on the load force and differ between single motors [74, 120, 326]. In the point-like cargo model, single motor velocities depend on the load force of the motor, but all motors have the same force-free forward velocity. Experiments, however, show a wide distribution of force-free single kinesin-3 velocities (see fig. 6.11a). The distribution ranges from very low velocities of about $50 - 100$ nm/s up to velocities of 2000 nm/s. This raises the question of whether individual, slow kinesin-3 motors are responsible for the slow state observed in the experiment (fig. 6.2).
To study the influence of different individual motor stepping velocities on cargo transport, the point-like cargo model is modified such that an individual force-free forward velocity is assigned to each motor. To apply the same single-motor force-free velocity distribution as in the experiment, first, the experimental single motor force-free velocity distribution needs to be characterized. The experimental single motor force-free velocity distribution (fig. 6.11a) is well described by a Weibull distribution (fig. 6.11b) with shape parameter $k = 2$ and mean $\lambda = v_\mathrm{f}$ given by the experiment (see table C.1 of the appendix C for parameter values):

$$f(x; \lambda, k) = \begin{cases} \frac{k}{\lambda} \left(\frac{x}{\lambda} \right)^{k-1} \mathrm{e}^{-(x/\lambda)^k}, & x \geq 0, \\ 0, & x < 0. \end{cases} \tag{6.9}$$

a)

b)
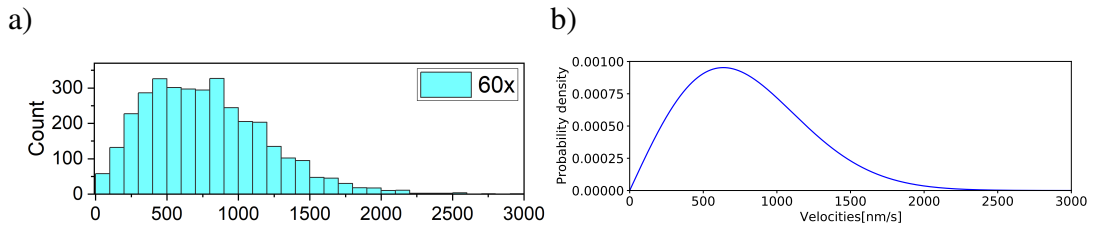
Figure 6.11: Weibull distributed velocities of single kinesin-3 motors.   a) Velocity histograms of experimental point-to-point velocities of single kinesin-3 motors in the absence of liposomes or beads. On the x-axis single molecule velocities in [nm/s] are depicted. The experiment was performed by Akhil Sai Naidu, Rahul Grover, and Ashwin D'Souza from Stefan Diez lab at B CUBE, TU-Dresden. *Print permission was given in a private communication by the Stefan Diez lab at B CUBE, TU-Dresden.* b) Weibull distribution with $k = 2$ and $\lambda = v_{\text{f}} = 900$ nm/s (see also eq. (6.9)). Since the original experimental data of the single kinesin-3 velocities was not available, the experimental data could not be fitted directly. However, it can be seen that the shown Weibull distribution reproduces well the single kinesin-3 velocity distribution.

Having characterized the experimental single kinesin-3 motor force-free forward velocity distribution, the point-like cargo model can be extended by giving each motor its own force-free forward velocity applying the Weibull distribution.

Results of Variation I: Applying Weibull distributed single motor force-free velocities, the velocity histograms (fig. 6.9b) show wider peaks at slightly lower velocities ($700 - 750$ nm/s). Variances of velocities (fig. 6.10b) have now the same order of magnitude as in the experiment (fig. 6.2c). However, the mean velocity of the simulation (fig. 6.10b) still increases with increasing number of motors, while the mean velocity of the experiment (fig. 6.2c) decreases with increasing kinesin-3 concentration. Moreover, simulation histograms (fig. 6.9b) still do not show the additional low velocity peak seen in the experiment (fig. 6.2a). This means the low velocities seen in the experiment are not caused by individual slow kinesin-3 motors.
In summary, Weibull-distributed single motor velocities widen the cargo velocity distribution but are not responsible for the experimentally observed slow state.

Variation II: add motor-motor exclusion on the MT: Results from dynein gliding assays of section 2.2.1 revealed that a reduction of the velocity at high number of motors is caused by a mutual steric hindrance of the MT-attached motors. Since motors in principle can attach to different protofilaments, but in the point-like cargo model only one protofilament is modeled, exclusion effects on the MT were not taken into account. However, it could be that at high number of motors, motors end up being attached to the same protofilament and hinder each other even though they can in principle attach to several protofilaments. To study the influence of sterical motor-motor hindrance, exclusion effects are added for motors attached to the MT. This means MT-attached motors, which occupy an area of $2R_{\text{kin3}}$ on one protofilament (see table C.1 for parameter values), are not allowed to overlap when being attached to the same protofilament. Here, it is assumed that motors can reach 7 out of 14 protofilaments, i.e. the upper half space of the MT. When a motor attaches, its protofilament is chosen according to a Gaussian distribution around the central protofilament with standard deviation $\sigma = 1$. The seven protofilaments are distributed over the Gaussian distribution in such a way that they

occupy an area of $\mu \pm 3\sigma$ of the Gaussian distribution and the Gaussian distribution is truncated at $\mu \pm 3\sigma$. Consequently, the motors preferentially attach to the central protofilaments, which are closest to the cargo. Note that exclusion effects and several protofilaments are added to the point-like cargo model including variation I (Weibull distributed single motor velocities).

Results of Variation II: Simulating cargo transport with motor-motor exclusion on the MT, the mean cargo velocity (fig. 6.10c) reduces from over 600 nm/s to around 500 nm/s with increasing number of motors. This means the experimentally observed reduction of the mean cargo velocity with increasing motor concentration (fig. 6.2a) can, indeed, be explained by a mutual sterical hindrance of MT-attached motors. Histograms of cargo velocities (fig. 6.9c) show the reduction of the velocity with increasing number of motors but do still not show the experimentally observed low velocity peak. Thus, the mutual steric hindrance of attached motors on the MT causes a reduction of the velocity with increasing number of motors, but not the experimentally observed slow state.

Variation III: add inactive motors: It has been shown that neither slow motors nor sterically hindered motors cause a slow velocity state of the cargo. To pause the cargo, there needs to be an opposing force, holding the cargo back. It could be that this opposing force is caused by MT-attached motors, which do not move at all and behave as an anker. Single kinesin-3 motor experiments revealed that about 20 % of the used kinesin-3 motors do not move at all[4]. To test their influence on cargo transport, 20 % non-moving, from now on called "inactive" motors are added to the point-like cargo model, which includes variations I and II (Weibull distributed single motor velocities and exclusion effects on the MT). In the model with variation III, attaching motors are chosen to be inactive with probability $p_{\text{inactive}} = 0.2$. Inactive motors attach and detach in the same way and at the same rates as the usual active motors. However, unlike active motors, inactive motors do not step at all. Thus, inactive motors stay on the spot on the MT, where they attached, until they detach again. Consequently, it can be assumed that inactive motors generate an opposing force, which holds the cargo back when active motors try to advance it. To advance the cargo, the active motors need to pull off the inactive motors.

Results of Variation III: Simulating cargo transport in the presence of inactive motors produces velocity histograms (fig. 6.9d), which show a low and a high velocity peak. Thus, inactive motors can explain the slow state. However, a more detailed comparison of the low velocity peaks yields that the peak is a lot narrower in the simulation than in the experiment (fig. 6.2a). Moreover, there are more negative velocities measured in the experiment than in the simulation. It remains unclear where the negative velocities of the experiment come from. Moreover, the presence of inactive motors slightly reduces the mean cargo velocities and increases the variance (see fig. 6.10d) such that both even better approximate the experimental values (see fig. 6.2c).

Variation IV: add cargo diffusion in the harmonic potential of MT-attached motor springs: Analyzing the experimental data revealed that the negative velocities are related to the slow state. It can therefore be assumed that the negative velocities are due to a diffusion of

---

[4]Experimental results are unpublished. Experiments were performed by Akhil Sai Naidu, Rahul Grover, and Ashwin D'Souza from Stefan Diez lab at B CUBE, TU-Dresden. Print permission was given in a private communication by the Stefan Diez lab at B CUBE, TU-Dresden.
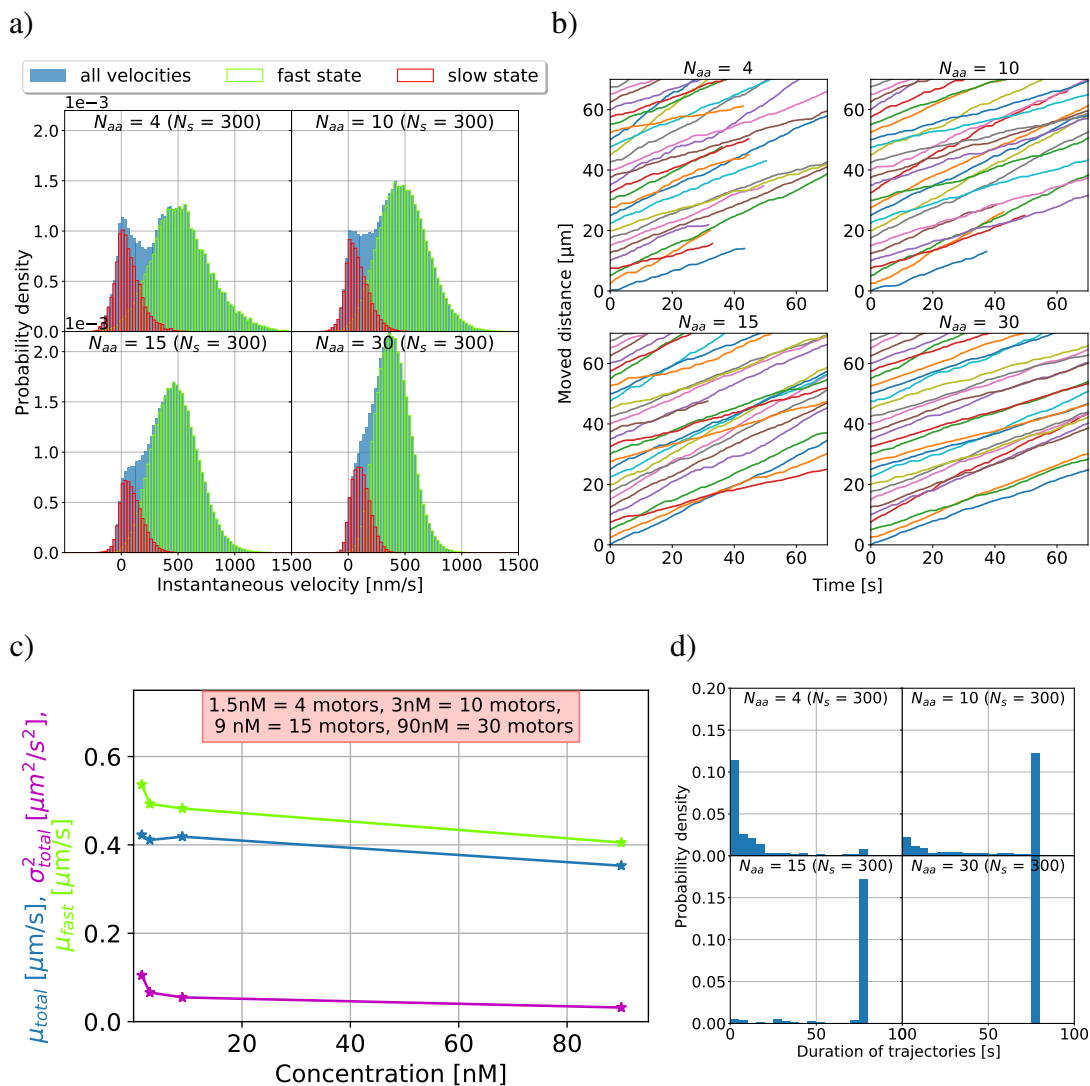
Figure 6.12: Point-like cargo model with variations I-IV. Simulation results produced with the point-like cargo model with variations I-IV. a) Cargo velocity histograms (blue) for varying numbers of motors in the attachment area N_{aa}. Using the segmentation algorithm (see main text and caption of fig. 6.3), trajectories can be divided into slow and fast states. Increasing the number of motors N_{aa}, the fast state velocity peak (green) moves to smaller velocities and finally merges with the slow state velocity peak (red). b) Example trajectories of simulated cargos (trajectory duration longer than 30 seconds) are depicted for varying numbers of motors in the attachment area N_{aa}. A stop-and-go-like motion with clear slow states can be seen for all numbers of motors. c) Mean (blue) and variance (magenta) of all cargo velocities as well as mean velocities of only the fast state (green) are depicted. All three observables decrease with increasing number of motors. d) Histograms of trajectory durations. Trajectories are longer in time for high number of motors. The program was terminated either if no motor was attached to the MT anymore or after 80 seconds. Number of samples (cargos) N_s are given in brackets (a +d).

the cargo in the harmonic potential of the MT-attached motors when being stalled. To test this assumption, the update mechanism in the model is changed. Instead of moving the cargo to

the closest force-free position, the Metropolis algorithm (see section 3.2) is used with number of proposals n_m and a proposal interval of d_m (see table C.1 of the appendix C). Using the Metropolis algorithm, transitions with lower energy are accepted with probability $p = 1$ and transitions with higher energy are accepted with probability $p = \exp\left[-\frac{\Delta E}{k_\mathrm{B}T}\right]$. That is how the diffusion of the cargo in the harmonic potential is modeled.

Results of Variation IV: Including the diffusion of the cargo in the harmonic potential of the MT-attached motors widens the low velocity peak in cargo velocity histograms (fig. 6.12a) such that negative velocities are reached. Comparing negative velocities of the simulation (fig. 6.12a) with negative velocities of the experiment (fig. 6.2a), it can be seen that negative velocities agree well. This means, the harmonic potential, given by the individual motor spring constant and the number of MT-attached motors, is well estimated. The number of MT-attached motors is determined by the attachment rate and the number of available motors in the attachment area on the cargo (N_aa). All these parameters, attachment rate, number of motors on the cargo/in the attachment area, and kinesin-3 stiffness (spring constant) are not given by the experiment. For attachment the commonly used attachment rate of $k_\mathrm{a} = 5\,\mathrm{s}^{-1}$ [34, 327] is applied. Because the stiffness of kinesin-3 is not given by the literature, a known stiffness of kinesin-1 is applied (see table C.1 of the appendix C). Assuming

Figure 6.13: Point-like cargo model: number of MT-attached motors. Mean number of MT-attached motors ($\mu \pm \sigma$) obtained from simulations with the point-like cargo model with variations I - IV. The total number of MT-attached motors (yellow), the number of active (green), and the number of inactive MT-attached motors (red) are shown as a function of the number of motors in the attachment area on the cargo N_aa. All three increase with increasing number of motors in the attachment area N_aa. The number of inactive motors increases slower than the number of active motors.

that kinesin-3 has a similar stiffness as kinesin-1, the simulation can give an estimate of the number of MT-attached motors (fig. 6.13). Furthermore, under the assumption of a good estimate of the attachment rate too, the simulation also gives a prediction of the number of motors in the attachment area on the cargo. Fig. 6.13 shows the number of MT-attached motors as a function of the number of motors available in the attachment area on the cargo. The number of MT-attached motors increases with the number of available motors. While for the lowest number of available motors, almost all of them are attached, for the highest number of motors less than half of them are attached to the MT. This means besides the attachment rate and the number of available motors, also the available space on the MT determines the number of MT-attached motors (exclusion effects, see variation II).

As discussed before, inactive motors cause a slow state of the cargo. Comparing velocities
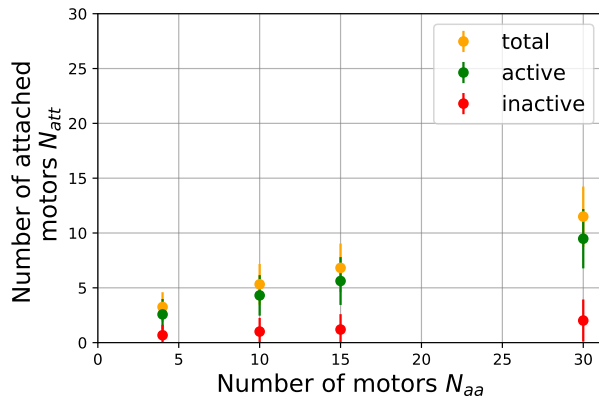
of the slow state for different motor numbers, it can be seen that they have a slightly higher drift (positive velocities) at higher number of motors (fig. 6.12a). Looking at the number of active and inactive MT-attached motors (fig. 6.13) reveals that the number of actively MT-attached motors increases faster with the number of available motors than the number of inactive MT-attached motors. Having a higher percentage of actively MT-attached motors (higher number of available motors) makes the team of active motors stronger, such that the slow velocity state shows a higher drift towards positive velocities compared to lower number of motors, where the percentage of actively MT-attached motors is lower.

Besides producing negative velocities, adding the diffusion of the cargo in the harmonic potential of the MT-attached motors slightly reduces the mean velocity and increases the variance (see fig. 6.12c). Velocity histograms as well as mean velocities and variances are now in alignment with the experimental findings. Furthermore, trajectories of the simulation (fig. 6.12b) show stops similar to the experiment (see fig. 6.2b). Consequently, the point-like cargo model with variations I-IV describes experimental observations.

Note that cargo trajectories are slightly longer in the simulation (fig. 6.12d) than in the experiment (fig. 6.2d). Simulation trajectories are supposed to be longer because they are only terminated when either no motor is attached to the MT anymore or the simulation time t_{end} (see table C.1 of the appendix C) is over. Experimental trajectories, in contrast, can additionally be terminated when the liposome reaches the MT end, when the tracked liposome moves out of the focus of the camera, when the liposome reaches an intersection of two MTs or can be shorted by the used tracking software. That is why experimental trajectories are supposed to be smaller than simulation trajectories. If simulation trajectories were smaller than experimental trajectories, the motor detachment would be overestimated or number of motors would be underestimated.

When dividing the trajectories into slow and fast states using the here developed segmentation algorithm (see section 6.1), the mean velocities of the fast state (fig. 6.12c) as well as duration and frequency of the slow state (fig. 6.14) can be calculated. Mean velocities of the fast state are in good alignment with the experiment. Duration of the slow state (fig. 6.14a) does not depend on the number of motors as seen in the experiments (fig. 6.4a), but is longer in the simulation than in the experiments. While in the experiments mean durations are longer than 2 seconds, they are less than 1 second in the simulation. A detailed look at the trajectories reveals that there are occasionally long stops in the experiment, which are not observed in the simulation. The origin of these long stops is possibly not due to inactive motors. Longer stops may occur when the cargo is sterically hindered by either another cargo or by the experimental set-up. Another possibility is that even advancing motors are not able to step anymore because of a roadblock on the MT or a defect in the MT lattice. Besides a hindrance of the cargo or the motors, also geometry could play a role. Having a point-like cargo, spatial effects of the sliding of motors to the backside of the cargo (side orientated towards the MT minus-end) due to diffusive motor tails are not taken into account. It is possible that the sliding to the backside of the cargo causes longer stops. That is why simulations including the spatial extensions of the liposome are necessary. Unlike durations, frequencies of the simulated slow state (fig. 6.14b) are similar to the frequencies of the experiment (fig. 6.4b). Taken together, cargos stop as often in the simulation as in the experiment but stay a bit longer in the slow state in the experiment compared to the simulation.

A summary of the point-like cargo model including variations I to IV is shown in fig. 6.6. Simulations of the point-like cargo model reveal the following three main findings:

a)

b)
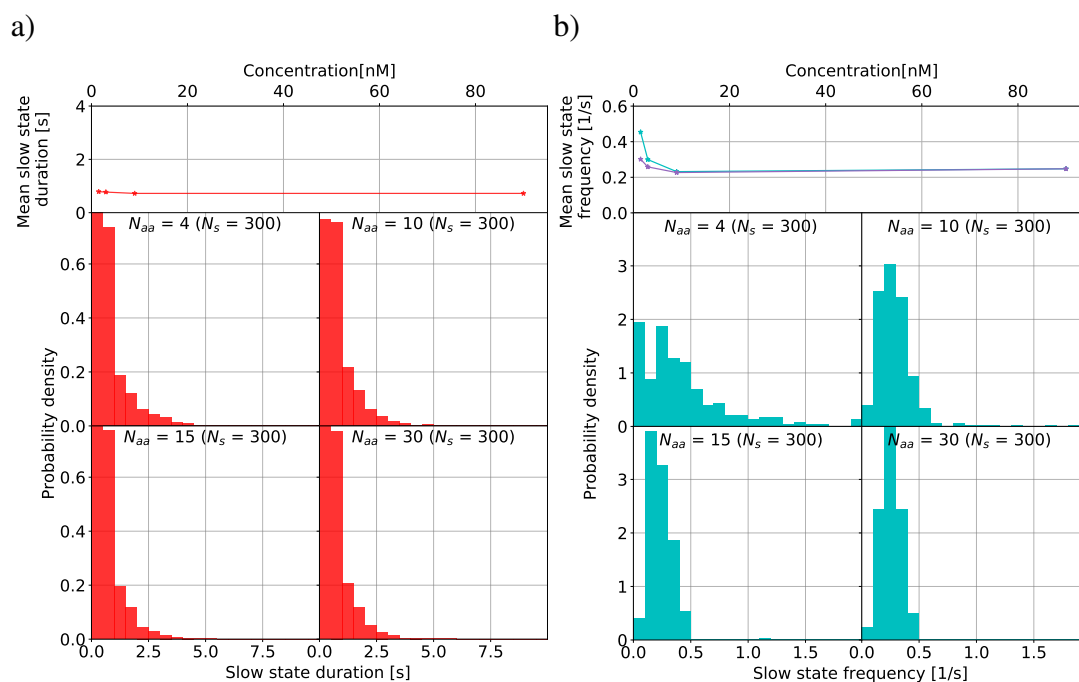
Figure 6.14: Point-like cargo model: duration and frequency of slow state. Duration and frequency of slow state obtained from simulation using the point-like cargo model with variations I - IV. a) Mean duration of the slow state as a function of the motor concentration as well as duration histograms for varying number of motors. Although in the simulation the number of motors in the attachment area on the cargo N_{aa} is given, the mean is drawn as a function of the motor concentration for a better comparison with the experimental data (fig. 6.4a). See fig. 6.12c for which concentration corresponds to which number of motors. Mean and histograms do not show a dependence of the slow state duration on the number of motors. b) Mean and histograms of slow state frequencies for varying numbers of motors. The individual frequency of slow states (blue) is the number of slow states divided by the trajectory duration. The total frequency of slow states (magenta, independent of the duration of the trajectories) is total number of slow states of all simulations divided by the sum of all trajectory durations. Slow state frequencies are slightly enhanced for low number of motors, otherwise independent of the number of motors.
Number of samples N_s is given in brackets.

- Inactive (non-moving) motors cause a slow velocity state. Inactive motors attach to the MT and hold the cargo back until they are pulled off by active motors.

- Negative velocities come from the diffusion of the cargo in the harmonic potential of the MT-attached motor springs.

- Sterical motor-motor hindrance (exclusion) on the MT causes a reduction of the velocity with increasing number of motors.

It might be thought that the inactive motors could also be responsible for the reduction of the velocity with increasing number of motors. However, simulating cargo transport with inactive motors, but no exclusion, the reduction of the velocity with increasing number of motors could not be observed (see appendix figure C.1a).

Taking together, the simulation results of the point-like cargo model are in alignment with the experimental observations and provide explanations for the slow state, the negative velocities, and the reduction of the cargo velocity with increasing number of motors. However, the point-like cargo model does not take into account the spatial extension of the liposome and consequently not the sliding of diffusive motor tails on the cargo surface. Effects raising from a possible more spread motor configuration due to the sliding of motor tails or a possible motor accumulation in the attachment area on the cargo are not captured. To understand the influence of the diffusive motor tails (fluid cargo surface), the spatial extension of the cargo needed to be added to the model.

6.2.2 Liposome model

Possible effects coming from the sliding of the diffusive motor tails on the cargo surface cannot be captured in a point-like cargo model. That is why, in this section, a cargo with radius R_C is modeled and sliding of motor tails are taken into account. The following one-dimensional liposome model is based on the point-like cargo model with variations I - IV (see previous section).

Liposome model   The liposome has a membrane of lipid bilayers (fluid cargo surface). Motors are known to rapidly diffuse in the membrane with a diffusion constant in the range of $1 - 20\mu m^2/s$ [22, 169, 256, 325]. Because of the rapid diffusion of the motor tails on the cargo surface, the typical traveled distance ($\Delta x \propto \sqrt{Dt}$) between two attachment events is much bigger than the diameter of the attachment area on the cargo ($2R_C\theta_1$, see fig. 6.15). That is why it can be assumed that motors uniformly distribute over the surface between two attachment events and only the fraction of motors which are in the attachment area on the cargo N_{aa} are taken into account. The attachment area on the cargo is the area from where motors are able to attach the MT (see fig. 6.15 for an illustration of the attachment area on the cargo). Motor forces are proportional to motor extensions. Since motor tails are diffusive, it is expected that tails of MT-attached motors slide to the position on the cargo, where the motor extension is minimal (compression effects are not explicitly taken into account, but a constant distance between cargo and MT is modeled). This means MT-attached motors stand perpendicularly from the surface of the sphere (see illustration in fig. 6.5). In the one-dimensional models, degrees of freedom in y- and z-direction as well as any rotational degrees of freedom are neglected. That is why the motor extension is given by the difference between the motor
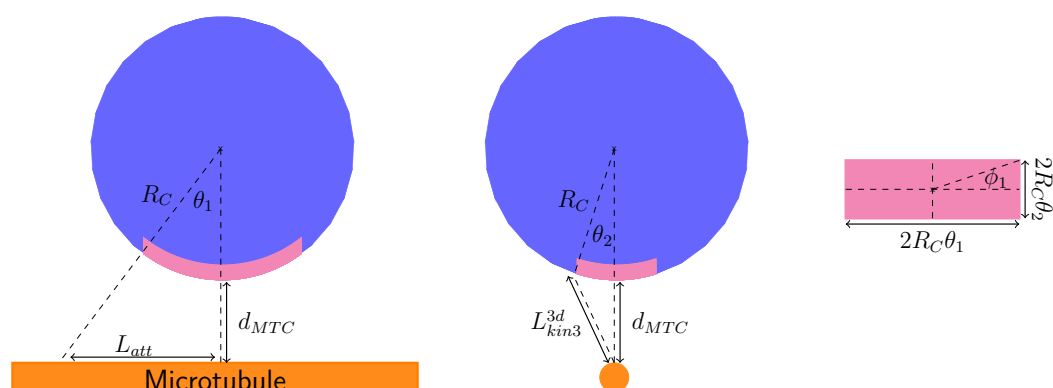
Figure 6.15: The attachment area on the cargo. The illustrations show the model attachment area on the cargo, from where the motors can attach to the MT. A side view is shown on the left, a front view in the middle, and just the rectangular attachment area on the right. The cargo radius is R_C and the distance between MT and cargo is d_{MTC}. The length of the attachment area on the cargo is defined by the half length of the attachment area on the MT L_{att} (see side view). The opening angle is labeled θ_1 and is used to calculate the length of the attachment area (see eq. (6.15) and illustration on the right). The width of the attachment area is defined by the three-dimensional correspondence L_{kin3}^{3d} of the one-dimensional motor rest length L_{kin3} (see front view and eq. (6.16)). The opening angle from the front is denoted by θ_2 and used to calculate the width of the attachment area. On the right side the attachment area, neglecting the curvature, is drawn to define the angle ϕ_1, which is needed to calculate the attachment area on the cargo including the curvature of the cargo (see eq. (6.15)).

head $x_h^i(t)$ and the motor tail position $x_t^i(t)$. The motor tail position can be calculated from the motor head position $x_h^i(t)$ and the center of the cargo position $X_C(t)$ as follows (see fig. 6.5 for an illustration of the geometry):

$$
\begin{aligned}
\sin(\theta_m^i) &= \frac{x_h^i(t) - X_C(t)}{\sqrt{(x_h^i(t) - X_C(t))^2 + (d_{MTC} + R_C)^2}} \\
&= \frac{x_h^i(t) - x_t(t)}{\sqrt{(x_h^i(t) - X_C(t))^2 + (d_{MTC} + R_C)^2} - R_C} \\
\iff \quad x_t^i(t) &= x_h^i(t) - \frac{x_h^i(t) - X_C(t)}{\sqrt{(x_h^i(t) - X_C(t))^2 + (d_{MTC} + R_C)^2}} \\
&\quad \times \left(\sqrt{(x_h^i(t) - X_C(t))^2 + (d_{MTC} + R_C)^2} - R_C \right) \quad (6.10)
\end{aligned}
$$

with d_{MTC} being the constant distance between MT and cargo and θ_m^i the angular between the vertical axis and the connection line between the center of the cargo and the motor head (see fig. 6.5). The motor extension is then:

$$
\begin{aligned}
\Delta x^i(t) = x_h^i(t) - x_t^i(t) &= \frac{x_h^i(t) - X_C(t)}{\sqrt{(x_h^i(t) - X_C(t))^2 + (d_{MTC} + R_C)^2}} \\
&\quad \times \left(\sqrt{(x_h^i(t) - X_C(t))^2 + (d_{MTC} + R_C)^2} - R_C \right). \quad (6.11)
\end{aligned}
$$

Plugging in this one-dimensional motor extension in the force calculation in eq. (6.4) gives the corresponding motor forces for the one-dimensional liposome model.

As for the point-like cargo cargo model, motors attach to a force-free position on the MT. Because of the spatial extension of the cargo and the diffusive motor tails, the attachment area $X_C(t) \pm L_{att}$ on the MT is more than twice the attachment area of the point-like cargo model, where $L_{att} = L_{kin3}$ holds. L_{att} of the liposome model is still given by L_{kin3} but takes into account that diffusive motor tails would slide to the position on the cargo, where motor extensions are minimal. To calculate L_{att}, the following equation needs to be solved:

$$
\Delta x^i(t) = L_{att} - x_t^i \overset{!}{=} L_{kin3} \tag{6.12}
$$

with $\Delta x^i(t)$ given by eq. (6.11). Table C.4 of the appendix shows L_{att} for different cargo radii. Even though motors are force-free over the whole range of $X_C(t) \pm L_{att}$, it is more likely that they attach close to the center of the cargo $X_C(t)$. Close to the center of the cargo $X_C(t)$, motor extensions are smaller, while at the edges of $X_C(t) \pm L_{att}$ motors are already almost stretched. That is why a truncated Gaussian distribution with mean $X_C(t)$ and standard deviation $\sigma = L_{att}/3$ is used to chose the motor head position x_h in the MT for attachment:

$$
p_{att}(x_h) = \begin{cases} \dfrac{A}{\sqrt{2\pi(L_{att}/3)^2}} e^{-\frac{(x_h - X_C(t))^2}{2(L_{att}/3)^2}}, & x_h \in X_C(t) \pm L_{att} \\ 0, & \text{else.} \end{cases} \tag{6.13}
$$

Thus, when a detached motor attaches to the MT, a force-free position x_h within $X_C(t) \pm L_{att}$ on the MT is chosen according to eq. (6.13). Besides choosing a position along the MT, also the protofilament has to be chosen. Like in the point-like cargo model, seven protofilaments are modeled and the attachment probabilities to the protofilaments are Gaussian distributed (see subsection 6.2.1 for details). Taking exclusion effects on the MT into account, before attaching, it has to be checked whether the range $x_h \pm R_{kin3}$ is empty on the chosen protofilament. If this is the case, the motor can attach. It is known from experiment that 20% of the kinesin-3 motors are inactive. Since motor tails rapidly diffuse on the cargo surface, the configuration of detached motors in the attachment area on the cargo changes over time. As said before, because diffusion is high compared to attachment, it is assumed that detached motors are uniformly distributed over the cargo surface. This means on average 20% of the detached motors in the attachment area on the cargo are inactive and when a motor attaches, it is chosen with probability $p_{inactive} = 0.2$ that the attaching motor is inactive.

In the liposome model, attachment and force-dependent detachment and stepping rates are used as in the point-like cargo model (see subsection 6.2.1). Furthermore, the same update mechanism for the cargo position, namely the Metropolis algorithm, is used to move the cargo in the harmonic potential of MT-attached motors. To calculate the harmonic potential, extensions of MT-attached motors as given by eq. (6.11) are used. It is thereby taken into account the sliding of the diffusive motor tails to the positions on the cargo, where motor extensions are minimal.

In summary, the diffusion of the motor tails on the cargo surface is taken into account in two ways. First, the configuration of motors in the attachment area changes over time such that each time a motor attaches, it is chosen randomly whether this motor is inactive or active. And second, motor extensions are reduced due to the sliding of the diffusive motor tails to the position with the shortest motor extension on the cargo surface. Consequently, the attachment area is bigger for the liposome model than for the point-like cargo model. Simulating the liposome model will show the influence on cargo transport.

Simulation results: To test the liposome model, first the liposome model is simulated with a point-like cargo $R_C = 0\,\text{nm}$ and a uniformly distributed attachment probability p_{att} within $X_C(t) \pm L_{att}$. Simulating the liposome model with a point-like cargo should lead to the same results as the point-like cargo model. Fig. C.1b of the appendix C shows that the liposome model with $R_C = 0\,\text{nm}$ reproduces the results of the point-like cargo model.

Next, the liposome is simulated as described above. This means, the radius of the cargo is $R_C = 60\,\text{nm}$ and the attachment probability along the MT p_{att} is Gaussian distributed (see eq. (6.13)). Simulating the liposome model with the same parameters as the point-like cargo model (see table C.1 of the appendix C) produces velocity histograms with less pronounced low velocity peaks (see fig. C.1c of the appendix C). The point-like cargo model simulations relate the low velocity peak to a stopping of the cargo (slow state) due to inactive motors. Having less pronounced low velocity peaks means that active motors pull off inactive motors more easily, which results in less pronounced slow states. Thus, active motors team up better in the liposome model than in the point-like cargo model. Thus, the force response differs between the point-like cargo model and the liposome model.

Having less pronounced low velocity peaks in the simulation means that inactive motors detach too easily. Active and inactive motors detach with the same force-dependent detachment rates. The detachment is characterized by the detachment force and the force-free detach-
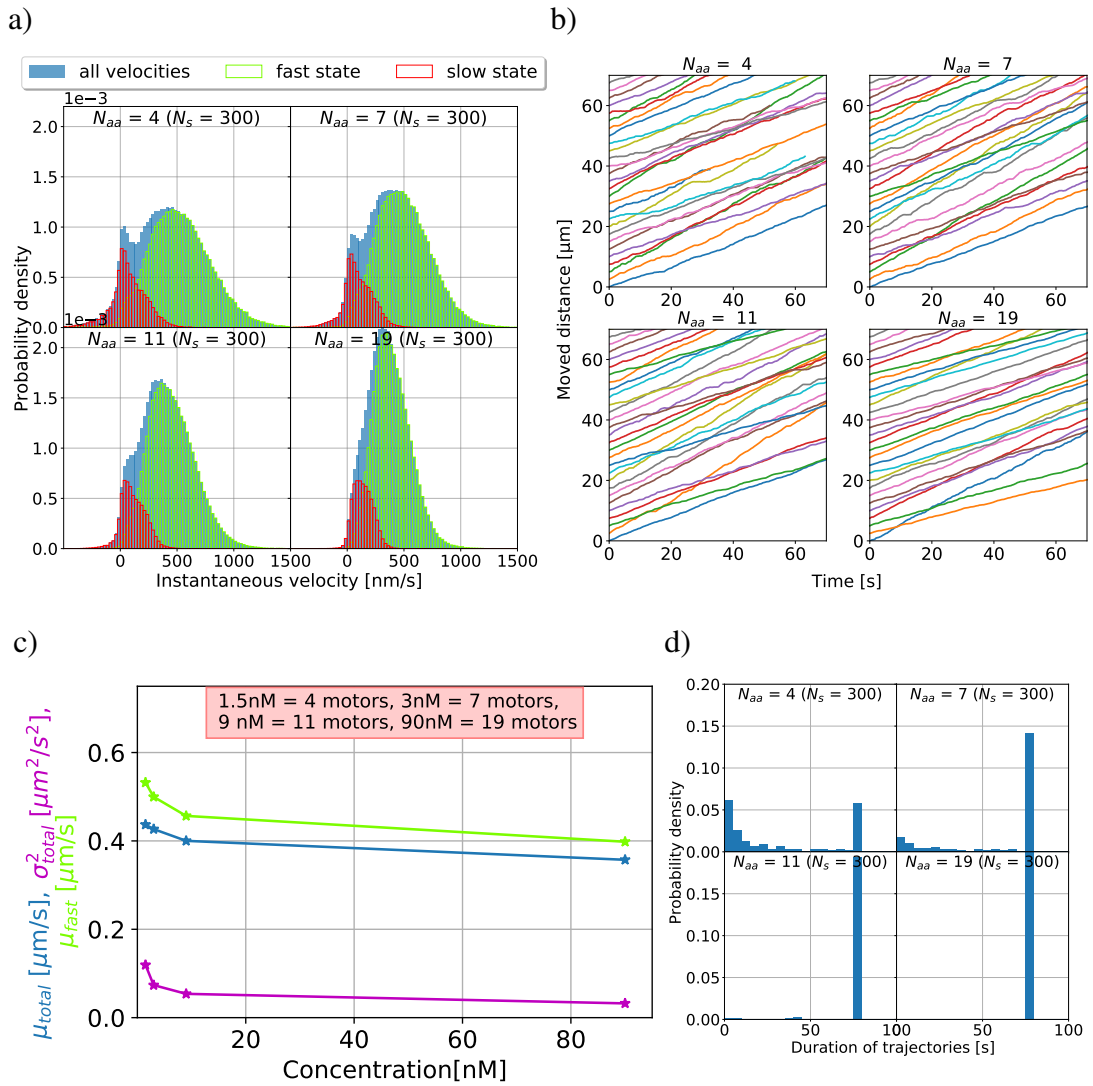
Figure 6.16: One-dimensional liposome model. Simulation results produced with the liposome model using an optimized number of motors N_{aa} and an increased detachment force ($F_{d,kin3} = 3\,pN$) compared to the point-like cargo model (fig. 6.12). See table C.1 for all parameter values. a) Cargo velocity histograms (blue) for varying numbers of motors in the attachment area N_{aa}. Using the segmentation algorithm (see main text and caption of fig. 6.3) trajectories can be divided into slow and fast states. Increasing the number of motors N_{aa}, the fast state velocity peak (green) moves to smaller velocities and finally merges with the slow state velocity peak (red). b) Example trajectories of simulated cargos (trajectory duration longer than 30 seconds) are depicted for varying numbers of motors in the attachment area N_{aa}. A stop-and-go-like motion with clear slow states can be seen for all numbers of motors. c) Mean (blue) and variance (magenta) of all cargo velocities as well as mean velocities of only the fast state (green) are depicted. All three observables decrease with increasing number of motors. d) Histograms of trajectory durations. Trajectories are longer in time for high number of motors.
The program was terminated either if no motor was attached to the MT anymore or after 80 seconds. Number of samples (cargos) N_s are given in brackets (a +d).

ment rate (see eq. (6.5)). While the latter is given by the experiment, the detachment force of KIF16B is neither known from the experiment nor given by the literature (to the author's knowledge). Detachment force values given for other members of the kinesin-3 subfamily range approximately from 1 pN to 2.7 pN [328]. When increasing the detachment force in
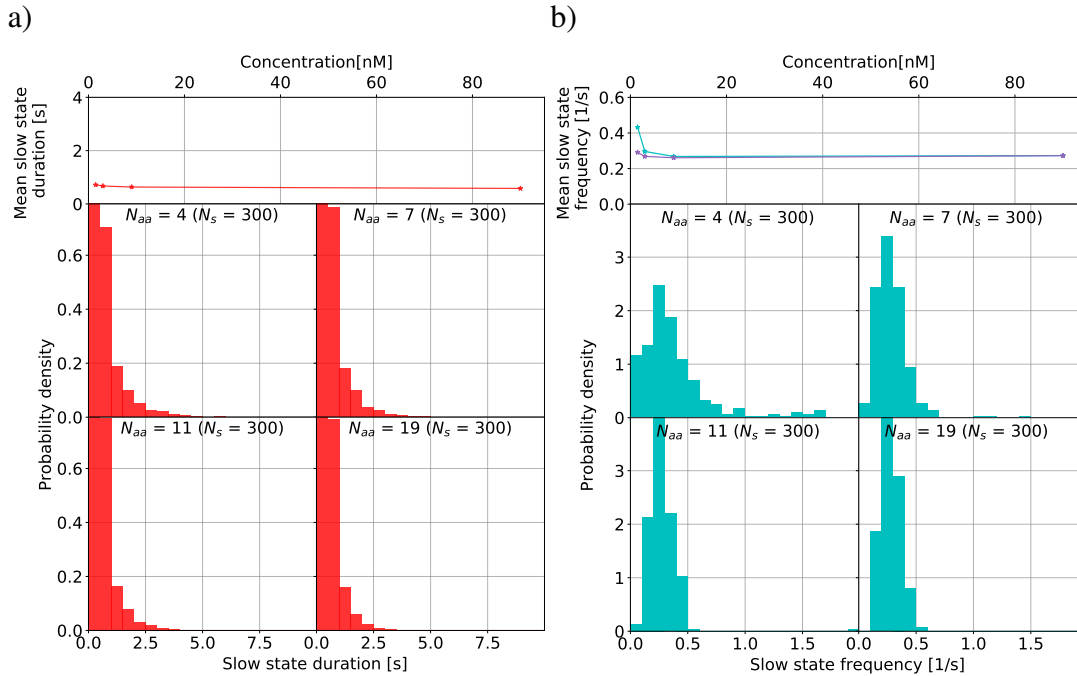
Figure 6.17: One-dimensional liposome model: slow state. Duration and frequency of the slow state obtained from simulations using the liposome model. a) Mean duration of the slow state as a function of the motor concentration as well as duration histograms for varying number of motors. Although in the simulation the number of motors in the attachment area on the cargo N_{aa} is given, the mean is drawn as a function of the motor concentration for a better comparison with the experimental data (fig. 6.4a). See fig. 6.16c for which concentration corresponds to which number of motors. Mean and histograms do not show a dependence of the slow state duration on the number of motors. b) Mean and histograms of slow state frequencies for varying numbers of motors. The individual frequency of slow states (blue) is the number of slow states divided by the trajectory duration. The total frequency of slow states (magenta, independent of the duration of the trajectories) is total number of slow states of all simulations divided by the sum of all trajectory durations. Slow state frequencies are slightly enhanced for low number of motors, otherwise independent of the number of motors.
Number of samples N_s is given in brackets.

the liposome model (from $F_d = 1$ pN to $F_d = 3$ pN) and optimizing the number of motors in the attachment area on the cargo N_{aa}, a reasonable set of parameters (see table C.1 of the appendix C for the used parameters including literature references) can be found for which the liposome model (fig. 6.16 and 6.17) is in alignment with the experimental observations (fig. 6.2 and 6.4). In detail, similar to the experiment, the velocity histograms (fig. 6.16a) show negative velocities, a low velocity peak, and a high velocity peak, which merges with the low velocity peak at higher number of motors N_{aa}. Cargo trajectories (fig. 6.16b) show a stop- and go-like motion. Moreover, the mean and variance of the veloci-

ties as well as the mean of the velocities of the running state decrease with increasing number of motors N_{aa} (fig. 6.16c). As in the point-like cargo model, trajectories are longer in the simulation (fig. 6.16d) than in the experiment (fig. 6.2d). Trajectories are supposed to be longer in the simulation than in the experiment because more factors terminate experimental trajectories (MT end for instance) than simulation trajectories (see subsection 6.2.1). Shorter trajectories in the simulation would mean that motor detachment is overestimated.

Duration and frequencies of the slow states (fig. 6.17) from the liposome model are similar to duration and frequencies from the point-like cargo model (fig. 6.14). Mean slow state durations are, however, still smaller than in the experiment (fig. 6.4a). As for the point-like cargo model, the number of MT-attached motors (fig. 6.18) increases with increasing number of available motors in the attachment area on the cargo. Especially at high number of available motors, the number of MT-attached motors is higher for the liposome model than for the point-like cargo model (fig. 6.13).
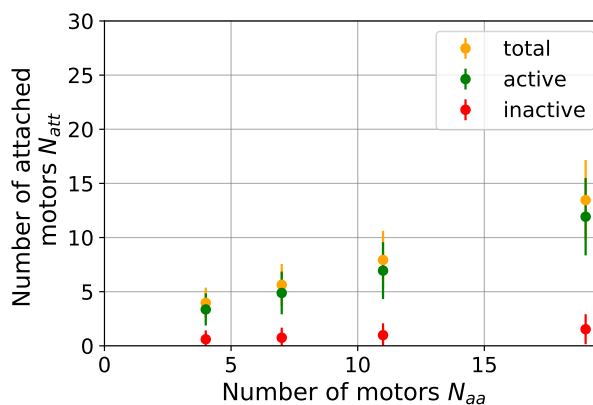
Figure 6.18: One-dimensional liposome model: number of MT-attached motors. Mean number of MT-attached motors ($\mu \pm \sigma$) obtained from simulation with the liposome model. The total number of MT-attached motors (yellow), the number of active (green), and the number of inactive MT-attached motors (red) are shown as a function of the number of motors in the attachment area on the cargo N_{aa}. All three increase with increasing number of motors in the attachment area N_{aa}. The number of inactive motors increases slower than the number of active motors.

In summary, adjusting the detachment force and the number of motors in the attachment area on the cargo in a reasonable, experimental range, aligns the simulation results produced with the liposome model with the experimental results. Compared to the point-like cargo model, a higher detachment force is needed to produce a low velocity peak in the histogram, which is similar to the experimentally given low velocities peaks. This means, in the liposome model, active motors team up better in order to pull off inactive motors. It might be that because of the sliding of the motor tails, active motors can better align and therefore increase their cooperation. However, the number of MT-attached motors revealed that slightly more motors are attached for the liposome model compared to the point-like cargo model. This indicates that in the liposome model, due to the spatial expansion of the cargo, there is more space on the MT for motors. More space also means less motor-motor hindrance, which could also be the reason for the better cooperation of active motors in the liposome model.

Furthermore, it was above suggested (see section 6.2.1) that the sliding of the motor tails might lead to "blocked" configurations, which causes an occasionally longer stopping of the cargo, which increases the duration of the slow states. The liposome model simulations, however, show that slow state durations are similar to those of the point-like cargo model.

This means the sliding of the motor tails does not lead to such a "blocked" configuration with a longer stopping of the cargo.

To gain a deeper understanding of the influences of the separate liposome model components, the following model variants are studied:

1. Liposome model with varied **motor forces**

2. Liposome model without **inactive motors**

3. Liposome model without motor-motor **exclusion on the MT**

4. Liposome model with **uniform attachment to protofilaments**

5. Liposome model with **uniform attachment along the MT** in the attachment area $X_C(t) \pm L_{att}$

6. Liposome model with varying **cargo sizes**

7. Liposome model with modeling **all motors on the cargo surface** (not only in attachment area on the cargo)

Note that the latter variants do not include the changes of the former variants.

1. Motor forces: Above it has been observed that the force response is different for the liposome and the point-like cargo model. Here, the individual influences of the kinesin-3 detachment force and stall force are studied explicitly.

To investigate the influence of the detachment force $F_{d,kin3}$, the kinesin-3 motor detachment force is increased from $F_{d,kin3} = 3\,\text{pN}$ to $F_{d,kin3} = 3.5\,\text{pN}$. Fig. 6.19a and fig. 6.19c show that increasing the detachment force leads to a higher low velocity peak and reduces the overall mean velocity as well as the mean velocity of the running state compared to the standard liposome model (fig. 6.16). This means first that inactive motors detach less easily, and active motors need to exert higher forces to pull off inactive motors. Second, the slightly reduced mean velocity of the running state means that active motors negatively affect each other more than in the standard liposome model. Active motors affect each other in two ways: first, they can sterically hinder each other (motor-motor exclusion effects) or second, they can impair each other by exerting opposite directed forces on the cargo. The latter is the case because usually, some motors advance slower than others (because of either simple stochastic, a lower individual motor stepping rate, or because of being hindered by an inactive motor). Consequently, some active motors are exerting a force on the cargo directed towards the MT plus-end and some towards the MT minus-end (motor-motor impairment). Both effects are enhanced when having a higher detachment force. Having a higher detachment force leads to reduced detachment such that more motors are attached to the MT and hinder each other sterically. Moreover, having a higher detachment force, motors, which pull the cargo towards the minus-end (opposite direction of kinesin-3), can be pulled off less easily from motors that pull the cargo towards the MT plus-end. Thus, the detachment force determines the strength of inactive motors and how much active motors are hindered or impaired by other motors.

Increasing the stall force $F_{s,kin3}$ from $5\,\text{pN}$ to $7\,\text{pN}$ leads to a reduction of the low velocity peak in the histograms (fig. 6.19b) and to higher means of all velocities as well as of the fast state (fig. 6.19d). Because inactive motors do not step at all, the stall force only affects active
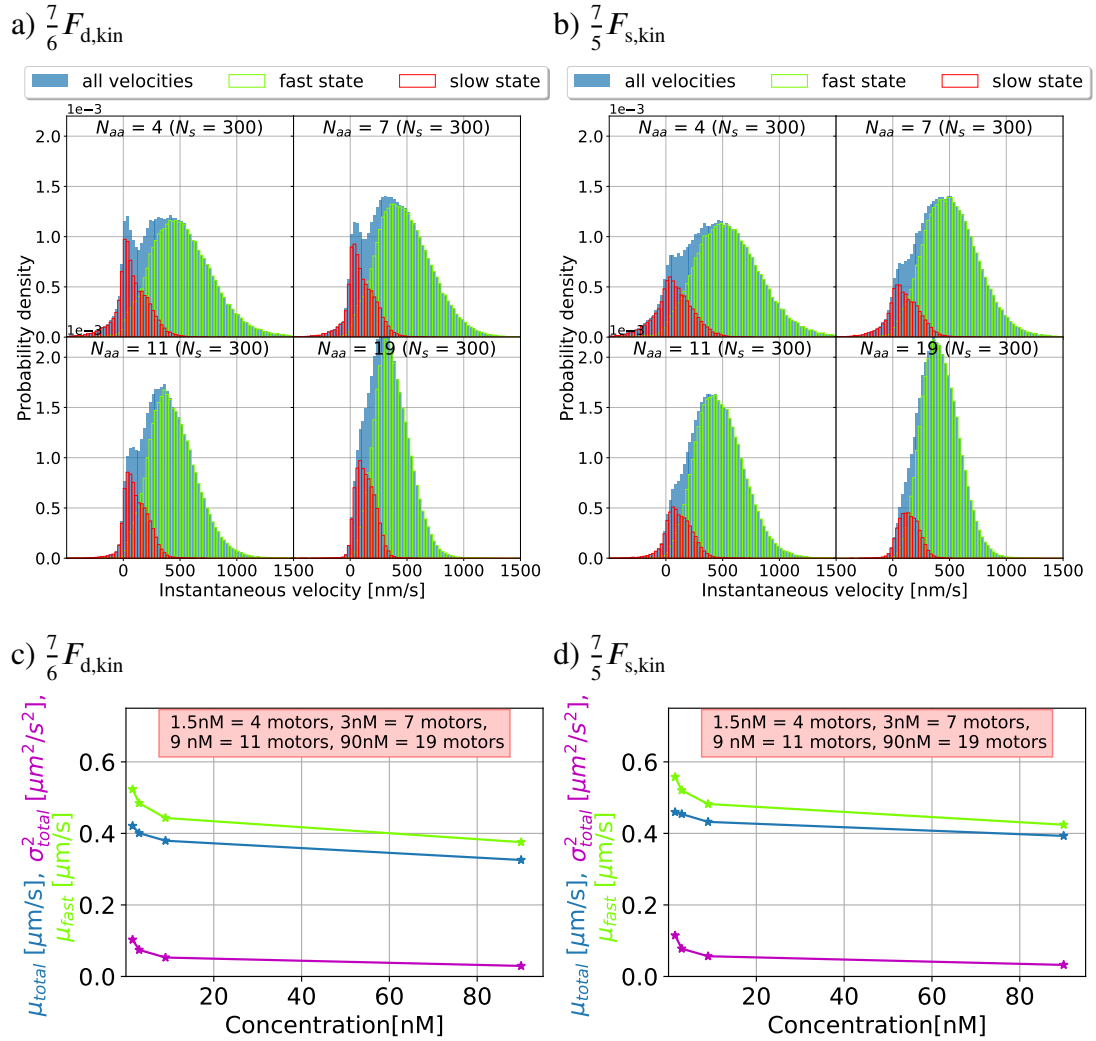
Figure 6.19: Liposome model variant 1: velocities. Simulation results produced with the liposome model using a higher detachment force ($\frac{7}{6}F_{d,kin}$, a+c) and a higher stall force ($\frac{7}{5}F_{s,kin}$, b+d). Velocity histograms (a+b) from all velocities (blue), the fast state (green) and the slow state (red) as well as mean (blue) and variance (magenta) of all cargo velocities as well as mean velocities of only the fast state (green). Left (a+c): Low velocity peaks (red) are more pronounced and fast velocity peaks (green) are shifted to lower velocities compared to the standard liposome model (fig. 6.16). Also, mean velocities (blue and green) and variances are reduced compared to the standard liposome model (fig. 6.16). Right (d+b): Low velocity peak is reduced and mean velocities (blue and green) are increased compared to the standard liposome model (fig. 6.16).

See table C.1 for the complete parameter list and brackets (a + b) for the number of samples N_s.

motors. In detail, a higher stall force means first that active motors step faster at higher forces. That is why the mean velocity of the fast state is increased. Second, a higher stall force means that active motors step further until stopping due to reaching the stall regime. This means that active motors can exert higher forces and are therefore more successful in pulling off inactive motors. In conclusion, the stall force determines the strength of the active motors.

Taken together, motor detachment and stall forces determine the force production of inactive and active motors. Higher detachment forces shift the force balance between inactive and active motors towards inactive motors, while higher stall forces shift the force balance towards active motors.

2. Inactive motors: Simulating the point-like cargo model revealed that the low velocity peak is caused by inactive motors (see section 6.2.1). While the point-like cargo model does not take the cargo extension and diffusive motor tails into account, the liposome model does. Consequently, in the liposome model, motors could at random slide to the backside of the cargo such that they pull the cargo backwards, i.e. towards the MT minus-end. Such MT-attached motor configurations could cause a slow velocity state similar to the one from inactive motors. To test this hypothesis, the liposome model is simulated only with active motors. Velocity histograms of simulations in the absence of inactive motors (fig. 6.20a) show that the low-velocity peak vanishes and mean velocities increase (fig. 6.21a). This means that motors that are at the backside of the cargo do not induce a slow velocity state as inactive motors do. Consequently, also the liposome model predicts that inactive motors are needed to induce a slow velocity state.

3. Exclusion on the MT: The point-like cargo model simulations found that the reduction of the velocity with increasing number of motors is caused by motor-motor exclusion effects on the MT (see section 6.2.1). However, when taking the cargo extension and diffusive motor tails into account (liposome model), it could also be that motors which slipped to the backside of the cargo (side facing the MT minus-end) are responsible for the reduction of the velocity with increasing number of motors (the more motors, the more motors at the backside and the harder it is for advancing motors to transport the cargo). Therefore, the liposome model is simulated neglecting exclusion effects, i.e. motors are allowed to overlap on the MT (same protofilament). When neglecting exclusion effects, mean velocities (fig. 6.21a) clearly increase with increasing number of motors. Thus, the sliding to the backside of the cargo does not reduce the velocity with increasing number of motors.
Velocity histograms (fig. 6.20b) in the absence of exclusion effects show that the low velocity peak is smaller compared to the standard liposome model (fig. 6.16a). For higher N_{aa} the low velocity peak and the slow state (red histogram at fig. 6.20b) vanish (almost) completely. This means, when not being hindered by other active or inactive, MT-attached motors, active motors are stronger and can pull off the inactive motors more efficiently. Consequently, in the liposome model with exclusion, inactive motors do not only hold the cargo back but also hinder active motors to advance on the MT track.

4. Uniform attachment to protofilaments: It has been shown that not having exclusion effects on the MT moves the force balances toward active motors. Here, the question is how the distribution over the protofilaments influences the cargo transport and the force balance between active and inactive motors. In the liposome model, the attachment to the protofilaments is Gaussian distributed such that MT-attached motors are Gaussian distributed over the protofilaments (no switching of the protofilament of MT-attached kinesin-3 motors[5]). To test the influence of the motor distribution over the protofilaments, a uniformly distributed attachment to the protofilaments is modeled instead of the Gaussian distributed attachment. If motors attach uniformly to all seven protofilaments (= upper half of the MT), the low velocity

---

[5]It is assumed that kinesin-3 motors stay on one protofilament as known for kinesin-1 [126].

a) No inactive motors
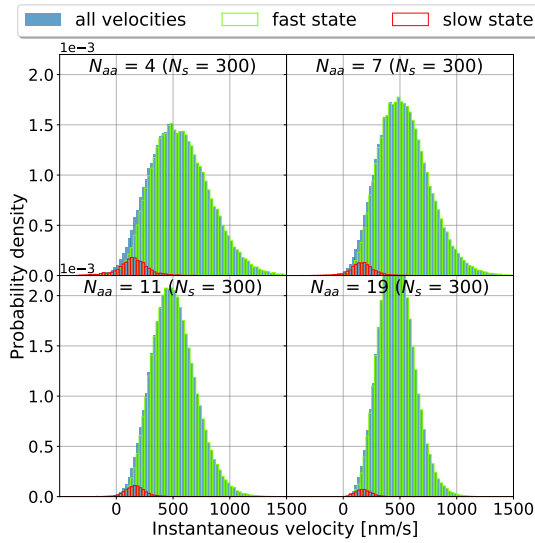
b) No exclusion
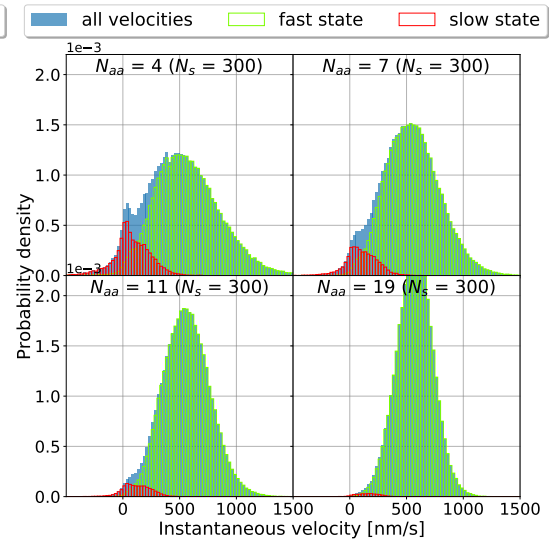
c) Uniform p_{PF}
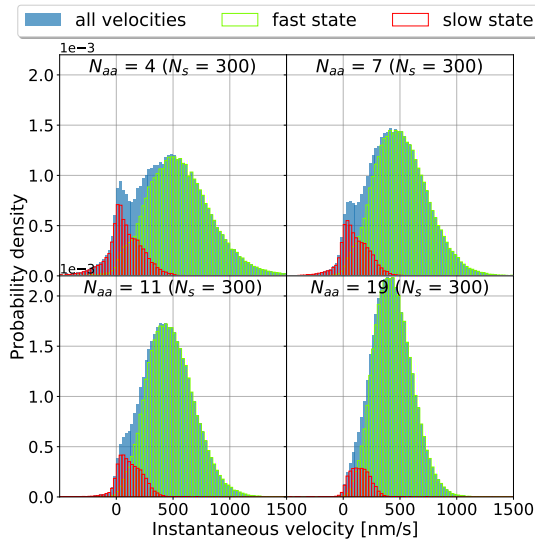
d) Uniform L_{att}
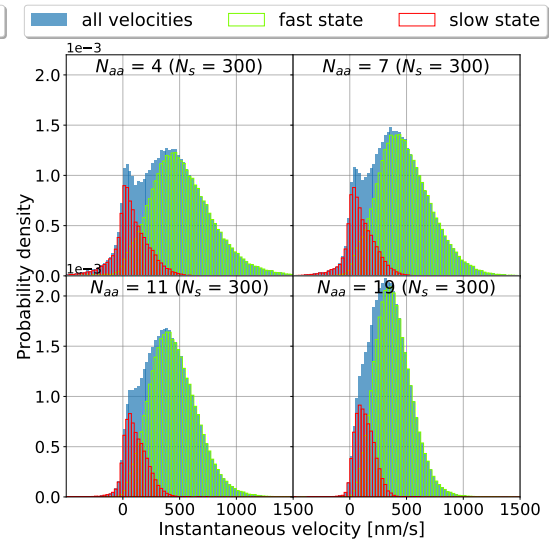
Figure 6.20: Liposome model variants 2-5: velocity histograms. Histograms of all velocities (blue) as well as from the fast state (green) and the slow state (red) from simulations with varying numbers of motors N_{aa}. a) 2. Model variant: no inactive motors. The low velocity peaks vanish completely and the slow state (red histogram) is strongly reduced. b) 3. Model variant: no exclusion effects on the MT. This means motors can overlap on the MT. The low velocity peaks are strongly reduced. c) 4. Model variant: motors attach uniformly to all protofilaments. The low velocity peaks are reduced compared to the standard liposome model (fig. 6.16). d) 5. Model variant: motors attach uniformly within the attachment area $X_C(t) \pm L_{att}$ along the MT. The low velocity peaks seem to be slightly increased compared to the standard liposome model (fig. 6.16).

peak of the velocity histogram is slightly reduced (fig. 6.20c) and mean velocities (fig. 6.21a) are higher than for the standard liposome model (fig. 6.16). This means the force balance

is shifted towards active motors as it has been seen in the absence of exclusion effects (fig. 6.20b and 6.21a). Thus, a uniform attachment to the protofilaments reduces exclusion effects on the MT. However, while in the absence of exclusion effects the mean velocity increases with increasing number of motors, a uniform attachment to the protofilaments still shows the reduction in mean velocities with increasing number of motors. This means, even though a uniform attachment to the protofilaments reduces exclusion effects, motors still hinder each other to advance.

Taken together, the distribution of the MT-attached motors over the protofilaments determines the degree of mutual hindrance of MT-attached motors and therefore how efficient active motors are in pulling off inactive motors.

5. Uniform attachment along the MT: The same effect is expected when the attachment probability within the attachment area $X_C(t) \pm L_{att}$ along the MT is uniformly distributed instead of Gaussian distributed. When they attach uniformly within $X_C(t) \pm L_{att}$, exclusion effects are expected to be reduced and active motors should be more efficient in pulling off inactive motors. However, when simulating a uniform attachment along the attachment area $X_C(t) \pm L_{att}$ the velocity histograms (fig. 6.20d) show a slightly increased low-velocity peak and mean velocities (fig. 6.21a) are reduced compared to the standard liposome model. This means the force balance is shifted towards inactive motors, the opposite of what was observed when having reduced or no exclusion effect on the MT (compare model variants 3-4). This
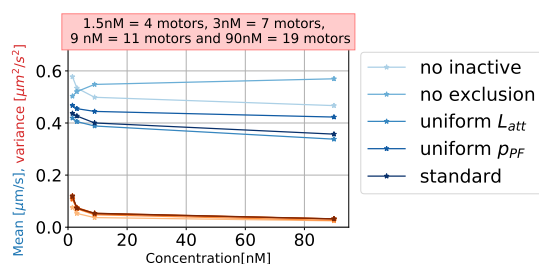
a) Modifications   b) Influence of radius
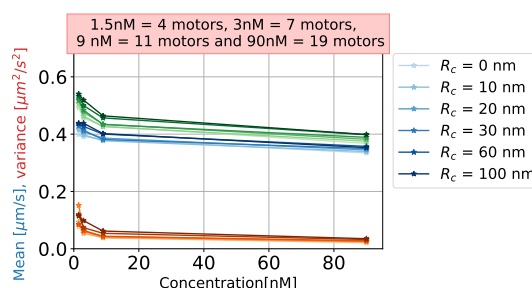
Figure 6.21: Liposome model variants 2-6: mean and variance of the velocity. a) Mean of the complete velocity distribution (blue) and the corresponding variance (red) for different model modifications (see fig. 6.20 and main text for explanations regarding model modifications). While the variance does not change much for the different model modifications, the mean does. Not having inactive motors increases the mean compared to the standard liposome model (indicated as "original"). When not modeling exclusion effects, the mean increases with increasing number of motors. When distributing the MT-attached motors uniformly among protofilaments instead of Gaussian, the mean decreases with increasing number of motors but is higher than for the standard liposome model. Attaching the motors uniformly along the MT in the attachment area $X_C \pm L_{att}$ instead of Gaussian reduces the mean compared to the standard liposome model. This is surprising since attaching uniformly along the MT should reduce the exclusion effects as it does when attaching uniformly to the protofilaments. See main text for an explanation. b) Mean (blue) and variance (red) of all velocities and mean of only the velocities stemming from running states (green) for different cargo radii. In the standard liposome model a radius of $R_C = 60$ nm is used. The variance as well as the mean of the complete histogram and the mean of the velocities stemming from running states increase with the cargo radius.

means there has to be another effect.

To understand why the force balance is shifted towards inactive motors when attaching uniformly along the attachment area on the MT, histograms of MT-attached motor extensions are calculated to see how motors are distributed along the MT (see fig. C.2b of the appendix C for uniform attachment and C.2a of the appendix C for Gaussian distributed attachment along the MT). Active motors would be most efficient in pulling off inactive motors when all active motors would be sorted toward the MT plus-end (positive motor extension) and all inactive motors towards the MT minus-end (negative motor extension). In this ideal case (see fig. 6.22a), active motors could continue stepping towards the MT plus-end without the need of passing an inactive motor, which acts as roadblocks for active motors. However, when an
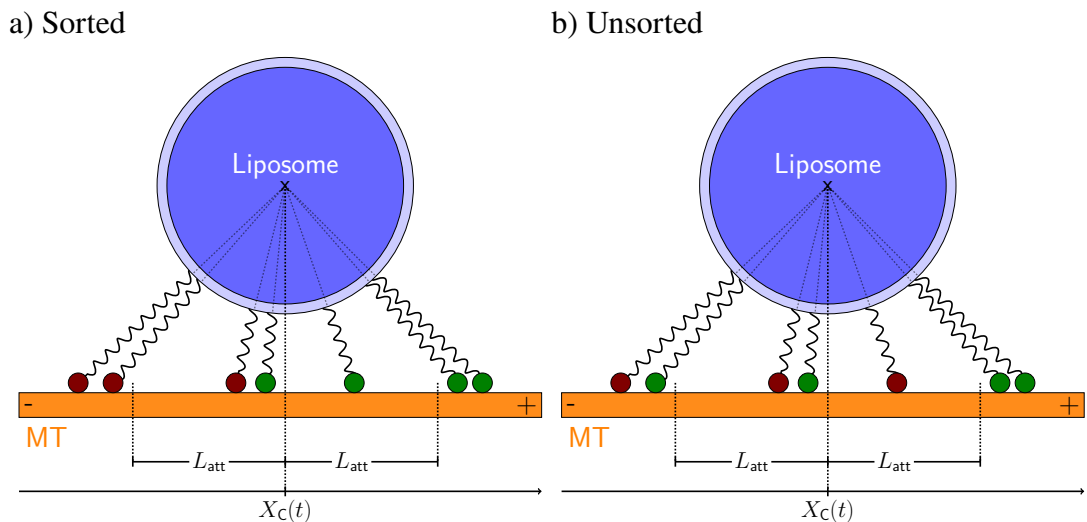
Figure 6.22: Sorted and unsorted motor configurations along MT. a) A motor configuration along the MT, where all inactive motors (red) are sorted towards the MT minus-end (left) and all active motors (green) towards the MT plus-end (right). In this ideal case, all active motors can continue stepping toward the plus-end without being blocked by an inactive motor. Consequently, active motors are most efficient in pulling off inactive motors. b) A motor configuration along the MT, where motors are not sorted. This means some inactive motors (red, two right motors) are closer to the MT plus-end than some active motors (green, two left motors). In this case, when the active motors continue stepping towards the MT plus-end they will be blocked by inactive motors at some point assuming that shown motors are all on the same protofilament (no switching of the protofilament allowed). Blocked active motors will not be able to contribute to pulling of inactive motors anymore, but need to be pulled off by other active motors as well in order to further transport the cargo. The further towards the MT minus-end (left) an active motor attaches, the higher is the chance to be blocked by an inactive motor at some point and the longer is the way until getting out of the force-free regime (attachment area on the MT $X_C(t) \pm L_{att}$) on the side facing the MT plus-end (right). Only when getting out of the force-free regime on the side facing the MT plus-end (two right motors), they contribute to pull off inactive or blocked motors and transport the cargo towards the MT plus-end. Note that active motors can even pull the cargo towards the MT minus-end (most left green motor). Altogether, this is why active motors are less efficient in pulling of inactive motors when motors are unsorted.

active and an inactive motor are on the same protofilament and the inactive motor is closer to

the plus-end than the active motor (unsorted motor configuration, see fig. 6.22b), the active motor will at some point be stopped by the inactive motor. Consequently, the active motor cannot continue stepping anymore (no switching of the protofilament allowed, see above) and need to be pulled off by other advancing active motors. The comparison of motor extensions from uniform and Gaussian attachment (fig. C.2b and C.2a of the appendix C) reveals that for the uniform attachment, slightly more inactive motors are sorted towards the MT plus-end. This means there are slightly more inactive motors, which could act as roadblocks for active motors, which are, by chance, sorted towards the MT minus-end. This is one reason why active motors are less efficient when motors attach uniformly within $X_C \pm L_{att}$.

A second reason is that when motors attach uniformly within $X_C \pm L_{att}$, there are also more active motors, which attach closer to the MT minus-end. Consequently, they have a "longer way" until getting out of the force-free regime towards the MT plus-end (positive motor extension greater than the motor rest length L_{kin3}). This means first that the chance is higher to be stopped by an inactive motor and second, it takes longer until the motor exerts a force on inactive motors, i.e., contributes to pulling off the inactive motors and transports the cargo towards the MT plus-end. This is the second reason for active motors being less efficient in pulling off inactive motors when attaching uniformly within $X_C \pm L_{att}$.

Taking together, the sorting of active motors to the front (facing the MT plus-end) and inactive motors to the back (facing the MT minus-end) plays a role (see fig. 6.22). When motors attach uniformly within $X_C \pm L_{att}$ instead of Gaussian distributed, motors are less sorted and active motors are, therefore, less efficient in pulling off inactive motors. Consequently, the force balance shifts towards inactive motors.

6. Cargo size: Previous studies of cargo transport show that transport properties can depend on the cargo size [88, 249, 324]. Here, it has been shown (see above) that including spatial extension of the cargo (and diffusive motor tails = liposome model) shifts the force balance towards active motors compared to the point-like cargo model (see section 6.2.1). Having the same number of motors on a bigger cargo, on one hand, it is expected that exclusion effects are reduced. Thus, motors hinder each other less, the force balance is shifted towards the active motors and higher velocities can be reached. On the other hand, when the cargo is bigger, the attachment area along the MT is bigger and the Gaussian for the attachment is stretched over a bigger area. Thus, the Gaussian would resemble a bit more a uniform attachment and motors would be less sorted (see fig. 6.22). Less sorted motors were shown to shift the force balance towards inactive motors (see model variant 5). It is therefore not clear how the radius influences the force balance.

To study the influence of the cargo radius, the liposome model is simulated for different cargo radii $R_C \in \{0, 10, 20, 30, 60, 100\}$ nm. Velocity histograms (fig. 6.23) show more separated low and high velocity peaks for bigger cargos. The same is reflected by the slightly higher variance of all velocities and slightly higher mean velocity of the fast state for bigger cargos (see fig. 6.21b). This leads also to a slightly higher total mean velocity of the bigger cargos. This means, even though the motors might be less sorted for the bigger cargoes, the reduced exclusion effects is the dominant factor. Thus, bigger cargos are slightly faster, because exclusion effects are reduced.

7. All motors on the cargo surface: The question arose whether the number of MT-attached motors increases over time because more motors would diffuse into the attachment area on the cargo over time and be able to attach the MT. To answer this question, the total

a) $R_c = 0\,\text{nm}$

b) $R_c = 10\,\text{nm}$

c) $R_c = 30\,\text{nm}$

d) $R_c = 100\,\text{nm}$
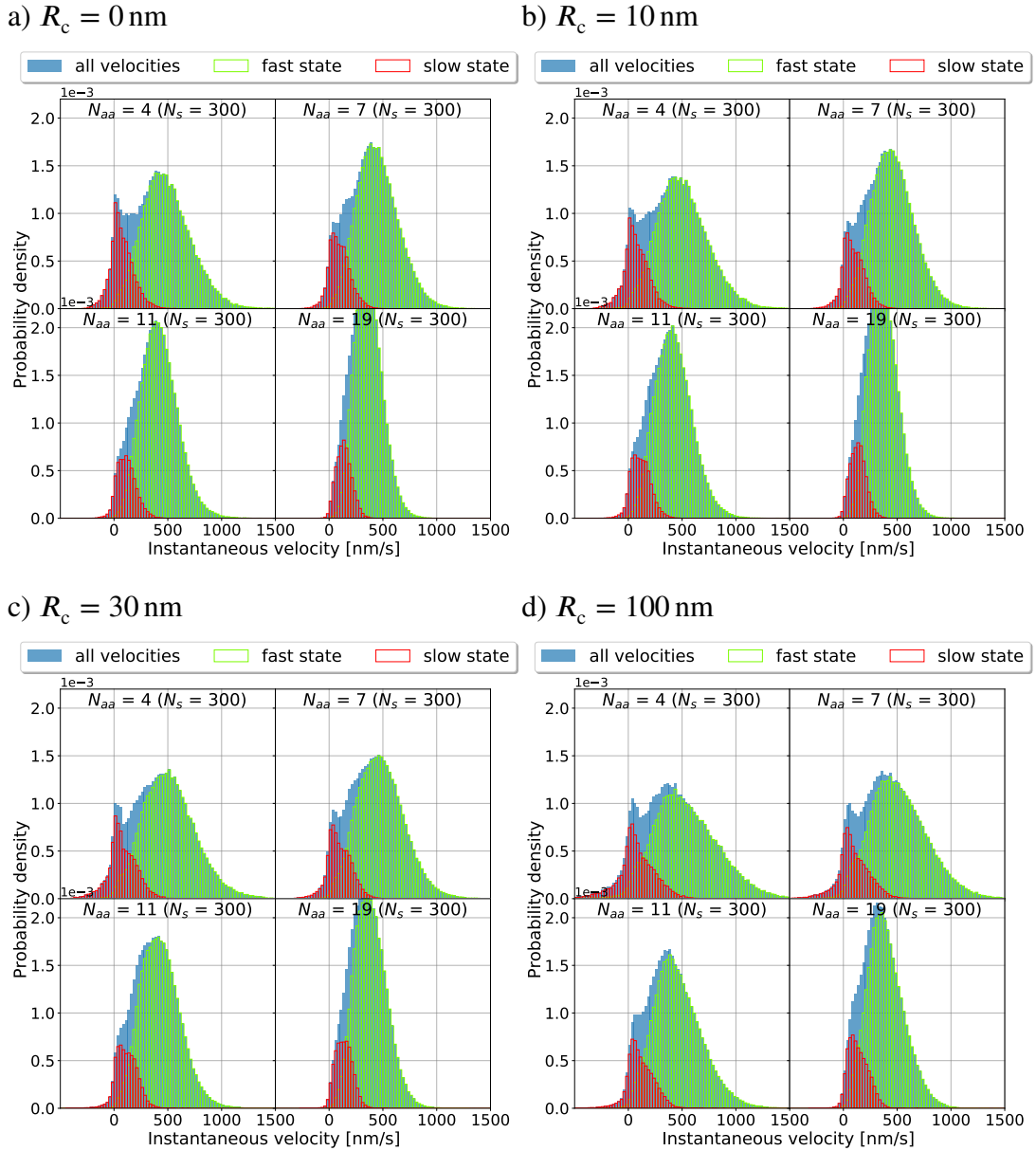
Figure 6.23: Liposome model variant 6: cargo velocity histograms for different cargo radii. Histograms of all velocities (blue) as well as from the fast state (green) and the slow state (red) from simulations with varying numbers of motors N_{aa} and different cargo radii (a $\rightarrow$ d, $R_C \in \{0, 10, 30, 100\}$ nm). The low and high velocity peaks are more separated for bigger cargos. Number of samples N_s are given in brackets.

number of motors N_{tot} on the cargo is taken into account. Because the diffusion of motors on the cargo surface is fast ($D \sim \mu\text{m}^2/\text{s}$ [22, 169, 256]), it can be assumed that motors are uniformly distributed over the cargo surface. This means that unbound motors attach the MT with probability:

$$r_{\text{att}} = \frac{A_{\text{att}}}{A_C} \tag{6.14}$$

with the attachment area on the cargo surface A_{att} and the surface area of the complete cargo $A_C = 4\pi R_C^2$. Taking the curvature of the cargo into account, the attachment area A_{att} is calculated as follows:

$$A_{att} = R_C^2 \left[\int_0^{\phi_1} d\phi \int_0^{\theta_1} \sin(\theta)\, d\theta + \int_{\phi_1}^{\pi-\phi_1} d\phi \int_0^{\theta_2} \sin(\theta)\, d\theta + \int_{\pi-\phi_1}^{\pi+\phi_1} d\phi \int_0^{\theta_1} \sin(\theta)\, d\theta \right.$$

$$\left. + \int_{\pi+\phi_1}^{2\pi-\phi_1} d\phi \int_0^{\theta_2} \sin(\theta)\, d\theta + \int_{2\pi-\phi_1}^{2\pi} d\phi \int_0^{\theta_1} \sin(\theta)\, d\theta \right]$$

$$= 4R_C^2 \left[\phi_1 \left(\cos(\theta_2) - \cos(\theta_2) \right) + \frac{\pi}{2} \left(1 - \cos(\theta_2) \right) \right]. \tag{6.15}$$

The angles θ_1, θ_2 and ϕ_1 are defined by the geometry (see fig. 6.15). The angle θ_1 is defined by the length of the attachment area on the MT, which is, in turn, defined by the one-dimensional motor length L_{kin3}. The angle θ_2 is determined by the three-dimensional motor length L_{kin3}^{3d}, which is the three-dimensional equivalent to the one-dimensional motor length L_{kin3} and can be calculated as:

$$L_{kin3}^{3d} = \sqrt{L_{att}^2 + (R_C + d_{MTC})^2)} - R_C \tag{6.16}$$

with d_{MTC} being the distance between cargo and MT. The three-dimensional motor rest length L_{kin3}^{3d} is the three-dimensional length a motor has at the border of the attachment area $X_C \pm L_{att}$ on the MT when the distance between the cargo and the MT is d_{MTC} and the cargo radius is R_C (see table C.1 for parameter values). Finally, the angle ϕ_1 is given by the rectangular attachment area on the cargo. In detail, the angles θ_1, θ_2 and ϕ_1 are given by the following formulas:

$$\cos(\theta_1) = \frac{R_C + d_{MTC}}{\sqrt{(R_C + d_{MTC})^2 + L_{att}^2}} \quad \cos(\theta_2) = \frac{R_C^2 + (R_C + d_{MTC})^2 - \left(L_{kin3}^{3d} \right)^2}{2R_C(R_C + d_{MTC})}$$

$$\tan(\phi_1) = \frac{2R_C\theta_2}{2R_C\theta_2} = \frac{\theta_2}{\theta_1}. \tag{6.17}$$

See fig. 6.15 for geometrical illustration of the angles.

To have a comparable result with simulations of the standard liposome model, where only the motors in the attachment area on the cargo A_{att} are taken into account, the total number of motors N_{tot} on the cargo is calculated from the ratio of the attachment area to the cargo surface r_{att} (see eq. (6.14)) and the previously used number of motors in the attachment area N_{aa} on the cargo (see fig. 6.16):

$$N_{tot} = \frac{N_{aa}}{r_{att}}. \tag{6.18}$$

Simulating all motors N_{tot} on the cargo, similar cargo velocity histograms (fig. 6.24a) are obtained as with the standard liposome model, where only the motors in the attachment area on the cargo where taken into account (fig. 6.16a). The comparison of the MT-attached

a)

b)
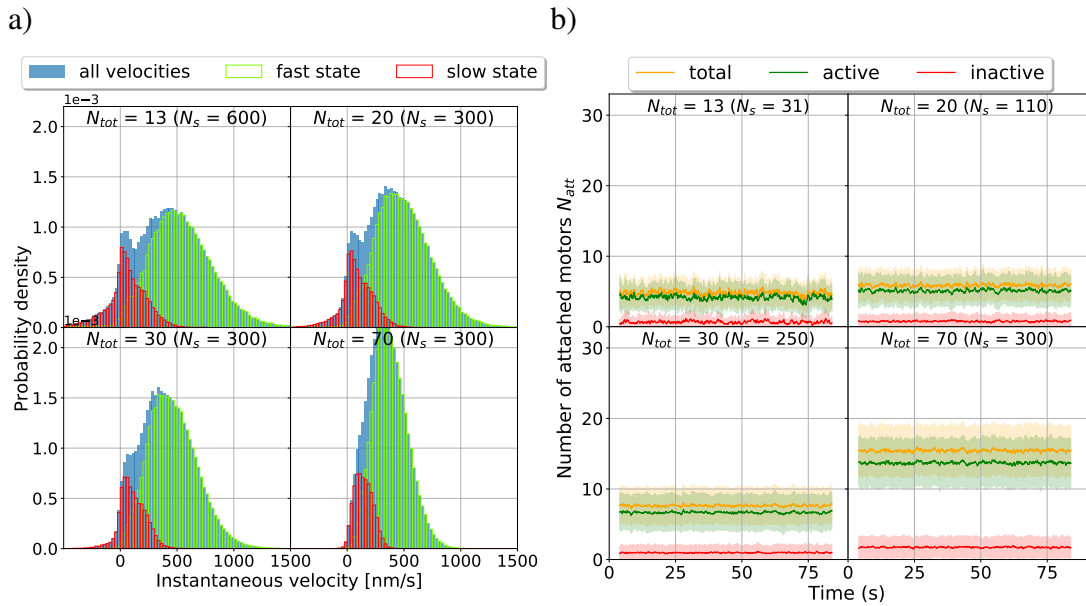
Figure 6.24: The liposome model variant 7. Simulation results from liposome model variant 7, where all motors on the cargo are taken into account instead of only the motors in the attachment area on the cargo. a) Histograms of all velocities (blue) as well as of the fast state (green) and the slow state (red) for varying numbers of total motors on the cargo N_{tot}. The velocity histograms are very similar to the velocity histograms of the standard liposome model (fig. 6.16a). b) Number of MT-attached motors ($\mu \pm \sigma$) as a function of time. To have comparable results only trajectories, which are 80 seconds long are taken into account (otherwise the mean number of motors would increase with time because trajectories are longer when having more motors.). Number of MT-attached motors remains unchanged over time.
Number of samples N_s are given in brackets.

motors (see fig. 6.18 for standard liposome model and 6.25 for liposome model with all motors) reveals that similar numbers of active and inactive motors are attached for the standard liposome model and the liposome model with all motors (variant 7). Moreover, the hypothesis that the number of MT-attached motors increases over time because more motors diffuse into the attachment area on the cargo is refuted. The number of MT-attached motors as a function of time (fig. 6.24b) shows no dependence on the time. This means attachment and detachment of motors are at equilibrium. The steady state is fast reached because the diffusion of motors on the cargo surface is fast. Together, this means modeling all motors on the cargo or just those in the attachment area on the cargo does not change the results. Consequently, the simplification of only modeling the motors in the attachment area on the cargo (standard liposome model) is justified.

Taking together, for both, the point-like cargo model and the liposome model, a reasonable set of parameters could be found, with which the simulation results are aligned with the experimental findings. While the point-like cargo model could not take the diffusive motor tails into account, the liposome model takes the sliding of the motor tails to the shortest motor extension into account and tries to answer the question whether the stopping of the cargo or the slow velocity state is caused by the diffusive motor tails. Duration and fre-

quency of the slow state, however, are similar for the liposome and the point-like cargo model.

Moreover, when simulating the liposome model without inactive motors, no slow state can be observed. Consequently, the diffusive motor tails are not responsible for the slow state seen in the experiment.

A direct comparison revealed that active motors are stronger in the liposome model than in the point-like cargo model. This arose the question whether this is due to the sliding of the diffusive motor tails to the position on the cargo with the shortest motor extension or due to reduced exclusion effects in the case of bigger cargos. Varying the size of the cargo in the liposome model simulations shows that exclusion effects are the dominant factor, which determines the velocity. Consequently, bigger cargos are transported faster than smaller cargos.
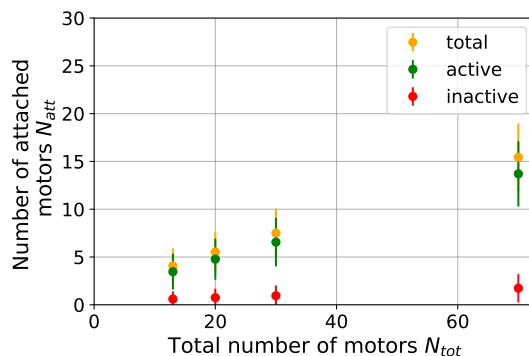
Figure 6.25: Liposome model variant 7: number of MT-attached motors. Mean number of MT-attached motors ($\mu \pm \sigma$) for the liposome model variant 7, where all motors on the cargo are taken into account. The total number of MT-attached motors (yellow), the number of active (green), and the number of inactive MT-attached motors (red) are shown as a function of the total number of motors on the cargo N_{tot}. The mean numbers of MT-attached motors are similar to the mean numbers of MT-attached motors of the standard liposome model (fig. 6.18), where only the motors in the attachment area on the cargo are taken into account.

Moreover, simulations show that the degree of sorting active motors to the front (towards the plus-end) and inactive motors to the back (towards the minus-end) plays a role. Having active and inactive motors well sorted, inactive motors hinder active motors less to step on the MT. That is why, the better the motors are sorted, the more efficiently the active motors step, the more efficiently the active motors pull off the inactive motors, and the faster the transport. In the simulation, the sorting efficiency was changed by changing the attachment probability distribution along the MT (Gaussian versus uniform). In the experiment, the sorting could be influenced by the way the motor tail is bound to the cargo. Sorting might be better in case of diffusive motor tails compared to motor tails which are fixed at one spot on the cargo surface as it is the case for beads. In the next section (section 6.2.3), beads are simulated and compared to liposome simulations.

Besides the exclusion effects and the motor sorting, also the detachment and the stall force determine the force balance between active and inactive motors. Simulations show that higher detachment forces enhance the low velocity peak and high stall forces reduce the low velocity peak. Thus, while higher detachment forces are found to strengthen the inactive motors, a higher stall force strengthens the active motors.

6.2.3 Bead model

Previous studies suggest that the cargo surface composition influence the cargo motility. The cargo surface composition (fluid or rigid cargo surface) influences the way motors are bound to the cargo [169, 248, 250]. While motor tails are able to diffuse on the surface of *in vivo* vesicles (fluid cargo surface), *in vitro* studies often use beads (rigid cargo surface), where motor tails are fixed at one position on the cargo surface. In the previous section, the liposome has been modeled with diffusive motor tails. To shield light on the influence of the diffusive versus the fixed motor tails, in this section a bead (fixed motor tails) is modeled and results are compared to the liposome model.

Bead model   As the liposome, the bead is modeled in one dimension (x-direction) neglecting degrees of freedom in y- and z-direction as well as any rotational degrees of freedom. Because the y-axis is not taken into account, also a rotation of the bead is not meaningful and therefore neglected. The bead is therefore approximated by a disk. In the bead model, all motors on the bead are taken into account (no matter whether they can reach the MT or not). To position motors uniformly on the surface of the disk, random angular tail positions ϕ_t in the interval $[0, 2\pi)$ are thrown. Exclusion effects of motor tails on the cargo surface are thereby taken into account. Motors with angular positions ϕ_t in the interval $\frac{3}{2}\pi \pm \theta_1$ are in the attachment area and can therefore attach to the MT. The opening angle θ_1 is the same as used to calculate the attachment area on the liposome (see fig. 6.15 for an illustration of the opening angle and the attachment area on the cargo). To compare the bead model to the liposome model, the same numbers of motors in the attachment area on cargos are used. This means the total number of motors N_{tot} on the bead is chosen such that:

$$N_{aa}^{bead} \overset{!}{=} N_{aa}^{liposome}$$
$$\Longleftrightarrow \quad r_{att}^{bead} N_{tot}^{bead} = r_{att}^{liposome} N_{tot}^{liposome}$$
$$\Longleftrightarrow \quad N_{tot}^{bead} = \frac{r_{att}^{liposome}}{r_{att}^{bead}} N_{tot}^{liposome} \tag{6.19}$$

where $r_{att}^{liposome}$ is the attachment ratio of the liposome, given by eq. (6.14) and r_{att}^{bead} the attachment ratio of the bead given by the following equation:

$$r_{att}^{bead} = \frac{2\theta_1}{2\pi} = \frac{\theta_1}{\pi} \tag{6.20}$$

with the opening angle θ_1 given by eq. (6.17).
The one-dimensional motor extension is calculated as the difference between the x-component of the motor head and motor tail positions

$$\Delta x^i(t) = x_h^i(t) - x_t^i(t) \tag{6.21}$$

with the motor tail position given by:

$$x_t(t) = X_C(t) + R_C \cos(\phi_t). \tag{6.22}$$

The one-dimensional motor force is then calculated using eq. (6.4).
The force-dependent kinesin-3 detachment and stepping rates remain the same as for the point-like cargo and the liposome model. Moreover, exclusion effects are taken into account on
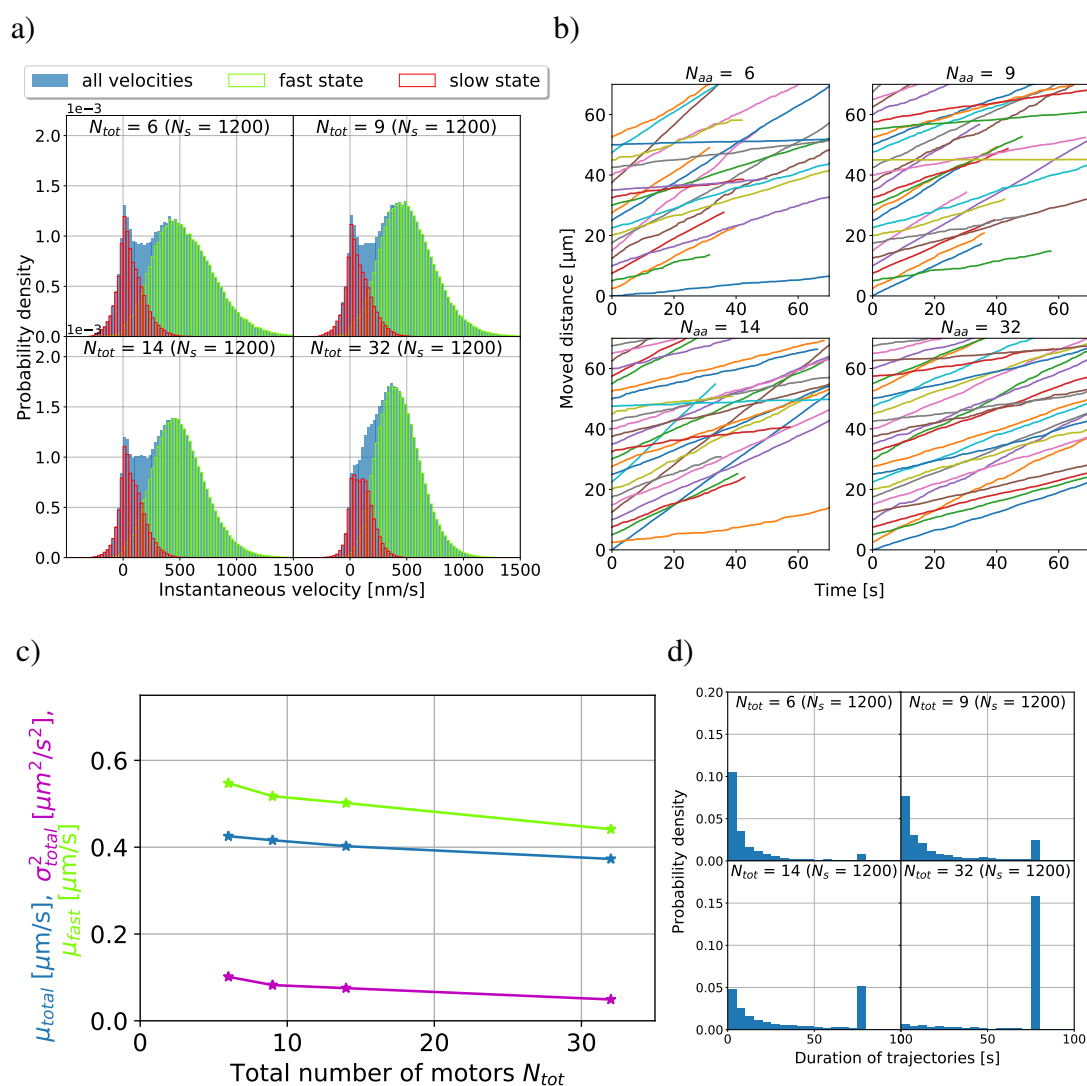
Figure 6.26: One-dimensional bead model. Simulation results produced with the bead model using the same number of motors in the attachment area on the cargo as the liposome model. a) Cargo velocity histograms (blue) for varying total number of motors N_{tot}. Using the segmentation algorithm (see main text and caption of fig. 6.3) trajectories can be divided into slow and fast states. The slow state velocity peak (red) slightly reduces with increasing number of motors. The fast state velocity peak (green) shifts to lower velocities for higher number of motors. For the highest number of motors, the two peaks merge. b) Example trajectories of simulated cargos (trajectory duration longer than 30 seconds) are depicted for varying total numbers of motors N_{tot}. A stop-and-go-like motion with clear slow states can be seen for all numbers of motors. Moreover, for the three lower numbers of motors, there are cargos that are transported with constantly slow velocities. c) Mean (blue) and variance (magenta) of all cargo velocities as well as mean velocities of only the fast state (green) are depicted. All three observables decrease with increasing number of motors. d) Histograms of trajectory durations. Trajectories are longer in time for high number of motors. The program was terminated either (*Continuation on next page.*)

Figure 6.26 (*previous page*): if no motor was attached to the MT anymore or after 80 seconds. Number of samples (cargos) N_s are given in brackets (a +d).

the MT and the Metropolis algorithm is used to propagate the bead along the MT (in one dimension) in the harmonic potential of the MT-attached motor springs.

As the force-dependent rates, also the attachment rate remains the same and a motor attaches along the MT in the attachment area $x_t^i \pm L_{att}$ around their tail position. In the attachment area along the MT, the motors are supposed to be force-free. Unlike for the liposome model, where $L_{att} \geq L_{kin3}$, for the bead, where motor tails cannot slide on the cargo surface, the half attachment length has to be $L_{att} = L_{kin3}$ to ensure that motors attach in a force-free state. As for the liposome model, the attachment probability p_{att} along the attachment area on the MT (along the MT length axis) is Gaussian distributed:

$$p_{att}(x_h) = \begin{cases} \dfrac{A}{\sqrt{2\pi(L_{kin3}/3)^2}} e^{-\frac{(x_h - X_t(t))^2}{2(L_{kin3}/3)^2}}, & x_h \in X_t(t) \pm L_{kin3} \\ 0, & \text{else.} \end{cases} \tag{6.23}$$

The attachment to the seven reachable protofilaments is also Gaussian distributed in the same manner as for the liposome and the point-like cargo model (see sections 6.2.2 and 6.2.1).

While in the liposome model, motors that can reach the MT could exchange with other motors in the reservoir (motors that are not in the attachment area on the cargo), the motors which can reach the MT are fixed for the bead model. This means motors on the bead have a fixed active/inactive status, while the active/inactive status of motors on the liposome was set when attaching. However, as for the liposome model, motors are inactive with probability $p_{inactive} = 0.2$.

In summary, in the bead model, the motor tails have a fixed tail position $x_t(t)$ on the cargo and a fixed active/inactive status. A fixed part of the motors on the cargo can attach the MT within the area $x_t(t) \pm L_{kin3}$ on the MT. The motor properties such as attachment, detachment, and stepping rates, as well as the mechanism to update the cargo position, remain the same as for the liposome model. To have comparable results from the bead and the liposome simulations the same number of motors in the attachment area on the cargos (bead and liposome) are chosen.
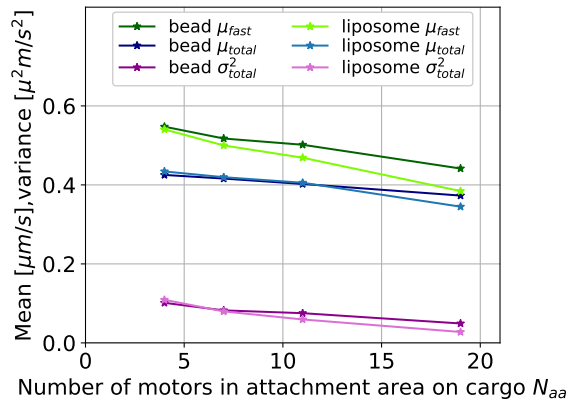
Figure 6.27: Comparing velocities from one-dimensional bead and liposome models. Mean (blue) and variance (magenta) of all cargo velocities as well as mean velocities of only the fast state (green) are depicted. Values from the liposome model are depicted in slightly lighter colors. No significant difference can be seen when comparing all velocities, but the fast state is slightly faster for the bead than for the liposome.

Simulation results: Fig. 6.26, 6.29, and 6.28 show simulation results produced with the

bead model. To study the influence of a fixed motor tail position (bead) versus a diffusive motor tail position on the cargo (liposome), the bead simulation results are compared to the liposome simulation results (fig. 6.24, 6.25 and fig. C.3 of the appendix C). Bead velocity histograms (fig. 6.26a) show a low velocity peak and a high velocity peak. The low velocity peak can be related to the slow state and the high velocity peak to the fast state as it is the case for the liposome. The high velocity peak moves towards slower velocities the higher the number of motors such that at the highest number of motors the two peaks merge. Unlike for the liposome model, where the peaks start to merge already for the second lowest number of motors, two separate peaks are visible for the three lower numbers of motors for the bead model. Variance and mean of all bead velocities as well as the mean of only the fast state decrease with increasing total number of motors on the cargo N_{tot} (fig. 6.26c). Comparing mean and variance of liposome and bead velocities (fig. 6.27) does not show a significant difference between liposome and bead transport. Only, the velocities of the fast state are slightly higher for the bead than for the liposome. Thus, for the one-dimensional models, velocity histograms and mean velocities reveal that the fast state of the bead is slightly faster than the fast state of the liposome model.

The reduction of the mean velocity of the fast state with increasing number of motors has been shown to be due to a mutual sterical hindrance of MT-attached motors. A comparison of MT-attached motors of the bead model (fig. 6.28) with MT-attached motors of the liposome model (fig. 6.25) reveals that fewer motors are attached to the MT in case of the bead model. There are two reasons for fewer motors being attached for the bead model compared to the liposome model: i) First in the liposome model, motors can diffuse from the other side of the cargo into the attachment area and then attach to the MT. The number of attaching motors can thereby increase. In the bead model, however, the number of motors in the attachment area on the cargo is fixed. This means that while in the bead model, the number of MT-attached motors cannot be higher than $r_{\text{att}}^{\text{bead}} N_{\text{tot}}^{\text{bead}}$, in the liposome model the number of MT-attached motors can be higher than $r_{\text{att}}^{\text{liposome}} N_{\text{tot}}^{\text{liposome}}$.

ii) The second reason for fewer motors being attached is that the motor extension does not relax like in the liposome model, where motor tails always slide to the position with the shortest motor extension. That is why forces are higher (see fig. C.5a for motor extensions in the bead model and fig. C.2a for motor extensions in the liposome model) in the bead model. Higher forces mean that motors detach faster leading to a reduced amount of MT-attached

Figure 6.28: **Bead: number of MT-attached motors.** Mean number of MT-attached motors ($\mu \pm \sigma$) for the one-dimensional bead model. The total number of MT-attached motors (yellow), the number of active (green), and the number of inactive MT-attached motors (red) increase with the total number of motors on the bead.

motors. The reduced amount of MT-attached motors leads to a reduced mutual, ster-
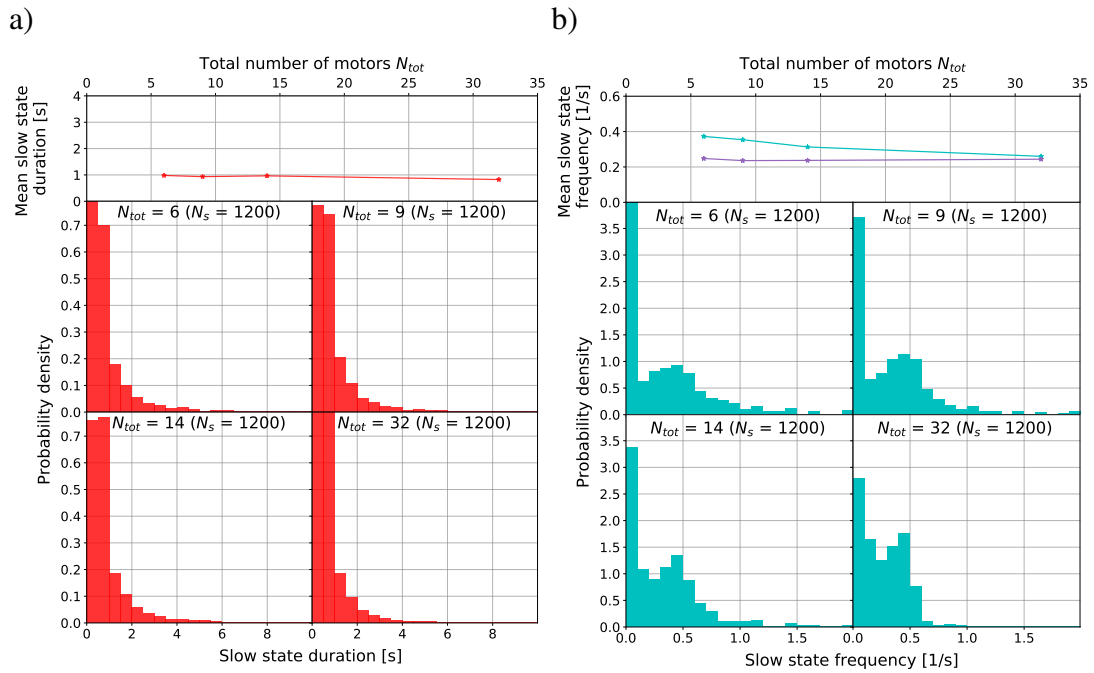
Figure 6.29: One-dimensional bead model: slow state. Duration and frequency of slow state obtained from simulations using the bead model. a) Mean duration of the slow state as a function of the total number of motors on the bead as well as duration histograms for varying total number of motors. Mean and histograms do not show a dependence of the slow state duration on the total number of motors. b) Mean and histograms of slow state frequencies for varying total number of motors. Individual slow state frequencies (blue) are calculated as number of slow states per trajectory duration. The total frequency of slow states (magenta, independent of the duration of the trajectories) is calculated as total number of slow states of all simulations divided by the sum of all trajectory durations. Slow state frequencies are slightly enhanced for low total number of motors.
Number of samples N_s is given in brackets.

ical motor-motor hindrance (reduced exclusion effects) such that velocities of the fast state are higher compared to the liposome model, where more motors are attached. Moreover, the reduced amount of MT-attaching motors leads to shorter trajectories for the bead model (fig. 6.26d) compared to the liposome model (fig. 6.16d). Taking together, the fixed motor tail positions versus the diffusive motor tail positions on the cargo surface lead to fewer MT-attached motors and therefore slightly higher velocities of the fast state, but shorter trajectories.

Trajectories of bead transport (fig. 6.26b) also show a stop- and go-like motion, which is comparable to the stop- and go motion observed with the liposome model (fig. 6.16b). Duration and frequency of the slow state of the bead (fig. 6.29) are similar to duration and frequency of the slow state of the liposome model (fig. 6.17). However, trajectories of the bead are less parallel than trajectories of the liposome. Some bead trajectories show very low velocities over the full range of the trajectory (fig. 6.26b). Such trajectories were not observed for the liposome model (fig. 6.16b). Comparing the variances of velocities per trajectory (fig. 6.30) confirms that the variance between trajectories is higher for the bead model compared to the liposome model. The reason could be that there are fewer variations in the kind of

MT-attached motors. While for the liposome model, motors exchange with the reservoir (= motors on the other side of the cargo, which are not in the attachment area), for the bead model a fixed configuration of motors (re)attach to the MT. Thus, MT-attached motors vary more in the active/inactive status for the liposome model than for the bead model. The result is that some trajectories of beads are very slow because there are not enough active motors to pull off the inactive motors, while others are faster because fewer inactive motors are involved. When resetting the active/inactive status each time a motor reattaches for the bead, trajectories are more parallel (fig. C.5b of the appendix). The variance of velocities per trajectories (fig. 6.30) is reduced, but still higher than for the liposome model. The reason is that for the liposome model, motors also vary in the force-free velocity. Resetting the force-free velocity each time a motor (re)attaches for the bead leads to a even more reduced variance of velocities per trajectory. However, the variance is still higher for the bead (fig. 6.30). The reason for the even lower variance per trajectory for the liposome lies in the higher number of MT-attached motors, which stabilize the transport. Consequently, while transport velocities depend on the local motor configuration in the one-dimensional bead model, transport velocities are more robust in the one-dimensional liposome model due to the diffusive motor tail positions.

In summary, it could be shown that the fixed motor tail positions (bead) lead to a reduced amount of MT-attached motors compared to diffusive motor tails case (liposome). Fewer motors are attached to the MT because due to the rigid cargo surface, there are first no additional motors diffusing into the attachment area as it happens for the diffusive motor tails and second, motors experience higher forces which lead to a faster detachment of the motors. The lower number of MT-attached motors leads on the one hand to less exclusion effects and therefore higher velocities of the fast state and on the other hand to shorter trajectories. Thus, beads are transported faster, but less robust.

Figure 6.30: **Variance of velocities per track: comparison between one-dimensional bead and one-dimensional liposome models.** The figure shows the variance of velocities per track as a function of the number of motors in the attachment area of the cargo N_{aa}. For the bead, simulations were performed for a fixed motor configuration in the attachment area (pink), fluctuations in the active/inactive status (= activity status is reset each time a motor (re)attaches, light blue), and for fluctuating motor configurations (= activity status and force-free velocities are reset each time a motor (re)attaches, dark blue). In all cases, variances decrease with increasing number of motors. Variances are highest for the bead model with fixed motor configurations. Variances are reduced for the bead model with fluctuations in the active/inactive status and even more reduced for the bead model with fluctuating motor configurations. Variances are lowest for the liposome model (orange). Number of samples is 300 for each simulation and each number of motors.

Besides being less robust because trajectories are shorter, bead transport is also less robust

because velocities per trajectory depend on the fixed motor configuration. It could be shown that the variance in velocities per trajectory reduces when the inactive/active status (and the force-free velocity) are newly set each time a motor reattaches. Such a high variation of the motor configuration is not realistic for the bead. However, fluctuations in the motor configuration might be higher than the fixed configuration, because the bead might randomly rotate around its center of gravity and thereby change the configuration of motors able to attach the MT. When rotating around its center of gravity, it could be that motors wrap around the bead. To take this extra motor extension into account, a one-dimensional model is not appropriate anymore. The bead needs to be modeled in three dimensions.

6.3 Three-dimensional models of cargo transport by kinesin-3

In the previous section, liposome and bead transport by kinesin-3 were modeled in one dimension. In one dimension, any translational degree of freedom perpendicular to the MT symmetry axis and any rotational degree of freedom has been neglected. However, rotation of the cargo around its center of gravity and around the MT could change motor forces and configurations of motors that can reach the MT. The latter is particularly interesting in the case of the bead where motor tails have fixed positions on the cargo surface. In the one-dimensional bead model, configurations of motors able to attach the MT did not change over time for a given cargo. However, due to bead rotations around its center of gravity, configurations of motors able to attach the MT could change over time. Therefore, liposome and bead transport by kinesin-3 is modeled in three dimensions.

In the following section, first, the three-dimensional liposome model and the corresponding results will be presented and thereafter, the three-dimensional bead model and results.

6.3.1 Liposome model

Before discussing simulation results, the three-dimensional liposome model will be presented in detail.

Three dimensional liposome model description   The three-dimensional liposome model is based on the one-dimensional liposome model, but takes the three-dimensional geometry of the cargo, the MT, and the motor extension of MT-attached motors into account. Since detached motors diffuse fast on the liposome surface (diffusion constant in the range of $1 - 20\mu m^2/s$ [22, 169, 256, 325]), it is assumed that detached motors are uniformly distributed on the cargo surface and the explicit positions of detached motors on the liposome surface are not taken into account.
Compared to the one-dimensional model, the following changes must be made:

1. Elaborate a three-dimensional coordinate system.

2. Motor forces/extensions need to be calculated in three dimensions.

3. Motors need to detach, step and attach to the MT in three dimensions.

4. The cargo needs to be moved in three dimensions.

1. Three-dimensional coordinate system   For the three-dimensional geometry, cylindrical coordinates are used. Thereby, the z-axis is chosen to be identical to the symmetry axis of the MT, which is modeled as a cylinder (see illustrational fig. 6.31). The origin of the three-dimensional coordinate system is chosen to be in the center of the MT with the z-axis pointing towards the MT plus-end. The cargo position, denoted by

$$\underline{\mathbf{X}}_C(t) = \begin{pmatrix} \rho_c \cos(\varphi_c) \\ \rho_c \sin(\varphi_c) \\ z_c \end{pmatrix}$$ (6.24)

is the position of the center of the cargo in the three-dimensional coordinate system. The position of an MT-attached motor head on the MT is denoted by

$$\underline{\mathbf{x}}_h^i(t) = \begin{pmatrix} R_{MT}\cos(\varphi_h^i) \\ R_{MT}\sin(\varphi_h^i) \\ z_h^i \end{pmatrix} \tag{6.25}$$

with R_{MT} being the radius of the MT (see illustrational fig. 6.31).
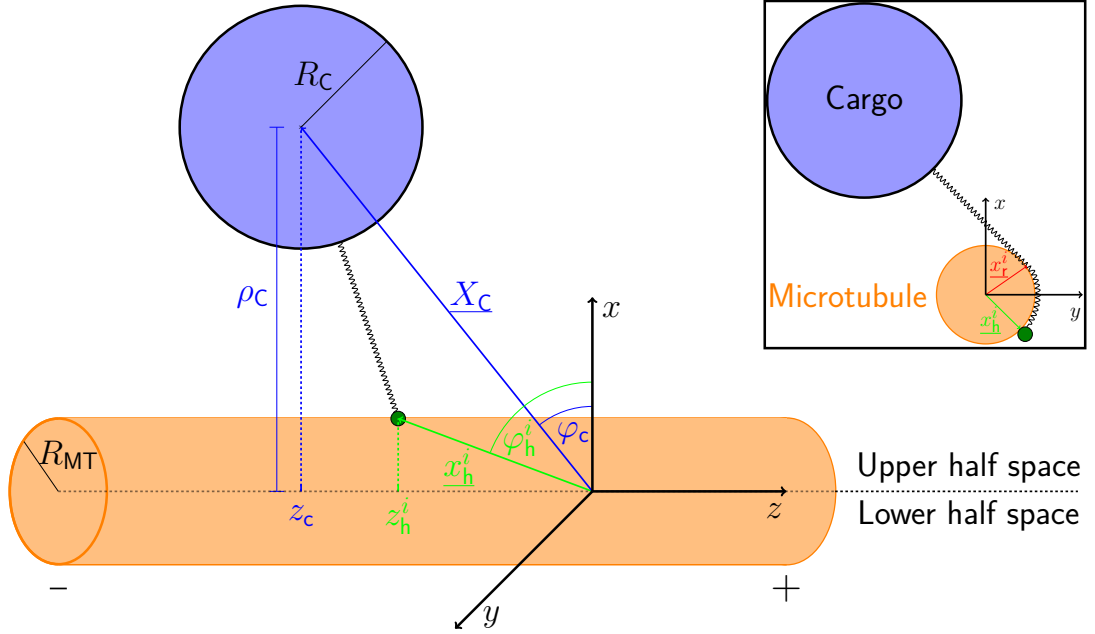
Figure 6.31: Three-dimensional liposome model: illustration of geometry. Illustration shows the three-dimensional geometry of the liposome model. The coordinate system is chosen such that the symmetry axis of the MT (orange cylinder with radius R_{MT}) is identical to the z-axis and the MT plus-end points in positive z-direction. The cargo (blue circle with radius R_C) has the position $\underline{\mathbf{X}}_C$ (blue) and the motor heads (green dots) the position $\underline{\mathbf{x}}_h^i$ (green). To describe any position in the three-dimensional space, cylindrical coordinates (ρ, φ, z) are chosen. The inset (upper right corner) shows a motor, which is partly winded around the MT. $\underline{\mathbf{x}}_r^i(t)$ (red) is the point where the motor meets the MT and $\underline{\mathbf{x}}_h^i(t)$ (green) is the motor head position on the MT.

2. Three-dimensional motor forces   Three-dimensional motor forces are characterized by the absolute force value and the force direction. The absolute force value is proportional to the absolute, three-dimensional motor extension. To calculate the motor extension, it has to be distinguished whether i) the motor head is in the same half space of the MT as the cargo ($\varphi_h \in \varphi_c \pm \frac{\pi}{2}$) or ii) whether the motor is partly winded around the MT (see inset of illustrational fig. 6.31). In the first case, the force direction can be calculated from the motor head position $\underline{\mathbf{x}}_h^i(t)$ and the center of the cargo position $\underline{\mathbf{X}}_C(t)$ because diffusive motor tails of MT-attached motors are radially bound to liposome

$$\underline{\mathbf{e}}_f = \frac{\underline{\mathbf{x}}_h^i(t) - \underline{\mathbf{X}}_C(t)}{|\underline{\mathbf{x}}_h^i(t) - \underline{\mathbf{X}}_C(t)|} \tag{6.26}$$

with

$$\underline{\mathbf{x}}_{\mathrm{h}}{}^{i}(t) - \underline{\mathbf{X}}_{\mathrm{C}}(t) = \begin{pmatrix} R_{\mathrm{MT}} \cos(\varphi_{\mathrm{h}}^{i}) - \rho_{\mathrm{c}} \cos(\varphi_{\mathrm{c}}) \\ R_{\mathrm{MT}} \sin(\varphi_{\mathrm{h}}^{i}) - \rho_{\mathrm{c}} \sin(\varphi_{\mathrm{c}}) \\ z_{\mathrm{h}}^{i} - z_{\mathrm{c}} \end{pmatrix} \tag{6.27}$$

and

$$|\underline{\mathbf{x}}_{\mathrm{h}}^{\mathbf{i}}(t) - \underline{\mathbf{X}}_{\mathrm{C}}(t)| = \sqrt{R_{\mathrm{MT}}^{2} + \rho_{\mathrm{c}}^{2} - 2R_{\mathrm{MT}}\rho_{\mathrm{c}} \cos(\varphi_{\mathrm{h}}^{i} - \varphi_{\mathrm{c}}) + (z_{\mathrm{h}}^{i} - z_{\mathrm{c}})}. \tag{6.28}$$

To calculate the motor extension the cargo radius R_{C} must be subtracted from the distance between the cargo center position and the motor head position:

$$\begin{aligned} |\underline{\mathbf{\Delta x}}^{i}(t)| &= |\underline{\mathbf{x}}_{\mathrm{h}}^{\mathbf{i}}(t) - \underline{\mathbf{X}}_{\mathrm{C}}(t)| - R_{\mathrm{C}} \\ &= \sqrt{R_{\mathrm{MT}}^{2} + \rho_{\mathrm{c}}^{2} - 2R_{\mathrm{MT}}\rho_{\mathrm{c}} \cos(\varphi_{\mathrm{h}}^{i} - \varphi_{\mathrm{c}}) + (z_{\mathrm{h}}^{i} - z_{\mathrm{c}})} - R_{\mathrm{C}}. \end{aligned} \tag{6.29}$$

In the second case, where the motor is partly winded around the MT, the force direction is

$$\underline{\mathbf{e}}_{\mathrm{f}} = \frac{\underline{\mathbf{x}}_{\mathrm{r}}^{\mathbf{i}}(t) - \underline{\mathbf{X}}_{\mathrm{C}}(t)}{|\underline{\mathbf{x}}_{\mathrm{r}}^{\mathbf{i}}(t) - \underline{\mathbf{X}}_{\mathrm{C}}(t)|} \tag{6.30}$$

with $\underline{\mathbf{x}}_{\mathrm{r}}^{\mathbf{i}}(t)$ being the point where the motor meets the MT. Thus, the motor has a straight extension from the surface of the cargo to the auxiliary point $\underline{\mathbf{x}}_{\mathrm{r}}^{\mathbf{i}}(t)$ and then winds around the MT until reaching the head position $\underline{\mathbf{x}}_{\mathrm{h}}^{\mathbf{i}}(t)$ on the MT. The hit point is given by

$$\underline{\mathbf{x}}_{\mathrm{r}}^{\mathbf{i}}(t) = \begin{pmatrix} R_{\mathrm{MT}} \cos(\varphi_{\mathrm{r}}^{i}) \\ R_{\mathrm{MT}} \sin(\varphi_{\mathrm{r}}^{i}) \\ z_{\mathrm{r}}^{i} \end{pmatrix} \tag{6.31}$$

whereby the azimuthal angle is $\varphi_{\mathrm{r}} = \varphi_{\mathrm{c}} \pm \frac{\pi}{2}$ depending on the direction of the winding and z_{r} has to be found by minimizing the complete motor extension. The complete motor extension is given by

$$|\underline{\mathbf{\Delta x}}^{i}(t)| = |\underline{\mathbf{x}}_{\mathrm{r}}^{\mathbf{i}}(t) - \underline{\mathbf{X}}_{\mathrm{C}}(t)| - R_{\mathrm{C}} + \mathcal{G}(\underline{\mathbf{x}}_{\mathrm{h}}^{\mathbf{i}}(t), \underline{\mathbf{x}}_{\mathrm{r}}^{\mathbf{i}}(t)) \tag{6.32}$$

whereby $\mathcal{G}(\underline{\mathbf{x}}_{\mathrm{h}}^{\mathbf{i}}(t), \underline{\mathbf{x}}_{\mathrm{r}}^{\mathbf{i}}(t))$ is the part of the motor, which is winded around the MT. $\mathcal{G}(\underline{\mathbf{x}}_{\mathrm{h}}^{\mathbf{i}}(t), \underline{\mathbf{x}}_{\mathrm{r}}^{\mathbf{i}}(t))$ is the geodesic on the MT surface connecting point $\underline{\mathbf{x}}_{\mathrm{h}}^{\mathbf{i}}(t)$ and $\underline{\mathbf{x}}_{\mathrm{r}}^{\mathbf{i}}(t)$ on the MT surface. The geodesic is calculated as

$$\mathcal{G}(\underline{\mathbf{x}}_{\mathrm{h}}^{\mathbf{i}}(t), \underline{\mathbf{x}}_{\mathrm{r}}^{\mathbf{i}}(t)) = \int_{0}^{\Delta\varphi} |\underline{\dot{\mathbf{s}}}(t')| \, dt' \tag{6.33}$$

with the differences in the azimuthal angle being $\Delta\varphi = |\varphi_{\mathrm{r}} - \varphi_{\mathrm{h}}|$. Since the shortest connection between $\underline{\mathbf{x}}_{\mathrm{r}}^{\mathbf{i}}(t)$ and $\underline{\mathbf{x}}_{\mathrm{h}}^{\mathbf{i}}(t)$ is a helix, the parameterization $\underline{\mathbf{s}}(t')$ is given by

$$\underline{\mathbf{s}}(t') = \begin{pmatrix} R_{\mathrm{MT}} \cos(t') \\ R_{\mathrm{MT}} \sin(t') \\ b \cdot t' \end{pmatrix} \tag{6.34}$$

with the pitch being $b = \frac{z_h - z_r}{\Delta \varphi}$ such that the difference in z-direction is equally distributed over $\Delta \varphi$. Taking together, the following expression can be found for the complete motor extension

$$|\underline{\Delta \mathbf{x}}^i(t)| = \left\| \begin{pmatrix} R_{MT} \cos(\varphi_r^i) - \rho_c \cos(\varphi_c) \\ R_{MT} \sin(\varphi_r^i) - \rho_c \sin(\varphi_c) \\ z_r^i - z_c \end{pmatrix} \right\| - R_c + \int_0^{\Delta \varphi} \sqrt{R_{MT}^2 + \left(\frac{z_h^i - z_r^i}{\Delta \varphi} \right)^2} \, dt'$$

$$= \sqrt{R_{MT}^2 + \rho_c^2 - 2 R_{MT} \rho_c (cos\varphi_c \cos \varphi_r^i + \sin \varphi_c \sin \varphi_r^i) + (z_r^i - z_c)^2} - R_C$$

$$+ \sqrt{R_{MT}^2 + \left(\frac{z_h^i - z_r^i}{\Delta \varphi} \right)^2} \Delta \varphi.$$

Using the theorem

$$\cos \alpha \cos \beta \pm \sin \alpha \sin \beta = \cos(\alpha \mp \beta) \tag{6.35}$$

and the definition of $\varphi_r = \varphi_c \pm \frac{\pi}{2}$, the following simplification can be achieved:

$$\cos \varphi_c \cos \varphi_r^i + \sin \varphi_c \sin \varphi_r^i = \cos(\varphi_c - \varphi_r^i) = \cos(\varphi_c - \varphi_c \mp \frac{\pi}{2}) = 0.$$

By further defining $A^2 \equiv \rho_c^2 + R_{RM}^2 > 0$ and $B^2 \equiv R_{MT}^2 (\Delta \varphi)^2 > 0$ the expression for the complete motor extension can be simplified:

$$|\underline{\Delta \mathbf{x}}^i(t)| = \sqrt{A^2 + \left(z_r^i - z_c \right)^2} - R_C + \sqrt{B^2 + \left(z_h^i - z_r^i \right)^2} \equiv f(z_r^i). \tag{6.36}$$

To find the z_r, which minimizes the complete motor extension, the derivative of the function $f(z_r)$ needs to be calculated and set to zero:

$$\frac{d}{dz_r^i} f(z_r^i) \stackrel{!}{=} 0$$

$$\iff \frac{\left(z_r^i - z_c \right)}{\sqrt{A^2 + \left(z_r^i - z_c \right)^2}} = \frac{\left(z_h^i - z_r^i \right)}{\sqrt{B^2 + \left(z_h^i - z_r^i \right)^2}}.$$

Solving this equation, the following expression is found for z_r^i:

$$(z_r^i)^\pm = \pm \frac{A B \left| z_h^i - z_c \right|}{\left| A^2 - B^2 \right|} + \frac{A^2 z_h^i - B^2 z_c}{A^2 - B^2}. \tag{6.37}$$

With

$$\frac{d^2}{d(z_r^i)^2} f(z_r^i) = \frac{A^2}{\left(A^2 + (z_r^i - z_c)^2 \right)^{3/2}} + \frac{B^2}{\left(B^2 + (z_h^i - z_r^i)^2 \right)^{3/2}} > 0 \quad \forall \quad z_r^i \tag{6.38}$$

both, z_r^+ and z_r^- are minima. Taking into account that $z_r^i \in \left[z_h^i, z_c \right]$ should hold, the correct z_r^i can be chosen and the motor extension can be calculated by plugging in the correct z_r^i in

equation 6.36. Having calculated the force direction and the complete motor extension for both cases, the complete motor force can be obtained by the following expression:

$$
\underline{\mathbf{F}}^i(t) = \begin{cases} \kappa_{\text{kin3}} \left(\left| \underline{\Delta \mathbf{x}}^i(t) \right| - L_{\text{kin3}}^{\text{3d}} \right) \underline{\mathbf{e}}_{\text{f}}, & \left| \underline{\Delta \mathbf{x}}^i(t) \right| > L_{\text{kin3}}^{\text{3d}} \\ 0, & \text{else} \end{cases} \tag{6.39}
$$

with $L_{\text{kin3}}^{\text{3d}}$ being the kinesin-3 length in three dimensions (= equivalent to the kinesin-3 length in one dimension L_{kin3}, see eq. (6.16) for the definition).

3. Three-dimensional motor detachment, stepping, and attachment   As for the one-dimensional models, the kinesin-3 motors detach and step with force-dependent rates. Having the three-dimensional motor force of MT-attached motors, the detachment rate is calculated by using the absolute value of the three-dimensional motor force:

$$
k_{\text{d}}(\underline{\mathbf{F}}^i(t)) = k_{\text{d}}^0 e^{\frac{|\underline{\mathbf{F}}^i(t)|}{F_{\text{d}}}} . \tag{6.40}
$$

For the stepping, instead of the absolute value of the three-dimensional motor force, the projection of the motor force in the direction of stepping is used. Since kinesin-1 is known to stay on the same protofilament [126], it is assumed that also kinesin-3 follows one protofilament. It is known that depending on the number of protofilaments, the protofilaments are either straight (13 protofilaments), i.e. parallel to the MT length axis or form a right- or left-handed super twisted helix (others than 13 protofilaments) around this axis [52, 329]. *In vivo*, the MT mostly nucleates from a ring of 13 gamma tubulins [52, 330]. That is why *in vivo* most of the MTs have 13, straight protofilaments [52]. Especially in crowded environments, like in dendritic cells, the straight protofilament conformation is advantageous because motors transporting organelles are not twisting around the MT [52]. *In vitro*, however, tubulin stochastically oligomerizes to nucleate a MT. That is why, a wider range of protofilament numbers are observed, but predominantly MTs with 14 protofilaments [52, 331]. Also, in our experiments, MTs with 14 protofilaments are used. It is known that MTs with 14 protofilaments have a left-handed supertwist with a pitch of 6 μm [126]. That is why, when a motor performs a step, the motor head displaces in z- and φ- direction and the stepping direction is obtained by

$$
\underline{\mathbf{e}}_{\text{step}} = \frac{\underline{\mathbf{x}}_{\text{h},+}^{\mathbf{i}}(t) - \underline{\mathbf{x}}_{\text{h}}^{\mathbf{i}}(t)}{|\underline{\mathbf{x}}_{\text{h},+}^{\mathbf{i}}(t) - \underline{\mathbf{x}}_{\text{h}}^{\mathbf{i}}(t)|} = \frac{1}{\text{d}} \begin{pmatrix} R_{\text{MT}} \cos(\varphi_{\text{h}} + \Delta\varphi_{\text{step}}) - R_{\text{MT}} \cos(\varphi_{\text{h}}) \\ R_{\text{MT}} \sin(\varphi_{\text{h}} + \Delta\varphi_{\text{step}}) - R_{\text{MT}} \sin(\varphi_{\text{h}}) \\ z_{\text{h}} + \Delta z_{\text{step}} - z_{\text{h}} \end{pmatrix} \tag{6.41}
$$

with $\underline{\mathbf{x}}_{\text{h},+}^{\mathbf{i}}(t)$ being the new motor head position after having performed a step of size d. Δz_{step} and $\Delta\varphi_{\text{step}}$ are the motor head displacements in z- and φ- direction during one step, respectively. Using again the theorem given by eq. (6.35) and the small-angle approximation

$$
\sin\alpha \approx \alpha \quad \text{and} \quad \cos\alpha \approx 1 \quad \text{for} \quad \alpha \ll 1 \tag{6.42}
$$

for $\Delta\varphi_{\text{step}} \ll 1$ (see below for the calculation of $\Delta\varphi_{\text{step}}$), the stepping direction can be simplified by:

$$
\underline{\mathbf{e}}_{\text{step}} \approx \frac{1}{\text{d}} \begin{pmatrix} -R_{\text{MT}} \sin(\varphi)\Delta\varphi_{\text{step}} \\ R_{\text{MT}} \cos(\varphi_{\text{h}})\Delta\varphi_{\text{step}} \\ \Delta z_{\text{step}} \end{pmatrix} = -\underline{\mathbf{e}}_{\text{step,back}}. \tag{6.43}
$$

The backward stepping direction $\underline{\mathbf{e}}_{\text{step,back}}$ is the opposite of the forward stepping direction $\underline{\mathbf{e}}_{\text{step}}$. The displacement in φ-direction $\Delta\varphi_{\text{step}}$ is calculated from how many steps the motor needs to perform to circle the MT once. Following one protofilament, the motor follows a helix with a pitch of $b = 6\,\mu\text{m}$ to circle the MT. As used before, the parameterization of a helix is

$$\gamma(t') = \begin{pmatrix} R_{\text{MT}}\cos t' \\ R_{\text{MT}}\sin t' \\ bt' \end{pmatrix} \quad \text{with} \quad t' \in [0, 2\pi] \tag{6.44}$$

and the arc length of one round is

$$L_{\text{helix}} == \int\limits_0^{2\pi} \left|\dot{\gamma}(t')\right| dt' = \int\limits_0^{2\pi} \sqrt{R_{\text{MT}}^2 + b^2}\, dt' = 2\pi\sqrt{R_{\text{MT}}^2 + b^2}. \tag{6.45}$$

with b being the pitch of $6\,\mu\text{m}$ divided by 2π. The number of steps a motor needs for one circle around the MT is then

$$N_{\text{steps}} = \frac{L_{\text{helix}}}{d} \tag{6.46}$$

and the displacement in φ-direction per step is

$$\Delta\varphi_{\text{step}} = \frac{2\pi}{N_{\text{step}}} = \frac{2\pi d}{L_{\text{helix}}} = \frac{d}{\sqrt{R_{\text{MT}}^2 + b^2}} \approx 0.01 \tag{6.47}$$

with applying $b = \frac{6\,\mu\text{m}}{2\pi}$ and a stepsize of $d = 8\,\text{nm}$. For calculating the displacement in z-direction, a right-angled triangle with a hypotenuse of length d and one leg of length Δz_{step} and the other leg of length $R_{\text{MT}}\Delta\varphi_{\text{step}}$ is assumed. Then, the displacement in z-direction is obtained by

$$\Delta z_{\text{step}} = \sqrt{d^2 - (\Delta\varphi_{\text{step}} R_{\text{MT}})^2}. \tag{6.48}$$

The projection of the motor force in stepping direction is then obtained by

$$F_{\text{step}}^i(t) = \underline{\mathbf{F}}^i(t) \cdot \underline{\mathbf{e}}_{\text{step}} \tag{6.49}$$

with $\underline{\mathbf{F}}^i(t)$ given by eq. (6.39) and $\underline{\mathbf{e}}_{\text{step}}$ given by eq. (6.43). The absolute value of the force projection in stepping direction $|F_{\text{step}}^i(t)|$ is used to calculate the stepping rates according to eq. (6.6) and eq. (6.7) (see subsection 6.2.1).

For stepping on the MT, exclusion effects are taken into account as it is done for the one-dimensional models. This means a motor head is only allowed to perform a step when the next motor head position on the MT is not (partly) occupied by a head of another MT-attached motor.

As for the stepping also for the motor attachment, exclusion effects matter. Thus, a motor head attaches to the MT at an empty, force-free position. The attachment for the three-dimensional model is similar to the attachment in the one-dimensional liposome model when taking the attachment area on the cargo into account (variant 7; see last part of subsection 6.2.2). Thus, all motors on the cargo are considered (in contrast to only considering the fraction of the motors in the attachment area on the cargo), from which a fraction given by eq. (6.14) is allowed to

a)

b)
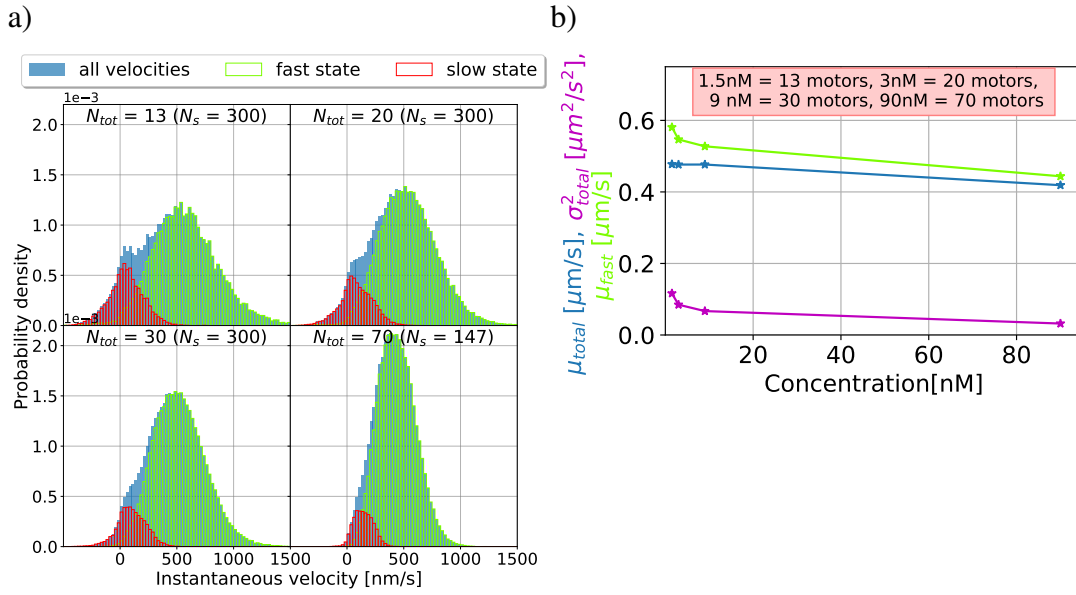
Figure 6.32: Three-dimensional liposome model: same parameters as one-dimensional liposome model. Simulation results were produced with the three-dimensional liposome model using the detachment force of the one-dimensional liposome model. a) Cargo velocity histograms (blue) for varying total number of motors N_{tot}. Using the segmentation algorithm (see main text and caption of fig. 6.3) trajectories can be divided into slow (red) and fast states (green). The low velocity peak related to the slow state is less pronounced than compared to the one-dimensional liposome model (fig. 6.16a). b) Mean (blue) and variance (magenta) of all cargo velocities as well as mean velocities of only the fast state (green) are depicted. All three observables decrease with increasing number of motors. Mean values reduce less with increasing number of motors than for the one-dimensional liposome model (fig. 6.16c).

The simulations were terminated either if no motor was attached to the MT anymore or after 80 seconds. Number of samples (cargos) N_{s} are given in brackets (a).

attach the MT. When attaching, a Gaussian distribution is used to find the protofilament (the φ-position) of the attaching motor head on the MT and another Gaussian distribution for the attachment along the MT within the area $X_{\text{C}}(t) \pm L_{\text{att}}$. Unlike for the one-dimensional model, where the half of the attachment area L_{att} is constant, L_{att} varies with the distance between the cargo and the MT given by $\rho_{\text{c}} - R_{\text{MT}}$. Assuming that the motor is force-free when its three-dimensional extension is less than the three-dimensional rest length of the motor $L_{\text{kin3}}^{\text{3d}}$, the half of the attachment area is given by

$$L_{\text{att}} = \sqrt{\left(R_{\text{C}} + L_{\text{kin3}}^{\text{3d}}\right)^2 - \left(\rho_{\text{c}} - R_{\text{MT}}\right)^2}. \tag{6.50}$$

4. Move the cargo in three dimensions To update the cargo position, again the Metropolis algorithm is used. Unlike in one dimension, where the cargo is displacement only along the MT-axis, the cargo can diffuse along the MT or perpendicular to the MT symmetry axis as well as rotate around the MT. Moreover, the cargo could rotate around its center of gravity. However, because diffusion on the cargo surface is fast, it is assumed that tails of

the MT-attached motors would relax instantaneously after cargo rotation. That is why, the rotation around the center of gravity of the cargo would not have any influence and is therefore neglected. Thus, to move the cargo in the three-dimensional space, random, new φ_c-, z_c- and ρ_c-positions are proposed and the Metropolis algorithm is used to decide whether the new, proposed position is accepted or rejected.

In summary, while the same kinesin-3 model as in the one-dimensional model is used, the three-dimensional model takes real extensions of the cargo, the motors, and the MT into account and does not neglect translational degrees of freedom perpendicular and rotational degrees of freedom around the MT.

Simulation results: To understand the influence of the three dimensions, the three-dimensional liposome model is first simulated with the same parameters as the one-dimensional liposome model. For the total number of motors N_{tot}, the same values are used as when modeling the one-dimensional liposome model with all motors on the cargo surface (variant 7, see section 6.2.2 and fig. 6.24). Simulating the three-dimensional liposome model, velocity histograms (fig. 6.32a) show a low velocity peak related to the slow state and a high velocity peak related to the fast state. The high velocity peak shifts towards lower velocities for increasing total number of motors N_{tot} and merges with the low velocity peak. Mean and variance of the complete velocity distribution as well as the mean of only the fast state (fig. 6.32b) decrease with increasing total number of motors N_{tot}. A comparison with the one-dimensional modeling results (fig. 6.16) reveals that the low velocity peaks around zero are less pronounced for the three-dimensional model than for the one-dimensional model. This means the influence of inactive motors is less strong in the three-dimensional model compared to the one-dimensional model. Moreover, the mean velocities are higher and reduce less with increasing number of motors in the three-dimensional model than in the one-dimensional model. This indicates that motors hinder each other less. Consequently, the force response and the motor-motor hindrance are slightly different due to the three-dimensional geometry.

The one-dimensional liposome model showed that increasing the detachment force strengthens the inactive motors. Increasing the detachment force by $1\,\mathrm{pN}$ (from $F_d = 3\,\mathrm{pN}$ to $F_d = 4\,\mathrm{pN}$) for the three-dimensional model simulations, velocity histograms show low and high velocity peaks similar to the results from the one-dimensional liposome model (fig. 6.16a), the point-like cargo model (fig. 6.12a) and the experiment (fig. 6.2a). Moreover, mean and variance from all velocities and the mean from just the fast state (fig. 6.33c) decrease with the total number of motors N_{tot} in a similar way than seen for the one-dimensional liposome model (fig. 6.16c), the point-like cargo model (fig. 6.12c) and the experiment (fig. 6.2c). Thus, also the three-dimensional liposome model simulation can be aligned with the experimental findings.

Trajectories of the three-dimensional liposome model (fig. 6.33b) show a stop- and go-like behavior for all total numbers of motors. Duration (fig. 6.34a) and frequency of the slow state (fig. 6.34b) are similar to the results from the one-dimensional liposome model (fig. 6.17) and the point-like cargo model (fig. 6.14). The duration of the slow state is still lower than in the experiment (fig. 6.4a). Thus, the three-dimensional liposome model reproduces the slow state of the one-dimensional models.

Trajectories of the three-dimensional liposome model (fig.6.33d) are slightly shorter than for the one-dimensional liposome model (fig. 6.16) or the point-like cargo model (fig. 6.12). But trajectories are still longer than in the experiment a.o. due to infinitely long MTs in the simulation (see fig. 6.2 for experimental trajectory length and section 6.2.1 for other reasons
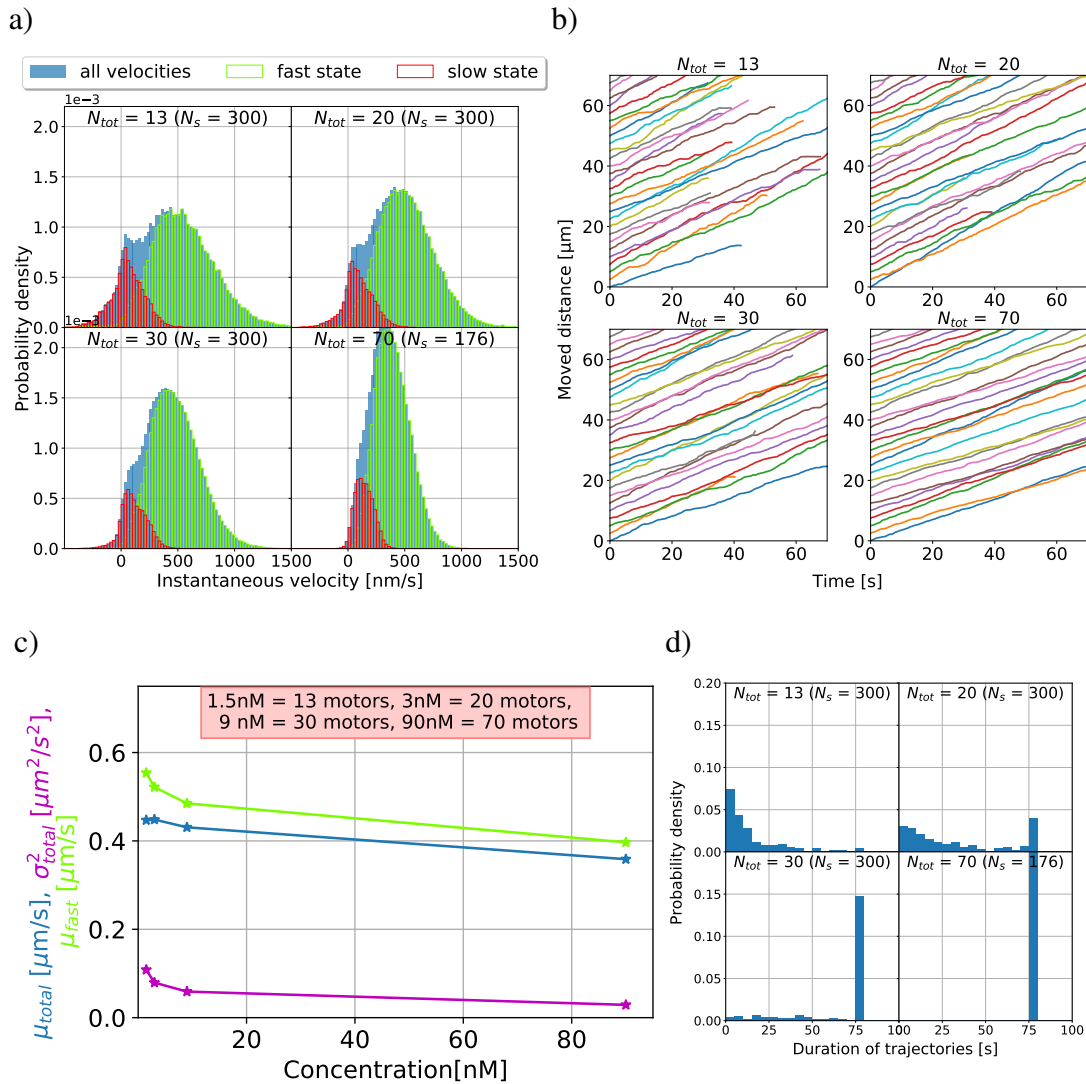
Figure 6.33: Three-dimensional liposome model with optimized parameter set. Simulation results were produced with the three-dimensional liposome model using the optimized parameter set (detachment force increased by 1 pN, see table C.1). a) Cargo velocity histograms (blue) for varying total number of motors N_{tot}. Using the segmentation algorithm (see main text and caption of fig. 6.3) trajectories can be divided into slow (red) and fast states (green). With increasing total number of motors N_{tot}, the high velocity peak moves towards smaller velocities and merges with the low velocity peak. b) Example trajectories of simulated cargos (trajectory duration longer than 30 seconds) show a stop-and-go-like motion for all varying total numbers of motors N_{tot}. c) Mean (blue) and variance (magenta) of all cargo velocities as well as mean velocities of only the fast state (green) decrease with increasing total number of motors N_{tot}. d) Histograms of trajectory durations. Trajectories are longer for higher number of motors.
The simulations were terminated either if no motor was attached to the MT anymore or after 80 seconds. Number of samples (cargos) N_s are given in brackets (a+d).

why trajectories are shorter for the experiment than for the simulation). A reason for the shorter trajectories of the three-dimensional liposome model compared to the one-dimensional

a)

b)
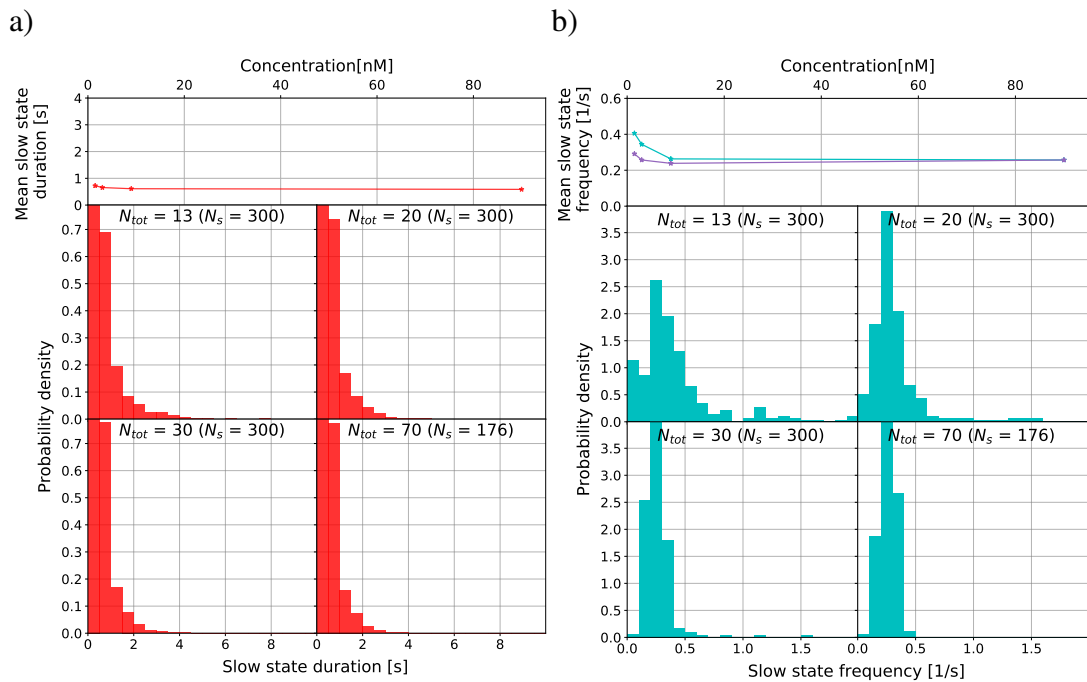
Figure 6.34: Three-dimensional liposome model with optimized parameter set: slow state.   a) Mean duration of the slow state as a function of the motor concentration and duration histograms for varying number of motors N_{tot}. The mean slow state duration is drawn as a function of the motor concentration for a better comparison with the experimental data. Mean and histograms of the slow state durations do not strongly depend on the total number of motors N_{tot}. Slow state durations are similar to the one-dimensional liposome model (see fig. 6.17a). b) Mean and histograms of slow state frequencies for varying total numbers of motors N_{tot}. The individual frequency of slow states (blue) is the number of slow states divided by the trajectory duration. The total frequency of slow states (magenta, independent of the duration of the trajectories) is total number of slow states of all simulations divided by the sum of all trajectory durations. Slow state frequencies are similar to the one-dimensional liposome model (see fig. 6.17b).
The number of samples N_{s} is given in brackets.

model might be the higher absolute values of the motor forces, which increase the detachment rate. The absolute value of the motor force is higher, because instead of using only the force component parallel to the MT length axis, in the three-dimensional model also force components perpendicular to the MT length axis contribute to the absolute value of the force. That is why forces are generally higher and detachment is enhanced.

As said before, a slow state is observed, which could be related to inactive motors. However, the origin of these inactive motors could be a geometrical effect. To find out whether the three-dimensional geometry in itself produces a slow state, the three-dimensional liposome model is simulated without inactive motors. When simulating the three-dimensional liposome model without inactive motors, the low velocity peak in the velocity histogram vanishes and almost no slow state could be detected (see fig. 6.35a). Furthermore, the mean of all velocities merges with the mean of only the velocities from the fast state (see fig. 6.35c). Consequently, the three-dimensional geometry in itself does not produce a slow velocity state of the cargo. In detail, this means neither the diffusive motor tails nor the rotation of the cargo around the

a)

b)

c)

d)
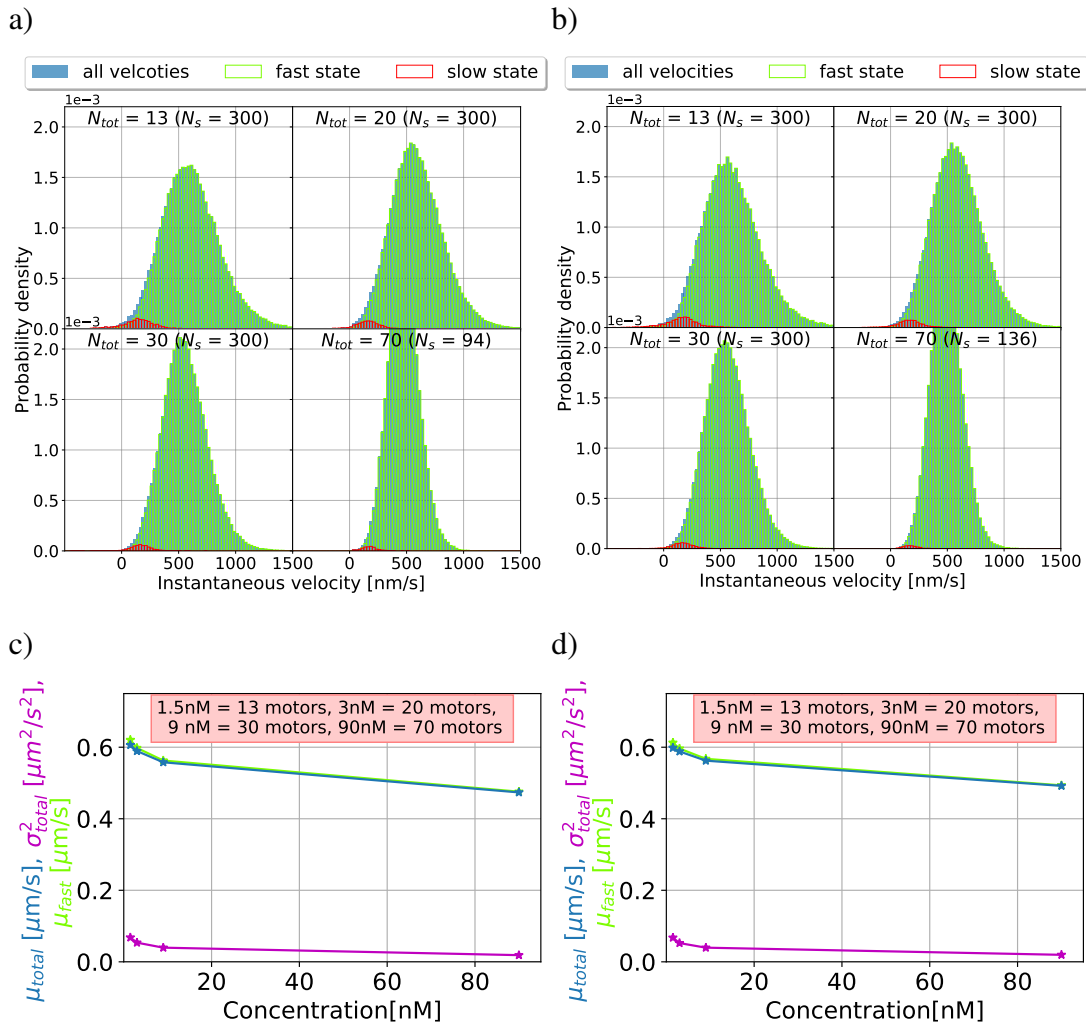
Figure 6.35: Three-dimensional liposome model: no inactive motors (and restriction on cargo position). Simulation results produced with the three-dimensional liposome model without inactive motors (a+c) and additionally a restriction on the cargo position (b+d). The restriction on the cargo position should mimic the influence of the coverslip in the experiment. In this simulation (b+d), the cargo is not allowed to move to the lower half space of the MT. Thus, it holds $\varphi_c \in [0, \pi]$. a+b) Cargo velocity histograms (blue) for varying total number of motors N_{tot}. Using the segmentation algorithm (see main text and caption of fig. 6.3) trajectories can be divided into slow (red) and fast states (green). Velocity histograms of both simulations show only a high velocity peak, but no low velocity peak. c+d) Mean (blue) and variance (magenta) of all cargo velocities as well as mean velocities of only the fast state (green) decrease with increasing total number of motors N_{tot}. Having a vanishing small slow state (see a+b), mean velocities of only the fast states are similar to the mean values of all velocities.

The simulations were terminated either if no motor was attached to the MT anymore or after 80 seconds. Number of samples (cargos) N_s are given in brackets (a+b).

MT when following the supertwist of the protofilaments cause a slow state.

So far in the simulation, the liposome and the motors can freely rotate around the MT following the supertwist of the protofilaments. In the experiment, however, the MT is fixed

on the bottom of the glass coverslip. This means the liposome cannot rotate around the MT which could cause the slow state. To test this assumption, the cargo position is restricted to the upper half space above the MT (see illustrational fig. 6.31). In detail, the cargo position is restricted to $\varphi_c \in [0, \pi]$. Not having inactive motors and not allowing the liposome to move to the underside of the MT, velocity histograms (fig. 6.35b) again show no low-velocity peak and the mean of all velocities coincides with the mean of only the velocities from the fast state (see fig. 6.35b). Velocity histograms and mean velocities are similar to velocity histograms and mean velocities from the simulation without inactive motors (fig. 6.35a and fig. 6.35c). Consequently, restricting the cargo position to the upper half space above the MT is not the reason for the slow state observed in the experiment.

While restricting the cargo to the upper half space did not cause a slow state, next it is tested whether restricting additionally the motor head positions to the upper half space would cause a slow state. Thus, in detail, motor positions are restricted to $\varphi_h^i(t) \in [0, \pi]$. When motors reach the border of the upper half space, they do not step any further, but stay attached until they are pulled off by other advancing motors. Motors at the border of the upper half space detach with the usual force-dependent detachment rates. Furthermore, motors are only allowed to attach to the upper half space above the MT. Not allowing the motors to move to the lower half space under the MT, velocity histograms show (fig. 6.36a) low velocity peaks related to a slow state and mean velocities split up in the mean of velocities from the fast state (higher) and the mean of all velocities (see fig. 6.36c). Furthermore, liposome trajectories show a stop- and go behavior (see fig. 6.36b). Thus, the slow state of the cargo motion can be reached when restricting the motors to the upper half space above the MT.

Comparing results from liposome transport with restricted motor positions (fig. 6.36) to the results from the three-dimensional liposome model with inactive motors (standard three-dimensional liposome model, fig. 6.33), it can be seen that the velocity peak of the slow state is higher for the liposome model with restrictions on the motor positions compared to the standard three-dimensional liposome model. Moreover, also the mean values of all velocities and the mean values of only the velocities from the fast states are reduced compared to the standard three-dimensional liposome model. This means, the restricted motor heads, holding back the cargo, are stronger than the inactive motors of the standard, three-dimensional liposome model. Comparing the slow state, it can be seen that durations of the slow state are similar for the three-dimensional liposome model with restrictions on the motor head positions (fig. 6.37) and the three-dimensional liposome model with inactive motors (fig. 6.34). Slow state frequencies, however, are higher in case of the three-dimensional model with restrictions on the motor positions. Consequently, motors restricted to the upper half of the MT cause slow states more often than inactive motors.

Taking together, simulations restricted to the upper half-space of the MT show that motors at the border of the upper half of the MT act like inactive motors. Thus, the hindrance by the surface could be the origin of the inactivity of a part of the motors. However, looking in more detail to the experimental set-up, it can be seen that MTs are fixed to the glass cover surface by antibodies and motors should in principle be able to pass to the lower half space of the MT. Moreover, some recent experiments using MT bridges[6] see some slow states of the liposome even though neither the liposome nor the motors should be hindered by the glass cover surface. Consequently, it is not likely that the motors restricted by the glass cover surface cause the observed slow state alone.

---

[6]In MT bridge experiments, the MT ends are placed and fixed on two pedestals such that the bulk of the MT is freely accessible and even the liposome can rotate around the MT.

Figure 6.36: Three-dimensional liposome model with restricting motor head positions to the upper half space. Figures show simulation results produced with the three-dimensional liposome model without inactive motors, but with restricting the cargo and the motor head position to the upper half space. Thus, it holds $\varphi_c \in [0, \pi]$ and $\varphi_h^i \in [0, \pi]$ for all MT-attached motors. a) Cargo velocity histograms (blue) for varying total number of motors N_{tot}. Using the segmentation algorithm (see main text and caption of fig. 6.3) trajectories can be divided into slow (red) and fast states (green). Besides a slightly more pronounced low velocity peak, histograms are comparable to the standard three-dimensional liposome model (fig. 6.33). b) Example trajectories of simulated cargos (trajectory duration longer than 30 seconds) show a stop-and-go-like motion for all varying total numbers of motors N_{tot} similar to the standard three-dimensional liposome model (fig. 6.33). c) Mean (blue) and variance (magenta) of all cargo velocities and mean velocities of only the fast state (green). Mean velocities reduce less compared to the standard three-dimensional liposome model 6.33. d) Histograms of trajectory durations are similar to the standard three-dimensional liposome model (fig. 6.33). (*Continuation on next page.*)
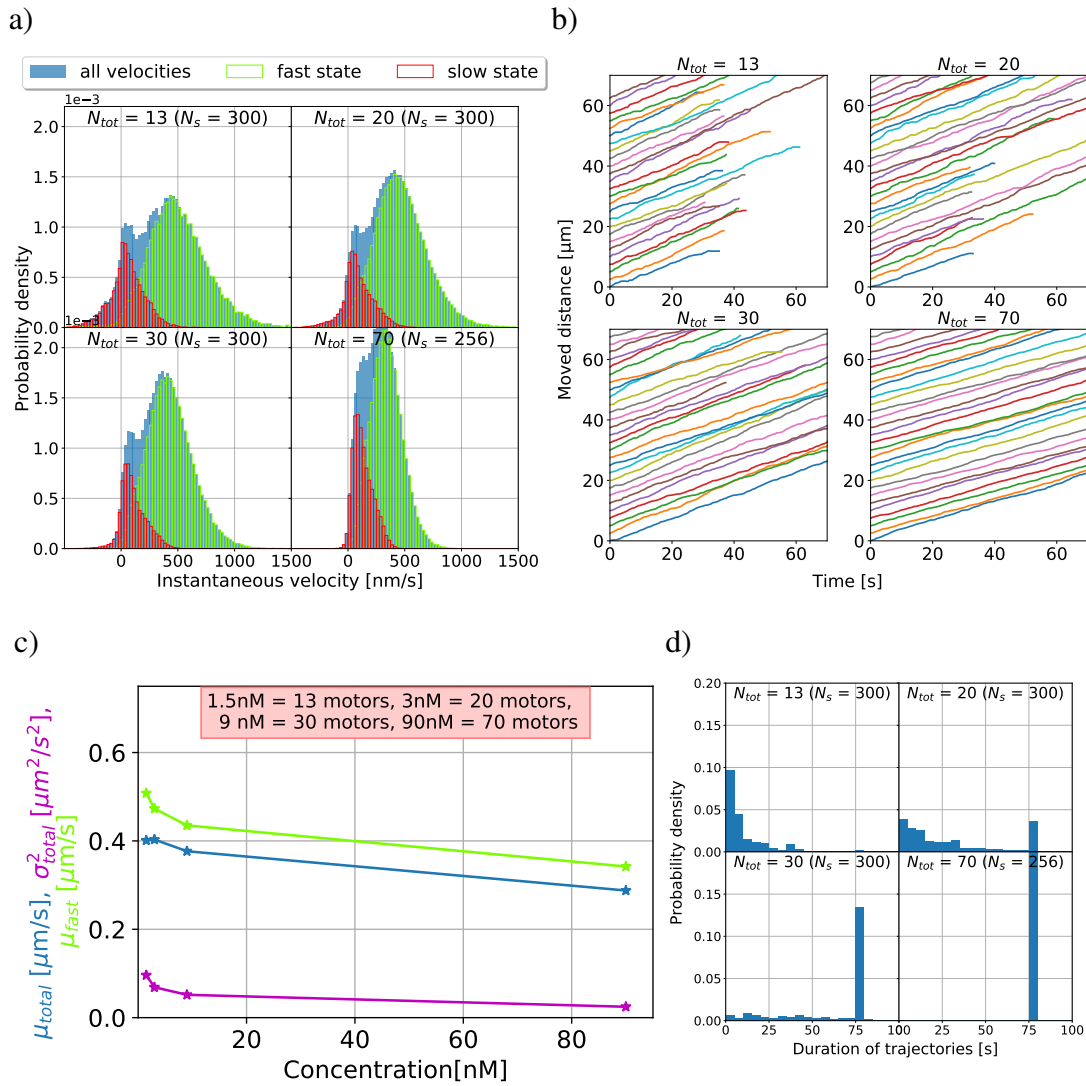
a) b)
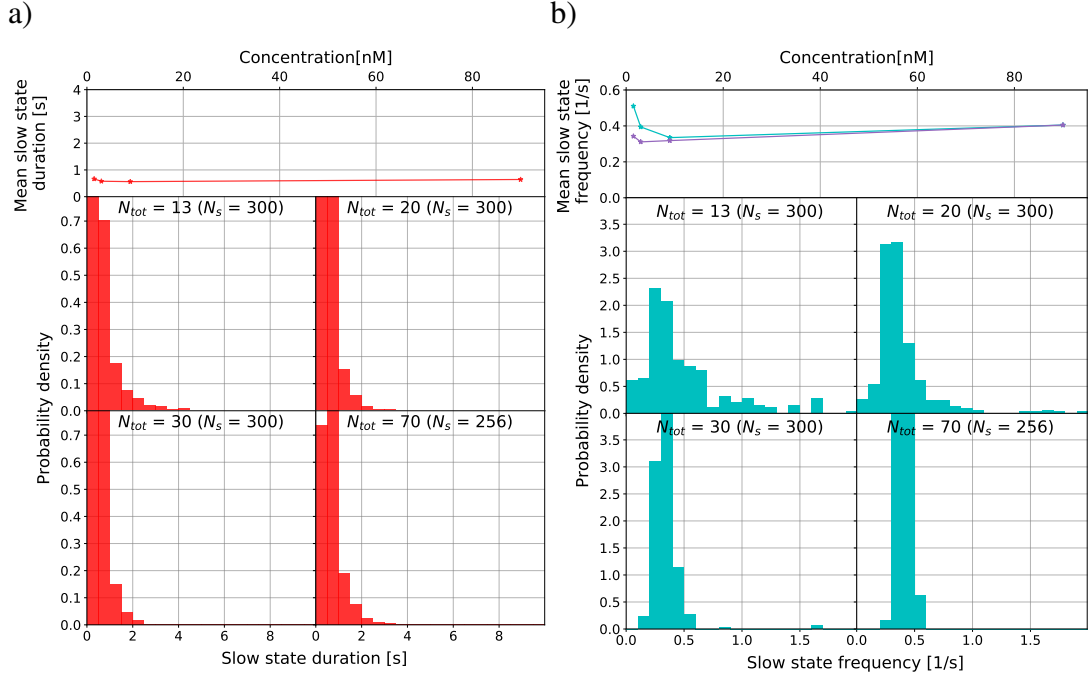
Figure 6.37: Three-dimensional liposome model with restricting motor head positions to the upper half space: slow state. Figures show simulation results produced with the three-dimensional liposome model without inactive motors, but with restricting the cargo and the motor heads to the upper half space. Thus, it holds $\varphi_c \in [0, \pi]$ and $\varphi_h^i \in [0, \pi]$ for all MT-attached motors. a) Mean duration of the slow state as a function of the motor concentration and duration histograms for varying number of motors N_{tot}. The mean slow state duration is drawn as a function of the motor concentration for a better comparison with the experimental data. Mean and histograms of slow state durations are similar to the slow state of the standard three-dimensional liposome model (see fig. 6.33). b) Mean and histograms of slow state frequencies for varying numbers of motors. The individual frequency of slow states (blue) is the number of slow states divided by the trajectory duration. The total frequency of slow states (magenta, independent of the duration of the trajectories) is total number of slow states of all simulations divided by the sum of all trajectory durations. Mean slow state frequencies are higher compared to the standard three-dimensional liposome model.
The number of samples N_s is given in brackets.

In general, simulations of this section show that non-stepping MT-attached motors cause a slow state of the cargo transport. The reason for the non-stepping of MT-attached motors could be a restriction by the glass cover surface, an inactivity of the motors, or other reasons such as defects in the MT lattice or roadblocks on the MT surface, which stop motors to further advance.

In summary, the three-dimensional liposome model with inactive motors leads to similar re-

sults as the one-dimensional liposome model, the point-like cargo model, and the experiment. Three-dimensional liposome model simulations confirm that the slow state is not caused by the diffusive motor tails due to a fluid cargo surface. Furthermore, three-dimensional simulations in the presence of the glass cover surface (constraint on the cargo position) could rule out that the slow state is due to a steric hindrance of the cargo by the glass cover surface. However, when a part of the motors stops stepping because they are hindered by the glass cover surface, a slow state of the liposome similar to the simulation with completely inactive motors can be observed. Motors could be temporarily hindered by the glass cover surface, by roadblocks on the MT, or by MT lattice defects. Together, this means, inactive motors (never step) as well as temporarily non-stepping motors (step and then stop) can cause a slow state of the liposome.

Compared to the one-dimensional model, motor forces are increased for the three-dimensional model such that detachment is enhanced. Consequently, trajectories are shorter and a slightly higher detachment force is needed to align simulation and experimental results. However, no additional effect was measured using the three-dimensional model such that the simpler, one-dimensional model is a valid approach to study liposome transport.

6.3.2 Bead model

The one-dimensional bead model showed before (see section 6.2.3) that the variance of velocities per trajectory depends on how much the configuration of motors, which are able to attach the MT, changes during the simulation. The one-dimensional bead model was once simulated with a constant motor configuration and once with a changing motor configuration, where the activity status and the force-free velocity were reset each time a motor reattaches. These scenarios are the two extreme cases. To obtain realistic changes in the motor configuration, the rotation of the bead around its center of gravity and around the MT needs to be modeled. Therefore, a three-dimensional bead model is developed in the following.

Three-dimensional bead model   The three-dimensional bead model is based on the three-dimensional liposome model. Changes that need to be made compared to the three-dimensional liposome model are as follows:

1. The bead (cargo) orientation needs to be taken into account.

2. The explicit motor tail positions on the cargo need to be taken into account.

3. Motor forces are determined by the explicit motor tail positions.

4. MT attachment is determined by the explicit motor tail positions.

5. Bead orientation needs to be updated.

1. Bead orientation   The bead is modeled as a rigid body (rigid sphere) characterized by its center of gravity position $\underline{\mathbf{X}}_c(t)$ and the orientation of its body-fixed coordinate system. The bead orientation (z-axis of the body-fixed coordinate system of the bead) is given in spherical coordinates:

$$\underline{\tilde{\mathbf{n}}}_c(t) = \begin{pmatrix} \cos(\Phi_c)\sin(\Theta_c) \\ \sin(\Phi_c)\sin(\Theta_c) \\ \cos(\Theta_c) \end{pmatrix}. \tag{6.51}$$

Thus, the orientation is characterized by $\{\Phi_c, \Theta_c\}$. See fig. 6.38 for an illustration of the geometry.

2. Explicit motor tail positions   To explicitly model the motor tails on the bead, N_{tot} motors are created with given tail positions on the surface of the bead, given force-free forward velocities, and given states: active or inactive. Again, a motor is inactive with probability $p = 0.2$. Motor tails are uniformly distributed on the bead surface. The polar and azimuth angles of uniformly distributed positions on a sphere are (see chapter 3):

$$\varphi_t = 2\pi u \quad \text{and} \quad \theta_t = \arccos(2u - 1) \tag{6.52}$$

where u is a uniformly distributed random variable between 0 and 1. With the polar and azimuth angles φ and θ, the motor tail positions in the body-fixed coordinate system of the bead are as follows:

$$\underline{\tilde{\mathbf{x}}}_t^i(t) = \begin{pmatrix} R_c\cos(\varphi_t)\sin(\theta_t) \\ R_c\sin(\varphi_t)\sin(\theta_t) \\ R_c\cos(\theta_t) \end{pmatrix} \tag{6.53}$$
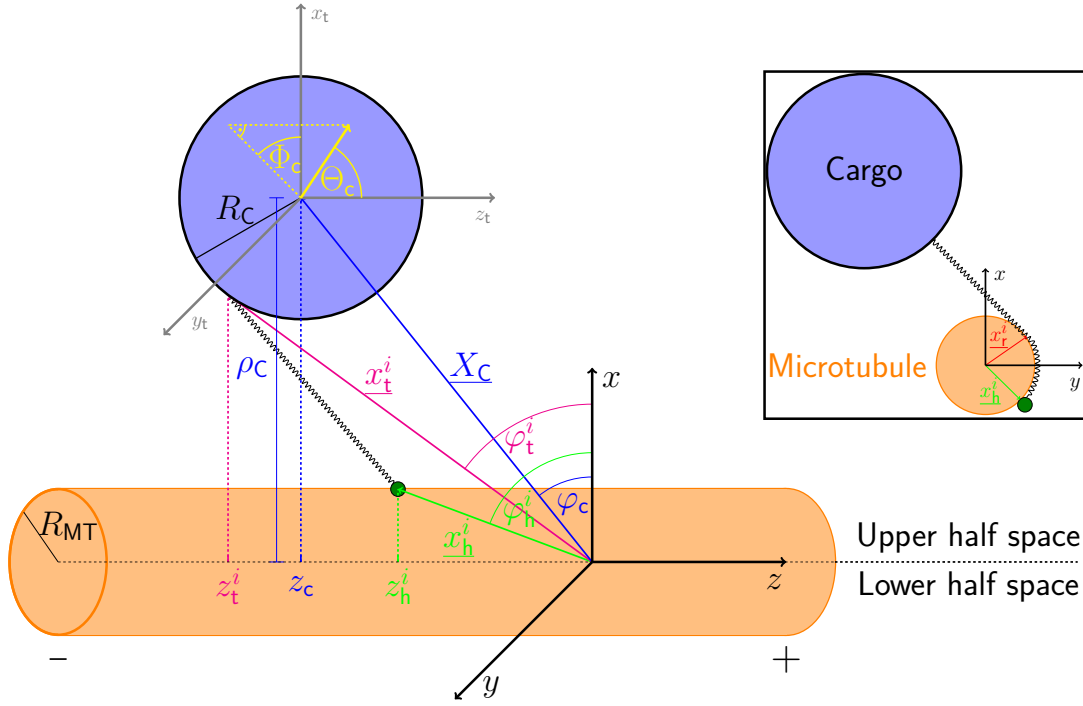
Figure 6.38: Three-dimensional bead model: illustration of geometry. Illustration shows the three-dimensional geometry of the bead model. The global coordinate system (black) is chosen such that the symmetry axis of the MT (orange cylinder with radius R_{MT}) is identical to the z-axis and the MT plus-end points in positive z-direction. The cargo (blue circle with radius R_C) has the position $\underline{X}_C$ (blue) and the motor heads (green dots) the position $\underline{x}_h{}^i$ (green). To describe any position in the global coordinate system, cylindrical coordinates (ρ, φ, z) are chosen. The orientation (yellow) of the body fixed coordinate system (gray) of the bead is determined by $\{\Phi_c, \Theta_c\}$ in the global coordinate system. The motor tail positions are denoted by $\underline{x}_t{}^i$ (magenta) in the global coordinate system. The inset (upper right corner) shows a motor, which is partly winded around the MT. $\underline{x}_r^i(t)$ (red) is the point where the motor meets the MT and $\underline{x}_h^i(t)$ (green) is the motor head position on the MT.

whereby, R_c is the radius of the sphere.

3. Motor forces   To calculate the motor extension and the motor force, the motor tail position is needed in the global coordinate system. Motor extensions are given by the difference between the motor tail and motor head positions in the global coordinate system. To obtain the motor tail positions in the global coordinate system $\underline{x}_t^i(t)$ (see illustrational fig. 6.38), the motor tail position in the body-fixed coordinate system of the bead $\underline{\tilde{x}}_t^i(t)$ needs to be rotated according to the orientation of the bead $\{\Phi_c, \Theta_c\}$ and translated by the center of gravity position of the bead $\underline{X}_c(t)$:

$$\underline{x}_t^i(t) = \underline{R}_z(\Theta_c)\underline{R}_y(\Phi_c)\,\underline{\tilde{x}}_t^i(t) + \underline{X}_c(t). \tag{6.54}$$

The rotation matrices are given by

$$\underline{R}_y(\Phi_c) = \begin{pmatrix} \cos(\Phi_c) & 0 & \sin(\Phi_c) \\ 0 & 1 & 0 \\ -\sin(\Phi_c) & 0 & \cos(\Phi_c) \end{pmatrix} \tag{6.55}$$

and

$$\underline{\underline{R}}_z(\Theta_c) = \begin{pmatrix} \cos(\Theta_c) & -\sin(\Theta_c) & 0 \\ \sin(\Theta_c) & \cos(\Theta_c) & 0 \\ 0 & 0 & 1 \end{pmatrix}. \tag{6.56}$$

As for the three-dimensional liposome model, it has to be distinguished whether i) the motor head is in the same half-space of the MT as the motor tail ($\varphi_h \in \varphi_t \pm \frac{\pi}{2}$) or ii) whether the motor is partly winded around the MT (see illustrational fig. 6.38) If the head is in the same half-space of the MT as the motor tail, the motor extension is

$$|\underline{\Delta x}^i(t)| = |\underline{x}_h^i(t) - \underline{x}_t^i(t)| \tag{6.57}$$

and the direction of the motor force is

$$\underline{e}_f = \frac{\underline{x}_h^i(t) - \underline{x}_t^i(t)}{|\underline{x}_h^i(t) - \underline{x}_t^i(t)|}. \tag{6.58}$$

If the motor is partly winded around the MT, the auxiliary point

$$\underline{x}_r^i(t) = \begin{pmatrix} R_{MT}\cos(\varphi_r) \\ R_{MT}\sin(\varphi_r) \\ z_r \end{pmatrix} \tag{6.59}$$

is needed. The auxiliary point $\underline{x}_r$ is the point on the MT, where the motor first meets the MT when coming from the cargo. The polar angular of the auxiliary point is given by $\varphi_r = \varphi_t \pm \frac{\pi}{2}$ depending on the direction of the winding. The z-position of the auxiliary point has to be found by minimizing the total motor extension

$$|\underline{\Delta x}^i(t)| = |\underline{x}_r^i(t) - \underline{x}_t^i(t)| + \mathcal{G}(\underline{x}_h^i(t), \underline{x}_r^i(t)) \tag{6.60}$$

(see section 6.3.1). The total motor extension is composed of the difference between the motor tail and the auxiliary point, and the geodesic $\mathcal{G}(\underline{x}_h^i(t), \underline{x}_r^i(t))$ around the MT (see section 6.3.1, eq. (6.33- 6.38)). The direction of the motor force is given by

$$\underline{e}_f = \frac{\underline{x}_r^i(t) - \underline{x}_t^i(t)}{|\underline{x}_r^i(t) - \underline{x}_t^i(t)|}. \tag{6.61}$$

To calculate the motor force, the motor extension $|\underline{\Delta x}^i(t)|$ and the direction of the motor force $\underline{e}_f$, has to be plugged in in eq. (6.39).

4. MT attachment   For stepping and detachment rates the same dependencies on the three-dimensional motor forces as for the three-dimensional liposome model are used (see section 6.3.1) and for the attachment the same, force-independent attachment rate. However, due to the diffusive motor tails in the three-dimensional liposome model, motors could attach over a wide range along the MT (see section 6.3.1 for L_{att} of the three-dimensional liposome model and table C.1 of appendix C). For the bead, on contrary, the motor tail positions are fixed such that motors can only attach around these given positions $\underline{x}_t^i(t)\underline{e}_x \pm L_{att}$. The half of the attachment area L_{att} is thereby given by:

$$L_{att} = \sqrt{\left(L_{kin3}^{3d}\right)^2 - \left(\underline{x}_t^i(t)\underline{e}_\rho - R_{MT}\right)^2} \tag{6.62}$$

such that at the borders of the attachment area the motor extension is equal to the three-dimensional motor rest length L_{kin3}^{3d}. Since it is more likely to attach to the MT directly under the motor tail position than further away, a truncated Gaussian is used to find the z- and φ-position of the attaching motor head on the MT. The means of the Gaussians are z_t and φ_t, respectively, and the standard deviation is chosen such that the force-free regime ($|\underline{\Delta\mathbf{x}}^i(t)| \leq L_{kin3}^{3d}$) ends at 3σ. Furthermore, exclusion effects on the MT are taken into account such that for a motor to bind, the chosen motor head position on the MT needs to be empty.

5. Update bead orientation   In the harmonic potential of MT-attached motors, the bead can translate in φ_c-, z_c- and ρ_c-directions and rotate around its center of gravity (bead orientation). To translate and rotate the bead, the Metropolis algorithm is used (see chapter 3). When translating the bead, random new values for φ_c, z_c and ρ_c are proposed and either taken as new bead positions or rejected according to the Metropolis algorithm. When rotating the bead around its center of gravity, the z-axis of the body-fixed coordinate system of the bead (denoting the bead orientation) is moved along a randomly chosen geodesic on the surface of the bead (in the global coordinate system). The geodesic has a small, random length of $\ell = R_c\beta$ with β being uniformly distributed between 0 and $\Delta\beta < \pi$ and a uniformly distributed random direction $\alpha \in [0, 2\pi)$ in the tangential circle at the z-axis of the body-fixed coordinate system of the bead. If the z-axis of the body-fixed coordinate system of the bead (bead orientation) is described by $\underline{\mathbf{e}}_r(\Theta_c, \Phi_c)$, $\underline{\mathbf{e}}_\theta(\Theta_c, \Phi_c)$ and $\underline{\mathbf{e}}_\varphi(\Phi_c)$ in the global coordinate system, the proposed new orientation of the z-axis of the body-fixed coordinate system of the bead is

$$\underline{\mathbf{p}} = R_c \left(\cos(\beta)\underline{\mathbf{e}}_r + \sin(\beta)\left(\cos(\alpha)\underline{\mathbf{e}}_\theta + \sin(\alpha)\underline{\mathbf{e}}_\varphi \right) \right). \tag{6.63}$$

The proposed orientation angles are then

$$\Theta_{c,p} = \arccos(p_z/\sqrt{p_x^2 + p_y^2 + p_z^2}) \quad \text{and} \quad \Phi_{c,p} = \arctan(p_y/p_x). \tag{6.64}$$

Again the Metropolis algorithm is used to decide whether the proposed orientation is accepted or rejected.

Taking together, the three-dimensional bead model is based on the three-dimensional liposome model but takes explicitly given motor tail positions on the bead surface into account. Moreover, the bead is able to rotate around its center of gravity in the harmonic potential of MT-attached motor springs such that the configuration of motors, being able to attach the MT, can change over time.

Simulation results: For the three-dimensional bead model simulations, the same number of motors and the same parameters as for the three-dimensional liposome model are used (see table C.1 of the appendix C)[7]. In the following, the bead simulation results will therefore be compared to the three-dimensional liposome model.
Velocity histograms of the three-dimensional bead model (fig. 6.39a) show low velocities which can be related to a slow state and high velocities which can be related to a fast state. For none of the number of motors, two clearly separated low and high velocity peaks could be seen. Thus, the low and fast velocity peaks already merge for the lowest number of motors.

---

[7]The detachment force of the three-dimensional liposome model is 1 pN higher than for the one-dimensional liposome and the bead model. It is therefore hard to directly compare the three-dimensional bead model with the one-dimensional bead model.
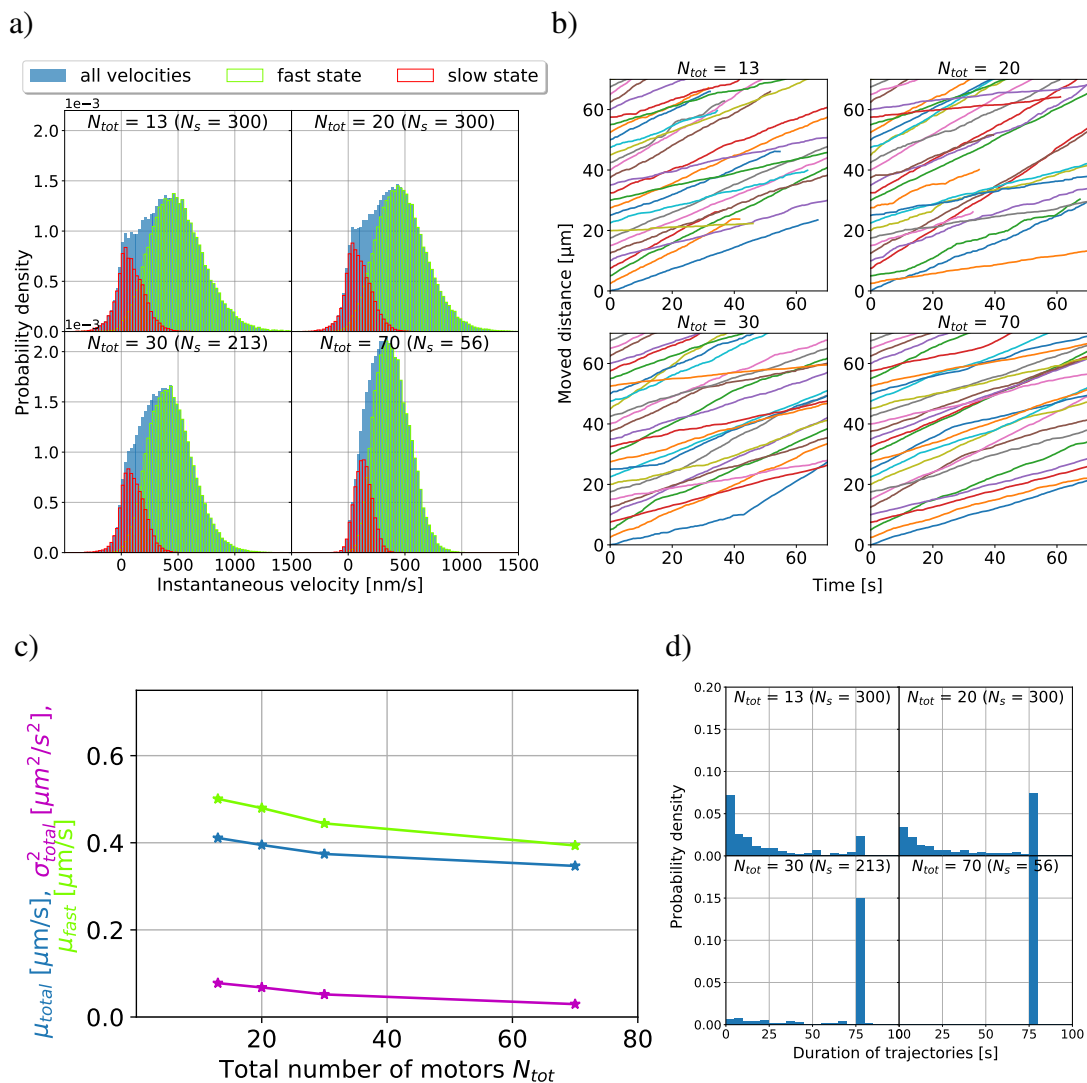
Figure 6.39: The three-dimensional bead model. Simulation results were produced with the three-dimensional bead model using the same parameter set as for the three-dimensional liposome model (see table C.1 of appendix C for parameter values). a) Cargo velocity histograms (blue) for varying total number of motors N_{tot}. Using the segmentation algorithm (see main text and caption of fig. 6.3) trajectories can be divided into slow (red) and fast states (green). Histograms do not show two separated low and high velocity peaks, but a wide distribution with velocities from slow and fast states. b) Example trajectories of simulated cargos (trajectory duration longer than 30 seconds) show a stop-and-go-like motion for all varying total numbers of motors N_{tot}. Occasionally, beads almost do not move at all or at very low velocities. c) Mean (blue) and variance (magenta) of all cargo velocities as well as mean velocities of only the fast state (green) decrease with increasing total number of motors N_{tot}. d) Histograms of trajectory durations. Trajectories are longer the higher the number of motors and slightly shorter than for the three-dimensional liposome model (fig. 6.33d).

The simulations were terminated either if no motor was attached to the MT anymore or after 80 seconds. Number of samples (cargos) N_s are given in brackets (a+d).

For the three-dimensional liposome model at least for the lowest number of motors two more separated peaks are visible (fig. 6.33a). As usual, variance and mean values of all velocities and mean values of velocities from the fast state (fig. 6.39c) decrease with increasing number of motors. Comparing mean values from liposome and bead models reveals that the bead

a)

b)
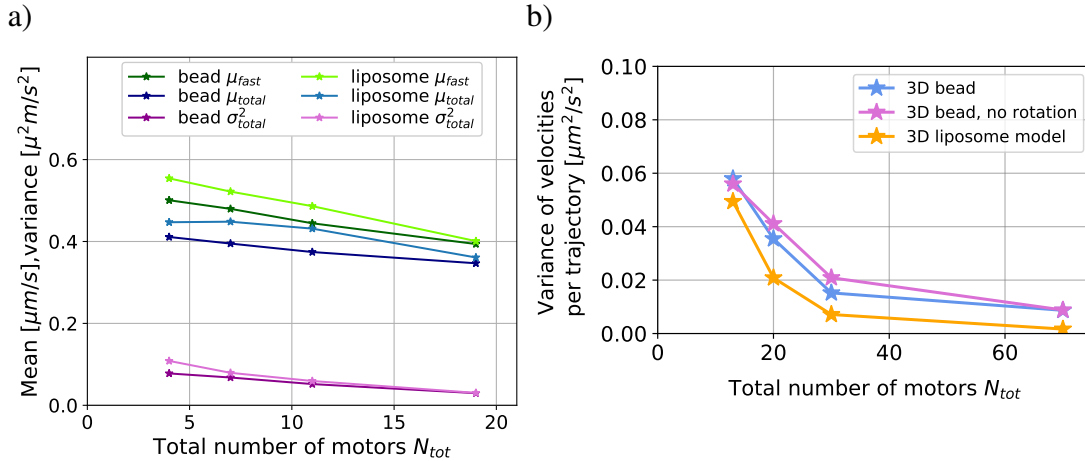
Figure 6.40: Three-dimensional models: comparison between bead and liposome. a) Mean (blue) and variance (magenta) of all cargo velocities as well as mean velocities of only the fast state (green) are depicted. Values from the liposome model are depicted in slightly lighter colors. Liposomes are transported at higher mean velocities compared to the bead. b) Variance of velocities per trajectory as a function of the total number of motors N_{tot} for the three-dimensional bead model (blue), the three-dimensional bead without random rotations of the bead around its center of gravity (magenta) and the three-dimensional liposome model (yellow). Variances are higher for the bead model compared to the liposome. Variances are even slightly higher, when not allowing the bead to randomly rotate around its center of gravity.

is transported at lower overall mean velocities and lower fast-state mean velocities (see fig. 6.40a). Lower mean velocities in the fast state explain why the histograms (fig. 6.39a) show a merged slow and fast state velocity peak rather than two separate low and high velocity peaks. While in three dimensions the liposome is transported faster than the bead, in one dimension the bead showed slightly higher mean velocities of the fast state than the liposome. Less MT-attached motors for the one-dimensional bead model lead to reduced exclusion effects and explained the slightly higher mean velocities in the fast state. For the three-dimensional models, again significantly fewer motors are attached for the bead (fig. 6.41a) than for the liposome (fig. 6.41b). In case of the liposome model, motors diffuse on the cargo surface. Therefore, additional motors can diffuse to the attachment area on the cargo and attach to the MT. That is how the number of MT-attached motors can be enhanced for the liposome model. In case of the bead model, motor tails have fixed positions on the cargo surface. Therefore, no additional motors can diffuse in the attachment area on the cargo and enhance the MT-attached number of motors. Additionally, in case of the bead, motor tails cannot slide to the positions on the cargo surface, where motor extensions are minimized how it is the case for the liposome model. Therefore, forces are generally higher leading to an enhanced detachment of motors in case of the bead. Consequently, fewer motors are attached to the MT for the bead than for the liposome model.

a)

b)
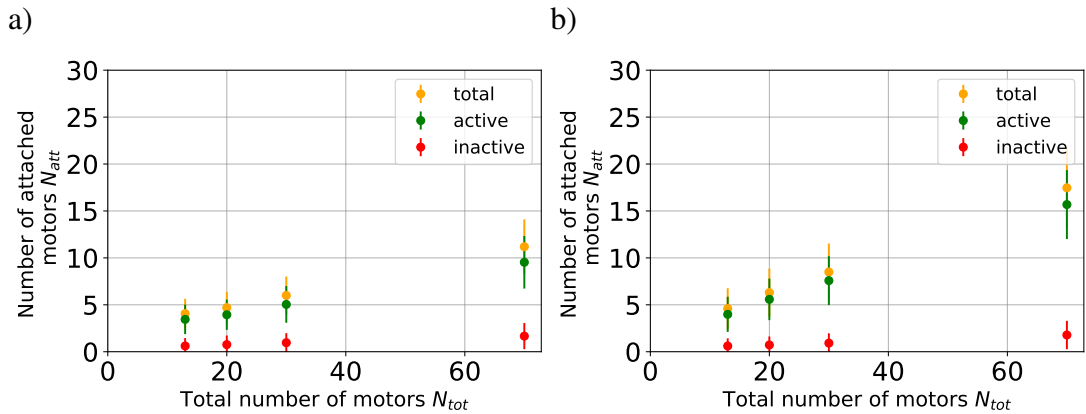
Figure 6.41: Three-dimensional models: MT-attached motors for beads and liposomes. Figures show the number of total (yellow), active (green), and inactive (red) MT-attached motors as a function of the total number of available motors N_{tot} for the three-dimensional bead model (left) and the three-dimensional liposome model (right). Number of all kind of motors increases with increasing total number of motors N_{tot}. Numbers of active MT-attached motors are higher in the liposome model compared to the bead model, while the number of inactive MT-attached motors is similar.

However, even though fewer motors are attached, velocities are lower for the bead than for the liposome model. Since fewer motors are attached, exclusion effects cannot be the reason for the lower velocities. This means, transport, i.e. stepping of the motors needs to be reduced for another reason. The stepping rates of the motors are force-dependent (see section 6.2.1 for the kinesin-3 model). Consequently, as enhanced motor forces in case of the bead lead to higher detachment rates, enhanced motor forces also lead to reduced stepping rates. The reduced stepping rates lead to lower transport velocities of the bead than the liposome in three dimensions.

Note that for the highest total number of motors, differences in mean velocities from beads and liposomes are negligible, while the difference in MT-attached motor numbers is maximal. Mean velocities are similar because even though stepping is reduced due to higher forces for the bead, the higher number of MT-attached motors for the liposome increases exclusion effects. Thus, the two effects, exclusion (liposome) and reduced stepping rates due to higher forces (bead) balance each other at the highest number of motors resulting in similar velocities for beads and liposomes.

The question arises why is the bead faster than the liposome in the one-dimensional model, but slower in the three-dimensional model. While reduced exclusion effects are the dominant effect in one dimension, reduced stepping rates due to higher motor forces are the dominant effect in three dimensions. The reduced stepping rates due to higher forces are more pronounced for the three-dimensional bead model than for the one-dimensional bead model because first, forces are higher due to the three dimensions and second, the applied detachment force is higher for the three-dimensional bead model. While for the one-dimensional bead model, the detachment force is $F_{\mathrm{d,kin3}} = 3\,\mathrm{pN}$, the detachment force is $F_{\mathrm{d,kin3}} = 4\,\mathrm{pN}$ for the three-dimensional model[8]. A higher detachment force means that motors experience higher

---

[8]For a comparison with the three-dimensional liposome model, the same detachment force as for the liposome model is applied. For the liposome model the detachment force has been increased by $1\,\mathrm{pN}$ to better align
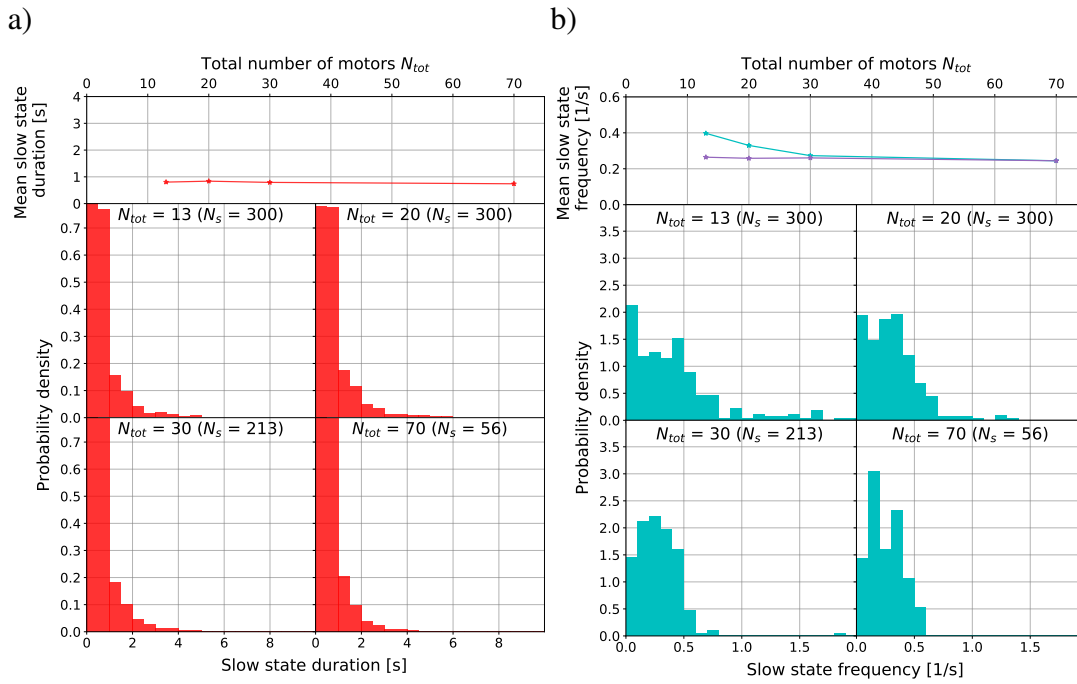
Figure 6.42: Three-dimensional bead model: slow state. Figures show simulation results produced with the three-dimensional bead model. a) Mean and histograms of durations of the slow state as a function of varying total number of motors on the cargo N_{tot}. Mean slow state durations remain constant under varying total numbers of motors and are similar to the slow state durations of the three-dimensional liposome model (fig.6.34a). b) Mean and histograms of slow state frequencies for varying total numbers of motors N_{tot}. The individual frequency of slow states (blue) is the number of slow states divided by the trajectory duration. The total frequency of slow states (magenta, independent of the duration of the trajectories) is total number of slow states of all simulations divided by the sum of all trajectory durations. Slow state frequencies are similar to the three-dimensional liposome model (fig.6.34b).

The number of samples N_s is given in brackets.

forces before they detach. Having a stall force of $F_{s,kin3} = 5\,\text{pN}$ and a detachment force of $F_{s,kin3} = 4\,\text{pN}$, fig. 6.8 shows that the motor stops before the detachment rate starts to strongly increase. Consequently, the mean forces motors experience are higher and stepping is reduced more. The higher force due to the three dimensions and due to the higher detachment force $F_{d,kin3} = 4\,\text{pN}$ is the reason why the reduced stepping due to higher forces dominates over the reduced exclusion effects for the three-dimensional model.

Comparing the length of trajectories for the three-dimensional bead model (fig. 6.39d) with the three-dimensional liposome model (fig. 6.33d), it can be seen that trajectories are shorter for the bead. Trajectories are shorter for the bead because fewer motors are attached due to higher forces. This means the fixed motor tail positions lead to a less robust transport.

Trajectories (fig. 6.39b) of the three-dimensional bead model show a stop- and go-like motion. Slow state duration (fig. 6.42a) and frequencies (fig. 6.42b) of the three-dimensional bead model are similar to the three-dimensional liposome model (fig. 6.34). This confirms that the

liposome experimental simulation results.

slow state is not related to the way the motor tails are bound to the cargo (diffusive or fixed). When comparing trajectories of the three-dimensional bead (fig. 6.39b) and liposome models (fig. 6.33b), it can be seen that liposome trajectories are more parallel, while some bead trajectories are overall slower than others. A comparison of the variance in velocities per trajectories (fig. 6.40b) demonstrates that the variance is higher for the bead than for the liposome model. The higher variance in the velocities per trajectory stems from a lower variation in the configuration of motors being able to attach the MT. While for the liposome model, motors can diffuse from the other side of the cargo into the attachment area and thereby change the configuration of motors being able to attach the MT, for the bead the motor configuration can only be changed when the bead randomly rotates around its center of gravity or when the orientation of the bead to the MT changes. Different motors differ in their force-free velocities and their activity status. That is why, the variance in velocities per trajectory is less for the bead model and reduces the robustness of the bead transport compared to the liposome transport.

In the one-dimensional bead model, only the two extreme cases of constant motor configuration versus a completely changing motor configurations (unrealistic) could be modeled. The variance in velocities per trajectories of the three-dimensional bead model lies between
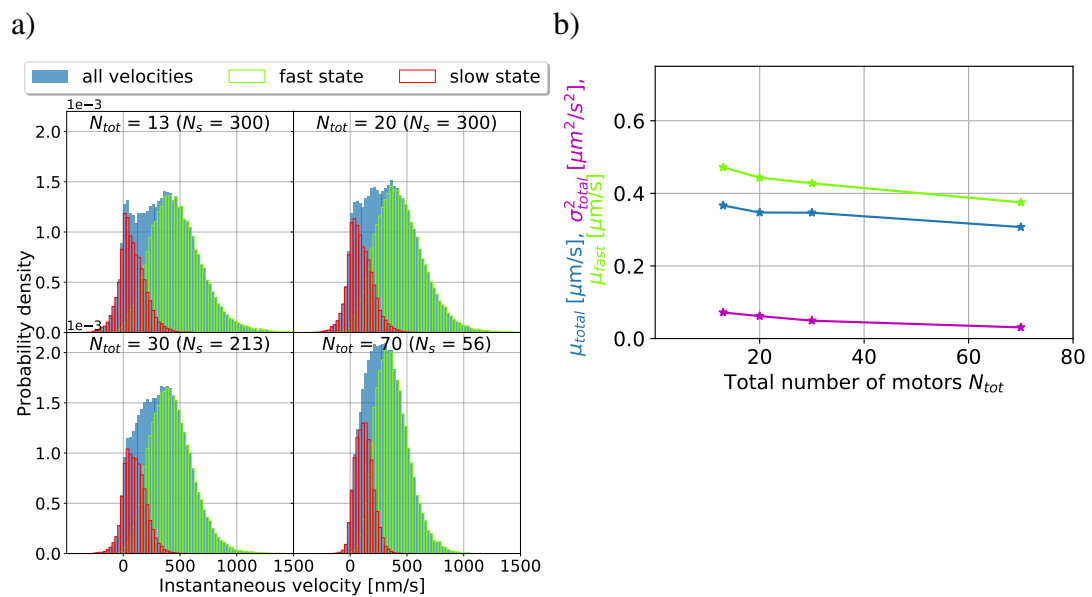
Figure 6.43: Three-dimensional bead model: no rotation of the bead around its center of gravity.
Simulations were produced with the three-dimensional bead model when not allowing the bead to randomly rotate around its center of gravity. a) Cargo velocity histograms (blue) for varying total number of motors N_{tot}. Using the segmentation algorithm (see main text and caption of fig. 6.3) trajectories can be divided into slow (red) and fast states (green). Velocity peaks from the slow states are more pronounced than compared to the bead model with rotation (fig. 6.39a). b) Mean (blue) and variance (magenta) of all cargo velocities as well as mean velocities of only the fast state (green) decrease with increasing total number of motors N_{tot}. Mean velocities are reduced compared to the bead model with bead rotation around its center of gravity (fig. 6.39c).

The simulations were terminated either if no motor was attached to the MT anymore or after 80 seconds. Number of samples (cargos) N_s are given in brackets (a).

two extreme cases of the one-dimensional model and gives more realistic values of the variance in velocities per trajectory (compare fig. 6.40b with fig. 6.30[9]). Not allowing the bead to randomly rotate around its center of gravity, shows only slightly increased variances of velocities per trajectory (see fig. 6.40b). This means the major effect changing the configuration of motors being able to attach the MT is the changing orientation of the bead towards the MT. When the bead is transported along the MT by kinesin-3 motors, it follows the protofilament axis which has a super twist around the MT. Thus, by rotation around the MT, the bead changes its orientation towards the MT, which results in a change in the configuration of motors being able to attach the MT. In summary, the rotation leads to fewer variances in the velocities per bead and therefore to a more robust transport.

Moreover, when not allowing the bead to randomly rotate around its center of gravity, mean velocities are reduced (fig. 6.43b) and velocity histograms show a higher low-velocity peak related to the slow state (see fig. 6.43a). This means active motors are less successful in pulling off inactive motors. It has been seen that mean velocities are reduced for the bead because of higher forces reducing the stepping rates. Not allowing the bead to rotate around its own axis, is expected to increase the forces even more and, therefore, reduce the stepping rates. However, in order to pull off inactive motors, active motors need to advance the bead. Thus, reducing the stepping rates results in active motors being less successful in pulling off inactive motors. Consequently, the rotation supports active motors to pull off inactive motors and leads to a more robust transport with higher mean velocities.

Taking together, studying the three-dimensional bead model reveals that besides exclusion effects influencing transport velocities, also reduced stepping rates of individual motors due to higher motor forces lower transport velocities. The latter effect is found to overall reduce transport velocities for the bead even though fewer motors are attached than for the liposome model. Less MT-attached motors, additionally, lead to shorter transport trajectories. Moreover, variances of velocities per trajectory are higher for the bead than for the liposome. Thus, transport depends more on the local motor configuration for the bead than for the liposome. To conclude, the fixed motor tail positions on the bead lead to higher forces and therefore less efficient transport due to reduced transport velocities and shorter trajectory lengths.

---

[9]Note that the detachment force F_{d} of the three-dimensional bead model is enhanced by 1 pN compared to the one-dimensional bead model, to be comparable to the three-dimensional liposome model. A by 1 pN different detachment force is not expected to drastically change the variance of velocities per trajectory.

6.4 Discussion

This chapter addressed the question of how the cargo surface, i.e., fluid or rigid, influences unidirectional cargo transport by kinesin-3. In detail the question was whether the diffusion of motor tails on fluid cargo surfaces changes the transport compared to motor tails which have fixed positions on the surface (rigid cargo). Studying cargo transport in one and three dimensions revealed that two antagonistic effects play a role. On one hand exclusion effects, i.e. sterical motor-motor hindrance on the MT, influence transport velocities. In detail, the more motors are attached to the MT, the more they hinder each other to step and the more the velocity is reduced. For the liposome, i.e. the fluid cargo with diffusive motor tails, more motors are attached to the MT than for the bead, i.e. the rigid cargo with fixed motor tails. This is in agreement with previous theoretical studies [250, 251]. There are two possible reasons why more motors are attached for the liposome than for the bead. First, due to motor diffusion on the cargo surface, motors could accumulate in the attachment area on the cargo. Second, due to the flexible (diffusive) motor tail position on the cargo surface motors can slide on the cargo surface and therefore reduce motor forces. Reduced motor forces lead to a reduced detachment. Consequently, more motors stay attached. A lower detachment is in agreement with the study by Sarpangala and Gopinathan [251]. The antagonistic effect to the exclusion effect is that on the other hand the enhanced/reduced forces lead to reduced/enhanced stepping rates, which has a direct influence of the transport velocities. For the bead, on one hand less motor are attached such that exclusion effects are reduced and the bead could be transported at higher velocities. On the other hand, forces are enhanced, such that stepping rates and therefore transport velocities would be reduced.

In one dimension these two antagonistic effects balance each other such that the mean transport velocities from beads and liposomes did not show a significant difference. In three dimensions, the reduced stepping due to higher motor forces dominates such that the bead velocity was reduced compared to the liposome. In three dimensions the used detachment force was 1 pN higher for both, beads and liposomes. This might be the reason why the reduced stepping due to higher motor forces dominates over the reduced exclusion effects in three-dimensions bead modeling. To better adjust the parameter set, further experiments are needed that study bead transport by kinesin-3 and kinesin-3 stall and detachment forces.

As said before, the force response is different for beads and liposomes, i.e. the cargo surface influences the number of MT-attached motors. The number of MT-attached motors also influences the duration of the transport. The more motors are attached the longer and farther the cargo is transported. Thus, the cargo surface regulates the robustness of the cargo transport.

Liposome transport experiments showed a stop-and-go-like motion. Using a segmentation algorithm, trajectories could be segmented into a slow and a fast state. The here presented simulations ruled out that the diffusive/fixed motor tails positions cause such a slow state. Instead, it was shown that for the slow state inactive, i.e. non-stepping motors are needed. Reasons for motors not to step could be that motors are not activated, motors are hindered by a roadblock or motors do not advance because of MT lattice defects or deformations. *In vivo*, it is also expected that roadblocks, MT lattice defects, not activated motors, or passive cross-linking proteins are present. Moreover, it was shown that the slow state is similar for bead and liposome transport. Slow states are achieved when non-stepping (here called inactive) motors are holding the cargo back. Thus, a slow state is a tug-of-war between active and inactive motors. When active and inactive motors are bound the same way to the cargo

(diffusive/fixed), both active and inactive motors are influenced by the cargo surface similarly and the tug-of-war is not changed. The same would be expected when having a tug-of-war between opposing motors with a similar way of binding motors to the cargo surface. This implies, as long as opposing motors are bound to the cargo in the same way, the tug-of-war between opposing motors would not be changed. Only, when opposing motors would be differently bound to the cargo (diffusive vs. fixed), the way they are bound would be expected to change the force response and therefore the force balance. The study of bidirectional transport (see chapter 4) showed first that the number of motors determines transport direction and second that factors influencing the force balance are expected to regulate the directionality of bidirectional transport. The way they are bound would therefore be expected to regulate the directionality of bidirectional transport.

Previous studies found higher cargo velocities for bigger cargos [88, 324]. The simulation results presented here confirm these findings for transport in the presence of inactive motors. Here, it is found that even though, inactive motors hinder the active motors more for bigger cargos, the overall exclusion effects are reduced. That is why, bigger cargos are transported at slightly higher velocities. Besides the cargo size, this work showed that also the stall and detachment force influences the cargo transport.

As previously stated, the number of MT-attached motors could not be measured in the experiment. Applying meaningful parameters and aligning experimental and simulation results, the simulation could be used for an estimate of the number of motors. However, the number of MT-attached motors depends on the total number of motors and the attachment rate. Both depend on the experiment and are not known. That is why, it is difficult to give an exact number of MT-attached motors. The here used attachment rate was previously found experimentally [327] and has been used many times in previous simulations [34, 151]. This means, at least the order of magnitude should be correct. Moreover, this work found that negative velocities of the simulation show a good agreement with the negative velocity distribution of the experiment. The negative velocities are expected to come from a diffusion of the cargo in the harmonic potential of the MT-attached motors. The diffusion depends on the number of MT-attached motors and the stiffness of the motors. Consequently, having similar negative velocity distributions means that the number of MT-attached motors is a good estimate under the assumption that the motor stiffness is correct. The stiffness is taken from kinesin-1 experiments [332, 333]. It is expected that the stiffness of kinesin-3 has at least the same order of magnitude. That is why it is expected that the predicted number of motors by the simulation at least matches the order of magnitude of the real values of the number of motors in the experiment. Thereby, especially the number of MT-attached motors should be close to the real values. However, for better values, experiments that measure the number of motors on the cargo are needed.

In this chapter, it is shown that the cargo surface composition fluid or rigid which leads to diffusive or fixed motor tails influence the force response and the number of MT-attached motors. Consequently, the cargo transport velocity and duration can differ for beads and liposomes. The next chapter studies liposome transport by opposing motors.

Chapter 7

Modeling bidirectional liposome transport by DDB and KIF16B

Contents

In this chapter bidirectional liposome transport by teams of dynein (DDB) and kinesin (KIF16B) motors is simulated. The goal of this chapter is to understand why cargos with a fluid surface, where motors have diffusive motor tail positions, reverse its direction, while artificial, rigid cargos of previous in vitro assays do not. Therefore, first unidirectional liposome transport and then bidirectional liposome transport are simulated and compared to the experimental findings. Moreover, simulation modifications have been used to derive three conditions which need to be fulfilled for bidirectional cargos to reverse its direction. The obtained results underline that the cargo surface can be a potential regulatory factor of bidirectional cargo transport.

While in the previous chapter, unidirectional transport by kinesin-3 was studied considering different cargo surfaces, this chapter deals with bidirectional cargo transport by opposing teams of kinesin-3 and cytoplasmic dynein motors. Previous *in vivo* studies found kinesin-3 and cytoplasmic dynein simultaneously bound to the same cargo showing bidirectional motility [9, 21, 25, 78, 141]. *In vivo*, bidirectional motor transport is characterized by phases of fast unidirectional runs, phases of stationary or diffusive pauses and directional reversals [7, 8, 25]. It remains unclear what causes the pauses and the directional reversals. It could be that the reversals and pauses are the results of self-organization or it could be that reversals and pauses are processes controlled by external regulators. External regulators could be passive crosslinkers (see also chapter 6) or roadblocks, which hold the motor-cargo system at a special position and thereby cause a pause. Or external regulators could be adaptor proteins, which activate or impede one motor type [94, 95, 141, 334] and thereby cause a directional reversal. Moreover, external regulators could be MT-associated proteins (MAPs), such as tau, which can cause the detachment of one type of motor or enhance the MT affinity of another type of motor [31, 40, 204, 313, 315]. To understand whether reversals are regulated or self-organized processes, model motor-cargo systems are studied *in vitro* in a controlled environment without any external regulators.

Previous *in vitro* assays used DNA origami assays, where a defined number of motors is rigidly coupled, MT gliding assay (see chapter 4), where motors are rigidly bound to a glass cover and propel MTs above them, or kinesin directly bound to dynein by DNA hybridization [88, 158, 309]. All of them showed unidirectional motion with cargos either going in one direction or not moving at all [88, 158, 309]. None of them showed directional reversals or bidirectional motion as seen *in vivo*. Thus, there needs to be something different *in vitro* compared to *in vivo*. Besides missing (potential) external regulators, motors were rigidly coupled in all previously used *in vitro* systems. Coupling cargos rigidly is far away from most *in vivo* systems, where motors are bound to fluid cargos, where motors can diffuse on the cargo surface [22, 169, 256]. The previous chapter (chapter 6) revealed significant differences between cargos with rigid (beads) and fluid surfaces (liposomes). Thus, it might be that reversals are observable *in vitro* when using a more *in vivo* like cargo such as a liposome with a fluid cargo surface where motors are able to move.

Recently, our collaborators[1] indeed could show that when using unilamellar vesicles (from now on called liposomes) coupled to teams of dynein-dynactin-BICD2 complexes (from now on referred to as DDB) and KIF16B motors from the kinesin-3 motor family (from now on called KIF16B), cargos paused and reversed their direction similar to *in vivo* [335]. Thus, using *in vivo* like cargos such as liposomes recapitulate the bidirectional *in vivo* motion without the need for additional regulators. This suggests that reversals are just the natural outcome of the interplay of DDB and KIF16B motors transporting fluid cargos.

However, it remains unclear, why directional reversals can be observed when having a fluid cargo surface, but are suppressed when having motors rigidly bound to the cargo. In the previous chapter (chapter 6), well-defined bead and liposome models were introduced. These models can be used to understand what is necessary to see reversals in transport performed by teams of DDB and KIF16B motors. Moreover, the simulation can shed light on what is happening during runs and pauses and what causes directional reversals. In detail, the simulation can discuss whether it is likely to have a continuous or an intermittent tug-of-war between DDB and KIF16B. A continuous tug-of-war would mean that DDB and KIF16B constantly exert forces against each other (also during fast runs), while for an intermittent tug-of-war, it is

---

[1]Ashwin D'Souza, Rahul Grover, and Stefan Diez from Stefan Diez lab at B CUBE, TU Dresden.

expected that the tug-of-war between DDB and KIF16B is interrupted by phases, where only one kind of motor is attached to the MT. To use the bidirectional cargo transport simulations to understand bidirectional cargo motion *in vitro*, first, the simulation needs to recapitulate the experimental observations. Therefore, first unidirectional liposome transport by only DDB and only KIF16B is modeled and compared to the experiment (section 7.1). Then, the two developed unidirectional models are brought together for the bidirectional transport and compared to the experiment (section 7.2). Finally, it is discussed what is necessary to see reversals.

Most of the work presented in this chapter is part of [335], which is published in *Nature Communications* (2023)14:7532 under the Creative Commons CC-BY license.

7.1 Unidirectional liposome transport by KIF16B and DDB

To model liposome transport by KIF16B and DDB, the point-like cargo model, introduced in chapter 6, section 6.2.1, is used. In chapter 6, the model was introduced for unidirectional KIF16B (there called kinesin-3) transport. Here it will be adapted to transport by teams of DDB motors. Furthermore, the KIF16B model will be compared to the here given experimental concentrations.

7.1.1 Liposome transport by DDB

For liposome transport by DDB, the point-like cargo model introduced in chapter 6 is adapted to the DDB motor. This means, the overall model remains the same, but the motor dynamic, i.e. the attachment, detachment, and stepping rates are adjusted to the DDB-specific behavior. A recent study found that DDB exists in the states *active*, *inactive* and *diffusive* [336] meaning that some DDB motors show directed motion, some diffusive motion and others did not move at all. The same behavior of DDB motors was observed in the here presented experiments. In detail, it was observed that about 10% of the DDB motors were diffusive, another 10% inactive, and the remaining 80% active (see our *publication* for details [335]). All three types of DDB motors are included in the model with the given percentages.

In the model, all (active, inactive, and diffusive) DDB motors bind to the MT with the constant attachment rate $k_{\mathrm{a,DDB}}$. For attachment, a Gaussian distribution is used to choose the protofilament as described in section 6.2.1. On each PF, exclusion effects are taken into account. Therefore, the DDB radius R_{DDB} is applied (see model description in section 6.2.1 for details).

For calculating forces of MT-attached motors, equation 6.4 is applied by substituting the kinesin-3 stiffness and length with the DDB stiffness κ_{DDB} and DDB length L_{DDB}, respectively:

$$F^i(t) = \begin{cases} \kappa_{\mathrm{DDB}} \left(\Delta x^i(t) - L_{\mathrm{DDB}} \right), & \Delta x^i(t) > L_{\mathrm{DDB}} \\ 0, & \left| \Delta x^i(t) \right| \leq L_{\mathrm{DDB}} \\ \kappa_{\mathrm{DDB}} \left(\Delta x^i(t) + L_{\mathrm{DDB}} \right), & \Delta x^i(t) < -L_{\mathrm{DDB}}. \end{cases} \quad (7.1)$$

Based on previous modeling work [34, 337], an exponential detachment is assumed for active, inactive, and diffusive DDB motors:

$$k_{\mathrm{d}}(F^i) = k_{\mathrm{d,DDB,s}}^0 \, \mathrm{e}^{\frac{|F^i|}{F_{\mathrm{d,DDB}}}} \quad \text{with} \quad s \in \{\mathrm{ac, in}\}. \quad (7.2)$$

While the same detachment force $F_{d,DDB}$ is assumed for all motors, diffusive and inactive DDB motors have a lower force-free detachment rate $k^0_{d,DDB,in}$ than active DDB motors ($k^0_{d,DDB,ac}$; see table D.1 of the appendix D).

The active DDB motor stepping depends on the amount and direction of force. Three different

a) Simulation   b) Experiment
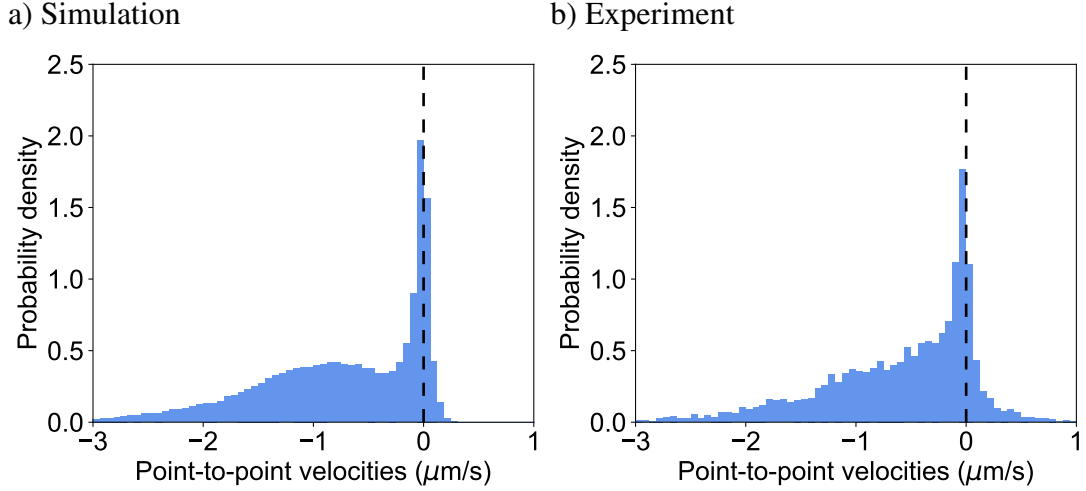
Figure 7.1: Velocities of liposome transport by DDB: experiment and simulation. Histograms of point-to-point velocities from simulation (a) and experiment (b). For simulation and experiment velocities are first calculated from two consecutive frames and then smoothed by a moving average of 600 ms. In the simulation, an average number of 8 DDB motors in the attachment area (see fig. 6.6 for the definition of the attachment area) is used, and in the experiment a DDB concentration of 38nM. Both histograms (simulation and experiment) show a zero velocity peak and a tail towards higher, negative velocities. Number of measured liposomes was 121 in the experiment and 150 in the simulation. All experiments were performed by Ashwin D'Souza and Rahul Grover from Stefan Diez lab at B CUBE, TU Dresden. Figures are published in *Nature Communications* (2023) 14:7532 [335]. Reprint with permission of *Nature Communications* under the Creative Commons CC-BY license.

force regimes are distinguished. First, if the active DDB motor experiences a backward load smaller than the stall force ($-F_{s,DDB} < F^i(t) < 0$), it steps forward with the following ATP and force-dependent stepping rate:

$$s_{DDB}(F^i, [ATP]) = \frac{v_{f,DDB}/d \cdot [ATP]}{[ATP] + K_M} = \frac{k_{cat}(F^i)[ATP]}{[ATP] + k_{cat}(F^i)/k_b(F^i)} \tag{7.3}$$

with the maximal, force-free forward velocity $v_{f,DDB}$, given by single molecule stepping velocities (from active DDB), with the stepsize d and $k_{cat}(F^i)$ and $k_b(F^i)$ given by eq. (4.20) (see section 4.2.1 for more details). Second, if the active DDB motor is pulled forward (forward load, $F^i(t) \geq 0$), the constant stepping rate $s_{DDB}(F^i = 0, [ATP])$ is used. And third, if the active DDB motor experiences a backward load greater than the stall force ($F^i(t) < -F_{s,DDB}$), the motor steps backward with the following constant rate:

$$s_{DDB}(F^i) = \frac{v_{b,DDB}}{d} \tag{7.4}$$

with $v_{b,DDB}$ being the backward stepping velocity of active DDB and d the stepsize. The here presented ATP and force dependence was previously found by Schnitzer et al. [120] for

kinesin-1. Using DDB-specific parameter values, a similar force dependence is obtained as previously found experimentally for DDB [70].

Unlike for active DDB, it is assumed that inactive DDB is strongly bound to the MT and therefore not able to step at all. Diffusive DDB, however, is assumed to diffuse along the MT in the harmonic potential of its motor spring. Therefore, the same force-dependent diffusion rate is used as introduced in section 4.2.2 for passive dynein without adaptor proteins:

$$s_{\pm,\text{DDB}}\left(F^i\right) = s_{0,\text{DDB}}\,\mathrm{e}^{\mp\frac{F^i \cdot d}{2k_\text{B}T}}. \tag{7.5}$$

The force-free diffusion rate $s_{0,\text{DDB}}$ is taken from the experimental work by Feng et al. [336]. See section 6.2.1 and our *publication* [335] for more details regarding the liposome model.

In total, the point-like model of liposome transport by DDB contains the following parameters: number of motors in the attachment area, percentage of active, inactive, and diffusive motors, attachment rate, force-free detachment rate of active motors, force-free detachment rate of inactive motors, stall force, detachment force, force-free velocities, backward velocities beyond stall, motor stiffness, diffusion rate of diffusive DDB motors and the untensioned length of DDB motors (see table D.1 of the appendix D). Directly measured or estimated from the here presented experiments are the percentage of inactive, active, and diffusive motors, the force-free detachment rate of active motors, and the distribution of single motor force-free velocities. Other parameters are, whenever possible, taken from the literature (table D.1 of the appendix D). Simulation velocity histograms (fig. 7.1) generated with the point-like cargo model of liposome transport by DDB show a high peak around zero, a second lower peak at around 1 μm/s (absolute value), and a long tail towards high negative velocities. Simulation velocity histograms are robust upon small changes in all parameter values except the force-free detachment rate of inactive DDB motors (see fig. D.1 of the appendix D). All histograms produced with small changes of the parameters (see fig. D.1 of the appendix D) show the peak around zero, the second, small peak at around 1 μm/s and a long tail towards high negative velocities. The peak around zero is sensitive to small changes in the force-free detachment rate of inactive motors and slight changes upon small changes of detachment force, backward velocity beyond stall, motor stiffness, diffusion rate of diffusive DDB motors, and untensioned DDB length. Since the force-free detachment rate of inactive DDB motors is not given by the literature and the peak at around zero is most sensitive to changes in the force-free detachment rate of inactive DDB motors, the value of the force-free detachment rate of inactive DDB motors is determined by optimizing the height of the peak around zero. For the other parameters, literature values are applied[2]. The number of motors involved in liposome transport is determined by first the number of available motors in the attachment area (see fig. 6.6 for an illustration of the attachment area) and second by the attachment rate. Higher attachment rates (fig. D.1a) and a higher number of motors (fig. D.1b) lead to slightly less very high velocities and a slightly increased second peak at around 1 μm/s. However, in general, the velocity histograms are quite robust to those changes in the attachment rate and the number of motors in the attachment area. That is why the standard attachment rate given by the literature is applied and the number of motors is selected by adjusting the outcome of the competition between DDB and KIF16B to the experimental results. For KIF16B, experimental velocity histograms are given for varying concentrations (fig. 7.2b). That is why the range of the number of motors is more defined by the experiment. In the competition between KIF16B

---

[2]The untensioned length of DDB motors is not directly given by the literature. Here the same value as for in this thesis presented and in Monzon et al. [300] published dynein model for gliding assay simulations (see chapter 4) is used.

and DDB, in the experiment, the same varying KIF16B concentrations and the same constant DDB concentration are used as in the unidirectional liposome transport by KIF16B or DDB alone. The number of DDB motors used in the simulations is selected such that the percentage of minus tracks decreases similarly to the experiment with increasing KIF16B concentration. In conclusion, DDB parameters were optimized such that simulated unidirectional liposome transport by DDB as well as simulated bidirectional liposome transport by DDB and KIF16B best align with the experimental results.
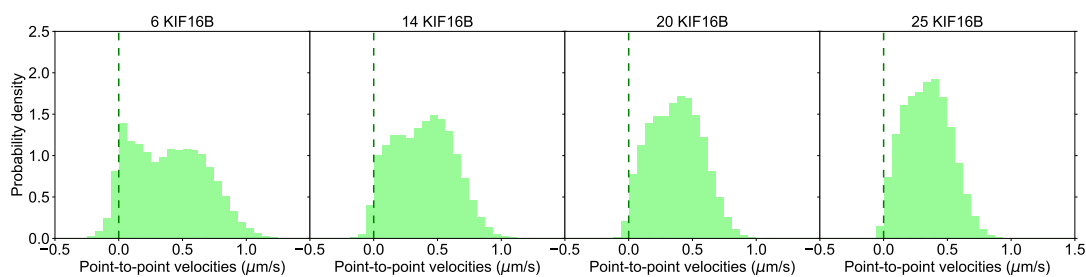
In detail, point-to-point velocity histograms from simulation (fig. 7.1a with parameter set given in table D.1 of the appendix D) and experiment (fig. 7.1b) show high peaks around zero with long tails towards high, negative velocities of up to $3\,\mu\mathrm{m/s}$ (absolute value). The peaks around zero are equally high and also the tails reach equally high negative velocities of up to $3\,\mu\mathrm{m/s}$ (absolute value) for simulation and experiment. However, the simulation histogram indicates a small second peak at approximately $1\,\mu\mathrm{m/s}$ (absolute value), which is not visible in the experimental histogram. Taken together, the simulated liposome transport by DDB widely reproduces experimental velocity histograms.

7.1.2 Liposome transport by KIF16B

Even though, liposome transport by kinesin-3 (from now on called KIF16B) is well characterized in the previous chapter (chapter 6), here again a comparison with the experiment is done because for the bidirectional liposome transport experiments a different buffer solution was used. A different buffer solution slightly changes the results such that the model had to be slightly adjusted. To adjust the simulated velocity histograms to the experimentally given velocity histograms, a different force-free detachment rate for inactive KIF16B $k^0_{\mathrm{d,KIF16B,\,in}}$ (see eq. 6.5) had to be introduced (similar as for DDB). Assuming that the inactive motors are strongly bound to the MT, the force-free detachment rate of inactive motors is lower than the force-free detachment rate of active KIF16B motors ($k^0_{\mathrm{d,KIF16B,\,in}} < k^0_{\mathrm{d,KIF16B,\,ac}}$). Besides the force-free detachment rate, also other parameter values were slightly modified (compare table C.1 of appendix C with table D.1 of appendix D).

In summary, the simulation of liposome transport by KIF16B using the point-like cargo model contains the following parameters: number of motors in the attachment area, percentage of inactive and active motors, attachment rate, force-free detachment rate of active motors, force-free detachment rate of inactive motors, stall force, detachment force, force-free forward velocity of single KIF16B motors, backward velocity beyond stall, motor stiffness, and untensioned length of KIF16B motors. The force-free detachment rate of active motors, the percentage of inactive motors, and the force-free forward velocity of single KIF16B motors are directly given by the experiment. Using the parameters listed in table D.1 of the appendix D, simulation velocity histograms (fig. 7.2a) are obtained which show a peak at low velocities close to zero and a peak at higher velocities (approximately $0.5\,\mu\mathrm{m/s}$). With increasing number of motors in the attachment area, the low velocity peak vanishes, and the high velocity peak moves to lower velocities. The number of motors in the attachment area (see fig. 6.6 for the definition of the attachment area) as well as the attachment rate determines how many motors are involved in transport. The simulation velocity histograms are sensitive to small changes of both parameters: a lower attachment rate ((fig. D.2a)) leads to a higher low velocity peak and higher velocities (high velocity peak at higher velocities) and as said before, an increasing number of motors reduces the low velocity peak and shifts the high velocity peak to lower velocities. Another free parameter is the force-free detachment rate of inactive motors. A higher force-free detachment rate of inactive motors leads to a disappearance of

a) Simulation

b) Experiment
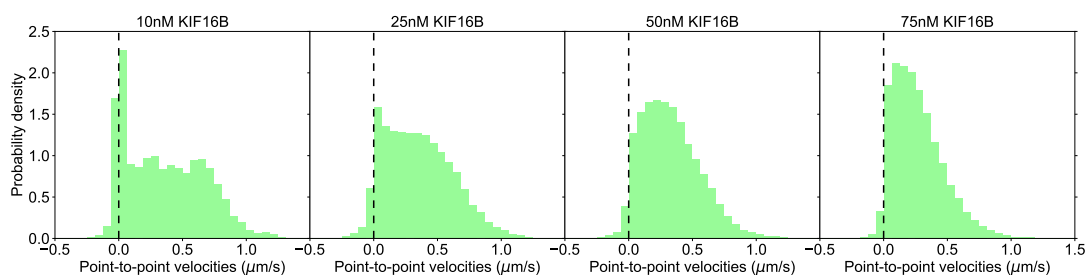
Figure 7.2: Velocities of liposome transport by KIF16B: experiment and simulation. Histograms of point-to-point velocities from simulation (a) and experiment (b). For simulation and experiment velocities are first calculated from two consecutive frames and then smoothed by a moving average of 600 ms. In the simulation, the average number of KIF16B motors in the attachment area (see fig. 6.6 for the definition of the attachment area) are $\{6, 14, 20, 25\}$, which account for the given experimental KIF16B concentrations in solution of $\{10, 25, 50, 75\}$ nM. For simulation and experiment, the histograms show a zero velocity peak and a high-velocity peak for low number of motors/motor concentrations. With increasing number of motors/motor concentrations the zero velocity peak vanishes and the high-velocity peak shifts towards lower velocities. Number of measured liposomes are 150 in the simulation for all number of motors and $n = \{33, 252, 377, 485\}$ for concentrations $\{10, 25, 50, 75\}$ nM in the experiment. All experiments were performed by Ashwin D'Souza and Rahul Grover from Stefan Diez lab at B CUBE, TU Dresden. Figures are published in *Nature Communications* (2023) 14:7532 [335]. Reprint with permission of *Nature Communications* under the Creative Commons CC-BY license.

the low velocity peak and in general higher velocities (fig. D.2b). The untensioned length of KIF16B can be varied within a certain range given by the literature (see table D.1 of appendix D). A lower untensioned length (fig. D.2g) has the opposite effect of the higher force-free detachment rate of inactive motors: a higher low velocity peak and generally lower velocities. The values of the force-free detachment rate of inactive motors and the untensioned length of KIF16B motors were optimized such that the low velocity peak and the high velocity peak fit best the experimental velocity histograms. The simulation velocity histograms are also sensitive to small changes in the stall force and the detachment force. A lower stall force (fig. D.2c) leads to slightly lower velocities and a higher detachment force (fig. D.2d) to a more pronounced low velocity peak, which increases with increasing number of motors. The stall force and detachment force values were chosen within a range given by the literature (see table D.1 of appendix D). The simulation velocity histograms are robust upon small changes of the backward velocity beyond stall (fig. D.2e) and the motor stiffness (fig. D.2f). For

these parameters also values from the literature are taken. Taking together, the best alignment between experiment and simulation (fig. 7.2) has been achieved when using the parameter set given by table D.1 of appendix D. All small parameter variations lead to a reduced alignment between experiment and simulation (compare fig. D.1 of the appendix D with fig. 7.2b).

Experiments of liposome transport by KIF16B were performed at four different KIF16B concentrations in solution $(10 - 75\,\text{nM})$. As for the simulation, point-to-point velocity histograms of experimental liposome transport by teams of KIF16B motors (fig. 7.2b) show a high velocity peak close to zero and a peak at higher velocities $(0.6\,\mu\text{m/s})$ for the lowest KIF16B concentration $(10\,\text{nM})$. Increasing the KIF16B concentration, the low velocity peak decreases, and the high velocity peak shifts to lower velocities (approximately around $0.2\,\mu\text{m/s}$ for the highest KIF16B concentration of $75\,\text{nM}$). At the two highest KIF16B concentrations, no zero-velocity peak is distinguishable anymore from the high velocity peak. Increasing the number of motors in the attachment area shows a similar trend as seen in the experiment (fig. 7.2),

Comparing, simulation and experimental velocity histograms presented in this chapter (fig. 7.2) with the previous chapter 6 reveal that the shapes and trends of the velocity histograms are the same. Consequently, explanations derived in the previous chapter 6 can be applied to this chapter. This means the low velocity peak close to zero can be assigned to a slow state (called pause in the following) caused by inactive motors, the high velocities to a fast state (called run state in the following) caused by active motors, and the reduction in velocity with increasing number of motors to an increasing exclusion effect (see also our *publication* [335]).

In summary, when optimizing the free parameters in the simulation, an alignment between simulation and experiment has been achieved for liposome transport by DDB or KIF16B motors alone. Consequently, the next step is to bring the two unidirectional models together and simulate bidirectional liposome transport by the oppositely directed motors KIF16B and DDB.

7.2 Bidirectional liposome transport by KIF16B and DDB

In this section, the presented models of unidirectional liposome transport by either only DDB or only KIF16B are brought together to simulate bidirectional liposome transport by KIF16B and DDB motors. First, bidirectional liposome transport simulations are analyzed as in the experiment and compared to the experiment. Then the simulation is used to understand what is necessary to obtain reversals in bidirectional transport and why previous *in vitro* studies using rigidly coupled motors could not see reversals [88, 158, 309]. Before showing the simulation results, first, the experimental results are presented.

7.2.1 Experimental results

In the experiment, fluorescent-labeled liposomes were incubated with DDB and KIF16B motors at given concentrations and added to polarity-marked MTs. Liposome positions were tracked over time. Time-distance plots (fig. 7.3a) show that a subset of liposomes moved towards the MT plus-end, another subset moved towards the MT minus-end and finally, some moved towards the plus and the minus-end showing directional reversals. To characterize the amount of reversing, minus-end, and plus-end directed liposomes, liposome tracks were classified into minus tracks, plus tracks, and reversal tracks. Therefore, a segmentation algorithm was needed, which detects pauses and positive and negative runs. In the previous chapter (chapter 6) a segmentation algorithm based on the instantaneous cargo velocity was used. Here an improved version of this segmentation algorithm is used because the transport pattern is more complex. The segmentation algorithm here includes a pre-step, where the track is segmented into sections of approximately equal velocities. To find the optimal piecewise linear approximation $f(t)$ of the track, the position-time coordinates (x_k^{cp}, t_k^{cp}) of the change points, which divide the track into pieces of approximately equal velocities, need to be optimized. Therefore, a Monte Carlo method is used, which minimizes the cost function:

$$E_{\text{err}} = \sum_{i=1}^{N} \left(x_i - f(t_i) \right)^2 \tag{7.6}$$

with N being the number of data points, x_i the position of the liposome at measurement time t_i. The linear approximation is given by

$$f(t) = x_k^{cp} + \frac{x_{k+1}^{cp} - x_k^{cp}}{t_{k+1}^{cp} - t_k^{cp}} \left(t - t_k^{cp} \right) \quad \text{for} \quad t_k^{cp} \le t < t_{k+1}^{cp}. \tag{7.7}$$

To also account for the adding and deleting of change points, the total energy (cost function) is given by

$$H = E_{\text{err}} + \mu N_{\text{cp}} \tag{7.8}$$

with the number of change points N_{cp} and the chemical potential μ. Best results were obtained for $\mu = 10000$. At the beginning of the algorithm, change points are placed after each 0.6 seconds of the track[3]. The change points at the beginning and end of the track are fixed to make sure to always cover the complete track. To find the optimal linear approximation

---

[3]At the beginning change points are identical with measurement data points. Later the position of the change point can slightly deviate from actual data point positions.

$f(t)$, the number of change points and their position-time coordinates are updated 8000 times. Therefore new change point positions and time points are proposed:

$$x^{\text{cp}}_{k,\text{new}} = x^{\text{cp}}_k + \epsilon_x \times (u - 0.5) \quad t^{\text{cp}}_{k,\text{new}} = t^{\text{cp}}_k + \epsilon_t \times (v - 0.5) \tag{7.9}$$

with u and v being uniformly distributed random numbers between zero and one. New position-time coordinates and number of change points are accepted according to the Metropolis algorithm (see chapter 3) using the total energy given by eq. (7.8). To stabilize the change points, the system is cooled down after 4000 updates. In detail, the applied $\beta = \frac{1}{k_{\text{B}}T}$ is increased by one order of magnitude every 1000 updates from $\beta = 0.005$ to $\beta = 50$. That is how a piecewise linear approximation is found, which divides the track in segments of approximately equal velocities. To distinguish between pauses and (negative/positive) runs, the mean velocity of the found segments is calculated. If the mean velocity is less than 100 nm/s, the segment is a pause otherwise a positive/negative run. To improve the segmentation algorithm, additional refinements are added. First, single data point segments are deleted, meaning they are assigned to the follow-up segment. Second, runs with a net displacement less than 500 nm are segmented as a pause. At the end of the algorithm, pauses at the end and the beginning of the track are deleted because it cannot be ruled out that the liposome has reached the beginning or end of the MT. For the same reason, completely stationary tracks were left out. Additionally, very short tracks (shorter than 3 seconds) were left out because the segmentation algorithm needs a minimum number of data points to find meaning full change point distributions. Using this segmentation algorithm, tracks can be segmented into positive, negative runs and pauses. Moreover, reversal and non-reversal pauses can be detected (see fig. 7.3a). Furthermore, tracks can be classified into minus/plus tracks, which contain only negative/positive runs and reversal tracks, which contain both, negative and positive runs (see fig. 7.3a). Fig. 7.3b shows the percentages of minus, plus, and reversal tracks for a constant DDB concentration (38 nM) and varying KIF16B concentrations (10 − 75 nM). Thereby, also the cases only DDB and only KIF16B are included as references. It can be seen that with increasing the KIF16B concentration the percentage of plus tracks increases and the percentage of minus tracks decreases. For all KIF16B concentrations and the only DDB case, a small percentage of reversal tracks was observable. The percentage of reversal tracks is maximal at the middle KIF16B concentration of 25 nM. To conclude, as seen for the bidirectional gliding assay (see chapter 4), the relative amount of KIF16B and DDB regulates the direction of bidirectional transport.

Next, the question of what happens during positive and negative runs is addressed. Is the opposing motor slowing down the transport suggesting a constant tug-of-war (assuming a tug-of-war during pauses) or is only one type of motor engaged during unidirectional runs suggesting an intermittent tug-of-war? Therefore, mean velocities of negative/positive runs from only DDB/only KIF16B liposomes are compared with mean velocities of negative/positive runs from minus/plus tracks and reversal tracks from DDB-KIF16B liposomes. For minus/plus tracks from only DDB/only KIF16B liposomes, it is clear that only one type of motor is present on the cargo. For reversal tracks from DDB-KIF16B liposomes, it is clear that both types of motors are present on the cargo. However, for minus/plus tracks it is not clear whether only one type of motor is present on the cargo or both. That is why mainly only DDB/only KIF16B liposomes should be compared to reversal tracks of DDB-KIF16B liposomes. Comparing mean velocities per run (fig. 7.4) for the KIF16B concentration with most reversal tracks (25 nM KIF16B and 38 nM DDB) reveals that mean velocities per run are similar for only DDB/only KIF16B liposomes and DDB-KIF16B liposomes (reversal tracks). This indicates that the opposing motor is not slowing down the leading motor during negative and positive

a) Trajectories
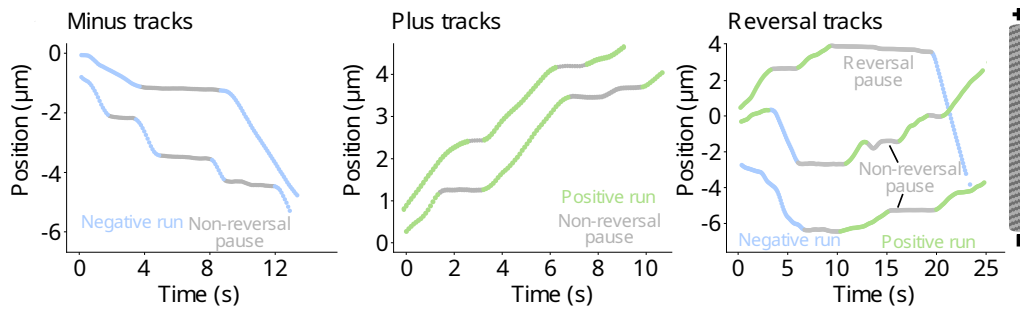
b) Classification
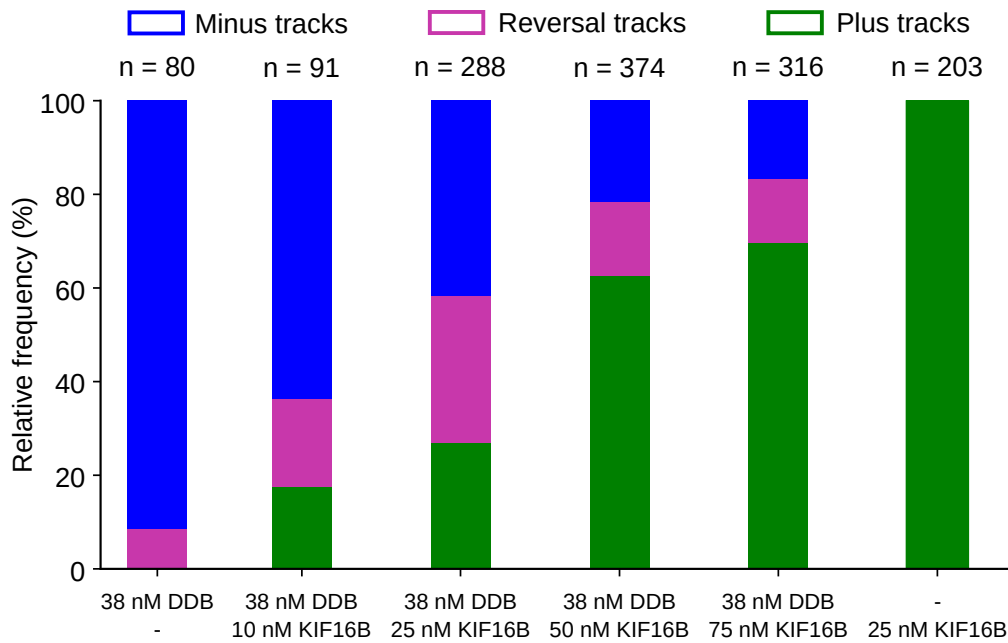
Figure 7.3: The KIF16B concentration regulates the direction of bidirectional liposome transport. a) Experimental time-distance plots of bidirectional liposome transport by KIF16B (25 nM) and DDB (38 nM). Transport towards the plus-end is assigned positive. A moving average of 600 ms was applied to the original time-distance tracks. Using our segmentation algorithm (see main text for details), tracks could be segmented into positive runs (light green), negative runs (light blue), reversal pauses (gray), and non-reversal pauses (gray). Moreover, tracks could be classified into minus tracks (first plot, negative runs, and non-reversal pauses), plus tracks (second plot, positive runs, and non-reversal pauses), and reversal tracks (third plot, positive and negative runs, reversal and eventually non-reversal pauses). b) Experimental percentages of minus, plus, and reversal tracks at varying KIF16B concentration ($10 - 75$ nM) and constant DDB concentration (38 nM). The only DDB and only KIF16B transport are added as a reference. Increasing the KIF16B concentration increases the number of plus tracks and decreases the number of minus tracks. Reversal tracks are obtained for all KIF16B concentrations in the presence of DDB and were maximal at the middle KIF16B concentration of 25 nM. n indicates the number of measured liposomes/number of tracks. All experiments were performed by Ashwin D'Souza and Rahul Grover from Stefan Diez lab at B CUBE, TU (*Continuation on next page.*)

Figure 7.3 *(previous page)*: Dresden. Figures a) (adapted) and b) are published in *Nature Communications* (2023) 14:7532 [335]. Reprint with permission of *Nature Communications* under the Creative Commons CC-BY license.
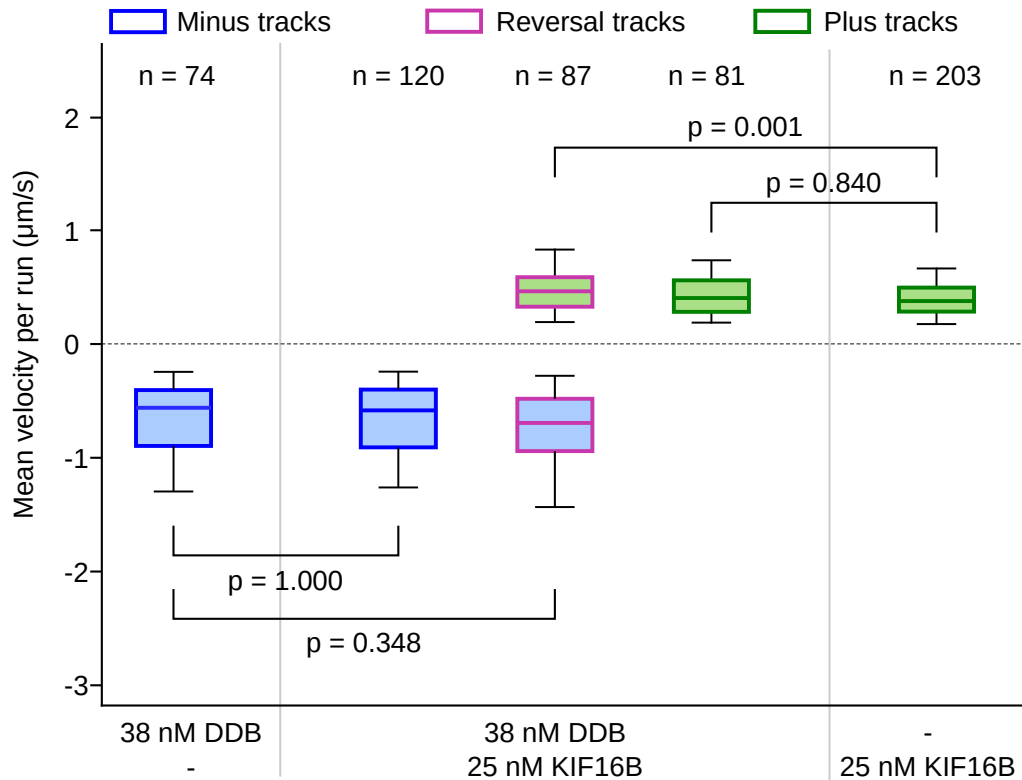
Figure 7.4: The presence of the opposing motor does not slow down transport during runs. Experimental boxplots show mean velocities per run for only DDB liposomes (38 nM), DDB and KIF16B liposomes (38 nM DDB and 25 nM KIF16B), and only KIF16B liposomes (25 nM). Mean velocities of negative runs are assigned light blue and mean velocities of positive runs light green. Borders of boxes show whether mean velocities per run were taken from minus tracks (middle blue), plus tracks (middle green), or reversal tracks (magenta). Mean velocities of negative/positive runs show no significant difference between DDB-KIF16B liposomes (minus/plus and reversal tracks) and only DDB/only KIF16B liposomes. n indicates the number of measured liposomes/number of tracks. p-values were obtained from pairwise, independent t-tests with Bonferroni correction. All experiments were performed by Ashwin D'Souza and Rahul Grover from Stefan Diez lab at B CUBE, TU Dresden. Figures are published in *Nature Communications* (2023) 14:7532 [335]. Reprint with permission of *Nature Communications* under the Creative Commons CC-BY license.

runs. However, it cannot be ruled out that the opposing motor is attached to the MT. Simulating bidirectional liposome transport by DDB and KIF16B motors can give an estimate of the configuration of MT-attached motors during runs and pauses.

Taken together, the experiments show directional reversals for DDB-KIF16B liposomes. Changing the relative concentrations of KIF16B and DDB regulates the net transport direction. Moreover, velocities reveal that the presence of the opposing motor does not slow down unidirectional runs of DDB-KIF16B liposomes. For more details about the experiment and

also an analysis of the pause state, see our *publication* [335].

7.2.2 Modeling bidirectional liposome transport

Before using the simulation to understand the underlying process leading to runs, pauses, and reversals, the model needs to be calibrated and the simulation results compared to the experiment.

To simulate liposome transport by DDB and KIF16B, the previously introduced unidirectional DDB and KIF16B liposome models (see section 7.1.1 and 7.1.2 and chapter 6) are combined.

Besides the fact that there are now two opposite-directed motors attached to the same liposome, the model did not change. Since the unidirectional liposome transport by KIF16B and DDB (see section 7.1.1 and 7.1.2) has been performed at similar experimental conditions as the unidirectional transport, also the parameters remain the same except for the attachment rate. For attachment, it is assumed that the attachment rate is lower in the presence of the oppositely directed motors because more motors are on the cargo and might hinder each other to reach the MT. Furthermore, the distance between cargo and MT might not be as optimal for binding as for the unidirectional case. A similar reduction in the attachment rate was also assumed for dynein in the bidirectional gliding assay simulation (see chapter 4). The number of motors, corresponding to the experimentally given concentrations, are given by the unidirectional simulations (see fig. 7.1 and 7.2). For the simulations of unidirectional liposome transport either by KIF16B or DDB alone, parameters were calibrated by finding the optimal alignment between simulation and experimental velocity histograms (see sections 7.1.1 and 7.1.2). Since liposome transport by DDB has been found to be quite robust upon changes in the number of motors (see section 7.1.1), the number of DDB motors is determined by adjusting the increase in percentages of minus tracks with decreasing KIF16B number of motors to the experiment (compare fig. 7.5b with fig. 7.3b). Thus, bidirectional liposome transport by KIF16B and DDB motors is simulated using the unidirectional liposome transport models with the parameters found for the unidirectional liposome transport simulations. See also the parameter table D.1 given in the appendix D.

Fig. 7.5a shows time-distance plots of DDB-KIF16B liposome transport simulations (on average 8 DDB motors and 14 KIF16B motors in the attachment area of the cargo, see section 6.2.1 for the definition of the attachment area). The tracks are segmented into negative and positive runs and reversal and non-reversal pauses using our segmentation algorithm (see section 7.2.1), which has also been used for segmenting the experimental tracks. Similar to the experiment, the simulation shows negative and positive runs, reversal and non-reversal pauses. One difference between simulation and experiment is that the MT is infinitely long in the simulation, but finite in the experiment. Consequently, simulation tracks are naturally longer than experimental tracks. A longer track means that one track includes more runs and pauses. That is why simulated and experimental tracks look somewhat different at first glance. However, when taking the time scale into account it can be seen that the overall behavior is similar (compare fig. 7.5a with fig. 7.3a). Future simulations should use finite MTs with lengths given by the experiment[4].

Segmented tracks could then be classified into minus, plus, and reversal tracks. To have the same track duration distribution as in the experiment, simulated tracks are shorten. To still

---

[4]Note: the distribution of MT lengths was not available to the author.
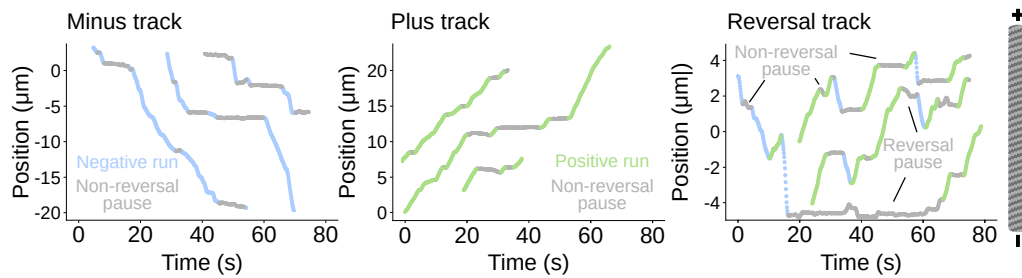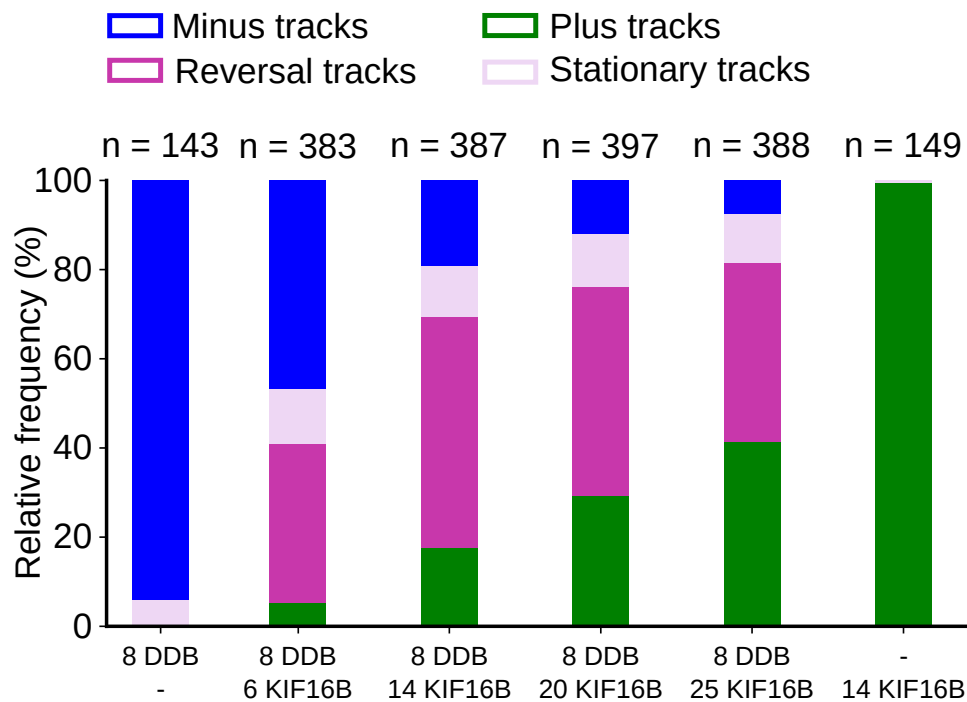
Figure 7.5: Simulations show reversal, minus, plus and stationary tracks. a) Time-distance plots of simulated liposome transport by DDB and KIF16B (25 DDB and 14 KIF16B motors on average in the attachment area). Transport towards the plus-end is assigned positive. A moving average of 600 ms is applied to the simulated time-distance tracks. Using our segmentation algorithm (see main text for details), tracks could be segmented into positive runs (light green), negative runs (light blue), reversal, and non-reversal pauses (gray). Moreover, tracks could be classified into minus tracks (first plot, negative runs, and non-reversal pauses), plus tracks (second plot, positive runs, and non-reversal pauses), reversal tracks (third plot, positive and negative runs, reversal and eventually non-reversal pauses) and stationary tracks (not shown), where the liposome does not move at all. b) Percentages of minus, plus, reversal, and stationary tracks at varying numbers of KIF16B and a constant number of DDB motors (6 − 25 KIF16B and 8 DDB motors on average in the attachment area). Percentages are calculated using the shortened simulated tracks (see main text for the procedure). The only DDB and only KIF16B transport are added as references. Increasing the number of KIF16B motors increases the number of plus tracks and decreases the number of minus tracks. Reversal tracks are obtained (*Continuation on next page.*)

Figure 7.5 (*previous page*): for all KIF16B numbers in the presence of DDB. n indicates the original number of simulated liposomes/number of tracks. Figures are published in *Nature Communications* (2023) 14:7532 [335]. Reprint with permission of *Nature Communications* under the Creative Commons CC-BY license.

keep a good statistic (not loosing long parts of the simulated tracks), each simulated track is dived into equally long pieces, the duration of which is given by one experimental track. The obtained short tracks are weighted with one divided by the number of pieces. This is done for all given experimental track durations. That is how a big data set of short simulated tracks is obtained. These short tracks are used to calculate the percentage of minus, plus and reversal tracks. Fig. 7.5b shows these percentages at varying average numbers of KIF16B and a constant average number of DDB motors in the attachment area of the cargo. Thereby also the only DDB and only KIF16B liposomes are included as references. As in the experiment, increasing the number of KIF16B motors increases the percentage of plus tracks and reduces the percentage of minus tracks. Moreover, at all KIF16B motor numbers and in the presence of DDB, a certain percentage of tracks shows reversals (reversal tracks). Furthermore, the simulation shows a fourth class of tracks, the stationary tracks. Stationary tracks contain no runs at all but only pauses. Stationary tracks were removed from the data set in the experiment since it could not be ruled out that liposomes are at the end of the MT. In the simulation, however, MTs are infinitely long such that liposomes never reach an end. Since the percentage of stationary tracks is very small in the simulation, it can be suggested that the stationary tracks might also be negligible in the experiment. To conclude simulations and experiments show that the transport direction of liposomes transported by DDB and KIF16B motors can be regulated by the relative number of KIF16B and DDB motors.

In addition to time-distance plots and percentages of track classes, the simulated mean velocities of runs can also be compared with the experiment. Fig. 7.6 shows simulated mean velocities of runs for the number of motors corresponding to the experimental concentrations shown in fig. 7.4. Thereby, the only DDB and only KIF16B liposome simulations are included to compare velocities in the presence of the opposing motor (reversal tracks) to velocities in the absence of opposing motors (only DDB or only KIF16B liposomes). As in the experiment, DDB-KIF16B liposomes do not slow down during unidirectional runs compared to the only DDB or only KIF16B cases. Thus, also for the bidirectional liposome transport by DDB and KIF16B motors an alignment between simulation and experiment has been achieved. In the following, the simulation will be used to understand the underlying processes leading to runs, pauses, and reversals during liposome transport.

Mean velocities of runs of simulation and experiment suggest that the opposing motor is not hindering the leading motor during unidirectional (positive or negative) runs. From the experimental data it could not be ruled out that the opposing motor is not bound to the MT. With the simulation, however, the configuration of MT-attached motors can be achieved. Fig. 7.7 shows the density of states of motors attached to the MT and the fraction of actively MT-attached motors (heat map). It can be seen that the distribution is quite broad meaning that many different MT-attached motor configurations exist. Furthermore, the figure shows that about 50% to 70% of the MT motors are active motors. To understand how transitions between run and pause states occur, it needs to be known what kind of motors are attached to the MT during runs and pauses. Fig. 7.10 (upper row, left) shows the mean number and type of motors attached to the MT during negative/positive runs and pauses. It can be seen that during runs on average $2 - 3$ active leading motors (active DDB or active KIF16B) are

attached to the MT and very rarely an inactive motor (inactive DDB or inactive KIF16B; mean of both less than 0.5). Occasionally, also an active opposing motor (active KIF16B or
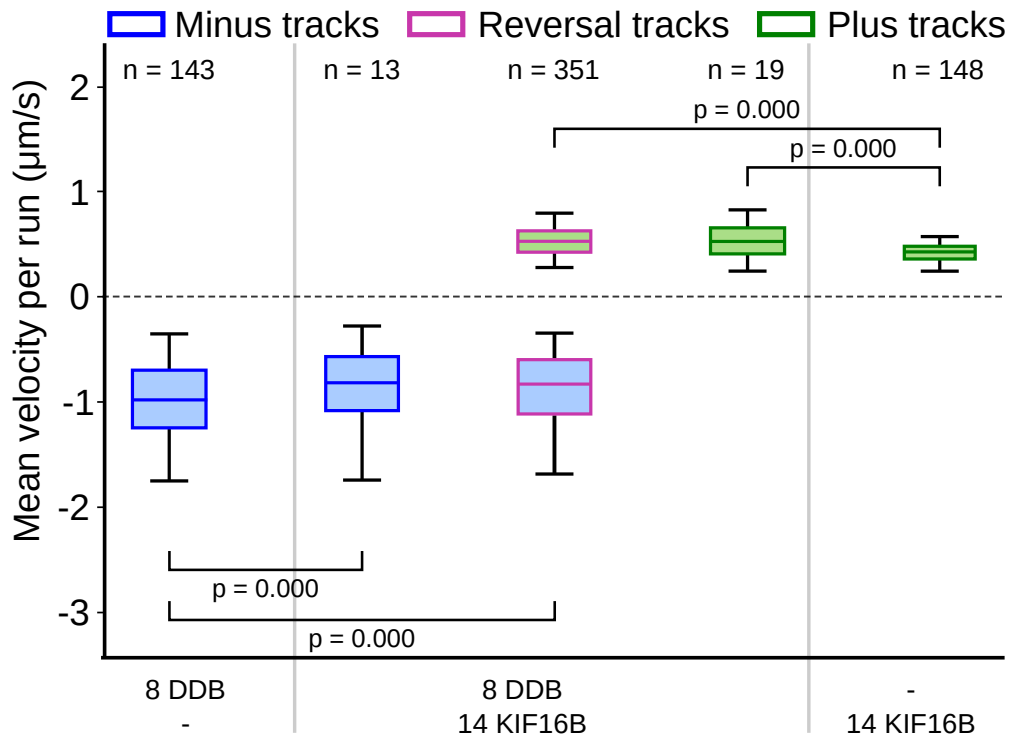
Figure 7.6: As the experiment, the simulation does not show a strong slow down of the velocity in the presence of the opposing motors. Boxplots show mean velocities per run for only DDB liposomes (8 motors on average in the attachment area), DDB and KIF16B liposomes (8 DDB and 14 KIF16B motors on average in the attachment area) and only KIF16B liposomes (14 motors on average in the attachment area). Mean velocities of segments were calculated from shortened simulated trajectories and weighted with one divided by the number of short tracks obtained from one simulated track for one experimental track duration (see main text). Mean velocities of negative runs are assigned light blue and mean velocities of positive runs light green. Borders of boxes show whether mean velocities per run were taken from minus tracks (middle blue), plus tracks (middle green), or reversal tracks (magenta). Even though p-values are small, mean velocities of positive/negative runs do not show a strong slowing down between DDB-KIF16B liposomes (plus/minus and reversal tracks) and only KIF16B/only DDB liposomes. n indicates the original number of simulated liposomes/number of tracks. p-values were obtained from weighted two-sample Kolmogorov-Smirnov tests with Bonferroni correction. Figures are published in *Nature Communications* (2023) 14:7532 [335]. Reprint with permission of *Nature Communications* under the Creative Commons CC-BY license.

active DDB) attaches (mean less than 1) but does not succeed to stop the team of leading motors. When an opposing motor attaches, the team of leading motors is confronted with a counterforce, which increases the motor tension and therefore the motor detachment rates. It can be seen (fig. 7.10, upper row, left) that for active KIF16B only a small amount of the MT-attached motors are under tension, while for DDB more than half of the actively MT-attached motors experience a force. This means teams of DDB and teams of KIF16B use distinct mechanisms to deal with opposing forces. Actively MT-attached DDB motors

distribute the opposing force over several motors (not necessarily equally) such that the tension of individual motors is only slightly increased and therefore also the detachment rate is only slightly increased. However, for KIF16B only one motor is counteracting the opposing force, which means this motor is stretched a lot and its detachment rate is increased drastically such that this motor likely detaches. When the tensioned KIF16B motor detaches, one of the untensioned active MT-attached KIF16B motors will take over to counterbalance the opposing motor. Meanwhile, a new KIF16B motor might attach and fill up the pool of untensioned motors, which are ready to help out in case the tensioned KIF16B motor detaches. Taking together, the distribution of MT-attached motors during unidirectional runs shows that mainly active leading motors are engaged in the transport indicating an intermittent tug-of-war during unidirectional runs.

After characterizing the runs, next the question of how pauses are achieved is addressed. The simulation shows (fig. 7.10, upper row, left) that during pauses on average $1 - 2$ active motors of each type are competing against each other. Again it can be seen that DDB motors distribute the opposing force more (not equally) than KIF16B motors. This means, i.a. to transition from a running state to a pausing state, on average $1 - 2$ active leading motors need to detach, and on average $1 - 2$ active opposing motors need to attach. Changes in motor

a)   b)
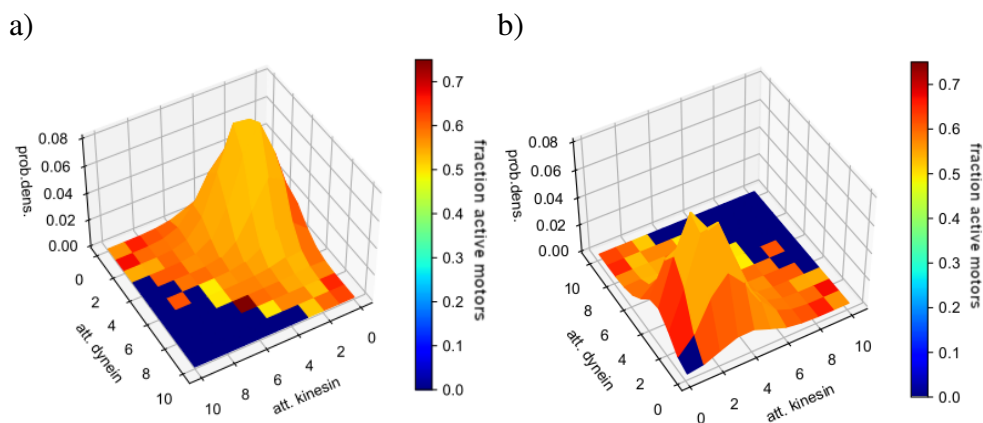
Figure 7.7: Density of states in the simulation. Distribution of motors attached to the MT. x- and y-axis show the number of MT-attached kinesin and dynein motors, respectively. The z-axis gives the corresponding probability density of the MT-attached motor configuration. The heat map in addition shows the fraction of the MT-attached motors which are active. b) Same as a), but turned by 180 degrees.

number occur due to stochastic motor attachment and stochastic, force-dependent motor detachment. Additionally, besides the amount and configuration of actively MT-attached motors, which need to change for a transition from a run to a pause, also the amount of MT-attached inactive motors is different between a run and a pause state. During pauses, the amount of inactive motors increases on average to $1 - 2$ motors (inactive DDB and inactive KIF16B together) compared to the run state, where very rarely an inactive motor is attached (mean of both less than 0.5). Inactive motors, no matter which kind, act as anchors, because they do not move at all along the MT. Unidirectional KIF16B simulations (see chapter 6) reveal that inactive KIF16B motors cause a slow state (pause) of the cargo transport. This arises the question of what is the role of inactive motors in bidirectional liposome transport by DDB and KIF16B. Are inactive motors causing the pauses which then occasionally lead

to reversals or can liposomes also reverse their direction in the absence of inactive motors? Simulating DDB-KIF16B liposome transport without inactive motors (also without diffusive
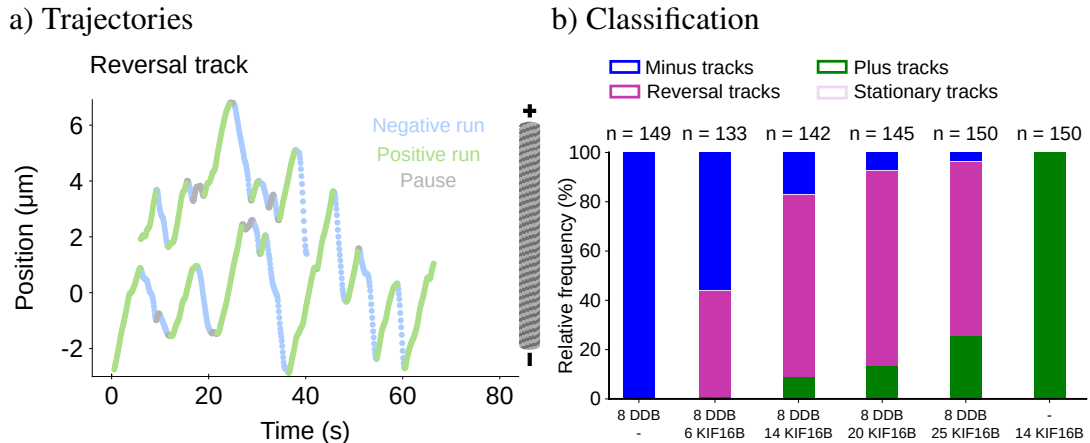
Figure 7.8: Simulations without inactive motors show reversals, but no stationary pauses. The shown tracks (a+b) are simulated without inactive motors (inactive DDB, diffusive DDB, and inactive KIF16B). a) Time-distance plot of DDB-KIF16B liposome transport (on average 14 KIF16B and 8 DDB motors in the attachment area) show tracks with frequent directional reversals, but no stationary pauses. b) Percentages of minus, plus, reversal and stationary tracks at varying numbers of KIF16B ($6 - 25$ on average in the attachment area) and a constant number of DDB motors (8 on average in the attachment area) are showing more reversal tracks than the simulation with inactive motors (see fig. 7.5b). Percentages are calculated using the shortened simulated tracks (see main text for the procedure). n indicates the original number of simulated liposomes/number of tracks. Figures are published in *Nature Communications* (2023) 14:7532 [335]. Reprint with permission of *Nature Communications* under the Creative Commons CC-BY license.

DDB motors), time-distance plots still show reversals (see fig. 7.8a) and the percentages of minus, plus, reversal and stationary tracks (fig. 7.8b) show even more reversal tracks. Tracks often show sequences of frequent directional reversals until the liposome finally moves in one direction for a longer distance. Stationary pauses, where the liposome does not move at all are suppressed. Consequently, inactive motors are not needed to observe directional reversals but stabilize the pauses.

Note that the amount of diffusive MT-attached dynein motors does not change significantly between negative and positive runs and pauses. The reason is that diffusive DDB always tends to diffuse back to their equilibrium position, where they exert no force. That is why diffusive DDB does not contribute much to the force balance and especially does not favor any direction.

In summary, after verifying that the simulation is in good agreement with the experiment, the simulation is used to understand motor dynamics during liposome transport. The simulation reveals that the attachment and detachment of a few active motors are enough to reverse the direction of liposomes transported by DDB and KIF16B motors. Inactive motors are not needed for directional reversals but stabilize the pauses.

7.2.3 Model modifications

We have seen how runs and pauses are characterized and how to transition between them. However, it remains unclear why fluid cargoes, where motor tails diffuse on the cargo surface, can experience reversals while rigidly coupled motors, as used in previous *in vitro* assays, cannot [88, 158, 309]. Therefore, the DDB-KIF16B liposome transport simulation is slightly modified to account for previous *in vitro* assays with rigidly coupled motors.

Higher attachment rate Comparing DNA origami assays [158] with liposomes, one can imagine that one parameter that differs between these two models is the (re)attachment rate. Once a motor detaches from the MT, it is assumed to diffuse away from the MT on the liposome surface (to the opposite side of the liposome for instance), while it stays near the MT in case of the DNA origami assay. Thus, for the DNA origami assay, the (re)attachment rate is likely to be higher. That is why, in the first model modification, the attachment rate of both DDB and KIF16B is increased by 32-fold. Increasing the attachment rate decreases the percentage of reversal tracks (fig. 7.9) and drastically increases the percentage of stationary tracks. A comparison of the number of motors attached to the MT indicates that more than twice as many motors are attached for the higher attachment rate than in the standard simulation (fig. 7.10, upper row, compare central with left). The relative amount of the different types of MT-attached motors, however, remains similar. For a transition from the run to the pause state in the standard simulation, on average $1 - 2$ active leading motors need to detach and $1-2$ active opposing motors need to attach. When having a higher attachment rate, on average about $3 - 4$ active leading motors need to detach, and about $1 - 2$ active opposing motors need to attach. When transitioning from a pause to a run state, on average about 5 inactive motors (inactive DDB and inactive KIF16B) need to detach additionally. With more motors, which need to be changed, but similar rates, it is more difficult to switch between states. Additionally, having more motors attach, first, there are fewer motors available which potentially could attach and change the configuration of MT-attached motors, and second, there is less space on the MT for new motors to attach. Thus, the more motors are attached, the more difficult the transition between the states gets. This means states are stabilized and transitions are suppressed such that it is likely to stay in one state for the complete simulation time. Consequently, the amount of stationary tracks is increased and the amount of reversal tracks is reduced.

In the case of the DNA origami assay, there are usually about 7 motors available such that it is assumable that there is enough space for all of them to attach. If then the attachment rate is high due to motors remaining near the MT after detachment, the configuration where all motors are attached is preferred. Consequently, no detached motors are available to change the configuration, and the state (pause or positive/negative run) is determined by the given motor configuration of the DNA origami assay.

Lower detachment rate Next, the force-dependent detachment rates are 20-fold decreased for all motors (active and inactive KIF16B; active, inactive, and diffusive DDB). Decreasing the detachment rate, drastically decreased the percentage of reversal tracks and drastically increased the percentage of stationary tracks (fig. 7.9). Measuring the number and types of motors attached to the MT (fig. 7.10, upper row, right) reveals that as for the higher
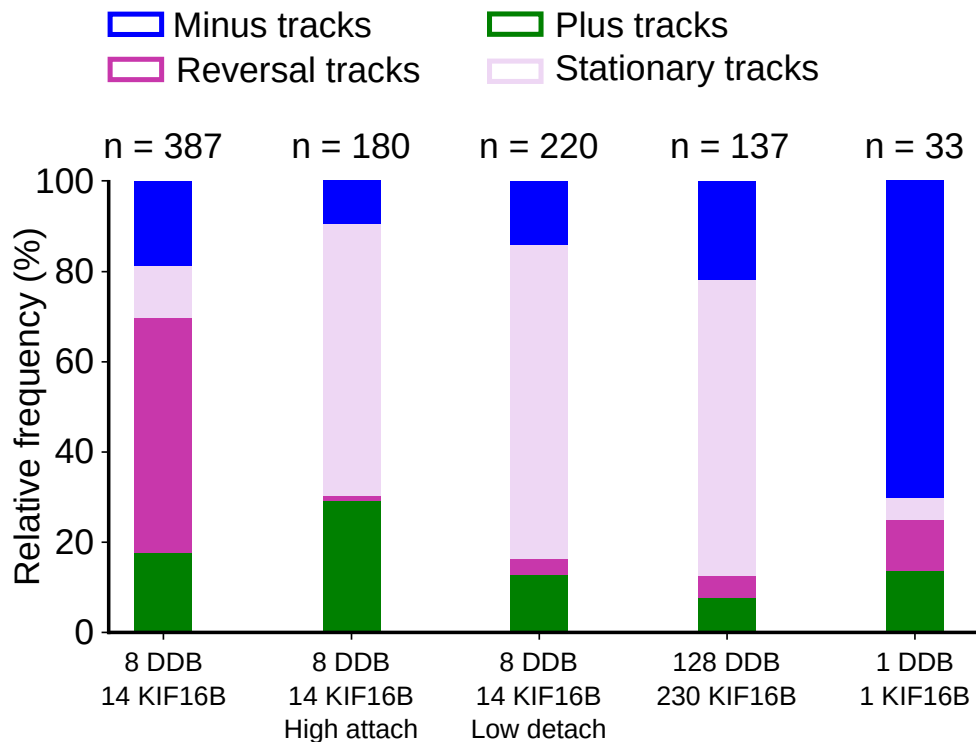
Figure 7.9: Model modifications reduce the percentage of reversal tracks and increase the percentage of stationary tracks. Percentages of minus, plus, reversal, and stationary tracks for different model modifications including only DDB and only KIF16B transport as reference. If not stated differently, 14 KIF16B and 8 DDB motors are on average in the attachment area. Percentages are shown for the simulation with the standard parameters (first bar), a simulation with 32-fold higher attachment rates for DDB and KIF16B (active, inactive, and diffusive; referred to as "High attach"), a simulation with 20-fold lower detachment rates for DDB and KIF16B (active, inactive and diffusive; referred to as "Low detach"), a simulation with a higher number of motors in the attachment area (230 KIF16B and 128 DDB motors on average in the attachment area) and a simulation, where one active DDB competes against one active KIF16B. All modifications reduce the percentage of reversal tracks. n indicates the number of simulated liposomes/number of tracks. Percentages are calculated using the shortened simulated tracks (see main text for the procedure). Figures (adapted simulation of "1DDB-1KIF16B" case) are published in *Nature Communications* (2023) 14:7532 [335]. Reprint with permission of *Nature Communications* under the Creative Commons CC-BY license.

attachment rate, almost twice the amount of motors is attached compared to the standard simulation. This means, as for the higher attachment rate, the higher number of MT-attached motors makes transitions difficult because first, more motors need to be changed, second less space is available for new motors to attach and change the configuration and third less motors are detached and available to attach and change the configuration. Hence, staying in one states is favored and transitions are suppressed. Since teams of DDB and KIF16B are similarly strong, the favored state is the pause state which results in many stalled tracks.

The dramatic increase in the proportion of stationary tracks is striking. The reason is that to
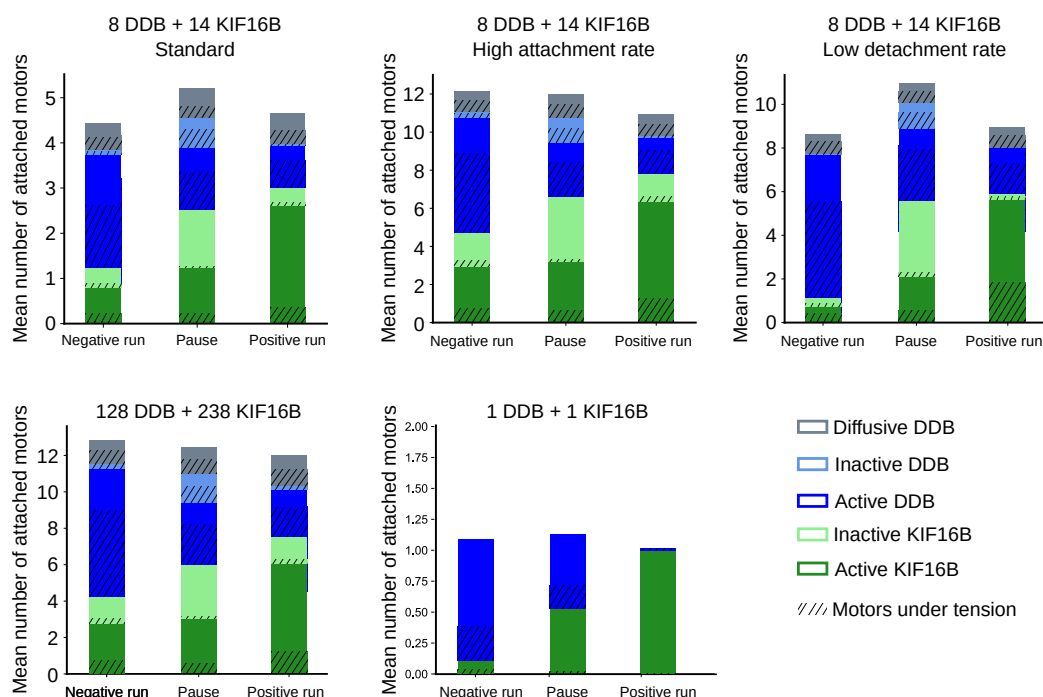
Figure 7.10: Twice the amount of motors are attached in case of a higher attachment rate, a lower detachment rate, and a higher number of motors. The bar plots show the mean number and types of motors attached to the MT during negative runs, pauses, and positive runs. Active KIF16B motors are denoted in middle green, inactive KIF16B in light green, active DDB in middle blue, inactive DDB in light blue and diffusive DDB in gray. The amount of each motor type, which is under tension is denoted by the hatches. The first row shows the mean number and types of MT-attached motors for the standard simulation (left), a 32-fold higher attachment rate for all motors (active, inactive, diffusive DDB and active, inactive KIF16B; middle) and a 20-fold lower detachment rate for all motors (active, inactive, diffusive DDB and active, inactive KIF16B; right). The number of motors in the attachment area is on average 8 DDB and 14 KIF16B for the simulations shown in the first row. The second row shows the mean number and types of MT-attached motors for a simulation with more motors in the attachment area (128 DDB and 230 KIF16B on average in the attachment area, left) and the competition between one active DDB and one active KIF16B (middle). See fig. 7.9 for the number of simulated liposomes/number of tracks of each modification. Figures (adapted simulation of "1DDB-1KIF16B" case) are published in *Nature Communications* (2023) 14:7532 [335]. Reprint with permission of *Nature Communications* under the Creative Commons CC-BY license.

get out of a pause state, many inactive motors need to be pulled off (about $4-5$). Inactive motors have a lower detachment rate than active motors. Overall lowering the detachment rate for all motors, enhances this effect and makes it very difficult for the active motors to pull off the inactive motors.

Higher number of motors A difference between the MT gliding assay (see also chapter 4) and the liposome transport might also be the number of available motors. It might be that in a MT gliding assay, more motors are available to attach to the MT than for the liposome

transport. That is why the next modification increases the number of motors. Here, 128 DDB motors (including active, inactive, and diffusive) and 230 KIF16B motors (including active and inactive) are on average in the attachment area. Increasing the number of motors also reduces the number of reversal tracks and increases the number of stationary tracks (fig. 7.9). Moreover, also twice as many motors are attached (fig. 7.10, second row, left) compared to the standard simulation (fig. 7.10, first row, left). Even though there are still many more detached motors available to attach, the amount of MT-attached motors is similar to the simulations with a high attachment rate or a low detachment rate. This suggests that there is no space left on the MT for more motors to attach. If about 12 motors are Gaussian distributed over the 7 reachable PFs, then about 4 motors are attached to the central PF. Assuming that 2 of the 4 motors are DDB motors and 2 KIF16B motors, the MT-attached motors would cover a space of 112 nm (see table D.1 of the appendix D for parameter values), which is about the size of the cargos used in the experiment. Thus, it is likely that also in the experiment not more than about 12 motors are able to simultaneously attach to the MT. Not having space left on the MT, no more new motors can attach to the MT and change the motor configuration. Consequently, it is difficult to transition between states, and reversals are suppressed.

The same can be observed when simulating the standard model with only one PF. Even though fewer motors are attached (fig. D.3b of the appendix D), the percentage of reversals is drastically reduced (fig. D.3a of the appendix D), because no space is left on the protofilament for new motors to attach. Taking together, in case of a high number of available motors transitions are suppressed because first, it is difficult to change many motors, and second no space on the MT is available anymore for new motors to attach and change the configuration of MT-attached motors.

In the case of the MT gliding assay, the first limiting factor would be that many motors are attached and need to be changed to transition to another state. Regarding the space left on the MT, it could be assumed that there should still be space for new motors to attach because MT-attached motors would be more spread out over the length of the MT (dependent on the motor density). However, the findings of chapter 4 suggest that the motors can only reach one protofilament in the MT gliding assay. Consequently, it might be that there is not too much space left for new motors to attach and change the configuration of MT-attached motors. Third, it is expected that also in the case of the gliding assay the attachment rate is increased because motors stay near the MT after detachment. A high attachment rate favors the state where all motors are attached and no detached motors are available anymore to attach and change the configuration of MT-attached motors. Thus, the high number of MT-attached motors, the missing space on the MT, and the high attachment rate are assumed to lead to a suppression of reversals for bidirectional MT gliding assays.

One DDB against one KIF16B The last modification deals with the case where one DDB motor competes against one KIF16B motor as it was measured *in vitro* by Belyy et al. [88]. Simulating the competition between one active DDB and one active KIF16B also reduces the amount of reversal tracks and increases the amount of minus tracks (fig. 7.9). Thus, DDB dominates over KIF16B. The number of MT-attached motors (fig. 7.10, second row, central) clearly shows that during positive runs the KIF16B motor is attached, during negative runs the DDB motor and during the pauses occasionally both motors, but mainly one of the two motors. This means for the one-to-one simulation pauses do not necessarily only occur when both motors are attached and a tug-of-war occurs. Pauses can also occur when

one motor is attached but in the force-free regime (see eq. (7.1) and (6.4) for the definition of motor forces). In this regime, the motor steps along the MT but does not exert any force on the liposome. The liposome in this case does not show any net motion. Moreover, the liposome is allowed to diffuse in the harmonic potential of MT-attached motors. Having just one (or two) motors attached, fluctuations due to the diffusive liposome motion become large. This, as well as the short duration of the tracks, also makes the segmentation of the tracks into pauses and runs difficult and it might be that a reversal is just a diffusive motion of the liposome. Therefore, it is better to directly compare attachment and detachment rates of active KIF16B and active DDB motors (see table D.1 of the appendix D) to understand why reversals are unlikely to happen for the one-to-one simulation. To see a reversal, the system needs to transition from one run state to a pause (both motors need to be attached for a short moment, motors cannot immediately be exchanged) and then to the other run state. Comparing DDB and KIF16B attachment and detachment rates reveal that when KIF16B attaches first, it is likely that the KIF16B motor detaches again before the DDB motor attaches. A transition to a pause state with both motors being attached is therefore unlikely. However, when DDB is attached first, then it is likely that KIF16B attaches before DDB detaches. Thus, a transition to a pause state with both motors being attached is likely. Being in this pause state means that both motors try to pull each other off. Since DDB has a higher detachment force and a lower force-free detachment rate, DDB likely pulls off KIF16B and a transition from the pause back to the negative run state occurs. Hence, transitions from the negative run state to the pause state and back to the negative run state are likely to happen but not the transition from the negative run state to the pause and then to the positive run state. Therefore, it is unlikely to observe reversals and why DDB dominates over KIF16B.

Belyy et al. [88] uses a kinesin-dynein complex, where both motors are bound to each other, and observed more stalled tracks than the here presented simulation with the standard parameter set (fig. 7.9). It might be that when kinesin is directly coupled to dynein, that attachment rates are enhanced. Moreover, Belyy et al. [88] uses kinesin-1 instead of kinesin-3 (KIF16B). Kinesin-1 is known to have a higher detachment force[33]. Thus, it is hard for dynein to pull off kinesin. Varying DDB and KIF16B parameters for the one-to-one case reveals that more stalled tracks can be observed, when both have higher attachment rates or when both are equally strong (same parameters, but opposite stepping directions). Thus, while reversals are reduced for all tested parameter sets, the used parameters/motors determine whether transport by one kinesin and one dynein is predominantly performed in one direction or stalled.

While for all the other modifications a high number of MT-attached motors makes it difficult to transition between one and another state, in the one-to-one competition maximal two motors can be attached. In this case, the missing pool of detached motors, which could attach and change the motor configuration, is the limiting factor why reversals cannot be observed with a one-to-one system.

In summary, model modifications reveal that three conditions must be met simultaneously to obtain directional reversals: first a low number of MT-attached motors such that the stochastic attachment and detachment of single motors change the configuration of MT-attached motors in such a way that transitions between states occur. Second, there needs to be enough space on the MT for new motors to attach and be able to change the configuration of MT-attached motors, and third, there needs to be a pool of detached motors, which can attach and change the configuration of MT-attached motors.

7.3 Discussion

In this chapter, it is shown that the following three conditions need to be fulfilled simultaneously to obtain reversals in bidirectional cargo transport:

1. A low number of MT-attached motors such that the stochastic detachment and attachment of individual motors can lead to transitions between states (condition one).

2. Enough space on the MT for new motors to attach and thereby change the configuration of MT-attached motors (condition two).

3. A pool of detached motors, which can attach and thereby change the configuration of MT-attached motors (condition three).

For all the presented model modifications at least one of the three conditions is not fulfilled such that reversals are reduced. Having a higher attachment rate or a lower detachment rate, none of the conditions are fulfilled. When having a higher number of motors, condition three is fulfilled, but not conditions one and two. And when having the one-to-one competition between one DDB and one KIF16B conditions one and two are fulfilled, but not condition three. Understandings obtained from model modifications can be used to understand why rigidly coupled motors as previously used *in vitro* do not show reversals, while cargos with fluid surfaces where motors can diffuse do. The main difference is that for fluid cargos motors diffuse away from the MT after detachment, while detached rigidly coupled motors stay near the MT. This leads to a higher (re)attachment rate for rigidly coupled motors. A higher attachment rate is also predicted by previous theoretical works simulating a dynein rigidly coupled to a kinesin [337, 338]. The here presented modeling results shows that a high attachment rate favors the MT-attached over the MT detached state such that whenever possible all motors are attached to the MT. Consequently, when having a high number of rigidly coupled motors as expected for the MT gliding assay, conditions one and two are not fulfilled, while condition three might be given. When having a low number of rigidly coupled motors as for DNA origami assays or the one-to-one competition, condition three is not fulfilled, while one and two might be given. In conclusion, a low attachment rate is mandatory to obtain reversals.

Besides the fluid cargo surface, there might be other factors reducing the attachment rate. MT-associated proteins (MAPs) are known to change the motor binding affinity to the MT. Monroy et al. [313] show how a series of MAPs alter the MT binding affinity of kinesin-3, kinesin-1, and cytoplasmic dynein. This means, based on the findings of the here presented work, it can be hypothesized that rigidly coupled motors might show reversals when the MT binding affinity is reduced by MAPs.

Moreover, the findings of this chapter suggest that rigidly coupled DDB and KIF16B motors transporting a bead would not show reversals. The last chapter (chapter 6) reveals that fewer motors are attached in case of the bead compared to the liposome. This means conditions one and two should be fulfilled. Because motors are rigidly coupled, one would assume that also the (re)attachment rate should be high such that all available motors are attached to the MT and no pool of detached motors exists (contradicting condition three). However, the bead can also rotate around its center of gravity. It might be that motors on the side of the bead facing away from the MT at some point can reach the MT and therefore build a pool of detached motors. In the last chapter (chapter 6), it is shown that the rotation of the bead leads to less fluctuations between tracks of different beads because a bigger pool of motors could attach. It remains unclear whether a stochastic rotation of the bead around its center of gravity could provide a pool

of detached motors that can attach to the MT and change the MT-attached motor configuration such that reversals occur. Thus, future modeling and experimental work should test whether beads show reversals or not.

In view of regulating bidirectional transport, the findings of this chapter suggest that in dependence on the motor-cargo coupling, two different motility modes can be achieved. One mode includes reversals such that the cargo is transported bidirectionally, the other mode suppresses reversals so that the cargo is transported in one direction or gets stuck. This means, when a cargo is needed to be transported only in the direction of the dominating motor team, a more rigid-like cargo (lower to no diffusion of motor tails) would be favorable. However, when a cargo should be transported bidirectionally, a fluid cargo (high diffusion of motor tails) would be needed. Thus, the cargo surface could be used to regulate the transport mode of intracellular transport. To conclude the cargo surface composition is an important factor to consider when studying the regulation of intracellular cargo transport by teams of opposing motors.

Chapter 8

Conclusion and Outlook

Intracellular cargo can be considered on different scales: i) one can consider many cargo systems and eventual interactions with other objects in the cellular environment, ii) one can consider single motor-cargo complexes where teams of (opposing) molecular motors transport a single cargo or iii) one can consider single molecular motor dynamics without any further interactions with other objects than the MT. Here, available knowledge of single molecular motors was used to study single motor-cargo complexes by means of stochastic simulations. Thereby, the following main research question was addressed:

How is bidirectional, intracellular cargo transport by teams of opposing kinesin and dynein motors regulated so that the cargo reaches its destination?

Bidirectional transport of single cargos *in vivo* is characterized by stationary and diffusive phases, fast directed runs, and directional reversals [7, 8]. Past *in vitro* assays, where teams of opposing kinesin and dynein motors are bound to artificial cargos, could not reproduce this rich behavior. Instead, *in vivo* cargo is typically transported at rather constant velocities or stalled. No reversals could be seen using artificial cargos *in vitro* [88, 158, 309]. However, using more *in vivo*-like cargos, such as liposomes, our collaborators[1], could reproduce *in vitro* cargo transport which shows fast unidirectional runs, pauses and directional reversals [335]. In particular, liposome transport simulations by opposing dynein (DDB) and kinesin (KIF16B) motors show similar trajectories (see chapter 7). Simulations reveal that for seeing reversals a low number of MT-attached motors, enough space on the MT, and a pool of detached motors are necessary. A low number of MT-attached motors is needed so that spontaneous at- or detachment of single motors changes the force balance significantly. An attachment of other motors to change the force balance is only possible if there is space on the MT for new motors to attach and if there is a pool of detached motors. Due to motor diffusion on the liposome surface, motors are expected to diffuse away from the MT and not (re)attach fast. Consequently, not all motors are attached such that there is a low number of MT-attached motors, enough space on the MT and a pool of detached motors.
Simulating, however, bidirectional MT gliding assays, many motors are attached to the MT. Moreover, due to motors staying in close proximity to the MT, (re)attachment is expected to be fast [337], such that the state where all available motors are attached is favored and no pool of detached motors exists. Consequently, neither at high nor at low number of motors under the MT, reversals can be produced with bidirectional MT gliding assays. Previous *in vitro* experiments [158] use DNA origami assays for bidirectional cargo transport by multiple motors with a fixed configuration. Due to the stiff nature of these artificial cargos, it is expected that motors stay in close proximity to the MT and therefore (re)attach fast.

---

[1]Lara Scharrel, Ashwin D'Souza, Rahul Grover, Akhil Sai Naidu from the Stefan Diez lab at B CUBE, TU-Dresden.

Consequently, all motors are attached such that no pool of detached motors exists and no reversals are observable.

Comparing unidirectional bead and liposome transport simulations shows that fewer motors are attached in case of the bead. This means, for bidirectional bead transport it is expected that a low number of MT-attached motors and enough space on the MT for other motors to attach are given. Moreover, there exists a pool of detached motors. However, most of them are not able to attach to the MT because they are too far away from the MT. Due to spontaneous or MT-attached motor-induced bead rotation, the configuration of motors, which are able to reach the MT, can change. Whether this would be enough to induce reversals, needs to be tested in future simulations and experiments.

Inactive motors were observed to induce pauses/slow velocity states in unidirectional bead and liposome transport (chapter 6). In bidirectional liposome transport simulations (chapter 7), it could be shown that inactive motors stabilize pauses. Simulating bidirectional liposome transport without inactive motors no long stable pause can be seen anymore, but frequent directional reversals. Passive crosslinkers might also be the reason for the observed stationary phases of *in vivo* cargo transport.

Having characterized the bidirectional cargo transport motion, the question, of how this transport might be regulated can be addressed. As above described, transport can be divided into a pause (or slow) state and a directional run state. Consequently, transport can be regulated during the pause state and/or the run state. The pause state is characterized by a force balance between opposing motor teams or between active and inactive motors. The run state, in contrast, is the outcome of an asymmetry between the (opposing) motor teams. One way of regulation would be to change the strength of one motor team such that the force balance or rather the asymmetry (run state) of the motor teams is changed. Another way of regulation is to change the motor activity (velocity) which determines how far the cargo can be transported during the run state. Speeding up one motor team, while the average strengths of the motor teams are kept constant, would lead to an overall higher distance traveled in this direction when the cargo transport pattern includes directional reversals. Here, different factors were found that influence the strengths of the motor teams and/or the motor activity.

The strengths of the motor teams are first given by the number of MT-attached kinesin and dynein motors. Using MT gliding assays (see chapter 4), it could clearly be shown that changing the relative number of available dynein to kinesin motors shifts the force balance such that the transport directionality can be regulated. Simulating liposome transport at a constant number of dynein motors and increasing number of kinesin motors increases the number of plus tracks, i.e. cargos that exclusively moved towards the MT plus-end. This means the asymmetry between kinesin and dynein teams is shifted more to the kinesin side. In summary, the relative amount of MT-attached kinesin and dynein motors determines the force balance or rather the asymmetry between opposing motor teams and therefore the overall transport direction.

Besides externally regulating the relative amount of MT-attached kinesin and dynein motors, also the MT track can do the work. *In vivo*, the surface of the MT is not homogeneous, but i.a. coated with various MT-associated proteins (MAPs) [31, 204]. Some of them increase the affinity for some types of motors, while others detach some types of motors [31, 40, 313–316]. The MAP tau, for instance, accumulates in stable tau islands on the MT. These tau islands are known to detach kinesin but leave dynein unchanged [31, 40]. By changing the MT-attached motors, tau islands could change the force balance and therefore the transport directionality. Here, the formation of stable tau islands is studied to better understand the impact on motor

transport. This work hypothesizes that also the tau island formation is guided by the MT lattice. Since *in vitro* experiments show that taxol-extended MT lattices are compacted by tau islands [317], there might be lattice sites where tau islands preferentially nucleate (initially compacted lattice sites) and others (non-compatible lattice sites) where tau islands cannot continue growing. The changes of the MT lattice might also be responsible for different motor affinities [339]. Besides non-motor MAPs, also motors themselves can change the MT lattice and change the motor affinity [222, 223, 340]. The theoretical work by Jose and Santen [224] shows that motor-induced MT lattice changes can lead to a regulation of dynein- and kinesin-driven cargos in crowded axons. This indicates, the MT track can also be a regulation factor of bidirectional transport and should be taken into account in future work.

Not only the relative number of motors but also the strength of individual motors influences the strengths of the motor teams. MT gliding assay simulations find that when kinesin-1 competes against cytoplasmic dynein without adaptor proteins, the balanced state is given by single kinesin motors, which compete against a pool of dynein motors including passive MT-attached motors. Passive MT-attached motors activate and help out in the case an active dynein motor is pulled off. When simulating liposome transport by kinesin-3 (KIF16B) and dynein with adaptor proteins (DDB) it is found that an equal average number of both motors is bound to the MT during force balance (slow/pause state). However, for kinesin-3 only one motor is carrying the load, while for dynein the load is shared (not necessarily equally) between almost all MT-bound motors. Thus, both cases reveal that in the presence of counteracting forces, kinesin is more a single fighter, while dynein motors are team players. The reason for the differences between kinesin and dynein lies in the different motor stall and detachment forces. Müller et al. [151] defines motor strength as the ratio of stall to detachment force. A strong motor (high stall force to detachment force ratio) detaches before stalling and a weak motor stalls before detaching. Dynein with adaptor proteins is stronger than without adaptor proteins (compare parameter tables A.1 of appendix A and D.1 of appendix C). This means the dynein adaptor proteins influence the single motor strength, the relative strengths of the opposing motor teams, and therefore the motor configurations in the force balance state. Consequently, adaptor proteins are factors, which can potentially regulate bidirectional transport.

Yet another factor influencing the strength of the individual motors is the ATP concentration. The ATP concentration is known to change the dynein and kinesin stall forces in certain regimes [101, 186]. Whether opposing motors respond sufficiently differently to changes in ATP concentration to regulate bidirectional transport remains uncertain. Bidirectional gliding assay simulations (see chapter 4) could not show that ATP concentrations change the force balance because changes were small compared to fluctuations. But, the theoretical work by Klein et al. [35] predicts that bidirectional cargo transport can be regulated by the ATP concentration. The work by Klein et al. [35] used a point-like cargo model with a fixed kinesin and dynein configuration which can attach to the MT. To test whether a regulation by the ATP concentration can be achieved, future work should use the here presented bidirectional liposome model where motor configurations, which are able to attach to the MT, change due to the exchange with the reservoir.

Additionally to influencing the motor stall forces, the ATP concentration changes motor activities, i.e. velocities in a different manner for dynein than kinesin (see chapter 4) [89, 120, 309]. As said before, bidirectional transport characterized by pauses and runs can either be regulated during pauses or runs. By influencing the motor velocities differently, changes in the ATP concentration could regulate the runs. Simulating bidirectional gliding

assays at different ATP concentrations, clearly shows that the velocities during kinesin-driven and dynein-driven states depend on the ATP concentration. However, since the regulation of the run state can only change the overall directionality if the transport exhibits reversals, MT gliding assay simulations could not show the regulation by the ATP concentration. Therefore, bidirectional liposome transport, which shows reversals, needs further to be simulated at varying ATP concentrations in the future.

Another factor influencing the motor stepping velocities are roadblocks. As for the ATP concentration, MT gliding assay simulations clearly show that roadblocks influence the dynein- and kinesin-driven states, but cannot regulate the directionality of MT gliding assays because they do not show reversals. Previous studies showed that kinesin gets stuck and eventually detaches when encountering a roadblock, while dynein circumvents the roadblock by shifting to the neighboring protofilament [39, 211]. These different mechanisms to overcome roadblocks might first influence the velocity of dynein and kinesin in the presence of roadblocks differently such that a regulation of the run state could be observed when using a transport system that shows reversals. Second, due to kinesin-1 motors detaching upon encountering a roadblock, roadblocks can even change the MT-attached motor configuration and therefore the strength of the opposing motor teams. Having a liposome transport system where only a low number of motors is attached and detached motors might diffuse away from the MT on the cargo surface, roadblock-induced changes of the MT-attached motor configurations might be enough to induce reversals. Bidirectional liposome transport in the presence of roadblocks should be tested in further studies.

In vivo, the crowded environment could also influence the transport. While *in vitro* the motor-cargo complex diffuses away from the MT when no motor is attached to the MT anymore, *in vivo* the crowded environment could keep the cargo in close proximity to the MT and thereby changing motor (re)attachment rates. Dependent on the crowdedness of the environment motor attachment rates, could be changed differently and consequently influence the cargo transport manner (see chapter 7 for how the attachment rate changes the transport manner).

In summary, this work studied motor-driven, intracellular transport by teams of opposing kinesin and dynein motors. The factors necessary for bidirectional transport to show reversals could be identified, as well as potential regulatory factors. Future work should focus on how the identified regulation factors influence the motor-driven, bidirectional transport of *in vivo*-like cargo such as liposomes. Understanding intracellular transport mechanisms and their regulation may help develop targeted treatments for cancer and neurodegenerative diseases in the future.

Appendix A

Appendix modeling microtubule gliding assays

Description:	Value	Reference:
Gliding assay		
MT length L_{MT}	See figures and figure captions	Given by the experiment
Kinesin surface density σ_{kin}	See figures and figure captions	Estimated from the experimental kinesin in solution
Dynein surface density σ_{dyn}	See figures and figure captions	Estimated from the experimental dynein in solution
ATP concentration	[ATP] = 2000 μM, if not further specified	Given by the experiment
Temperature	$T = 300\,\mathrm{K}$	Given by the experiment
Simulation parameters		
Relaxation time (=time until measurements start)	$t_{relax} = 20\,\mathrm{s}$	
Total simulation time	$t_{end} = 220\,\mathrm{s}$	
Number of runs/samples	$N_{samples} = 15 - 20$	
Number of measurements during one sample	$n_{mes} = 200$	
Total number of measurements of all samples together	$N_{mes} = 3000 - 4000$	
Standard deviation of MT position	$\sigma_{Pos} = 30\,\mathrm{nm}$	Measurement uncertainty from experiment
Common dynein and kinesin parameters		
Stepsize of kinesin and dynein	$d = 8\,\mathrm{nm}$	[101, 183, 186]
Unloaded second-order rate constant for ATP binding	$k_b^0 = 1.3\,\mu\mathrm{M}^{-1}\mathrm{s}^{-1}$	[120]
Fraction of unloaded catalytic cycle	$q_{cat} = 6.2,\ p_{cat} = 1 - q_{cat}$	[120]

Fraction of unloaded ATP binding	$q_b = 4.0$, $p_b = 1 - q_b$	[120]
Kinesin:		
Motor radius	$R_{kin} = 4\,nm$	Same order of magnitude as [193]
Untensioned length	$L_{0,kin} = 30\,nm$	[341]
Width of attachment area $\approx$ twice kinesin contour length	$L_{attach,kin} = 100\,nm$	Same order of magnitude as [341–343]
Stiffness	$\kappa_{2,kin} = 3.0 \cdot 10^{-4}\,kg/s^2$	[34, 332, 333]
Stall force	$F_{s,kin} = 6\,pN$	[33, 186]
Detachment force	$F_{d,kin} = 6\,pN$	[33]
Force-free detachment rate	$k_{d,kin}^0 = 0.66\,s^{-1}$	Taken from [34], same order of magnitude as [120]
Attachment rate	$k_{a,kin} = 20\,s^{-1}$	
Forward velocity	$v_{f,kin} = 1000\,nm/s$	[183, 186]
Backward velocity	$v_{b,kin} = 6\,nm/s$	Same order of magnitude as [124]
Dynein:		
Motor radius	$R_{dyn}^i = 24\,nm$	Approximated from EM images of [89, 95]
Length of deactivation area	$L_{0,dyn} = 30\,nm$	Unknown
Width of attachment area	$L_{attach,dyn} = 30\,nm$	= dynein length, approximated from EM images of [89, 95]
Stiffness within L_0	$\kappa_{1,dyn} = 0.019272\,pN/nm$	Unknown
Stiffness beyond L_0	$\kappa_{2,dyn} = 0.065\,pN/nm$	[34]
Stall force	$F_{s,dyn} = 1.25\,pN$	Same as [33, 34], same order of magnitude as [88, 99, 101, 344]
Attachment rate	$k_{a,dyn} = 0.2\,s^{-1}$	Unknown
Mean forward velocity	$v_{f,mean,dyn} = 1300\,nm/s$	[89] (motility assay)
Backward velocity	$v_{b,dyn} = 15\,nm/s$	[100] (yeast dynein)
Standard deviation of max. velocity distribution	$\sigma_v = 1500\,nm/s$	Relatively wide velocity distributions were measured in [94, 95], too.
Left velocity border	$v_{f,low} = 300\,nm/s$	
Right velocity border	$v_{f,high} = 2300\,nm/s$	
Diffusion rate	$s_{0,max} = 92.9\,s^{-1}$, $s_0([ATP] = 2000\,\mu M) = 85\,s^{-1}$	From [300] (fit of experimental data)
Activation rate constant	$r_a^0 = 40\,s^{-1}$	Unknown
Deactivation rate	$r_d = 1\,s^{-1}$	Unknown

Motor radius	$R_{\text{dyn}}^i = 24\,\text{nm}$	Approximated from EM images of [89, 95]
Roadblocks		
Roadblocks line density	$\lambda_{\text{RB}} = 0 - 16\,\mu\text{m}^{-1}$ (stated in the figures)	Range chosen similar to [39]
Number of Roadblocks on the MT	N_{RB}	Calculated from the roadblock line density λ_{RB} and the MT length L_{MT}
Radius of roadblocks (rigor binding kinesin motor mutants)	$R_{\text{RB}} = 4\,\text{nm}$	As kinesin motor
Multiple protofilament simulations		
Number of protofilaments	$N_{\text{L}} = 7$	Optimized until obtaining the kinesin result shown by [39] for multiple kinesin motors
Dynein side stepping rate	$s_{\text{side}} = 4\,\text{s}^{-1}$	Same order of magnitude as calculated from results of [39] (mammalian) and [67] (yeast)

Table A.1: Table shows parameters used for kinesin and dynein motor models in unidirectional and bidirectional gliding assay simulations. Parameter values are used as given by this table, if not stated differently. See figures and figure captions for varied parameters.
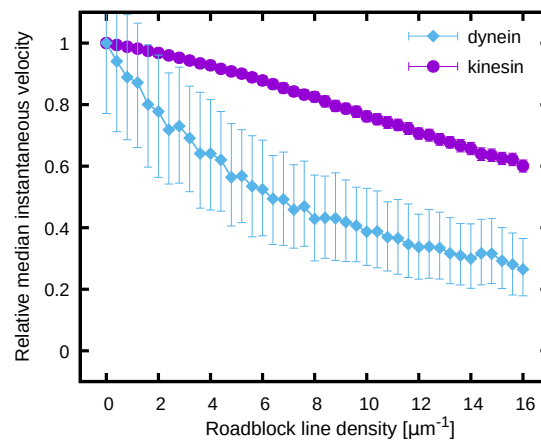
Figure A.1: Without side-stepping, dynein is more affected by roadblocks than kinesin. a) Multiple protofilament simulations of unidirectional dynein and kinesin gliding assays in the presence of roadblocks. Using the multiple protofilament simulations seven PFs are modeled instead of just one protofilament. In the here presented, modified simulation neither kinesin nor dynein is allowed to change the protofilament, even though there are seven PFs modeled. The dynein density was $\sigma_{\mathrm{dyn}} = 50\,\mu\mathrm{m}^{-2}$ and a MT of length $L_{\mathrm{MT}} = 30\,\mu\mathrm{m}$ was used. Relative median instantaneous velocities (instantaneous velocity divided by the instantaneous velocity in the absence of roadblocks) are depicted as a function of the roadblock line density. Not being able to change the protofilament, dynein is more affected by roadblocks than kinesin as it could be seen for the one protofilament simulation (see fig. 4.21a)

A.1 Diffusion

In this appendix section, a relation between the one-dimensional diffusion coefficient and the mean square velocity is derived for a constant measurement interval Δt and a zero mean velocity. Therefore, first, the instantaneous velocity is calculated as usual:

$$v_i = \frac{(\Delta x)_i}{(\Delta t)_i} \tag{A.1}$$

Since the measurement interval Δt is constant, the mean square velocity is obtained by:

$$\left\langle v^2 \right\rangle = \frac{\left\langle (\Delta x)^2 \right\rangle}{(\Delta t)^2}. \tag{A.2}$$

Since in case of a diffusive motion, the displacements Δx are independent, identically distributed random variables with zero mean, the mean square displacement can be calculated as follows:

$$\left\langle x^2 \right\rangle = \left\langle \sum_{k=1}^{n} (\Delta x)_k \sum_{l=1}^{n} (\Delta x)_l \right\rangle \tag{A.3}$$

$$= \underbrace{\sum_{k=1}^{n} \left\langle (\Delta x)_k^2 \right\rangle}_{k=l} + \sum_{l,k,k \neq l} \underbrace{\left\langle (\Delta x)_k \right\rangle \left\langle (\Delta x)_l \right\rangle}_{=0} \tag{A.4}$$

$$= n \left\langle (\Delta x)^2 \right\rangle. \tag{A.5}$$

Using $n = \frac{t}{\Delta t}$ and equation A.2 the following relation between the mean square displacement and the mean square velocity can be obtained:

$$\left\langle x^2 \right\rangle = \frac{t}{\Delta t} (\Delta t)^2 \left\langle v^2 \right\rangle \tag{A.6}$$

$$= t (\Delta t) \left\langle v^2 \right\rangle. \tag{A.7}$$

With the one-dimensional diffusion coefficient being [259]

$$\left\langle x^2 \right\rangle = 2Dt \tag{A.8}$$

a relation between the diffusion coefficient D and the mean square velocity $\left\langle v^2 \right\rangle$ can be found:

$$2Dt = \left\langle x^2 \right\rangle = t (\Delta t) \left\langle v^2 \right\rangle \tag{A.9}$$

$$\iff D = \left\langle v^2 \right\rangle \frac{\Delta t}{2} \tag{A.10}$$

Appendix B

Appendix modeling tau adsorption

Parameter	Value	Reference
Global adsorption rate	$\Omega_a = 0.003\,\text{s}^{-1}$	Calculated using the standard Langmuir adsorption model
Global desorption rate	$\Omega_d = 0.046\,\text{s}^{-1}$	Calculated using the standard Langmuir adsorption model
Diffusion rate	$s = 4220\,\text{s}^{-1}$	From the diffusion constant $D_{\text{mes}} = 0.27\,\mu\text{m}^2/\text{s}$ given by Siahaan et al. [40]
Binding energy	$B = 0.1$	Unknown
Intrinsic detachment rate of MTBRs	$\omega_d = 0.207\,\text{s}^{-1}$	From mean first detachment time $\langle t \rangle = \Omega_d^{-1}$ for given binding energy B
Intrinsic attachment rate of MTBRs	$\omega_a = \omega_d \cdot \text{e}^{-B} = 0.229 s^{-1}$	Using the binding energy B, the detachment rate ω_d and the detailed balance (see eq. (5.4)).
Tau-tau interaction energy	$I = 5$	Unknown
Preference of preferential adsorption	$p = 500$	Unknown
Minimum number of occupied sites for the external island definition (up to 3 three empty sites within an island)	$N_{\text{min}} = 7$	
Tau reservoir = number of tau molecules in solution	$N_{\text{res}} = 80$	
Number of sites	$N_L = 1250$	Correspond to a MT length of $L_{\text{MT}} = 10\,\mu\text{m}$
End of simulation	$T_{\text{end}} = 200 - 300\,\text{s}$	$T_{\text{end}} = 200\,\text{s}$ for section 5.1 and $T_{\text{end}} = 300\,\text{s}$ for section 5.2
Measurement time interval	$\Delta t_{\text{mes}} = 0.12\,\text{s}$	
Number of samples (=simulated MTs)	$N_{\text{samples}} = 50$	

Table B.1: Table shows the standard parameter set used in the tau adsorption model, if not stated differently (see therefore captions of figures showing simulation results).

a) Tau with 4 MTBRs   b) Tau with diffusion   c) Tau-tau interaction

d) Preferential adsorp.   e) Tau reservoir
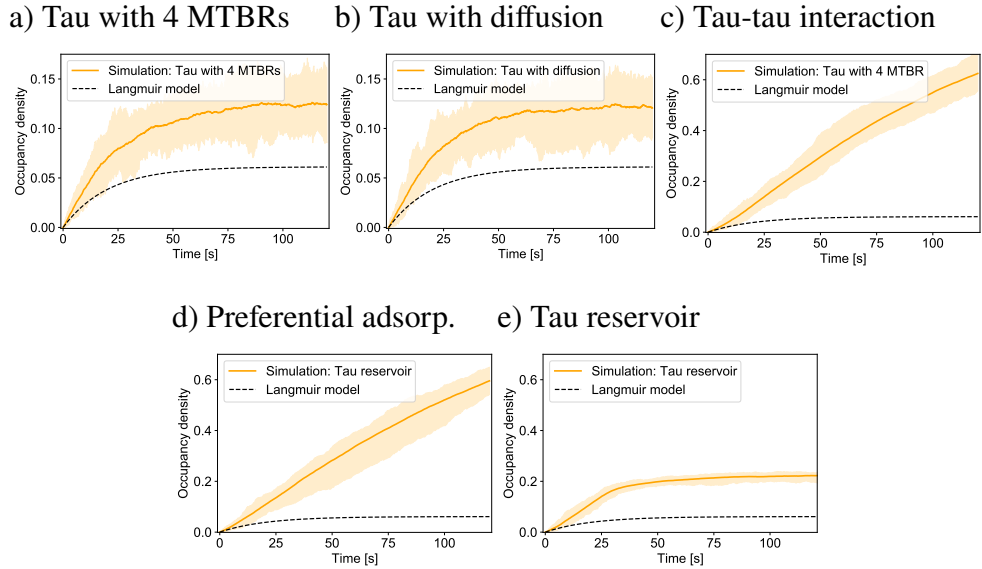
Figure B.1: Building up tau adsorption model - occupancy density. Occupancy densities for different stages of the tau adsorption model. The occupancy density is defined as the number of occupied sites divided by the total number of sites N_{L}. Moreover, the Langmuir adsorption model fit of the experimental density is shown. a) Tau adsorption and desorption are modeled with tau having 4 MT binding repeats (MTBRs). Since one tau molecule can occupy 1-4 sites, the occupancy density is higher than for the pure Langmuir model. b) To the model of a) a one-dimensional tau diffusion along the lattice is added. The occupancy density remains unchanged. c) A tau-tau interaction energy is added to the model of b). A tau-tau interaction occurs between two tau molecules that are next neighbors on the lattice. The interaction energy reduces the intrinsic tau detachment rate and the tau diffusion rate leading to an increased occupancy density. d) A preferential tau adsorption at the empty boundary sites of existing tau islands is added (internal island definition, see main text for detailed definition). Therefore, the adsorption rate at the island boundary sites is increased and the adsorption rate for the other sites is reduced such that the overall adsorption remains unchanged. The occupancy density, therefore, is similar to c). e) To the model of d), a tau reservoir is added, which limits the available tau molecules in the solution. This leads to a saturation of the occupancy density with time.

a) $N_{\min} = 5$ b) $N_{\min} = 7$ c) $N_{\min} = 9$ d)
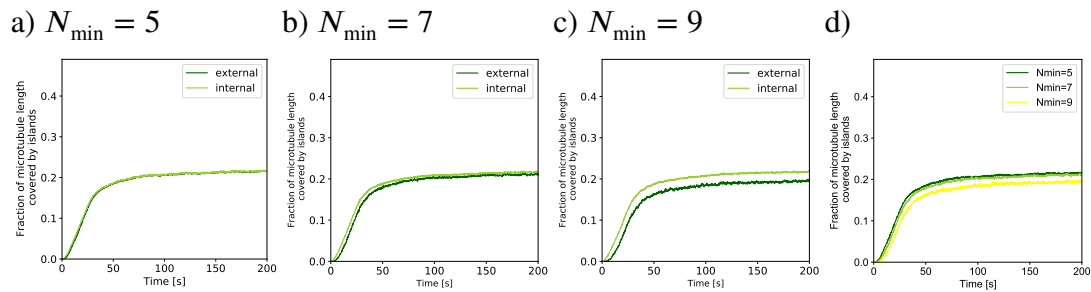
Figure B.2: Internal and external island definition. In the simulation, an island is formed when two tau molecules are next neighbors on the lattice (internal definition). However, in the kymograph, it is not distinguishable whether two occupied spots are from one or two tau molecules. Therefore, another definition is needed to segment into island and surrounding regions. The external island definition says that when $N_{\min}$ consecutive sites are occupied they form an island. Within islands, up to three empty sites are allowed for both definitions. This figure compares island coverages from the internal and external definitions with a) $N_{\min} = 5$ (minimal meaningful value), b) $N_{\min} = 7$, and c) $N_{\min} = 9$. d) Graph directly compares coverages from the external definitions with $N_{\min} = 5$, $N_{\min} = 7$, and $N_{\min} = 9$.

Appendix C

Appendix modeling cargo transport by kinesin-3

Parameter	point-like	1d L	1d B	3d L	3d B	Reference
Attachment rate k_a [s^{-1}]	5	5	5	5	5	[327], standard, also used in the modeling of [34, 151]
Mean force-free velocity v_f [nm/s]	900	900	900	900	900	Estimated from experimental single molecule data
Backward velocity v_b [nm/s]	6	6	6	6	6	Same order of magnitude as Carter and Cross [124] found for kinesin-1
Stall force F_s [pN]	5	5	5	5	5	[74] for kinesin-3
Detachment force F_d [pN]	1	3	3	4	4	Budaitis et al. [328] find a range of approx. $1 - 3$ pN for different members of the kinesin-3 family, not including KIF16B
Force-free detachment rate k_d^0 [s^{-1}]	0.8	0.8	0.8	0.8	0.8	From experiment
Stepsize d [nm]	8	8	8	8	8	[183, 186] for kinesin-1
Stiffness κ_{kin3} [pN/nm]	0.3	0.3	0.3	0.3	0.3	[332, 333] for kinesin-1, [34] modeling kinesin-1 and kinesin-2

Kinesin radius (area occupied by both heads) R_{kin3} [nm]	4	4	4	4	4	[193] same order of magnitude (kinesin-1)
Untensioned kinesin length (1d) L_{kin3} [nm]	30	30	30	30	30	From kinesin-1 gliding assays
Untensioned kinesin length (3d) L_{kin3}^{3d} [nm]	/	/	/	43.52	43.52	Consistent with L_{kin3} for 1d L with $R_C = 60$ nm
Half of attachment area on MT L_{att} [nm]	L_{kin3}	71.36	L_{kin3}	eq. (6.50)	eq. (6.62)	Given by the untensioned kinesin length
Cargo radius R_C [nm]	60	60	60	60	60	Given by the experiment
Minimal distance between MT and cargo d_{MTC} [nm]	/	/	/	15	15	Estimated
Number of reachable PFs N_{PF}	7	7	7	7 (var.)	7 (var.)	Estimated
Total number of PFs	14	14	14	14	14	Given by the experiment
Number of motors in the attachment area on the cargo N_{aa}	see fig.	see fig.	see fig.	/	/	Optimized
Total number of motors N_{tot}	/	see fig.	see fig.	see fig.	see fig.	Optimized
ATP concentration [μM]	1000	1000	1000	1000	1000	Given by the experiment
Number of proposals for the Metropolis algorithm n_m	200	200	200	2000	2000	
Number of samples N_s	300	300	300	300	300	
End of simulation T_{end} [s]	80	80	80	80	80	
Relaxation time at beginning of simulation T_{rel} [s]	4	4	4	4	4	
Measurement interval ΔT_{mes} [s]	0.1	0.1	0.1	0.1	0.1	Given by experiment

Table C.1: Table shows parameter values used in the simulations, when not stated differently (see therefore captions of figures showing simulation results). The abbreviation "point-like" stands for "point-like cargo model", "1d L" for "one-dimensional liposome model", "1d B" for "one-dimensional bead model", "3d L" for "three-dimensional liposome model" and "3d B" for "three-dimensional bead model". The number of reachable protofilaments is noted by "7 (var.)" for the three-dimensional models, because even though always 7 protofilaments can be reached, the protofilaments change in dependence of the angular cargo position. The number of motors in the attachment area N_{aa} and the total number of motors N_{tot} are varied and can always be found in figures showing the respective simulation results.

	μ_r	μ_p	α	β	c_1	c_2
$c = 1.5\,\text{nM}$	589.26	380.89	$6.98 \cdot 10^{-6}$	$6.81 \cdot 10^{-5}$	$1.13 \cdot 10^{-3}$	$1.18 \cdot 10^{-3}$
$c = 3\,\text{nM}$	516.13	62.39	$1.02 \cdot 10^{-5}$	$5.55 \cdot 10^{-5}$	$1.51 \cdot 10^{-3}$	$7.09 \cdot 10^{-4}$
$c = 9\,\text{nM}$	488.27	89.2	$1.27 \cdot 10^{-5}$	$3.57 \cdot 10^{-5}$	$1.56 \cdot 10^{-3}$	$7.59 \cdot 10^{-4}$
$c = 90\,\text{nM}$	322.06	23.43	$1.28 \cdot 10^{-5}$	$3.58 \cdot 10^{-4}$	$1.95 \cdot 10^{-3}$	$3.24 \cdot 10^{-4}$

Table C.2: Fit parameters for the double Gaussian fit of the two peaks in the experimental velocity distribution. See fig. 6.2a for the experimental velocity distribution and eq. (6.1) for the double Gaussian.

	P_f	P_s
$c = 1.5\,\text{nM}$	92.71 %	97.06 %
$c = 3\,\text{nM}$	92.37 %	92.65 %
$c = 9\,\text{nM}$	92.66 %	82.55 %
$c = 90\,\text{nM}$	73.14 %	99.99 %

Table C.3: Table shows percentages of the Gaussian peaks, which would correctly be detected as fast (P_f) or slow states (P_s) when using a limit of $v_{limit} = 200\,\text{nm/s}$ for segmentation.

R_C [nm]	L_{att} [nm]
0	30 (= L_{kin3})
10	38.38
20	45.90
30	52.84
60	71.36
100	92.8

Table C.4: Half length of the attachment area on the MT L_{att} as a function of the cargo radius R_C for the one-dimensional liposome model. The length of the attachment area is chosen such that the motor is force-free over the whole attachment area $X_C(t) \pm L_{att}$ on the MT and experience a force when stretched outside $X_C(t) \pm L_{att}$.
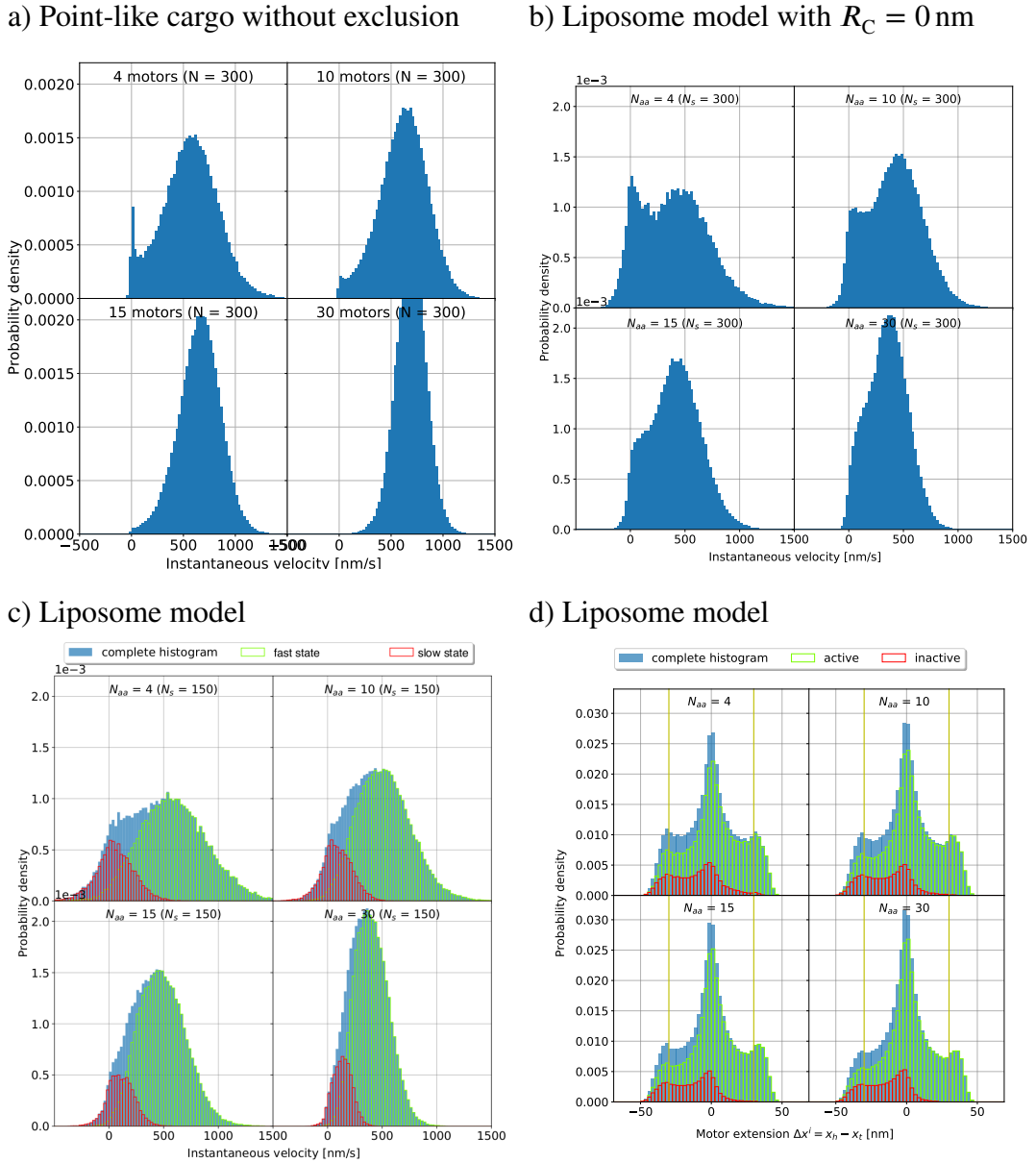
a) Point-like cargo without exclusion

b) Liposome model with $R_C = 0\,\mathrm{nm}$

c) Liposome model

d) Liposome model

Figure C.1: More simulations with the point-like cargo and the one-dimensional liposome model.
a) Figure shows simulation histograms using the point-like cargo model with variations I,III, and IV, but without the motor-motor exclusion on the MT (variation II). Not having the motor-motor exclusion on the MT, the high velocity peak does not move to lower velocities with increasing number of motors and the low velocity peak disappears for higher number of motors. b) Velocity histograms of the one-dimensional liposome with $R_C = 0\,\mathrm{nm}$ and a uniform attachment along L_{att} as a cross check for the one-dimensional liposome model. Results agree with velocity histograms of the point-like cargo model with variations I-IV (see fig. 6.12a). c) Velocity histograms of the one-dimensional liposome model using parameter values from the point-like cargo model with variations I-IV (see table C.1). Low-velocity peaks are less pronounced than for the point-like cargo model (see fig. 6.12a). d) Histograms of motor extensions defined as the (*Continuation on next page.*)

one-dimensional difference between the motor head position x_h on the MT and the motor tail position x_t on the liposome. The vertical yellow lines show the boundaries of the force-free regime. Motor extensions are produced using the liposome model with parameter values of the point-like cargo model with variations I-IV (see table C.1).

a) Standard liposome model
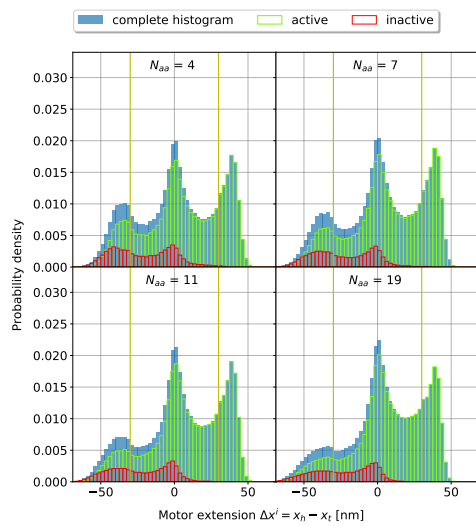
b) Liposome with L_{att} uniform
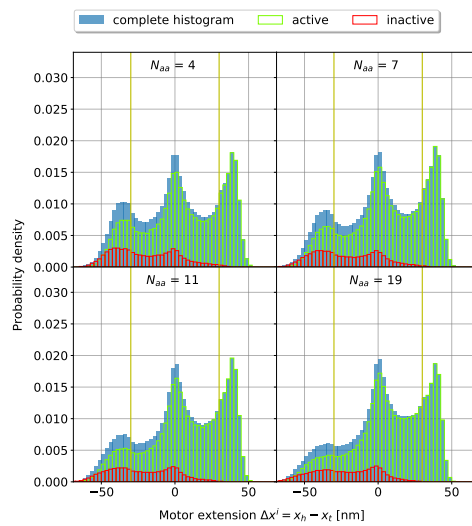
Figure C.2: Motor extensions of the one-dimensional liposome model. Histograms of motor extensions defined as the one-dimensional difference between the motor head position x_h on the MT and the motor tail position x_t on the liposome. Histograms are depicted for the liposome model with the optimized parameter set (see table C.1)) in a) and for the liposome model with the optimized parameter set, but a uniform attachment along L_{att} instead of a Gaussian distributed attachment in b). The vertical yellow lines in the histograms show the boundaries of the force-free regime. While the histograms do not show a big difference outside the force-free regime, the peak at zero is reduced for the liposome model with uniform attachment and slightly higher, force-free motor extensions can be observed.

a)

b)

c)
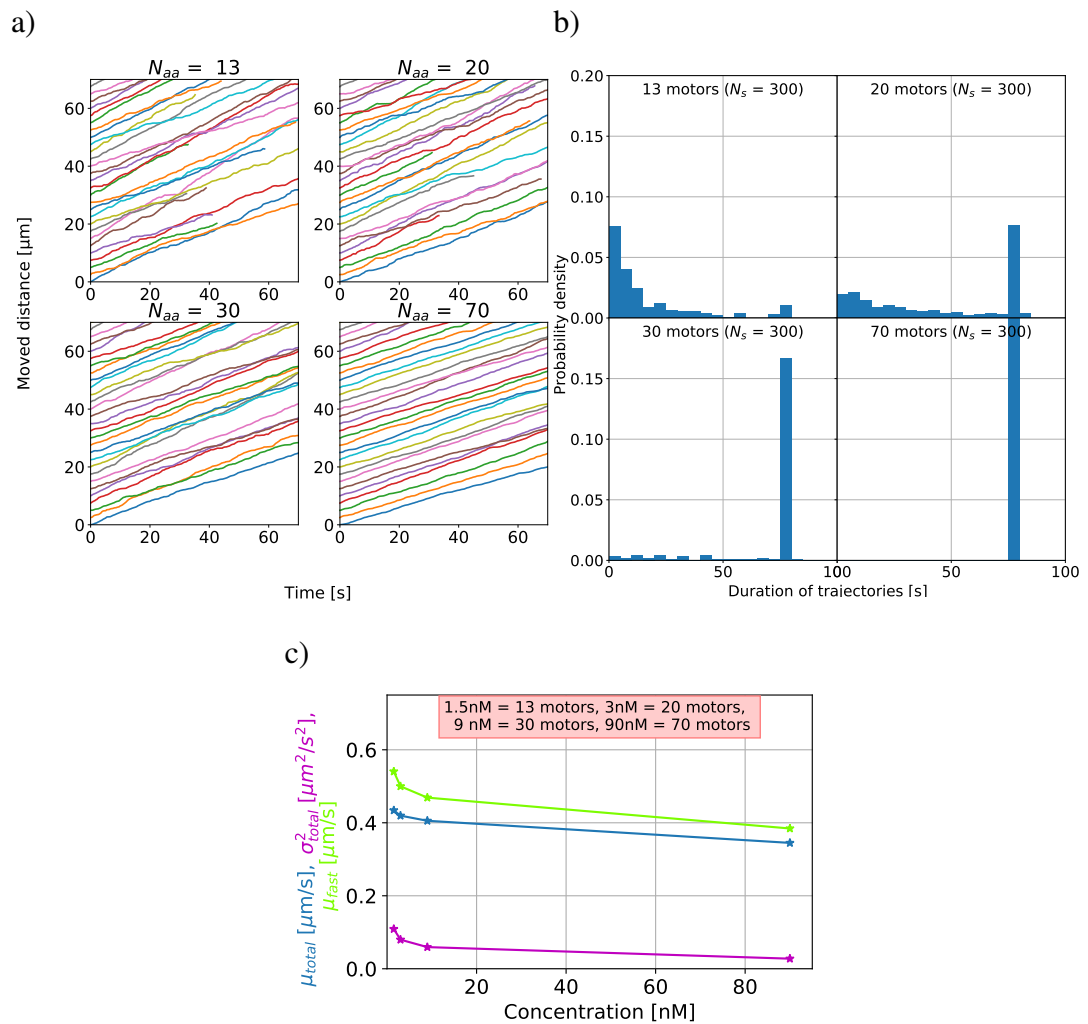
Figure C.3: One-dimensional liposome model variant 7: more plots. Instead of modeling only the motors, which are able to attach the MT, in this simulation the one-dimensional liposome model takes all motors on the cargo into account and an attachment area on the cargo from where the motors can attach the MT. Cargo trajectories (longer than 30 seconds), length of trajectories in seconds and mean values and variances of all velocities as well as mean values of only the running state are similar to the results of the liposome model, where only the motors able to attach the MT are taken into account (see fig. 6.16).
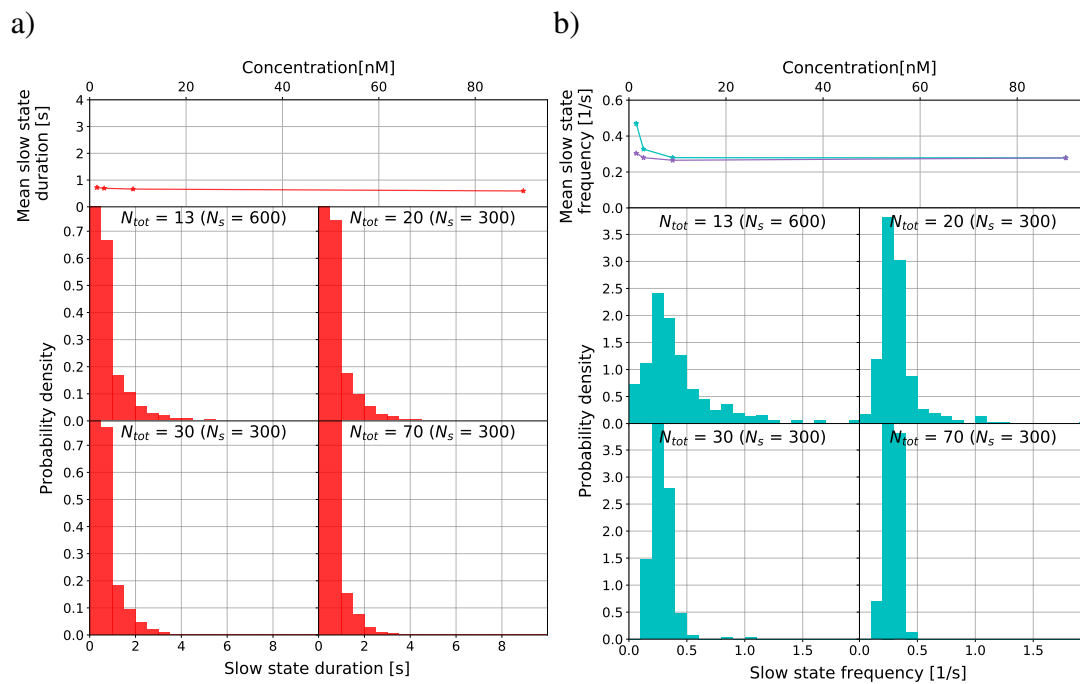
Figure C.4: One-dimensional liposome model variant 7: slow state. Instead of modeling only the motors, which are able to attach the MT, in this simulation the one-dimensional liposome model takes all motors on the cargo into account and an attachment area on the cargo from where the motors can attach the MT. Duration and frequency of the slow state are similar to the results of the liposome model, where only the motors able to attach the MT are modeled (see fig. 6.17).

a)

b)
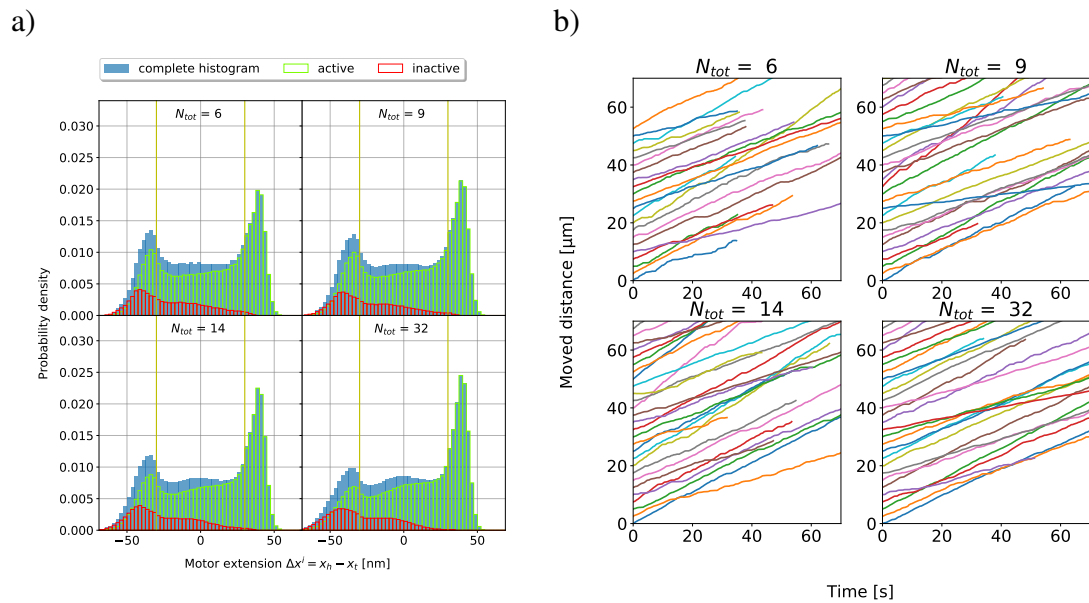
Figure C.5: One-dimensional bead model: motor extensions and trajectories. a) Histograms of motor extensions defined as the one-dimensional difference between the motor head position x_h on the MT and the fixed motor tail position x_t on the bead. The vertical yellow lines show the boundaries of the force-free regime. The motor configuration is constant in this model. It can be seen that more motors are experiencing a force (more motor extension are left/right to the yellow vertical lines) compared to the liposome model, where the motor extension histograms show a high peak around zero (see fig. C.2a). b) Trajectories of the bead model when resetting the active/inactive status each time a motor reattaches. Trajectories are more parallel than for the bead model with a constant active/inactive status of motors attaching the MT (constant motor configuration, see fig. 6.26b).

Appendix D

Appendix modeling bidirectional liposome transport by DDB and KIF16B

Parameter	Value	Reference
DDB parameters		
Attachment rate	$k_{a,DDB} = 2.5\,s^{-1}$ $(0.625\,s^{-1})$	Standard (in the presence of KIF16B) same order of magnitude as [34, 151, 327]
Force-free detachment rate, active motors	$k_{d,DDB,ac} = 0.44\,s^{-1}$	Obtained from experiments [335]
Force-free detachment rate, inactive motors	$k_{d,DDB,in} = 0.18\,s^{-1}$	Obtained from comparing simulated and experimental point-to-point velocities from only DDB liposome transport
Stall force	$F_{s,DDB} = 4\,pN$	[88]
Detachment force	$F_{d,DDB} = 3\,pN$	[337]
Force-free velocity at 2.5 mM ATP	$s_{DDB}(F^i = 0, [ATP] = 2.5\,mM) \times d$, instantaneous velocity distribution of single DDB (ignoring positive velocities)	From experiments [335]
Backward velocity	$v_{b,DDB} = 6\,nm/s$	Same order of magnitude as [124]
Diffusion rate of diffusive DDB motors per 8 nm	$s_{0,DDB} = 250\,s^{-1}$	[336]
Stiffness	$\kappa_{DDB} = 0.065\,pN \cdot nm^{-1}$	[34]
Untensioned length	$L_{DDB} = 30\,nm$	Unknown, same as in appendix A and [309]
Motor radius on the microtubule	$R_{DDB} = 24\,nm$	Approximated from EM images of [89, 95]
KIF16B parameters		
Attachment rate	$k_{a,KIF16B} = 5\,s^{-1}$ $(1.25\,s^{-1})$	Standard (in the presence of DDB) same order of magnitude as [34, 151, 327]
Force-free detachment rate, active motors	$k_{d,KIF16B,ac} = 1.27\,s^{-1}$	Obtained from experiments [335]

Force-free detachment rate, inactive motors	$k_{\mathrm{d,KIF16B,in}} = 0.70\,\mathrm{s}^{-1}$	Obtained from comparing simulated and experimental point-to-point velocities from only KIF16B liposome transport
Stall force	$F_{\mathrm{s,KIF16B}} = 6\,\mathrm{pN}$	[74, 338]
Detachment force	$F_{\mathrm{d,KIF16B}} = 2\,\mathrm{pN}$	Budaitis et al. [328] find a range of approx. $1 - 3\,\mathrm{pN}$ for different members of the kinesin-3 family, not including KIF16B, modeling in [338]
Force-free velocity at 2.5 mM ATP	$s_{\mathrm{KIF16B}}(F^i = 0, [\mathrm{ATP}] = 2.5\,\mathrm{mM}) \times d$, instantaneous velocity distribution of single KIF16B (ignoring negative velocities)	From experiments [335]
Backward velocity	$v_{\mathrm{b,KIF16B}} = 6\,\mathrm{nm/s}$	Same order of magnitude as Carter and Cross [124] found for kinesin-1
Stiffness	$\kappa_{\mathrm{KIF16B}} = 0.3\,\mathrm{pN} \cdot \mathrm{nm}^{-1}$	[332, 333] for kinesin-1, [34] modeling kinesin-1 and kinesin-2
Untensioned length	$L_{\mathrm{KIF16B}} = 70\,\mathrm{nm}$	Same order of magnitude as [341, 342]
Motor radius on the MT	$R_{\mathrm{KIF16B}} = 4\,\mathrm{nm}$	Same order of magnitude [193] (kinesin-1)
Common parameters		
Stepsize	$d = 8\,\mathrm{nm}$	[101, 183, 186]
Unloaded second-order rate constant for ATP binding	$k_{\mathrm{b}}^0 = 1.3\,\mathrm{\mu M}^{-1}\mathrm{s}^{-1}$	[120] (kinesin-1)
Fraction of unloaded catalytic cycle	$q_{\mathrm{cat}} = 6.2, p_{\mathrm{cat}} = 1 - q_{\mathrm{cat}}$	[120] (kinesin-1)
Fraction of unloaded ATP binding	$q_{\mathrm{b}} = 4.0, p_{\mathrm{b}} = 1 - q_{\mathrm{b}}$	[120] (kinesin-1)
Temperature	$T = 300\,\mathrm{K}$	Given by the experiment
Number of reachable protofilaments	7	Estimated
End of simulation	$80\,\mathrm{s}$	
Measurement time interval	$\Delta T_{\mathrm{mes}} = 0.1\,\mathrm{s}$	Given by experiment
Number of proposals for the Metropolis algorithm n_{m}	200	

Table D.1: Table shows parameters unidirectional and bidirectional DDB and KIF16B liposome transport. Parameter values are used as given by this table, if not stated differently. See also figure and figure captions for varied parameters.

Figure D.1: Parameter changes in simulations of liposome transport by DDB. Histograms of point-to-point velocities from simulations using the point-like cargo model with DDB motors. Individual parameters changed as follows: a) a 1.5 times higher number of motors (12 instead of 8 DDB motors), b) a two times higher attachment rate, c) a two times higher force-free detachment rate of inactive motors, d) a 1.5 times higher stall force, e) a 1.33 times higher detachment force, f) a two times higher backward velocity, g) a 0.4 times lower diffusion rate, h) a two times higher stiffness and i) a 0.66 times lower untensioned length. All other parameters are kept like in the standard simulation (see fig. 7.1a) and are listed in table D.1.

a) $0.2\,k_{\text{a,KIF16B}}$

b) $2\,k_{\text{d,KIF16B,in}}$

c) $0.5\,F_{\text{s,KIF16B}}$
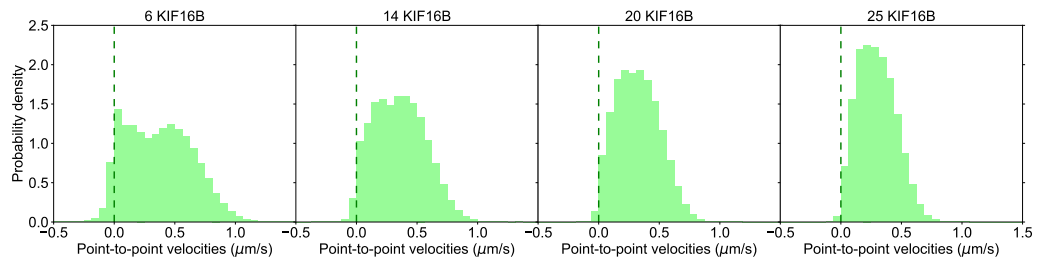
d) $2\,F_{\text{d,KIF16B}}$
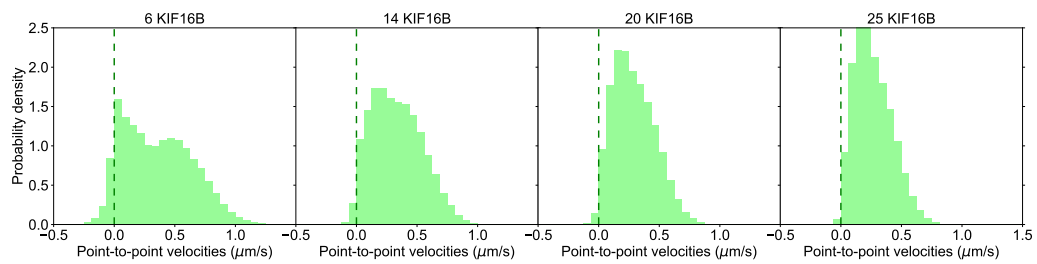
e) $2\,v_{\text{b,KIF16B}}$
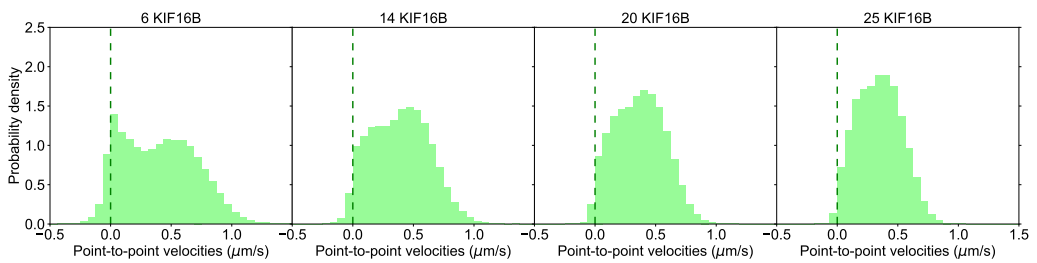
f) $2\,\kappa_{\text{KIF16B}}$
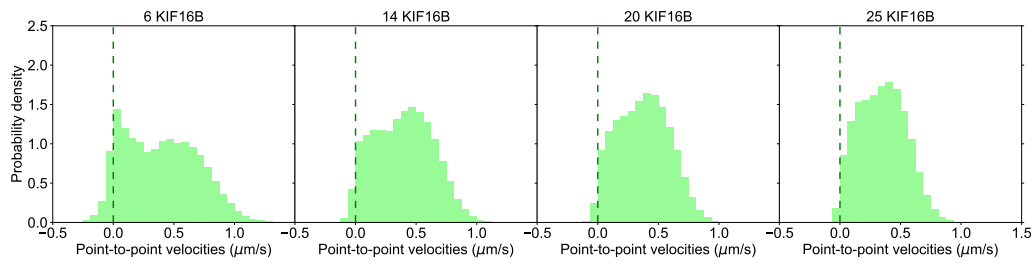
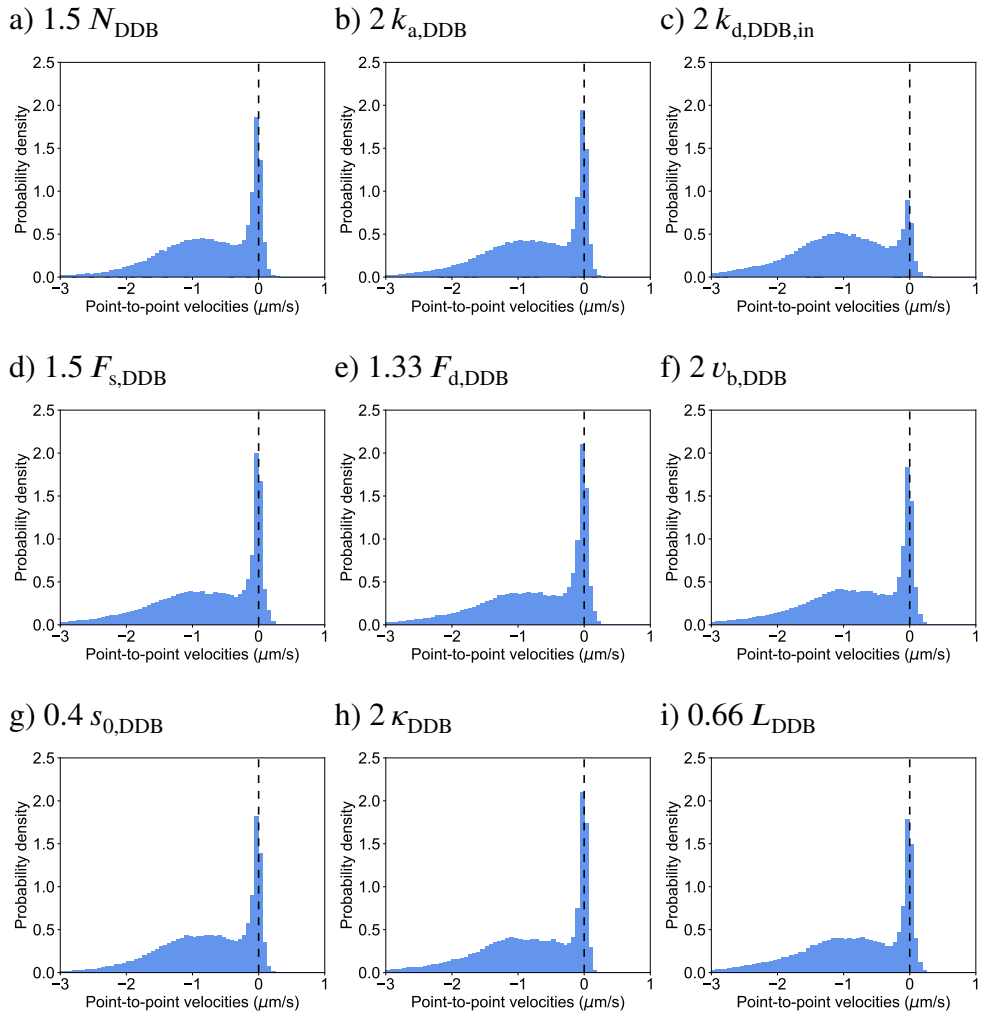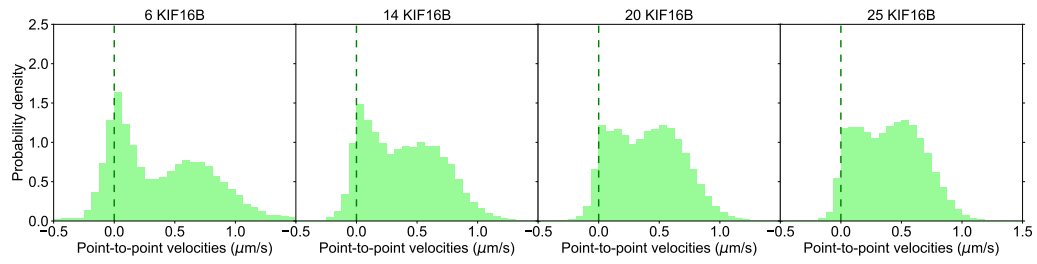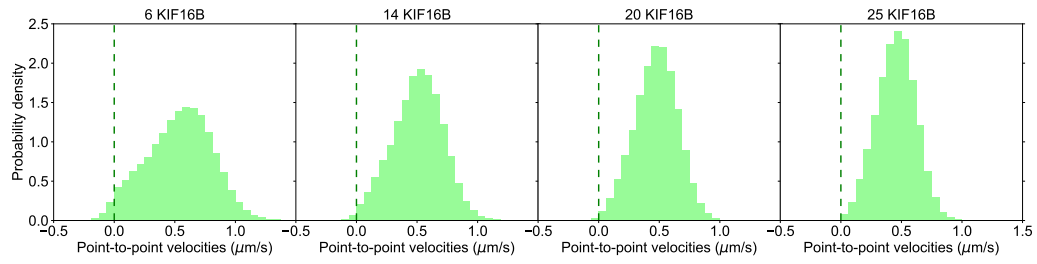g) $5/7\,L_{\text{KIF16B}}$
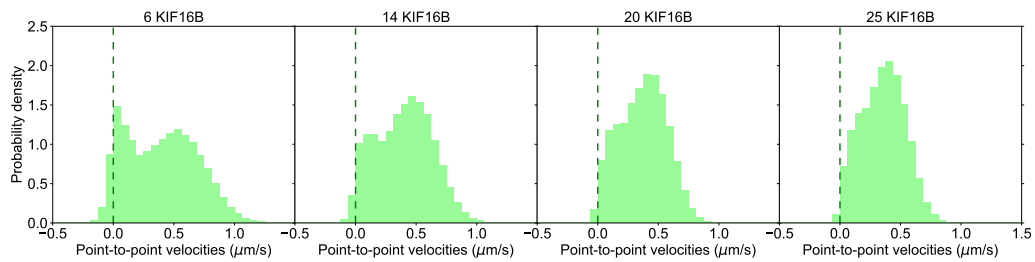
Figure D.2 *(previous page)***: Parameter changes in simulations of liposome transport by KIF16B.** Histograms of point-to-point velocities from simulations using the point-like cargo model with KIF16B motors. Individual parameters were changed as follows: a) a 0.2 times lower attachment rate, b) a two times higher force-free detachment rate of inactive motors, c) a 0.5 times lower stall force, d) a two times higher detachment force, e) a two times higher backward velocity, f) a two times higher stiffness, and g) a 5/7 times lower untensioned length. All other parameters are kept like in the standard simulation (see fig. 7.2a) and are listed in table D.1.

a) Classification
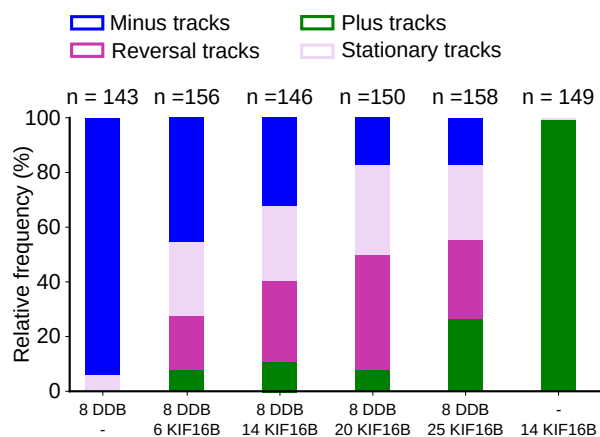
b) Number of motors
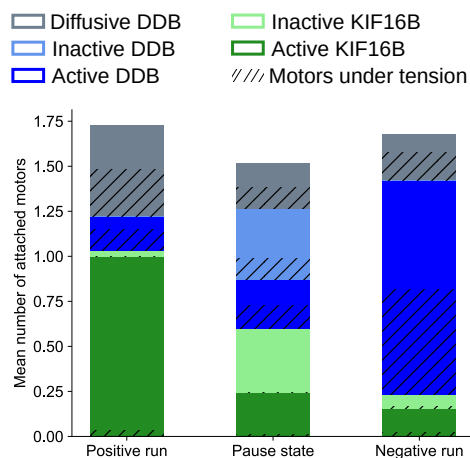
Figure D.3: The simulation with only one protofilament almost does not show reversals. a) Percentages of minus, plus, reversal and stationary tracks at varying number of KIF16B and a constant number of DDB motors (6 − 25 KIF16B and 8 DDB motors on average in the attachment area) using the standard simulation with only one PF. The only DDB and only KIF16B transport are added as references. Simulating just one PF, reduces the number of reversal tracks. Percentages are calculated using the shortened simulated tracks (see main text for the procedure). n indicates the number of simulated liposomes/number of tracks. b) The bar plots show the mean number and types of motors attached to the MT during positive runs, pauses and negative runs for the standard simulation with only one PF. Active KIF16B motors are denoted in middle green, inactive KIF16B in light green, active DDB in middle blue, inactive DDB in lightblue and diffusive DDB in gray. The amount of each motor type, which is under tension, is denoted by the hatches. See a) for the number of simulated liposomes/number of tracks.

Publications

- Gina A. Monzon*, Lara Scharrel*, Ludger Santen, and Stefan Diez. Activation of mammalian cytoplasmic dynein in multimotor motility assays. *Journal of Cell Science*, 132(4):jcs220079, 2019. doi: 10.1242/jcs.220079.

- Gina A. Monzon, Lara Scharrel, Ashwin D'Souza, Verena Henrichs, Ludger Santen, and Stefan Diez. Stable tug-of-war between kinesin-1 and cytoplasmic dynein upon different ATP and roadblock concentrations. *Journal of Cell Science*, 133(22):jcs249938, 2020. doi: 10.1242/jcs.249938.

- Ashwin I. D'Souza*, Rahul Grover*, Gina A. Monzon*, Ludger Santen, and Stefan Diez. Vesicles driven by dynein and kinesin exhibit directional reversals without regulators. *Nature Communications*,14:7532, 2023. doi: 10.1038/s41467-023-42605-8.

* equal contribution

Bibliography

[1] William Stillwell. Membrane Transport. In *An Introduction to Biological Membranes.*, chapter 19, pages 423–51. 2016. ISBN PMC7182109. doi: http://dx.doi.org/10.1016/B978-0-444-63772-7.00019-1423.

[2] Bruce Alberts, Alexander Johnson, Julian Lewis, Martin Raff, Keith Roberts, and Peter Walter. *Molecular Biology of the Cell*. New York: Garland Science, 4 edition, 2002.

[3] Robert L. Morris and Peter J. Hollenbeck. The regulation of bidirectional mitochondrial transport is coordinated with axonal outgrowth. *Journal of Cell Science*, 104(3):917–927, 1993. ISSN 00219533. doi: 10.1242/jcs.104.3.917.

[4] Sher Karki and Erika L.F. Holzbaur. Cytoplasmic dynein and dynactin in cell division and intracellular transport. *Current Opinion in Cell Biology*, 11(1):45–53, 1999. ISSN 09550674. doi: 10.1016/S0955-0674(99)80006-4.

[5] Gohta Goshima and Ronald D. Vale. The roles of microtubule-based motor proteins in mitosis: Comprehensive RNAi analysis in the Drosophila S2 cell line. *Journal of Cell Biology*, 162(6):1003–1016, 2003. ISSN 00219525. doi: 10.1083/jcb.200303022.

[6] Harvey Lodish, Arnold Berk, Paul Matsudaira, and Chri Kaiser. *Molecular Cell Biology*. W. H. Freeman and Co., 5 edition, 2004.

[7] Sandra Maday, Karen E. Wallace, and Erika L.F. Holzbaur. Autophagosomes initiate distally and mature during transport toward the cell soma in primary neurons. *Journal of Cell Biology*, 196(4):407–417, 2012. ISSN 00219525. doi: 10.1083/jcb.201106120.

[8] Joseph A. White, Thomas J. Krzystek, Hayley Hoffmar-Glennon, Claire Thant, Katherine Zimmerman, Gary Iacobucci, Julia Vail, Layne Thurston, Saad Rahman, and Shermali Gunawardena. Excess Rab4 rescues synaptic and behavioral dysfunction caused by defective HTT-Rab4 axonal transport in Huntington's disease. *Acta Neuropathologica Communications*, 8(1):1–22, 2020. ISSN 20515960. doi: 10.1186/s40478-020-00964-z.

[9] Amber L. Jolly and Vladimir I. Gelfand. Bidirectional intracellular transport: Utility and mechanism. *Biochemical Society Transactions*, 39(5):1126–1130, 2011. ISSN 03005127. doi: 10.1042/BST0391126.

[10] Benjamin H. Blehm and Paul R. Selvin. Single Molecule Fluorescence and In-Vivo Optical Traps: How Multiple Dyneins & Kinesins Interact. *Chemical Reviews*, 114(6):3335–3352, 2014. ISSN 15378276. doi: 10.1021/cr4005555.

[11] Adam G. Hendricks, Eran Perlson, Jennifer L. Ross, Harry W. Schroeder, Mariko Tokito, and Erika L.F. Holzbaur. Motor Coordination via a Tug-of-War Mechanism Drives Bidirectional Vesicle Transport. *Current Biology*, 20(8):697–702, 2010. ISSN 09609822. doi: 10.1016/j.cub.2010.02.058.

[12] Virgil Muresan, Chris P. Godek, Thomas S. Reese, and Bruce J. Schnapp. Plus-end motors override minus-end motors during transport of squid axon vesicles on microtubules. *Journal of Cell Biology*, 135(2):383–397, 1996. ISSN 00219525. doi: 10.1083/jcb.135.2.383.

[13] Shabeen Ally, Adam G. Larson, Kari Barlan, Sarah E. Rice, and Vladimir I. Gelfand. Opposite-polarity motors activate one another to trigger cargo transport in live cells. *Journal of Cell Biology*, 187(7):1071–1082, 2009. ISSN 00219525. doi: 10.1083/jcb. 200908075.

[14] Shuo-Chien Ling, Peter S. Fahrner, William T. Greenough, and Vladimir I. Gelfand. Transport of Drosophila fragile X mental retardation protein-containing ribonucleoprotein granules by kinesin-1 and cytoplasmic dynein. *Proceedings of the National Academy of Sciences of the United States of America*, 101(50):17428–17433, 2004. ISSN 00278424. doi: 10.1073/pnas.0408114101.

[15] George T. Shubeita, Susan L. Tran, Jing Xu, Michael Vershinin, Silvia Cermelli, Sean L. Cotton, Michael A. Welte, and Steven P. Gross. Kinesin-1–driven lipid droplets: Consequences of motor copy number for intracellular transport. *Cell*, 135(6):1098–1107, 2008. ISSN 15378276. doi: 10.1038/jid.2014.371.

[16] Christina Leidel, Rafael A. Longoria, Franciso Marquez Gutierrez, and George T. Shubeita. Measuring molecular motor forces in VIVO: Implications for tug-of-war models of bidirectional transport. *Biophysical Journal*, 103(3):492–500, 2012. ISSN 00063495. doi: 10.1016/j.bpj.2012.06.038.

[17] Arpan K. Rai, Ashim Rai, Avin J. Ramaiya, Rupam Jha, and Roop Mallik. Molecular adaptations allow dynein to generate large collective forces inside cells. *Cell*, 152(1-2): 172–182, 2013. ISSN 00928674. doi: 10.1016/j.cell.2012.11.044.

[18] Sandra E. Encalada, Lukasz Szpankowski, Chun-hong Xia, and Lawrence S. B. Goldstein. Stable Kinesin and Dynein Assemblies Drive the Axonal Transport of Mammalian Prion Protein Vesicles. *Cell*, 144(4):551–565, 2011. doi: 10.1038/jid.2014.371.

[19] Shuo Ma and Rex L. Chisholm. Cytoplasmic dynein-associated structures move bidirectionally in vivo. *Journal of Cell Science*, 115(7):1453–1460, 2002. ISSN 00219533. doi: 10.1242/jcs.115.7.1453.

[20] Michael A. Welte, Steven P. Gross, Marya Postner, Steven M. Block, and Eric F. Wieschaus. Developmental regulation of vesicle transport in Drosophila embryos: Forces and kinetics. *Cell*, 92(4):547–557, 1998. ISSN 00928674. doi: 10.1016/ S0092-8674(00)80947-2.

[21] Steven P. Gross. Hither and yon: A review of bi-directional microtubule-based transport. *Physical Biology*, 1(2), 2004. ISSN 14783975. doi: 10.1088/1478-3967/1/2/R01.

[22] Paulomi Sanghavi, Ashwin D'Souza, Ashim Rai, Arpan Rai, Ranjith Padinhatheeri, and Roop Mallik. Coin Tossing Explains the Activity of Opposing Microtubule Motors on Phagosomes. *Current Biology*, 28(9):1460–1466, 2018. ISSN 09609822. doi: 10. 1016/j.cub.2018.03.041.

[23] Michael A. Welte. Bidirectional transport along microtubules. *Current Biology*, 14(13): 525–537, 2004. ISSN 09609822. doi: 10.1016/j.cub.2004.06.045.

[24] Abdullah R. Chaudhary, Florian Berger, Christopher L. Berger, and Adam G. Hendricks. Tau directs intracellular trafficking by regulating the forces exerted by kinesin and dynein teams. *Traffic*, 19(2):111–121, 2018. ISSN 16000854. doi: 10.1111/tra.12537.

[25] Virupakshi Soppina, Arpan K. Rai, Avin J. Ramaiya, Pradeep Barak, and Roop Mallik. Tug-of-war between dissimilar teams of microtubule motors regulates transport and fission of endosomes. *Proceedings of the National Academy of Sciences of the United States of America*, 106(46):19381–19386, 2009. doi: 10.1073/pnas.0906524106.

[26] Carlo Ballatore, Virginia M.Y. Lee, and John Q. Trojanowski. Tau-mediated neurodegeneration in Alzheimer's disease and related disorders. *Nature Reviews Neuroscience*, 8(9):663–672, 2007. ISSN 1471003X. doi: 10.1038/nrn2194.

[27] Erica Chevalier-Larsen and Erika L.F. Holzbaur. Axonal transport and neurodegenerative disease. *Biochimica et Biophysica Acta - Molecular Basis of Disease*, 1762(11-12): 1094–1108, 2006. ISSN 09254439. doi: 10.1016/j.bbadis.2006.04.002.

[28] Iman H. Ibrahim, Amany Balah, Abrar G. A.E. Hassan, and Heba G.A. El-Aziz. Role of motor proteins in human cancers. *Saudi Journal of Biological Sciences*, 29(12):103436, 2022. ISSN 1319562X. doi: 10.1016/j.sjbs.2022.103436.

[29] A. Ebneth, R. Godemann, K. Stamer, S. Illenberger, B. Trinczek, E.-M. Mandelkow, and E. Mandelkow. Overexpression of Tau Protein Inhibits Kinesin-dependent Overexpression of Vesicles , Mitochondria , and Endoplasmic Trafficking Reticulum : for Alzheimer's Disease Implications. *The Journal of cell biology*, 143(3):777–794, 1998. doi: 10.1083/jcb.143.3.777.

[30] Jesus Avila, Juan S. Jiménez, Carmen L. Sayas, Marta Bolós, Juan C. Zabala, Germán Rivas, and Felix Hernández. Tau Structures. *Frontiers in Aging Neuroscience*, 8:262, 2016. ISSN 16634365. doi: 10.3389/fnagi.2016.00262.

[31] Ruensern Tan, Aileen J. Lam, Tracy Tan, Jisoo Han, Dan W. Nowakowski, Michael Vershinin, Sergi Simó, Kassandra M. Ori-McKenney, and Richard J. McKenney. Microtubules gate tau condensation to spatially regulate microtubule functions. *Nature Cell Biology*, 21(9):1078–1085, 2019. ISSN 14764679. doi: 10.1038/s41556-019-0375-5.

[32] Melanie J.I. Müller, Stefan Klumpp, and Reinhard Lipowsky. Motility states of molecular motors engaged in a stochastic tug-of-war. *Journal of Statistical Physics*, 133(6): 1059–1081, 2008. ISSN 00224715. doi: 10.1007/s10955-008-9651-7.

[33] Ambarish Kunwar, Suvranta K. Tripathy, Jing Xu, Michelle K. Mattson, Preetha Anand, Roby Sigua, Michael Vershinin, Richard J. McKenney, Clare C. Yu, Alexander Mogilner, and Steven P. Gross. Mechanical stochastic tug-of-war models cannot explain bidirectional lipid-droplet transport. *Proceedings of the National Academy of Sciences of the United States of America*, 108(47):18960–18965, 2011. doi: 10.1073/pnas.1107841108.

[34] Kazuka G. Ohashi, Lifeng Han, Brandon Mentley, Jiaxuan Wang, John Fricks, and William O. Hancock. Load-dependent detachment kinetics plays a key role in bidirectional cargo transport by kinesin and dynein. *Traffic*, 20(4):284–294, 2019. ISSN 16000854. doi: 10.1111/tra.12639.

[35] Sarah Klein, Cécile Appert-Rolland, and Ludger Santen. Environmental control of microtubule-based bidirectional cargo-transport. *EPL*, 107(1):1–6, 2014. doi: 10.1209/0295-5075/107/18004.

[36] S. Klein, C. Appert-Rolland, and L. Santen. Fluctuation effects in bidirectional cargo transport. *European Physical Journal: Special Topics*, 223(14):3215–3225, 2014. ISSN 19516401. doi: 10.1140/epjst/e2014-02328-2.

[37] Karim Rezaul, Dipika Gupta, Irina Semenova, Kazuho Ikeda, Pavel Kraikivski, Ji Yu, Ann Cowan, Ilya Zaliapin, and Vladimir Rodionov. Engineered tug-of-war between kinesin and dynein controls direction of microtubule transport in vivo. *Physiology & behavior*, 17(5):475–486, 2016. doi: 10.1111/tra.12385.

[38] Ronald D. Vale, Fady Malik, and Diane Brown. Directional instability of microtubule transport in the presence of kinesin and dynein, two opposite polarity motor proteins. *The Journal of cell biology*, 119(6):1589–1596, 1992. doi: 10.1083/jcb.119.6.1589.

[39] Luke S. Ferro, Sinan Can, Meghan A. Turner, Mohamed M. Elshenawy, and Ahmet Yildiz. Kinesin-1 and dynein use distinct mechanisms to bypass obstacles. *eLife*, 8: e48629, 2019. doi: 10.7554/eLife.48629.

[40] Valerie Siahaan, Jochen Krattenmacher, Anthony A. Hyman, Stefan Diez, Amayra Hernández-Vega, Zdenek Lansky, and Marcus Braun. Kinetically distinct phases of tau on microtubules regulate kinesin motors and severing enzymes. *Nature Cell Biology*, 21(9):1086–1092, 2019. ISSN 1465-7392. doi: 10.1038/s41556-019-0374-6.

[41] Jacques Ferlay, Isabelle Soerjomataram, Rajesh Dikshit, Sultan Eser, Colin Mathers, Marise Rebelo, Donald Maxwell Parkin, David Forman, and Freddie Bray. Cancer incidence and mortality worldwide: Sources, methods and major patterns in GLOBOCAN 2012. *International Journal of Cancer*, 136(5):E359–E386, 2015. ISSN 10970215. doi: 10.1002/ijc.29210.

[42] Rebecca L. Siegel, Kimberly D. Miller, and Ahmedin Jemal. Cancer statistics, 2020. *CA: A Cancer Journal for Clinicians*, 70(1):7–30, 2020. ISSN 0007-9235. doi: 10.3322/caac.21590.

[43] Mary Deraitus and Kris Freeman. *Essentials of cell biology*. Cambridge, MA: NPG Education, 2001. doi: 10.1145/634295.634339.

[44] Thomas D. Pollard, William C. Earnshaw, Jennifer Lippincott-Schwartz, and Graham T. Johnson. Actin and Actin-Binding Proteins. In *Cell Biology*, chapter Chapter 33, pages 575–591. Elsevier, 3 edition, 2017. doi: https://doi.org/10.1016/B978-0-323-34126-4.00033-5.

[45] Daniel A. Fletcher and R. Dyche Mullins. Cell mechanics and the cytoskeleton. *Nature*, 463:485–492, 2010. ISSN 00280836. doi: 10.1038/nature08908.

[46] Azzurra Margiotta and Cecilia Bucci. Role of Intermediate Filaments in Vesicular Traffic. *Cells*, 5(2):20, 2016. ISSN 2073-4409. doi: 10.3390/cells5020020.

[47] Ron Milo and Rob Phillips. *CELL BIOLOGY by the numbers*. Garland Science - Taylor and Francis Group, 2015.

[48] Yuta Nihongaki, Hideaki T. Matsubayashi, and Takanari Inoue. A molecular trap inside microtubules probes luminal access by soluble proteins. *Nature Chemical Biology*, 17 (8):888–895, 2021. ISSN 15524469. doi: 10.1038/s41589-021-00791-w.

[49] Gary J. Brouhard and Luke M. Rice. Microtubule dynamics: An interplay of biochemistry and mechanics. *Nature Reviews Molecular Cell Biology*, 19(7):451–463, 2018. ISSN 14710080. doi: 10.1038/s41580-018-0009-y.

[50] O. Valiron, N. Caudron, and D. Job. Microtubule dynamics. *Cellular and Molecular Life Sciences*, 58(14):2069–2084, 2001. ISSN 1420682X. doi: 10.1007/PL00000837.

[51] P. T. Tran, L. Marsh, V. Doye, S. Inoué, and F. Chang. A mechanism for nuclear positioning in fission yeast based on microtubule pushing. *Journal of Cell Biology*, 153(2): 397–411, 2001. ISSN 00219525. doi: 10.1083/jcb.153.2.397.

[52] Sami Chaaban and Gary J. Brouhard. A microtubule bestiary: Structural diversity in tubulin polymers. *Molecular Biology of the Cell*, 28(22):2924–2931, 2017. ISSN 19394586. doi: 10.1091/mbc.E16-05-0271.

[53] Joe Howard and Anthony A. Hyman. Dynamics and mechanics of the microtubule plus end. *Nature*, 422(6933):753–758, 2003. ISSN 00280836. doi: 10.1038/nature01600.

[54] Juan Estévez-Gallego, Fernando Josa-Prado, Siou Ku, Ruben M. Buey, Francisco A. Balaguer, Andrea E. Prota, Daniel Lucena-Agell, Christina Kamma-Lorger, Toshiki Yagi, Hiroyuki Iwamoto, Laurence Duchesne, Isabel Barasoain, Michel O. Steinmetz, Denis Chrétien, Shinji Kamimura, J. Fernando Díaz, and Maria A. Oliva. Structural model for differential cap maturation at growing microtubule ends. *eLife*, 9:1–26, 2020. ISSN 2050084X. doi: 10.7554/eLife.50155.

[55] Henry T. Schek, Melissa K. Gardner, Jun Cheng, David J. Odde, and Alan J. Hunt. Microtubule Assembly Dynamics at the Nanoscale. *Current Biology*, 17(17):1445–1455, 2007. ISSN 09609822. doi: 10.1016/j.cub.2007.07.011.

[56] Johanna Roostalu, Claire Thomas, Nicholas Ian Cade, Simone Kunzelmann, Ian A. Taylor, and Thomas Surrey. The speed of GTP hydrolysis determines GTP cap size and controls microtubule stability. *eLife*, 9:1–22, 2020. ISSN 2050084X. doi: 10.7554/eLife.51992.

[57] Andrew W. Hunter and Linda Wordeman. How motor proteins influence microtubule polymerization dynamics. *Journal of Cell Science*, 113(24):4379–4389, 2000. ISSN 00219533. doi: 10.1242/jcs.113.24.4379.

[58] Ram Dixit, Brian Barnett, Jacob E. Lazarus, Mariko Tokito, Yale E. Goldman, and Erika L.F. Holzbaur. Microtubule plus-end tracking by CLIP-170 requires EB1. *Proceedings of the National Academy of Sciences of the United States of America*, 106(2): 492–497, 2009. ISSN 00278424. doi: 10.1073/pnas.0807614106.

[59] Michal Wieczorek, Susanne Bechstedt, Sami Chaaban, and Gary J. Brouhard. Microtubule-associated proteins control the kinetics of microtubule nucleation. *Nature Cell Biology*, 17(7):907–916, 2015. ISSN 14764679. doi: 10.1038/ncb3188.

[60] Peter Bieling, Liedewij Laan, Henry Schek, E. Laura Munteanu, Linda Sandblad, Marileen Dogterom, Damian Brunner, and Thomas Surrey. Reconstitution of a microtubule plus-end tracking system in vitro. *Nature*, 450(7172):1100–1105, 2007. ISSN 14764687. doi: 10.1038/nature06386.

[61] Sarah Triclin, Daisuke Inoue, Jérémie Gaillard, Zaw Min Htet, Morgan E. DeSantis, Didier Portran, Emmanuel Derivery, Charlotte Aumeier, Laura Schaedel, Karin John, Christophe Leterrier, Samara L. Reck-Peterson, Laurent Blanchoin, and Manuel Théry. Self-repair protects microtubules from destruction by molecular motors. *Nature Materials*, 20(6):883–891, 2021. ISSN 14764660. doi: 10.1038/s41563-020-00905-0.

[62] R. B. Dye, P. F. Flicker, D. Y. Lien, and R. C. Williams Jr. End-stabilized microtubules observed in vitro: stability, subunit, interchange, and breakage. *Cell Motil Cytoskeleton*, 21(3):171–86, 1992. ISSN 14764660. doi: 10.1038/nmat4396.

[63] Laura Schaedel, Karin John, Jérémie Gaillard, Maxence V Nachury, Laurent Blanchoin, and Manuel Théry. Europe PMC Funders Group Microtubules self-repair in response to mechanical stress. *Nature Materials*, 14(11):1156–1163, 2015. doi: 10.1038/nmat4396. Microtubules.

[64] Amol Aher, Dipti Rai, Laura Schaedel, Jeremie Gaillard, Karin John, Qingyang Liu, Maarten Altelaar, Laurent Blanchoin, Manuel Thery, and Anna Akhmanova. CLASP Mediates Microtubule Repair by Restricting Lattice Damage and Regulating Tubulin Incorporation. *Current Biology*, 30:2175–2183, 2020. ISSN 18790445. doi: 10.1016/j.cub.2020.03.070.

[65] Charlotte Aumeier, Laura Schaedel, Jérémie Gaillard, Karin John, Laurent Blanchoin, and Manuel Théry. Self-repair promotes microtubule rescue. *Nature Cell Biology*, 18 (10):1054–1064, 2016. ISSN 14764679. doi: 10.1038/ncb3406.

[66] Sanghamitra Ray, Edgar Meyhöfer, Ronald A. Milligan, and Jonathon Howard. Kinesin follows the microtubule's protofilament axis. *Journal of Cell Biology*, 121(5):1083–1093, 1993. ISSN 00219525. doi: 10.1083/jcb.121.5.1083.

[67] Sinan Can, Mark A. Dewitt, and Ahmet Yildiz. Bidirectional helical motility of cytoplasmic dynein around microtubules. *eLife*, pages 1–12, 2014. doi: 10.7554/eLife.03205.

[68] Alexander Marx, Andreas Hoenger, and Eckhard Mandelkow. Structures of kinesin motor proteins. *Cell Motility and the Cytoskeleton*, 66(11):958–966, 2009. ISSN 08861544. doi: 10.1002/cm.20392.

[69] Gira Bhabha, Graham T. Johnson, Courtney M. Schroeder, and Ronald D. Vale. How Dynein Moves Along Microtubules. *Trends in Biochemical Sciences*, 41(1):94–105, 2016. doi: 10.1016/j.tibs.2015.11.004.

[70] Mohamed M. Elshenawy, John T. Canty, Liya Oster, Luke S. Ferro, Zhou Zhou, Scott C. Blanchard, and Ahmet Yildiz. Cargo adaptors regulate stepping and force generation of mammalian dynein-dynactin. *Nature Chemical Biology*, 15(11):1093–1101, 2019. doi: 10.1038/s41589-019-0352-0.Cargo.

[71] Mark A. Dewitt, Caroline A. Cypranowska, Frank B. Cleary, Vladislav Belyy, and Ahmet Yildiz. THE AAA3 DOMAIN OF CYTOPLASMIC DYNEIN ACTS AS A SWITCH TO FACILITATE MICROTUBULE RELEASE. *Nature Structural and Molecular Biology*, 22(1):73–80, 2015. doi: 10.1038/nsmb.2930.

[72] Charles L. Asbury, Adrian N. Fehr, and Steven M. Block. Kinesin Moves by an Asymmetric Hand-Over-Hand Mechanism. *Science*, 302(5653):2130–2134, 2003. ISSN 00368075. doi: 10.1126/science.1092985.

[73] Kristen J. Verhey, Neha Kaul, and Virupakshi Soppina. Kinesin Assembly and Movement in Cells. *Annual Review of Biophysics*, 40:267–288, 2011. doi: 10.1146/annurev-biophys-042910-155310.

[74] Si Kao Guo, Xiao Xuan Shi, Peng Ye Wang, and Ping Xie. Run length distribution of dimerized kinesin-3 molecular motors: comparison with dimeric kinesin-1. *Scientific Reports*, 9(1):1–14, 2019. ISSN 20452322. doi: 10.1038/s41598-019-53550-2.

[75] Jennetta W. Hammond, Dawen Cai, T. Lynne Blasius, Zhe Li, Yuyang Jiang, Gloria T. Jih, Edgar Meyhofer, and Kristen J. Verhey. Mammalian Kinesin-3 motors are dimeric in vivo and move by processive motility upon release of autoinhibition. *PLoS Biology*, 7(3):0650–0663, 2009. ISSN 15449173. doi: 10.1371/journal.pbio.1000072.

[76] Peter Höök and Richard B. Vallee. The dynein family at a glance. *Journal of Cell Science*, 119(21):4369–4371, 2006. ISSN 00219533. doi: 10.1242/jcs.03176.

[77] Kristen J. Verhey and Jennetta W. Hammond. Traffic control: Regulation of kinesin motors. *Nature Reviews Molecular Cell Biology*, 10(11):765–777, 2009. ISSN 14710072. doi: 10.1038/nrm2782.

[78] N. Siddiqui and A. Straube. Intracellular Cargo Transport by Kinesin-3 Motors. *Biochemistry (Moscow)*, 82(7):803–815, 2017. doi: 10.1134/S0006297917070057.

[79] Zhen Yu She and Wan Xi Yang. Molecular mechanisms of kinesin-14 motors in spindle assembly and chromosome segregation. *Journal of Cell Science*, 130(13):2097–2110, 2017. ISSN 14779137. doi: 10.1242/jcs.200261.

[80] William O. Hancock and Jonathon Howard. Processivity of the motor protein kinesin requires two heads. *Journal of Cell Biology*, 140(6):1395–1405, 1998. ISSN 00219525. doi: 10.1083/jcb.140.6.1395.

[81] Weihong Qiu, Nathan D. Derr, Brian S. Goodman, Elizabeth Villa, David Wu, William Shih, and Samara L. Reck-peterson. Dynein achieves processive motion using both stochastic and coordinated stepping. *Nature Structural and Molecular Biology*, 19(2):193–200, 2012. doi: 10.1038/nsmb.2205.Dynein.

[82] Manfred Schliwa and Günther Woehlke. Molecular motors. *Nature*, 422(April):759–765, 2003. doi: 10.1038/nature01601.

[83] Michael A. Cianfrocco, Morgan E. DeSantis, Andres E. Leschziner, and Samara L. Reck-Peterson. Mechanism and Regulation of Cytoplasmic Dynein. *Annual Review of Cell and Developmental Biology*, 31:83–108, 2015. doi: 10.1146/annurev-cellbio-100814-125438.

[84] K. Kevin Pfister, Paresh R. Shah, Holger Hummerich, Andreas Russ, James Cotton, Azlina Ahmad Annuar, Stephen M. King, and Elizabeth M.C. Fisher. Genetic analysis of the cytoplasmic dynein subunit families. *PLoS Genetics*, 2(1):11–26, 2006. ISSN 15537390. doi: 10.1371/journal.pgen.0020001.

[85] Mark A. DeWitt, Amy Y. Chang, Peter A. Combs, and Ahmet Yildiz. Cytoplasmic dynein moves through uncoordinated stepping of the AAA+ ring domains. *Science*, 335(6065):221–225, 2012. ISSN 10959203. doi: 10.1126/science.1215804.

[86] Frank B. Cleary, Mark A. Dewitt, Thomas Bilyard, Zaw Min Htet, Vladislav Belyy, Danna D. Chan, Amy Y. Chang, and Ahmet Yildiz. Tension on the linker gates the ATP-dependent release of dynein from microtubules. *Nature Communications*, 5, 2014. ISSN 20411723. doi: 10.1038/ncomms5587.

[87] Matthew P. Nicholas, Peter Höök, Sibylle Brenner, Caitlin L. Wynne, Richard B. Vallee, and Arne Gennerich. Control of cytoplasmic dynein force production and processivity by its C-terminal domain. *Nature Communications*, 6, 2015. ISSN 20411723. doi: 10.1038/ncomms7206.

[88] Vladislav Belyy, Max A. Schlager, Helen Foster, Armando E. Reimer, Andrew P. Carter, and Ahmet Yildiz. The mammalian dynein-dynactin complex is a strong opponent to kinesin in a tug-of-war competition. *Nature Cell Biology*, 18(9):1018–1024, 2016. doi: 10.1038/ncb3393.

[89] Takayuki Torisawa, Muneyoshi Ichikawa, Akane Furuta, Kei Saito, Kazuhiro Oiwa, Hiroaki Kojima, Yoko Y Toyoshima, and Ken'ya Furuta. Autoinhibition and cooperative activation mechanisms of cytoplasmic dynein. *Nature Cell Biology*, 16(11):1118–1124, 2014. doi: 10.1038/ncb3048.

[90] Kai Zhang, Helen E. Foster, Arnaud Rondelet, Samuel E. Lacey, Nadia Bahi-Buisson, Alexander W. Bird, and Andrew P. Carter. Cryo-EM Reveals How Human Cytoplasmic Dynein Is Auto-inhibited and Activated. *Cell*, 169(7):1303–1314.e18, 2017. ISSN 10974172. doi: 10.1016/j.cell.2017.05.025.

[91] Arne Gennerich and Ronald D. Vale. Walking the walk: how kinesin and dynein coordinate their steps. *Current Opinion in Cell Biology*, 21(1):59–67, 2009. doi: 10.1016/j.ceb.2008.12.002.

[92] Lu Rao, Florian Berger, Matthew P. Nicholas, and Arne Gennerich. Molecular mechanism of cytoplasmic dynein tension sensing. *Nature Communications*, 10(1), 2019. ISSN 20411723. doi: 10.1038/s41467-019-11231-8.

[93] I. R. Gibbons, Joan E. Garbarino, Carol E. Tan, Samara L. Reck-Peterson, Ronald D. Vale, and Andrew P. Carter. The affinity of the dynein microtubule-binding domain is modulated by the conformation of its coiled-coil stalk. *Journal of Biological Chemistry*, 280(25):23960–23965, 2005. ISSN 00219258. doi: 10.1074/jbc.M501636200.

[94] Richard J. McKenney, Walter Huynh, Marvin E. Tanenbaum, Gira Bhabha, and Ronald D. Vale. Activation of cytoplasmic dynein motility by dynactin-cargo adapter complexes. *Science*, 345(6194):337–341, 2014. ISSN 10959203. doi: 10.1126/science. 1254198.

[95] Max A. Schlager, Ha T. Hoang, Linas Urnavicius, Simon L. Bullock, and Andrew P. Carter. In vitro reconstitution of a highly processive recombinant human dynein complex. *The EMBO Journal*, 33(17):1855–1868, 2014. doi: 10.15252/embj.201488792.

[96] Mara A. Olenick and Erika L.F. Holzbaur. Cell science at a glance dynein activators and adaptors at a glance. *Journal of Cell Science*, 132(6):1–7, 2019. ISSN 14779137. doi: 10.1242/jcs.227132.

[97] Stephen J. King and Trina A. Schroer. Dynactin increases the processivity of the cytoplasmic dynein motor. *Nature Cell Biology*, 2(1):20–24, 2000. ISSN 14657392. doi: 10.1038/71338.

[98] Katerina Toropova, Miroslav Mladenov, and Anthony J Roberts. Intraflagellar transport dynein is autoinhibited by trapping of its mechanical and track-binding elements. *Nature Publishing Group*, 24(5):461–468, 2017. ISSN 1545-9993. doi: 10.1038/nsmb.3391.

[99] Sibylle Brenner, Florian Berger, Lu Rao, Matthew P. Nicholas, and Arne Gennerich. Force production of human cytoplasmic dynein is limited by its processivity. *Science Advances*, 6(15), 2020. ISSN 23752548. doi: 10.1126/sciadv.aaz4295.

[100] Arne Gennerich, Andrew P. Carter, Samara L. Reck-Peterson, and Ronald D. Vale. Force-Induced Bidirectional Stepping of Cytoplasmic Dynein. *Cell*, 131:952–965, 2007. doi: 10.1016/j.cell.2007.10.016.

[101] Roop Mallik, Brian C. Carter, Stephanie A. Lex, Stephen J. King, and Steven P. Gross. Cytoplasmic dynein functions as a gear in response to load. *Nature*, 427(6975):649–652, 2004. ISSN 0028-0836. doi: 10.1038/nature02293.

[102] Richard J. McKenney, Michael Vershinin, Ambarish Kunwar, Richard B. Vallee, and Steven P. Gross. LIS1 and NudE Induce a Persistent Dynein Force-Producing State. *Cell*, 141(2):304–314, 2010. ISSN 15378276. doi: 10.1038/jid.2014.371.

[103] Kassandra M. Ori-Mckenney, Jing Xu, Steven P. Gross, and Richard B. Vallee. A cytoplasmic dynein tail mutation impairs motor processivity. *Nature Cell Biology*, 12(12): 1228–1234, 2010. ISSN 14657392. doi: 10.1038/ncb2127.

[104] Samara L. Reck-Peterson, Ahmet Yildiz, Andrew P. Carter, Arne Gennerich, Nan Zhang, and Ronald D. Vale. Single-Molecule Analysis of Dynein Processivity and Stepping Behavior. *Cell*, 126(2):335–348, 2006. ISSN 00928674. doi: 10.1016/j.cell.2006. 05.046.

[105] Gaia Pigino and Stephen M. King. Switching dynein motors on and off. *Nature Structural and Molecular Biology*, 24(7):557–559, 2017. ISSN 15459985. doi: 10.1038/nsmb.3429.

[106] Daniël Splinter, David S. Razafsky, Max A. Schlager, Andrea Serra-Marques, Ilya Grigoriev, Jeroen Demmers, Nanda Keijzer, Kai Jiang, Ina Poser, Anthony A. Hyman, Casper C. Hoogenraad, Stephen J. King, and Anna Akhmanova. BICD2, dynactin, and LIS1 cooperate in regulating dynein recruitment to cellular structures. *Molecular Biology of the Cell*, 23(21):4226–4241, 2012. ISSN 10591524. doi: 10.1091/mbc.E12-03-0210.

[107] Mohamed M. Elshenawy, Emre Kusakci, Sara Volz, Janina Baumbach, Simon L. Bullock, and Ahmet Yildiz. Lis1 activates dynein motility by modulating its pairing with dynactin. *Nature Cell Biology*, 22(5):570–578, 2020. ISSN 14764679. doi: 10.1038/s41556-020-0501-4.

[108] Matthew P. Nicholas, Florian Berger, Lu Rao, Sibylle Brenner, Carol Cho, and Arne Gennerich. Cytoplasmic dynein regulates its attachment to microtubules via nucleotide state-switched mechanosensing at multiple AAA domains. *Proceedings of the National Academy of Sciences of the United States of America*, 112(20):6371–6376, 2015. doi: 10.1073/pnas.1417422112.

[109] Vladislav Belyy, Nathan L. Hendel, Alexander Chien, and Ahmet Yildiz. Cytoplasmic dynein transports cargos via load-sharing between the heads. *Nature Communications*, 5:5544 l, 2014. ISSN 20411723. doi: 10.1038/ncomms6544.

[110] Ronald D. Vale, Thomas S. Reese, and Michael P. Sheetz. Identification of a Novel Force-Generating Protein, Kinesin, Involved in Microtubule-Based Motility Ronald. *Cell*, 42(1):39–50, 1985. ISSN 15378276. doi: 10.1038/jid.2014.371.

[111] Scott T. Brady. A novel brain ATPase with properties expected for the fast axonal transport motor. *Nature*, 317:73-75:73–75, 1985. doi: 10.1038/317073a0.

[112] Carolyn J. Lawrence, R. Kelly Dawe, Karen R. Christie, Don W. Cleveland, Scott C. Dawson, Sharyn A. Endow, Lawrence S.B. Goldstein, Holly V. Goodson, Nobutaka Hirokawa, Jonathon Howard, Russell L. Malmberg, J. Richard McIntosh, Harukata Miki, Timothy J. Mitchison, Yasushi Okada, Anireddy S.N. Reddy, William M. Saxton, Manfred Schliwa, Jonathan M. Scholey, Ronald D. Vale, Claire E. Walczak, and Linda Wordeman. A standardized kinesin nomenclature. *Journal of Cell Biology*, 167 (1):19–22, 2004. ISSN 00219525. doi: 10.1083/jcb.200408113.

[113] Harukata Miki, Yasushi Okada, and Nobutaka Hirokawa. Analysis of the kinesin superfamily: Insights into structure and function. *Trends in Cell Biology*, 15(9):467–476, 2005. ISSN 09628924. doi: 10.1016/j.tcb.2005.07.006.

[114] Charles L. Asbury. Kinesin: World's tiniest biped. *Current Opinion in Cell Biology*, 17 (1):89–97, 2005. ISSN 09550674. doi: 10.1016/j.ceb.2004.12.002.

[115] Ahmet Yildiz, Michio Tomishige, Ronald D. Vale, and Paul R. Selvin. Kinesin Walks Hand-Over-Hand. *Science*, 303:676–678, 2004. doi: 10.1126/science.1093753.

[116] Bason E. Clancy, William M. Behnke-Parks, Johan O. L. Andreasson, Steven S. Rosenfeld, and Steven M. Block. A universal pathway for kinesin stepping. *Nature Structural and Molecular Biology*, 18(9):1020–1028, 2011. doi: 10.1038/nsmb.2104.

[117] Dawen Cai, Adam D. Hoppe, Joel A. Swanson, and Kristen J. Verhey. Kinesin-1 structural organization and conformational changes revealed by FRET stoichiometry in live cells. *Journal of Cell Biology*, 176(1):51–63, 2007. ISSN 00219525. doi: 10.1083/jcb.200605097.

[118] Hung Yi Kristal Kaan, David D. Hackney, and Frank Kozielski. The structure of the kinesin-1 motor-tail complex reveals the mechanism of autoinhibition. *Science*, 333 (6044):883–885, 2011. ISSN 00368075. doi: 10.1126/science.1204824.

[119] Wei Hua, Johnson Chung, and Jeff Gelles. Distinguishing inchworm and hand-over-hand processive kinesin movement by neck rotation measurements. *Science*, 295(5556): 844–848, 2002. ISSN 00368075. doi: 10.1126/science.1063089.

[120] Mark J. Schnitzer, Koen Visscher, and Steven M. Block. Force production by single kinesin motors. *Nature Cell Biology*, 2(10):718–723, 2000. doi: 10.1038/35036345.

[121] Bojan Milic, Johan O.L. Andreasson, William O. Hancock, and Steven M. Block. Kinesin processivity is gated by phosphate release. *Proceedings of the National Academy of Sciences of the United States of America*, 111(39):14136–14140, 2014. ISSN 10916490. doi: 10.1073/pnas.1410943111.

[122] Megan T. Valentine and Susan P. Gilbert. To step or not to step? How biochemistry and mechanics influence processivity in Kinesin and Eg5. *Current Opinion in Cell Biology*, 19:75–81, 2007. ISSN 15378276. doi: 10.1038/jid.2014.371.

[123] Teppei Mori, Ronald D. Vale, and Michio Tomishige. How kinesin waits between steps. *Nature*, 450(7170):750–754, 2007. ISSN 14764687. doi: 10.1038/nature06346.

[124] N. J. Carter and R. A. Cross. Mechanics of the kinesin step. *Nature*, 435:308–312, 2005. doi: 10.1038/nature03528.

[125] Sarah Rice, Abel W. Lin, Daniel Safer, Cynthia L. Hart, Nariman Naberk, Bridget O. Carragher, Shane M. Cain, Elena Pechatnikova, Elizabeth M. Wilson-Kubalek, Michael Whittaker, Edward Pate, Roger Cookek, Edwin W. Taylor, Ronald A. Milligan, and Ronald D. Vale. A structural change in the kinesin motor protein that drives motility. *Nature*, 402:778–784, 1999. doi: 10.1038/45483.

[126] Sanghamitra Ray, Edgar Meyhöfer, Ronald A. Milligan, and Jonathon Howard. Kinesin follows the microtubule's protofilament axis. *Journal of Cell Biology*, 121(5):1083–1093, 1993. ISSN 00219525. doi: 10.1083/jcb.121.5.1083.

[127] Johan O.L. Andreasson, Bojan Milic, Geng Yuan Chen, Nicholas R. Guydosh, William O. Hancock, and Steven M. Block. Examining kinesin processivity within a general gating framework. *eLife*, 2015(4):1–44, 2015. ISSN 2050084X. doi: 10.7554/eLife.07403.

[128] Steven M. Block, Charles L. Asbury, Joshua W. Shaevitz, and Matthew J. Lang. Probing the kinesin reaction cycle with a 2D optical force clamp. *Proceedings of the National Academy of Sciences of the United States of America*, 100(5):2351–2356, 2003. ISSN 00278424. doi: 10.1073/pnas.0436709100.

[129] Rosemarie V. Barkus, Olga Klyachko, Dai Horiuchi, Barry J. Dickson, and William M. Saxton. Identification of an Axonal Kinesin-3 Motor for Fast Anterograde Vesicle Transport that Facilitates Retrograde Transport of Neuropeptides. *Molecular Biology of the Cell*, 19:274–283, 2008. doi: 10.1091/mbc.E07.

[130] Virupakshi Soppina, Stephen R. Norris, Aslan S. Dizaji, Matt Kortus, Sarah Veatch, Michelle Peckham, and Kristen J. Verhey. Dimerization of mammalian kinesin-3 motors results in superprocessive motion. *Proceedings of the National Academy of Sciences of the United States of America*, 111(15):5562–5567, 2014. ISSN 10916490. doi: 10. 1073/pnas.1400759111.

[131] Anthony J. Otsuka, Ayyamperumal Jeyaprakash, Jaime García-Añoveros, Lan Zhao Tang, Gregory Fisk, Toinette Hartshorne, Rodrigo Franco, and Teresa Bornt. The C. elegans unc-104 4 gene encodes a putative kinesin heavy chain-like protein. *Neuron*, 6 (1):113–122, 1991. ISSN 08966273. doi: 10.1016/0896-6273(91)90126-K.

[132] Jae Ran Lee, Hyewon Shin, Jeonghoon Choi, Jaewon Ko, Seho Kim, Hyun Woo Lee, Karam Kim, Seong Hwan Rho, Jun Hyuck Lee, Hye Eun Song, Soo Hyun Eom, and Eunjoon Kim. An intramolecular interaction between the FHA domain and a coiled coil negatively regulates the kinesin motor KIF1A. *EMBO Journal*, 23(7):1506–1515, 2004. ISSN 02614189. doi: 10.1038/sj.emboj.7600164.

[133] Virupakshi Soppina and Kristen J. Verhey. The family-specific K-loop influences the microtubule on-rate but not the superprocessivity of kinesin-3 motors. *Molecular Biology of the Cell*, 25(14):2161–2170, 2014. ISSN 19394586. doi: 10.1091/mbc.E14-01-0696.

[134] Yasushi Okada, Hiroto Yamazaki, Yoko Sekine-Aizawa, and Nobutaka Hirokawa. The neuron-specific kinesin superfamily protein KIF1A is a uniqye monomeric motor for anterograde axonal transport of synaptic vesicle precursors. *Cell*, 81(5):769–780, 1995. ISSN 00928674. doi: 10.1016/0092-8674(95)90538-3.

[135] Michio Tomishige, Dieter R. Klopfenstein, and Ronald D. Vale. Conversion of Unc104/KIF1A kinesin into a processive motor after dimerization. *Science*, 297(5590): 2263–2267, 2002. ISSN 00368075. doi: 10.1126/science.1073386.

[136] Kaori H. Yamada, Toshihiko Hanada, and Athar H. Chishti. The effector domain of human Dlg tumor suppressor acts as a switch that relieves autoinhibition of kinesin-3 motor GAKIN/KIF13B. *Biochemistry*, 46(35):10039–10045, 2007. ISSN 00062960. doi: 10.1021/bi701169w.

[137] Atena Farkhondeh, Shinsuke Niwa, Yosuke Takei, and Nobutaka Hirokawa. Characterizing KIF16B in neurons reveals a novel intramolecular "stalk inhibition" mechanism that regulates its capacity to potentiate the selective somatodendritic localization of early endosomes. *Journal of Neuroscience*, 35(12):5067–5086, 2015. ISSN 15292401. doi: 10.1523/JNEUROSCI.4240-14.2015.

[138] Yasushi Okada and Nobutaka Hirokawa. A processive single-headed motor: Kinesin superfamily protein KIF1A. *Science*, 283(5405):1152–1157, 1999. ISSN 00368075. doi: 10.1126/science.283.5405.1152.

[139] Michael Vershinin, Brian C. Carter, David S. Razafsky, Stephen J. King, and Steven P. Gross. Multiple-motor based transport and its regulation by Tau. *Proceedings of the National Academy of Sciences of the United States of America*, 104(1):87–92, 2007. doi: 10.1073/pnas.0607919104.

[140] Adeela Kamal and Lawrence S.B. Goldstein. Principles of cargo attachment to cytoplasmic motor proteins. *Current Opinion in Cell Biology*, 14(1):63–68, 2002. ISSN 09550674. doi: 10.1016/S0955-0674(01)00295-2.

[141] Ewa Bielska, Martin Schuster, Yvonne Roger, Adokiye Berepiki, Darren M. Soanes, Nicholas J. Talbot, and Gero Steinberg. Hook is an adapter that coordinates kinesin-3 and dynein cargo attachment on early endosomes. *Journal of Cell Biology*, 204(6): 989–1007, 2014. ISSN 15408140. doi: 10.1083/jcb.201309022.

[142] Adam G. Hendricks, Erika L.F. Holzbaur, and Yale E. Goldman. Force measurements on cargoes in living cells reveal collective dynamics of microtubule motors. *Proceedings of the National Academy of Sciences of the United States of America*, 109(45):18447–18452, 2012. ISSN 00278424. doi: 10.1073/pnas.1215462109.

[143] William O. Hancock. Bidirectional cargo transport: Moving beyond tug of war. *Nature Reviews Molecular Cell Biology*, 15(9):615–628, 2014. ISSN 14710080. doi: 10.1038/nrm3853.

[144] Maryann Martin, Stanley J. Iyadurai, Andrew Gassman, Joseph G. Gindhart, Thomas S. Hays, and William M. Saxton. Cytoplasmic Dynein, the Dynactin Complex, and Kinesin Are Interdependent and Essential for Fast Axonal Transport. *Molecular biology of the cell*, 10:3717–3728, 1999. doi: 10.1091/mbc.10.11.3717.

[145] Kari Barlan, Molly J. Rossow, and Vladimir I. Gelfand. The Journey of the Organelle: Teamwork and Regulation in Intracellular Transport. *Current Opinion in Cell Biology*, 25:483–488, 2013. doi: 10.1016/j.ceb.2013.02.018.

[146] Marjan Haghnia, Valeria Cavalli, Sameer B. Shah, Kristina Schimmelpfeng, Richard Brusch, Ge Yang, Cheryl Herrera, Aaron Pilling, and Lawrence S.B. Goldstein. Dynactin Is Required for Coordinated Bidirectional Motility, but Not for Dynein Membrane Attachment. *Molecular biology of the cell*, 18:2081–2089, 2007. ISSN 1059-1524. doi: 10.1091/mbc.E06.

[147] Benjamin H. Blehm, Trina A. Schroer, Kathleen M. Trybus, Yann R. Chemla, and Paul R. Selvin. In vivo optical trapping indicates kinesin's stall force is reduced by dynein during intracellular transport. *Proceedings of the National Academy of Sciences of the United States of America*, 110(23):3381–3386, 2013. ISSN 00278424. doi: 10.1073/pnas.1308350110.

[148] Jeneva A. Laib, John A. Marin, Robert A. Bloodgood, and William H. Guilford. The reciprocal coordination and mechanics of molecular motors in living cells. *Proceedings of the National Academy of Sciences of the United States of America*, 106(9):3190–3195, 2009. ISSN 00278424. doi: 10.1073/pnas.0809849106.

[149] Meng-meng Fu and Erika L.F. Holzbaur. Integrated regulation of motor-driven organelle transport by scaffolding proteins. *Trends in Cell Biology*, 24(10):564–574, 2014. ISSN 18793088. doi: 10.1016/j.tcb.2014.05.002.

[150] Arne Gennerich and Detlev Schild. Finite-particle tracking reveals submicroscopic-size changes of mitochondria during transport in mitral cell dendrites. *Physical Biology*, 3 (1):45–53, 2006. ISSN 14783975. doi: 10.1088/1478-3975/3/1/005.

[151] Melanie J. I. Müller, Stefan Klumpp, and Reinhard Lipowsky. Tug-of-war as a cooperative mechanism for bidirectional cargo transport by molecular motors. *Proceedings of the National Academy of Sciences of the United States of America*, 105(12):4609–4614, 2008. doi: 10.1073/pnas.0706825105.

[152] Marco Tjioe, Saurabh Shukla, Rohit Vaidya, Alice Troitskaia, Carol Bookwalter, Kathleen M. Trybus, Yann R. Chemla, and Paul R. Selvin. Multiple Kinesins Induce Tension for Smooth Cargo Transport. *eLife*, 8:e50974, 2019. doi: 10.7554/eLife.50974.

[153] Sarah Klein, Cécile Appert-Rolland, and Ludger Santen. Motility states in bidirectional cargo transport. *Europhysics Letter*, 111(6):1–6, 2015. ISSN 12864854. doi: 10.1209/0295-5075/111/68005.

[154] Michael Vershinin, Jing Xu, David S. Razafsky, Stephen J. King, and Steven P. Gross. Tuning microtubule-based transport via filamentous MAPs: the problem of dynein. *Traffic*, 9:882–892, 2008. doi: 10.1111/j.1600-0854.2008.00741.x.

[155] Babu J.N. Reddy, Michelle Mattson, Caitlin L. Wynne, Omid Vadpey, Abdo Durra, Dail Chapman, Richard B. Vallee, and Steven P. Gross. Load-induced enhancement of Dynein force production by LIS1-NudE in vivo and in vitro. *Nature Communications*, 7:1–14, 2016. ISSN 20411723. doi: 10.1038/ncomms12259.

[156] Arthur R. Rogers, Jonathan W. Driver, Pamela E. Constantinou, D. Kenneth Jamison, and Michael R. Diehl. Negative interference dominates collective transport of kinesin motors in the absence of load. *Physical Chemistry Chemical Physics*, 11:4882–4889, 2009. ISSN 14639076. doi: 10.1039/b901646e.

[157] Ken'ya Furuta, Akane Furuta, Yoko Y. Toyoshima, Misako Amino, Kazuhiro Oiwa, and Hiroaki Kojima. Measuring collective transport by defined numbers of processive and nonprocessive kinesin motors. *Proceedings of the National Academy of Sciences of the United States of America*, 110(2):501–506, 2013. ISSN 10916490. doi: 10.1073/pnas.1201390110.

[158] N. D. Derr, B.S. Goodman, R. Jungmann, A. E. Leschziner, W.M. Shih, and S. L. Reck-Peterson. Tug-of-War in Motor Protein Ensembles Revealed with a Programmable DNA Origami Scaffold. *Science*, 338(6107):662–666, 2012. ISSN 0036-8075. doi: 10.1126/science.1226734.

[159] Christoph Herold, Cecile Leduc, Robert Stock, Stefan Diez, and Petra Schwille. Long-Range Transport of Giant Vesicles along Microtubule Networks. *Chem. Phys. Chem.*, 13:1001–1006, 2012. doi: 10.1007/978-94-007-4698-5_4.

[160] Hamid Khataee and Jonathon Howard. Force Generated by Two Kinesin Motors Depends on the Load Direction and Intermolecular Coupling. *Physical Review Letters*, 122(18), 2019. ISSN 10797114. doi: 10.1103/PhysRevLett.122.188101.

[161] Stephen R. Norris, Virupakshi Soppina, Aslan S. Dizaji, Kristin I. Schimert, David Sept, Dawen Cai, Sivaraj Sivaramakrishnan, and Kristen J. Verhey. A method for multiprotein assembly in cells reveals independent action of kinesins in complex. *Journal of Cell Biology*, 207(3):393–406, 2014. ISSN 15408140. doi: 10.1083/jcb.201407086.

[162] D. Kenneth Jamison, Jonathan W. Driver, Arthur R. Rogers, Pamela E. Constantinou, and Michael R. Diehl. Two kinesins transport cargo primarily via the action of one motor: Implications for intracellular transport. *Biophysical Journal*, 99(9):2967–2977, 2010. ISSN 15420086. doi: 10.1016/j.bpj.2010.08.025.

[163] Mehmet Can Uçar and Reinhard Lipowsky. Collective Force Generation by Molecular Motors Is Determined by Strain-Induced Unbinding. *Nano Letters*, 20(1):669–676, 2019. ISSN 15306992. doi: 10.1021/acs.nanolett.9b04445.

[164] Göker Arpag, Shankar Shastry, William O. Hancock, and Erkan Tüzel. Transport by populations of fast and slow kinesins uncovers novel family-dependent motor characteristics important for in vivo function. *Biophysical Journal*, 107(8):1896–1904, 2014. ISSN 15420086. doi: 10.1016/j.bpj.2014.09.009.

[165] Peter Bieling, Ivo A. Telley, Jacob Piehler, and Thomas Surrey. Processive kinesins require loose mechanical coupling for efficient collective motility. *EMBO reports*, 9 (11):1121–1127, 2008. doi: 10.1038/embor.2008.169.

[166] Taikopaul Kaneko, Suguru Ando, Ken'Ya Furuta, Kazuhiro Oiwa, Hirofumi Shintaku, Hidetoshi Kotera, and Ryuji Yokokawa. Transport of microtubules according to the number and spacing of kinesin motors on gold nano-pillars. *Nanoscale*, 11(20):9879–9887, 2019. ISSN 20403372. doi: 10.1039/c9nr01324e.

[167] Alvaro H. Crevenna, Sineej Madathil, Daniel N. Cohen, Michael Wagenbach, Karim Fahmy, and Jonathon Howard. Secondary structure and compliance of a predicted flexible domain in kinesin-1 necessary for cooperation of motors. *Biophysical Journal*, 95 (11):5216–5227, 2008. ISSN 15420086. doi: 10.1529/biophysj.108.132449.

[168] Qiaochu Li, Kuo Fu Tseng, Stephen J. King, Weihong Qiu, and Jing Xu. A fluid membrane enhances the velocity of cargo transport by small teams of kinesin-1. *Journal of Chemical Physics*, 148:123318, 2018. ISSN 00219606. doi: 10.1063/1.5006806.

[169] Rahul Grover, Janine Fischer, Friedrich W. Schwarz, Wilhelm J. Walter, Petra Schwille, and Stefan Diez. Transport efficiency of membrane-anchored kinesin-1 motors depends on motor density and diffusivity. *Proceedings of the National Academy of Sciences of the United States of America*, 113(46):E7185–E7193, 2016. ISSN 10916490. doi: 10.1073/pnas.1611398113.

[170] Michael R. Diehl, Kechun Zhang, Heun Jin-Lee, and David A. Tirrell. Engineering Cooperativity in Biomotor-Protein Assemblies. *Science*, 311(5766):1468–1471, 2006. ISSN 0036-8075. doi: 10.1126/science.1122125.

[171] Cécile Leduc, Felix Ruhnow, Jonathon Howard, and Stefan Diez. Detection of fractional steps in cargo movement by the collective operation of kinesin-1 motors. *Proceedings of the National Academy of Sciences of the United States of America*, 104(26):10847–10852, 2007. ISSN 00278424. doi: 10.1073/pnas.0701864104.

[172] Roop Mallik, Dmitri Petrov, S. A. Lex, S .J. King, and S. P. Gross. Building complexity: An in vitro study of cytoplasmic dynein with in vivo implications. *Current Biology*, 15 (23):2075–2085, 2005. ISSN 09609822. doi: 10.1016/j.cub.2005.10.039.

[173] Ronald D. Vale and Yoko Y. Toyoshima. Microtubule translocation properties of intact and proteolytically digested dyneins from Tetrahymena cilia. *The Journal of cell biology*, 108(6):2327–2334, 1989. ISSN 00219525. doi: 10.1083/jcb.108.6.2327.

[174] Hitoshi Sakakibara, Hiroaki Kojima, Yukako Sakai, Eisaku Katayama, and Kazuhiro Oiwa. Inner-arm dynein c of Chlamydomonas flagella is a single-headed processive motor. *Nature*, 400(6744):586–590, 1999. ISSN 00280836. doi: 10.1038/23066.

[175] Jonathan W. Driver, D. Kenneth Jamison, Karthik Uppulury, Arthur R. Rogers, Anatoly B. Kolomeisky, and Michael R. Diehl. Productive cooperation among processive motors depends inversely on their mechanochemical efficiency. *Biophysical Journal*, 101(2):386–395, 2011. ISSN 00063495. doi: 10.1016/j.bpj.2011.05.067.

[176] Cecile Leduc, Nenad Pavin, Frank Jülicher, and Stefan Diez. Collective Behavior of Antagonistically Acting Kinesin-1 Motors. *Physical Review Letters*, 105:1–4, 2010. doi: 10.1103/PhysRevLett.105.128103.

[177] Saumya Yadav and Ambarish Kunwar. Temperature-Dependent Activity of Motor Proteins: Energetics and Their Implications for Collective Behavior. *Frontiers in Cell and Developmental Biology*, 9:1–11, 2021. ISSN 2296634X. doi: 10.3389/fcell.2021. 610899.

[178] Vladimir Rodionov, Julie Yi, Anna Kashina, Abiola Oladipo, and Steven P. Gross. Switching between Microtubule- and Actin-Based Transport Systems in Melanophores Is Controlled by cAMP Levels. *Current Biology*, 13(21):1837–1847, 2003. ISSN 09609822. doi: 10.1016/j.cub.2003.10.027.

[179] Peter J. Hollenbeck and William M. Saxton. The axonal transport of mitochondria. *Journal of Cell Science*, 118(23):5411–5419, 2005. ISSN 00219533. doi: 10.1242/jcs. 02745.

[180] Hiromi Imamura, Kim P. Huynh Nhat, Hiroko Togawa, Kenta Saito, Ryota Iino, Yasuyuki Kato-Yamada, Takeharu Nagai, and Hiroyuki Noji. Visualization of ATP levels inside single living cells with fluorescence resonance energy transfer-based genetically encoded indicators. *Proceedings of the National Academy of Sciences of the United States of America*, 106(37):15651–15656, 2009. ISSN 00278424. doi: 10.1073/pnas.0904764106.

[181] Lynal S. Albert and Derick G. Brown. Variation in bacterial ATP concentration during rapid changes in extracellular pH and implications for the activity of attached bacteria. *Colloids and Surfaces B: Biointerfaces*, 132:111–116, 2015. ISSN 18734367. doi: 10.1016/j.colsurfb.2015.05.020.

[182] Judit Oláh, Péter Klivényi, Gabriella Gardián, László Vécsei, Ferenc Orosz, Gabor G. Kovacs, Hans V. Westerhoff, and Judit Ovádi. Increased glucose metabolism and ATP level in brain tissue of Huntington's disease transgenic mice. *Federation of European Biochemical Societies Journal*, 275(19):4740–4755, 2008. ISSN 1742464X. doi: 10. 1111/j.1742-4658.2008.06612.x.

[183] David L. Coy, Michael Wagenbach, and Jonathon Howard. Kinesin Takes One 8-nm Step for Each ATP That It Hydrolyzes. *THE JOURNAL OF BIOLOGICAL CHEMISTRY*, 274(6):3667–3671, 1999. doi: 10.1074/jbc.274.6.3667.

[184] Hannah A. DeBerg, Benjamin H. Blehm, Janet Sheung, Andrew R. Thompson, Carol S. Bookwalter, Seyed F. Torabi, Trina A. Schroer, Christopher L. Berger, Yi Lu, Kathleen M. Trybus, and Paul R. Selvin. Motor domain phosphorylation modulates kinesin-1 transport. *Journal of Biological Chemistry*, 288(45):32612–32621, 2013. ISSN 00219258. doi: 10.1074/jbc.M113.515510.

[185] J. Howard, A. J. Hudspeth, and R. D. Vale. Movement of microtubules by single kinesin molecules. *Nature*, 342:154–158, 1989. doi: 10.1038/342154a0.

[186] Koen Visscher, Mark J. Schnitzer, and Steven M. Block. Single kinesin molecules studied with a molecular force clamp. *letters to nature*, 400:184–189, 1999. doi: 10.1038/22146.

[187] Susan B. Rivera, Steven J. Koch, Joseph M. Bauer, J. Matthew Edwards, and George D. Bachand. Temperature dependent properties of a kinesin-3 motor protein from Thermomyces lanuginosus. *Fungal Genetics and Biology*, 44(11):1170–1179, 2007. ISSN 10871845. doi: 10.1016/j.fgb.2007.02.004.

[188] Mary E. Porter, Jonathan M. Scholey, Derek L. Stemple, Guy P. Vigers, Ronald D. Vale, Michael P. Sheetz, and J. Richard McIntosh. Characterization of the microtubule movement produced by sea urchin egg kinesin. *Journal of Biological Chemistry*, 262 (6):2794–2802, 1987. ISSN 00219258. doi: 10.1016/s0021-9258(18)61576-5.

[189] K. J. Boehm, R. Stracke, and E. Unger. Speeding up kinesin-driven microtubule gliding in vitro by variation of cofactor composition and physicochemical parameters. *Cell Biology International*, 24(6):335–341, 2000. ISSN 10656995. doi: 10.1006/cbir.1999. 0515.

[190] Jennifer L. Ross, Karen Wallace, Henry Shuman, Yale E. Goldman, and Erika L.F. Holzbaur. Processive bidirectional motion of dynein-dynactin complexes in vitro. *Nature Cell Biology*, 8(6):562–570, 2006. ISSN 14657392. doi: 10.1038/ncb1421.

[191] Shiori Toba and Yoko Yano Toyoshima. Dissociation of double-headed cytoplasmic dynein into single-headed species and its motile properties. *Cell Motility and the Cytoskeleton*, 58(4):281–289, 2004. ISSN 08861544. doi: 10.1002/cm.20018.

[192] Youske Shimizu, Hitoshi Sakakibara, Hiroaki Kojima, and Kazuhiro Oiwa. Slow axonemal dynein e facilitates the motility of faster dynein c. *Biophysical Journal*, 106 (10):2157–2165, 2014. ISSN 15420086. doi: 10.1016/j.bpj.2014.04.009.

[193] Krzysztof Sozanski, Felix Ruhnow, Agnieszka Wisniewska, Marcin Tabaka, Stefan Diez, and Robert Holyst. Small Crowders Slow Down Kinesin-1 Stepping by Hindering Motor Domain Diffusion. *Physical Review Letters*, 115(21):1–5, 2015. ISSN 10797114. doi: 10.1103/PhysRevLett.115.218102.

[194] Dominique Chretien, Paule Benit, Hyung-Ho Ha, Susanne Keipert, Riyad El-Khoury, Young-Tae Chang, Martin Jastroch, Howard T. Jacobs, Pierre Rustin, and Malgorzata

Rak. Mitochondria are physiologically maintained at close to 50 C. *PLoS Biology*, 16 (1):e2003992, 2018. doi: 10.3726/978-3-653-07022-4.

[195] Kohki Okabe, Noriko Inada, Chie Gota, Yoshie Harada, Takashi Funatsu, and Seiichi Uchiyama. Intracellular temperature mapping with a fluorescent polymeric thermometer and fluorescence lifetime imaging microscopy. *Nature Communications*, 3, 2012. ISSN 20411723. doi: 10.1038/ncomms1714.

[196] Ikuko Nara and Shin'ichi Ishiwata. Processivity of kinesin motility is enhanced on increasing temperature. *Biophysics*, 2:13–21, 2006. ISSN 1349-2942. doi: 10.2142/biophysics.2.13.

[197] Weili Hong, Anjneya Takshak, Olaolu Osunbayo, Ambarish Kunwar, and Michael Vershinin. The Effect of Temperature on Microtubule-Based Transport by Cytoplasmic Dynein and Kinesin-1 Motors. *Biophysical Journal*, 111(6):1287–1292, 2016. doi: 10.1016/j.bpj.2016.08.006.

[198] Kenji Kawaguchi and Shi N.Ichi Ishiwata. Thermal activation of single kinesin molecules with temperature pulse microscopy. *Cell Motility and the Cytoskeleton*, 49 (1):41–47, 2001. ISSN 08861544. doi: 10.1002/cm.1019.

[199] F. Doval, K. Chiba, R. J. McKenney, K. M. Ori-McKenney, and M. D. Vershinin. Temperature-dependent activity of kinesins is regulable. *Biochemical and Biophysical Research Communications*, 528(3):528–530, 2020. ISSN 0006-291X. doi: https://doi.org/10.1016/j.bbrc.2020.05.157.

[200] Julia R. Kardon and Ronald D. Vale. Regulators of the cytoplasmic dynein motor. *Nature Reviews Molecular Cell Biology*, 10(12):854–865, 2009. ISSN 14710072. doi: 10.1038/nrm2804.

[201] Irina Semenova, Kazuho Ikeda, Karim Resaul, Pavel Kraikivski, Mike Aguiar, Steven Gygi, Ilya Zaliapin, Ann Cowan, and Vladimir Rodionov. Regulation of microtubule-based transport by MAP4. *Molecular Biology of the Cell*, 25(20):3119–3132, 2014. ISSN 19394586. doi: 10.1091/mbc.E14-01-0022.

[202] Viktoriya Syrovatkina. *Role of Molecular Motors and Maps in Spindle Dynamics and Chromosome Segregation in the Fission Yeast Schizosaccharomyces Pombe*. PhD thesis, 2015.

[203] Hiroki Hagiwara, Hiroshi Yorifuji, Reiko Sato-Yoshitake, and Nobutaka Hirokawa. Competition between motor molecules (kinesin and cytoplasmic dynein) and fibrous microtubule-associated proteins in binding to microtubules. *Journal of Biological Chemistry*, 269(5):3581–3589, 1994. ISSN 00219258.

[204] Brigette Y. Monroy, Danielle L. Sawyer, Bryce E. Ackermann, Melissa M. Borden, Tracy C. Tan, and Kassandra M. Ori-Mckenney. Competition between microtubule-associated proteins directs motor transport. *Nature Communications*, 9(1):1–12, 2018. ISSN 20411723. doi: 10.1038/s41467-018-03909-2.

[205] Luis A. Lopez and Michael P. Sheetz. Steric inhibition of cytoplasmic dynein and kinesin motility by MAP2. *Cell Motility and the Cytoskeleton*, 24(1):1–16, 1993. ISSN 10970169. doi: 10.1002/cm.970240102.

[206] Ione Verdeny-Vilanova, Fabian Wehnekamp, Nitin Mohan, ángel Sandoval Álvarez, Joseph Steven Borbely, Jason John Otterstrom, Don C. Lamb, and Melike Lakadamyali. 3D motion of vesicles along microtubules helps them to circumvent obstacles in cells. *Journal of Cell Science*, 130(11):1904–1916, 2017. ISSN 14779137. doi: 10.1242/jcs. 201178.

[207] Nichole E. LaPointe, Gerardo Morfini, Gustavo Pigino, Irina N. Gaisina, P. Alan, Lester I. Binder, and Scott T. Brady. The Amino Terminus of Tau Inhibits Kinesin-Dependent Axonal Transport: Implications for Filament Toxicity. *Journal of Neuroscience*, 87(2):440–451, 2009. doi: 10.1002/jnr.21850.The.

[208] Hsin Ho Sung, Ivo A. Telley, Piyi Papadaki, Anne Ephrussi, Thomas Surrey, and Pernille Rørth. Drosophila Ensconsin Promotes Productive Recruitment of Kinesin-1 to Microtubules. *Developmental Cell*, 15(6):866–876, 2008. ISSN 15345807. doi: 10.1016/j.devcel.2008.10.006.

[209] Ram Dixit, Jennifer L. Ross, Yale E. Goldman, and Erika L. F. Holzbaur. Differential Regulation of Dynein and Kinesin Motor Proteins by Tau. *Science*, 319(5866):1086–1089, 2008. doi: 10.1126/science.1152993.Differential.

[210] Elizabeth H. Kellogg, Nisreen M. A Hejab, Simon Poepsel, Kenneth H. Downing, Frank DiMaio, and Eva Nogales. Near-atomic model of microtubule-tau interactions. *Science*, 1246(June):1242–1246, 2018. doi: 10.1126/science.aat1780.

[211] René Schneider, Till Korten, Wilhelm J. Walter, and Stefan Diez. Kinesin-1 Motors Can Circumvent Permanent Roadblocks by Side-Shifting to Neighboring Protofilaments. *Biophysical Journal*, 108(9):2249–2257, 2015. doi: 10.1016/j.bpj.2015.03.048.

[212] Ivo A. Telley, Peter Bieling, and Thomas Surrey. Obstacles on the microtubule reduce the processivity of kinesin-1 in a minimal in vitro system and in cell extract. *Biophysical Journal*, 96(8):3341–3353, 2009. ISSN 15420086. doi: 10.1016/j.bpj.2009.01.015.

[213] Arne Seitz and Thomas Surrey. Processive movement of single kinesins on crowded microtubules visualized using quantum dots. *EMBO Journal*, 25(2):267–277, 2006. ISSN 02614189. doi: 10.1038/sj.emboj.7600937.

[214] Kerstin Dreblow, Nikolina Kalchishkova, and Konrad J. Böhm. Kinesin passing permanent blockages along its protofilament track. *Biochemical and Biophysical Research Communications*, 395(4):490–495, 2010. ISSN 0006291X. doi: 10.1016/j.bbrc.2010. 04.035.

[215] Till Korten and Stefan Diez. Setting up roadblocks for kinesin-1: Mechanism for the selective speed control of cargo carrying microtubules. *Lab on a Chip*, 8(9):1441–1447, 2008. ISSN 14730189. doi: 10.1039/b803585g.

[216] Jeff Gelles, Bruce J. Schnappt, and Michael P. Sheetz. Tracking kinesin-driven movements with nanometre-scale precision. *Nature*, 331(4):450–453, 1988. doi: 10.1038/ 331450a0.

[217] Zhaohui Wang, Shahid Khan, and Michael P. Sheetz. Single cytoplasmic dynein molecule movements: characterization and comparison with kinesin. *Biophysical Journal*, 69(5):2011–2023, 1995. ISSN 00063495. doi: 10.1016/S0006-3495(95)80071-8.

[218] Heidi N. Fridolfsson and Daniel A. Starr. Kinesin-1 and dynein at the nuclear envelope mediate the bidirectional migrations of nuclei. *Journal of Cell Biology*, 191(1):115–128, 2010. ISSN 00219525. doi: 10.1083/jcb.201004118.

[219] Dawen Cai, Dyke P. McEwen, Jeffery R. Martens, Edgar Meyhofer, and Kristen J. Verhey. Single molecule imaging reveals differences in microtubule track selection between kinesin motors. *PLoS Biology*, 7(10), 2009. ISSN 15449173. doi: 10.1371/journal.pbio.1000216.

[220] Sarah Dunn, Ewan E. Morisson, Tanniemola B. Liverpool, Carmen Molina-París, Robert A. Cross, Maria C. Alonso, and Michelle Peckham. Differential trafficking of Kif5c on tyrosinated and detyrosinated microtubules in live cells. *Journal of Cell Science*, 121(7):1085–1095, 2008. ISSN 00219533. doi: 10.1242/jcs.026492.

[221] Roderick P. Tas, Anaël Chazeau, Bas M.C. Cloin, Maaike L.A. Lambers, Casper C. Hoogenraad, and Lukas C. Kapitein. Differentiation between Oppositely Oriented Microtubules Controls Polarized Neuronal Transport. *Neuron*, 96(6):1264–1271, 2017. ISSN 10974199. doi: 10.1016/j.neuron.2017.11.018.

[222] Daniel R. Peet, Nigel J. Burroughs, and Robert A. Cross. Kinesin expands and stabilizes the GDP-microtubule lattice. *Nature Nanotechnology*, 13(5):386–391, 2018. ISSN 17483395. doi: 10.1038/s41565-018-0084-4.

[223] Tomohiro Shima, Manatsu Morikawa, Junichi Kaneshiro, Taketoshi Kambara, Shinji Kamimura, Toshiki Yagi, Hiroyuki Iwamoto, Sotaro Uemura, Hideki Shigematsu, Mikako Shirouzu, Taro Ichimura, Tomonobu M. Watanabe, Ryo Nitta, Yasushi Okada, and Nobutaka Hirokawa. Kinesin-binding – triggered conformation switching of microtubules contributes to polarized transport. *Journal of Cell Biology*, 217(12):4164–4183, 2018. doi: 10.1083/jcb.201711178.

[224] Robin Jose and Ludger Santen. Self-Organized Lane Formation in Bidirectional Transport by Molecular Motors. *Physical Review Letters*, 124(19):198103, 2020. ISSN 10797114. doi: 10.1103/PhysRevLett.124.198103.

[225] Richard J. McKenney, Walter Huynh, Ronald D. Vale, and Minhajuddin Sirajuddin. Tyrosination of α-tubulin controls the initiation of processive dynein–dynactin motility. *The EMBO Journal*, 35(11):1175–1185, 2016. ISSN 0261-4189. doi: 10.15252/embj. 201593071.

[226] Minhajuddin Sirajuddin, Luke M. Rice, and Ronald D. Vale. Regulation of microtubule motors by tubulin isotypes and post-translational modifications. *Nature Cell Biology*, 16(4):335–344, 2014. ISSN 14764679. doi: 10.1038/ncb2920.

[227] M. D. Weingarten, A. H. Lockwood, S. Y. Hwo, and M. W. Kirschner. A protein factor essential for microtubule assembly. *Proceedings of the National Academy of Sciences of the United States of America*, 72(5):1858–1862, 1975. ISSN 00278424. doi: 10. 1073/pnas.72.5.1858.

[228] Amayra Hernández-Vega, Marcus Braun, Lara Scharrel, Marcus Jahnel, Susanne Wegmann, Bradley T. Hyman, Simon Alberti, Stefan Diez, and Anthony A. Hyman. Local nucleation of microtubule bundles through tubulin concentration into a condensed tau

phase. *Cell Reports*, 20:2304–2312, 2017. ISSN 1556-5068. doi: 10.1016/j.celrep. 2017.08.042.

[229] Diane P. Hanger, Brian H. Anderton, and Wendy Noble. Tau phosphorylation: the therapeutic challenge for neurodegenerative disease. *Trends in Molecular Medicine*, 15 (3):112–119, 2009. ISSN 14714914. doi: 10.1016/j.molmed.2009.01.003.

[230] Guy Lippens, Isabelle Landrieu, Caroline Smet, Isabelle Huvent, Neha S. Gandhi, Benoît Gigant, Clément Despres, Haoling Qi, and Juan Lopez. NMR meets Tau: Insights into its function and pathology. *Biomolecules*, 6(2):1–21, 2016. ISSN 2218273X. doi: 10.3390/biom6020028.

[231] Anthony W.P. Fitzpatrick, Benjamin Falcon, Shaoda He, Alexey G. Murzin, Garib Murshudov, Holly J. Garringer, R. Anthony Crowther, Bernardino Ghetti, Michel Goedert, and Sjors H.W. Scheres. Cryo-EM structures of tau filaments from Alzheimer's disease. *Nature*, 547(7662):185–190, 2017. ISSN 14764687. doi: 10.1038/nature23002.

[232] Hans Zempel and Eckhard Mandelkow. Lost after translation: Missorting of Tau protein and consequences for Alzheimer disease. *Trends in Neurosciences*, 37(12):721–732, 2014. ISSN 1878108X. doi: 10.1016/j.tins.2014.08.004.

[233] Liviu Gabriel Bodea, Anne Eckert, Lars Matthias Ittner, Olivier Piguet, and Jürgen Götz. Tau physiology and pathomechanisms in frontotemporal lobar degeneration. *Journal of Neurochemistry*, 138:71–94, 2016. ISSN 14714159. doi: 10.1111/jnc.13600.

[234] Sven Konzack, Edda Thies, Alexander Marx, Eva Maria Mandelkow, and Eckhard Mandelkow. Swimming against the tide: Mobility of the microtubule-associated protein tau in neurons. *Journal of Neuroscience*, 27(37):9916–9927, 2007. ISSN 02706474. doi: 10.1523/JNEUROSCI.0927-07.2007.

[235] Susmitha Ambadipudi, Jacek Biernat, Dietmar Riedel, Eckhard Mandelkow, and Markus Zweckstetter. Liquid-liquid phase separation of the microtubule-binding repeats of the Alzheimer-related protein Tau. *Nature Communications*, 8(1):1–13, 2017. ISSN 20411723. doi: 10.1038/s41467-017-00480-0.

[236] Xiao Han Li and Elizabeth Rhoades. Heterogeneous Tau-Tubulin Complexes Accelerate Microtubule Polymerization. *Biophysical Journal*, 112(12):2567–2574, 2017. ISSN 15420086. doi: 10.1016/j.bpj.2017.05.006.

[237] Sarah Bachmann, Michael Bell, Jennifer Klimek, and Hans Zempel. Differential Effects of the Six Human TAU Isoforms: Somatic Retention of 2N-TAU and Increased Microtubule Number Induced by 4R-TAU. *Frontiers in Neuroscience*, 15(May):1–10, 2021. ISSN 1662453X. doi: 10.3389/fnins.2021.643115.

[238] Jawdat Al-Bassam, Rachel S. Ozer, Daniel Safer, Shelley Halpain, and Ronald A. Milligan. MAP2 and tau bind longitudinally along the outer ridges of microtubule protofilaments. *Journal of Cell Biology*, 157(7):1187–1196, 2002. ISSN 00219525. doi: 10.1083/jcb.200201048.

[239] Xiao-Han Li, Jacob A. Culver, and Elizabeth Rhoades. Tau Binds to Multiple Tubulin Dimers with Helical Structure. *Journal of the American Chemical Society*, 137(29): 9218–9221, 2015. doi: 10.1021/jacs.5b04561.

[240] Karen A. Butner and Marc W. Kirschner. Tau protein binds to microtubules through a flexible array of distributed weak sites. *Journal of Cell Biology*, 115(3 I):717–730, 1991. ISSN 00219525. doi: 10.1083/jcb.115.3.717.

[241] Maike H. Hinrichs, Avesta Jalal, Bernhard Brenner, Eckhard Mandelkow, Satish Kumar, and Tim Scholz. Tau protein diffuses along the microtubule lattice. *Journal of Biological Chemistry*, 287(46):38559–38568, 2012. ISSN 00219258. doi: 10.1074/jbc.M112.369785.

[242] Derrick P. McVicker, Gregory J. Hoeprich, Andrew R. Thompson, and Christopher L. Berger. Tau Interconverts Between Diffusive and Stable Populations on the Microtubule Surface in an Isoform and Lattice Specific Manner. *Cytoskeleton (Hoboken)*, 71(3): 184–194, 2014. ISSN 15378276. doi: 10.1038/jid.2014.371.

[243] Kenneth J. Rosenberg, Jennifer L. Ross, H. Eric Feinstein, Stuart C. Feinstein, and Jacob Israelachvili. Complementary dimerization of microtubule-associated tau protein: Implications for microtubule bundling and tau-mediated pathogenesis. *Proceedings of the National Academy of Sciences of the United States of America*, 105(21):7445–7450, 2008. ISSN 00278424. doi: 10.1073/pnas.0802036105.

[244] Rui Zhang, Gregory M. Alushin, Alan Brown, and Eva Nogales. Mechanistic origin of microtubule dynamic instability and its modulation by EB proteins. *Cell*, 162(4): 849–859, 2015. ISSN 10974172. doi: 10.1016/j.cell.2015.07.012.

[245] Ashim Rai, Divya Pathak, Shreyasi Thakur, Shampa Singh, Alok Kumar Dubey, and Roop Mallik. Dynein Clusters into Lipid Microdomains on Phagosomes to Drive Rapid Transport toward Lysosomes. *Cell*, 164(4):722–734, 2016. ISSN 10974172. doi: 10. 1016/j.cell.2015.12.054.

[246] Rui Jiang, Steven Vandal, Soohyun Park, Sheereen Majd, Erkan Tüzel, and William O. Hancock. Microtubule binding kinetics of membrane-bound kinesin-1 predicts high motor copy numbers on intracellular cargo. *Proceedings of the National Academy of Sciences of the United States of America*, 116(52):26564–26570, 2019. doi: 10.1101/ 627174.

[247] Robert P. Erickson, Zhiyuan Jia, Steven P. Gross, and Clare C. Yu. How molecular motors are arranged on a cargo is important for vesicular transport. *PLoS Computational Biology*, 7(5), 2011. ISSN 1553734X. doi: 10.1371/journal.pcbi.1002032.

[248] Shane R. Nelson, Kathleen M. Trybus, and David M. Warshaw. Motor coupling through lipid membranes enhances transport velocities for ensembles of myosin Va. *Proceedings of the National Academy of Sciences of the United States of America*, 111(38):E3986–E3995, 2014. ISSN 10916490. doi: 10.1073/pnas.1406535111.

[249] Serapion Pyrpassopoulos, Henry Shuman, and E. Michael Ostap. Modulation of Kinesin's Load-Bearing Capacity by Force Geometry and the Microtubule Track. *Biophysical Journal*, 118(1):243–253, 2019. ISSN 15420086. doi: 10.1016/j.bpj.2019.10.045.

[250] Matthew Bovyn, Babu Reddy Janakaloti Narayanareddy, Steven Gross, and Jun Allard. Diffusion of kinesin motors on cargo can enhance binding and run lengths during intracellular transport. *Molecular Biology of the Cell*, 32(9):984–994, 2021. ISSN 19394586. doi: 10.1091/MBC.E20-10-0658.

[251] Niranjan Sarpangala and Ajay Gopinathan. Cargo surface fluidity reduces inter-motor mechanical interference, promotes load-sharing and enhances run-lengths in an ATP-dependent manner. *PLOS Computational Biology*, 18(6):e1010217, 2021. doi: 10. 1371/journal.pcbi.1010217.

[252] Gerrit Van Meer, Dennis R. Voelker, and Gerald W. Feigenson. Membrane lipids: Where they are and how they behave. *Nature Reviews Molecular Cell Biology*, 9(2): 112–124, 2008. ISSN 14710072. doi: 10.1038/nrm2330.

[253] Divya Pathak and Roop Mallik. Lipid - Motor Interactions: Soap Opera or Symphony? *Current Opinion in Cell Biology*, 44:79–85, 2017. ISSN 18790410. doi: 10.1016/j.ceb. 2016.09.005.

[254] Raz Jelinek. Membranes. In *Membranes*, chapter 3. Membran, pages 59–65. De Gruyter, 2018. ISBN 9783110453690. doi: 10.1515/9783110453690-003.

[255] J.M. Berg, J.L. Tymoczko, and L. Stryer. Biochemistry. In *Biochemistry*, chapter 12.6 Lipid. New York: W H Freeman, 5 edition, 2002.

[256] Kerstin Weiß, Andreas Neef, Qui Van, Stefanie Kramer, Ingo Gregor, and Jörg Enderlein. Quantifying the diffusion of membrane proteins and peptides in black lipid membranes with 2-focus fluorescence correlation spectroscopy. *Biophysical Journal*, 105(2):455–462, 2013. ISSN 00063495. doi: 10.1016/j.bpj.2013.06.004.

[257] Otger Campàs, Cécile Leduc, Patricia Bassereau, Jaume Casademunt, Jean François Joanny, and Jacques Prost. Coordination of kinesin motors pulling on fluid membranes. *Biophysical Journal*, 94(12):5009–5017, 2008. ISSN 15420086. doi: 10.1529/biophysj. 107.118554.

[258] Gerald F. Reis, Ge Yang, Lukasz Szpankowski, Carole Weaver, Sameer B. Shah, John T. Robinson, Thomas S. Hays, Gaudenz Danuser, and Lawrence S.B. Goldstein. Molecular motor function in axonal transport in vivo probed by genetic and computational analysis in Drosophila. *Molecular Biology of the Cell*, 23(9):1700–1714, 2012. ISSN 10591524. doi: 10.1091/mbc.E11-11-0938.

[259] Paul C. Bressloff. *Stochastic Processes in Cell Biology*. Springer, 2014.

[260] Nino Boccara. *Modeling Complex Systems*. Springer-Verlag, New York, 1 edition, 2004. ISBN 0-387-40462-7.

[261] N.G. van Kampen. *Stochastic Processes in Physics and Chemistry*. Elsevier, 3 edition, 2007.

[262] C. W: Gardiner. *Handbook of Stohcastic Methods for Physics, Chemestry and the Natural Science*. Springer, 2 edition.

[263] Albert Einstein. INVESTIGATIONS ON THE THEORY OF THE BROWNIAN MOVEMENT. *Annalen der Physik*, 17:549, 1905. ISSN 00219673. doi: 10.1016/ j.chroma.2008.07.021.

[264] Don S. Lemons. Paul Langevin's 1908 paper "On the Theory of Brownian Motion" ["Sur la théorie du mouvement brownien," C. R. Acad. Sci. (Paris) 146, 530–533 (1908)]. *American Journal of Physics*, 65:1079–1081, 19997. ISSN 00029505.

[265] J. Honerkamp. *Stochastische Dynamische Systeme: Konzepte, numerische Methoden, Datenanalyse*. VCH, 1990.

[266] S. Redner. *A Guide to First-Passage Processes*. Cambridge University Press, 2001.

[267] W. Krauth. *Statistical Mechanics: Algorithms and Computations*. Oxford University Press, 2006.

[268] Daniel T. Gillespie. A General Method for Numerically Simulating the Stochastic Time Evolution of Coupled Chemical Reactions. *Journal of Computational Physics*, 22(4): 403–434, 1976. doi: 10.1016/0021-9991(76)90041-3.

[269] Ronald D. Vale, David R. Soll, and I. R. Gibbons. One-dimensional diffusion of microtubules bound to flagellar dynein. *Cell*, 59(5):915–925, 1989. ISSN 00928674. doi: 10.1016/0092-8674(89)90614-4.

[270] John Happel and Howard Brenner. *Low Reynolds number hydrodynamics*. MARTINUS NIJHOFF PUBLISHERS, 1983.

[271] G.K. Batchelor. *AN INTRODUCTION TO FLUID DYNAMICS*. Cambridge University Press, 1967.

[272] Victor A. Bloomfield. Hydrodynamic properties of complex, rigid, biological macromolecules: Theory and applications. *Quarterly Reviews of Biophysics*, 14(1):81–139, 1981. ISSN 14698994. doi: 10.1017/S0033583500002080.

[273] Maria M. Tirado and Jose Garcia de la Torre. Translational friction coefficients of rigid, symmetric top macromolecules. Application to circular cylinders. *The Journal of Chemical Physics*, 71(6):2581–2587, 1979. doi: 10.1063/1.438613.

[274] S. Broersma. Viscous force constant for a closed cylinder. *The Journal of Chemical Physics*, 32(6):1632–1635, 1960. ISSN 00219606. doi: 10.1063/1.1730995.

[275] R. A. Blythe and M. R. Evans. Nonequilibrium steady states of matrix-product form: A solver's guide. *Journal of Physics A: Mathematical and Theoretical*, 40(46), 2007. ISSN 17518113. doi: 10.1088/1751-8113/40/46/R01.

[276] Pavel L. Krapivsky, Sidney Redner, and Eli Ben–Naim. *A Kinetic View of Statistical Physics*. Cambridge University Press, 2010.

[277] Hans Swenson and Nicholas P. Stadie. Langmuir's Theory of Adsorption: A Centennial Review. *Langmuir*, 35(16):5409–5426, 2019. ISSN 15205827. doi: 10.1021/acs.langmuir.9b00154.

[278] Xin Li, Reinhard Lipowsky, and Jan Kierfeld. Critical motor number for fractional steps of cytoskeletal filaments in gliding assays. *PLoS ONE*, 7(8):1–14, 2012. ISSN 19326203. doi: 10.1371/journal.pone.0043219.

[279] Christian B. Korn, Stefan Klumpp, Reinhard Lipowsky, and Ulrich S. Schwarz. Stochastic simulations of cargo transport by processive molecular motors. *Journal of Chemical Physics*, 131(24), 2009. ISSN 00219606. doi: 10.1063/1.3279305.

[280] Ambarish Kunwar, Michael Vershinin, Jing Xu, and Steven P. Gross. Stepping, Strain Gating, and an Unexpected Force-Velocity Curve for Multiple-Motor-Based Transport. *Current Biology*, 18(16):1173–1183, 2008. ISSN 09609822. doi: 10.1016/j.cub.2008. 07.027.

[281] Mehmet Can Uçar and Reinhard Lipowsky. Tug-of-war between two elastically coupled molecular motors: a case study on force generation and force balance. *Soft Matter*, 13 (2):328–344, 2017. ISSN 17446848. doi: 10.1039/c6sm01853j.

[282] Adam G. Larson, Eric C. Landahl, and Sarah E. Rice. Mechanism of cooperative behaviour in systems of slow and fast molecular motors. *Physical Chemistry Chemical Physics*, 11:4890–4898, 2009. ISSN 14639076. doi: 10.1039/b901646e.

[283] Stefan Klumpp and Reinhard Lipowsky. Cooperative cargo transport by several molecular motors. *Proceedings of the National Academy of Sciences of the United States of America*, 102(48):17284–17289, 2005. ISSN 00278424. doi: 10.1073/pnas. 0507363102.

[284] Yunxin Zhang. Cargo transportation by two species of motor protein. *Physical Review E - Statistical, Nonlinear, and Soft Matter Physics*, 87(5):1–10, 2013. ISSN 15393755. doi: 10.1103/PhysRevE.87.052705.

[285] Xin Li, Reinhard Lipowsky, and Jan Kierfeld. Bifurcation of velocity distributions in cooperative transport of filaments by fast and slow motors. *Biophysical Journal*, 104 (3):666–676, 2013. ISSN 00063495. doi: 10.1016/j.bpj.2012.11.3834.

[286] Kejie Chen, Woochul Nam, and Bogdan I. Epureanu. Collective intracellular cargo transport by multiple kinesins on multiple microtubules. *Physical Review E*, 101(5): 52413, 2020. ISSN 24700053. doi: 10.1103/PhysRevE.101.052413.

[287] Kunalika Jain, Neha Khetan, and Chaitanya A. Athale. Collective effects of yeast cytoplasmic dynein based microtubule transport. *Soft Matter*, 15(7):1571–1581, 2019. ISSN 17446848. doi: 10.1039/c8sm01434e.

[288] Neha Khetan and Chaitanya A. Athale. Aster swarming by symmetry breaking of cortical dynein transport and coupling kinesins. *Soft Matter*, 16(37):8554–8564, 2020. ISSN 17446848. doi: 10.1039/d0sm01086c.

[289] François Nédélec. Computer simulations reveal motor properties generating stable antiparallel microtubule interactions. *Journal of Cell Biology*, 158(6):1005–1015, 2002. ISSN 00219525. doi: 10.1083/jcb.200202051.

[290] H. A. Kramers. Brownian motion in a field of force and the diffusion model of chemical reactions. *Physica*, 7(4):284–304, 1940. ISSN 00318914. doi: 10.1016/ S0031-8914(40)90098-2.

[291] George I. Bell. Models for the specific adhesion of cells to cells. *Science*, 200(4342): 618–627, 1978. ISSN 00368075. doi: 10.1126/science.347575.

[292] Lara Scharrel, Rui Ma, René Schneider, Frank Jülicher, and Stefan Diez. Multimotor transport in a system of active and inactive kinesin-1 motors. *Biophysical Journal*, 107 (2):365–372, 2014. ISSN 15420086. doi: 10.1016/j.bpj.2014.06.014.

[293] Manoranjan P. Singh, Roop Mallik, Steven P. Gross, and Clare C. Yu. Monte Carlo modeling of single-molecule cytoplasmic dynein. *Proceedings of the National Academy of Sciences of the United States of America*, 102(34):12059–12064, 2005. ISSN 00278424. doi: 10.1073/pnas.0501570102.

[294] Frank Gibbons, Jean François Chauwin, Marcelo Despósito, and Jorge V. José. A dynamical model of kinesin-microtubule motility assays. *Biophysical Journal*, 80(6): 2515–2526, 2001. ISSN 00063495. doi: 10.1016/S0006-3495(01)76223-6.

[295] Pavel Kraikivski, Reinhard Lipowsky, and Jan Kierfeld. Enhanced ordering of interacting filaments by molecular motors. *Physical Review Letters*, 96(25):1–4, 2006. ISSN 00319007. doi: 10.1103/PhysRevLett.96.258103.

[296] J. Kierfeld, K. Frentzel, P. Kraikivski, and R. Lipowsky. Active dynamics of filaments in motility assays. *European Physical Journal: Special Topics*, 157(1):123–133, 2008. ISSN 19516355. doi: 10.1140/epjst/e2008-00635-9.

[297] Cécile Leduc, Kathrin Padberg-Gehle, Vladimír Varga, Dirk Helbing, Stefan Diez, and Jonathon Howard. Molecular crowding creates traffic jams of kinesin motors on microtubules. *Proceedings of the National Academy of Sciences of the United States of America*, 109(16):6100–6105, 2012. ISSN 00278424. doi: 10.1073/pnas.1107281109.

[298] Daniel T. Gillespie. Exact stochastic simulation of coupled chemical reactions. *The Journal of Physical Chemistry*, 81(25):2340–2361, 1977. doi: 10.1021/j100540a008.

[299] Lara Maresa Scharrel. *Cooperative transport by groups of different microtubule motors*. dissertation, Technische Universitaet Dresden, 2017.

[300] Gina A. Monzon, Lara Scharrel, Ludger Santen, and Stefan Diez. Activation of mammalian cytoplasmic dynein in multimotor motility assays. *Journal of Cell Science*, 132 (4):jcs220079, feb 2019. doi: 10.1242/jcs.220079.

[301] Alan J. Hunt, Frederick Gittes, and Jonathan Howard. The force exerted by a single kinesin molecule against a viscous load. *Biophysical Journal*, 67(2):766–781, 1994. ISSN 00063495. doi: 10.1016/S0006-3495(94)80537-5.

[302] José García de la Torre and Victor A. Bloomfield. Hydrodynamic properties of complex rigid, biological macromolecules: theory and applications. *Quarterly Review of Biophysics*, 14(1):81–139, 1981. doi: 10.1017/s0033583500002080.

[303] E. M. Purcell. Life at low Reynolds number. *American Journal of Physics*, 45(3), 1977. doi: 10.1119/1.10903.

[304] Adrian N. Fehr, Braulio Gutiérrez-Medina, Charles L. Asbury, and Steven M. Block. On the origin of kinesin limping. *Biophysical Journal*, 97(6):1663–1670, 2009. ISSN 15420086. doi: 10.1016/j.bpj.2009.07.004.

[305] Edgar Meyhöfer and Jonathon Howard. The force generated by a single kinesin molecule against an elastic load. *Proceedings of the National Academy of Sciences of the United States of America*, 92(2):574–578, 1995. ISSN 00278424. doi: 10.1073/pnas.92.2.574.

[306] Chris M. Coppin, Daniel W. Pierce, Long Hsu, and Ronald D. Vale. The load dependence of kinesin's mechanical cycle. *Proceedings of the National Academy of Sciences of the United States of America*, 94(16):8539–8544, 1997. ISSN 00278424. doi: 10.1073/pnas.94.16.8539.

[307] Zhaohui Wang and Michael P. Sheetz. One-dimensional Diffusion on Microtubules of Particles Coated with Cytoplasmic Dynein and Immunoglobulins. *Cell Structure and Function*, 24(5):373–383, 1999. ISSN 0386-7196. doi: 10.1247/csf.24.373.

[308] Martina Trokter, Norbert Muecke, and Thomas Surrey. Reconstitution of the human cytoplasmic dynein complex. *Proceedings of the National Academy of Sciences of the United States of America*, 109(51):20895–20900, 2012. ISSN 00278424. doi: 10.1073/pnas.1210573110.

[309] Gina A. Monzon, Lara Scharrel, Ashwin D'Souza, Verena Henrichs, Ludger Santen, and Stefan Diez. Stable tug-of-war between kinesin-1 and cytoplasmic dynein upon different ATP and roadblock concentrations. *Journal of Cell Science*, 133(22):jcs249938, 2020. ISSN 14779137. doi: 10.1242/jcs.249938.

[310] Joshua Niclas, Viki J. Allan, and Ronald D. Vale. Cell cycle regulation of dynein association with membranes modulates microtubule-based organelle transport. *Journal of Cell Biology*, 133(3):585–593, 1996. ISSN 00219525. doi: 10.1083/jcb.133.3.585.

[311] Sharron X.H. Lin, K. Kevin Pfister, and Christine A. Collins. Comparison of the intracellular distribution of cytoplasmic dynein and kinesin in cultured cells: Motor protein location does not reliably predict function. *Cell Motility and the Cytoskeleton*, 34(4): 299–312, 1996. ISSN 08861544. doi: 10.1002/(SICI)1097-0169(1996)34:4<299:: AID-CM5>3.0.CO;2-3.

[312] Verena Henrichs, Lenka Grycova, Cyril Barinka, Zuzana Nahacka, Jiri Neuzil, Stefan Diez, Jakub Rohlena, Marcus Braun, and Zdenek Lansky. Mitochondria-adaptor TRAK1 promotes kinesin-1 driven transport in crowded environments. *Nature Communications*, 11(1):1–13, 2020. ISSN 20411723. doi: 10.1038/s41467-020-16972-5.

[313] Brigette Y. Monroy, Tracy C. Tan, Janah May Oclaman, Jisoo S. Han, Sergi Simó, Shinsuke Niwa, Dan W. Nowakowski, Richard J. McKenney, and Kassandra M. Ori-McKenney. A Combinatorial MAP Code Dictates Polarized Microtubule Transport. *Developmental Cell*, 53(1):60–72.e4, 2020. ISSN 18781551. doi: 10.1016/j.devcel.2020.01.029.

[314] Luke S. Ferro, Qianglin Fang, Lisa Eshun-Wilson, Jonathan Fernandes, Amanda Jack, Daniel P. Farrell, Mert Golcuk, Teun Huijben, Katelyn Costa, Mert Gur, Frank DiMaio, Eva Nogales, and Ahmet Yildiz. Structural and functional insight into regulation o kinesin-1 by microtubule-associated protein MAP7. *Science*, 375(6578):326–331, 2022. ISSN 10959203. doi: 10.1126/science.abf6154.

[315] Abdullah R. Chaudhary, Hailong Lu, Elena B. Krementsova, Carol S. Bookwalter, Kathleen M. Trybus, and Adam G. Hendricks. MAP7 regulates organelle transport by recruiting kinesin-1 to microtubules. *Journal of Biological Chemistry*, 294(26):10160–10171, 2019. ISSN 1083351X. doi: 10.1074/jbc.RA119.008052.

[316] B. Trinczek, A. Ebneth, E. M. Mandelkow, and E. Mandelkow. Tau regulates the attachment/detachment but not the speed of motors in microtubule-dependent transport of single vesicles and organelles. *Journal of Cell Science*, 112(14):2355–2367, 1999. ISSN 00219533. doi: 10.1242/jcs.112.14.2355.

[317] Valerie Siahaan, Ruensern Tan, Tereza Humhalova, Lenka Libusova, Samuel E. Lacey, Tracy Tan, Mariah Dacy, Kassandra M. Ori-McKenney, Richard J. McKenney, Marcus Braun, and Zdenek Lansky. Microtubule Lattice Spacing Governs Cohesive Envelope Formation of Tau Family Proteins. *Nature Chemical Biology*, 18:1224–1235, 2021. doi: 10.1038/s41589-022-01096-2.

[318] Yong-Lei Gao, Nan Wang, Fu-Rong Sun, Xi-Peng Cao, Wei Zhang, and Jin-Tai Yu. Review Article on Translational Neurodegeneration Tau in neurodegenerative disease. *Annals of Translational Medicine*, 6(10):175, 2018. ISSN 1023294X. doi: 10.1007/978-3-319-43589-3_7.

[319] Susanne Wegmann, Bahareh Eftekharzadeh, Katharina Tepper, Katarzyna M. Zoltowska, Rachel E. Bennett, Simon Dujardin, Pawel R. Laskowski, Danny MacKenzie, Tarun Kamath, Caitlin Commins, Charles Vanderburg, Allyson D. Roe, Zhanyun Fan, Amandine M. Molliex, Amayra Hernandez-Vega, Daniel Muller, Anthony A. Hyman, Eckhard Mandelkow, J. Paul Taylor, and Bradley T. Hyman. Tau protein liquid–liquid phase separation can initiate tau aggregation. *The EMBO Journal*, 37(7): 1–21, 2018. ISSN 0261-4189. doi: 10.15252/embj.201798049.

[320] Janine Hochmair, Christian Exner, Maximilian Franck, Alvaro Dominguez-Baquero, Lisa Diez, Hévila Brognaro, Matthew L. Kraushar, Thorsten Mielke, Helena Radbruch, Senthilvelrajan Kaniyappan, Sven Falke, Eckhard Mandelkow, Christian Betzel, and Susanne Wegmann. Molecular crowding and RNA synergize to promote phase separation, microtubule interaction, and seeding of Tau condensates. *The EMBO Journal*, 41 (11):1–28, 2022. ISSN 0261-4189. doi: 10.15252/embj.2021108882.

[321] Laura Schaedel, Sarah Triclin, Denis Chrétien, Ariane Abrieu, Charlotte Aumeier, Jérémie Gaillard, Laurent Blanchoin, Manuel Théry, and Karin John. Lattice defects induce microtubule self-renewal. *Nature Physics*, 15(8):830–838, 2019. ISSN 17452481. doi: 10.1038/s41567-019-0542-4.

[322] Taylor A. Reid, Courtney Coombes, and Melissa K. Gardner. Manipulation and quantification of microtubule lattice integrity. *Biology Open*, 6(8):1245–1256, 2017. ISSN 20466390. doi: 10.1242/bio.025320.

[323] Charlotte Guyomar, Clément Bousquet, Siou Ku, John Heumann, Gabriel Guilloux, Natacha Gaillard, Claire Heichette, Laurence Duchesne, Michel O. Steinmetz, Romain Gibeaux, and Denis Chrétien. Changes in seam number and location induce holes within microtubules assembled from porcine brain tubulin and in Xenopus egg cytoplasmic extracts. *eLife*, 11:83021, 2022. doi: 10.7554/eLife.83021.

[324] S. Keller, K. Berghoff, and H. Kress. Phagosomal transport depends strongly on phagosome size. *Scientific Reports*, 7(1):1–15, 2017. ISSN 20452322. doi: 10.1038/s41598-017-17183-7.

[325] Salvatore Chiantia, Petra Schwille, Andrey S. Klymchenko, and Erwin London. Asymmetric GUVs prepared by MβCD-mediated lipid exchange: An FCS study. *Biophysical Journal*, 100(1):L1–L3, 2011. ISSN 15420086. doi: 10.1016/j.bpj.2010.11.051.

[326] Dawen Cai, Kristen J. Verhey, and Edgar Meyhöfer. Tracking single kinesin molecules in the cytoplasm of mammalian cells. *Biophysical Journal*, 92(12):4137–4144, 2007. ISSN 00063495. doi: 10.1529/biophysj.106.100206.

[327] Cecile Leduc, Otger Campàs, Konstantin B. Zeldovich, Aurelien Roux, Pascale Jolimaitre, Line Bourel-Bonnet, Bruno Goud, Jean-Francois Joanny, Patricia Bassereau, and Jaques Prost. Cooperative extraction of membrane nanotubes by molecular motors. *Proceedings of the National Academy of Sciences of the United States of America*, 101 (49):17096–17101, 2004. ISSN 0027-8424. doi: 10.1073/pnas.0406598101.

[328] Breane G. Budaitis, Shashank Jariwala, Lu Rao, Yang Yue, David Sept, Kristen J. Verhey, and Arne Gennerich. Pathogenic mutations in the kinesin-3 motor KIF1A diminish force generation and movement through allosteric mechanisms. *Journal of Cell Biology*, 220(4), 2021. ISSN 15408140. doi: 10.1083/JCB.202004227.

[329] Zachary J. Donhauser, William B. Jobs, and Edem C. Binka. Mechanics of microtubules: Effects of protofilament orientation. *Biophysical Journal*, 99(5):1668–1675, 2010. ISSN 15420086. doi: 10.1016/j.bpj.2010.06.065.

[330] Michelle Moritz, Michael B. Braunfeld, John W. Sedat, Bruce Alberts, and David A. Agard. Microtubule nucleation by gamma-tubulin rings in the centrosome. *Nature*, 378 (6557):638–640, 1995. doi: 10.1038/378638a0.

[331] George B. Pierson, Paul R. Burton, and Richard H. Himes. ALTERATIONS IN NUMBER OF PROTOFILAMENTS IN MICROTUBULES ASSEMBLED IN VITRO. *The Journal of Cell biology*, 76(1):223–228, 1978. doi: 10.1083/jcb.76.1.223.

[332] Sylvia Jeney, Ernst H. K. Stelzer, Helmut Grubmüller, and Ernst-Ludwig Florin. Mechanical Properties of Single Motor Molecules Studied by Three-Dimensional Thermal Force Probing in Optical Tweezers. *ChemPhysChem*, 5:1150–1158, 2004. doi: 10.1002/cphc.200301027.

[333] Kenji Kawaguchi and Shin'ichi Ishiwata. Nucleotide-dependent single- to double-headed binding of kinesin. *Science*, 291(5504):667–669, 2001. ISSN 00368075. doi: 10.1126/science.291.5504.667.

[334] Kyoko Chiba, Kassandra M. Ori-McKenney, Shinsuke Niwa, and Richard J. McKenney. Synergistic autoinhibition and activation mechanisms control kinesin-1 motor activity. *Cell Reports*, 39(13):111016, 2022. ISSN 22111247. doi: 10.1016/j.celrep.2022.110900.

[335] Ashwin I. D'Souza, Rahul Grover, Gina A. Monzon, Ludger Santen, and Stefan Diez. Vesicles driven by dynein and kinesin exhibit directional reversals without regulators. *Nature Communications*, 14:7532, 2023. doi: 10.1038/s41467-023-42605-8.

[336] Qingzhou Feng, Allison M. Gicking, and William O. Hancock. Dynactin p150 promotes processive motility of DDB complexes by minimizing diffusional behavior of dynein.

Molecular Biology of the Cell, 31(8):782–792, 2020. ISSN 19394586. doi: 10.1091/MBC.E19-09-0495.

[337] Tzu-chen Ma, Allison M. Gicking, Qingzhou Feng, and William O. Hancock. Simulations reveal slow detachment and fast reattachment of kinesin and dynein in antagonistic pairs. *bioRxiv*, pages 1–40, 2022.

[338] Allison M. Gicking, Tzu-chen Ma, Qingzhou Feng, Rui Jiang, Somayesadat Badieyan, Michael A. Cianfrocco, and William O. Hancock. Kinesin-1 , -2 and -3 motors use family-specific mechanochemical strategies to effectively compete with dynein during bidirectional transport. *eLife*, 11:e82228, 2022. doi: 10.7554/eLife.82228.

[339] Kristen J. Verhey and Ryoma Ohi. Causes, costs and consequences of kinesin motors communicating through the microtubule lattice. *Journal of Cell Science*, 136(5), 2023. ISSN 14779137. doi: 10.1242/jcs.260735.

[340] Sithara S. Wijeratne, Shane A. Fiorenza, Alex E. Neary, Radhika Subramanian, and Meredith D. Betterton. Motor guidance by long-range communication on the microtubule highway. *Proceedings of the National Academy of Sciences of the United States of America*, 119(28), 2022. ISSN 10916490. doi: 10.1073/pnas.2120193119.

[341] Jacob Kerssemakers, Jonathon Howard, Henry Hess, and Stefan Diez. The distance that kinesin-1 holds its cargo from the microtubule surface measured by fluorescence interference contrast microscopy. *Proceedings of the National Academy of Sciences of the United States of America*, 103(43):15812–15817, 2006. ISSN 00278424. doi: 10.1073/pnas.0510400103.

[342] Nobutaka Hirokawa, K. Kevin Pfister, Hiroshi Yorifuji, Mark C. Wagner, Scott T. Brady, and George S. Bloom. Submolecular domains of bovine brain kinesin identified by electron microscopy and monoclonal antibody decoration. *Cell*, 56(5):867–878, 1989. doi: 10.1016/0092-8674(89)90691-0.

[343] Jonathan M. Scholey, John Heuser, Joy T. Yang, and Lawrence S. B. Goldstein. Identification of globular mechanochemical heads of kinesin. *Nature*, 338(6213):355–357, 1989. ISSN 1476-4687. doi: 10.1038/338355a0.

[344] Steven P. Gross, Michael A. Welte, Steven M. Block, and Eric F. Wieschaus. Dynein-mediated cargo transport in vivo: A switch controls travel distance. *Journal of Cell Biology*, 148(5):945–955, 2000. ISSN 00219525. doi: 10.1083/jcb.148.5.945.

Acknowledgments

Just as molecular motors work in teams, so was I surrounded by a marvelous team that always stood behind me.

First of all and foremost, I would like to thank my supervisor Prof. Ludger Santen for motivating me to deeply dive into the world of modeling intracellular transport. He enormously supported me over the past years by always being there for answering my questions and improving the models with his profound knowledge.

Second, I would like to offer my special thanks to Prof. Stefan Diez for the fruitful and enjoyable collaboration during my doctoral study. I am very grateful to him for motivating and inspiring me to continue my work in the intracellular research field and the cherished time I could spend in Dresden.

A huge thank you also goes to the Santen Lab, in particular to Erik Maikranz, Neda Safaridehkohneh, and Robin Jose, and the Diez Lab, in particular to Ashwin D'Souza, Lara Scharrel, Rachele Catalano and Rahul Grover. I really appreciated the pleasant atmosphere in the offices and our lively and inspiring (online) discussions, from which I learned a lot.

For providing me with an extra kymograph of tau adsorption and for the enthusiastic scientific exchange during the Lab retreat, I thank the Lansky and Braun Lab.

Finally, I am so glad to have my family and would like to express my deep thank you especially to my father, my mother, my sister and my cousin for always having been there for me my whole life.

At this point, a special thanks to my mother for the intensive proofreading of my work.

I also would like to point out my partner Niklas, who I cannot thank enough for his positive attitude which always motivated me to continue.